SECTION 9
WCOBRA/TRAC ONE-DIMENSIONAL COMPONENT MODELS

9-1 Introduction

The one-dimensional components in WCOBRA/TRAC are modules derived from TRAC-PD2 to model the reactor primary system. These components provide models for accumulators, pressurizers, pipes, tees, pumps, steam generators, and valves. In addition, there are two modules that provide boundary conditions for parts of the system not modelled, consisting of either a pressure sink/source or a flow boundary.

The conservation equations used for the one-dimensional components are discussed in Section 2-4. The following sections will describe the features of each of the one-dimensional components and elaborate on their unique characteristics. Many of the modules are virtually unchanged from their original TRAC-PD2 versions, so many of the descriptions are the same as those given by Liles et al. (1981).

9-2 PIPE Component

Model Basis The PIPE component is used to model one-dimensional thermal-hydraulic flow in a duct or pipe. A PIPE can be used alone in a problem or can connect other components together to model a system. Area changes, wall heat sources and heat transfer across the inner and outer wall surfaces can be modelled in the PIPE component.

Figure 9-1 shows a typical noding diagram for a PIPE containing a venturi and an abrupt area change. The numbers within the PIPE indicate cell numbers, and those above it are cell boundary numbers. The geometry is specified by providing a volume and length for each cell and a flow area and hydraulic diameter at each cell boundary. The junction variables JUN1 and JUN2 provide reference numbers for connecting this PIPE to other components.

Wall friction losses and form losses associated with bends, orifices, etc. are set where required at the appropriate node boundaries. Five options are available to determine the wall friction losses based on a variety of flow configurations and correlations. These options are described in Section 4-7.

Wall heat transfer from the inner and outer surfaces of the PIPE may be calculated as well as heat generation within the wall. The calculation of critical heat flux may be determined by the Biasi et al. (1967) correlation. Section 6-3 describes the selection of heat transfer coefficients in the one-dimensional components. The wall material properties are selected from stainless steel (304, 316, and 347), carbon steel A508, or Inconel 600.

The PIPE component includes an option that allows the user to simulate the effect of a non-condensible gas on the condensation rate. This option is used to simulate the suppression of the condensation rates in the PIPE caused by nitrogen injection from the accumulator or from ingestion of air from the containment. Application of the condensation suppression factor to the interfacial heat transfer coefficients is described in Section 5-3-5.

The numerical solution method used for the PIPE component is specified by the user. The semi-implicit method is adopted due to its increased computational efficiency. In components which can expect high flow velocities, the fully implicit solution method is used to avoid the restriction set by the low Courant limit. The junctions of the one-dimensional components are always solved semi-implicitly.

Model as Coded No special models or correlations are applied in a PIPE component. The conservation equations are solved as described in Section 2, with the closure relations discussed in Sections 3 through 8, referring to one-dimensional components. The thermodynamic and material properties are described in Section 10. During the execution of a problem, the solution procedure is controlled by subroutines PIPE1, PIPE2, and PIPE3. At the beginning of each time step, PIPE1 calls subroutine SLIP to obtain relative velocities, and subroutine FWALL for wall friction and irrecoverable loss coefficients to determine the interfacial drag coefficients and calculate the relative phase velocities. Subroutine HTPIPE is then called to determine the wall heat transfer coefficients. During the timestep iteration, PIPE2 calls DF1D, which is the controlling routine for the hydrodynamics solution.

DF1D calls DF1DS or DF1DI depending on whether the semi-implicit or implicit solution scheme has been chosen. In these routines the interfacial mass and heat transfer, condensation suppression, and in the case of DF1DS, water packing logic are applied or calculated. The controlling routine PF1CHK is called if the critical flow model has been selected. After a timestep is successfully completed, PIPE3 calls CYLHT and FPROP to determine the wall temperatures and calculate the new fluid properties, respectively. The boundary arrays are again updated for the converged solution. If the time step fails to converge, the calculation is backed up to the previous time step values, and a new time step, half the size of the old one, is tried.

9-3 TEE Component

Model Basis The TEE component models the thermal-hydraulics of three piping branches, two of which lie along a common line with the third entering at some angle β from the main axis of the other two. The code basically treats a TEE component as two PIPEs, as indicated in Figure 9-2. The angle β is from the low-numbered end of PIPE 1 to PIPE 2. The low-numbered end of PIPE 2 always connects to PIPE 1. The straight PIPE segment is numbered from cell 1 to NCELL1, with the connection to PIPE 2 at cell JCELL. The branch PIPE segment is numbered from the cell immediately adjacent to JCELL, beginning with cell 1 and ending with cell NCELL2.

The connection to PIPE 1 from PIPE 2 is treated with mass, momentum, and energy source terms. For PIPE 2 the conditions in cell JCELL of PIPE 1 form the inlet boundary conditions. The mass and energy terms associated with the side branch flow are added to the governing mass and energy equations representing the main branch flow. The losses at the junction are modelled in terms of the momentum change resulting from the combining or dividing flow. For the combining case an additional momentum source term is added to the main branch momentum equations. This term represents the momentum source or sink associated with the secondary flow in relation to the main branch flow. The time differencing and iteration procedures guarantee conservation of scalar quantities within a convergence tolerance. The levels of implicitness for the finite-difference equations applied to PIPE 1 and PIPE 2 can be specified independently using the input variables IHYD1 and IHYD2. Since the junction between PIPE 1 and PIPE 2 is always treated semi-implicitly, the velocity at that point is always included in the computation of the time step stability limit. Phase separation at the junction is calculated if the flag ISEP is set to one. Phase separation is computed if the void fraction in the junction cell JCELL exceeds the user-specified value ALSEP.

Model as Coded Since the TEE is modelled as two connected PIPEs, the PIPE model description in Section 9-2 should be consulted for additional information. The calculational sequence for a TEE includes separate calculations of the primary and secondary sides. For the junction momentum source, an additional source term is calculated in subroutine ETEE and is incorporated in the momentum equation in DF1DS or DF1DI depending on the solution option chosen. This source term is set to zero when the TEE is a dividing tee.

9-4 PUMP Component

Model Basis The pump model employed in WCOBRA/TRAC describes the interaction of the system fluid with a centrifugal pump. The model calculates the pressure differential across the pump and its angular velocity as a function of the fluid flowrate and the fluid properties. The model is designed to treat any centrifugal pump and can include two-phase effects.

The pump model is represented by a one-dimensional component with N cells, where N must be greater than 1. A typical noding diagram for the pump component is shown in Figure 9-3. The pump momentum is modelled as a source Ω that is included between cells 1 and 2. The source is positive for normal operation with the pressure rise occurring from cell 1 to cell 2, so it is necessary to number the cells so that the cell number increases in the normal flow direction.

The pump model is identical to the one-dimensional pipe model except that a momentum source is included in the mixture momentum equation written between cells 1 and 2:

$$\frac{U_{1.5} - U_{1.5}^n}{\Delta t} = \frac{(P_1 - P_2)}{\rho_{1.5}^n \Delta x} - C^n - g_z - \frac{f U_{1.5}^n |U_{1.5}^n|}{D_h} + \Omega \tag{9-1}$$

where U is the mixture velocity, P is the pressure, C represents the convective terms, g_z is the gravity term, f is the friction factor, ρ is the fluid density, Δx is the cell length, D_h is the hydraulic diameter, the subscript 1.5 refers to the average value between cell 1 and cell 2, and the superscript n indicates that the parameter was evaluated at the previous timestep. Parameters without a superscript are the updated, new time values. The source term Ω is taken to be:

$$\Omega = \frac{\Delta P_{pump}}{\rho_{1.5}^n \Delta X} + C^n + g_z + \frac{f}{D_h} U_{1.5}^n |U_{1.5}^n| \tag{9-2}$$

where ΔP_{pump} is the pressure rise across the pump evaluated from the pump characteristic curves. With this definition of the momentum source, the steady-state solution of Equation 9-1 is $P_2 - P_1 = \Delta P_{pump}$. The model for ΔP_{pump} is described next.

The Pump Characteristic Curves - The Homologous Curves

It has been well known that for single-phase flow the characteristics of a pump can be quite accurately obtained from those of a geometrically similar scale-model using the similarity laws. Following these laws, the head and the torque of the pump can be represented in nondimensional forms which are independent of the scale of the pump model. The approach used to establish the so-called homologous curves is one of the methods that has utilized the similarity laws to nondimensionalize the variables involved in pump operations. In this approach, four homologous curve segments (one curve segment represents a family of curves) are established. These curves describe in a compact manner all the operating states of the pump. The following definitions are employed in the subsequent development:

H	=	pump head = $\Delta P_{pump}/\rho$
ρ	=	fluid density at pump inlet
Q	=	volumetric flow rate through pump
ω	=	pump impeller angular speed
T	=	pump hydraulic torque

To allow one set of curves to be used for a variety of pumps, the following normalized quantities are used:

$$\upsilon = Q/Q_R$$
$$\alpha_N = \omega/\omega_R$$
$$h = H/H_R$$
$$\beta = (T/T_R)/(\rho_R/\rho)$$

where the subscript R denotes the rated conditions. Use of the pump similarity relations (Olson, 1974a) shows that

$$\frac{h}{\alpha_N^2} = f\left(\frac{\upsilon}{\alpha_N}\right) \tag{9-3}$$

and

$$\frac{\beta}{\alpha_N^2} = f\left(\frac{\upsilon}{\alpha_N}\right) \tag{9-4}$$

for

$$\left| \frac{\upsilon}{\alpha_N} \right| \le 1 ,$$

and

$$\frac{h}{\upsilon^2} = f\left(\frac{\alpha_N}{\upsilon}\right) \tag{9-5}$$

and

$$\frac{\beta}{\upsilon^2} = f\left(\frac{\alpha_N}{\upsilon}\right) \tag{9-6}$$

for

$$\left| \frac{\alpha_N}{\upsilon} \right| \le 1$$

Table 9-1 shows the resulting four segments of the homologous head and torque curves that represent the complete pump operational characteristics.

Pump Single-Phase Head and Torque Homologous Curves

Figures 9-4 and 9-6 show typical single-phase homologous head and torque characteristic curves for Westinghouse designed pumps.

Pump Fully-Degraded Head and Torque Homologous Curves

A basic assumption of the WCOBRA/TRAC pump model is that the same type of scaling laws, which are applied under single-phase conditions, can also be applied under two-phase conditions. It is assumed that there exists a condition at an intermediate range of void fractions in which the pump head and torque can be described by a set of homologous curves, similar to the single-phase curves. A typical set of curves is illustrated in Figures 9-5 and 9-7.

The Head and Torque Multipliers

To provide for a transition from single- to two-phase conditions, the following correlations are used:

$$H_* = H_1 - M(\alpha)\ (H_1 - H_2) \tag{9-7}$$[1]

and

$$T_* = T_1 - N(\alpha)\ (T_1 - T_2) \tag{9-8}$$[1]

where

M = head multiplier

N = torque multiplier

α = donor-cell vapor void fraction at pump inlet and the subscript 1 denotes the single-phase value, the subscript 2 denotes the two-phase value, both calculated from the homologous curves, and the subscript $_*$ denotes the derived value for a given two-phase condition.

Pump Impeller Speed

The angular speed of the pump impeller is calculated from the equation

$$I \frac{d\omega}{dt} = T_M - (T_* + T_{FR} + T_E) \tag{9-9}$$

where

I = moment of inertia of the pump rotor assembly

T_M = torque supplied by motor (after trip, T_M = 0.0)

T_{FR} = total friction torque (including all mechanical, bearing friction and windage loss)

T_E = electric torque (caused by induced voltage after trip)

The total friction torque is (Bordelon et al., 1974) [

]^{a,c} (9-10)

where

[

]^{a,c}

for the 93A pump, and is assumed to apply to other pumps of similar design. The pump hydraulic torque (T_*) is evaluated from the homologous curves and Equation 9-8 as a function of the fluid density and flow rate as well as pump angular velocity.

Pump Options and Limitations

The wall heat transfer, wall friction, CHF calculation and implicit hydrodynamics options for the PUMP module are the same as for the PIPE module. In addition, the following options are specified: pump type, motor action, reverse speed option, two-phase option, and pump curve option.

If the pump motor is energized, its angular velocity is assumed to be the constant value specified. If the motor is not energized, a pump coastdown calculation is performed using the specified initial pump speed.

There are two pump options available. For pump option 1 (IPMPTY = 1) the pump speed variation is specified by input. The pump is initially energized at a constant speed specified by input (OMEGA). The pump motor may be tripped by a TRIP signal. If a pump trip has occurred, the pump speed is taken from a table of pump speed versus time-after-trip (array SPTBL).

Pump option 2 (IPMPTY = 2) is similar to option 1 except that the pump speed is calculated from Equation 9-9 after a trip has occurred rather than from an input table. The electric torque T_E is assumed to be zero. The relationships between the various pump input parameters as well as the algorithm for the pump speed calculation are shown in Table 9-2. The value entered for IPMPTR is the TRIP identification number for pump trip initiation and NPMPTX is the number of pairs of points in the pump speed table (SPTBL). If IPMPTR = 0, the pump will maintain a constant speed.

If the reverse speed option is specified (IRP = 1), the pump can rotate in both the forward and reverse directions. If reverse speed is not allowed (IRP = 0), the pump will rotate in the forward direction only. For this case, if a negative speed is calculated (after trip with option 2), the speed will be set to zero.

If the two-phase option is turned on (IPM = 1), the degraded pump head and torque will be calculated from Equations 9-7 and 9-8. If the two-phase option is turned off (IPM = 0), only the single-phase head and torque homologous curves will be used.

The user may either specify pump homologous curves in the input or use the built-in pump curves. The built-in pump curves are for the MOD-1 Semiscale system pump and are based on the data of Olson (1974a, b) and Loomis (1974). For other types of PWR pumps their corresponding homologous curves and multiplier values would be specified. Since these homologous curves are dimensionless, they can be used to describe a variety of pumps by specifying as input the rated values for density, head, torque, flow, and angular velocity.

There are several restrictions and limitations in the current version of the pump component. Since there is no pump motor torque-versus-speed model, the pump speed is assumed at the input value if the motor is energized. The pump momentum source must be located between cells 1 and 2 of the pump model. Finally, the head degradation multiplier $M(\alpha)$ and the torque degradation multiplier $N(\alpha)$ are assumed to apply to all operating states of the pump.

The PUMP module input consists of the same geometric and hydrodynamic data and initial conditions that are required for the PIPE module. In addition, information specific to the PUMP is required. The speed table (SPTBL) as well as the homologous pump curve arrays must be input.

<u>Model as Coded</u> For the new timestep, Equation 9-9 is evaluated explicitly:

$$\omega = \omega^n + \left(\frac{d\omega}{dt}\right)^n \Delta t \tag{9-11}$$

The momentum source for a pump cell is evaluated once each timestep, and the source is applied only during the explicit pass in subroutine DF1DI or subroutine DF1DS. The mixture velocity and mixture density from the donor component (i.e., conditions at the upstream boundary of the pump component) are used to establish the volumetric flowrate through the pump. Standard curve fitting techniques are then used to compute the pump head. The pump source evaluation is performed by subroutine PUMPSR.

Scaling Considerations During blowdown and reflood periods, reactor coolant pumps will be under two-phase flow conditions, and both the pump head and the pump torque will be degraded. Although the physical mechanisms responsible for the performance degradation in two-phase flows are not well understood, analysis of tests on pumps (Kamath and Swift, 1982) revealed that "scaling down the size of the pump while maintaining the same design specific speed produces very similar performance characteristics both in single and two-phase flows." The study also indicated that effects due to size and operating speed were not discernible within the range of test conditions and within experimental uncertainties. The system pressure, however, appeared to affect the rate of degradation even for the same pump. Similar results were also observed in the scaled-pump experimental tests conducted by KWU (Kostner and Seeburger, 1983). These test results suggest that uncertainties due to scaling distortion from the pump are small compared to other contributors. The effect of scaling and other uncertainties is minimized in the WCOBRA/TRAC model by using data from a 1/3-scale model similar in design to the Westinghouse pump (Snyder and Grigsby, 1982).

Conclusions The pump model is constructed by combining the experimentally-established pump characteristic correlations and the WCOBRA/TRAC PIPE module based on a one-dimensional drift-flux formulation. The frictional torque correlation was also experimentally established. The pump model can handle all single- and two-phase operations (with or without phase separation) and provide accurate speed, flow, and head predictions during the transient (including coastdown). The options of the model provide the users with the flexibility to model a variety of system operating conditions. The WCOBRA/TRAC pump model has been assessed against LOFT L2-5 test data (Bayless et al., 1982) with satisfactory results. The model can be utilized to simulate any PWR pump for which the homologous characteristic curves have been adequately established.

9-5 Steam Generator Component (STGEN)

Model Basis In a PWR, the steam generators transfer energy from the primary coolant loop to the secondary coolant to produce steam. The STGEN module can model either "U-tube" or "once-through" steam generators; the basic operation is similar for both types. Primary coolant enters an inlet plenum, flows through a tube bank in which the primary coolant exchanges heat with a secondary coolant that flows over the exterior of the tube bank, and finally discharges into an outlet plenum. Figure 9-8 provides typical noding diagrams for U-tube and once-through steam generators. In both cases the tube bank is represented by a single effective tube that has heat transfer characteristics of the entire tube bank.

Model as Coded The number of fluid mesh cells is specified by NCELL1 on the primary side and by NCELL2 on the secondary side. There are some constraints imposed on the possible values for (NCELL1, NCELL2) combinations. For a once-through type, it is required that NCELL2=NCELL1-2. For a U-tube type, it is assumed that there is a one-to-one correspondence between two active primary cells and one active secondary cell (Figure 9-8). Thus for the fluid cells on the secondary side to reach the U-tube bundle top, it is required that NCELL2 ≥ (NCELL1-2)/2. The secondary-side cells that are greater than (NCELL1-2)/2 are treated adiabatically and are used to model possible area changes and volumes above the tube bank. In Figure 9-8, these are cells 6 through 8 on the secondary side. There is an inlet plenum (cell 1) and outlet plenum (last cell) on the primary side; these two cells are assumed adiabatic.

The steam generator, primary-side, and secondary-side hydrodynamics are treated separately. Coupling between the two sides is achieved through wall heat transfer, which is modelled in a semi-implicit fashion. The calculational sequence for a steam generator is identical to that for a PIPE (component) except that it is performed twice, once for the primary side and once for the secondary side. It is possible to connect the secondary-side junctions to any TRAC component, but the most common arrangement is to connect the inlet to a FILL, specifying the secondary-side fluid inlet conditions and flow rate, and to a BREAK at the discharge, specifying the steam-generator secondary discharge pressure.

The cylindrical heat conduction equation for a typical tube is solved as described in Section 7-7. There must be at least one wall temperature node, but three are suggested, placing one at each tube surface and one at the tube wall center. The tube material is selected from the material options given in Section 10-5. Wall friction correlations and additional frictional losses for the primary and secondary sides can be specified as described in Section 4-7. Either fully implicit or semi-implicit hydrodynamics may be selected for the steam generator component.

9-6 Pressurizer Component (PRIZER)

Model Basis The pressurizer in a PWR is used to control the primary coolant system operating pressure and accommodate any change in the coolant volume during normal operation. It consists of a pressure vessel connected to one of the hot legs by a surge line. Approximately half of the vessel is filled with water, which is pressurized by saturated steam above it. The pressure is maintained at the operating setpoint value by a system of heaters and sprays which regulate the energy input to the water.

Model as Coded The pressurizer is simulated by the PRIZER component. It can connect only to another one-dimensional component, and its nodes are numbered, 1 to NCELL, from the top (closed end) to the junction at the bottom as shown in Figure 9-9. The PRIZER component is treated in most respects as a PIPE; however, the drift velocities are not obtained from the slip routine, but are specified in subroutine PRIZR1, which imposes a sharp liquid/vapor interface during the pressurizer discharge. This is done by setting the relative velocity to a large value, [

]^{a,c} (9-12)[(2)]

The negative sign is included to be consistent with the sign conventions used in the code.

The controlling action of the heater/spray can be simulated in the PRIZER component. The heater/spray model is available as an input option and is used as a system pressure controller. If this option is used, the setpoint pressure and the pressure deviation DPMAX at which the heaters deliver their maximum power QHEAT are input. The calculated heater power is directly proportional to the difference between PSET and P(1), the pressure in node 1.

$$Q_{pressurizer} = QHEAT(PSET - P(1))/DPMAX$$

This power ($Q_{pressurizer}$) is limited to $+/-\ QHEAT$ and is distributed to each node as a function of the node liquid fraction to total pressurizer liquid fraction. Power is not added if the collapsed liquid level falls below the input height ZHTR. The collapsed liquid level within the PRIZER component is given by the following equation:

$$z = V_\ell / A \qquad (9\text{-}13)$$

where

$$V_\ell = \sum_{i=1}^{NCELLS} (1 - \alpha_i)\ V_i \qquad (9\text{-}14)$$

and V_i and V_ℓ are the volume of the node i and the total volume of liquid in the pressurizer, respectively. A is the maximum flow area of nodes 1 and 2.

9-7 VALVE Component

Model Basis The VALVE component is used to simulate the controlling action of a valve fitting. It comprises at least two fluid nodes. The flow area and hydraulic diameter at a given node boundary are used as the controlling parameters to model the valve operation. In all other respects, the VALVE component is identical to the PIPE component.

Model as Coded The noding scheme is shown in Figure 9-10. Node IVPS defines the node boundary where the valve action is modelled. Five options are provided to describe the valve operation (Table 9-3). Options 1 through 4 open or close the valve with a trip. The action can be instantaneous or a function of time. Option 5 models a check valve with the open or closed condition determined by a pressure differential between the specified nodes (IVPS and IVPS-1) and a set point. For this option the valve opening and closing is damped to prevent pressure oscillations.

9-8 Accumulator Component (ACCUM)

An accumulator is a pressure vessel partially filled with water and pressurized with nitrogen gas. The accumulator is isolated from the primary coolant system (RCS) by a check valve. If reactor coolant pressure falls below accumulator pressure, the check valve opens and the accumulator water is forced into the RCS. This flow continues until the accumulator is empty, after which the nitrogen cover gas is discharged.

During a LOCA transient, the accumulators of a PWR will deliver ECC water to the cold legs. The accumulator injection period may be divided into two time intervals:

Phase A: $t_{ACC} \le t \le t_o$

Phase B: $t_o \le t \le t_*$

where t_{ACC} is the time when the accumulator starts to deliver ECC water, t_o is the time when the accumulator is empty of water, t_* is the time when the pressure in the accumulator is in equilibrium with that of the *RCS*, and no more flow issues from the accumulator. *Although the core recovers during a small break LOCA event prior to the time at which the accumulator empties, Phase B is discussed for completeness.*

During phase A, only water enters the *RCS*. The nitrogen in the accumulator continues to expand in volume as the pressure in the accumulator decreases. The nitrogen cools as it expands. During this phase, accumulator water begins to fill the reactor vessel downcomer and core. Meanwhile, the reactor pressure falls to near the containment pressure. During phase B a water/nitrogen mixture, and finally only the-nitrogen gas, enters the *RCS*. Because of the width of the tank, the water-nitrogen interface is likely to be well-defined. Consequently, the time during which a water-nitrogen mixture flows from the tank is expected to be small.

As the nitrogen flows into the vessel, the upper portion of the downcomer may be pressurized due to the presence of the nitrogen flow. This increase in pressure may affect the cooling flow entering or leaving the core. The way in which these phenomena are simulated in WCOBRA/TRAC is described below.

Accumulator Model Basis (Phase A) The accumulator component is simulated in the ACCUM module in WCOBRA/TRAC. This component can only be connected at one junction to other WCOBRA/TRAC components. This connection is the highest number cell, and it is assumed that cell 1 is closed, as shown in the typical noding diagram in Figure 9-11. It is also assumed that the accumulator is not connected to a nitrogen pressure source. Therefore, the nitrogen pressure results from the expansion of the initial gas volume.

The following additional assumptions are made for the ACCUM component during Phase A:

1. The vapor phase in the accumulator is an ideal gas with the properties of nitrogen.

2. The relative velocity between the vapor and liquid is set to a large value to create a sharp interface between the liquid and vapor. This assumption is made because the relatively large diameter of the tank leads to low fluid velocities and rapid phase separation.

3. The mixture properties at the last accumulator cell are controlled such that only pure liquid is discharged. This assumption is also a result of the expected sharp interface between liquid and vapor.

4. The wall friction factor for each accumulator tank cell is set to a constant value of 0.005. The accumulator is expected to represent a negligible portion of the overall resistance to flow.

5. The accumulator tank walls are assumed to be adiabatic. Heat transfer from the accumulator walls is not expected to be significant, due to the small surface area per unit volume.

Nitrogen Discharge Model Basis (Phase B) During the accumulator water injection period, a nitrogen gas field is assumed to exist in the accumulator, while steam is assumed everywhere else in WCOBRA/TRAC. While the nitrogen field can be extended (as an input option) to all other WCOBRA/TRAC components, a combined nitrogen-steam-water model is not available. To simulate the nitrogen discharge, the subcooled vapor model in WCOBRA/TRAC is used to provide similar pressure/flow characteristics to those obtained from a nitrogen model. In this model, the normal hydrodynamics package is used. However, the following additional assumptions are made:

1. Phase B is assumed to begin when the water level in the accumulator tank falls below [ ]^{a,c} (the basis for this value is described in Section 16-2-5). At this point, a mixture of water and nitrogen is assumed to flow out of the tank.

2. During Phase B, heat transfer between liquid and vapor is suppressed in regions of the RCS expected to contain significant amounts of nitrogen. This is assumed to occur as long as the accumulator pressure remains significantly above the RCS pressure (implying significant flow of nitrogen).

   The region over which the condensation suppression is assumed to occur is shown in Figure 9-12 and consists of the accumulator and line, the intact cold leg, the upper downcomer region, and the broken cold leg on the vessel side. The nitrogen influence is assumed to be limited to this region as discussed below.

   At the time nitrogen begins to inject, the lower plenum and downcomer are full of water, and the core has begun to reflood. Any steam generated in the core will flow up the core and out through the loops and upper head vent paths. In addition, the high downcomer water level provides a driving force for this flow. It is therefore unlikely that accumulator nitrogen flow will cause reverse flow in the loop or upper head. If it does, this flow would have to be sustained for a substantial period of time before the nitrogen will reach the upper plenum.

In the reactor vessel, the accumulator water isolates the nitrogen from the core. The region of influence is assumed to extend to a point in the downcomer level with the bottom of the core. If the downcomer is full above this level, no steam will be available for condensation and the condensation suppression will make no difference.

3. During Phase B, the behavior of the nitrogen can be simulated using the subcooled vapor models in the code.

   This assumption was checked by comparing two simple models of the accumulator, one in which the entire process takes place with nitrogen, and one where the nitrogen model is replaced during Phase B with a model using the one-dimensional component subcooled vapor equations.[3] In the nitrogen model, the pressure/temperature/density relationships are for a perfect gas.

   The simple models were used to predict pressure and flow, using a linear ramp for the pressure at the accumulator exit and representative accumulator dimensions.

<u>Accumulator and Nitrogen Model as Coded</u> The procedures for data input, initialization of arrays, advancement of time-dependent variables, and editing are similar to those given for a PIPE component. The hydrodynamics are treated using the one-dimensional, semi-implicit drift-flux routine DF1DS.

No metal heat transfer is permitted for the accumulator. In addition, the following special coding is employed for each of the phases. During Phase A:

1. Nitrogen properties are calculated in subroutine THERMO. The gas constant used is 287.12 $Pa\ m^3/kg\ °K$ ($53.4\ ft\ lb_f/lb_m\ °R$), which is consistent with standard values found in handbooks.

2. The liquid vapor interface is sharply defined by setting the relative velocity to a large value. This is set in ACCUM1 and is [

]^{a,c} (9-15)

The negative sign is included to be consistent with the sign conventions used in the code.

3. The discharge at accumulator exit during Phase A is limited to liquid only by setting the component boundary array elements representing the void fraction to zero. This is done in subroutine ACCUMBD.

4. Accumulator wall friction is set to 0.005 in ACCUM1. User specified friction factors, input via the parameter FRIC, may be added to this value.

The end of Phase A is determined by the collapsed liquid level. The collapsed liquid level is calculated in subroutine ACCMIX by computing the total liquid volume in the accumulator tank and then determining the height of this volume at the bottom of the tank. This collapsed level is used to signal that the accumulator is nearly empty. The signal is set when the collapsed level falls below [ ]^{a,c}. The time when this occurs is t_o, and the code moves to Phase B.

For Phase B (simulated nitrogen injection), additional special coding is required as described below.

1. In the accumulator, [

]^{a,c} as described in Section 5-3.

2. The steam properties for [

]^{a,c}.

3. Discharge from the accumulator becomes two-phase.

Scaling Considerations The model was tested in simulations of the accumulator in the *integral* test facility *simultaneous*, and against data obtained from in-plant tests. A description of *the in-plant* test simulation as it applies to the accumulator model is given in *Section 22 of* this report.

Conclusions The basic assumptions which are made in the application of this model to the PWR and which introduce uncertainty into the calculation are:

1. The condensation is assumed to be suppressed in the intact cold legs, upper downcomer, and broken nozzle until all nitrogen has been exhausted from the accumulator and swept from the systems.

2. The nitrogen vapor properties are approximated by subcooled vapor flow.

These uncertainties *are not relevant to a small break LOCA scenario, and do not need to be considered in the uncertainty methodology.*

9-9 BREAK and FILL Components

These models differ from other components in that they do not model any system component per se, and no hydrodynamic or heat transfer calculations are performed for them. In all other respects, they are treated as any other component, with the same input, initialization, and identification procedures.

A BREAK component is used to impose a pressure boundary condition adjacent to the one-dimensional component with which it connects (Figure 9-13). The boundary conditions specified by the BREAK are pressure, mixture temperature and node void fraction, all of which may be time dependent. Care is required when setting the mixture temperature and void fraction values, as these are used to determine the properties of the fluid if the flow is calculated to be in the reverse direction, i.e., into the system from the BREAK. In the normal mode of operation, where the fluid flows out through the BREAK, the mixture temperature and void fraction do not affect the calculation.

The FILL component is used to impose a velocity boundary condition at the junction between the FILL and the adjoining one-dimensional component (Figure 9-14). The boundary velocity may be specified by one of the five different input options. The options define the velocity as a constant, or as a function of time or pressure, or as a constant until a trip signal is reached, then again as a function of time or pressure. The fluid properties within the FILL node are determined from the user input values of void fraction, mixture temperature, and pressure.

9-10 References

Bayless, P. D., et al., 1982, "Experimental Data Report for LOFT Large-Break Loss-of-Coolant Experiment L2-5," NUREG/CR-2826, EGG-2210.

Biasi, L., et al., 1967, "Studies on Burnout, Part 3: A New Correlation for Round Ducts and Uniform Heating and Its Comparison with World Data," Energia Nucleare, Vol. 14, pp. 530-536.

Bordelon, F. M., et al., 1974, "SATAN VI Program: Comprehensive Space-Time Dependent Analysis of Loss-of-Coolant," WCAP-8302.

Kamath, P. S. and Swift, W. J., 1982, "Two-Phase Performance of Scale Models of a Primary Coolant Pump," EPRI NP-2578, Final Report.

Kostner, W. and Seeburger, G. J., 1983, "Pump Behaviour and Its Impact on a Loss of Coolant Accident in a Pressurized Water Reactor," Nuclear Technology, Vol. 60.

Liles, D. R., et al., 1981, "TRAC-PD2, An Advanced Best Estimate Computer Program for Pressurized Water Reactor Loss-of-Coolant Accident Analysis," NUREG/CR-2054.

Loomis, G. G., 1974, "Intact Loop Pump Performance During the Semiscale MOD-1 Isothermal Test Series," Aerojet Nuclear Company, Report-1240.

Olson, D. J., 1974a, "Single- and Two-Phase Performance Characteristics of the MOD-1 Semiscale Pump Under Steady-State and Transient Fluid Conditions," Aerojet Nuclear Company, Report ANCR-1165.

Olson, D. J., 1974b, "Experimental Data Report for Single- and Two-phase Steady-State Test of the 1 Loop MOD-1 Semiscale System Pump," Aerojet Nuclear Company, Report ANCR-1150.

Snyder, P. H., and Grigsby, J. M., 1982, "EVA Project on Two-Phase Reactor Coolant Pump Performance - Data Analysis and Model," Vol. 1-3, WCAP-10109.

9-11 RAI Listing

1. RAI1-233
2. RAI1-234
3. RAIS-21

Table 9-1

The Four Segments of Pump Homologous Curves

Curve Segment	Homologous Head	Homologous Torque	Variable Range	Operating Condition
1	h/α_N^2	β/α_N^2	$\lvert v/\alpha_N \rvert \leq 1$	$\omega > 0$
2	h/v^2	β/v^2	$\lvert v/\alpha_N \rvert > 1$	$Q > 0$
3	h/v^2	β/v^2	$\lvert v/\alpha_N \rvert > 1$	$Q < 0$

Note: A fourth segment may also be input for negative pump roation ($\omega < 0$). This condition will not occur in Westinghouse PWR's due to locking devices on the pumps.

Table 9-2
Pump Control Input Parameter

IPMPTY Pump Option	IMPPTR Pump Trip I.D.	NPMPTX (SPTBL) Pair of Points	Pump Speed Speed Table	Algorithm
1	x = pump trip desired	x	x	OMEGA before trip
	0 = no pump trip	0		SPTBL after trip
2	x = pump trip desired	x		OMEGA before trip
	0 = no pump trip	0		Code calculated after trip

Table 9-3

Valve Control Options

1. Valve is normally open and is closed instantly on a trip signal.
   Controlling logic is as follows:

   Before trip,

   $A_{(valve)}$ = AVLVE
   $D_{h(valve)}$ = HVLVE

   After trip,

   $A_{(valve)}$ = 0.0
   VM = 1.E-10
   VR = 0.0

   where,

   AVLVE equals completely open valve area
   HVLVE equals completely open valve hydraulic diameter
   VM equals mixture velocity of phases
   VR equals relative velocity of phases

2. Valve is normally closed and is opened instantly on a trip signal.
   Controlling logic is as follows:

   Before trip,

   $A_{(valve)}$ = 0.0
   VM = 1.E-10
   VR = 0.0

   After trip,

   $A_{(valve)}$ = AVLVE
   $D_{h(valve)}$ = HVLVE

3. Valve is normally open and is closed on a trip signal according to a time-dependent valve table.
   Controlling logic is as follows:

   Before trip,

   $A_{(valve)}$ = AVLVE
   $D_{h(valve)}$ = HVLVE

   After trip,

   $A_{(valve)}$ = AVLVE * SCALE
   $D_{h(valve)}$ = HVLVE * SCALE

   where SCALE equals the linear interpolated multiplier from the user input forcing factor versus time table. If SCALE equals 0.0,

   VM = 1.E-10
   VR = 0.0

Table 9-3 (Cont'd)
Valve Control Options

4. Valve is normally closed and is opened on a trip signal according to a time-dependent valve table.
   Controlling logic is as follows:
   Before trip,
   $A_{(valve)}$ = 0.0
   VM = 1.E-10
   VR = 0.0
   After trip,
   $A_{(valve)}$ = AVLVE * SCALE
   $D_{h(valve)}$ = HVLVE * SCALE
   where,
   SCALE has the same definition as given above.

5. Check valve is controlled by a static pressure gradient. If IVPG = 1, then DP = P(IVPS - 1) - P(IVPS); if IVPG = 2 then DP = P(IVPS) - P(IVPS-1)

   If DP+PVS $\geq$ 0, the valve opens.
   If DP+PVS < 0, the valve closes.

   For this option the valve opening and closing action is damped according to the following equations.
   Opening,
   $A_{(valve)} = A_{(valve)} * 0.99 + 0.01 * AVLVE$
   $D_{h(valve)} = D_{h(valve)} * 0.99 + 1.0E-5$

   The above equations are applied at each timestep until the opening or closing action has been completed.

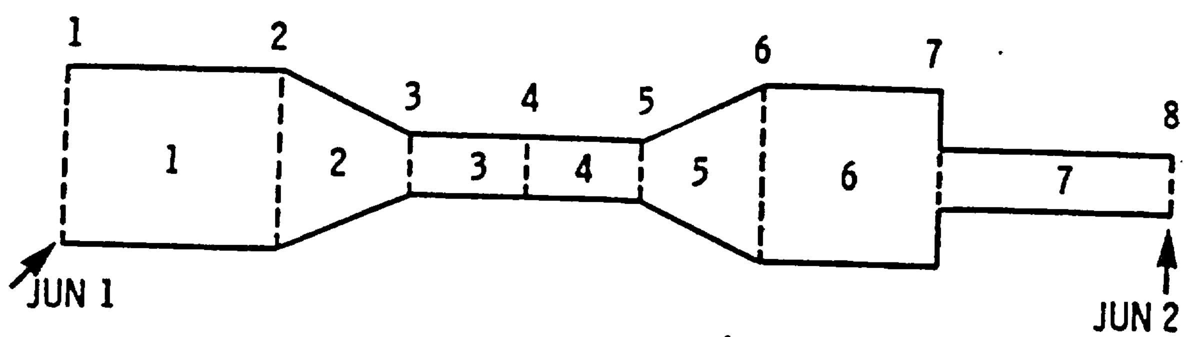

Figure 9-1. PIPE Component Noding

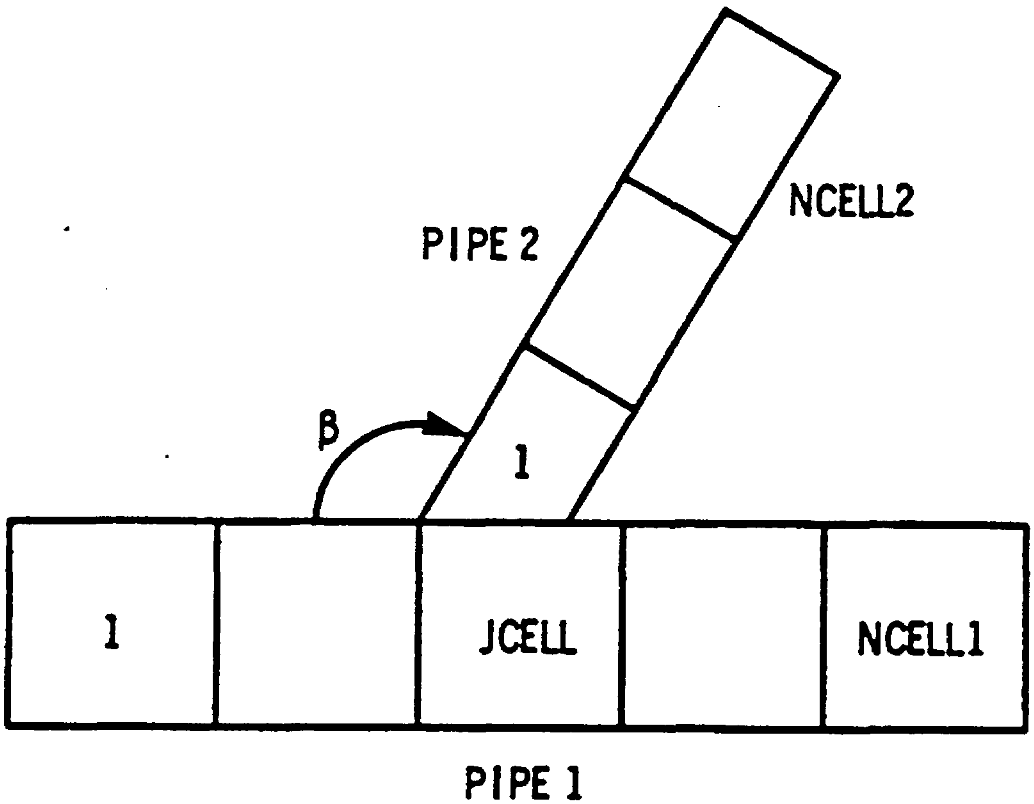

Figure 9-2. TEE Component Noding

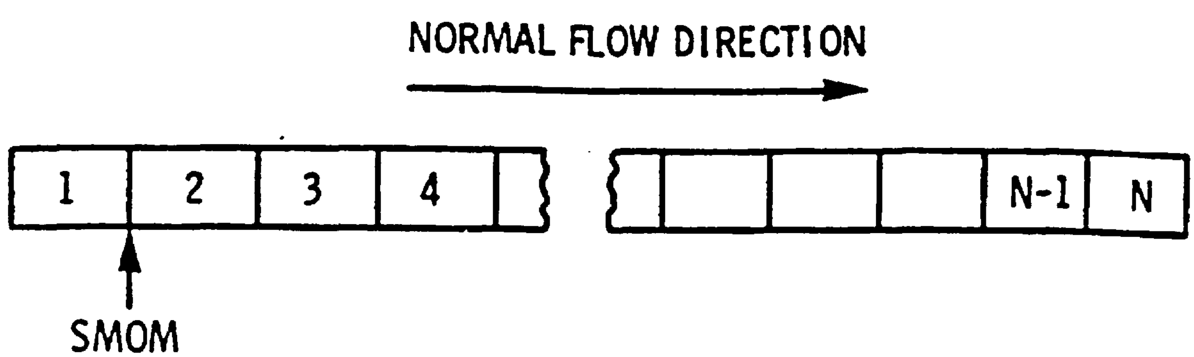

Figure 9-3. PUMP Noding Diagram

a,c

Figure 9-4. 93A Pump Single-Phase Homologous Head Curves

a,c

Figure 9-5. 93A Pump Two-Phase Homologous Head Curves

a,c

Figure 9-6. 93A Pump Single-Phase Homologous Torque Curves

a,c

Figure 9-7. 93A Pump Two-Phase Homologous Torque Curves

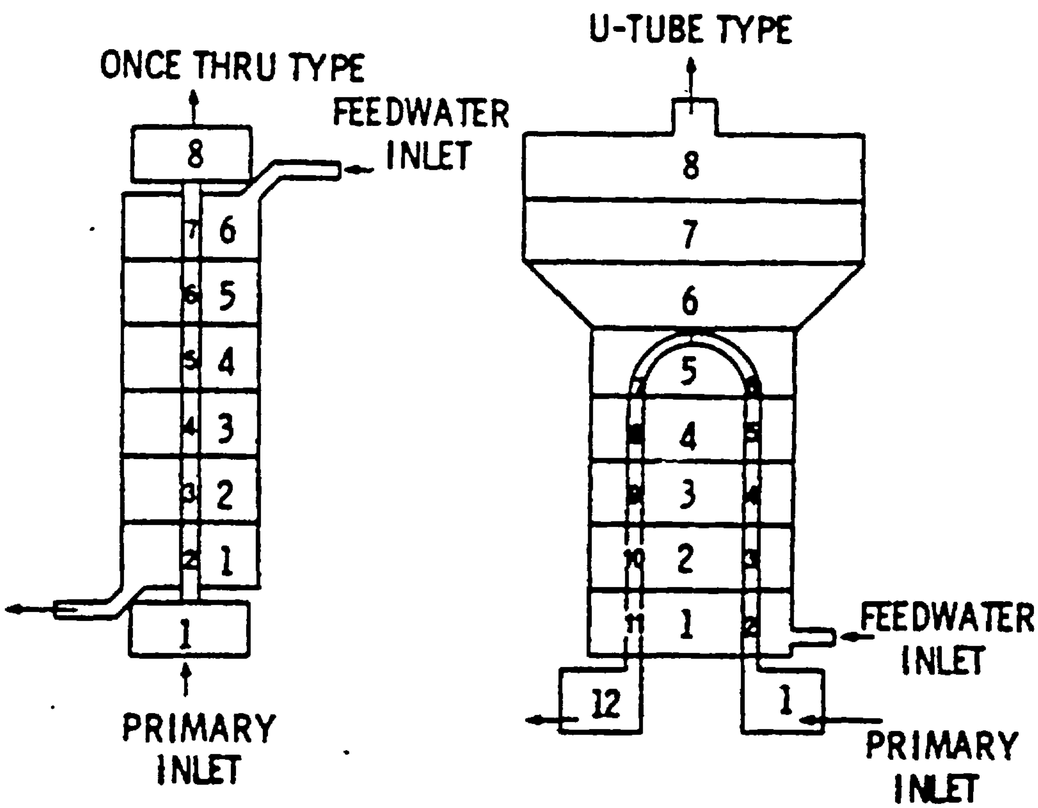

Figure 9-8. Steam Generator Noding Diagram

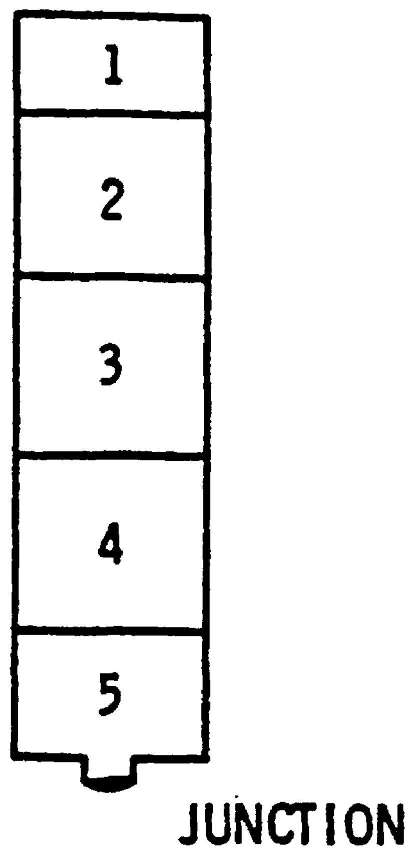

Figure 9-9. Pressurizer (PRIZER) Component Noding

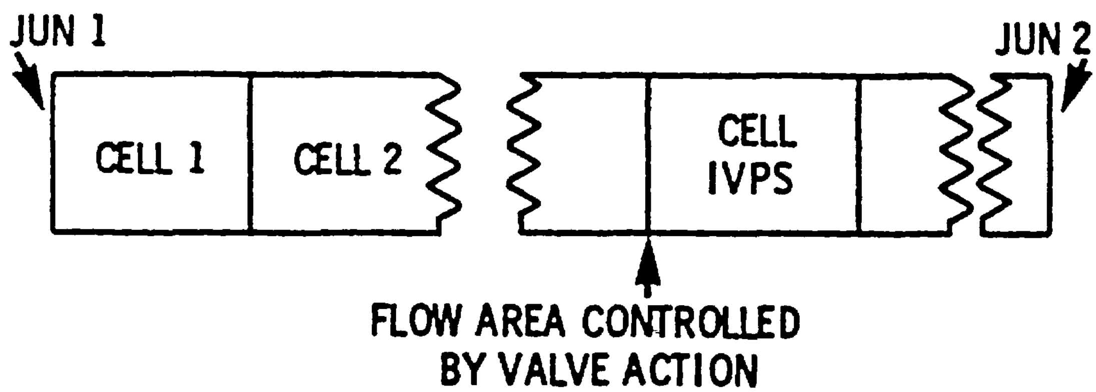

Figure 9-10. VALVE Component Noding

a,c

Figure 9-11. Accumulator Noding Diagram

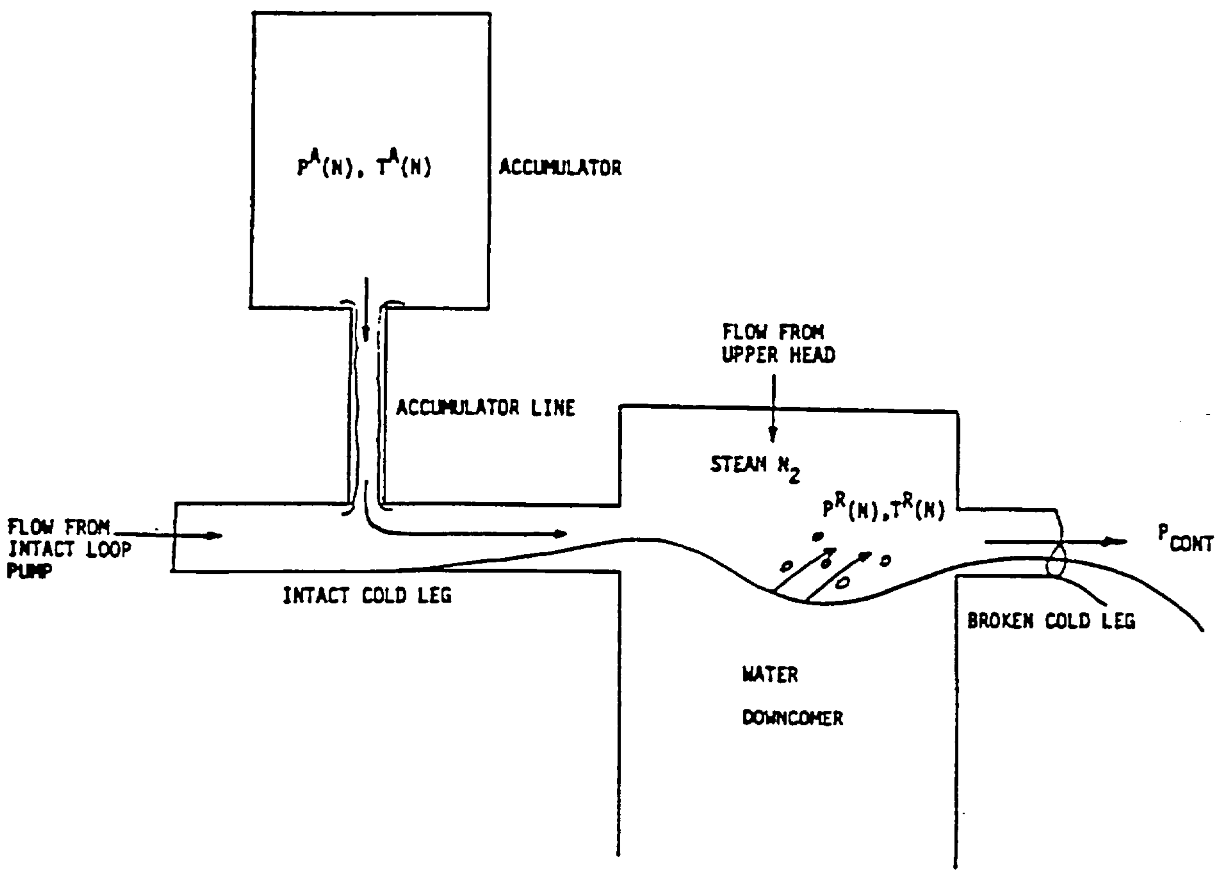

Figure 9-12. Condensation Suppression Region for Accumulator/Nitrogen Model

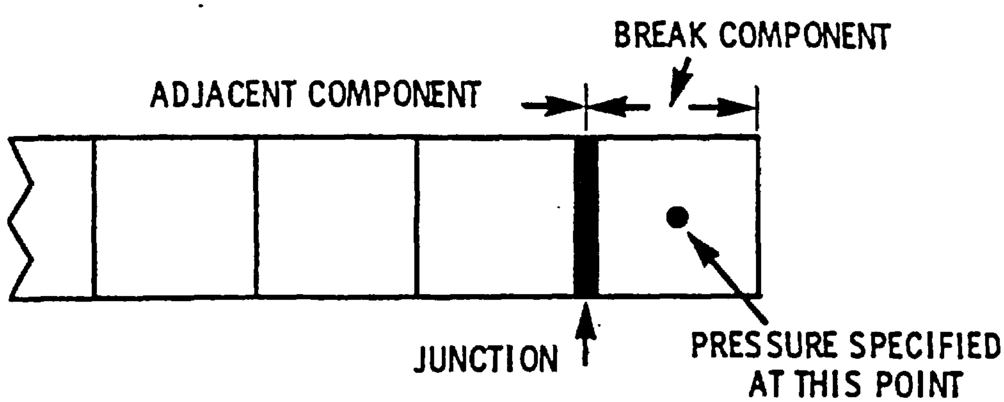

Figure 9-13. Pressure Boundary Condition Using BREAK Component

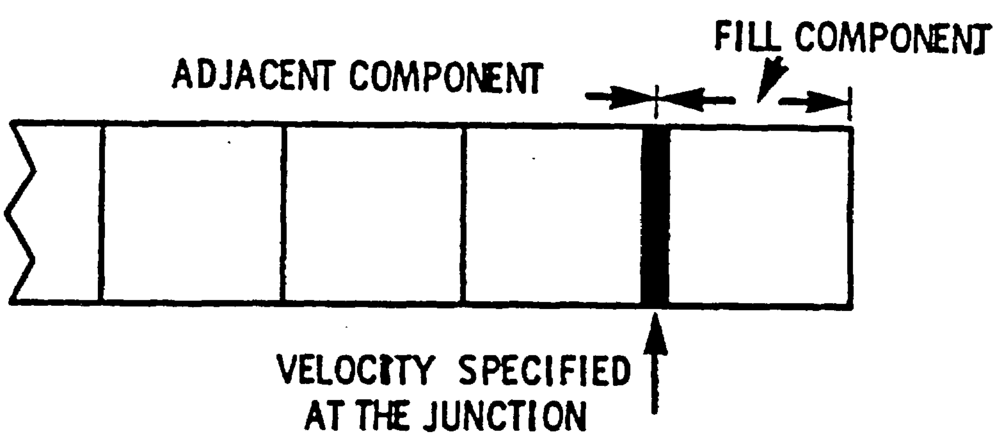

Figure 9-14. Velocity Boundary Condition Using FILL Component

SECTION 10
THERMOPHYSICAL PROPERTIES

10-1 Introduction

WCOBRA/TRAC includes a set of functional routines and individual correlations to calculate the thermal properties of water, air, nuclear rods and several common structural materials. This section describes the manner in which the thermal properties are calculated for the vessel and one-dimensional components. Section 10-2 describes calculation of the thermodynamic properties of water. Section 10-3 describes the WCOBRA/TRAC calculation of air thermal properties. Section 10-4 describes the thermal properties of materials used in nuclear fuel rods including mixed oxide fuel, clad materials, and fuel rod gap gases. WCOBRA/TRAC can also calculate the thermal properties of several common PWR structural materials such as stainless steel. These calculations are described in Section 10-5.

10-2 Thermophysical Properties of Water

10-2-1 Vessel Component Water Properties

The thermal-hydraulic calculations performed by the WCOBRA/TRAC vessel component frequently require the thermal conductivity, specific heat, viscosity, Prandtl number, and surface tension for water as functions of the fluid pressure and specific enthalpy. This section describes the thermodynamic property calculations performed by WCOBRA/TRAC for saturated, superheated, and subcooled fluid conditions.

10-2-1-1 Saturated Fluid Properties

Model Basis The saturated liquid and saturated vapor enthalpies are calculated as functions of the pressure. Values for the saturation temperature, densities of saturated liquid and vapor, thermal conductivities and viscosities of saturated liquid and vapor, saturated liquid specific heat, and the surface tension are interpolated from tables indexed by saturated liquid enthalpy. The saturated liquid and saturated vapor specific enthalpies are determined from polynomial representations of the saturation curve. This representation provides close agreement with ASME Steam Tables (1968) and the NBS/NRC Steam Tables (Haar, Gallagher, and Kell, 1984).

The tables of values at saturation for the other properties (conductivities, viscosities, etc.) are also in close agreement with the standard tables.

The saturation enthalpies are calculated in Btu/lbm as functions of pressure based on expressions developed for EPRI (McFadden et al., 1980).

The polynomial expansions for saturated liquid enthalpy are

$$H_f(P) = \sum_{n=1}^{9} A_n \, [\ln(P)]^{n-1} \tag{10-1}$$

if P < 2529.9 psia and

$$H_f(P) = \sum_{n=1}^{9} A_n \left[(3208.2 - P)^{0.41}\right]^{n-1} \tag{10-2}$$

for 2529.9 ≤ P < 3208.0 psia.

The constants A_n for Equations 10-1 and 10-2 are shown in Table 10-1.

The saturated vapor enthalpy is calculated using

$$H_g(P) = \sum_{n=1}^{5} B_n [\ln(P)]^{n-1} + \sum_{n=6}^{8} B_n [\ln(P)]^{n+3} \tag{10-3}$$

if 0.1 ≤ P < 1467.6 psia, by

$$H_g(P) = \sum_{n=1}^{9} B_n [\ln(P)]^{n-1} \tag{10-4}$$

if $1467.6 \leq P < 2586.0$ psia and by

$$H_g(P) = \sum_{n=1}^{9} B_n\left[(3208.2 - P)^{0.41}\right]^{n-1} \tag{10-5}$$

if $2586.0 \leq P < 3208.0$ psia.

The constants B_n for Equations 10-3 through 10-5 are listed in Table 10-2.

These expressions are compared to values from the ASME Steam Tables (1968, 1983) in Figures 10-1 and 10-2.

Table 10-3 lists values of the saturation temperature, density, viscosity, thermal conductivity, specific heat, and surface tension that are used to represent the saturation curve for those properties. The saturation curves defined by these tables are compared to values from the standard tables in Figures 10-3 through 10-11.

Model as Coded For a known pressure P the saturated liquid enthalpy is calculated using either Equation 10-1 or 10-2 in subroutine SAT. From that calculated value of saturated liquid enthalpy, the other properties are determined in subroutine PROP by linearly interpolating between the 90 values listed in Table 10-3.

Scale Considerations Calculation of saturated water thermophysical properties is not dependent on scale.

Conclusions The WCOBRA/TRAC vessel component calculates saturated liquid and saturated vapor enthalpies as functions of pressure using polynomial representations, and then uses the saturated liquid enthalpy to determine the other thermal properties by linear interpolation. All of the saturated properties agree very closely with values found in the standardized Steam Tables.

10-2-1-2 Properties of Superheated Vapor

Model Basis

Vapor Enthalpy The enthalpy of superheated vapor as a function of pressure and temperature is calculated by the expression developed by Keenan and Keys (1936):

$$H_v = 0.43 \left[0.10129 \left(F_0 P + \frac{F_1}{2} P^2 + \frac{F_3}{4} P^4 + \frac{F_{12}}{13} P^{13} \right) + F^1 \right] \tag{10-6}$$

where, F_0, F_1, F_3, and F_{12} are defined by

$$F_k = \frac{\partial}{\partial \tau} (B_k \tau),\ k = 0,1,3,12 \tag{10-7}$$

The coefficients B_k are defined as:

$$\tau = 1/T \tag{10-8}$$

$$B_0 = 1.89 - 2641.62\ \tau\ 10^{80870\tau^2} \tag{10-9}$$

$$B_1 = B_0^2(82.546\ \tau^2 - 1.6246(10)^5\tau^3) \tag{10-10}$$

$$B_3 = B_0^4\ (0.21828\ \tau^3 - 1.2697(10)^5\tau^5) \tag{10-11}$$

$$B_{12} = -B_0^{13}\ (3.635(10)^{-4}\ \tau^{12} - 6.768(10)^{64}\tau^{36}) \tag{10-12}$$

and F^1 is given by

$$F^1 = 2502.36 + \int_{273.16}^{T} (1.472 + 0.00075566T + \frac{47.8365}{T})dT \tag{10-13}$$

In Equations 10-6 through 10-13, T is in °K, P is in atmospheres, and H_v is in J/g.

Vapor Temperature Values for superheated vapor temperature as a function of pressure and enthalpy are calculated using an iterative method described by McClintock and Silvestri (1936). Estimates for T and C_p are computed from the expressions

$$\begin{aligned} T = {} & A_1 + A_2H_v + A_3H_v^2 + A_4H_v^3 + A_5P + A_6P^2 \\ & + A_7P^3 + P(A_8H_v + A_9H_v^2 + A_{10}H_v^3) \end{aligned} \tag{10-14}$$

$$\begin{aligned} 1/C_p = {} & B_1 + B_2H + B_3H^2 + B_4H^3 + B_5\ln P + B_6(\ln P)^2 \\ & + B_7(\ln P)^3 + (\ln P)(B_8H + B_9H^2 + B_{10}H^3) \end{aligned} \tag{10-15}$$

where T is in °F, P is in psia, H_v is in Btu/lbm, and C_p is in Btu/lbm-°F. The constants A_n and B_n depend on the range of pressure and enthalpy as shown in Table 10-4.

The estimated temperature is then used to approximate the enthalpy as

$$H_v^1(P,T) = f(P,T) \tag{10-16}$$

where the function $f(P,T)$ is described by Equations 10-6 through 10-13. A temperature correction is calculated as

$$\Delta T = \frac{1}{C_p} (H_v - H_v^1) \tag{10-17}$$

and a new estimated temperature is defined as

$$T^1 = T + \Delta T \tag{10-18}$$

A new enthalpy is calculated and the iteration is continued until

$$|\Delta T| < 1.0°F$$

$$or\ |H_v - H_v^1| < 0.5\ Btu/lbm$$

<u>Vapor Density</u> The vapor specific volume is calculated as a function of pressure and enthalpy using equations from Keenan and Keys (1936):

$$\upsilon_v = \frac{1}{P_v} = E_1 + E_2 P + \frac{E_3}{P} + E_4 H_v + E_5 P H_v + E_6 \frac{H_v}{P} \tag{10-19}$$

where P is in psia, H_v is in Btu/lbm, and υ is in ft^3/lbm. The constants for these equations are

E_1 = -0.81735849E-03
E_2 = 0.12378514E-04
E_3 = -0.10339904E+04
E_4 = -0.62941689E-05
E_5 = -0.872921608E-08
E_6 = 0.12460225E+01

<u>Vapor Thermal Conductivity</u> The thermal conductivity for superheated vapor is calculated as a function of temperature and density using equations given in the ASME Steam Tables (1968). The expression for thermal conductivity is:

$$k_v = k_1 + (103.51 + 0.4198\ T - 2.771(10)^{-5}T^2)\rho_v + 2.1482(10)^{14}\frac{\rho_v^2}{T^{4.2}} \tag{10-20}$$

where:

$$k_1 = 17.6 + 5.87(10)^{-2}T + 1.04(10)^{-4}T^2 - 4.51(10)^{-8}T^3 \tag{10-21}$$

In Equations 10-20 and 10-21, T is in °C, ρ_v is in g/cm³, and k_v is in mW/m-°K.

<u>Vapor Viscosity</u> The viscosity for superheated vapor is calculated as a function of temperature and density using equations given in the ASME Steam Tables (1968).

The viscosity is given by

$$\mu_v = \begin{cases} \mu_1 - \rho(1858 - 5.9T)\ , \ if\ T < 340°C \\ \mu_1 + 353\rho + 676.5\rho^2 + 102.1\rho^3\ , \ if\ T > 365°C \end{cases} \tag{10-22}$$

$$\mu_1 = 0.407T + 80.4 \tag{10-23}$$

For values of T between 340°C and 365°C the viscosity is interpolated between the values given by the two expressions in Equation 10-22. In Equations 10-22 and 10-23 temperature is in °C, density is in g/cm³, and viscosity is in micropoise.

Values of superheated vapor enthalpy, temperature, density, thermal conductivity, and viscosity defined by the foregoing expressions are compared with the ASME tables (1968, 1983) and the National Bureau of Standards/National Research Council tables (Haar, Gallagher, and Kell, 1984) in Figures 10-12 through 10-16.

<u>Model as Coded</u> The properties for superheated vapor represented by Equations 10-6 through 10-23 are coded as described above without modification in subroutines HGAS, TGAS, VOLVAP, and TRANSP. Properties are not calculated if $P < 0.1$ psia or if $P > 3208.0$ psia, in which cases an error message is printed and execution is terminated.

In the calculation of vapor temperature as a function of pressure and enthalpy, Equations 10-14 through 10-18 describe an iterative method. A maximum of 10 iterations are permitted.

Scaling Considerations The equations and methods used to calculate the properties for superheated vapor are independent of scale.

Conclusions

The WCOBRA/TRAC vessel component calculates superheated vapor enthalpy as a function of temperature and pressure, density as a function of pressure and enthalpy, and thermal conductivity as a function of temperature and density, using generalized polynomials. Temperature as a function of pressure and enthalpy is found iteratively using the enthalpy function. All of these properties agree closely with values found in standard steam tables.

10-2-1-3 Subcooled Liquid Properties

Model Basis Subcooled liquid specific volume is calculated using the equation

$$v_\ell = \exp\left[\sum_{i=1}^{5}\left(\sum_{j=1}^{3} C_{CXij}\, P^{j-1}\right) H_\ell^{i-1}\right] \tag{10-24}$$

where H_ℓ is in Btu/lbm, P is in psia, and the values of the coefficients C_{CXij} are given in Table 10-5.

The liquid temperature at enthalpy (H_ℓ) is assumed to be equal to the saturation temperature at H_ℓ. The properties C_p, k, and μ for subcooled liquid at temperature T are assumed to be equal to the saturated liquid properties at T. These properties are only weakly dependent on pressure in the low to moderate pressure range.

The liquid Prandtl number is calculated as

$$Pr_\ell = \frac{\mu_f C_{pf}}{k_f} \tag{10-25}$$

Model as Coded The equation for subcooled liquid specific volume is programmed as shown in subroutine VOLLIQ. Other subcooled liquid properties are determined by linear interpolation of the saturation properties listed in Table 10-3. The liquid enthalpy is used as the index to determine the appropriate location in the table in which to perform the interpolation.

Scaling Considerations The method in which subcooled liquid properties are determined is scale independent.

Conclusions Subcooled liquid properties are estimated to be equal to the properties of saturated liquid corresponding to the liquid temperature. Since these properties are only weakly dependent on pressure, only a negligible error is introduced into the calculation.

10-2-2 One-Dimensional Component Water Properties

The thermodynamic and transport properties used in the WCOBRA/TRAC one-dimensional (1D) components are based on polynomial fits to steam table data for water, and on ideal gas behavior for air. The fits for transport properties were obtained from Coffman and Lynn (1966).

10-2-2-1 Saturated Fluid Properties

Model Basis

Saturation Temperature and Pressure Saturation temperature as a function of pressure, and saturation pressure as a function of temperature, are calculated using expressions recommended by Rivard and Torrey (1975). These are

$$P_{sat} = 10^5\left(\frac{T_{sat} - 255.2}{117.8}\right)^{\frac{1}{0.223}} \qquad (10\text{-}26)$$

and

$$T_{sat} = 117.8\left(10^{-5}P_{sat}\right)^{0.223} + 255.2 \qquad (10\text{-}27)$$

The derivative of saturation temperature with respect to pressure is given by

$$\frac{dT_{sat}}{dP_{sat}} = \frac{0.223\left(T_{sat} - 255.2\right)}{P_{sat}} \tag{10-28}$$

Saturated Vapor Internal Energy and Enthalpy Two main pressure regions are used in the calculation of water vapor internal energy and enthalpy. The low pressure range is $P < 2.0 \times 106$ Pa and the high pressure range is 2.0×10^6 Pa $\leq P$, where P is the pressure and T_{sat} is its corresponding saturation temperature.

Low Pressure Region: The internal energy of saturated vapor and its derivative with respect to pressure are

$$e_g = AVE(1) + BVE(1)T_1 \tag{10-29}$$

$$\frac{de_g}{dP} = -BVE(1)\ T_1^2 \tag{10-30}$$

where:

$$T_1 = 1/(P + 3.403E5) \tag{10-31}$$

High Pressure Region:

$$e_g = AVE(2) + BVE(2)\ P + CVE(2)\ P^2 \tag{10-32}$$

$$\frac{de_g}{dP} = BVE(2) + 2\ CVE(2)\ P \tag{10-33}$$

The values of the constants $AVE(i)$, $BVE(i)$, and $CVE(i)$ are listed in Table 10-6.

All pressures: The ratio of specific heats, saturated vapor enthalpy, and derivatives with respect to pressure are calculated from:

$$\gamma_g = AVG(i) + BVG(i)\ P + CVG(i)\ P^2 \tag{10-34}$$

$$\frac{d\gamma_g}{dP} = BVG(i) + 2\ CVG(i)\ P \tag{10-35}$$

$$H_g = \gamma_g\ e_g \tag{10-36}$$

$$\frac{dH_g}{dP} = \gamma_g \frac{de_g}{dP} \tag{10-37}$$

The values of the constants $AVG(i)$, $BVG(i)$, and $CVG(i)$ are listed in Table 10-7.

<u>Saturated Liquid Internal Energy and Enthalpy</u> A series of polynomials in T_{sat} is used to calculate the internal energy of saturated liquid and its derivative with respect to saturation temperature. These are given by:

$$e_f = ALE(i) + BLE(i)\ T_{sat} + CLE(i)\ T_{sat}^2 + DLE(i)\ T_{sat}^3 + ELE(i)\ T_{sat}^4 \tag{10-38}$$

and

$$\frac{de_f}{dT_{sat}} = BLE(i) + 2\ CLE(i)\ T_{sat} + 3\ DLE(i)\ T_{sat}^2 + 4\ ELE(i)\ T_{sat}^3 \tag{10-39}$$

where:

i = 1 for $T_{sat} < 548.15\ K,$

i = 2 for $548.15 \leq T_{sat} < 611.15\ K,$

i = 3 for $611.15 \leq T_{sat}$

Table 10-8 lists the constants *ALE(i), BLE(i), CLE(i), DLE(i), and ELE(i)* for the given temperature ranges.

Saturated liquid enthalpy is calculated using the definition

$$H_f = e_f + \frac{P}{\rho_f} \tag{10-40}$$

and its derivative by

$$\frac{dH_f}{dP} = \frac{de_f}{dT_{sat}}\frac{dT_{sat}}{dP} + \frac{1}{\rho_f} - \frac{P}{\rho_f^2}\left[\left(\frac{\partial\rho_\ell}{\partial P}\right)_{T_{sat}} + \left(\frac{\partial\rho_\ell}{\partial T_{sat}}\right)_P \frac{\partial T_{sat}}{dP}\right] \tag{10-41}$$

where e_f and its derivative are evaluated as shown earlier, and where $\rho_f = \rho_\ell(P, T_{sat})$ and its derivatives are evaluated using the equations in Section 10-2-2-4 with T_ℓ equal to T_{sat}.

<u>Saturated Vapor Specific Heat Capacity</u> The heat capacity of saturated steam at constant pressure is also calculated using a polynomial representation in T_{sat}. The saturated vapor specific heat and its derivative are given by

$$C_{pg} = ACP\ \Theta_r^{-2} + BCP\ \Theta_r^{-1} + CCP + DCP\ \Theta_r + ECP\ \Theta_r^2 \tag{10-42}$$

$$\frac{dC_{pg}}{dP} = \left[2ACP\ \Theta_r^{-3} + BCP\ \Theta_r^{-2} - DCP\ -2ECP\ \Theta_r\right] T_{cr}\frac{dT_{sat}}{dP} \tag{10-43}$$

where:

$$\Theta_r = 1 - T_{sat} / T_{crit}$$

$$T_{crit} = 647.3 \; K$$

and

$ACP = 8.349824$
$BCP = 349.519444$
$CCP = 2996.018036$
$DCP = -8448.077393$
$ECP = 9700.016602$

Model as Coded Subroutine THERMO supplies thermodynamic properties for WCOBRA/TRAC one-dimensional components. The input variables are the pressure and the liquid- and vapor-phase temperatures. The output variables include the saturation temperature, saturated liquid, and saturated vapor enthalpies corresponding to the pressure, and their derivatives with respect to pressure. These variables also include the internal energies and densities of the liquid and vapor phases, and their partial derivatives with respect to pressure (at constant temperature) and with respect to temperature (at constant pressure).

THERMO supplies thermodynamic properties valid for temperatures and pressures within the following ranges:

$$280 \; K \le T_\ell \le 697 \; K$$

and

$$1000 \; Pa \le P \le 19.0 \times 10^6 \; Pa.$$

If THERMO is provided with a temperature outside this range, the calculation stops. Given a pressure outside this range, it adjusts the data to the corresponding limit and issues a warning message.

Subroutine RHOLIQ calculates liquid densities and density derivatives used in THERMO.

Saturation pressure, and phasic densities and enthalpies as calculated are compared with NBS/NRC tables (Haar, Gallagher, and Kell, 1984) in Figures 10-17 through 10-21.

Scaling Considerations Not applicable.

Conclusions The saturation conditions for the WCOBRA/TRAC one-dimensional components are calculated using polynomial expressions that provide a close approximation to the Steam Table values. The error introduced by the WCOBRA/TRAC routines is small and is not considered a major contributor to the overall code calculational uncertainty.

10-2-2-2 Properties of Superheated Vapor

Model Basis Specific Heat at Constant Pressure The constant pressure specific heat of steam at temperature T_v is approximated as

$$C_{pv} = \left(\frac{\partial h_v}{\partial T_v}\right)_P = \frac{C_{pv,ideal}}{2}\left[1 + \frac{T_v}{\left(T_v^2 - \beta\right)^{1/2}}\right], \tag{10-44}$$

where:

$$\beta = T_{sat}^2\left[1 - \frac{1}{\left(\frac{2\,C_{pg}}{C_{pv,\,ideal}} - 1\right)^2}\right] \tag{10-45}$$

The term C_{pg} is calculated as defined in Equation 10-42 and $C_{pv,\,ideal}$ is defined by ideal gas behavior, such that

$$C_{pv,ideal} = \frac{R_v\,\gamma_{ideal}}{\gamma_{ideal} - 1} \tag{10-46}$$

where R_v is the gas constant for steam (461.7 J/kg-K) and $\gamma_{ideal} = 1.3$ is the ratio of ideal specific heats for steam.

Internal Energy The internal energy is obtained by integrating the expression for C_{pv} along a line of constant pressure P. Integrating Equation 10-44 gives

$$h_v = h_g + \frac{C_{pv,ideal}}{2}\left[(T_v - T_{sat}) + (T_v^2 - \beta)^{1/2} - \frac{T_{sat}}{\left(\dfrac{2C_{pg}}{C_{pv,ideal}} - 1\right)}\right] \tag{10-47}$$

The internal energy of vapor is therefore

$$e_v = e_g + \frac{C_{pv,ideal}}{2}\left[\left(T_v - T_{sat}\right) + \left(T_v^2 - \beta\right)^{1/2} - \frac{T_{sat}}{\left(\dfrac{2C_{pg}}{C_{pv,ideal}} - 1\right)}\right] - P\left(\frac{1}{\rho_v} - \frac{1}{\rho_g}\right)$$

(10-48)

The definitions of enthalpy and internal energy allow the density of the water vapor to be written such that

$$\rho_v = \frac{P}{h_v - e_v} = \frac{P}{\left[\ h_g + C_{pv,ideal}\left(T_v - T_{sat}\right)\right] - \left[\ e_g + C_{vv,ideal}\left(T_v - T_{sat}\right)\right]}$$

$$= \frac{P}{\left(h_g - e_g\right) + \left(\gamma_{ideal} - 1\right)\left(e_v - e_g\right)} \tag{10-49}$$

Substitution of ρ_v and ρ_g, as defined by the preceding equation, into the equation for the internal energy of the vapor, gives

$$e_v = e_g + \frac{C_{vv,ideal}}{2}\left[\left(T_v - T_{sat}\right) + \left(T_v^2 - \beta\right)^{1/2} - \frac{T_{sat}}{\left(2\frac{C_{pg}}{C_{pv,ideal}} - 1\right)}\right] \tag{10-50}$$

where $C_{vv,ideal}$ is the constant volume specific heat for steam as defined by ideal gas behavior given by

$$C_{vv,ideal} = \frac{R_v}{\gamma_{ideal} - 1} \tag{10-51}$$

The partial derivatives are given by

$$\left(\frac{\partial e_v}{\partial T_v}\right)_P = \frac{C_{vv,ideal}}{\left(1 - \frac{\beta}{\kappa^2}\right)} \tag{10-52}$$

$$\left(\frac{\partial e_v}{\partial P}\right)_{T_v} = -\frac{1}{2}\left(\frac{\partial e_v}{\partial T_g}\right)_P\left[\left(1 - \frac{\beta}{\kappa^2}\right)\kappa_P' + \frac{1}{\kappa}\frac{d\beta}{dP}\right] \tag{10-53}$$

where:

$$\kappa = \frac{2}{C_{vv,ideal}}\left(e_v - e_g\right) + T_{sat}\left[1 + \frac{1}{\frac{2C_{pg}}{C_{pv,ideal}} - 1}\right] \tag{10-54}$$

and

$$\kappa_P' = \left(\frac{\partial \kappa}{\partial P}\right)_{T_v} = -\frac{2}{C_{vv,ideal}}\frac{de_g}{dP} + \left[1 + \frac{1}{\left(\frac{2C_{pg}}{C_{pv,ideal}} - 1\right)}\right]\frac{dT_{sat}}{dP} \tag{10-55}$$

$$-\frac{2}{C_{pv,ideal}}\left[\frac{T_{sat}}{\left(\frac{2C_{pg}}{C_{pv,ideal}} - 1\right)^2}\right]\frac{dC_{pg}}{dP}$$

and

$$\frac{d\beta}{dP} = \frac{2}{T_{sat}}\left\{\beta\frac{dT_{sat}}{dP} + \frac{2}{C_{pv,ideal}}\left[\frac{T_{sat}}{\left(\frac{2C_{pg}}{C_{pv,ideal}} - 1\right)}\right]^3\frac{dC_{pg}}{dP}\right\} \tag{10-56}$$

<u>Superheated Vapor Density</u> The vapor density is calculated as

$$\rho_v = \frac{P}{(\gamma_g - 1)\, e_g + (\gamma_{ideal} - 1)(e_v - e_g)} \tag{10-57}$$

Therefore, the partial derivatives are calculated by

$$\left(\frac{\partial \rho_v}{\partial T_v}\right)_P = -\left(\frac{\partial e_v}{\partial T_v}\right)_P\left[\frac{(\gamma_{ideal} - 1)\,\rho_v}{(\gamma_g - 1)\, e_g + (\gamma_{ideal} - 1)(e_v - e_g)}\right] \tag{10-58}$$

and

$$\left(\frac{\partial \rho_v}{\partial P}\right)_{T_v} = \left\{1 - \rho_v \left[e_g \frac{d\gamma_g}{dP} + (\gamma_g - \gamma_{ideal}) \frac{de_g}{dP}\right] \cdot \left[\frac{1}{(\gamma_g - 1)e_g + (\gamma_{ideal} - 1)(e_v - e_g)}\right]\right\} + \left(\frac{\partial \rho_v}{\partial e_v}\right)_P \left(\frac{\partial e_v}{\partial P}\right)_{T_v} \tag{10-59}$$

where:

$$\left(\frac{\partial \rho_v}{\partial e_v}\right)_P = -\frac{(\gamma_{ideal}-1)\rho_v}{(\gamma_g-1)e_g+(\gamma_{ideal}-1)(e_v-e_g)} \tag{10-60}$$

Enthalpy The enthalpy of superheated vapor is calculated using the definition of enthalpy,

$$h_v = e_v+\frac{P}{\rho_v} \tag{10-61}$$

where e_v is calculated from Equation 10-50, and ρ_v is calculated using Equation 10-57.

Model as Coded Thermodynamic properties for superheated water vapor are calculated in subroutine THERMO as described in this section. For superheated vapor, however, minimum and maximum limits are placed on the calculated values of the density and its partial derivatives. In low pressure regions where the above equations may predict a negative density, and near the critical point, it is necessary to impose the following limits on the density ratio

$$0 < \frac{\rho_v}{\rho_\ell} \leq 0.9 \tag{10-62}$$

to avoid singularities when calculating certain parameters. If the calculated value of ρ_v is outside these bounds, the vapor density and its derivatives are superseded by

$$\rho_v = 0.9\rho_\ell \tag{10-63}$$

$$\left(\frac{\partial \rho_v}{\partial T_v}\right)_P = 0.9\left(\frac{\partial \rho_\ell}{\partial T_\ell}\right)_P \tag{10-64}$$

$$\left(\frac{\partial \rho_v}{\partial P}\right)_{T_v} = 0.9\left(\frac{\partial \rho_\ell}{\partial P}\right)_{T_\ell} \tag{10-65}$$

<u>Scaling Considerations</u> Not applicable.

<u>Conclusions</u> The thermodynamic properties for superheated vapor in <u>W</u>COBRA/TRAC one-dimensional components are calculated from thermodynamic first principles. The calculated values are in good agreement with those found in the Steam Tables. The error introduced by the <u>W</u>COBRA/TRAC routines is small and thus is not considered a major contributor to the overall code calculational uncertainty.

10-2-2-3 Subcooled Vapor Properties

<u>Model Basis</u> <u>W</u>COBRA/TRAC calculates internal energy, density, and enthalpy in one-dimensional components in the following manner when the vapor is subcooled.

<u>Internal Energy</u> The internal energy and its derivatives for subcooled vapor are calculated as

$$e_v = e_g + (T_v - T_{sat})\frac{C_{pg}}{\gamma_{ideal}} \tag{10-66}$$

$$\left(\frac{\partial e_v}{\partial T_v}\right)_P = \frac{C_{pg}}{\gamma_{ideal}} \tag{10-67}$$

$$\left(\frac{\partial e_v}{\partial P}\right)_{T_v} = \frac{de_g}{dP} + \left(\frac{e_v - e_g}{C_{pg}}\right)\frac{dC_{pg}}{dP} - \left(\frac{\partial e_v}{\partial T_v}\right)_P \frac{dT_{sat}}{dP} \tag{10-68}$$

where T_{sat} is the saturation temperature corresponding to the vapor pressure (P_v).

The subcooled vapor density is calculated using Equation 10-57. If this value falls outside of the range

$$0 < \rho_v < 0.9\rho_\ell$$

then the internal energy and its derivatives are recalculated and used in subsequent density recalculations. A new value of constant-pressure specific heat for vapor at the saturation condition is estimated:

$$C_{pg} = 958.75\ (1 - \frac{T_{sat}}{T_{crit}})^{-0.8566} \tag{10-69}$$

and its derivative is

$$\frac{dC_{pg}}{dP} = (958.75)\ (0.8566)\left(1 - \frac{T_{sat}}{T_{crit}}\right)^{-1.8566} \frac{1}{T_{crit}}\frac{dT_{sat}}{dP} \tag{10-70}$$

Vapor internal energy and its derivatives are

$$e_v = e_g + (T_v - T_{sat})\, C_{pg} / \gamma_{ideal} \tag{10-71}$$

$$\left(\frac{\partial e_v}{\partial T_v}\right)_P = C_{pg} \,/\, \gamma_{ideal} \tag{10-72}$$

$$\left(\frac{\partial e_v}{\partial P}\right)_{T_v} = \frac{de_g}{dP} + \frac{(e_v - e_g)}{C_{pg}} \frac{dC_{pg}}{dP} - \left(\frac{\partial e_v}{\partial T_v}\right)_P \frac{dT_{sat}}{dP} \tag{10-73}$$

<u>Density</u> Subcooled vapor density and its derivatives are determined using the same method of calculation as in the case of superheated vapor, as described in Section 10-2-2-2.

If the subcooled vapor density calculated with Equation 10-57 falls outside the range

$$0 < \rho_v < 0.9\, \rho_\ell$$

then the vapor internal energy is recalculated using Equations 10-69 through 10-73 and the density and its derivatives are recalculated:

$$\rho_v = P \,/\, ((\gamma_g - 1)\, e_v) \tag{10-74}$$

$$\left(\frac{\partial \rho_v}{\partial T_v}\right)_P = \frac{-\rho_\upsilon}{e_v} \left(\frac{\partial e_v}{\partial T_v}\right)_P \tag{10-75}$$

$$\left(\frac{\partial \rho_v}{\partial P}\right)_{T_v} = \frac{\rho_v}{P}\left[1 - \frac{P}{(\gamma_g - 1)}\frac{d\gamma_g}{dP} - \frac{P}{e_v}\left(\frac{\partial e_v}{\partial P}\right)_{T_v}\right] \tag{10-76}$$

Enthalpy The enthalpy of subcooled vapor is calculated using the definition of enthalpy,

$$h_v = e_v + \frac{P}{\rho_v} \tag{10-77}$$

where e_v is calculated from Equation 10-66 or 10-71, and ρ_v is calculated using Equation 10-57 or 10-74.

Model as Coded The thermodynamic properties for subcooled vapor are calculated directly as described in this section, in subroutine THERMO. The enthalpy is calculated in subroutine FPROP.

Scaling Considerations Not applicable.

Conclusions The thermodynamic properties for subcooled vapor in WCOBRA/TRAC one-dimensional components are calculated in a manner consistent with calculations for superheated vapor, which are derived from thermodynamic first principles. Subcooled vapor occurs only infrequently during a LOCA transient. As such, the error introduced by WCOBRA/TRAC subcooled vapor property calculations is assumed minor and is not considered a contributor to the code uncertainty.

10-2-2-4 Subcooled Liquid Properties

Model Basis

Internal Energy For a liquid at a subcooled temperature T_ℓ and pressure P the liquid internal energy associated with that state is calculated starting with the internal energy of the saturated liquid state described by T_ℓ and $P_{sat}(T_\ell)$, which is the saturation pressure corresponding to T_ℓ, and adding an additional term which represents the change in internal energy from the state $(T_\ell,\ P_{sat}(T_\ell))$ to the state $(T_\ell,\ P)$. That is,

$$e_\ell(T_\ell,\ P) = e_f(T_\ell) + \theta_1(P,T_\ell) \tag{10-78}$$

The additional term θ_1, which represents the change in energy required to move along the isotherm at T_ℓ between two different pressure values, namely $P_{sat}(T_\ell)$ and P, is represented as

$$\theta_1 = (P - P_{sat}(T_\ell))\left(\frac{\partial e_\ell}{\partial P}\right)_{T_\ell} \tag{10-79}$$

where:

$$P_{sat}(T_\ell) = \left(10^5\right)\left[\frac{T_\ell - 255.2}{117.8}\right]^{1/0.223} \tag{10-80}$$

The partial derivative with respect to pressure of the internal energy is

$$\left(\frac{\partial e_\ell}{\partial P}\right)_{T_\ell} = C_{KO} + C_{K2}\ P_{sat}\ (T_\ell) \tag{10-81}$$

where:

$$C_{KO} = -8.33544\ x\ 10^{-4}$$
$$C_{K2} = -2.24745\ x\ 10^{-17}$$

Therefore the partial derivative with respect to T_ℓ of the internal energy increment is calculated as

$$\left(\frac{\partial \theta_1}{\partial T_\ell}\right)_P = \frac{-C_{KO} - C_{K2}\left[2\,P_{sat}(T_\ell)P - 3\,P_{sat}(T_\ell)^2\right]}{\dfrac{(117.8)(0.223)}{10^5}\left[\dfrac{P_{sat}(T_\ell)}{10^5}\right]^{-0.767}} \tag{10-82}$$

and the derivative of internal energy is

$$\left(\frac{\partial e_\ell}{\partial T_\ell}\right)_P = \frac{de_f}{dT_{sat}} + \left(\frac{\partial \theta_1}{\partial T_\ell}\right)_P \tag{10-83}$$

The saturated liquid internal energy and its derivative with respect to temperature are determined over three temperature domains as was previously described (Equations 10-38 and 10-39).

Density Liquid density is also calculated over three temperature domains. Defining $P_{BAR} = (10^{-5})P$ and $T_{\ell c} = T_\ell - 273.15$, density and its derivatives are as follows.

For $T_\ell > 525.15$:

$$\rho_\ell = 1.43 + 1000\left[C_{\ell 1} + C_{\ell 2}P_{BAR} + C_{\ell 3}P_{BAR}^2 + \beta_1 T_{\ell c} + \beta_2 T_{\ell c}^2\right]^{-1} \tag{10-84}$$

$$\left(\frac{\partial \rho_\ell}{\partial P}\right)_{T_\ell} = -(\rho_\ell - 1.43)^2(10^{-8})\left[C_{\ell 2} + 2C_{\ell 3}P_{BAR} + T_{\ell c}(C_{\ell 5} + 2C_{\ell 6}P_{BAR}) + T_{\ell c}^2(C_{\ell 8} + 2C_{\ell 9}P_{BAR})\right] \tag{10-85}$$

$$\left(\frac{\partial \rho_\ell}{\partial T_\ell}\right)_P = -(\rho_\ell - 1.43)^2(10^{-3})(\beta_1 + 2\beta_2 T_{\ell c}) \tag{10-86}$$

where:

$$\beta_1 = C_{\ell 4} + C_{\ell 5}P_{BAR} + C_{\ell 6}P_{BAR}^2 \tag{10-87}$$

and

$$\beta_2 = C_{\ell 7} + C_{\ell 8} P_{BAR} + C_{\ell 9} P_{BAR}^2 \tag{10-88}$$

For T_ℓ<521.15:

$$\rho_\ell = 1000\left[d_{\ell 1} + d_{\ell 2} P_{BAR} + d_{\ell 3} P_{BAR}^2 + \beta_3 T_{\ell c} + \beta_4 T_{\ell c}^2\right] - 2.01 \tag{10-89}$$

$$\left(\frac{\partial \rho_\ell}{\partial P}\right)_{T_\ell} = -\left(\rho_\ell + 2.01\right)^2 \left(10^{-8}\right)\left[d_{\ell 2} + 2d_{\ell 3} P_{BAR} + T_{\ell c}\left(d_{\ell 5} + 2d_{\ell 6} P_{BAR}\right) + T_{\ell c}^2\left(d_{\ell 8} + 2d_{\ell 9} P_{BAR}\right)\right] \tag{10-90}$$

$$\left(\frac{\partial \rho_\ell}{\partial T_\ell}\right)_P = -\left(\rho_\ell + 2.01\right)^2 \left(10^{-3}\right)\left(\beta_3 + 2\beta_4 T_{\ell c}\right) \tag{10-91}$$

where:

$$\beta_3 = d_{\ell 4} + d_{\ell 5} P_{BAR} + d_{\ell 6} P_{BAR}^2 \tag{10-92}$$

and

$$\beta_4 = d_{\ell 7} + d_{\ell 8} P_{BAR} + d_{\ell 9} P_{BAR}^2 \tag{10-93}$$

For $521.15 \leq T_\ell \leq 525.15$ a linear interpolation of the above two ranges is used. Representing the values from Equations 10-84 through 10-88 by $\rho_{\ell a}$ and those from Equations 10-89 through 10-93 by $\rho_{\ell b}$, then

$$\rho_\ell = F_b \rho_{\ell b} + F_a \rho_{\ell a} \tag{10-94}$$

$$\frac{\partial \rho_\ell}{\partial p} = F_b \frac{\partial \rho_{\ell b}}{\partial P} + F_a \frac{\partial \rho_{\ell a}}{\partial P} \tag{10-95}$$

$$\frac{\partial \rho_\ell}{\partial T_\ell} = F_b \frac{\partial \rho_{\ell b}}{\partial T_\ell} + F_a \frac{\partial \rho_{\ell a}}{\partial T_\ell} + \frac{\rho_{\ell a} - \rho_{\ell b}}{4.0} \tag{10-96}$$

where:

$$F_a = (T_\ell - 521.15)/4 \tag{10-97}$$

$$F_b = 1 - F_a \tag{10-98}$$

The coefficients used in Equations 10-84 through 10-93 are:

$$
\begin{aligned}
C_{\ell 1} &= 2.25262 & d_{\ell 1} &= 1.00213623 \\
C_{\ell 2} &= 0.014859 & d_{\ell 2} &= -5.632785E-05 \\
C_{\ell 3} &= -7.15488E-05 & d_{\ell 3} &= -8.971304E-09 \\
C_{\ell 4} &= -0.0104588 & d_{\ell 4} &= -2.28287459E-05 \\
C_{\ell 5} &= -1.02962E-04 & d_{\ell 5} &= 4.76596787E-07 \\
C_{\ell 6} &= 5.09135E-07 & d_{\ell 6} &= 5.021318E-10 \\
C_{\ell 7} &= 2.59266E-05 & d_{\ell 7} &= 4.10115658E-06 \\
C_{\ell 8} &= 1.7241E-07 & d_{\ell 8} &= -3.803989E-09 \\
C_{\ell 9} &= -8.98419E-10 & d_{\ell 9} &= -1.42199752E-12
\end{aligned}
$$

Model as Coded The thermodynamic properties for subcooled liquid are calculated in subroutine THERMO as described in the previous paragraphs. For subcooled liquid, however, the density and its derivatives are corrected to reflect a residual void fraction. The correction is shown below.

In the following, the liquid values calculated in the previous section are denoted by a tilde (~).

For $P \geq 0.4 \times 10^6 Pa$

$$\rho_\ell = \left(1 - \frac{1000}{P}\right)\tilde{\rho}_\ell \tag{10-99}$$

and

$$\left(\frac{\partial \rho_\ell}{\partial T_\ell}\right)_P = \left(1 - \frac{1000}{P}\right)\left(\frac{\partial \tilde{\rho}_\ell}{\partial T_\ell}\right)_P \tag{10-100}$$

$$\left(\frac{\partial \rho_\ell}{\partial P}\right)_{T_\ell} = \left(1 - \frac{1000}{P}\right)\left(\frac{\partial \tilde{\rho}_\ell}{\partial P}\right)_{T_\ell} + \frac{1000\rho_\ell}{P^2} \tag{10-101}$$

For $P < 0.4 \times 10^6 Pa$

$$\rho_\ell = (0.995 + 6.25 \times 10^{-9} P)\tilde{\rho}_\ell \tag{10-102}$$

and,

$$\left(\frac{\partial \rho_\ell}{\partial T_\ell}\right)_P = (0.995 + 6.25 \times 10^{-9} P)\left(\frac{\partial \tilde{\rho}_\ell}{\partial T_\ell}\right)_P \tag{10-103}$$

$$\left(\frac{\partial \rho_\ell}{\partial_P}\right)_{T_\ell} = \left(0.995 + 6.25\times10^{-9}P\right)\left(\frac{\partial \tilde{\rho}_\ell}{\partial P}\right)_{T_\ell} + 6.25\times10^{-9}\tilde{\rho}_\ell \qquad (10\text{-}104)$$

Scaling Considerations Not applicable.

Conclusions The TRAC-PD2 subcooled water thermodynamic property routines used in WCOBRA/TRAC for one dimensional components have been compared by Rivard and Torrey (1975) with steam table data. The agreement is good in the region for $373\ K < T_\ell < 523\ K$ and $0.4178\ x\ 10^6\ J/Kg < e_\ell < 1.0808\ x\ 10^6\ J/Kg$. Comparison with the WATER package (Coffman and Lynn, 1966) over a wider range also showed good agreement except for very extreme cases not expected in a PWR LOCA.

10-2-2-5 Transport Properties

Model Basis This section describes the WCOBRA/TRAC calculations performed to obtain the specific heat, fluid viscosity, thermal conductivity, and surface tension for one-dimensional components. The equations used for these quantities are polynomial fits to data.

Specific Heat The constant pressure specific heat for liquid water is given in J/kg°K as a function of enthalpy and pressure by

$$C_{P\ell} = \left\{H_\ell\left[H_\ell\left(D_{O\ell}+D_{1\ell}P\right)+\left(C_{O\ell}+C_{1\ell}P\right)\right]+B_{O\ell}+B_{1\ell}P\right\}^{-1} \qquad (10\text{-}105)$$

For vapor, the constant pressure specific heat is given by:

$$C_{pv} = C_{1v}+C_{2v}T_v+\frac{C_{3v}P}{\left(C_{5v}T_v-C_{6v}\right)^{2.4}}+\frac{C_{4v}P^3}{\left(C_{5v}T_v-C_{6v}\right)^9} \qquad (10\text{-}106)$$

where the coefficients of Equations 10-105 and 10-106 are listed in Table 10-9.

Liquid Viscosity Calculation of liquid viscosity is divided into three different ranges based on the liquid enthalpy.

For $H_\ell \leq 0.276\times10^6\ J/kg$, liquid viscosity in $N\text{-}s/m^2$

$$\mu_\ell = \left\{A_{0\ell}+A_{1\ell}\chi+A_{2\ell}\chi^2+A_{3\ell}\chi^3+A_{4\ell}\chi^4\right\} - \left[B_{0\ell}+B_{1\ell}\eta+B_{2\ell}\eta^2+B_{3\ell}\eta^3\right]\left(P-P_o\right) \tag{10-107}$$

where:

$$\chi = \left(H_\ell-c_{0n}\right)H_0 \tag{10-108}$$

and

$$\eta = \left(H_\ell-e_{c0n}\right)e_{h0} \tag{10-109}$$

For $0.276\times10^6\ J/kg < H_\ell \leq 0.394\times10^6\ J/kg$ the liquid viscosity is,

$$\mu_\ell = \left[E_{0\ell}+E_{1\ell}H_\ell+E_{2\ell}H_\ell^2+E_{3\ell}H_\ell^3\right] + \left[F_{0\ell}+F_{1\ell}H_\ell+F_{2\ell}H_\ell^2+F_{3\ell}H_\ell^3\right]\left(P-P_o\right) \tag{10-110}$$

and for $H_\ell > 0.394\times10^6\ J/kg$

$$\mu_\ell = \left[D_{0\ell}+D_{1\ell}z+D_{2\ell}z^2+D_{3\ell}z^3+D_{4\ell}z^4\right] \tag{10-111}$$

$$z = \left(H_\ell-c_n\right)H_{OO} \tag{10-112}$$

The coefficients for the liquid viscosity equations are found in Table 10-10.

Vapor Viscosity Calculation of the viscosity of vapor is divided into three different temperature ranges. The ranges and expressions used for vapor viscosity are:

For $T_v < 280\ K$,

$$\mu_v = 17.08 \times 10^{-6} + 5.927 \times 10^{-8}(T_v - 273.15)$$

$$-8.14\times10^{-11}(T_v - 273.15)^2 \qquad (10\text{-}113a)$$

For $280\ K \le T_v \le 573.15\ K$,

$$\mu_v = \left[B_{1v}\left(T_v - 273.15\right) + C_{1v}\right] - \rho_v\left[D_{1v} - E_{1v}\left(T_v - 273.15\right)\right] \qquad (10\text{-}113b)$$

For $573.15\ K < T_v < 648.15\ K$,

$$\mu_v = B_{1v}\left(T_v - 273.15\right) + C_{1v} + \rho_v\left[F_{Ov} - F_{1v}\left(T_v - 273.15\right)\right. \qquad (10\text{-}114)$$

$$\left. + F_{2v}\left(T_v - 273.15\right)^2 + F_{3v}\left(T_v - 273.15\right)^3\right]$$

$$+ \rho_v\left[G_{Ov} + G_{1v}\left(T_v - 273.15\right) + G_{2v}\left(T_v - 273.15\right)^2\right]$$

$$+ G_{3v}\left(T_v - 273.15\right)^3\Big]\left(A_{Ov} + A_{1v}\rho_v + A_{2v}\rho_v^2\right).$$

and for $T_v \ge 648.15\ K$,

$$\mu_v = B_{1v}\left(T_v - 273.15\right) + C_{1v} + \rho_v\left(A_{Ov} + A_{1v}\rho_v + A_{2v}\rho_v^2\right). \qquad (10\text{-}115)$$

The coefficients for Equations 10-113 through 10-115 are listed in Table 10-11.

Liquid Thermal Conductivity The liquid thermal conductivity is given $W/m-K$ by

$$k_\ell = A_{\ell 0}+A_{\ell 1}\chi_\kappa+A_{\ell 2}\chi_\kappa^2+A_{\ell 3}\chi_\kappa^3, \tag{10-116}$$

where:

$$\chi_\kappa = \frac{H_\ell}{A_{\ell 4}} \tag{10-117}$$

Vapor Thermal Conductivity

If 280.0 $K \le T_v$

$$k_v = \chi_1+\rho_v\left[\chi_2+\frac{A_{v4}\rho_v}{(T_v-273.15)^{4.2}}\right] \tag{10-118}$$

where:

$$\chi_1 = A_{v0}+A_{v1}(T_v-273.15)+A_{v2}(T_v-273.15)^2+A_{v3}(T_v-273.15)^3 \tag{10-119}$$

and

$$\chi_2 = B_{v0}+B_{v1}(T_v-273.15)+B_{v2}(T_v-273.15)^2 \tag{10-120}$$

The coefficients used in Equations 10-116 through 10-120 are listed in Table 10-12.

If $T_v < 280.0$ K, the vapor conductivity is

$$k_v = 0.0228 \tag{10-121}$$

Surface Tension The surface tension is calculated in N/m as,

$$\sigma = \left(a_2 + \frac{a_1}{1+0.83\theta} \right) \theta^2 + a_3\theta^3 + a_4\theta^4 + a_5\theta^5 \tag{10-122}$$

where:

$$\theta = 647.3 - T_{sat} \tag{10-123}$$

The coefficients for Equation 10-122 are given in Table 10-13.

Model as Coded Subroutine FPROP is used to obtain transport properties for liquid and vapor water. The input variables for this subroutine are the saturation temperature corresponding to the total pressure, the internal energies, densities, and temperatures of the liquid and vapor phases and the total pressure. The output transport variables include the constant pressure specific heats, viscosities, and thermal conductivities of the liquid and gas phases, and the surface tension of the liquid.

The transport property calls are function calls within the FPROP subroutine. Function CPLL calculates the constant pressure specific heat of the liquid, while function CPVV1 determines the value of the constant pressure specific heat of the vapor. Function THCL evaluates the liquid thermal conductivity, and function THCV calculates the steam thermal conductivity. Similarly, functions VISCL and VISCV determine viscosity values. Finally, function SIGMA calculates the surface tension.

The equations shown are coded directly. Sample curves of liquid and vapor specific heat, viscosity, thermal conductivity, and the surface tension calculated by these routines along the saturation line are shown in Figures 10-22 through 10-28.

In some instances, upper and lower limits are maintained on the calculated values of the transport properties. These limits are summarized as follows:

Specific Heat The maximum permitted value for the liquid specific heat is $C_{p\ell}=4.0\times10^4$. If the calculation of $C_{p\ell}$ by Equation 10-105 performed by function CPLL yields a value greater than this, $C_{p\ell}$ is reset to 4.0×10^4. No limits are placed on the calculation of the vapor specific heat.

Viscosity The minimum permitted value of vapor viscosity is $\mu_v=10^{-7}$. If the calculation of μ_v by Equations 10-113 through 10-115 yields a value less than this in function VISCV, μ_v is reset to 10^{-7}. No limits are imposed on the liquid phase viscosity.

Thermal Conductivity The minimum permitted value of the liquid thermal conductivity is $k_\ell=0.09$. If, in function THCL, Equation 10-116 yields a value lower than this, k_ℓ is reset to 0.09.

The minimum permitted value for vapor thermal conductivity is $k_v=10^{-4}$. If Equation 10-118 in function THCV calculates a value less than 10^{-4}, k_v is reset to 10^{-4}.

Surface Tension If $T_{sat} > 647.3$, the surface tension is set to $\sigma = 0.0$.

Scaling Considerations Not applicable.

Conclusions In NUREG/CR-2054, it was reported that the thermodynamic and transport property fits used in TRAC-PD2 were compared by Rivard and Torrey (1975) with steam table data over a wide range of parameters. The agreement is satisfactory in the saturation region and in the superheated steam region for 1.0×10^5 Pa < P < 100.0×10^5 Pa and 423.0 K < T_v < 823.0 K. The agreement also is good in the subcooled water region for 373.0 K < T_ℓ < 523.0 K and $0.417\,8 \times 10^6$ J/kg < e_ℓ < $1.080\,8 \times 10^6$ J/kg.

Further verification was performed by comparing the TRAC-PD2 polynomial fits with the WATER package (Coffman and Lynn, 1966) over a wider range of nonequilibrium (99 K of both superheat and subcooling) for a pressure variation of 1.0×10^5 Pa to 2.0×10^7 Pa. The comparisons showed good agreement for both the thermodynamic and transport properties throughout the saturation and nonequilibrium regions except for very extreme cases, which are not expected in a PWR LOCA.

The WCOBRA/TRAC property package for one-dimensional components is identical to the TRAC-PD2 package. Therefore, for most WCOBRA/TRAC applications, the thermodynamic and transport property routines will provide realistic values over a wide range. The simplified polynomial fits provide an efficient and low-cost method compared to other approaches such as steam table interpolation.

10-3 Thermophysical Properties of Air

10-3-1 Vessel Component

Model Basis WCOBRA/TRAC can perform calculations for conditions in which there is air in the vessel component. This section describes the thermodynamic properties which are defined for air in the WCOBRA/TRAC vessel component.

Enthalpy The enthalpy of air is calculated as

$$H_{air} = C_{p,ref}\left(T_{air}-T_{ref}\right)+H_{ref} \tag{10-124}$$

where the reference values are $T_{ref} = 40.0°F$, $H_{ref} = 188.49$ Btu/lbm, and $C_{p,ref} =$ 0.249 Btu/ lbm-°F.

Density The density of air is calculated from the ideal gas law with the gas constant for air assumed to be $R_{air} = 0.37042\ psi/°R\ (lb/ft^3)$. Thus, the density of air is given by

$$\rho_{air} = \frac{P}{R_{air}(T_{air}+459.6)} \tag{10-125}$$

Gas Temperature The air temperature is estimated from the enthalpy using the inverse of Equation 10-124.

Specific Heat The specific heat for air in BTU/lbm-°F is determined in two different temperature ranges.

If $T_{air} \leq 600K$,

$$C_p = 0.244388 + A_1 T_{air} + A_2 T_{air}^2 + A_3 T_{air}^3 \tag{10-126}$$

and if $T_{air} > 600K$,

$$C_p = 0.208831 + B_1 T_{air} + B_2 T_{air}^2 + B_3 T_{air}^3 \tag{10-127}$$

where the coefficients A_i and B_i are listed in Table 10-14, and T_{air} is in degrees K.

Model as Coded The equations used to calculate the thermodynamic properties of air, Equations 10-124 through 10-127, are coded as shown without modification. No upper or lower limits are imposed on the values calculated. Calculations are performed in Subroutines HGAS and TGAS.

Scaling Considerations Not Applicable

Conclusions The WCOBRA/TRAC vessel component can perform calculations to estimate the thermodynamic properties of air. This option, however, is not used in a LOCA analysis.

10-3-2 One-Dimensional Components

Model Basis This section describes the calculation of thermodynamic and transport properties in WCOBRA/TRAC one-dimensional components for air.

Internal Energy The internal energy and its derivatives for air are given by

$$e_{air} = C_{vair} T_{air} \tag{10-128}$$

$$\left(\frac{\partial e_{air}}{\partial T_{air}} \right)_P = C_{vair} \tag{10-129}$$

and

$$\left(\frac{\partial e_{air}}{\partial P} \right)_{Tair} = 0.0 \tag{10-130}$$

The constant volume specific heat (C_{vair}) is

$$C_{vair} = 714.9 \ J/kg\text{-}K \tag{10-131}$$

Density The density and its derivatives are based on the Ideal Gas Law and are given by

$$\rho_{air} = \frac{P}{R_{air} T_{air}} \tag{10-132}$$

$$\left(\frac{\partial \rho_{air}}{\partial P_{air}} \right)_{Tair} = \frac{1}{R_{air} T_{air}} \tag{10-133}$$

$$\left(\frac{\partial \rho_{air}}{\partial T_{air}} \right)_P = -R_{air} \rho_{air} \left(\frac{\partial \rho_{air}}{\partial P} \right)_{T_{air}} \tag{10-134}$$

where

$$R_{air} = 287.12 \ J/kg\text{-}K \qquad (10\text{-}135)$$

Enthalpy The enthalpy of air is calculated using the definition of enthalpy:

$$H_{air} = e_{air} + \frac{P}{\rho_{air}} \qquad (10\text{-}136)$$

where e_{air} is determined by Equation 10-128, and ρ_{air} is given by Equation 10-132.

Viscosity Two different temperature ranges are used to calculate the viscosity of air.

If $T_{air} \leq 502.15 \ K$,

$$\mu_{air} = a_{a0} + a_{a1}\left(T_{air} - 273.15\right) + a_{a2}\left(T_{air} - 273.15\right)^2 \qquad (10\text{-}137)$$

and if $T_{air} > 502.15 \ K$,

$$\mu_{air} = a_{b0} + a_{b1}\left(T_{air} - 273.15\right) + a_{b2}\left(T_{air} - 273.15\right)^2 \qquad (10\text{-}138)$$

where the coefficients a_{ai} and a_{bi} are listed in Table 10-15.

Thermal Conductivity The thermal conductivity of air is assumed to be constant,

$$k_{air} = 0.0228 \ W/m\text{-}K \qquad (10\text{-}139)$$

Model as Coded The internal energy and its derivatives and the density and its derivatives for air are calculated in subroutine THERMO. Subroutine FPROP calculates the enthalpy. The transport properties viscosity and thermal conductivity are determined in subroutines VISCV and THCV, respectively.

Scaling Considerations Not applicable.

Conclusions The WCOBRA/TRAC one-dimensional components calculate thermodynamic properties for air assuming it behaves as an ideal gas. The transport properties are based on polynomial fits to data. The correlations approximately calculate properties for air at low temperatures.

10-4 Thermal Properties of Nuclear Fuel Rod Materials

A typical nuclear fuel rod is composed of uranium-dioxide fuel pellets and a zirconium based clad material. The gap between the fuel pellets and the clad is filled with the initial backfill gas and fission gas. As part of the WCOBRA/TRAC default nuclear fuel rod model, the material properties of uranium-dioxide, Zircaloy-4, ZIRLO™, and of gas mixtures are included. This section describes the calculation of the thermal properties for these fuel rod materials.

10-4-1 Uranium Dioxide

Model Basis The material properties of uranium dioxide are based on MATPRO-9 (MacDonald et al., 1976) and on MATPRO-11, Rev. 1 (Hagrman, Reymann, and Mason, 1980) calculations.

Density The (cold) density for uranium-dioxide is assumed to be

$$\rho_{UO_2} = 684.86\, f_D \tag{10-140}$$

where f_D is the fraction of theoretical density and is input by the user. The density ρ_{UO_2} has units of lbm/ft^3.

Thermal Conductivity The UO_2 thermal conductivity is computed from the MATPRO-9 correlation instead of the more complex version in MATPRO-11 to reduce computer time. Both correlations have the same error band (0.2 $W/m-°K$) and give very nearly the same conductivity over the expected operating range of 500-3000° K. The thermal conductivity in Btu/hr-ft-°F is determined from

$$k_{UO_2} = \left[\max \left(0.0191, \frac{40.4}{(T_c+464)} \right) + 1.216\times10^{-4}\exp\left(1.867\times10^{-3}T_c\right) \right] C \tag{10-141}$$

where T_c is the temperature in °Celsius and

$$C = (0.5779)100[1.0 - \beta(1.0 - f_D)]/(1.0-0.05\beta) \tag{10-142}$$

and

$$\beta = 2.58-(5.8\times10^{-4})T_c \tag{10-143}$$

Specific Heat The specific heat in Btu/lbm-°F for uranium dioxide is given by

$$C_{P_{UO_2}} = (2.388\times10^{-4})\left\{ \frac{K_1\theta^2\exp(\theta/T_K)}{T_K^2[\exp(\theta/T_K)-1]^2} + K_2T_K + \frac{F_{OM}}{2}\frac{K_3E_D}{RT_K^2}\exp(-E_D/RT_K) \right\} \tag{10-144}$$

where T_K is the temperature in °K and

$$\begin{aligned}
\theta &= \textit{Einstein temperature}(535.285°K) \\
R &= 8.3143\ (J/mol-°K) \\
K_1 &= 296.7(J/kg-°K) \\
K_2 &= 2.43\text{x}10^{-2}(J/kg-°K^2) \\
K_3 &= 8.745\text{x}10^{7}(J/kg) \\
E_D &= 1.577\text{x}10^{5}(J/mol) \\
F_{OM} &= \textit{oxygen/metal ratio}(2.0)
\end{aligned}$$

Model as Coded The equations representing the density, thermal conductivity and specific heat for uranium dioxide are coded into WCOBRA/TRAC as described by Equations 10-140 through 10-144 without modification.

Calculations for uranium dioxide density are performed in Subroutine SETUP, those for thermal conductivity in subroutines SSTEMP and TEMP, and those for specific heat in Subroutines TEMP and MOVE. Values of conductivity and specific heat versus temperature are shown in Figures 10-29 and 10-30.

Scaling Considerations Not applicable.

Conclusions The WCOBRA/TRAC correlations for UO_2 density, specific heat and thermal conductivity are based on MATPRO-9 and MATPRO-11. The models and correlations for these properties were used in simulations of NRU and LOFT. Therefore, the uncertainty and reliability of these models is accounted for in the overall code bias and uncertainty.

10-4-2 Zircaloy-4

Model Basis The material properties of Zircaloy-4 are based on MATPRO-9 and MATPRO-11 calculations.

Density The (cold) density of Zircaloy-4 clad material is assumed to be ρ_{Zr}=409.0 lbm/ft^3.

Thermal Conductivity The thermal conductivity in Btu/hr-ft-°F for Zircaloy-4 clad is given by

$$k_{Zr} = 0.5779\left[7.51 + 0.0209T_K - \left(1.45\times10^{-5}\right)T_K^{\,2} + \left(7.67\times10^{-9}\right)T_K^{\,3}\right] \tag{10-145}$$

where T_K is temperature in °Kelvin.

Specific Heat WCOBRA/TRAC calculates the specific heat for Zircaloy-4 by linearly interpolating between values from a built-in table. Table 10-16 lists the values used to determine the specific heat of Zircaloy-4.

Model as Coded The equations for the density, thermal conductivity and specific heat of Zircaloy-4 are coded into WCOBRA/TRAC as described above without modification. Density is calculated in Subroutine SETUP and HEAT, conductivity in Subroutines STEMP, TEMP, and HEAT and specific heat in Subroutines TEMP, HEAT, and MOVE. Curves of conductivity and specific heat versus temperature are shown in Figures 10-31 and 10-32.

Scaling Considerations Not applicable.

Conclusions The WCOBRA/TRAC correlations for the density, thermal conductivity, and specific heat of Zircaloy-4 are based on MATPRO-9 and MATPRO-11. These property relations were used in simulations of NRU and LOFT.

10-4-3 ZIRLO™

Model Basis The ZIRLO™ alloy developed by Westinghouse represents a modification to Zircaloy-4 which was achieved by reducing the tin and iron content, eliminating the chromium, and adding a nominal one percent niobium. Table 10-17 shows a comparison of the two alloys.

Since tin is an alpha phase stabilizer and niobium is a beta phase stabilizer, the reduction in tin and the addition of niobium result in reductions in the temperatures at which the ZIRLO™ alloy undergoes the alpha to beta phase change, relative to Zircaloy-4. Measurements performed by Westinghouse show that the ZIRLO™ alloy starts the transformation at 1023°K and ends at 1213°K.

Since the ZIRLO™ and Zircaloy-4 alloys are both about 98 percent zirconium, it should not be expected that the material properties are significantly different, except to the extent that they are affected by the differences in the phase change temperatures. Density, thermal expansion, thermal conductivity, and specific heat of both alloys have been measured by the Properties Research Laboratory using samples cut from Westinghouse production tubing (Taylor, Groot, and Larimore, 1989). Evaluation of the test results indicated that the materials are sufficiently similar that the Zircaloy-4 material properties can be used for the ZIRLO™ alloy, with the exception of the specific heat (Davidson and Nuhfer, 1990). The specific heat of the ZIRLO™ alloy is based on an adjustment to Table 10-16, which considers the difference in phase change temperatures.

Density The (cold) density of the ZIRLO™ cladding material is taken to be identical to that of Zircaloy-4 (409.0 lbm/ft^3).

Thermal Conductivity The thermal conductivity of the ZIRLO™ cladding material is taken to be identical to that of Zircaloy-4, given by Equation 10-145.

Specific Heat The specific heat shown in Table 10-16 for Zircaloy-4 includes both the true specific heat and the alpha to beta phase heat of transformation. The specific heat for the ZIRLO™ cladding material was obtained by adjusting Table 10-*16* to account for the difference in phase change temperatures, assuming both the true specific heat and the heat of transformation are the same for the two alloys. The true specific heat is taken to be equal to the total specific heat in Table 10-16 for $T \leq 1090$°K, 0.085 Btu/lbm-°F for $T \geq 1213$°K, and[

(10-146)

]^{a,c} (10-147)

where: [

]^{a,c} (10-148)

WCOBRA/TRAC calculates the specific heat for the ZIRLO™ cladding material using the resulting total specific heat values, shown in Table 10-18.

Model as Coded The density, thermal conductivity, and specific heat of the ZIRLO™ cladding material are coded into WCOBRA/TRAC as described above, without modification. Figure 10-33 shows a comparison of specific heat for ZIRLO™ with that of Zircaloy-4.

Scaling Considerations Not applicable.

Conclusions Comparisons of the material properties for the ZIRLO™ and Zircaloy-4 cladding materials have shown that the Zircaloy-4 relations for density and thermal conductivity can also be applied to the ZIRLO™ alloy. The difference in the phase change temperatures of the two alloys requires that different specific heat correlations be used. The specific heat correlation for the ZIRLO™ alloy is based on an adjustment to the Zircaloy-4 correlation, which accounts for the different phase change temperature range. This correlation will be used for analyses of nuclear reactors which utilize the ZIRLO™ cladding material.

10-4-4 Fuel Rod Gas Mixtures

Model Basis For the gas mixture in the fuel-clad gap, only the thermal conductivity is calculated. The fill gas in the WCOBRA/TRAC fuel rod model assumes that the gas is a mixture composed of helium, xenon, argon, krypton, hydrogen, and nitrogen. The thermal conductivity of the gas mixture as a function of temperature is determined, as described in MATPRO-11 Rev. 1 (Hagrman, Reymann, and Mason, 1980), from the relation

$$k_{gas} = \sum_{i=1}^{N} \frac{k_i}{1 + \sum_{\substack{j=1 \\ j \neq i}}^{N} \Psi_{ij} \frac{n_j}{n_i}} \tag{10-149}$$

where N = number of component gases, and where

$$\Psi_{ij} = \Phi_{ij} \left[1 + 2.41 \frac{(M_i - M_j)(M_i - 0.142 M_j)}{(M_i + M_j)^2} \right] \tag{10-150}$$

and

$$\Phi_{ij} = \frac{\left[1 + \left(\frac{k_i}{k_j}\right)^{1/2} \left(\frac{M_i}{M_j}\right)^{1/4}\right]^2}{2^{3/2}\left(1 + \frac{M_i}{M_j}\right)^{1/2}} \tag{10-151}$$

where:

M_i = molecular weight of gas species i

n_i = mole fraction of gas species i

k_i = thermal conductivity of gas species I

The thermal conductivities of the six component gases are evaluated in Btu/hr-ft-°F as a function of temperature from the following relations:

Gas	k(Btu/hr-ft-°F)	
Helium	$(1.314x10^{-3})T_{gas}^{0.668}$	(10-152)
Argon	$(1.31x10^{-3})T_{gas}^{0.701}$	(10-153)
Krypton	$(1.588x10^{-5})T_{gas}^{0.92331}$	(10-154)
Xenon	$(1.395x10^{-5})T_{gas}^{0.872}$	(10-155)
Hydrogen	$(5.834x10^{-4})T_{gas}^{0.8213}$	(10-156)

$$\text{Nitrogen} \quad (7.35\text{x}10^{-5})T_{gas}^{0.846} \tag{10-157}$$

where T_{gas} = gas temperature (°R).

Model as Coded Equations 10-149 through 10-151 for gap gas thermal conductivity are coded in WCOBRA/TRAC as described without modification in subroutine GTHCON.

Scaling Consideration Not applicable.

Conclusions Thermal conductivity for the gas mixture in the fuel-clad gap is calculated using the equations in MATPRO-11 Rev. 1 (Hagrman, Reymann, and Mason, 1980).

10-5 Thermal Properties of Structural Materials

10-5-1 Vessel Component Structural Material Properties

Model Basis The density, specific heat, and thermal conductivity for structural materials within the vessel are specified by the user for a range of temperatures. Values for each material are obtained from standard references for thermal properties such as Touloukian (1967). When available, material properties provided by the material supplier are used.

Model as Coded Values for the material specific heat and thermal conductivity are linearly interpolated with temperature. A warning message is printed if the temperature is outside of the range supplied by the user.

Scaling Considerations Not applicable.

Conclusion Material thermal properties are supplied by the user. This permits the representation of the material properties by the actual measured values and minimizes uncertainty.

10-5-2 One-Dimensional Component Structural Material Properties

<u>Model Basis</u> A library of temperature-dependent material properties is incorporated in <u>W</u>COBRA/TRAC for the one-dimensional components. There are five sets of material properties that make up the library. Each set supplies values for the density, thermal conductivity, specific heat, and spectral emissivity for use in heat transfer calculations. The material sets are for Types 304, 316, and 347 Stainless Steel, Medium Carbon Steel, and Inconel 600.

In the following expressions,

$$
\begin{aligned}
\rho &= density \left(\frac{kg}{m^3}\right) \\
C_p &= specific\ heat \left(\frac{J}{kg\text{-}K}\right) \\
k &= thermal\ conductivity \left(\frac{W}{m\text{-}K}\right) \\
T_K &= temperature (K) \\
T_F &= temperature\ (^\circ F)
\end{aligned}
$$

<u>Stainless Steel, Type 304</u> The density is given by

$$\rho(T_F) = 8054.65 - 0.2595 T_F \tag{10-158}$$

Specific heat is given by

$$C_p(T_F) = 426.17 + 0.43816 T_F - (6.3759\times10^{-4}) T_F^2 + (4.4803\times10^{-7}) T_F^3 - (1.0729\times10^{-10}) T_F^4 \tag{10-159}$$

Thermal conductivity is calculated by

$$k(T_F) = 14.79 + 0.00714 T_F \tag{10-160}$$

Stainless Steel, Type 316 Density is given by

$$\rho(T_K) = 8084.0 - 0.4209T_K - (3.894\times10^{-5})T_K^{\,2} \tag{10-161}$$

Specific heat is given by Equation 10-159 and thermal conductivity is given by

$$k(T_K) = 9.248 + 0.01571T_K \tag{10-162}$$

Stainless Steel, Type 347 The density is assumed constant at

$$\rho = 7913\frac{kg}{m^3} \tag{10-163}$$

The specific heat is given by

$$C_p(T_F) = 502.416 + 0.0984(T_F - 240) \tag{10-164}$$

and the thermal conductivity is

$$k(T_F) = 14.1926 + (7.269\times10^{-3})T_F \tag{10-165}$$

Carbon Steel The density for carbon steel is assumed constant:

$$\rho = 7855.23\frac{kg}{m^3} \tag{10-166}$$

The specific heat is given by

$$C_p(T_F) = 400.48 + 0.4582T_F - (6.5532\times10^{-4})T_F^{\,2} + (5.3706\times10^{-7})T_F^{\,3} \tag{10-167}$$

and the thermal conductivity is given by

$$k(T_F) = 48.43 - 0.011366 T_F \tag{10-168}$$

Inconel 600 The density for Inconel 600 is assumed constant,

$$\rho = 8409.45 \frac{kg}{m^3} \tag{10-169}$$

The specific heat is given by

$$C_p(T_F) = 4184.\left[0.1014456 + (4.378952\times10^{-5})T_F - (2.046138\times10^{-8})T_F^{\,2} + (3.418111\times10^{-11})T_F^{\,3} - (2.060318\times10^{-13})T_F^{\,4} + (3.682836\times10^{-16})T_F^{5} - (2.458648\times10^{-19})T_F^{\,6} + (5.597571\times10^{-23})T_F^{\,7}\right] \tag{10-170}$$

and thermal conductivity is given by

$$k(T_F) = 1.730\left[8.011332 + (4.643719\times10^{-3})T_F + (1.872857\times10^{-6})T_F^{\,2} - (3.914512\times10^{-9})T_F^{\,3} + (3.475513\times10^{-12})T_F^{\,4} - (9.936696\times10^{-16})T_F^{\,5}\right] \tag{10-171}$$

Model as Coded The correlations described by Equations 10-158 through 10-171 are programmed as shown without modification in subroutine MSTRCT. Curves of specific heat and thermal conductivity as functions of temperature calculated with this subroutine are shown in Figures 10-34 through 10-42.

Scaling Considerations Not applicable.

Conclusions The WCOBRA/TRAC code uses built-in correlations to calculate the thermal properties of common structural materials modeled by one dimensional components. Comparisons to data show that these correlations provide a good estimate of the properties at low temperature. Since the one-dimensional components generally remain at low temperature during a LOCA transient, use of these correlations introduces only a small uncertainty into the transient calculation.

10-6 Conclusions

WCOBRA/TRAC routines provide appropriate means for calculation of thermodynamic and transport properties of liquid water, steam, and air for the vessel component and for one-dimensional components. Routines to calculate properties of fuel rod materials, i.e., fuel, cladding, and gap gas, are also included. Properties of structural materials in the vessel component are interpolated from user-provided tables. For one-dimensional components, routines to calculate properties of common structural materials are included. The routines generally calculate properties in the form of equations, for example as functions of temperature and pressure, or by linear interpolation in built-in tables. These property calculations have been compared with standard references and found to agree satisfactorily over the range of conditions expected for PWR LOCA calculations. No scaling uncertainty is required for the use of these models in reactor analysis.

10-7 References

ASME Steam Tables, 1968, American Society of Mechanical Engineers, 2nd Edition.

ASME Steam Tables, 1983, Thermodynamic and Transport Properties of Steam, 5th ed., The American Society of Mechanical Engineers, New York.

Coffman, W. A. and Lynn, L. L., 1966, "WATER: A Large Range Thermodynamic and Transport Water Property FORTRAN-IV Computer Program," Bettis Atomic Power Laboratory Report WAPD-TM-568.

Davidson, S. L. and Nuhfer, D. L. (Eds.), 1990, "VANTAGE+ Fuel Assembly Reference Core Report," WCAP-12610, Westinghouse Electric Corporation, Pittsburgh, Pennsylvania. [PROPRIETARY].

Haar, L., Gallagher, J. S., and Kell, G. S., 1984, NBS/NRC Steam Tables, Hemisphere Publishing Corporation, New York.

Hagrman, D. L., Reymann, G. A., and Mason, R. E., 1980, "MATPRO - Version 11 (Revision 1): A Handbook of Materials Properties for Use in the Analysis of Light Water Reactor Fuel Rod Behavior," USNRC Report NUREG/CR-0497, TREE-1280, Revision 1.

Keenan, J. H. and Keyes, F. G., 1936, Thermodynamic Properties of Steam, John Wiley & Sons, New York.

MacDonald, P. E., et al., 1976, "MATPRO - Version 9: A Handbook of Materials Properties for Use in the Analysis of Light Water Reactor Fuel Rod Behavior," Idaho National Engineering Laboratories, TREE-NUREG-1005.

McClintock, R. B. and Silvestri, G. J., 1936, Formulations and Iterative Procedures for the Calculation of Properties of Steam, American Society of Mechanical Engineers.

McFadden, J. H., et al., 1980, "RETRAN-02 A Program for Transient Thermal-Hydraulic Analysis of Complex Fluid Flow Systems, Volume 1: Equations and Numbers," Report NP-850, Electric Power Research Institute, Palo Alto, California.

Rivard, W. C. and Torrey, M. D., 1975, "Numerical Calculation of Flashing from Long Pipes Using a Two-Field Model," Los Alamos Scientific Laboratory Report LA-6104-MS.

Taylor, R. E., Groot, H., and Larimore, J., 1989, "Thermophysical Properties of ZR-4 and ZIRLO," PRL-820, Properties Research Laboratory, West Lafayette, Indiana. [PROPRIETARY].

Touloukian, Y. S., 1967, Thermophysical Properties of High Temperature Materials, Thermophysical Properties Research Center, Purdue University, The Macmillan Co., New York.

Table 10-1
Constants for Saturated Liquid Enthalpy

A_n	$0.1 \le P < 898.7$	Pressure: $898.7 \le P < 2529.9$	$2529.9 \le 3208$
1	0.6970887859E+02	0.8408618802E+06	0.9060030436E+03
2	0.3337529994E+02	0.3637413208E+06	-0.1426813520E+02
3	0.2318240735E+01	-0.4634506669E+06	0.1522233257E+01
4	0.1840599513E+00	0.1130306339E+06	-0.6973992961E+00
5	-0.5245502294E-02	-0.4350217298E+03	0.1743091663E+00
6	0.2878007027E-02	-0.3898988188E+04	-0.2319717696E-01
7	0.1753652324E-02	0.6697399434E+03	0.1694019149E-02
8	-0.4334859620E-03	-0.4730726377E+02	-0.6454771710E-04
9	0.3325699282E-04	0.1265125057E+01	0.1003003098E-05

Table 10-2
Constants for Saturated Vapor Enthalpy

B_n	$P < 1467.6$	Pressure: $1467.6 \le P < 2586.0$	$2586.0 \le 3208.0$
1	0.1105836875E+04	0.5918671729E+06	0.9059978254E+03
2	0.1436943768E+02	-0.2559433320E+06	0.5561957539E+01
3	0.8018288621E+00	0.3032474387E+05	0.3434189609E+01
4	0.1617232913E-01	0.4109051958E+01	-0.6406390628E+00
5	-0.1501147505E-02	0.3475066877E+00	0.5918579484E-01
6	-0.1237675562E-04	-0.3026047262E+00	-0.2725378570E-02
7	0.3004773304E-05	-0.1022018012E+02	0.5006336938E-04
8	-0.2062390734E-06	0.1591215116E+01	0.0
9	0.0	-0.6768383759E-01	0.0

Table 10-3
Vessel Component Saturated Water Thermal Properties

P_{sat} (psia)	T_{sat} (°F)	ρ_f (lbm/ft^3)	ρ_g (lbm/ft^3)	H_f (Btu/lbm)	H_g (Btu/lbm)	μ_f (lbm/hr/ft)	μ_g (lbm/hr/ft)	k_f (Btu/hr/ft/F)	k_g (Btu/hr/ft/F)	C_{pf} (Btu/lbm/F)	C_{pg} (Btu/lbm/F)	σ (lbf/ft)
0.1	41.97	62.42	0.000	10.00	1079.83	3.61570	0.02262	0.33023	0.01002	1.00440	0.44426	0.00513
0.2	51.93	62.40	0.001	20.00	1084.18	3.06850	0.02295	0.33627	0.01022	1.00320	0.44477	0.00508
0.3	61.91	62.36	0.001	30.00	1088.55	2.64160	0.02331	0.34218	0.01041	1.00140	0.44542	0.00502
0.4	71.90	62.29	0.001	40.00	1092.92	2.30190	0.02368	0.34791	0.01062	0.99975	0.44623	0.00496
0.5	81.91	62.20	0.002	50.00	1097.28	2.02710	0.02406	0.35338	0.01083	0.99851	0.44723	0.00491
0.7	91.93	62.09	0.002	60.00	1101.62	1.80170	0.02445	0.35848	0.01105	0.99776	0.44844	0.00484
1.0	101.95	61.97	0.003	70.00	1105.94	1.61440	0.02485	0.36334	0.01128	0.99743	0.44988	0.00478
1.4	111.98	61.83	0.004	80.00	1110.23	1.45700	0.02526	0.36765	0.01152	0.99745	0.45157	0.00472
1.8	122.00	61.68	0.005	90.00	1114.49	1.32340	0.02568	0.37183	0.01177	0.99774	0.45353	0.00465
2.3	132.02	61.52	0.007	100.00	1118.70	1.20900	0.02611	0.37530	0.01203	0.99823	0.45577	0.00459
3.0	142.04	61.34	0.009	110.00	1122.86	1.11020	0.02654	0.37863	0.01230	0.99888	0.45832	0.00452
3.9	152.04	61.15	0.011	120.00	1126.97	1.02440	0.02698	0.38146	0.01258	0.99965	0.46117	0.00445
5.0	162.04	60.95	0.014	130.00	1131.04	0.94915	0.02742	0.38403	0.01287	1.00050	0.46435	0.00438
6.3	172.02	60.75	0.017	140.00	1135.03	0.88297	0.02787	0.38624	0.01318	1.00150	0.46786	0.00432
7.9	182.01	60.53	0.021	150.00	1138.98	0.82425	0.02832	0.38814	0.01349	1.00270	0.47172	0.00424
9.7	191.96	60.31	0.025	160.00	1142.85	0.77208	0.02877	0.38984	0.01381	1.00390	0.47591	0.00417
12.0	201.92	60.07	0.031	170.00	1146.66	0.72533	0.02923	0.39115	0.01415	1.00530	0.48047	0.00410
14.7	211.84	59.83	0.037	180.00	1150.39	0.68345	0.02969	0.39236	0.01449	1.00690	0.48538	0.00403

Table 10-3 (Cont'd)
Vessel Component Saturated Water Thermal Properties

P_{sat} (psia)	T_{sat} (°F)	ρ_f (lbm/ft^3)	ρ_g (lbm/ft^3)	H_f (Btu/lbm)	H_g (Btu/lbm)	μ_f (lbm/hr/ft)	μ_g (lbm/hr/ft)	k_f (Btu/hr/ft/F)	k_g (Btu/hr/ft/F)	C_{pf} (Btu/lbm/F)	C_{pg} (Btu/lbm/F)	σ (lbf/ft)
17.8	221.78	59.58	0.045	190.00	1154.05	0.64561	0.03015	0.39320	0.01486	1.00860	0.49067	0.00396
21.4	231.66	59.32	0.053	200.00	1157.62	0.61149	0.03061	0.39397	0.01523	1.01050	0.49633	0.00388
25.7	241.55	59.05	0.063	210.00	1161.12	0.58043	0.03107	0.39444	0.01561	1.01260	0.50239	0.00381
30.6	251.39	58.78	0.074	220.00	1164.50	0.55228	0.03153	0.39481	0.01601	1.01490	0.50882	0.00373
36.2	261.22	58.50	0.087	230.00	1167.79	0.52655	0.03199	0.39496	0.01642	1.01740	0.51569	0.00366
42.5	271.02	58.21	0.101	240.00	1170.98	0.50302	0.03245	0.39498	0.01684	1.02010	0.52299	0.00358
49.8	280.80	57.92	0.117	250.00	1174.05	0.48145	0.03291	0.39485	0.01727	1.02300	0.53075	0.00351
58.0	290.54	57.61	0.135	260.00	1177.01	0.46163	0.03337	0.39456	0.01772	1.02610	0.53899	0.00343
67.2	300.26	57.30	0.155	270.00	1179.84	0.44339	0.03383	0.39418	0.01817	1.02940	0.54775	0.00335
77.6	309.93	56.99	0.177	280.00	1182.54	0.42656	0.03429	0.39358	0.01864	1.03290	0.55706	0.00327
89.1	319.58	56.66	0.202	290.00	1185.10	0.41101	0.03474	0.39293	0.01912	1.03670	0.56696	0.00320
101.8	329.19	56.34	0.229	300.00	1187.53	0.39661	0.03520	0.39205	0.01962	1.04060	0.57748	0.00312
116.0	338.76	56.00	0.260	310.00	1189.82	0.38325	0.03565	0.39113	0.02012	1.04470	0.58869	0.00304
131.6	348.28	55.66	0.293	320.00	1191.95	0.37083	0.03610	0.39000	0.02064	1.04910	0.60063	0.00296
148.6	357.77	55.31	0.329	330.00	1193.94	0.35927	0.03655	0.38882	0.02116	1.05380	0.61336	0.00288
167.4	367.21	54.95	0.368	340.00	1195.77	0.34849	0.03699	0.38743	0.02170	1.05870	0.62693	0.00280
187.8	376.61	54.59	0.411	350.00	1197.44	0.33842	0.03744	0.38597	0.02225	1.06390	0.64141	0.00272

Table 10-3 (Cont'd)
Vessel Component Saturated Water Thermal Properties

P_{sat} (psia)	T_{sat} (°F)	ρ_f (lbm/ft^3)	ρ_g (lbm/ft^3)	H_f (Btu/lbm)	H_g (Btu/lbm)	μ_f (lbm/hr/ft)	μ_g (lbm/hr/ft)	k_f (Btu/hr/ft/F)	k_g (Btu/hr/ft/F)	C_{pf} (Btu/lbm/F)	C_{pg} (Btu/lbm/F)	σ (lbf/ft)
210.0	385.96	54.22	0.458	360.00	1198.96	0.32898	0.03788	0.38435	0.02281	1.06940	0.65687	0.00264
234.0	395.26	53.85	0.508	370.00	1200.30	0.32014	0.03832	0.38265	0.02338	1.07530	0.67338	0.00256
260.0	404.50	53.47	0.563	380.00	1201.48	0.31182	0.03876	0.38078	0.02396	1.08150	0.69101	0.00248
288.0	413.69	53.08	0.622	390.00	1202.49	0.30399	0.03920	0.37881	0.02455	1.08820	0.70984	0.00240
318.1	422.83	52.69	0.686	400.00	1203.32	0.29660	0.03964	0.37667	0.02516	1.09540	0.72995	0.00232
350.4	431.90	52.29	0.755	410.00	1203.97	0.28961	0.04008	0.37441	0.02578	1.10300	0.75144	0.00224
384.9	440.91	51.88	0.828	420.00	1204.44	0.28299	0.04052	0.37199	0.02642	1.11130	0.77439	0.00216
421.6	449.86	51.47	0.907	430.00	1204.71	0.27670	0.04095	0.36946	0.02707	1.12010	0.79891	0.00208
460.7	458.73	51.05	0.992	440.00	1204.79	0.27072	0.04139	0.36679	0.02773	1.12970	0.82510	0.00200
502.1	467.53	50.62	1.082	450.00	1204.67	0.26501	0.04183	0.36401	0.02841	1.13990	0.85307	0.00192
546.0	476.26	50.18	1.178	460.00	1204.34	0.25954	0.04227	0.36106	0.02912	1.15100	0.88295	0.00185
592.2	484.91	49.74	1.281	470.00	1203.79	0.25431	0.04271	0.35800	0.02984	1.16290	0.91488	0.00177
641.2	493.51	49.29	1.391	480.00	1203.02	0.24926	0.04315	0.35472	0.03059	1.17590	0.94916	0.00169
692.1	501.94	48.84	1.507	490.00	1202.04	0.24444	0.04359	0.35138	0.03136	1.18980	0.98549	0.00161
745.9	510.35	48.37	1.631	500.00	1200.81	0.23976	0.04404	0.34782	0.03218	1.20490	1.02460	0.00154
802.0	518.65	47.90	1.762	510.00	1199.35	0.23524	0.04450	0.34426	0.03300	1.22130	1.06650	0.00146
860.5	526.84	47.42	1.901	520.00	1197.64	0.23086	0.04495	0.34043	0.03390	1.23890	1.11140	0.00139

Table 10-3 (Cont'd)
Vessel Component Saturated Water Thermal Properties

P_{sat} (psia)	T_{sat} (°F)	ρ_f (lbm/ft³)	ρ_g (lbm/ft³)	H_f (Btu/lbm)	H_g (Btu/lbm)	μ_f (lbm/hr/ft)	μ_g (lbm/hr/ft)	k_f (Btu/hr/ft/F)	k_g (Btu/hr/ft/F)	C_{pf} (Btu/lbm/F)	C_{pg} (Btu/lbm/F)	σ (lbf/ft)
921.3	534.91	46.93	2.048	530.00	1195.69	0.22662	0.04541	0.33660	0.03480	1.25800	1.15940	0.00132
984.4	542.86	46.44	2.204	540.00	1193.50	0.22250	0.04588	0.33255	0.03581	1.27870	1.21100	0.00124
1050.0	550.72	45.93	2.368	550.00	1191.03	0.21846	0.04636	0.32846	0.03684	1.30120	1.26690	0.00117
1117.8	558.47	45.42	2.543	560.00	1188.31	0.21452	0.04685	0.32427	0.03795	1.32560	1.32710	0.00111
1187.8	566.10	44.89	2.727	570.00	1185.33	0.21067	0.04734	0.31999	0.03915	1.35220	1.39240	0.00104
1259.9	573.61	44.36	2.922	580.00	1182.08	0.20689	0.04785	0.31571	0.04038	1.38120	1.46330	0.00097
1334.0	580.98	43.82	3.127	590.00	1178.57	0.20318	0.04837	0.31134	0.04174	1.41290	1.54050	0.00091
1410.0	588.22	43.27	3.344	600.00	1174.80	0.19953	0.04891	0.30694	0.04324	1.44770	1.62510	0.00084
1487.8	595.33	42.71	3.574	610.00	1170.75	0.19594	0.04946	0.30255	0.04486	1.48590	1.71800	0.00078
1567.2	602.29	42.14	3.816	620.00	1166.42	0.19239	0.05004	0.29817	0.04663	1.52810	1.82060	0.00073
1648.2	609.11	41.56	4.072	630.00	1161.76	0.18889	0.05063	0.29382	0.04854	1.57490	1.93450	0.00067
1730.4	615.77	40.96	4.343	640.00	1156.76	0.18543	0.05125	0.28954	0.05069	1.62710	2.06150	0.00061
1813.8	622.28	40.36	4.629	650.00	1151.40	0.18200	0.05190	0.28531	0.05307	1.68570	2.20410	0.00056
1898.2	628.62	39.74	4.931	660.00	1145.66	0.17859	0.05258	0.28115	0.05565	1.75180	2.36520	0.00051
1983.9	634.84	39.11	5.253	670.00	1139.49	0.17518	0.05330	0.27709	0.05848	1.82770	2.55010	0.00046
2069.5	640.84	38.47	5.593	680.00	1132.96	0.17181	0.05405	0.27314	0.06173	1.91440	2.76120	0.00042
2155.4	646.65	37.81	5.953	690.00	1126.01	0.16845	0.05485	0.26926	0.06527	2.01490	3.00550	0.00037

Table 10-3 (Cont'd)
Vessel Component Saturated Water Thermal Properties

P_{sat} (psia)	T_{sat} (°F)	ρ_f (lbm/ft^3)	ρ_g (lbm/ft^3)	H_f (Btu/lbm)	H_g (Btu/lbm)	μ_f (lbm/hr/ft)	μ_g (lbm/hr/ft)	k_f (Btu/hr/ft/F)	k_g (Btu/hr/ft/F)	C_{pf} (Btu/lbm/F)	C_{pg} (Btu/lbm/F)	σ (lbf/ft)
2241.1	652.28	37.14	6.335	700.00	1118.63	0.16509	0.05570	0.26545	0.06919	2.13280	3.29110	0.00033
2326.3	657.69	36.46	6.740	710.00	1110.82	0.16173	0.05661	0.26186	0.07374	2.27250	3.62830	0.00029
2410.6	662.89	35.76	7.170	720.00	1102.59	0.15837	0.05758	0.25836	0.07854	2.44030	4.03110	0.00025
2494.0	667.89	35.03	7.630	730.00	1093.91	0.15497	0.05863	0.25520	0.08401	2.64650	4.52210	0.00022
2575.2	672.62	34.29	8.117	740.00	1084.90	0.15156	0.05975	0.25212	0.08983	2.90110	5.12290	0.00019
2653.8	677.08	33.53	8.635	750.00	1075.52	0.14813	0.06096	0.24935	0.09704	3.22290	5.87350	0.00016
2729.8	681.29	32.75	9.190	760.00	1065.74	0.14464	0.06228	0.24673	0.10465	3.64070	6.14500	0.00013
2801.8	685.18	31.95	9.777	770.00	1055.59	0.14113	0.06371	0.24493	0.11447	4.19150	6.14500	0.00011
2869.6	688.77	31.12	10.403	780.00	1045.00	0.13755	0.06526	0.24313	0.12429	4.94400	6.14500	0.00008
2931.9	692.01	30.27	11.066	790.00	1034.06	0.13393	0.06694	0.24418	0.13890	5.99630	6.14500	0.00007
2988.5	694.90	29.39	11.771	800.00	1022.75	0.13024	0.06878	0.24576	0.15442	6.14500	6.14500	0.00005
3038.4	697.40	28.48	12.513	810.00	1011.17	0.12649	0.07076	0.24734	0.16993	6.14500	6.14500	0.00004
3081.4	699.53	27.55	13.293	820.00	999.32	0.12268	0.07291	0.25288	0.19158	6.14500	6.14500	0.00002
3116.7	701.26	26.60	14.101	830.00	987.40	0.11885	0.07520	0.26470	0.22270	6.14500	6.14500	0.00002
3144.7	702.62	25.63	14.927	840.00	975.50	0.11500	0.07761	0.29237	0.27220	6.14500	6.14500	0.00001
3165.7	703.63	24.65	15.750	850.00	963.98	0.11119	0.08008	0.81017	0.80644	6.14500	6.14500	0.00000
3180.5	704.34	23.68	16.541	860.00	953.38	0.10744	0.08253	2.55507	2.55265	6.14500	6.14500	0.00000

Table 10-3 (Cont'd)

Vessel Component Saturated Water Thermal Properties

P_{sat} (psia)	T_{sat} (°F)	ρ_f (lbm/ft^3)	ρ_g (lbm/ft^3)	H_f (Btu/lbm)	H_g (Btu/lbm)	μ_f (lbm/hr/ft)	μ_g (lbm/hr/ft)	k_f (Btu/hr/ft/F)	k_g (Btu/hr/ft/F)	C_{pf} (Btu/lbm/F)	C_{pg} (Btu/lbm/F)	σ (lbf/ft)
3190.3	704.81	22.72	17.243	870.00	944.22	0.10382	0.08475	4.29997	4.29886	6.14500	6.14500	0.00000
3196.0	705.08	21.78	17.759	880.00	937.47	0.10034	0.08642	10.00000	10.00000	6.14500	6.14500	0.00000
3198.3	705.19	20.87	17.987	890.00	934.25	0.09704	0.08717	50.00000	50.00000	6.14500	6.14500	0.00000
3206.4	705.39	20.16	19.244	900.00	917.46	0.09704	0.08717	100.00000	100.00000	6.14500	6.14500	0.00000

Table 10-4
Superheated Vapor Temperature Constants

Term	P ≤ 1000 psia or P > 1000 psia and h ≥ 1280 Btu/lbm	P > 1000 psia and H_v < 1280 Btu/lbm
A_1	-1.0659659E+04	-4.5298646E+03
A_2	2.0110905E+01	1.5358850E+01
A_3	-1.250954E-02	-1.5655537E-02
A_4	2.8274992E-06	5.2687849E-06
A_5	4.9815820	4.4185386E-01
A_6	-7.7618225E-06	-9.1654905E-06
A_7	2.4391612E-10	2.7549766E-10
A_8	-9.8147341E-03	-1.1541553E-03
A_9	6.5824890E-06	1.2384560E-06
A_{10}	-1.4749938E-09	-4.1724604E-10
B_1	-2.8557816	1.2659960E+02
B_2	1.3250230E-02	-2.5611614E-01
B_3	-1.0521514E-05	2.2270593E-04
B_4	2.5007955E-09	-5.9928922E-08
B_5	-3.4620214	-2.1818030E+01
B_6	-3.6261637E-02	1.3424036
B_7	7.3529479E-04	-4.9110372E-02
B_8	5.7703098E-03	2.7966370E-02
B_9	-2.9972073E-06	-2.4665012E-05
B_{10}	5.2037300E-10	6.7723080E-09

Table 10-5

Subcooled Water Density Constants

C_{CXij}					
i=	1	2	3	4	5
j=1	-0.413450E1	0.13252E-4	0.15812E-5	-0.21959E-8	0.21683E-11
j=2	-0.59428E-5	0.63377E-7	-0.39974E-9	0.69391E-12	-0.36159E-15
j=3	0.15681E-8	-0.40711E-10	0.25401E-12	-0.52372E-15	0.32503E-18

Table 10-6

Saturated Steam Internal Energy Constants

i	*P*	AVE(*i*)	BVE(*i*)	CVE(*i*)
1	≤ 2E+6	2.619410618E+6	-4.995E+10	--
2	> 2E+6	2.5896E+6	6.350E-3	-1.0582E-9

Table 10-7

Saturated Steam Enthalpy Constants

i	*P*	AVG(*i*)	BVG(*i*)	CVG(*i*)
1	≤ 2E+6	1.06655448	1.02E-8	-2.548E-15
2	> 2E+6	1.0764	3.625E-10	-9.063E-17

Table 10-8

Saturated Liquid Internal Energy Constants

i	*ALE(i)*	*BLE(i)*	*CLE(i)*	*DLE(i)*	*ELE(i)*
1	1.75880E+4	3.7402E+3	4.02435	-0.0157294	3.1301E-5
2	6.18527E+6	-8.14547E+4	4.46598E+2	-1.04116	9.26022E-4
3	2.283789029E+9	-2.62215677E+7	1.12948667E+5	-2.16233985E+2	0.155283438

Table 10-9
Constants for Specific Heat

$B_{0\ell} = 2.394907 \times 10^{-4}$ $C_{0\ell} = 1.193203 \times 10^{-11}$ $D_{0\ell} = -3.944067 \times 10^{-17}$	$B_{1\ell} = -5.196250 \times 10^{-13}$ $C_{1\ell} = 2.412704 \times 10^{-18}$ $D_{1\ell} = -1.680771 \times 10^{-24}$	$C_{1v} = 1.68835968 \times 10^{3}$ $C_{2v} = 0.6029856$ $C_{3v} = 4.820979623 \times 10^{2}$ $C_{4v} = 2.95317905 \times 10^{7}$ $C_{5v} = 1.8$ $C_{6v} = 4.60 \times 10^{2}$

Table 10-10
Liquid Viscosity Constants

$A_{0\ell} = 1.299470299\times10^{-3}$ $A_{1\ell} = -9.264032108\times10^{-4}$ $A_{2\ell} = 3.81047061\times10^{-4}$ $A_{3\ell} = -8.219444458\times10^{-5}$ $A_{4\ell} = 7.022437984\times10^{-6}$	$B_{0\ell} = -6.5959\times10^{-12}$ $B_{1\ell} = 6.763\times10^{-12}$ $B_{2\ell} = -2.88825\times10^{-12}$ $B_{3\ell} = 4.4525\times10^{-13}$
$D_{0\ell} = 3.026032306\times10^{-4}$ $D_{1\ell} = -1.836606896\times10^{-4}$ $D_{2\ell} = 7.567075775\times10^{-5}$ $D_{3\ell} = -1.647878879\times10^{-5}$ $D_{4\ell} = 1.416457633\times10^{-6}$	$E_{0\ell} = 1.4526052612\times10^{-3}$ $E_{1\ell} = -6.9880084985\times10^{-9}$ $E_{2\ell} = 1.5210230334\times10^{-14}$ $E_{3\ell} = -1.2303194946\times10^{-20}$
$F_{0\ell} = -3.8063507533\times10^{-11}$ $F_{1\ell} = 3.9285207677\times10^{-16}$ $F_{2\ell} = -1.2585799292\times10^{-21}$ $F_{3\ell} = 1.2860180788\times10^{-27}$	$H_O = 8.581289699\times10^{-6}$ $c_{0n} = 4.265884\times10^{4}$ $P_o = 6.894575293\times10^{5}$
$H_{OO} = 3.892077365\times10^{-6}$ $e_{c0n} = 5.53588\times10^{4}$	$e_{h0} = 6.484503981\times10^{-6}$ $c_n = 4.014676\times10^{5}$

Table 10-11
Vapor Viscosity Constants

$A_{0v} = 3.53\times10^{-8}$ $A_{1v} = 6.765\times10^{-11}$ $A_{2v} = 1.021\times10^{-14}$	$B_{1v} = 0.407\times10^{-7}$ $C_{1v} = 8.04\times10^{-6}$ $D_{1v} = 1.858\times10^{-7}$ $E_{1v} = 5.9\times10^{-10}$
$F_{0v} = -0.2885\times10^{-5}$ $F_{1v} = 0.2427\times10^{-7}$ $F_{2v} = -0.67893333333\times10^{-10}$ $F_{3v} = 0.6317037037\times10^{-13}$	$G_{0v} = 0.176\times10^{3}$ $G_{1v} = -1.6$ $G_{2v} = 0.0048$ $G_{3v} = -0.47407407407\times10^{-5}$

Table 10-12
Liquid and Vapor Thermal Conductivity Constants

$A_{\ell 0} = 0.573738622$ $A_{\ell 1} = 0.2536103551$ $A_{\ell 2} = -0.145468269$ $A_{\ell 3} = 0.01387472485$ $A_{\ell 4} = 5.815\times10^{5}$	$A_{v0} = 1.76\times10^{-2}$ $A_{v1} = 5.87\times10^{-5}$ $A_{v2} = 1.04\times10^{-7}$ $A_{v3} = -4.51\times10^{-11}$ $A_{v4} = 2.1482\times10^{5}$	$B_{v0} = 1.0351\times10^{-4}$ $B_{v1} = 0.4198\times10^{-6}$ $B_{v2} = -2.771\times10^{-11}$

Table 10-13
Surface Tension Constants

$$
\begin{aligned}
a_1 &= 1.160936807E-04 \\
a_2 &= 1.12140468E-06 \\
a_3 &= -5.752805180E-09 \\
a_4 &= 1.286274650E-11 \\
a_5 &= -1.149719290E-14
\end{aligned}
$$

Table 10-14
Constants for Specific Heat of Air

i	A_i	B_i
1	-4.20419E-05	7.71027E-05
2	9.61128E-08	-8.56726E-09
3	-1.16383E-11	-4.75772E-12

Table 10-15
Constants for Viscosity of Air

i	a_{ai}	a_{bi}
0	1.708×10^{-5}	1.735×10^{-5}
1	5.927×10^{-8}	4.193×10^{-8}
2	-8.14×10^{-11}	-1.09×10^{-11}

Table 10-16
Specific Heat of Zircaloy-4

T(°K)	C_p (Btu/lbm - °F)
300.0	0.0671
400.0	0.0721
640.0	0.0790
1090.0	0.0896
1093.0	0.1199
1113.0	0.1409
1133.0	0.1469
1153.0	0.1717
1173.0	0.1949
1193.0	0.1839
1213.0	0.1478
1233.0	0.1120
1248.0	0.0850
>1248.0	0.0850

Table 10-17
Chemical Composition of ZIRLO™ and Zircaloy-4 Alloys

Element (wt %)	ZIRLO™ Alloy	Zircaloy-4 Alloy
Sn	0.8-1.2	1.2-1.7
Fe	0.09-0.13	0.18-0.24
Cr	--	0.07-0.13
Fe+Cr	--	0.28-0.37
Nb	0.8-1.2	--
Zr	Balance	Balance

Table 10-18
Specific Heat of ZIRLO™ Alloy

[	
	]a,c

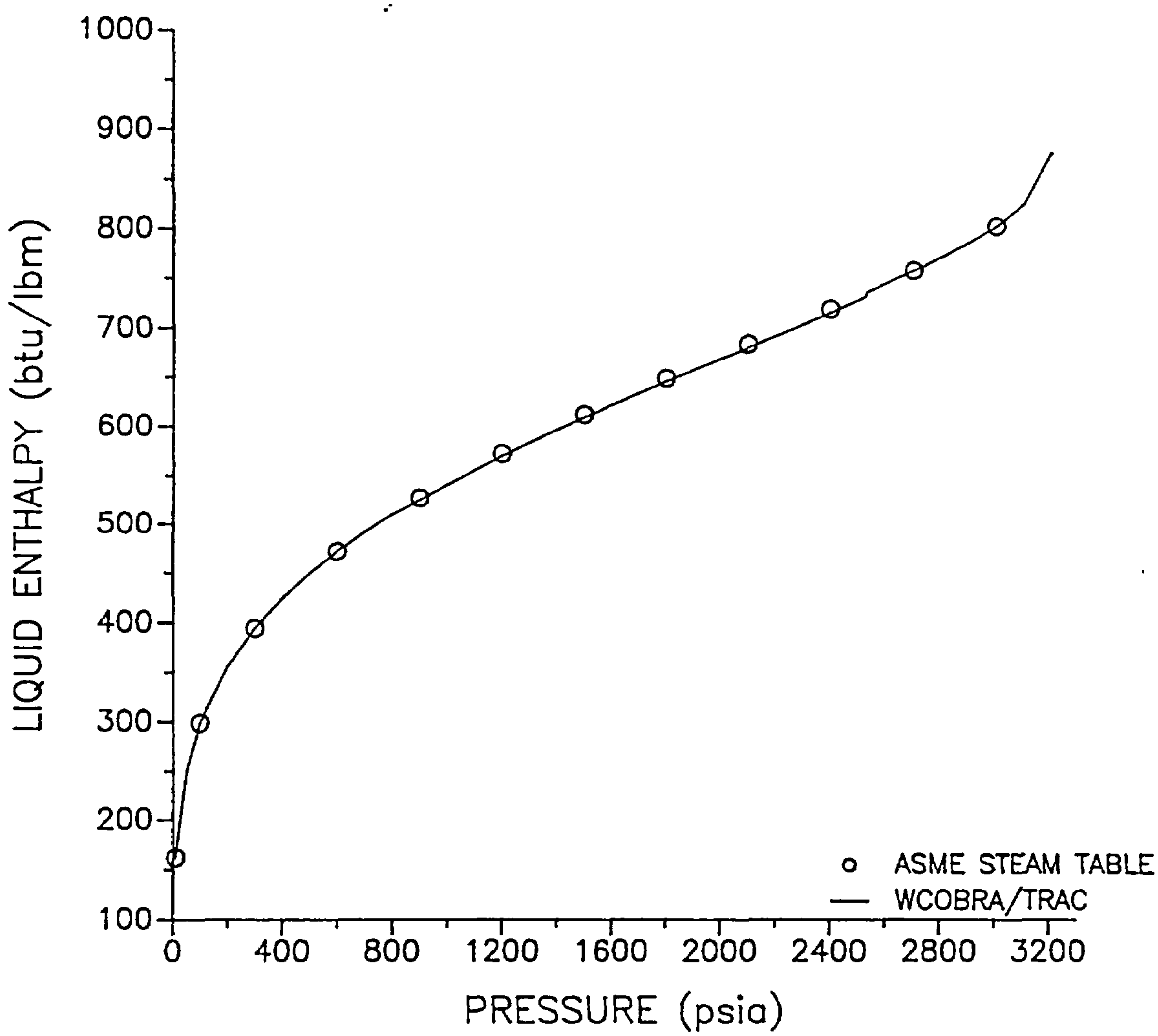

Figure 10-1. WCOBRA/TRAC Vessel Component Saturated Liquid Enthalpy Function

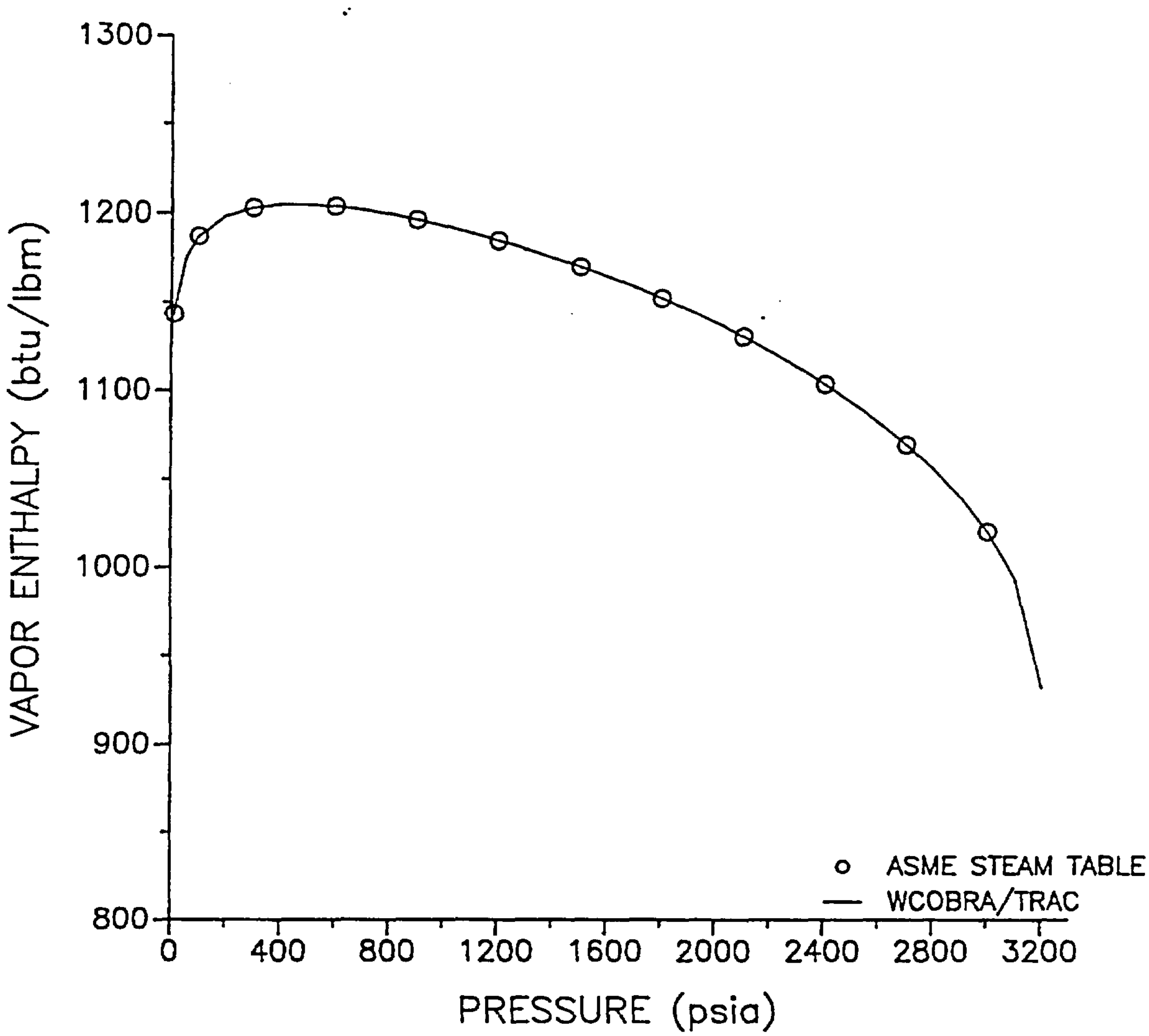

Figure 10-2. WCOBRA/TRAC Vessel Component Saturated Vapor Enthalpy Function

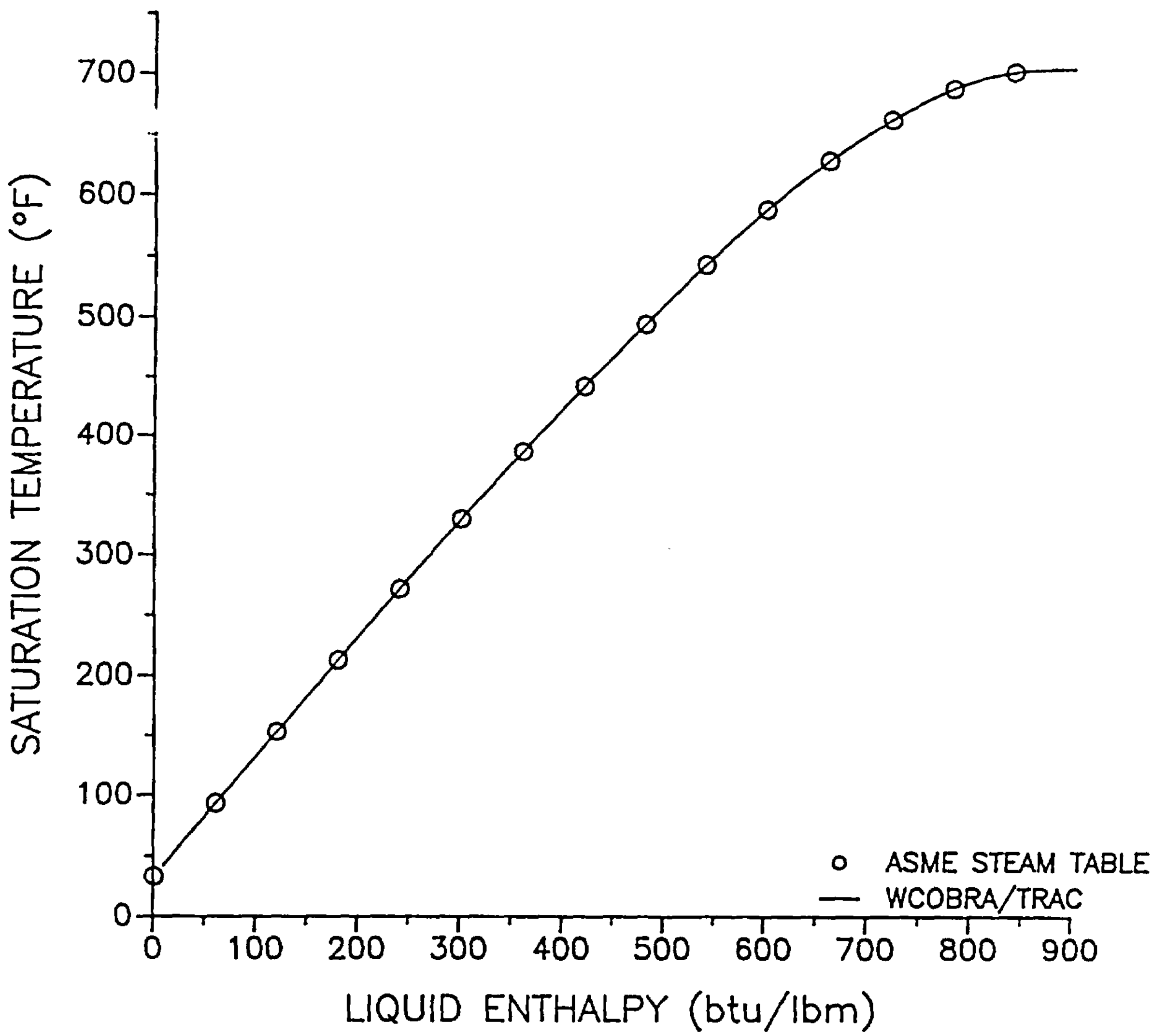

Figure 10-3. WCOBRA/TRAC Vessel Component Saturation Temperature

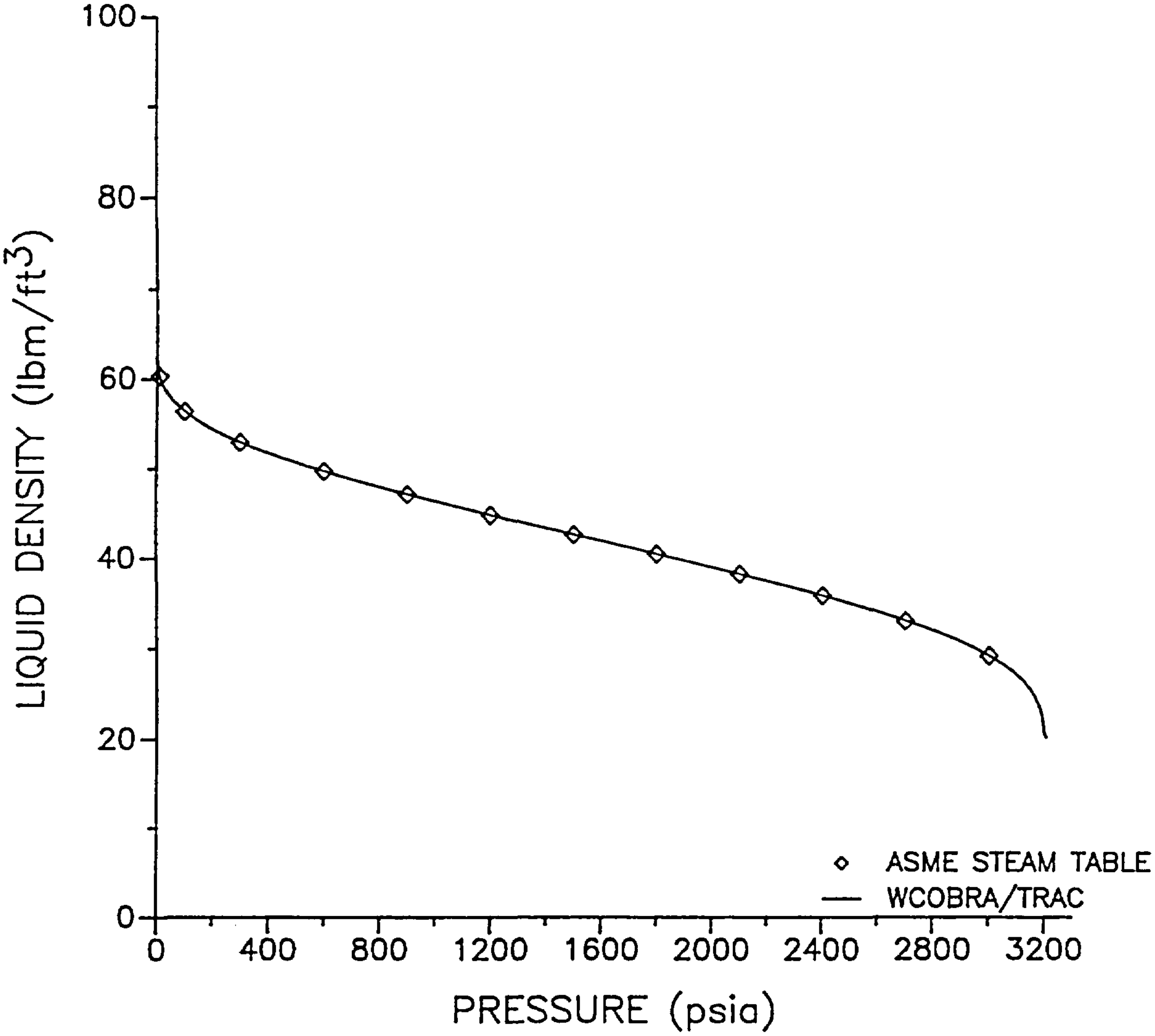

Figure 10-4. WCOBRA/TRAC Vessel Component Saturated Liquid Density

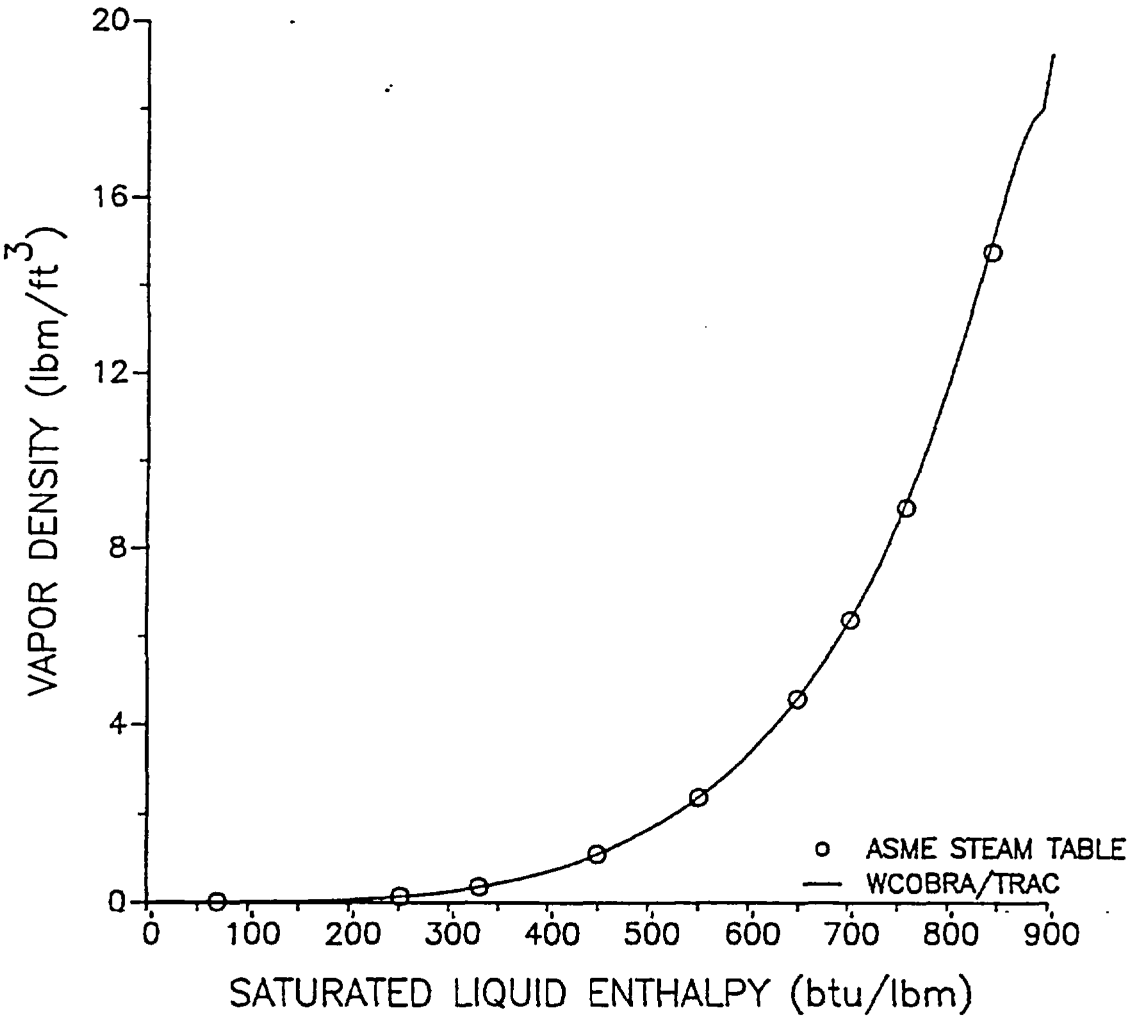

Figure 10-5. WCOBRA/TRAC Vessel Component Saturated Vapor Density

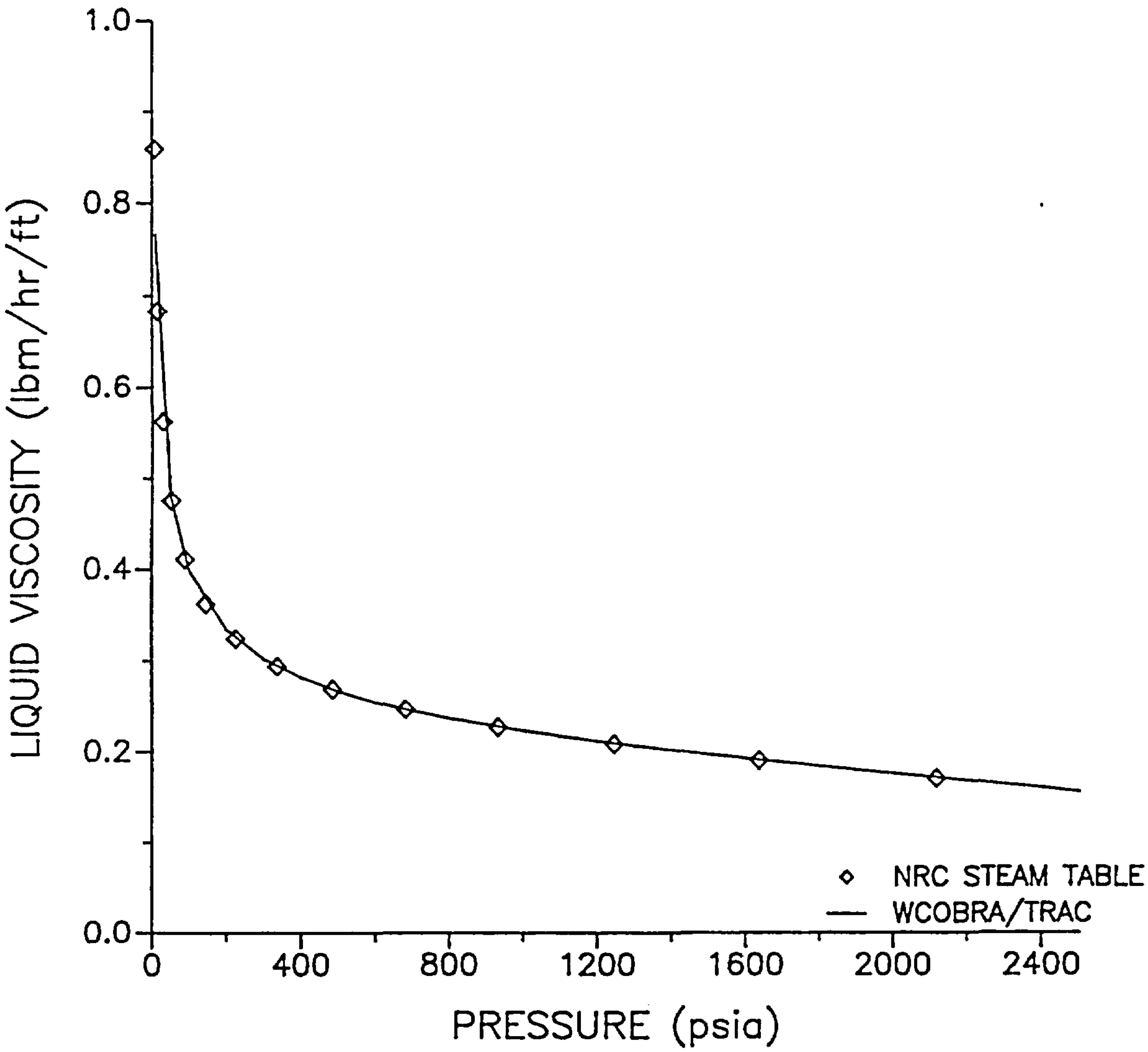

Figure 10-6. WCOBRA/TRAC Vessel Component Saturated Liquid Viscosity

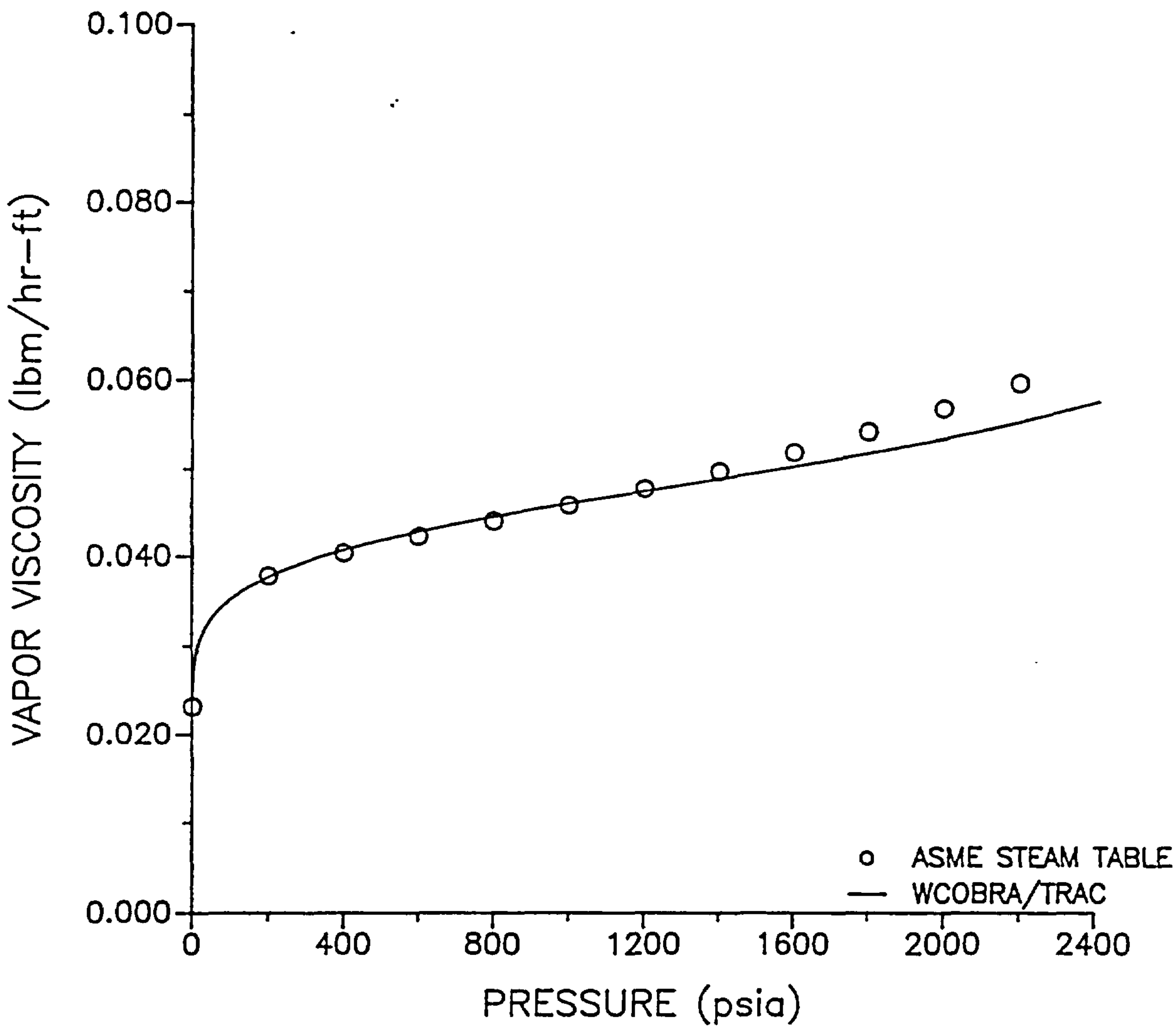

Figure 10-7. WCOBRA/TRAC Vessel Component Saturated Vapor Viscosity

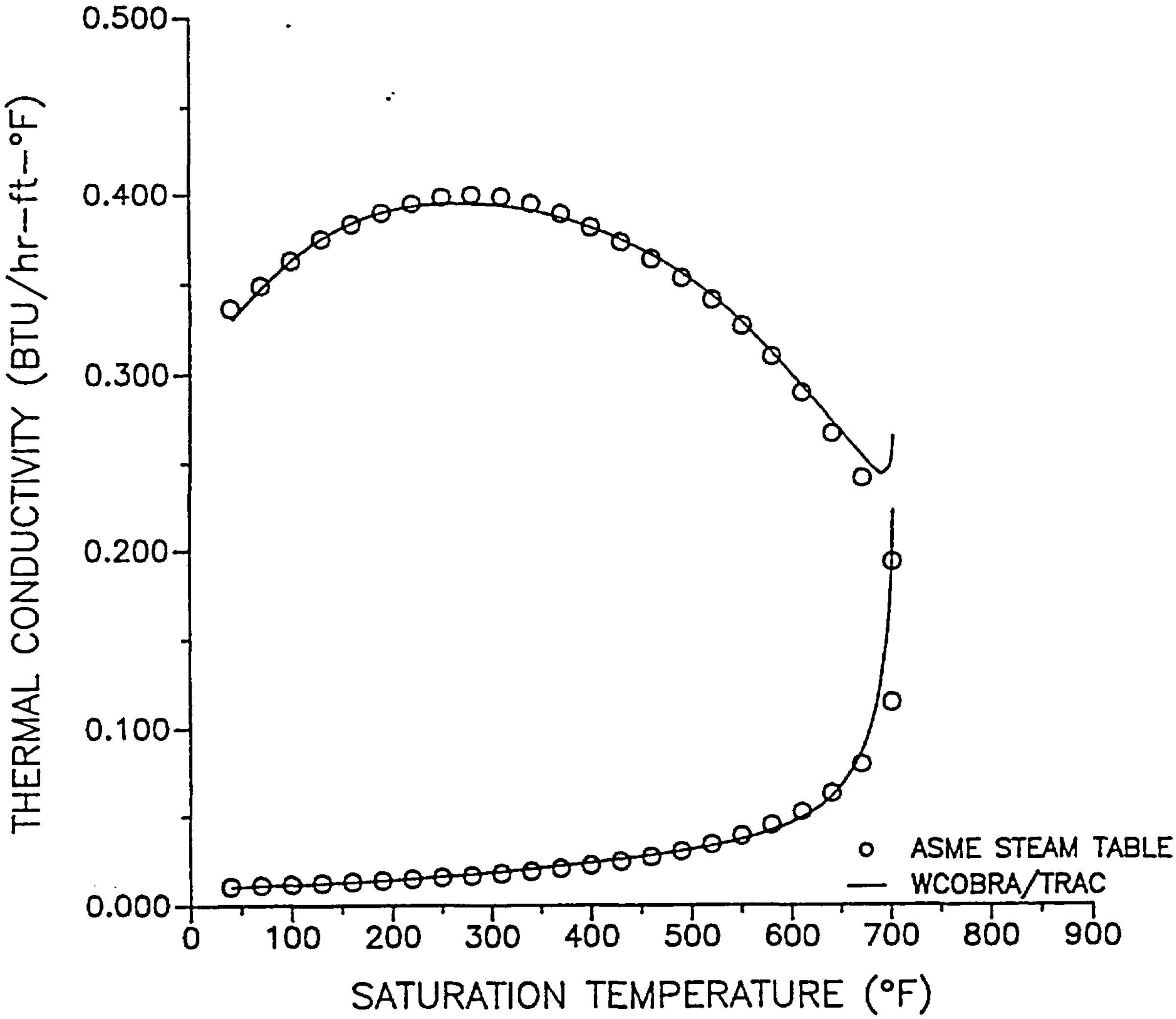

Figure 10-8. WCOBRA/TRAC Vessel Component Saturated Liquid and Vapor Thermal Conductivity

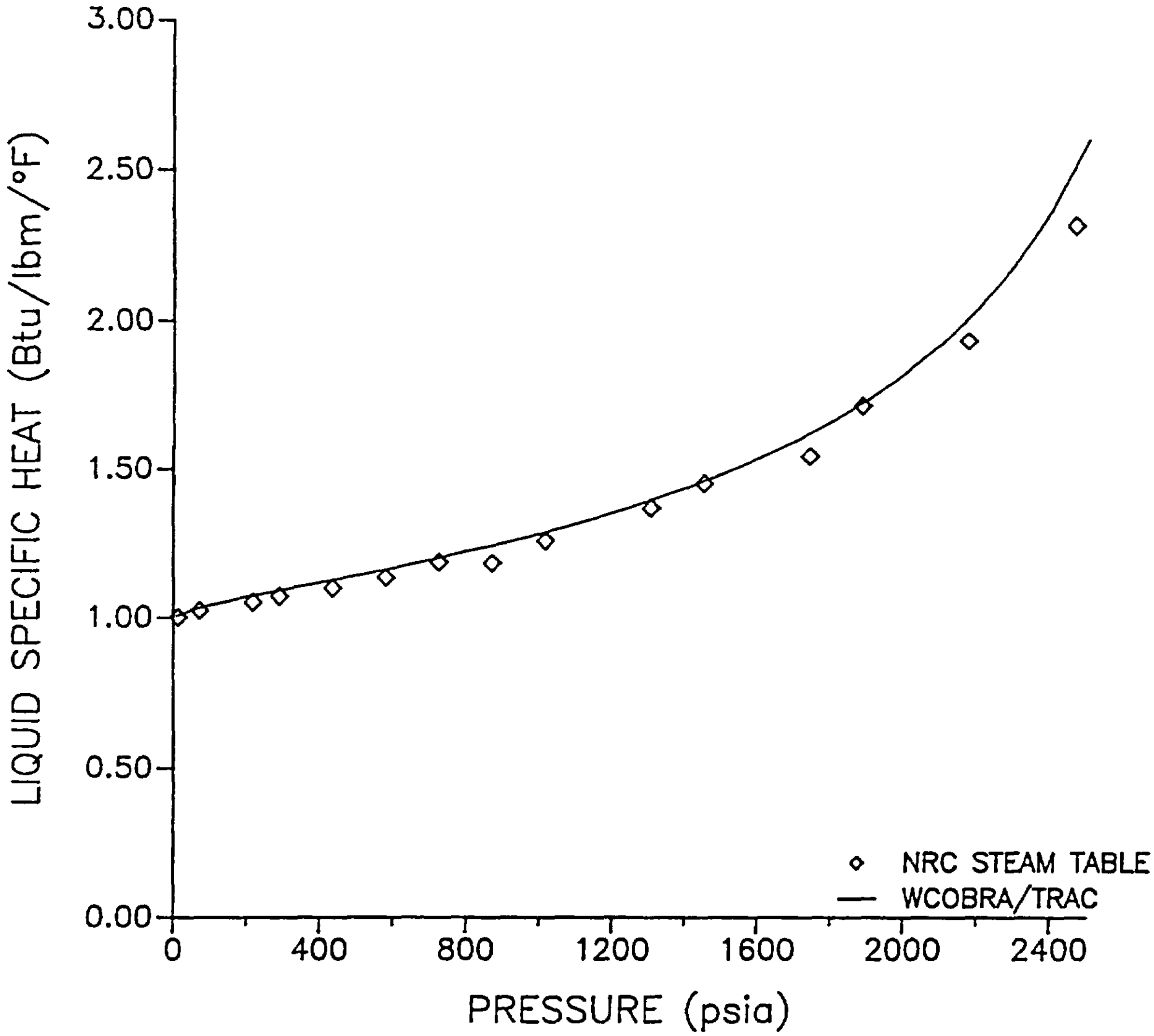

Figure 10-9. WCOBRA/TRAC Vessel Component Saturated Liquid Specific Heat

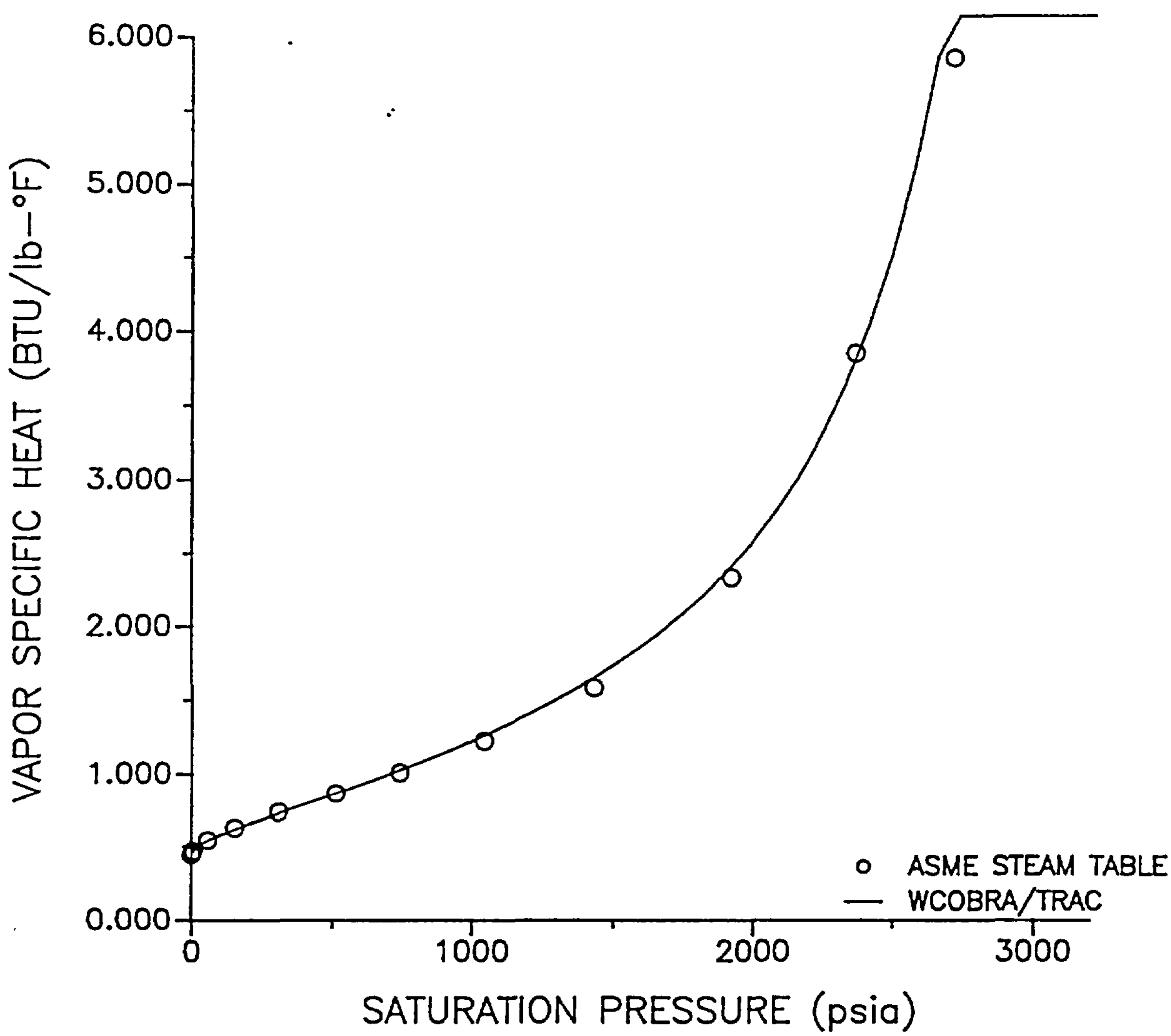

Figure 10-10. WCOBRA/TRAC Vessel Component Saturated Vapor Specific Heat

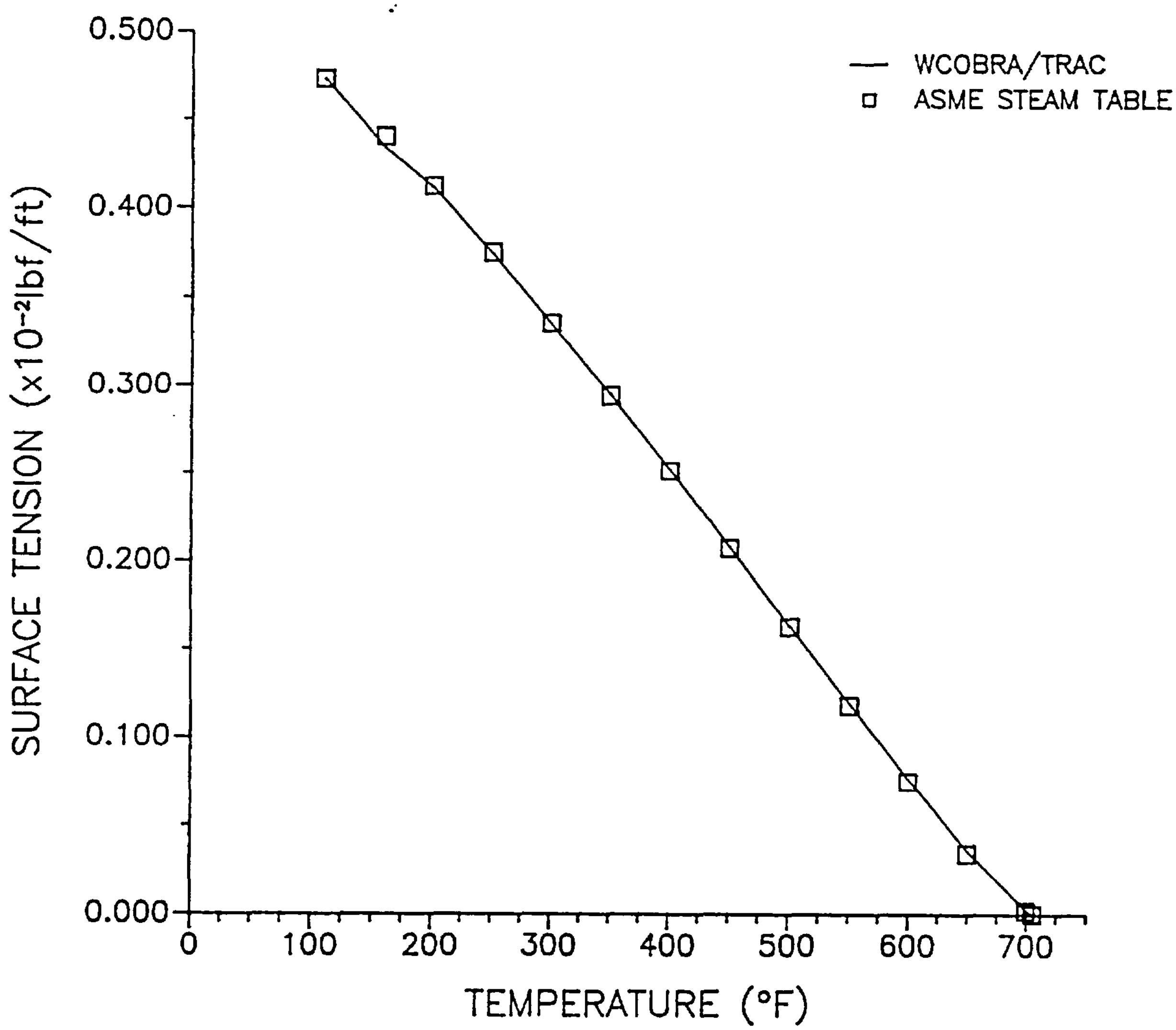

Figure 10-11. WCOBRA/TRAC Vessel Component Saturated Liquid Surface Tension

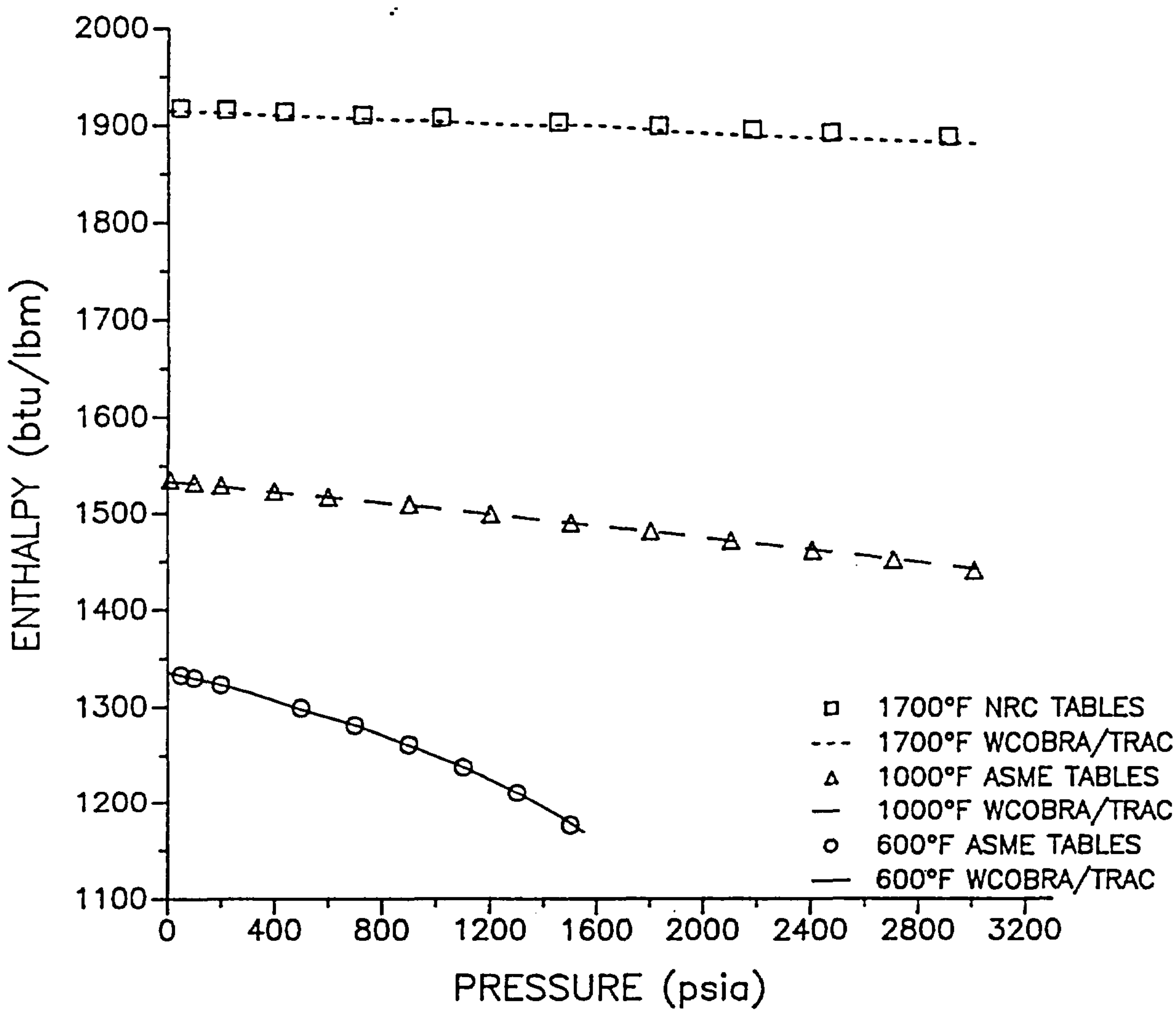

Figure 10-12. WCOBRA/TRAC Vessel Component Superheated Vapor Enthalpy

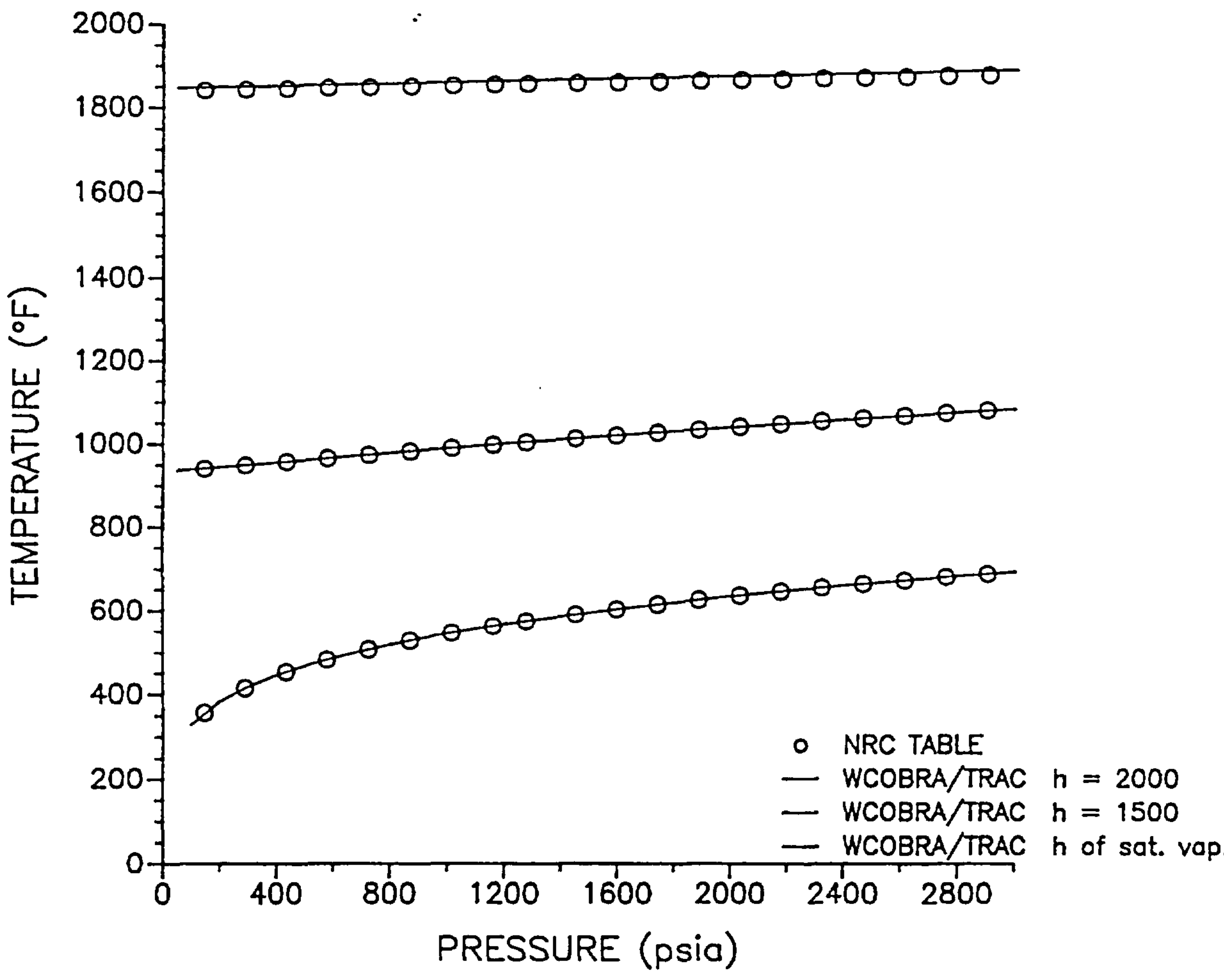

Figure 10-13. WCOBRA/TRAC Vessel Component Superheated Vapor Temperature

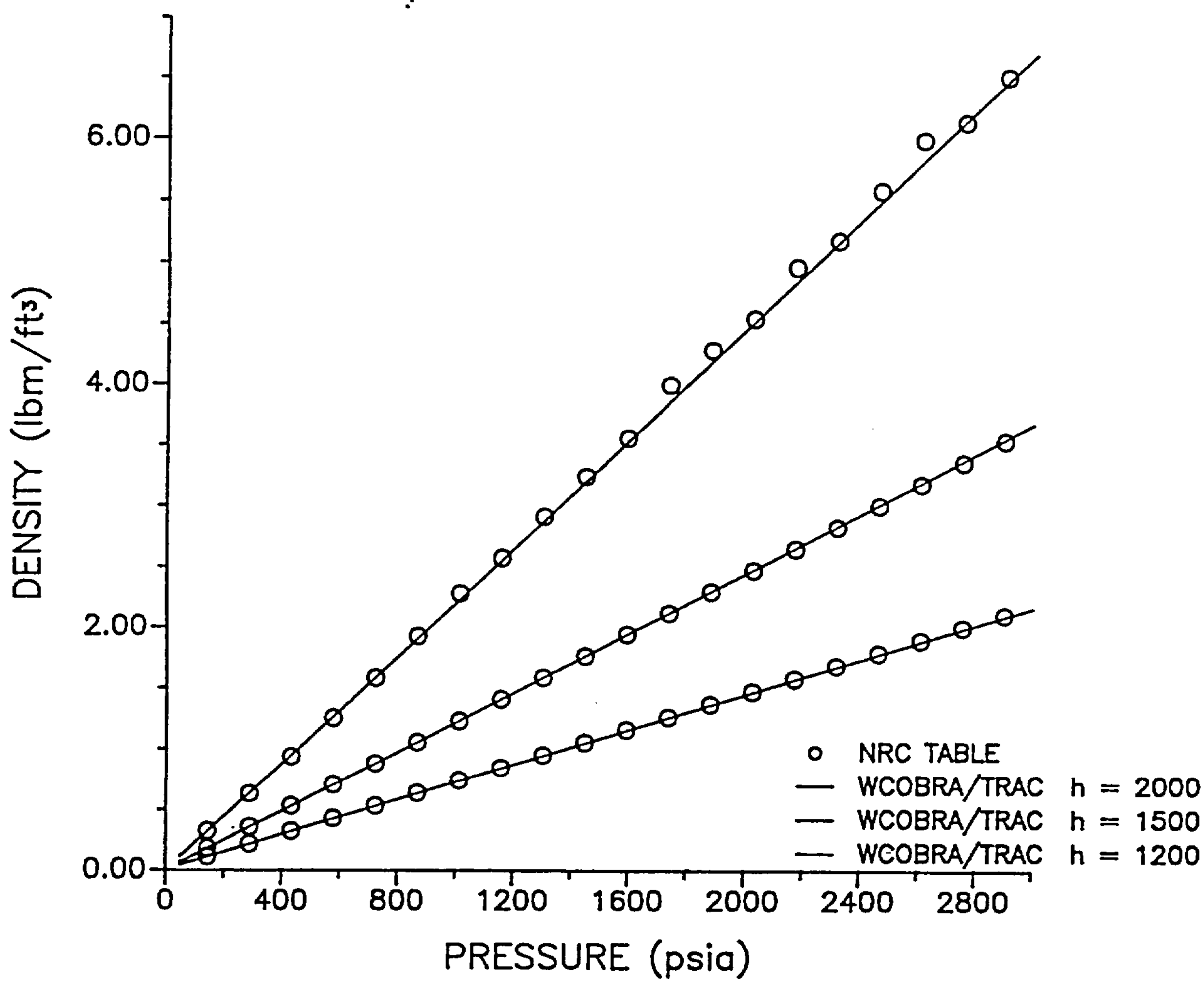

Figure 10-14. WCOBRA/TRAC Vessel Component Superheated Vapor Density

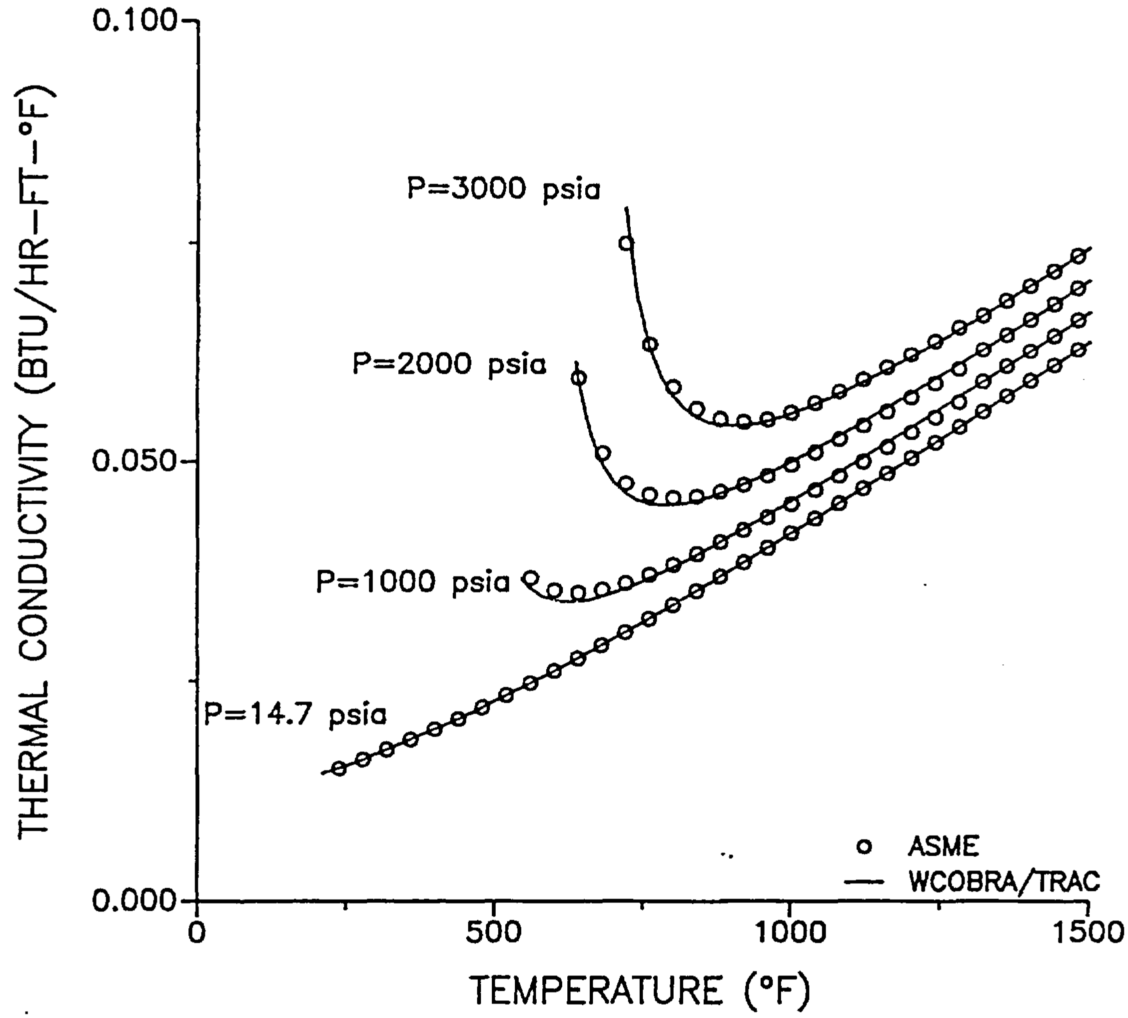

Figure 10-15. WCOBRA/TRAC Vessel Component Superheated Vapor Thermal Conductivity

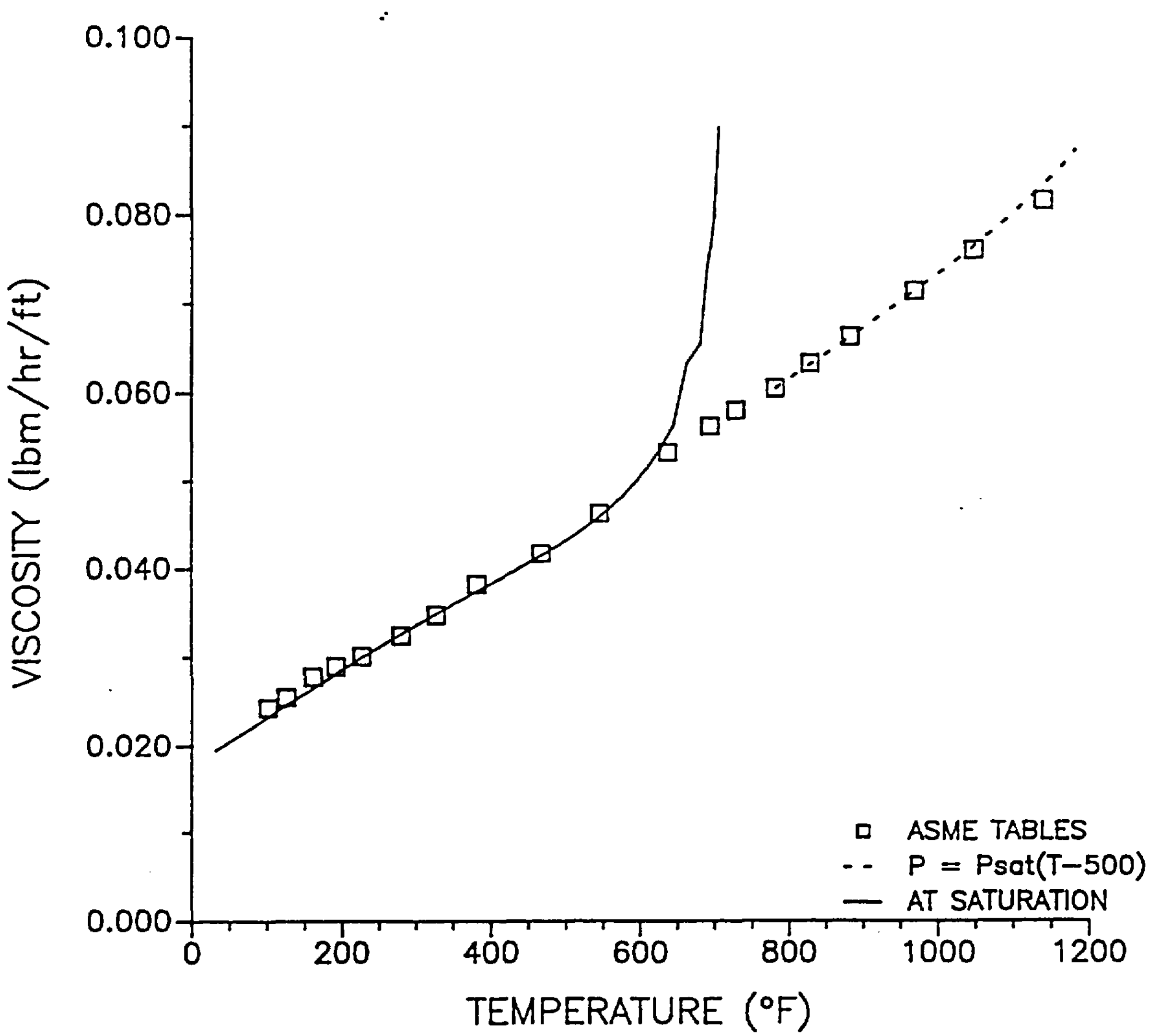

Figure 10-16. WCOBRA/TRAC Vessel Component Superheated Vapor Viscosity

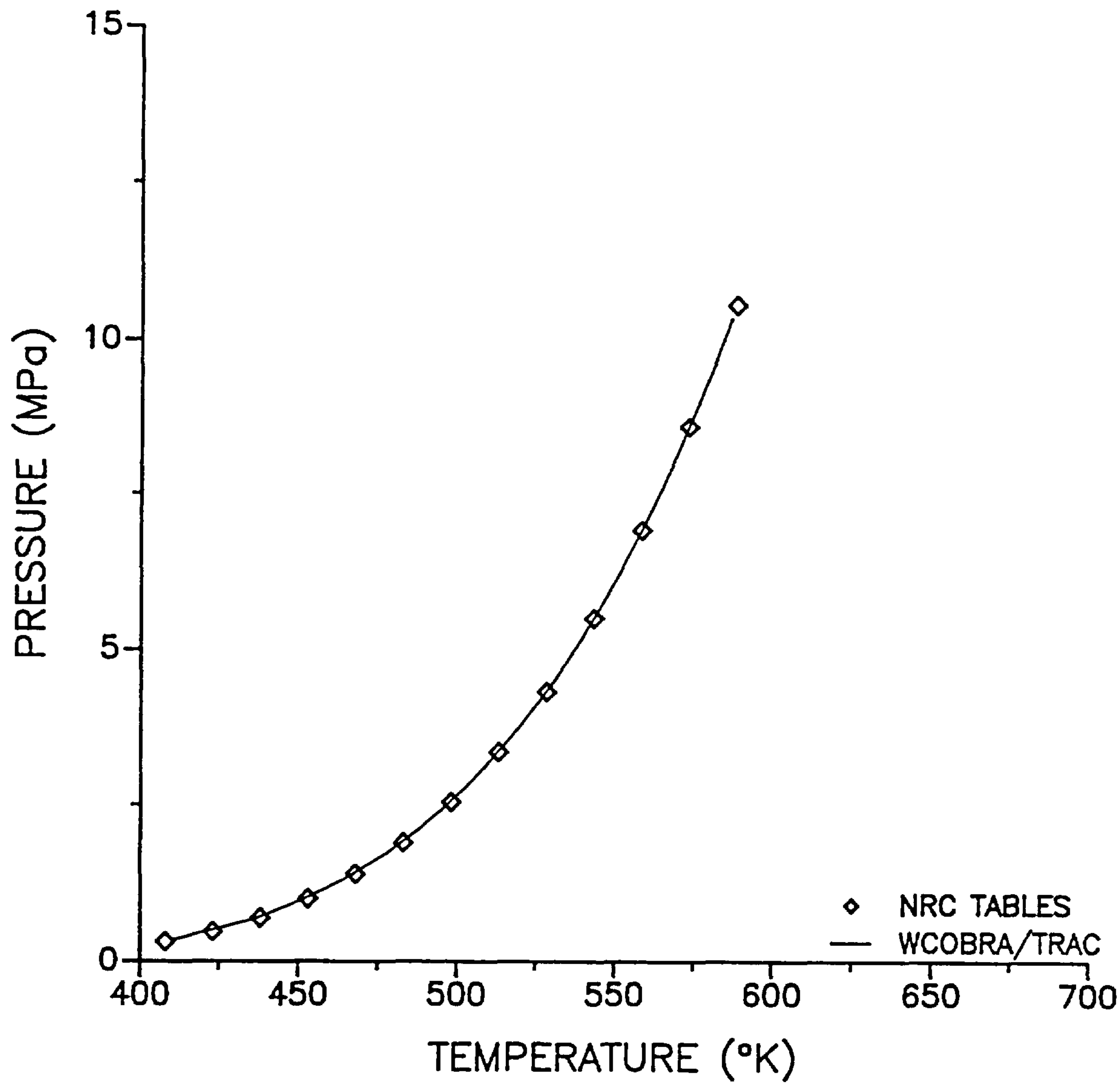

Figure 10-17. WCOBRA/TRAC 1-D Component Saturation Pressure

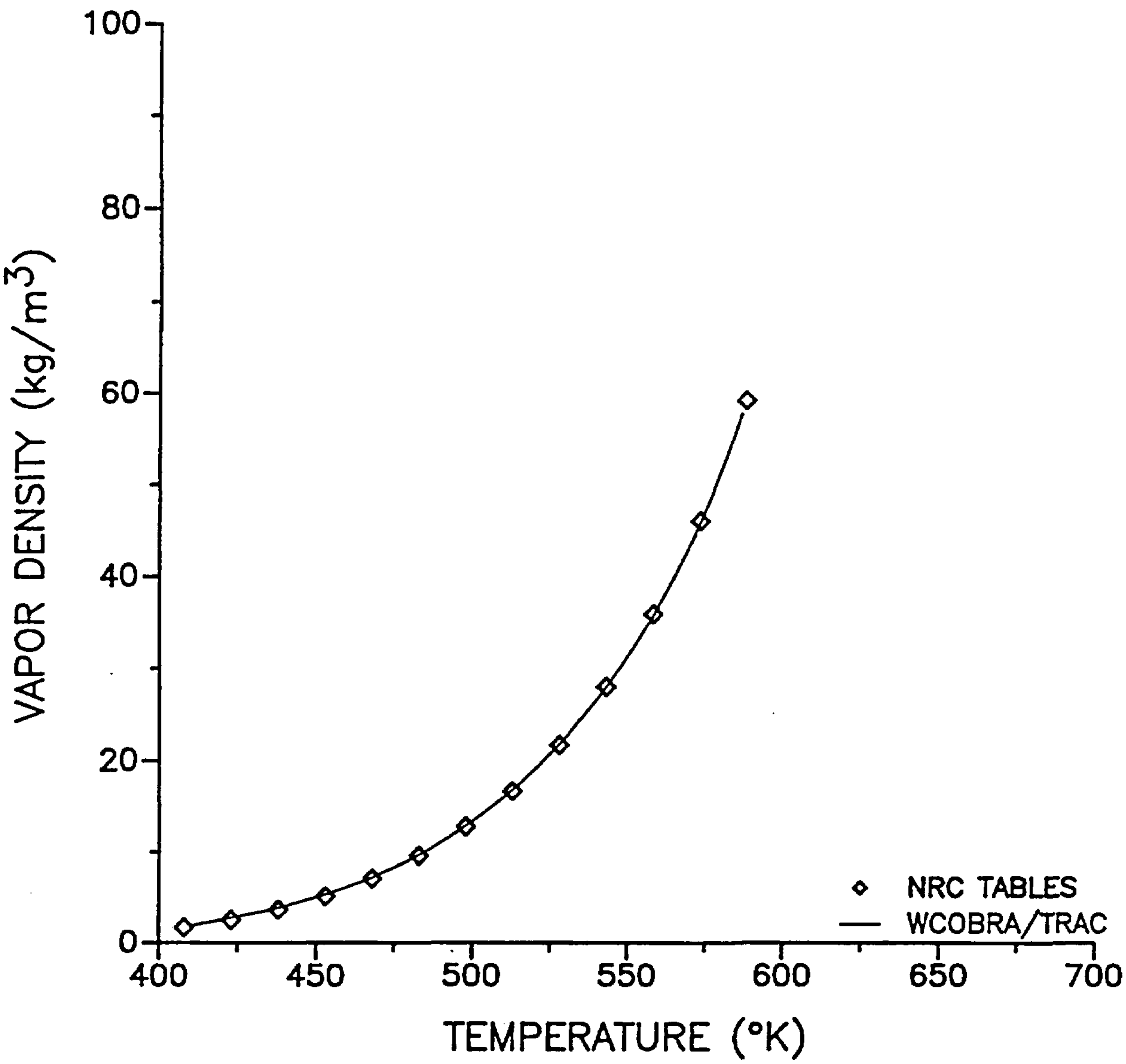

Figure 10-18. WCOBRA/TRAC 1-D Component Saturated Vapor Density

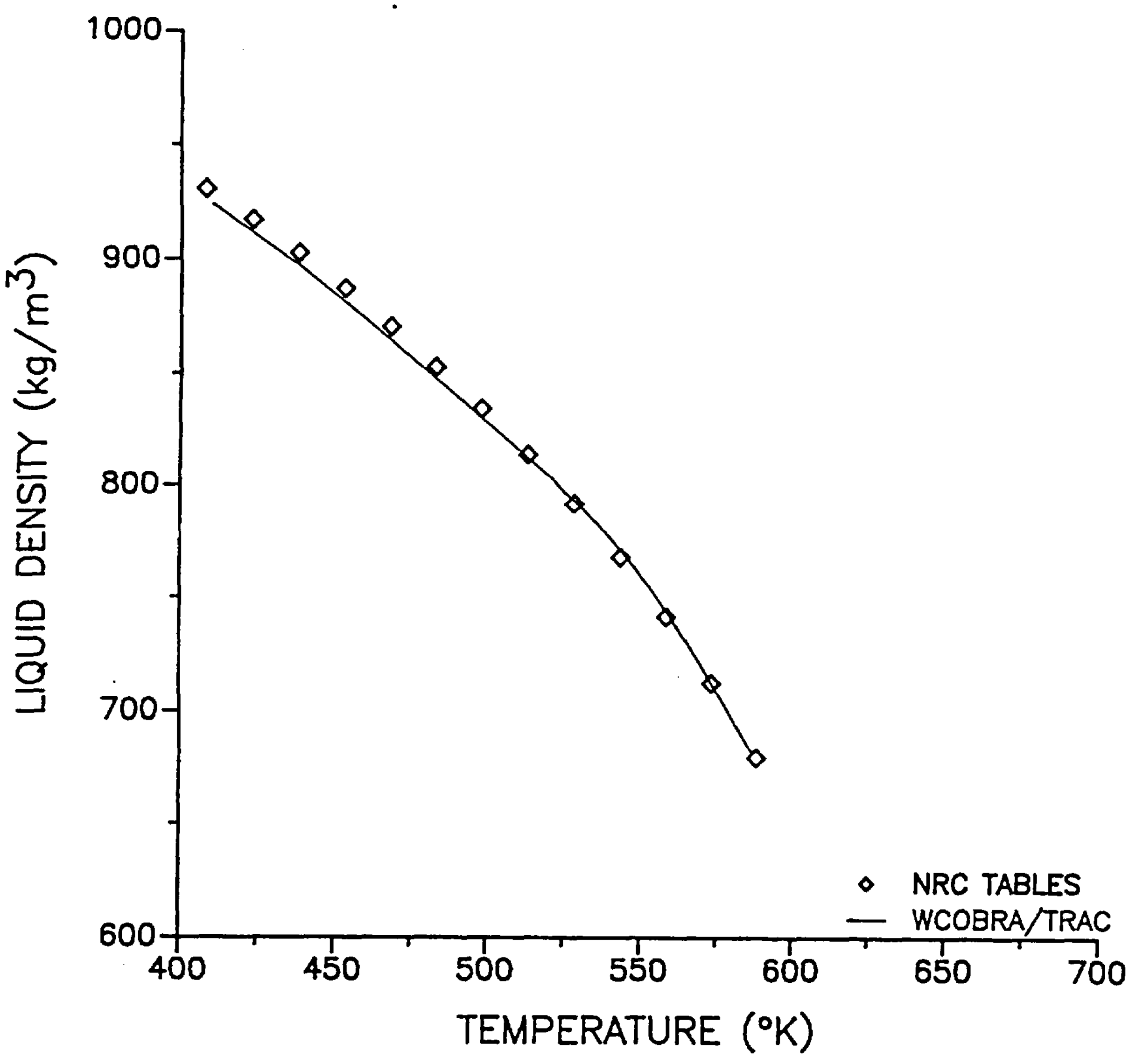

Figure 10-19. WCOBRA/TRAC 1-D Component Saturated Liquid Density

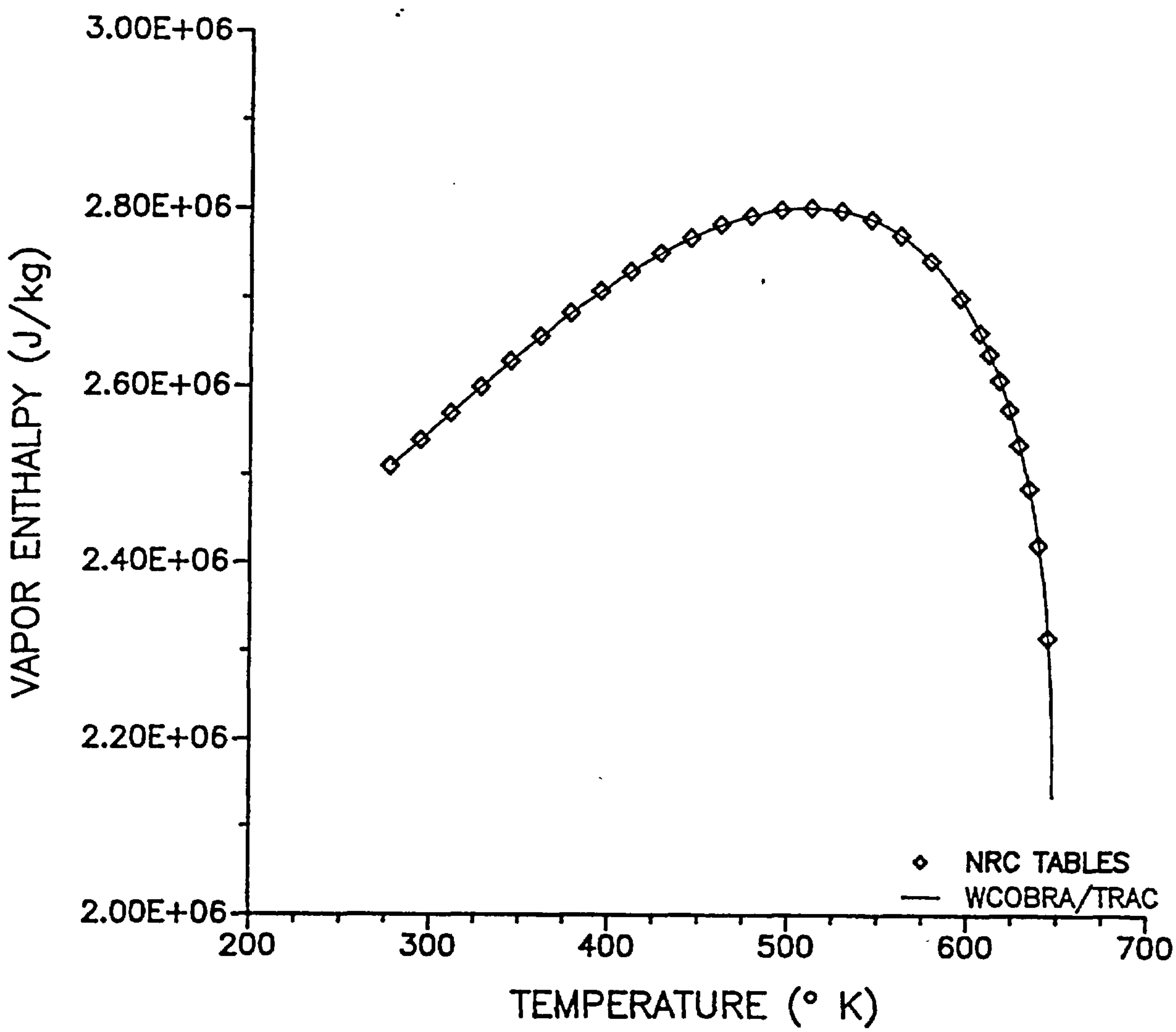

Figure 10-20. WCOBRA/TRAC 1-D Component Saturated Vapor Enthalpy

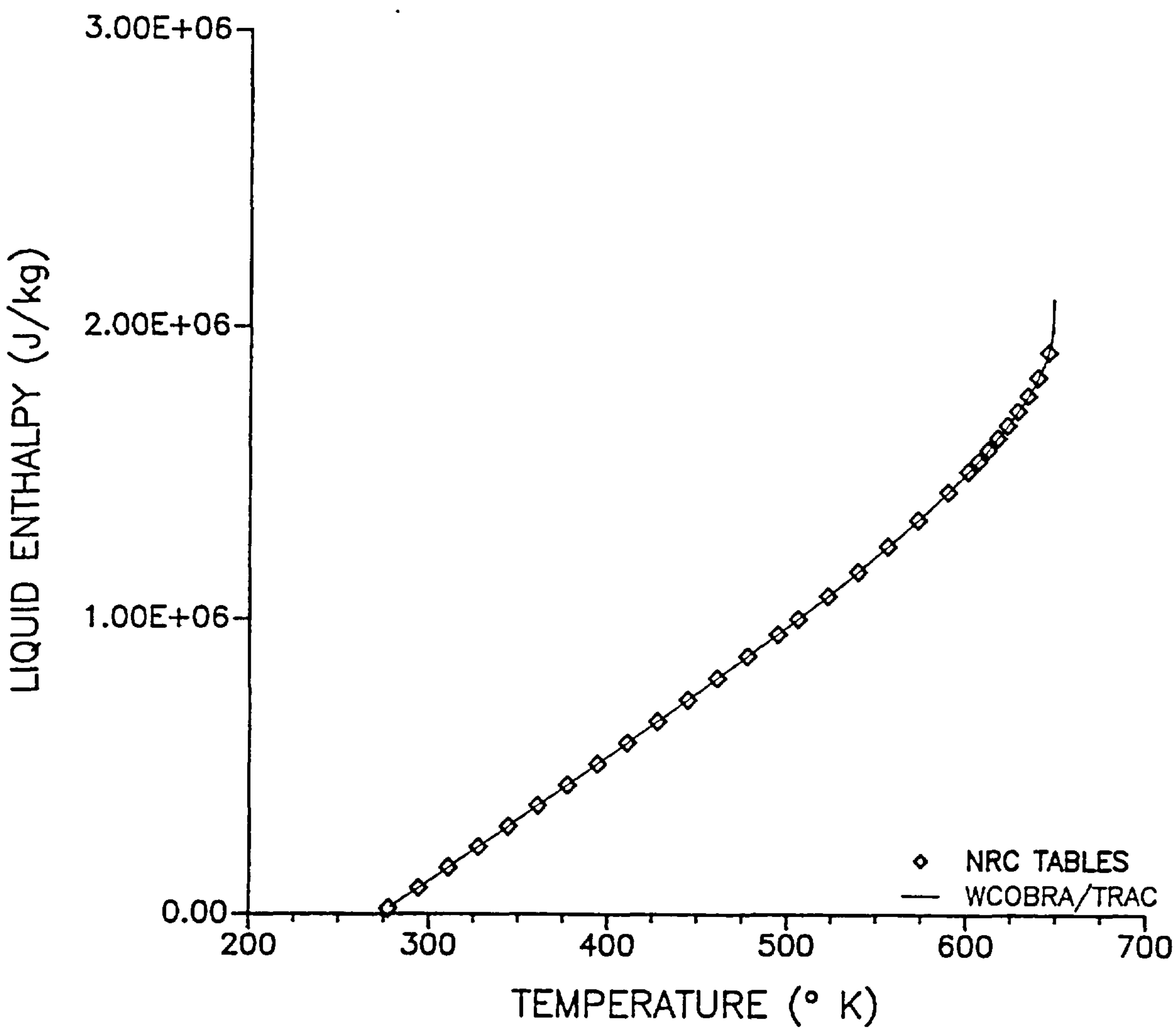

Figure 10-21. WCOBRA/TRAC 1-D Component Saturated Liquid Enthalpy

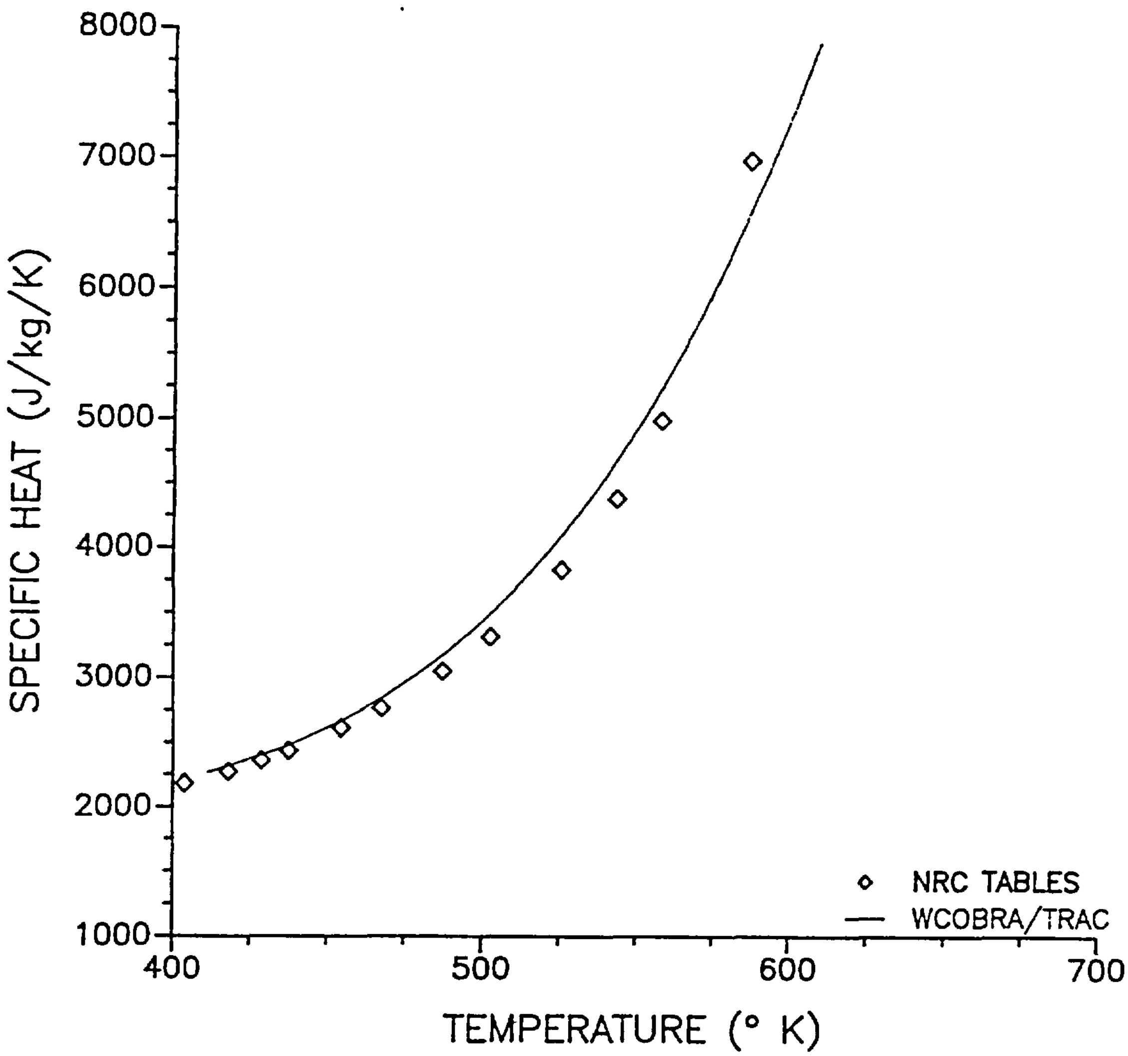

Figure 10-22. WCOBRA/TRAC 1-D Component Saturated Vapor Specific Heat

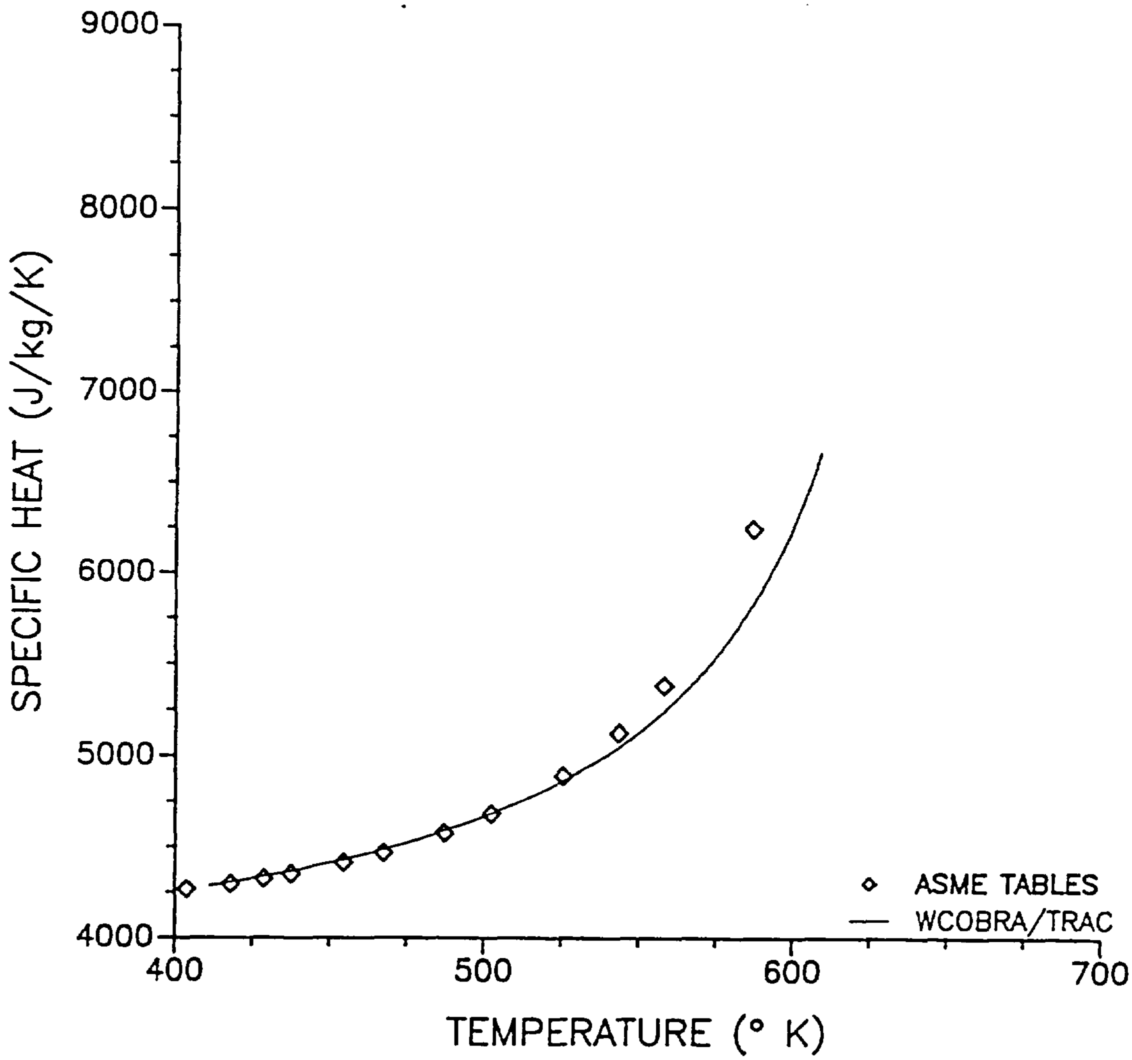

Figure 10-23. W̲COBRA/TRAC 1-D Component Saturated Liquid Specific Heat

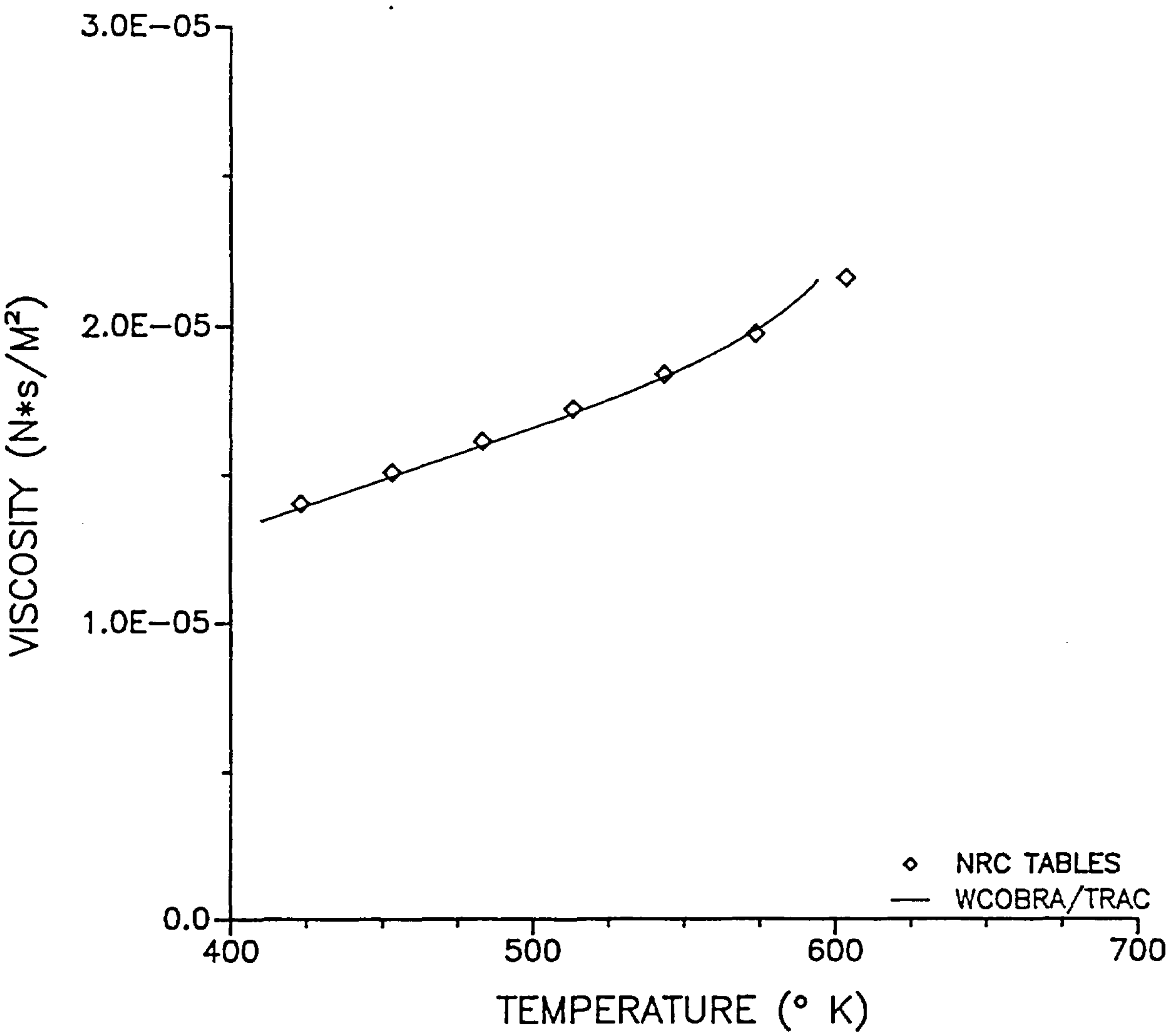

Figure 10-24. WCOBRA/TRAC 1-D Component Saturated Vapor Viscosity

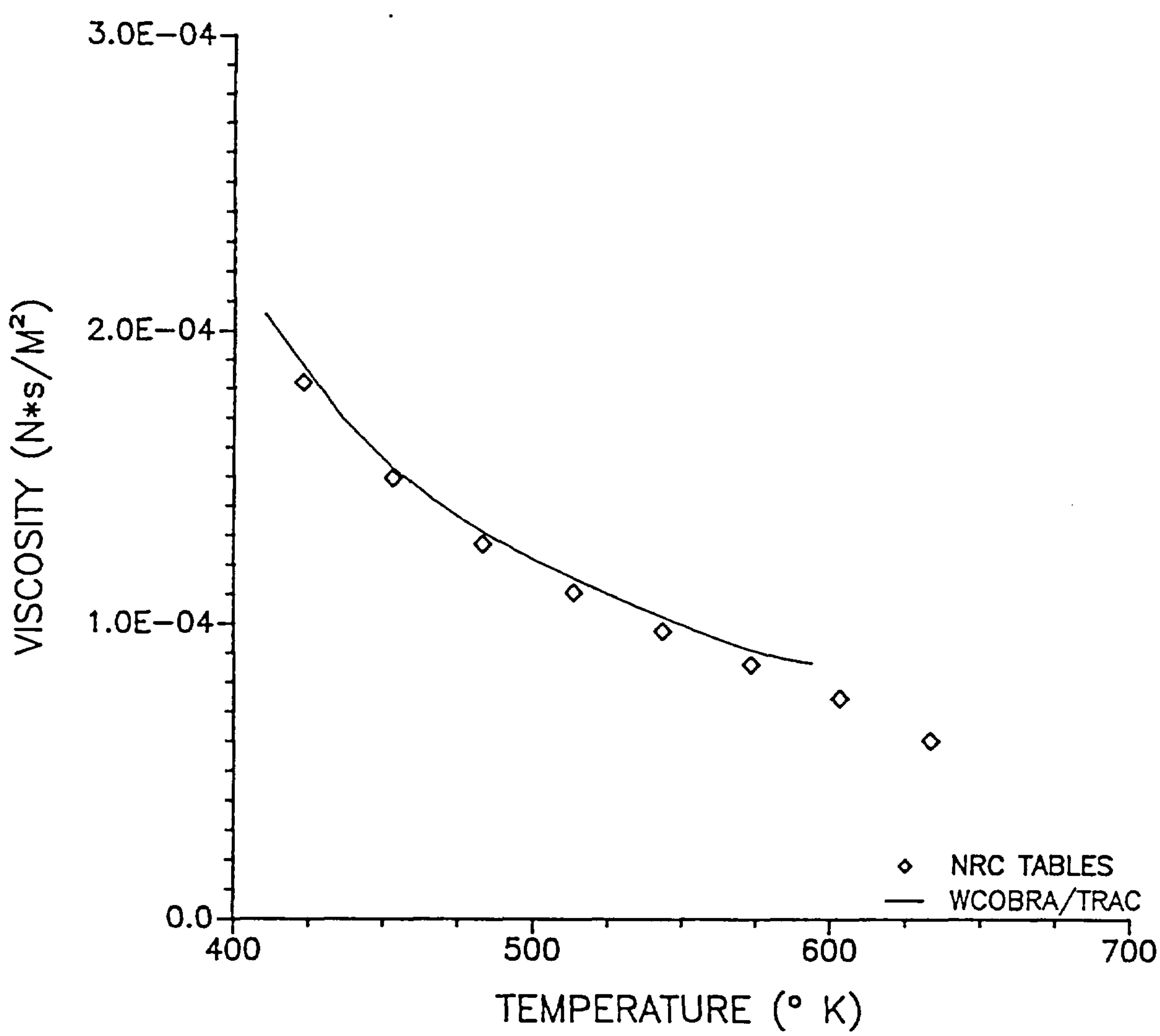

Figure 10-25. WCOBRA/TRAC 1-D Component Saturated Liquid Viscosity

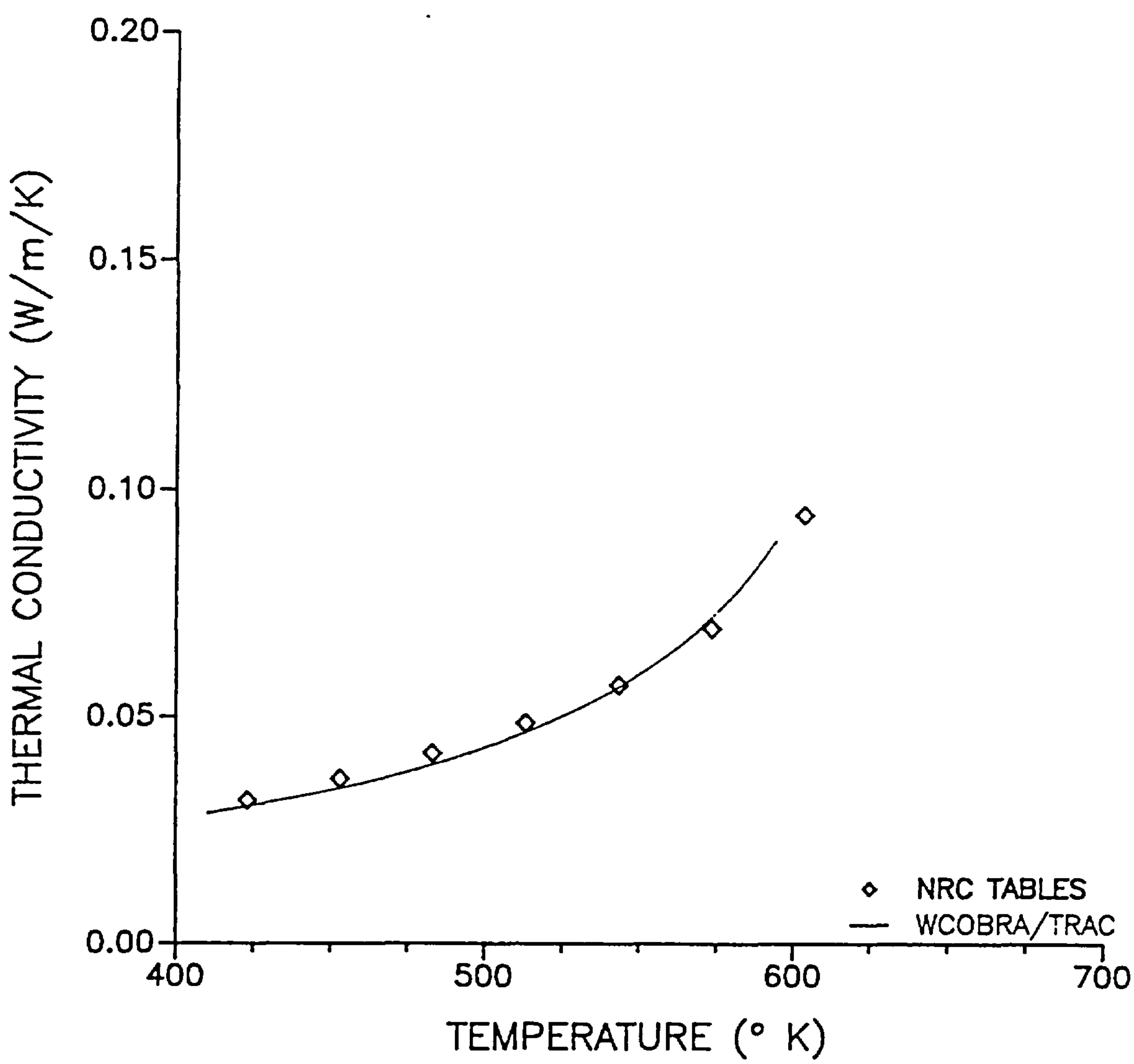

Figure 10-26. WCOBRA/TRAC 1-D Component Saturated Vapor Thermal Conductivity

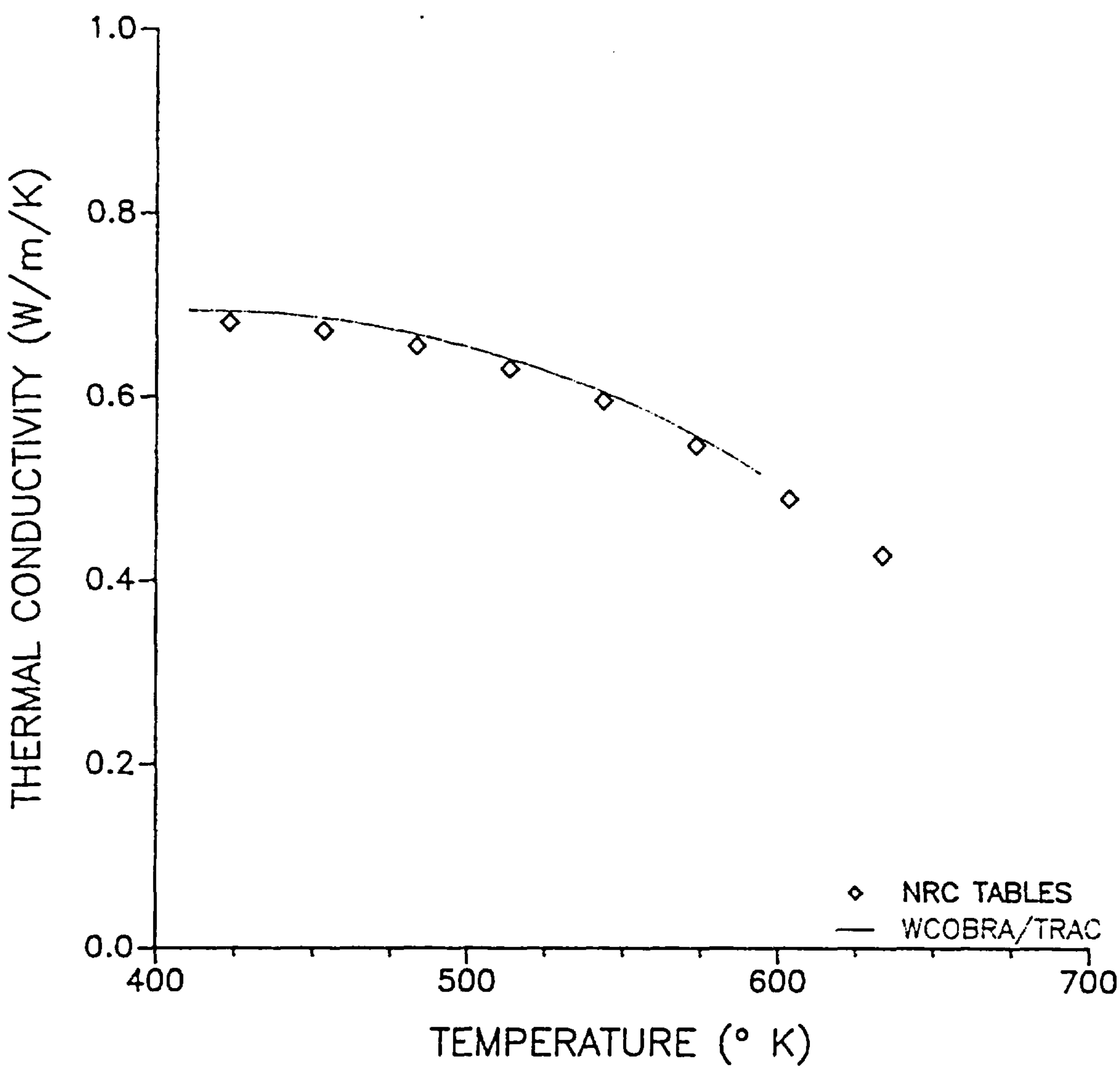

Figure 10-27. WCOBRA/TRAC 1-D Component Saturated Liquid Thermal Conductivity

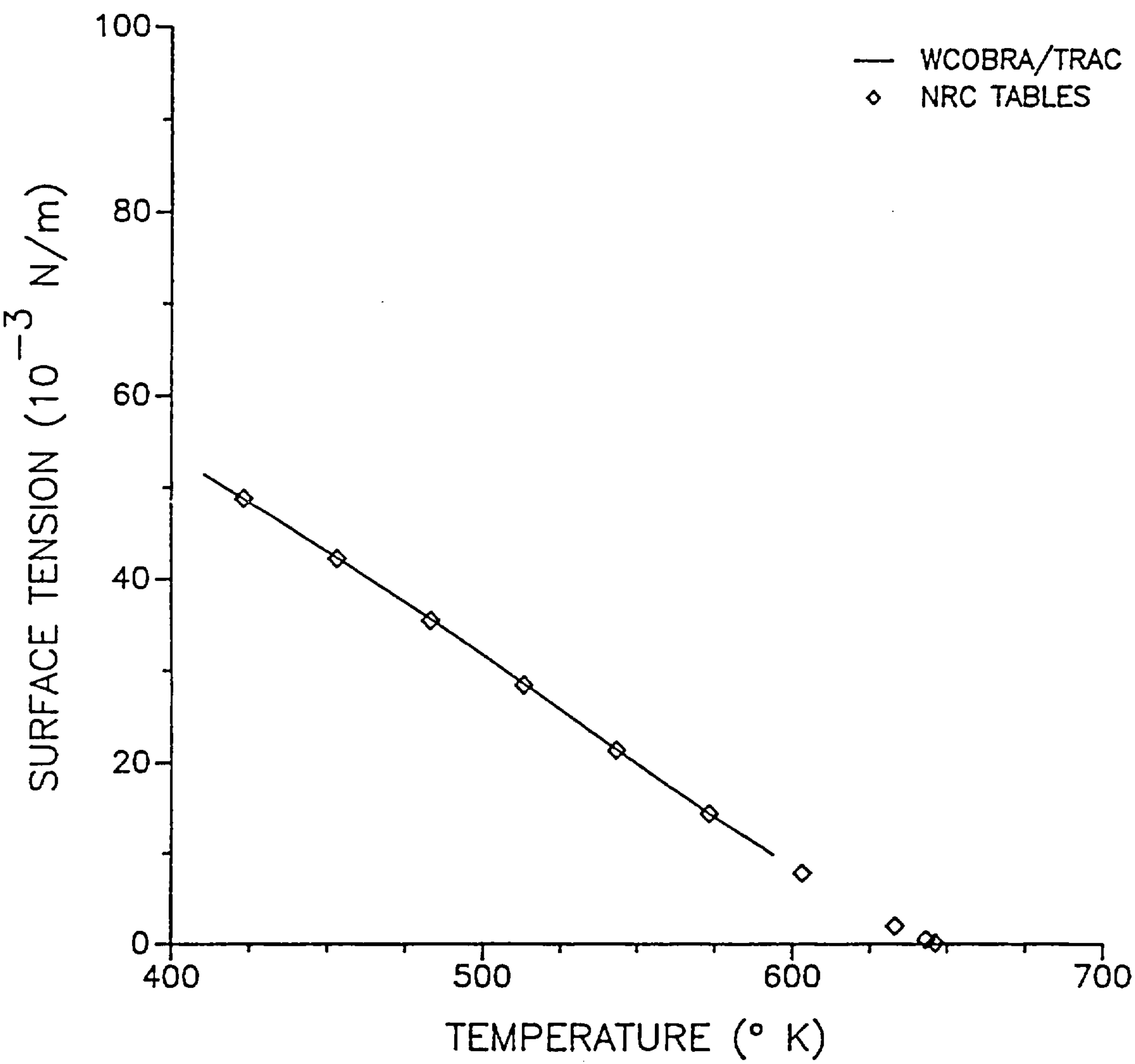

Figure 10-28. WCOBRA/TRAC 1-D Component Surface Tension

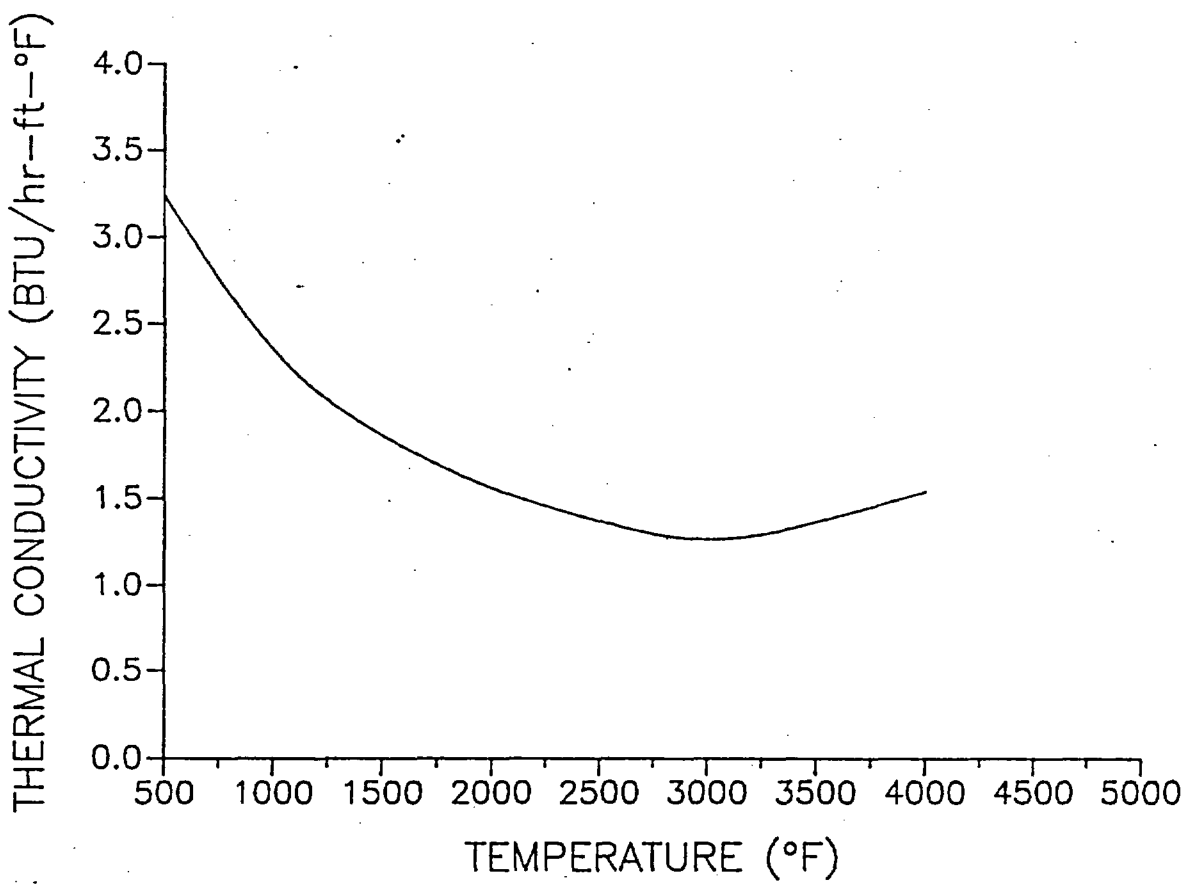

Figure 10-29. WCOBRA/TRAC UO_2 Thermal Conductivity (95% of Theoretical Density)

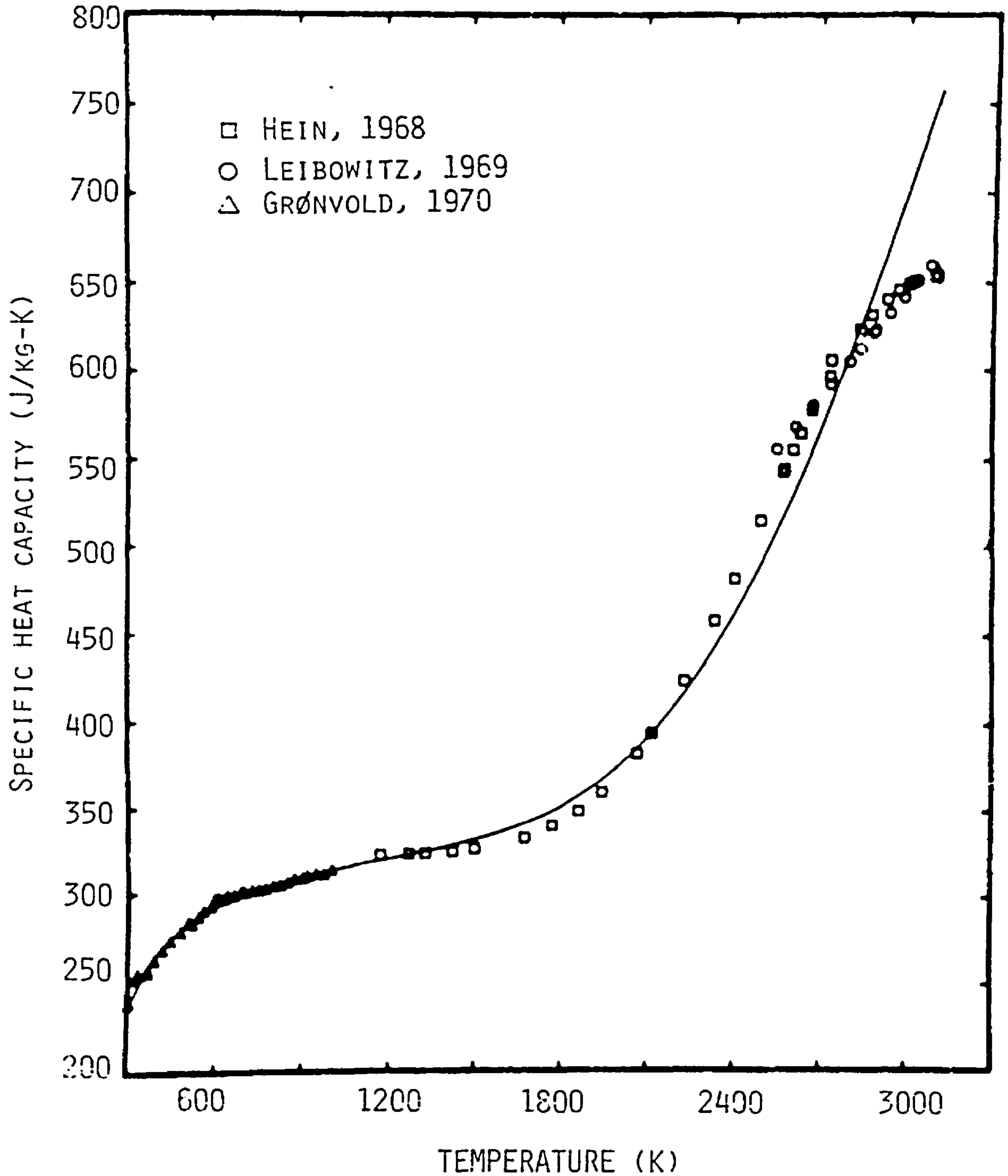

Figure 10-30. WCOBRA/TRAC UO_2 Specific Heat

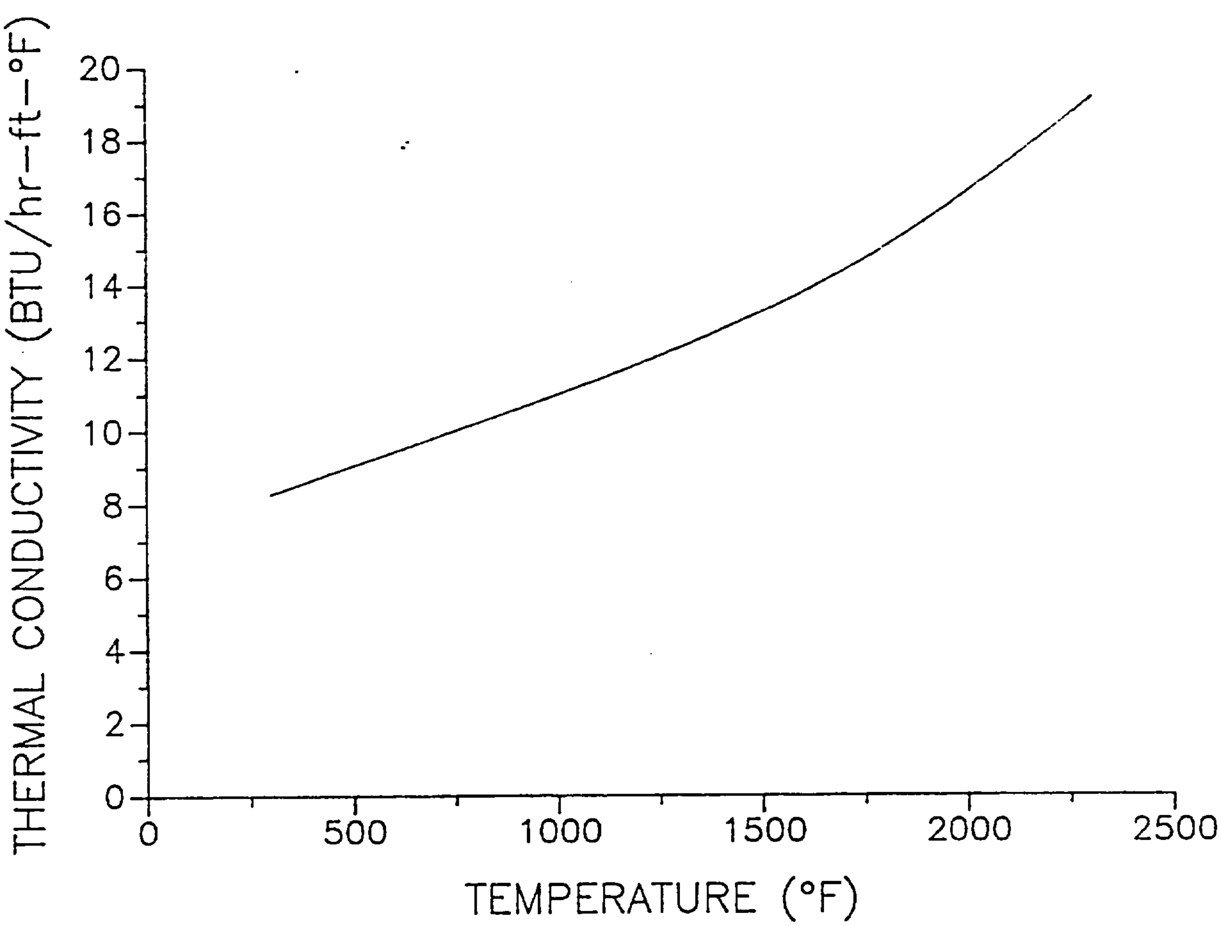

Figure 10-31. WCOBRA/TRAC Zircaloy-4 Thermal Conductivity

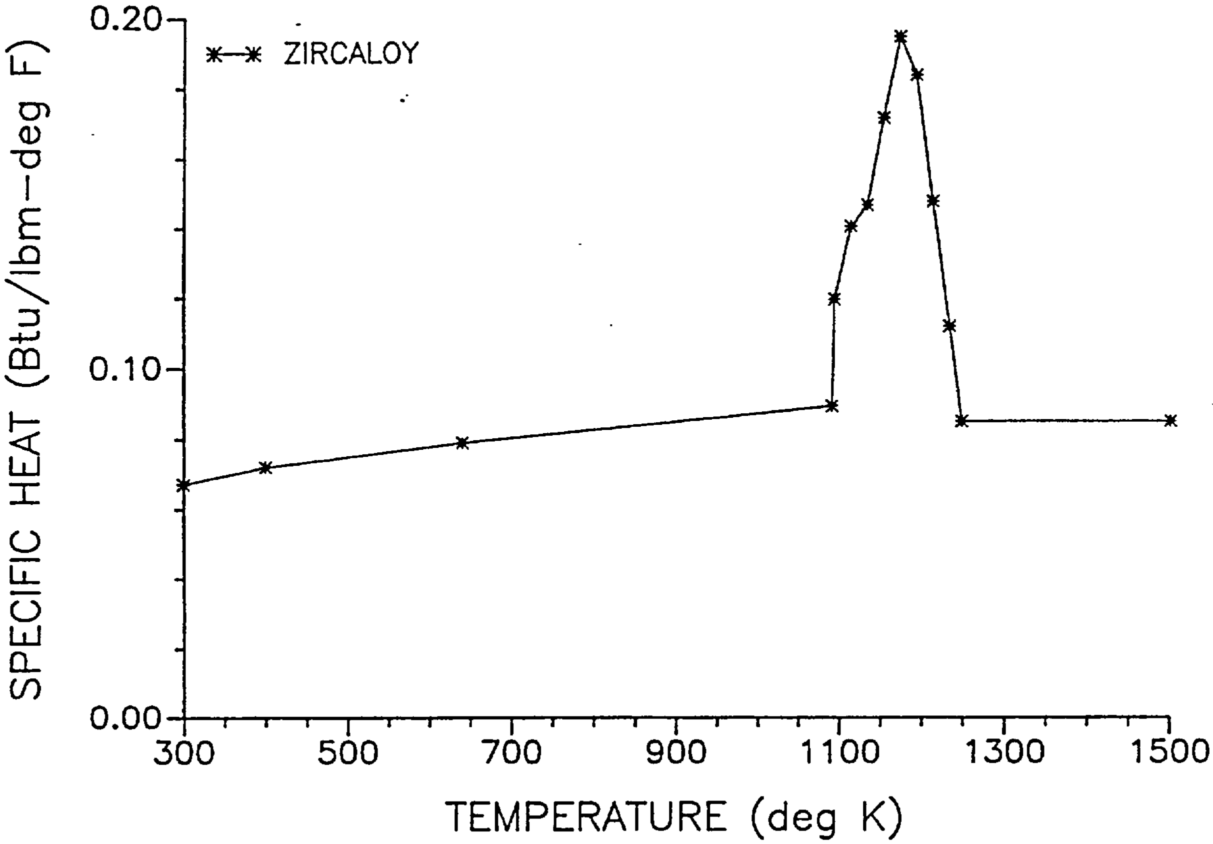

Figure 10-32. WCOBRA/TRAC Zircaloy-4 Specific Heat

a,c

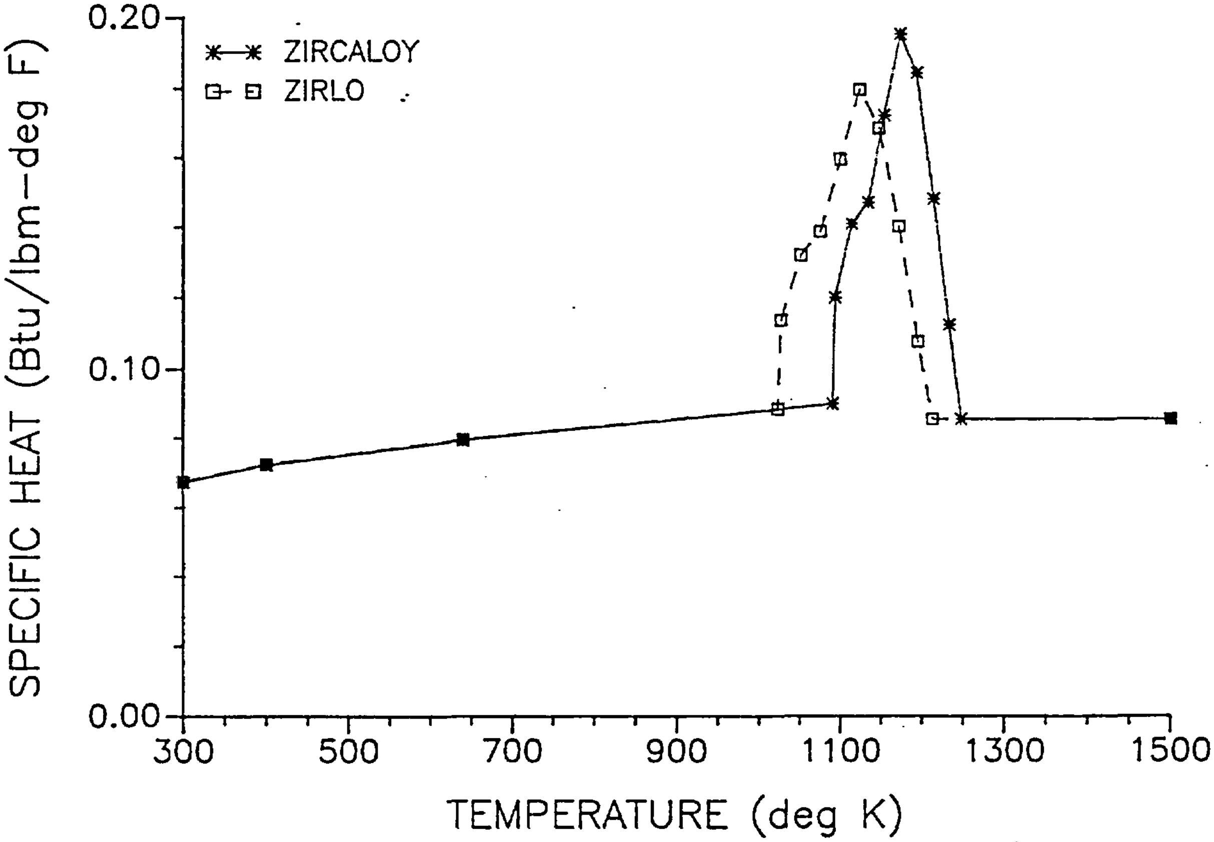

Figure 10-33. Comparison of ZIRLO™ and Zircaloy-4 Specific Heat

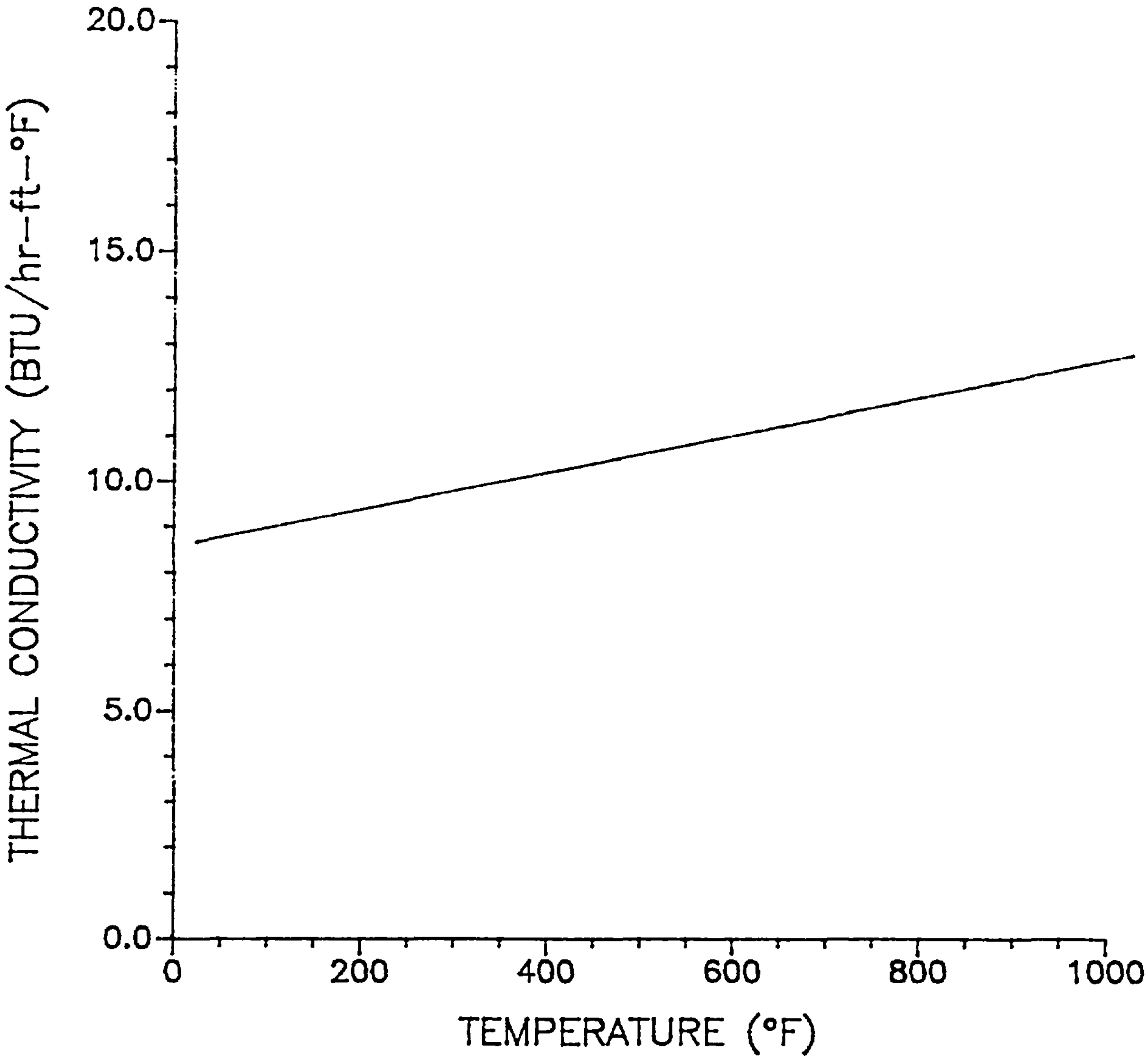

Figure 10-34. WCOBRA/TRAC 1-D Component 304 Stainless Steel Thermal Conductivity

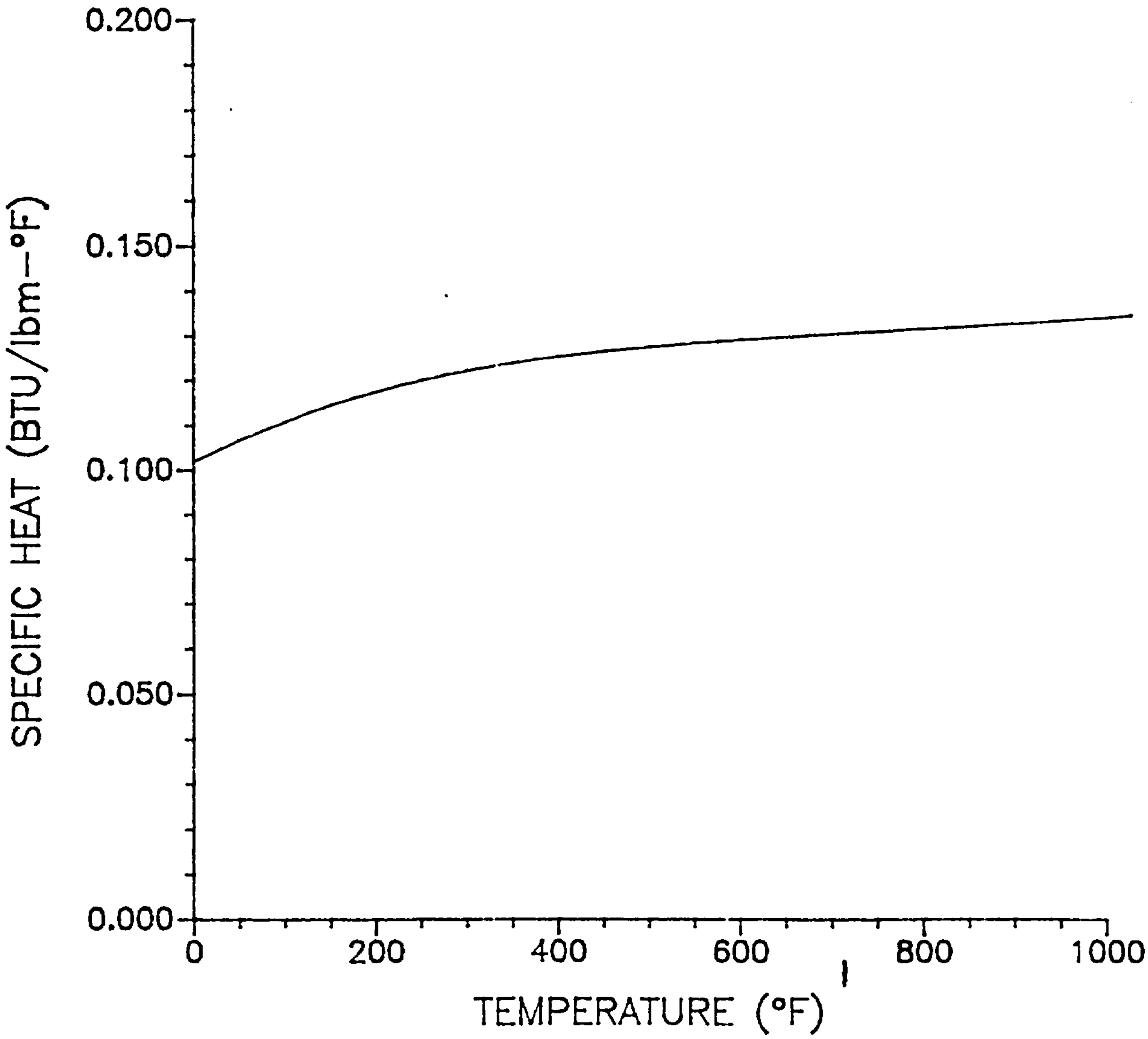

Figure 10-35. W COBRA/TRAC 1-D Component 304 and 316 Stainless Steel Specific Heat

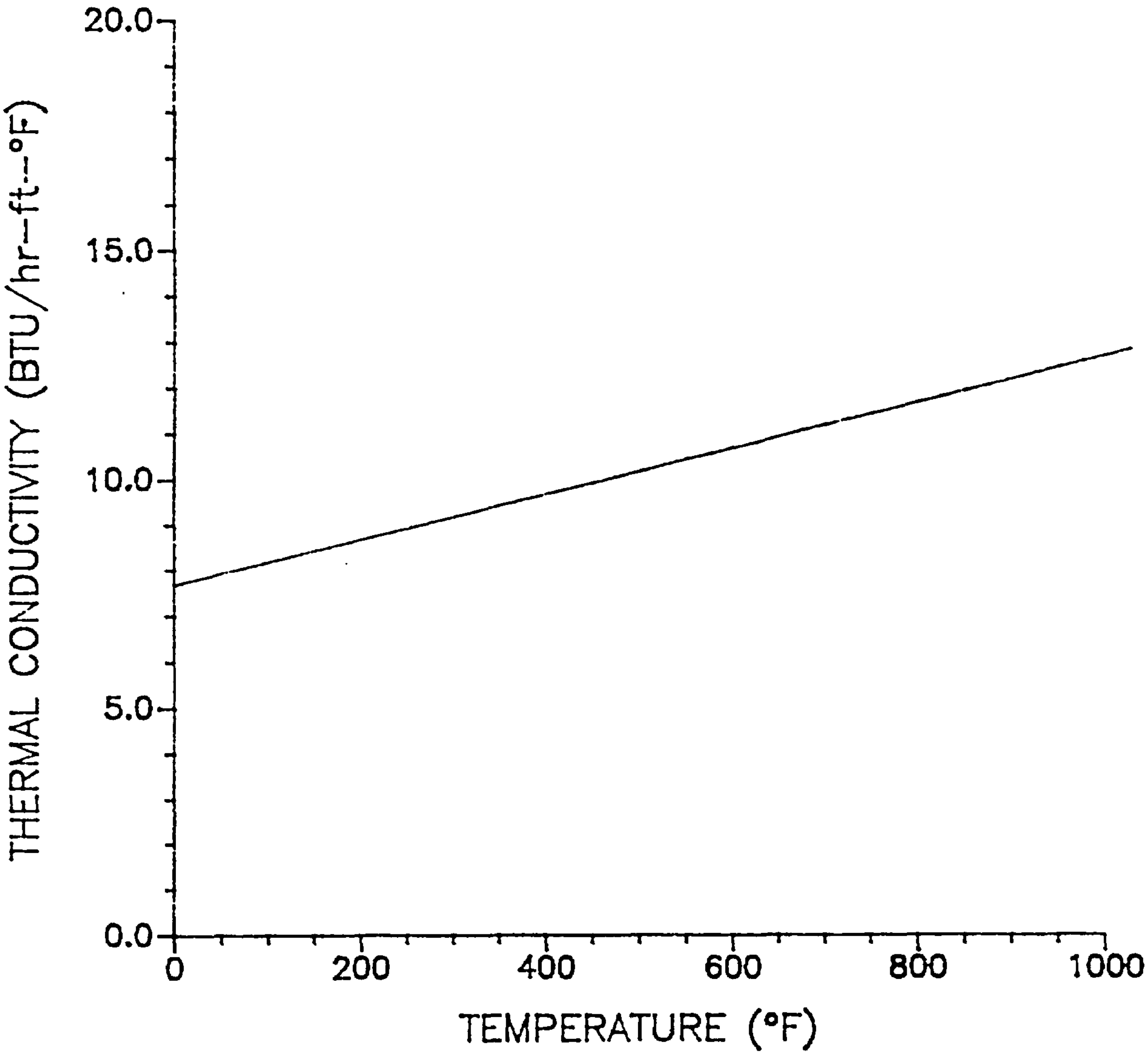

Figure 10-36. W̲COBRA/TRAC 1-D Component 316 Stainless Steel Thermal Conductivity

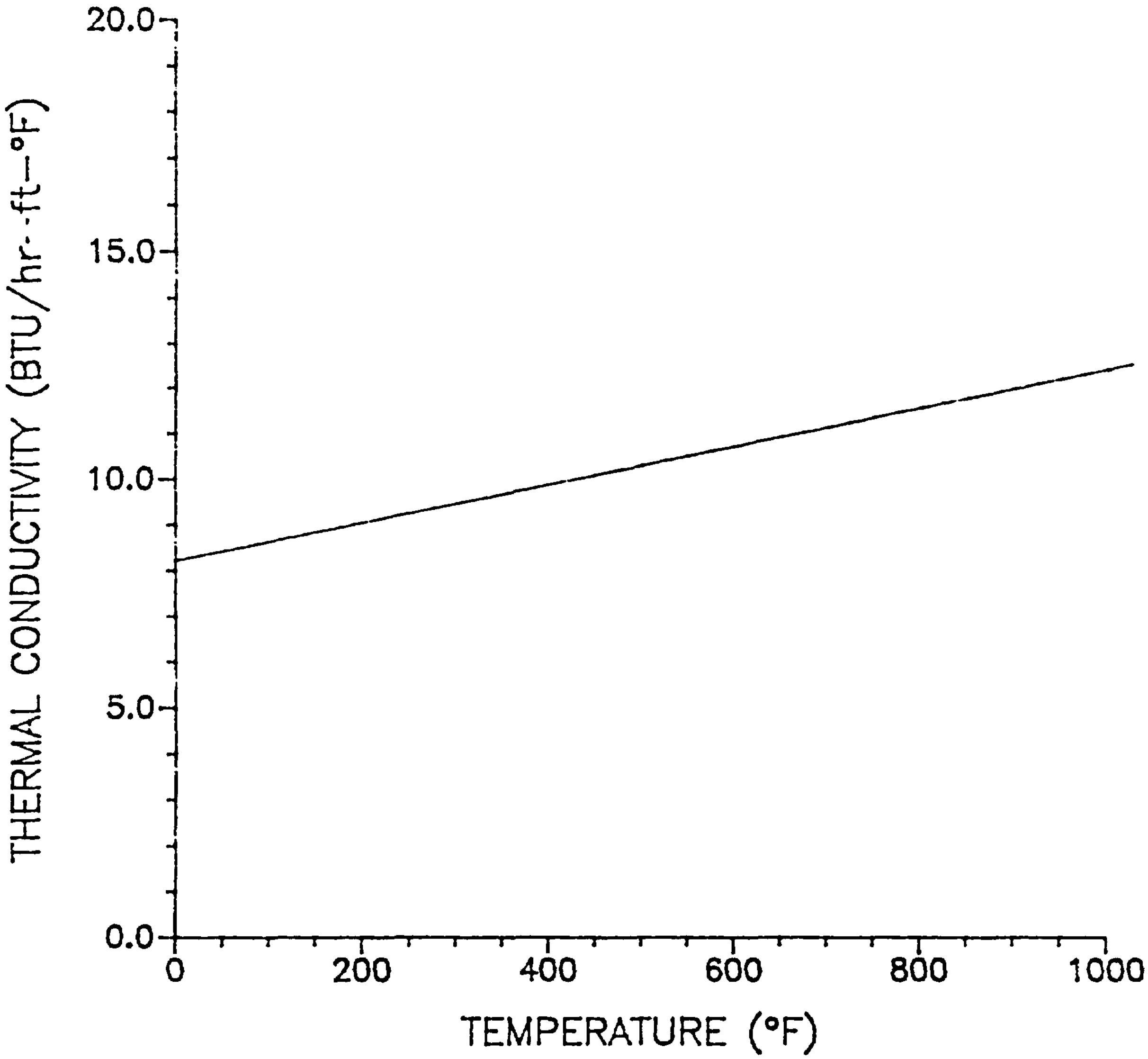

Figure 10-37. W̲COBRA/TRAC 1-D Component 347 Stainless Steel Thermal Conductivity

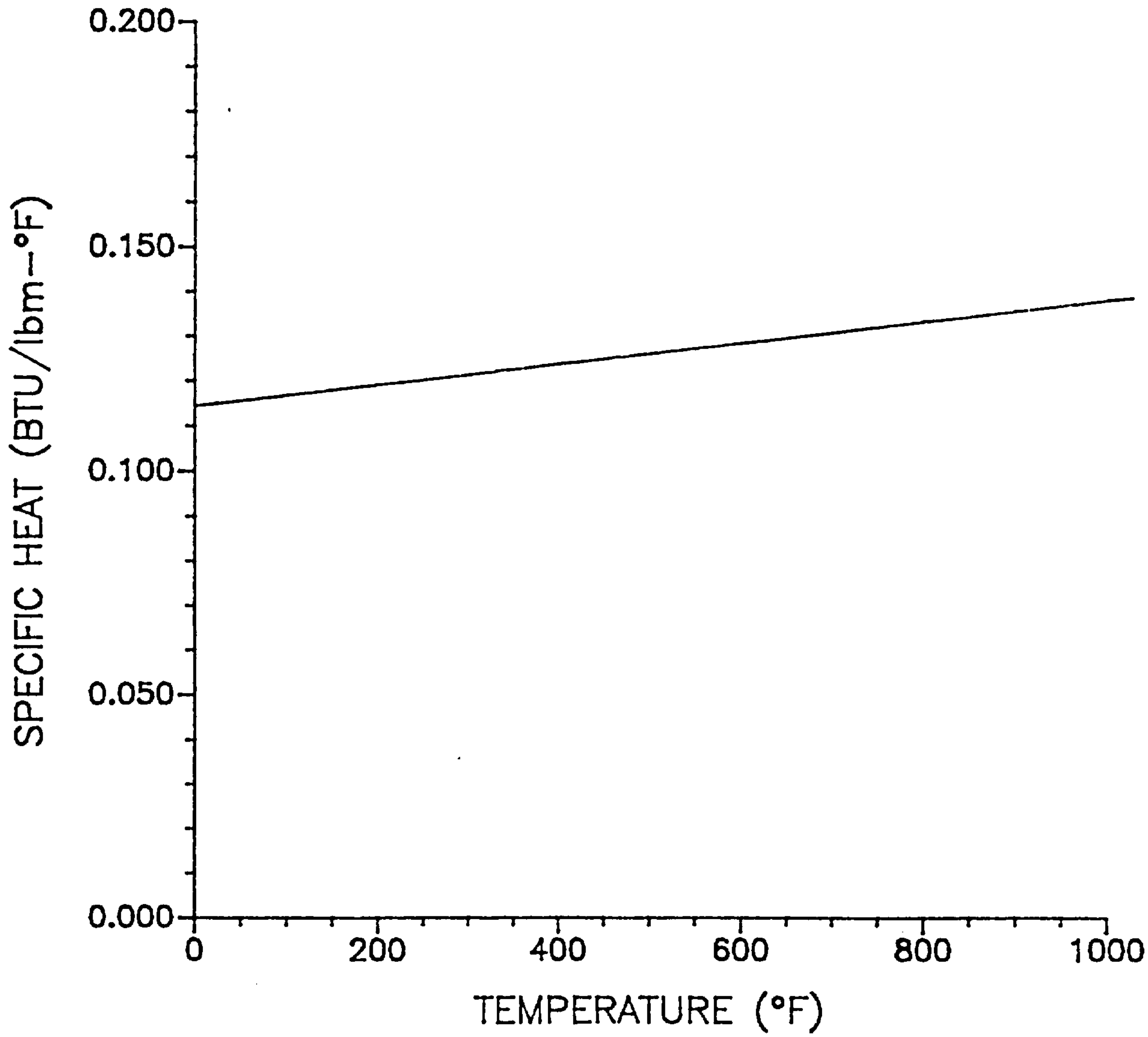

Figure 10-38. WCOBRA/TRAC 1-D Component 347 Stainless Steel Specific Heat

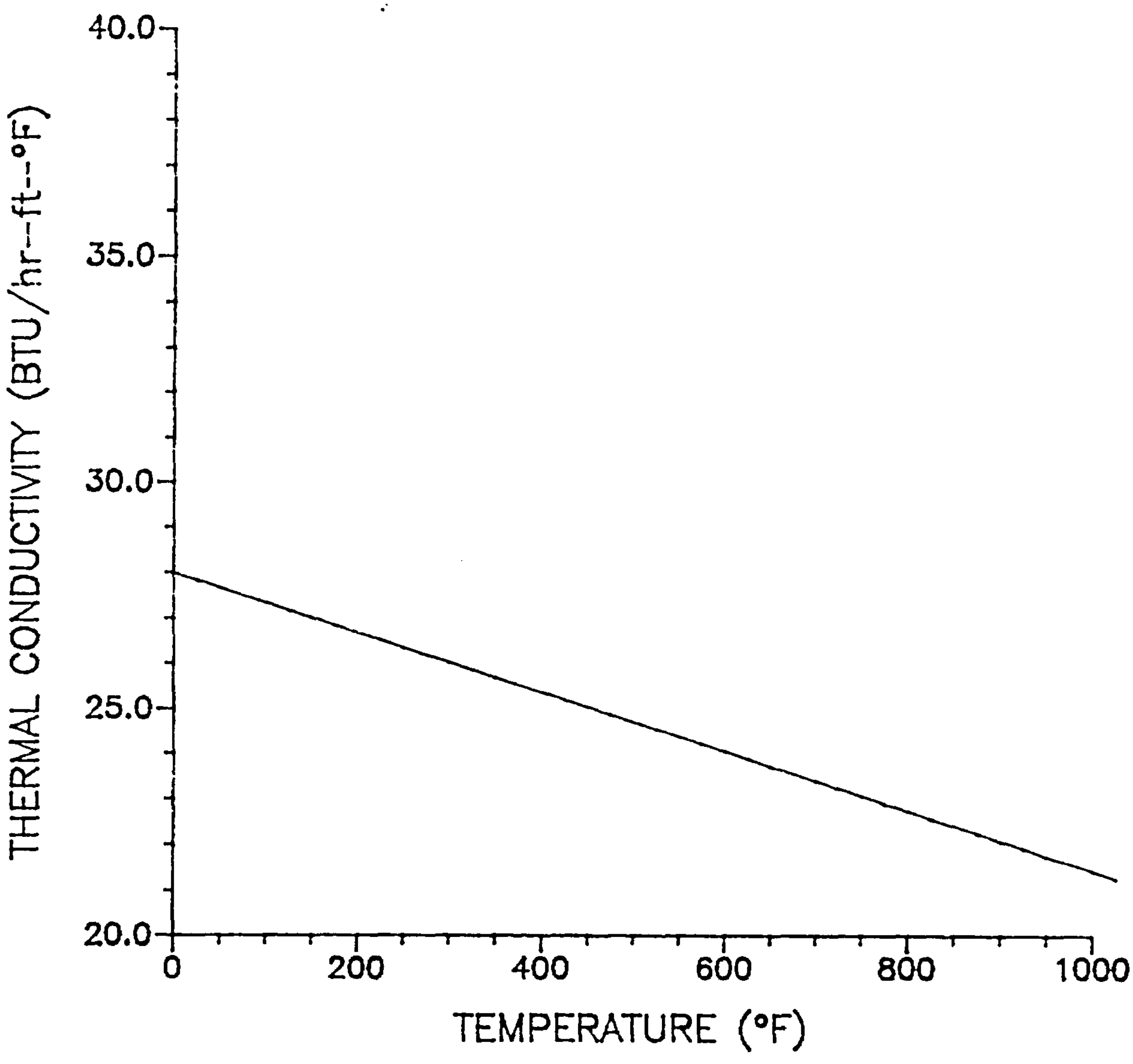

Figure 10-39. WCOBRA/TRAC 1-D Component Carbon Steel Thermal Conductivity

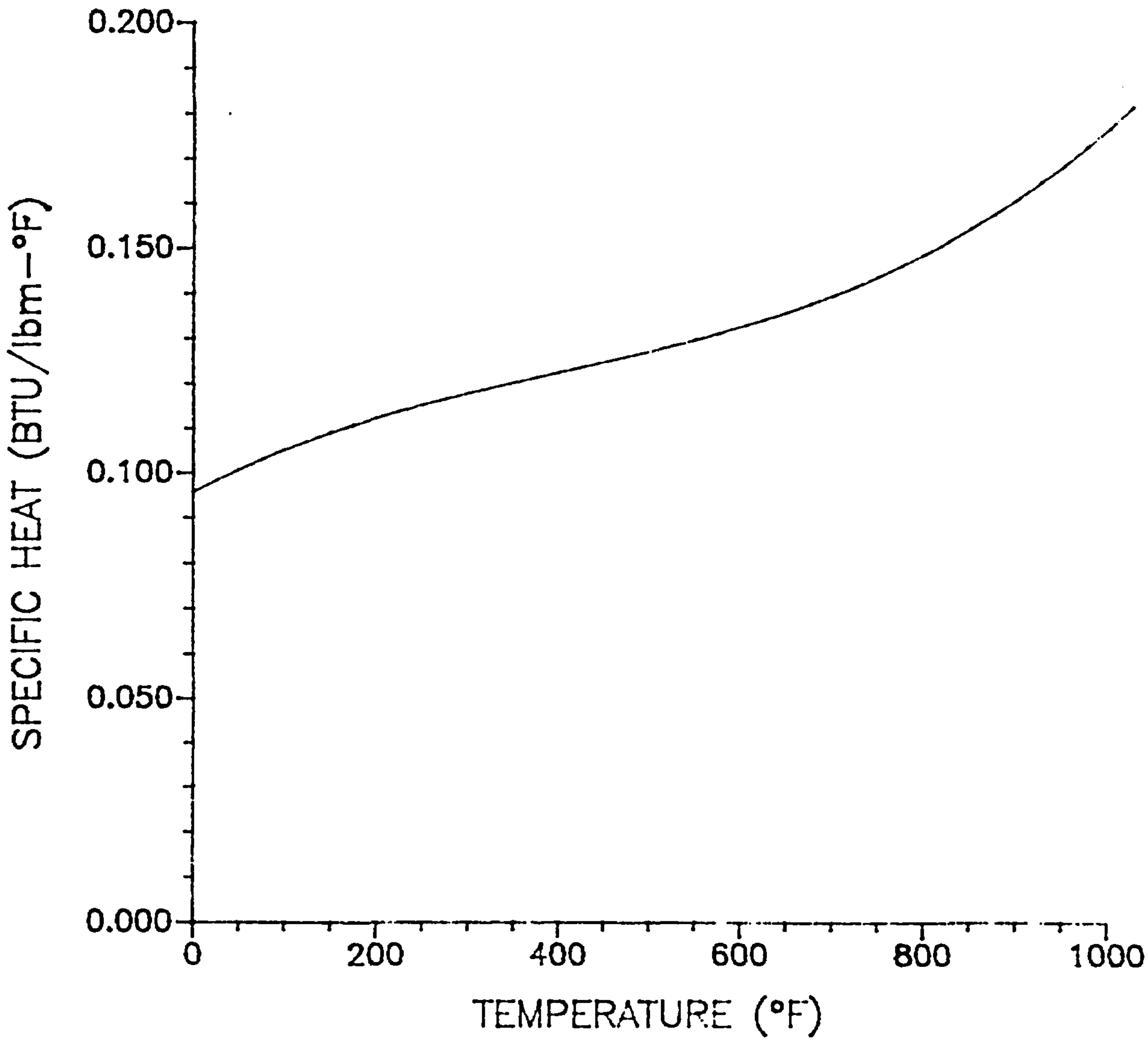

Figure 10-40. WCOBRA/TRAC 1-D Carbon Steel Specific Heat

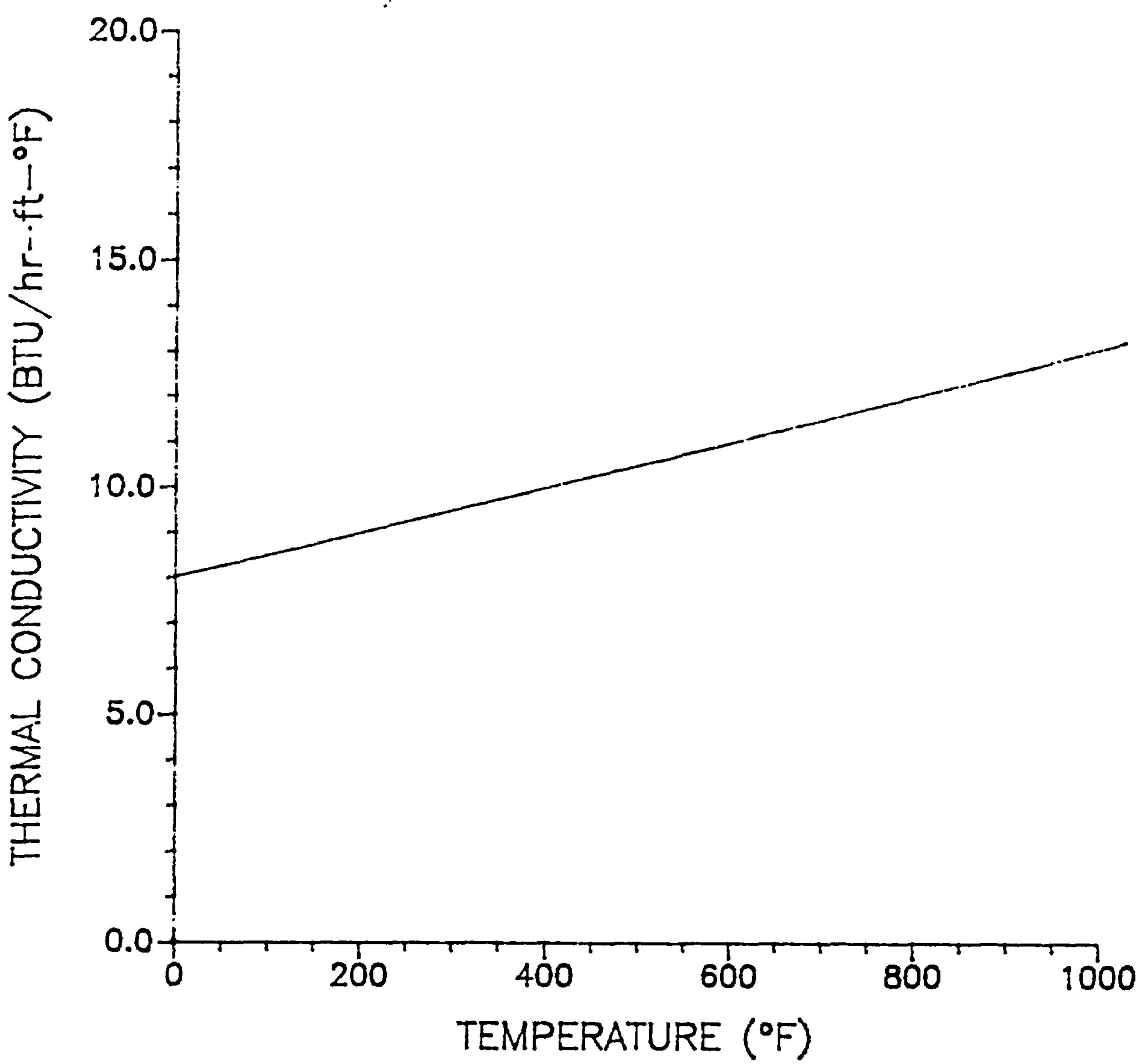

Figure 10-41. WCOBRA/TRAC 1-D Component Inconel 600 Thermal Conductivity

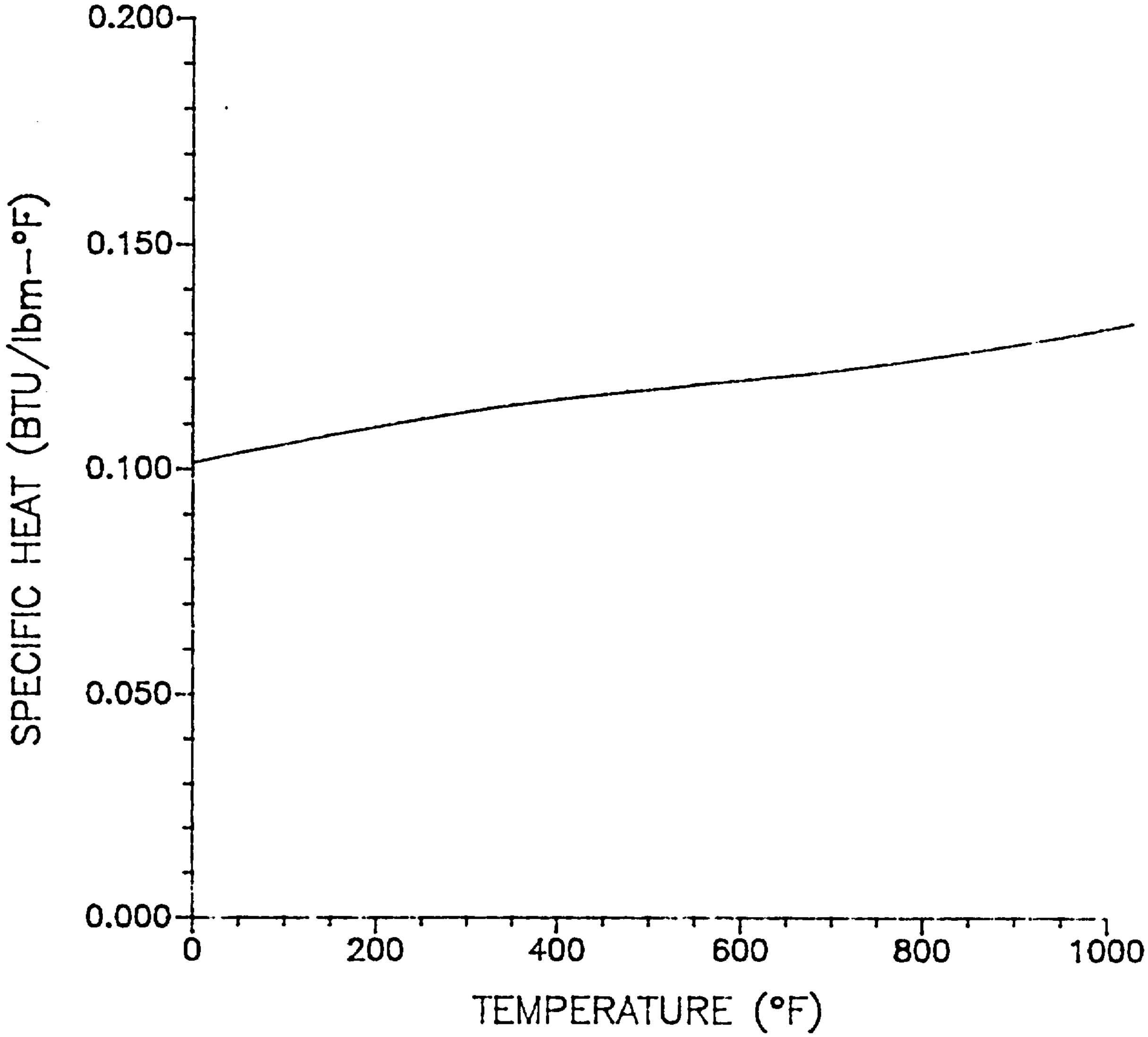

Figure 10-42. WCOBRA/TRAC 1-D Component Inconel 600 Specific Heat

SECTION 11
SMALL BREAK LOCA-RELATED CAPABILITIES

11-1 Introduction

To enable modelling of small break LOCA events in a CSAU methodology, certain features to facilitate WCOBRA/TRAC execution were added. This section describes these features, added to enable pertinent model sensitivity studies and to increase modelling flexibilities. In addition, the models and correlations added to permit accurate predictions of small break LOCA phenomena which have been previously described are summarized; consult Volume 2 for validation results of the small break LOCA code version, WCOBRA/TRAC-SB.

11-2 WCOBRA/TRAC-SB Additional Features

WCOBRA/TRAC Mod7A is the computer code developed by Westinghouse (Bajorek et al., 1998) for the best estimate analysis of large break LOCAs and approved by the NRC staff for that purpose (Jones, 1996). Some extra features have been added during development of the WCOBRA/TRAC-SB code version.

11-2-1 Features Previously Developed

The following WCOBRA/TRAC modification previously introduced to enable modelling of certain AP600 components (Garner et al., 1998) has been placed into the small break code version.

Check Valve Option, Type 6

The MOD7A code has five control options for the VALVE component. These options are described in Section 9-7. Option 5 is used for check valve simulation. For this option, a *specified ramp opens or closes the valve, taking several hundred timesteps. Under certain circumstances, the valve stays partially open and allows flow in both directions.*

A Type 6 check valve option has been added to the WCOBRA/TRAC code version for small break LOCA analysis. The Type 6 valve is either fully opened or fully closed in one timestep. The check valve opens when the pressure gradient across the valve reaches a user-specified value and closes when the pressure gradient is less than the specified value, or when reverse flow is detected.

11-2-2 Features Introduced to Enable Parameter Ranging

In order to perform response surface and/or uncertainty analyses, parameters important to the small break LOCA analysis must be ranged. To facilitate this, the following variables are introduced into WCOBRA/TRAC-SB; the default value for each is 1.0.

11-2-2-1 Variable "YDRAG"

This modification enables the user to apply a multiplier to the vertical interfacial drag coefficient. This multiplier is applied to the vertical flow regimes. User-supplied input allows specification of multipliers for individual channels.

11-2-2-2 Variable "XCNDSB"

This modification enables the user to apply a multiplier to the interfacial condensation heat transfer coefficient. User-supplied input allows specification of multipliers for individual channels.

11-2-2-3 Variable "XSHASB"

This modification enables the user to apply a multiplier to the wall condensation heat transfer coefficient for unheated conductors. User-supplied input allows specification of multipliers for individual channels.

11-2-3 Multiple Regions in VESSEL Channels

As described in the simulations presented in Volumes 2 and 3 of this report, VESSEL channels are used to model almost the entire primary coolant loop. Because their use is more widespread than in the large break LOCA WCOBRA/TRAC model, more flexibility in specifying channel input is necessary. One of the restrictions associated with the use of VESSEL channels is that one set of cell height variations is applied to all channels in a section. To relax this restriction, an update has been implemented into WCOBRA/TRAC-SB making multiple sets of cell height variation tables available for channels in a section. Figure 11-1 shows the primary circuit of the PWR and the approximate elevation of major components, i.e., the pressure vessel, cold and hot legs, steam generator, cross-over pipe and RCP. To model a loop using VESSEL channels, the cell heights in the steam generator plenum and tubes would previously have been restricted to the same value as the VESSEL upper plenum nodes. Similarly, the cross-over leg [

]a,c

Channels are [

]a,c

must match between the two connecting regions. Regions can also be connected through a gap. In this case, [

]^{a,c} to assist debugging of input.

11-2-4 Hydraulic Cell Level Tracking for Heat Transfer Computations

The WCOBRA/TRAC code does not contain an explicit mixture level tracking model. Rather, level tracking is accomplished by nodalization, and prediction of the axial void gradient between hydraulic cells. In most regions of the vessel and reactor coolant system (RCS), nodalization is sufficient to track the mixture level, as the structures do not have a quench front. A detailed tracking of the mixture level is not necessary.

In the reactor core, however, an accurate assessment of the mixture level is vital in the prediction of the peak cladding temperature (PCT). Local void fractions for use in heat transfer calculations are typically linearly interpolated between adjoining axial hydraulic cells. The detailed nodalization in the core [ ]^{a,c} helps to resolve the axial void fraction gradient. However, the linear interpolation of void fraction does not allow the location of a sharp interface to be identified. Therefore, WCOBRA/TRAC-SB includes logic to detect the possible presence of a sharp void fraction gradient in the vicinity of a quench front. This new logic is used in conjunction with the linear interpolation logic so that the calculation affects only the hydraulic cell in which the sharp gradient is assumed to occur; it is employed in fuel rod heat transfer computations.

Figure 11-3 shows an example of the linear interpolation scheme. Continuity cell 'j' is at the boundary [

]^{a,c}

[

]a,c

[

]a,c

If a sharp gradient is detected [

]a,c (11-2-1)

[

(11-2-2)

]a,c

With this example of level sharpening logic, [

]^{a,c}

11-2-5 T_{min} Definition

A variable (ITMINHN) is introduced to enable the user to define T_{min}, the minimum stable film boiling temperature, to be the homogeneous nucleation temperature. If chosen by the user, the calculation of T_{min} previously described herein is not performed; T_{min} is always calculated to be the homogeneous nucleation temperature, which is generally regarded as the lowest value of T_{min}, according to Equation 6-97 in this volume. Setting ITMINHN to equal 1 allows a conservative approach to be taken in PWR calculations.

11-2-6 Momentum Transfer at Pipe Elbows

When WCOBRA/TRAC-SB VESSEL component channels are used to model the loop piping in a PWR, pipe elbows in the hot leg and at the loop seal in the crossover leg (two elbows) are considered in which the flow turns from a horizontal to a vertical direction (or vice-versa). Because the flow velocity is stopped in one direction, then restarted in another with the staggered mesh used in the WCOBRA/TRAC-SB model, inappropriate pressure drop conditions are predicted. This situation has been corrected by introducing a VESSEL component momentum scheme for a U-bend region.

Figure 11-5 presents the Momentum Cell A case, when a vertical flow turns into a horizontal channel. In this case, the momentum convection is calculated as follows:

[

]^{a,c}

[

]a,c

Figure 11-6 presents the Momentum Cell B case, when a gap between horizontal flow channels is stopped at a wall. In this case, the cell momentum in Cell B is ρVA_{gap} but the associated
[

]a,c

Figure 11-7 presents the Momentum Cell C case, when the horizontal flow is redirected into a vertical channel. In this case, the cell momentum in Cell C is ρUA_x, the associated convection velocity is U. The axial momentum [

]a,c

[

]a,c

11-2-7 Enhanced Reactivity Insertion Model

In a small break LOCA event negative reactivity is introduced into the core both by voiding of the fluid and by the insertion of the control rods. WCOBRA/TRAC-SB has been programmed with the capability to use the internal reactivity feedback models described in Section 8 together with an input reactivity table. The user can specify a negative reactivity insertion as a function of time to model the action of the control rods.

11-3 Summary of Identified Improvements Necessary to Model Small Break LOCAs

The capability of WCOBRA/TRAC MOD7A to model high ranked small break LOCA processes was assessed. Modelling of the following processes was judged to require new and/or upgraded capability in the WCOBRA/TRAC-SB code version used in small break LOCA analysis:

- *Horizontal Stratified Flow Phenomena*
- *Break Flow*
- *Steam Generator Tube Condensation*
- *Heat Transfer to Uncovered Fuel*

The models/correlations implemented in WCOBRA/TRAC-SB for each of these phenomena is identified in preceding sections of Volume 1. Other model features which are unique to WCOBRA/TRAC-SB are also presented. Overall, this volume presents a complete description of the models and correlations contained in the WCOBRA/TRAC-SB code version.

11-4 References

Bajorek, S. M. et al., 1998 "Code Qualification Document for Best Estimate LOCA Analysis," WCAP-12945-P-A, Revision 2, Volumes 1 through 4.

Jones, R. C. Jr. (USNRC) letter to N. J. Liparulo (W), "Acceptance for Referencing of the Topical Report, WCAP-12945(P), Westinghouse Code Qualification Document for Best-Estimate Loss-of-Coolant Analysis," June 28, 1996.

Garner, D. C. et al., 1998 "WCOBRA/TRAC OSU Long-Term Cooling Final Validation Report," WCAP-14776, Revision 4.

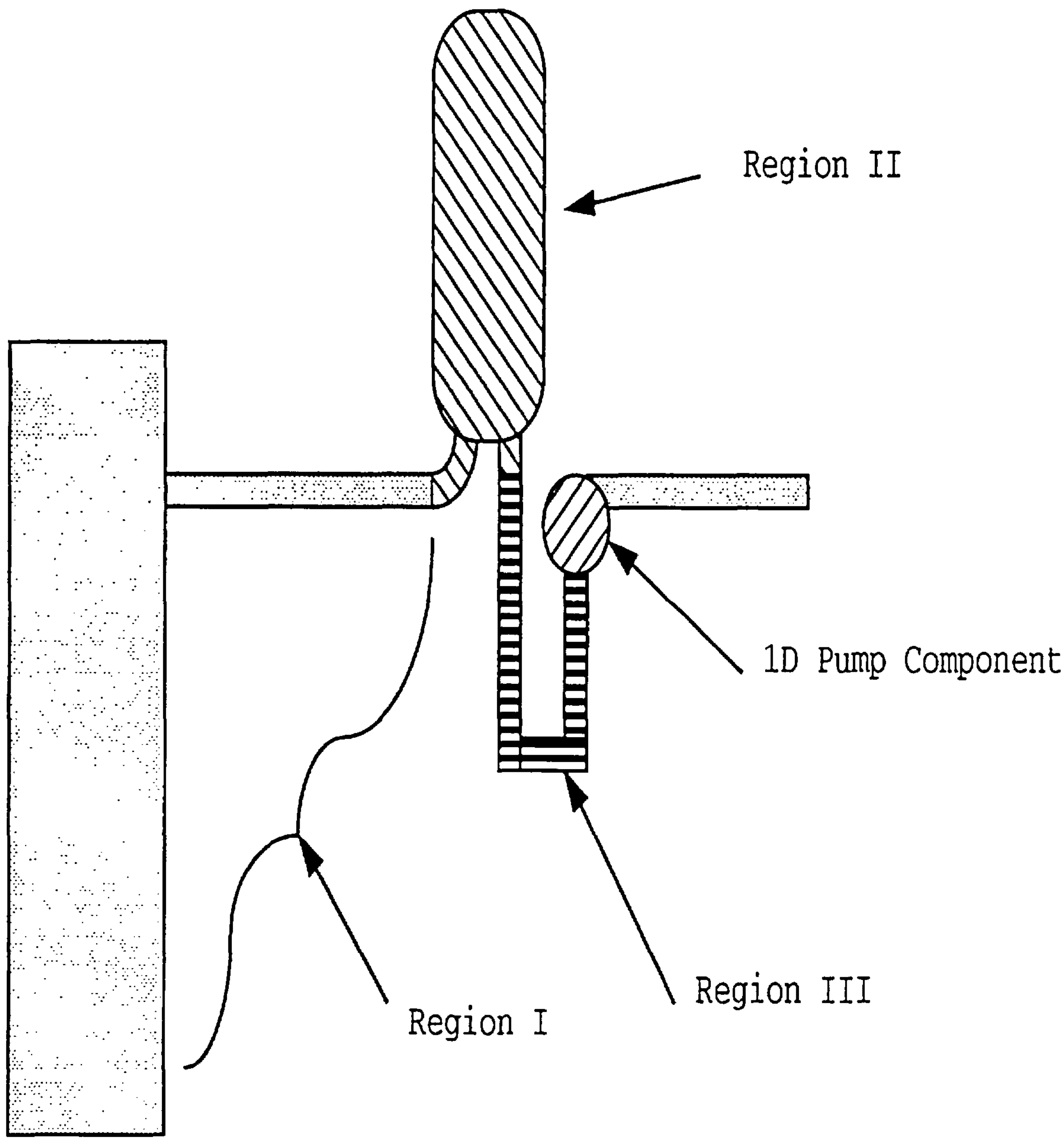

Figure 11-1. PWR Primary Circuit

a,c

Figure 11-2. Channel and Cell Identification

a,c

Figure 11-3. WCOBRA/TRAC Void Fraction Interpolation for Rod Heat Transfer Calculations

a,c

Figure 11-4. WCOBRA/TRAC Level Sharpening for Rod Heat Transfer Calculations

a,c

Figure 11-5. Momentum Cell A

a,c

Figure 11-6. Momentum Cell B

a,c

Figure 11-7. Momentum Cell C

ATTACHMENT A

SBLOCA PIRT

Independent Review

PMX INCORPORATED
209 MAIN STREET
P.O. BOX 153
NORTHPORT, NY 11768-0153
516-754-4721
FAX 516-754-4727

November 17, 1998

Mr. Bob Kemper
Westinghouse Electric Corporation
P.O. Box 355
Pittsburgh, PA 15230-0355

Dear Bob:

Please find enclosed a mini-report that contains a Table of Contents, discussions by the evaluators and the PIRT.

This work was performed independently by Drs. Dan Speyer, Yassin Hassan, Peter Griffith and Tom Fernandez. They evaluated various events for Small Break LOCA and determined their rankings for the PIRT. Please note that some of the items, discussed by the evaluators, need analysis and/or evaluation by Westinghouse.

Mini-Report Prepared by

Paul Malik

Paul Malik

Approved By

Arthur Ginsberg

Dr. Arthur Ginsberg
Chairman

SBLOCA PIRT

Evaluations

&

Rankings

Prepared for

Consolidated Edison
Nuclear Safety & Licensing Section
Indian Point Station
Buchanan, New York 10511

November 1998

Compiled by

Paul Malik
PMX Incorporated
209 Main Street
Northport, NY 11768

TABLE OF CONTENTS

Dan Speyer

CORE

Former Plate Region The former plate region was added since it contains a potentially significant source of water (about 25% of that residing in the core) and has small drain holes distributed axial (and radially). The modeling of this volume, as regards the draining and refilling processes, may be of greatest (relative) importance during the period after natural circulation and prior to core recovery.

UPPER HEAD

Metal Heat Release & Initial Fluid Temperature The upper head metal release and initial fluid temperature were added as these effect when the upper head reaches saturation and (thus) acts as a pressurizer. This has importance in larger breaks (due to core stagnation and reverse flow as it flashes), and may also have greater impact on smaller breaks.

For small breaks it can effect the system pressure and thus break flow rate, and thus time to cessation of natural circulation. The upper head temperature is established (at steady state) by the inflow (downcomer-to-upper head and peripheral upper plenum-to-upper head flows), and the outflow (central upper head-to-upper plenum flow); and this temperature in turn establishes when the region will flash.
Depending on the degree of complexity/3D modeling in the WCOBRA/TRAC code and IP2 model, the upper head-upper plenum region hydraulics may establish a initial temperature between the TCOLD and THOT. The reasonableness of this temperature (compared to plant data and/or other sources) could be part of the code/model V&V and, if not reasonable, require model "adjustment."

Of somewhat lesser importance, but similar in effect, is the modeling of the metal mass heat release which will tend to maintain the upper head temperature, as it flashes and cools. This is potentially effected by CRDM fans, etc.

PRESSURIZER

Interfacial Heat Transfer & Metal Heat Release The metal heat release and interphase heat transfer were added. Although of lesser importance than for pressurizer insurge (increasing pressure) transients, the pressurizer heat transfer model is of greater importance for the slower small break transients, than for large break LOCA in which the pressurizer steam space is essentially subject to an adiabatic expansion. This pressurizer heat transfer includes both the liquid-steam interface and metal-to-liquid/steam heat transfer. These will effect the RCS pressure and thus will effect the blowdown phase break flow.

STEAM GENERATOR

ADV/SRV Mass Flow & Energy Release (Equipment Available/Operator Action Considerations) The operator actions on AFW (and equipment available) were added as they can effect the small break LOCA and because the emergency operating procedures (EOPs) also include directions for operator actions on SG level. The assumptions as regards M/D and S/D (motor and steam driven) AFW pumps included the number of pumps, and presumably 2 M/D and 1 S/D pump is best estimate, and operator actions to control SG level. The other assumption on equipment relates to the SG relief valves, and the best estimate condition would presumably be relief valve available.

The latter (SG relief valves) would have an effect on the SG pressure, and thus the RCS pressure and break flow from approximately end of blowdown to loop seal clearing. The assumptions on AFW flow also may effect the results, e.g., the effect on SG fluid temperature, etc.

PUMP

Pumps ON/OFF was an area in which the post TMI Westinghouse Owners Group (WOG) analyses established (and NRC accepted), as I recall, about 2 minute operator action. These results, from the time period 1980 to 1982, may be different than current assumptions (Is best estimate about 2 minutes?).

Running the pumps longer maintains a liquid or two-phase mixture at the break, and (thus) when pumps are tripped the subsequent core uncovery can be severe; but, on the other hand, other transients are significantly benefitted by RCPs ON--notably SGTR, in which RCP(s) ON allow use of normal PZR spray, which is a significant help for operators to rapidly terminate the SG filling, and lessen likelihood of filling steam lines with water.

Is there a possibility that using WCOBRA/TRAC could allow loss of RCPs at longer times and still yield acceptable results? If this were the case (and credit could be taken by allowing RCPs to operate) what would be the RCP trip criteria, and would the calculation of the 95th percentile PCT value be a problem in this case, as it would also consider the mean and variance for operator action times?

ACCUMULATOR

Interfacial Heat Transfer & Metal Heat Release Although the accumulators are probably of lesser importance, these and other areas (such as pressurizer discussed above) are subject to essentially adiabatic expansion in large LOCAs, where the transient time is small; but small LOCAs occur over considerably longer duration and heat transfer is more important.

Specifically, where the two phases are a non-condensing gas and subcooled water (as in accumulators) how realistic is the code? Perhaps control model(s) are, or can, be used to describe the differential equation for gas pressure--both for the adiabatic case, and with heat transfer. (I have developed such an approach for RETRAN, but never actually implemented it!)

Yassin Hassan

CORE

Heat Transfer Patterns can be organized in the order as they are experienced during the accident scenario. It should start with single-phase flow. It is followed by nucleate boiling heat transfer and so on. Then, plant responses are listed. As an example, the table can be listed in this order:

Heat Transfer to covered Core.
DNB
Post-CHF Heat Transfer
Radiation Heat Transfer
Entrainment/De-Entrainment
Rwet/T_{min}
Mixture Level (This is a plant response)
Etc.

STEAM GENERATOR

Primary Side Heat Transfer

BLD Period During the blowdown period, the tube heat transfer from the primary to the secondary system is important and is ranked high (H). It represents the main mechanism by which the core power is removed from the core. The accurate estimation of this convection heat transfer is important.

LSC Period The primary side heat transfer can be divided into two subdivisions: heat transfer and condensation heat transfer. Or, the brackets (condensation) can be omitted.

Secondary Side Heat Transfer

The secondary side heat transfer is ranked Medium during blowdown and natural circulation periods. The secondary side is a heat sink during these periods. The direction of heat transfer reverses (i.e., secondary-to-primary) following loop seal clearance. Consequently, low ranking is assigned for boiloff and recovery periods.

PUMP

Mixing Pump mixing is ranked Medium* during the blowdown period. This is due to turbulence induced by flow through reactor coolant impellers following pump coastdown. This influence is limited by the short duration of the coastdown.

BREAK

Critical Flow in Complex Geometries Break mass flow is ranked High. Choking in complex geometries is also ranked High. Due to the difficulty of estimating the break flow, it is recommended to perform a sensitivity study with bounding calculations. Several parameters should be tested and varied as:

- Flow resistance
- Upstream flow conditions
- Break quality
- Spectrum of flow locations
- Various critical flow models.

The sensitivity calculations may reduce the ranking during certain phases.

Peter Griffith

CORE

Rewet/ T_{min} It would appear that T_{quench} should be added to this item. However, for the small break LOCA of concern, the process in which T_{quench} appears is never expected to arise. For quenching a fuel rod from below the rewet temperature or T_{min} are sufficient. Inverted annular flow uses the rewet temperature while dispersed flow film boiling the T_{min}. T_{quench} is appropriate for rewetting from above. This never occurs during this transient as the core cannot overheat as long as there water in the upper plenum and there isn't any at this point in the transient. The core always rewets from below in this transient.

STEAM GENERATOR

Primary side two-phase ▲P The key to allowing the liquid in the core to come to the same level as in the downcommer is to clear at least one of the loop seals. This can only happen when the pressure drop in the steam generators is small enough. A large part of this pressure drop is due to gravity so it is very important to get the pressure in the risers of the steam generators correct. For this reason primary side two phase ▲P is rated High for the loop seal clearing part of the transient.

COLD LEG

Water Hammer This concern is rated low for this transient because its effect on the average flows and temperatures into and out of the cold leg are low and fleeting. A condensation induced water hammer occurs over in a small fraction of a second and does not reoccur (if it ever does) for a relatively long time afterwards. To explore the possible consequences of a condensation induced water hammer would entail altering the scenario for this transient. This is beyond the scope of this review.

Tom Fernandez

FUEL ROD

Decay Heat refers to the decay heat model and its uncertainties (range and distribution type) used for the fuel rods. This affects the local heat generation rate for all fuel rods throughout the core, including the hot rod and PCT location. The decay heat model and associated uncertainties are well defined in the 1979 ANS Stand for Decay Heat, independent of other phenomena discussed under Local Power. Decay heat is a primary driver for fuel rod thermal response. Therefore, it is considered an important effect throughout the accident, and is assigned a high (H) ranking for all periods.

Local Power (Local Peaking & Relocation) phenomena refer to the axial power shape, linear heat generation rate (especially the Peak LHGR), and potential fuel relocation after accident initiation. The modeling techniques and uncertainties are considered to be distinctly different from decay heat. The first two phenomena affect the initial power distribution in the hot assembly, hot rod, and PCT location. During the accident, the axial power shape affects the mixture level in the two-phase region, and the vapor superheat in the deficient cooling region. The PLHGR affects the magnitude of the PCT. These two phenomena are considered to have medium (M) importance during the Blowdown, Natural Circulation and Loop Seal Clearing periods when the core is generally well cooled for long periods. They are considered to have (H) importance during the Boiloff and Recovery periods when higher peak clad temperature, including the PCT occur.

Relocation refers to the potential for fuel to relocate inside the cladding toward the rupture zone after accident initiation. This is considered to be unlikely for SBLOCA conditions since even if cladding rupture occurs, the local cladding strain is expected to be relatively small, asymmetrical, and localized ("warts").

CORE

3D Power Distribution referee to the combined radial and axial power distribution in the core. First, this affects the initial stored energy in the fuel roads and core internal structures. This alone is expected to have low (L) importance during the Blowdown and Natural Circulation periods for SBLOCAs; however it is considered to have medium importance for IBLOCAs ($0.1 \leq A_{brk} \leq 1.0\ ft^2$ where core recovery may occur sooner. Thus, it is ranked a L^* for these periods to indicate the rank (*) depends on the scenario. Second, this increasingly affects the core internal 3D circulation, two-phase level, and vapor superheat as the accident progresses through the Loop Seal Clearing, Boiloff, and Recovery periods. Therefore, it is ranked medium (M) during the LSC and High (H) during BO and REC phases.

Top Nozzle/Tie Plate CCFL refers to the Counter Current Flow Limitation (Liquid down flow limited by vapor upflow) than occur at the top of the core during two-phase conditions. This affects the ability of Liquid to drain gravity back down into the core region to retain a well cooled core as RPV inventory is depleted through the break. This is considered to have low (L) importance during SBLOCA Blowdown and medium (M) importance during the subsequent SBLOCA periods as tow-phase flow conditions and core uncovery become more manifest. It is expected to become more important during the BLD, NC and LSC periods for IBLOCAs since two-phase conditions and core uncovery will occur sooner. Therefore it is ranked L* and M* for BLD, NC and LSC periods.

UPPER PLENUM

Hot Leg-Downcomer Gaps refer to the leakage paths that exist between the hot leg nozzles and upper downcomer region during all operating modes. Physically these represent the small residual radial gaps between the core barrel hot leg nozzle tips and the reactor vessel hot leg nozzle inner surfaces. Their presence, by design, allows the upper plenum shroud/core barrel to be installed and removed. These gaps exist even after differential thermal expansion of the core barrel, relative to the RPV, has occurred at rated operating conditions. These gaps can account for on the order of 1% leakage flow directly the upper downcomer to the hot legs during normal operation. These gaps open up as the reactor is shut down and brought to cold conditions. The radial gap is on the order of 0.1 inch for cold conditions, and about 0.01 to 0.02 inches for hot operating conditions. The hot leg circumference is about 94 inches (π times 30 inches) for each leg.

The leakage associated with these gaps can occur during all accident periods; the leakage direction is controlled by the pressure difference between the upper downcomer and inner region of the hot leg nozzles. These leakage paths are expected have a small affect (L) during Blowdown when the system and core flow rates are dominated by other stronger forces (RCP, SG heat sink, break). They are considered to have medium importance during the Natural Circulation periods (as small sneak circuits) that short circuit flow otherwise headed to the core region. They are expected to have High (H) importance during the Loop Seal Clearing period when they provide alternative paths from the upper plenum to the break location to vent some hot core fluid enthalpy and relive some two-phase level depression. Thereafter, they are considered to have increasingly diminished importance of medium (M) during the Boiloff and low (L) during the Recovery periods.

APPENDIX

This appendix contains the PIRT Ranking Tables for Small Break LOCA processes.

Ranking Table - PIRT for Small Break Processes

	Period					
Process	BLD	NC	LSC	BO	REC	NOTES
FUEL ROD						
Stored Energy	L*	L	L	L	L	
Oxidation	L	L	L	H*	H*	
Decay Heat	H	H	H	H	H	TF
Local Power (Local Peaking , Relocation)	M	M	M	H	H	Added : TF
Clad Deformation (Burst Strain, Temp.)	L	L	L	M	M	Added
Gap Conductance	L	L	L	L	L	
CORE						
DNB	L	L	L	L	L	
Post-CHF Heat Transfer	L	L	M	H	H	
Rewet/T_{min}	L	L	M	H	H	PG
Heat Transfer to Covered Core	M	L	L	L	L	
Radiation Heat Transfer	L	L	L	M	M	
Mixture Level	M	M	H	H	H	
3-D Flow/Core Natural Circulation	L	L	L	M	M	
Entrainment /De-Entrainment	L	L	L	M	M	
Flow Resistance	L	M	M	L	L	
3-D Power Distribution	L*	L*	M	H	H	Added: TF
Top Nozzle/Tie Plate CCFL	L*	M*	M*	M	M	Added: TF
Former Plate Region	L	L	M	M	L	Added: DS
UPPER HEAD						
Draining/Mixture Level	M	M	L	L	L	
Metal Heat Release	L	L	L	L	L	
Initial Fluid Temperature	M	L	L	L	L	Added: DS
UPPER PLENUM						
Hot Assembly Location	L*	L	L	L	L	
Entrainment/De-Entrainment	L*	L	L	M	L	
Draining/Fallback/CCFL	L*	M*	M*	M	M	
Mixture Level	M	M	M	L	L	
Horizontal Stratification	L	M	M	L	L	
Phase Separation at Pressurizer Tee	L	L	L	L	L	
Counter-Current Flow & CCFL	L	H	H	L	L	
Hot Leg – Downcomer Gap Flow	L	M	H	M	L	Added: TF
Condensation	N/A	L	L	L	L	Added
Metal Heat Release	L	L	L	L	L	Added

Ranking Table - PIRT for Small Break Processes

	Period					
Process	BLD	NC	LSC	BO	REC	NOTES
PRESSURIZER/SURGE LINE (CL Break)						
Level Swell/Flashing	M	L	L	L	L	
Surge Line Flow/Flooding	L	L	L	L	L	
Entrainment/De-Entrainment	L	L	L	L	L	
Interface Heat Transfer	M	L	L	L	L	
Metal Heat Release (including PZR Heater)	M	L	L	L	L	Added
Interface Heat Transfer	M	L	L	L	L	Added: DS
STEAM GENERATOR						
Primary Side Heat Transfer (condensation)	H	M	H	M	M	YH
Non-condensable Gas Effects	L	L	L	L	L	
CCFL/Tube Voiding	L	M	H	L	L	
Primary Side 2-Phase ΔP	L	M	H	L	L	PG
Multi-tube Behavior	L	M	M	L	L	
Secondary Side Stratification & Recirc.	L	M	L	L	L	
Secondary Side Level	L	M	L	L	L	
ADV/SRV Mass Flow & Energy Release	L	M	L	L	L	DS
Tube Plugging/SGTP asymmetry	L	M	M	M	M	
Secondary Side Heat Transfer	M	M	L	L	L	YH
Metal Heat Release	L	L	L	L	L	Added
HOT LEG						
Entrainment/De-Entrainment	L	L	L	L	L	
PUMP SUCTION PIPING/LOOP SEAL						
CCFL	L	L	L	L	L	WEST.
Entrainment/Flow Regime/Interfacial Drag	L	L	H	M	L	
Horizontal Stratification	L	L	H	M	L	
Flow Resistance	L	L	M	L	L	
Metal Heat Release	L	L	L	L	L	Added
PUMP						
Mixing	M*	NL	N	N	N	
2-Phase Performance	M*	N/A	N/A	N/A	N/A	
Flow Resistance	L	M	M	L	L	
Coastdown Performance	M*	N/A	N/A	N/A	N/A	
Friction/Windage Losses	M	M	M	L	L	Added
Pump CCFL	N/A	L	M	M	M	
Metal Heat Release	L	L	L	L	L	Added

Ranking Table - PIRT for Small Break Processes

	Period					
Process	BLD	NC	LSC	BO	REC	NOTES
ACCUMULATOR						
Injection Flow Rate	N/A	N/A	N/A	N/A	M*	
Line Resistance	N/A	N/A	N/A	N/A	L*	
Nitrogen Effects	N/A	N/A	N/A	N/A	L*	
Check Valve Hysteresis	N/A	N/A	N/A	N/A	L*	
Dissolved Nitrogen Effects	N/A	N/A	N/A	N/A	L*	Added
Interfacial Heat Transfer	N/A	N/A	N/A	N/A	M*	Added: DS
Metal Heat Release	L	L	L	L	L	Added: DS
COLD LEG						
Condensation (Stratified)	N/A	L	M	H	H	
Non-Condensable Effects	N/A	L	L	L	L	
Horizontal Stratification/Flow Regime	L	L	H	H	H	
Flow Resistance	L	L	L	L	L	Added
Water Hammer	L	L	L	L	L	Added: PG
Metal Heat Release	L	L	L	L	L	Added
SAFETY INJECTION						
Condensation/ Jet Efficiency	N/A	L	L	L	L	
DOWNCOMER/LOWER PLENUM						
Condensation	N/A	L	L	L	L	
Non-Condensable Effects	N/A	L	L	L	L	
3-D Effects	M*	L	L	L	L	
Mixture Level/Flashing/Void Fraction	M	M	H	H	H	
Enterainment/De-Enterainment	L	L	L	L	L	
Flow Resistance	L	L	L	L	L	Added
Vessel Metal Wall/RPV Int. Heat Release Effects	L	L	L	L	L	
BREAK						
Critical Flow In Complex Geometries	H	H	H	H	H	YH
Upstream Flow Regime & Break Quality	H	H	H	H	H	
Non-condensable Effects	L	L	L	L	L	

Note: * means that the ranking is "Break Size" dependent.

Ranking Table - PIRT for Small Break Processes

	Period					
Process	BLD	NC	LSC	BO	REC	NOTES
PRESSURIZER/SURGE LINE (CL Break)						
Level Swell/Flashing	M	L	L	L	L	
Surge Line Flow/Flooding	L	L	L	L	L	
Entrainment/De-Entrainment	L	L	L	L	L	
Interface Heat Transfer	M	L	L	L	L	
Metal Heat Release (including PZR Heater)	M	L	L	L	L	Added
Interface Heat Transfer	M	L	L	L	L	Added: DS
STEAM GENERATOR						
Primary Side Heat Transfer (condensation)	H	M	H	M	M	YH
Non-condensable Gas Effects	L	L	L	L	L	
CCFL/Tube Voiding	L	M	H	L	L	
Primary Side 2-Phase ΔP	L	M	H	L	L	PG
Multi-tube Behavior	L	M	M	L	L	
Secondary Side Stratification & Recirc.	L	M	L	L	L	
Secondary Side Level	L	M	L	L	L	
ADV/SRV Mass Flow & Energy Release	L	M	L	L	L	DS
Tube Plugging/SGTP asymmetry	L	M	M	M	M	
Secondary Side Heat Transfer	M	M	L	L	L	YH
Metal Heat Release	L	L	L	L	L	Added
HOT LEG						
Entrainment/De-Entrainment	L	L	L	L	L	
PUMP SUCTION PIPING/LOOP SEAL						
CCFL	L	L	L	L	L	WEST.
Entrainment/Flow Regime/Interfacial Drag	L	L	H	M	L	
Horizontal Stratification	L	L	H	M	L	
Flow Resistance	L	L	M	L	L	
Metal Heat Release	L	L	L	L	L	Added
PUMP						
Mixing	M*	NL	N	N	N	
2-Phase Performance	M*	N/A	N/A	N/A	N/A	
Flow Resistance	L	M	M	L	L	
Coastdown Performance	M*	N/A	N/A	N/A	N/A	
Friction/Windage Losses	M	M	M	L	L	Added
Pump CCFL	N/A	L	M	M	M	
Metal Heat Release	L	L	L	L	L	Added

Ranking Table - PIRT for Small Break Processes

Process	BLD	NC	LSC	BO	REC	NOTES
	Period					
ACCUMULATOR						
Injection Flow Rate	N/A	N/A	N/A	N/A	M*	
Line Resistance	N/A	N/A	N/A	N/A	L*	
Nitrogen Effects	N/A	N/A	N/A	N/A	L*	
Check Valve Hysteresis	N/A	N/A	N/A	N/A	L*	
Dissolved Nitrogen Effects	N/A	N/A	N/A	N/A	L*	Added
Interfacial Heat Transfer	N/A	N/A	N/A	N/A	M*	Added: DS
Metal Heat Release	L	L	L	L	L	Added: DS
COLD LEG						
Condensation (Stratified)	N/A	L	M	H	H	
Non-Condensable Effects	N/A	L	L	L	L	
Horizontal Stratification/Flow Regime	L	L	H	H	H	
Flow Resistance	L	L	L	L	L	Added
Water Hammer	L	L	L	L	L	Added: PG
Metal Heat Release	L	L	L	L	L	Added
SAFETY INJECTION						
Condensation/ Jet Efficiency	N/A	L	L	L	L	
DOWNCOMER/LOWER PLENUM						
Condensation	N/A	L	L	L	L	
Non-Condensable Effects	N/A	L	L	L	L	
3-D Effects	M*	L	L	L	L	
Mixture Level/Flashing/Void Fraction	M	M	H	H	H	
Enterainment/De-Enterainment	L	L	L	L	L	
Flow Resistance	L	L	L	L	L	Added
Vessel Metal Wall/RPV Int. Heat Release Effects	L	L	L	L	L	
BREAK						
Critical Flow In Complex Geometries	H	H	H	H	H	YH
Upstream Flow Regime & Break Quality	H	H	H	H	H	
Non-condensable Effects	L	L	L	L	L	

Note: * means that the ranking is "Break Size" dependent.

WCAP-14936-NP
Volume 2, Rev. 0
Sections 12-23

Code Qualification Document for Best Estimate Small Break LOCA Analysis

Volume 2: Small Break Code Validation

R. M. Kemper
S. M. Bajorek
D. C. Golden
K. Ohkawa
D. J. Shimeck
A. K. Muftuoglu
D. Paramonov
M. Dzodzo
M. Y. Young

April 2003

Westinghouse Electric Company LLC
P.O. Box 355
Pittsburgh, PA 15230-0355

ABSTRACT

The document "Code Qualification Document for Best Estimate Loss of Coolant Accident Analysis" (WCAP-12945-P-A) discussed the WCOBRA/TRAC computer code and the methodology used to determine the 95th percentile peak cladding temperature (PCT) for a large break loss of coolant accident (LOCA) scenario. Westinghouse has reviewed the large break code and methodology to determine if the same principles could be adapted to reliably predict the processes that occur in a small break LOCA lasting from several hundred to several thousand seconds. This document, "Code Qualification Document for Best Estimate Small Break LOCA Analysis," (WCAP-14936), describes the WCOBRA/TRAC small break LOCA code version, the code validation performed and a methodology to determine the 95th percentile PCT for small break LOCA transients.

Volume 1 describes the features, models and correlations contained in the small break LOCA version of the WCOBRA/TRAC computer code. First, the small break processes considered to have the greatest effect during a small LOCA event are identified and ranked in the phenomena identification and ranking table (PIRT). The sufficiency of the large break WCOBRA/TRAC models and correlations for small LOCA analysis is then evaluated. A comprehensive presentation of the WCOBRA/TRAC-SB models and correlations follows.

Volume 2 documents simulations of a large number of separate and integral effects tests using this small break version of the code. The simulations provide, at different scales, predicted transients in which all of the important processes are compared with experimental data. The information obtained from the simulations is used to assess errors within the code. The test simulations and subsequent comparison to experimental data determine the bias and uncertainty of major model packages as they apply to small break LOCA thermal-hydraulic conditions.

Volume 3 reviews the operator actions pertinent to a small break loss-of-coolant accident (LOCA) event using Indian Point Unit 2, a four-loop pressurized water reactor (PWR), as the reference. Sources of uncertainty in the plant condition and the limiting accident analysis assumptions are identified. The effects of various assumptions on small break LOCA transient behavior are investigated through numerous calculations using WCOBRA/TRAC-SB. The calculations examine the sensitivity of the results to the break size, location, orientation, and offsite power availability.

Volume 4 presents calculations that are performed to determine the sensitivity of results to the plant core power distribution, the initial and boundary conditions, and code modelling assumptions. These studies, in which parameters are varied one at a time, are performed for Indian Point Unit 2 to quantify the sensitivity of plant behavior to changes in plant initial conditions and accident modelling. An uncertainty methodology consistent with the application of the Code Scaling, Applicability, and Uncertainty (CSAU) methodology is identified to define the overall plant analysis uncertainty and is applied to determine the 95th percentile PCT for the Indian Point Unit 2 small break LOCA analysis. Volume 4 also demonstrates the compliance of the Westinghouse best estimate large break LOCA methodology with U.S. Nuclear Regulatory Commission (NRC) Regulatory Guide 1.157 and with 10CFR50.46.

TABLE OF CONTENTS

Volume 1 Models and Correlations
Volume 2 Small Break Code Validation
Volume 3 PWR Uncertainties and Sensitivities for Small Break LOCA
Volume 4 Small Break Uncertainty Methodology

TABLE OF CONTENTS (Cont'd)

TABLE OF CONTENTS (Cont'd)

TABLE OF CONTENTS (Cont'd)

TABLE OF CONTENTS (Cont'd)

TABLE OF CONTENTS (Cont'd)

TABLE OF CONTENTS (Cont'd)

TABLE OF CONTENTS (Cont'd)

TABLE OF CONTENTS (Cont'd)

LIST OF TABLES

LIST OF TABLES (Cont'd)

LIST OF FIGURES

LIST OF FIGURES (Cont'd)

LIST OF FIGURES (Cont'd)

LIST OF FIGURES (Cont'd)

LIST OF FIGURES (Cont'd)

LIST OF FIGURES (Cont'd)

LIST OF FIGURES (Cont'd)

LIST OF FIGURES (Cont'd)

LIST OF FIGURES (Cont'd)

LIST OF FIGURES (Cont'd)

LIST OF FIGURES (Cont'd)

LIST OF FIGURES (Cont'd)

LIST OF FIGURES (Cont'd)

LIST OF FIGURES (Cont'd)

LIST OF FIGURES (Cont'd)

LIST OF FIGURES (Cont'd)

LIST OF ACRONYMS AND ABBREVIATIONS

A. O.	Axial Offset
ACRS	Advisory Committee on Reactor Safeguards
AFLUX	Core Average Heat Flux
ANS	American Nuclear Society
ANSI	American National Standards Institute
BE-SBLOCA	Best Estimate Small Break LOCA
BLD	Blowdown
BO	Boil-off
BOL	Beginning of Life
CAOC	Constant Axial Offset Control
CCFL	Counter-current Flow Limitation
CD	Discharge Coefficient for Two-phase Break Flow
CE	Combustion Engineering
CHF	Critical Heat Flux
COLR	Core Operating Limits Report
COSI	Condensation On Safety Injection
CP	Conditional Probability
CQD	Code Qualification Document
CSAU	Code Scaling Applicability and Uncertainty
DFFB	Dispersed Flow Film Boiling
DNB	Departure from Nucleate Boiling
ECCS	Emergency Core Cooling System
EOP	Emergency Operating Procedure
FAC	Final Acceptance Criteria
FEM	Entrained Droplet Flowrate
FLM	Continuous Liquid Flowrate
GEDM	Generalized Energy Deposition Model
H	High (Importance Level in Los Alamos PIRT Ranking Scheme)
HAFLUX	Hot Assembly Average Power
HAPHR	Hot Assembly Peak Heat Rate
HHSI	High Head Safety Injection
HRFLUX	Hot Rod Average Power
HTC	Heat Transfer Coefficient
IADF	Inverted Annular Dispersed Flow

LIST OF ACRONYMS AND ABBREVIATIONS (Cont'd)

IAFB	Inverted Annular Film Boiling
INEL	Idaho National Engineering Laboratory
IP2	Indian Point Unit 2
JAERI	Japan Atomic Energy Research Institute
L	Low (Importance Level in Los Alamos PIRT ranking scheme)
LOCA	Loss of Coolant Accident
LOCE	Loss of Coolant Experiment
LOFT	Loss of Fluid Test
LOOP	Loss of Offsite Power
LSC	Loop Seal Clearance
LSTF	Large Scale Test Facility
M	Medium (Importance Level in Los Alamos PIRT ranking scheme)
MSSV	Main Steam Safety Valve
MSIV	Main Steam Isolation Valve
MTC	Moderator Temperature Coefficient
N/A	Not Applicable
NC	Natural Circulation
NPP	Nuclear Power Plant
NRC	Nuclear Regulatory Commission
NRU	National Research Universal
NSSS	Nuclear Steam Supply System
NUCL	Saturated Nucleate Boiling
OPA	Offsite Power Available
ORNL	Oak Ridge National Laboratory
PCT	Peak Cladding Temperature
PIRT	Phenomena Identification and Ranking Table
PLHGR	Peak Linear Heat Generation Rate
PLHR	Peak Linear Heat Rate
PLOW	Low Power Region Relative Power
PORV	Pressure-operated Relief Valve
PWR	Pressurized Water Reactor
RABL	Reflood Assist Bypass Line
RAI	Request for Additional Information
RAOC	Relaxed Axial Offset Control

LIST OF ACRONYMS AND ABBREVIATIONS (Cont'd)

RCP	Reactor Coolant Pump
RCS	Reactor Coolant System
REC	Core Recovery
RHR	Residual Heat Removal
ROSA	Rig-of-Safety Assessment
RSIC	Radiation Shielding Information Center
RWST	Refueling Water Storage Tank
SBLOCA	Small Break Loss of Coolant Accident
SCNB	Subcooled Nucleate Boiling
SG	Steam Generator
SGTP	Steam Generator Tube Plugging
SI	Safety Injection
SIS	Safety Injection Systems
SPL	Single-phase Liquid Convection
SPV	Single-phase Vapor Convection
THTF	Thermal Hydraulic Test Facility
TPFL	Two-Phase Flow Loop
TRAN	Transition Boiling
TS	Technical Specifications
TSI	Safety Injection Water Temperature
UHI	Upper Head Injection
UPTF	Upper Plenum Test Facility

COMMONLY USED EQUATION NOMENCLATURE

a	sonic velocity
a_r	grid blockage ratio
a_v	vapor absorption coefficient
a_ℓ	liquid absorption coefficient
A	area
A_X	axial flow area
A_z	lateral flow area
A_w	wall heat transfer area
A_I	intercell friction area
A_i	interfacial area
B	mass transfer number
C_o	slip distribution parameter
C_D	drag coefficient
C_p	specific heat at constant pressure
C_v	specific heat at constant volume
D	diameter
D_h	hydraulic diameter
$\underline{\underline{D}}$	deformation tensor
e	specific energy
f_w	wall friction factor
f_i	interfacial friction factor
f	theoretical density fraction (Ch. 7)
F	ramping function
$\underline{\underline{F}}$	turbulence anisotropy tensor
F	gray body factor (Ch. 6)
F_{CHEN}	Chen convective boiling multiplier
$\mathscr{F}$	force
g	gravitational acceleration
g_c	gravitational conversion constant
$\underline{g}$	gravitational acceleration vector
G	mass flux
G_X	axial mass flux
G_Z	transverse mass flux
h	heat transfer coefficient
h	normalized pump head (Ch. 9)
h_i	interfacial heat transfer coefficient
H	enthalpy
H_{fg}	enthalpy of vaporization
H_m	Meyer hardness
I	grid rewet index (Ch. 5,6)
I	pump moment of inertion (Ch. 9)
k	thermal conductivity
K	loss coefficient (Ch. 2,4)
K	conductance (Ch. 7)
K_{iX}	vertical interfacial drag coefficient
K_{iZ}	transverse interfacial drag coefficient
K_{wX}	vertical wall drag coefficient
K_{wZ}	transverse wall drag coefficient
K_X	axial flow form loss coefficient
K_Z	transverse flow form loss coefficient
L	length
L_g	gap width
L_g^o	orthogonal gap width
L_b	mean beam length
ℓ_m	momentum mixing length
ℓ_H	energy mixing length
$\dot{m}$	mass flowrate
M	momentum (Ch. 2)
M	molecular weight (Ch. 7)
n	pump head multiplier (Ch. 9)
N	mole fraction
N	number density
N_μ	pump torque multiplier (Ch. 9)
P	viscosity number
P	pressure
P_W	wetted perimeter

COMMONLY USED EQUATION NOMENCLATURE (Cont'd)

Pr	Prandtl number
P_{rod}	fuel rod pitch
$q_{w\ell}$	wall-liquid heat transfer rate
q_{wv}	wall-vapor heat transfer rate
$q_{i\ell}$	interface-liquid heat transfer rate
q_{iv}	interface-vapor heat transfer rate
$Q_{w\ell}$	wall-liquid heat transfer
Q_{wv}	wall-vapor heat transfer
r	bubble/drop radius
r	radial coordinate
R	internode resistance (Ch. 7)
R	radiation resistance (Ch. 6)
R	gas constant (Ch. 10)
R_o	orifice hole radius
Re	Reynolds number
s	specific entropy
S	net rate of entrainment
S_{CHEN}	Chen building suppression factor
S_E	rate of entrainment
S_{DE}	rate of de-entrainment
St	Stanton number
t	time
T	temperature
T	pump torque (Ch. 9)
$\underline{\underline{T}}$	stress tensor
$\underline{T}^T$	Reynold stress tensor
u	vertical velocity component, Cartesion coordinates
U	vertical velocity component, subchannel coordinates
v	transverse velocity component, Cartesian coordinates
V	volume
V_c	mesh cell volume
w	transverse velocity component, Cartesian coordinates
W	transverse velocity, subchannel coordinates
W^o	orthogonal transverse velocity, subchannel coordinates
We	Weber number
x	quality
x	vertical direction, Cartesian coordinates (Ch. 2)
X	vertical direction, subchannel coordinates
X	axial direction, 1D components
y	transverse direction, Cartesian coordinates
z	transverse direction, Cartesian coordinates
Z	transverse direction, subchannel coordinates

<u>Greek</u>

α	void fraction
α_N	normalized pump speed
β	volumetric coefficient of expansion
Γ	net rate of mass transfer
δ	film thickness
δ_{ij}	Kronecker delta
ε	thermal emissivity
ε	strain
η	fraction of vapor generation coming from entrained liquid

η_{NR}	de-entrainment efficiency
κ	thermal diffusivity
λ	characteristic wave length
μ	viscosity
μ^T	turbulent viscosity
ρ	density
Σ	absorption cross section
σ	surface tension
σ	stress (Ch. 2, 7)
$\underline{\underline{\sigma}}$	fluid-fluid stress tensor
σ_{SB}	Stephan-Boltzmann constant
τ	shear stress
$\underline{\underline{\tau}}$	viscous drag force
$\underline{\underline{\tau}}_i$	interfacial drag force
v	specific volume
v	normalized pump volumetric flow
χ	Martinelli-Nelson factor
ψ_a	absorption efficiency
Ω	source term
ω	specific speed

Subscripts

am	annular-mist flow regime
ACC	accumulator
b	bubble
br	bubble rise
bubbly	bubbly flow regime
Brom	Bromley correlation
crit	critical
cwv	convection wall-vapor
CHEN	Chen correlation
CHF	critical heat flux
churn	churn flow regime
CT	churn-turbulent flow regime
d	drop
dcht	direct contact heat transfer
DD	dispersed droplet flow regime
DE	de-entrainment
dffb	dispersed flow film boiling
DFFB	dispersed flow film boiling
e	entrained field
E	entrainment
f	saturated liquid
fb	film boiling
fr	flow regime
fric	friction loss
form	form loss
FC	forced convection
FD	film/drop flow regime
FF	falling film flow regime
g	saturated vapor
gas	gas
gv	grid to vapor
Gr	Grashof number
h	hydraulic
Henry	Henry correlation
i	interfacial
IVA	inverted annular flow regime
IVS	inverted liquid slug flow regime
k	phase k
ℓ	liquid field
liq	liquid
LB	large bubble
m	mixture

COMMONLY USED EQUATION NOMENCLATURE (Cont'd)

MIN	minimum film boiling point
nc	natural convection
lnc	laminar natural convection
lfc	laminar forced convection
N	normalized
NB	nucleate boiling
o	orifice
p	pipe
QF	quench front
r	relative
r	radial (Ch. 7)
rwe	radiation wall-entrained field
rwg	radiation wall to grid
$rw\ell$	radiation wall-liquid field
rwv	radiation wall-vapor field
s	drop formation
sat	saturation
slug	slug flow regime
s	slug
SB	small bubble flow regime
SCL	subcooled liquid
SCNB	subcooled nucleate boiling
SCV	subcooled vapor
SNL	superheated liquid
SLV	superheated vapor
SLB	small to large bubble flow regime
SPL	single-phase liquid
SPV	single-phase vapor
sup	suppression
TB	transition boiling
TD	top deluge flow regime
tnc	turbulent natural convection
TQ	top quench
UO_2	uranium dioxide
v	vapor field
vap	vapor
ve	between vapor and entrained fields
$v\ell$	between vapor and liquid fields
w	wall
wb	wall to fluid as latent heat
$w\ell$	wall to liquid
wv	wall to vapor
x	vertical direction, Cartesian coordinates
X	vertical direction, subchannel coordinates
X	axial direction, 1D components
y	transverse direction, Cartesian coordinates
z	transverse direction, Cartesian coordinates
Z	transverse direction, subchannel coordinates
Zr	Zirconium
2ϕ	two-phase
Γ	phase change

Superscripts

i	interfacial surface average
n	old time value
$\tilde{n}$	donor cell old time value
T	turbulent
t	transpose
$''$	per unit area
$'''$	per unit volume

SECTION 12
CORE HEAT TRANSFER DURING A SMALL BREAK LOCA

12-1 Introduction

The small break LOCA transient is characterized by the draining of the initial Reactor Coolant System (RCS) inventory to the break location. Five distinct periods have been identified during a small break LOCA event: blowdown, natural circulation, loop seal clearance, boiloff, and core recovery. The duration of each period is break-size dependent. Each small break LOCA period is described in the detailed discussion of the small break LOCA PIRT (Volume 1, Section 1-4, of this document).

In Westinghouse-designed pressurized water reactors (PWRs), core uncovery and fuel rod heatup occur in the boiloff period and terminate in the recovery period. During the boiloff period, the vessel mixture level reaches a minimum value as the liquid inventory gradually boils away. If this two-phase mixture level is low enough, core uncovery occurs. The recovery phase begins when the RCS is depressurized to the point where boiloff is exceeded by the delivery of safety injection to the vessel. The fuel rod heatup transient is terminated once the entire core is quenched and the safety injection flow from the safety injection pumps and/or accumulators exceeds the break flow.

The core flowrates during the fuel rod heatup period of a small break LOCA are lower than those associated with large break LOCAs. In general, the core flowrates in all phases of the large break LOCA are large enough for the convective flow to be turbulent. This is not always the case during a small break LOCA. For example, in a 3-inch cold leg break analysis of Indian Point Unit 2, similar to the case reported in Section 27 in Volume 3 of this document, the steam flow in the hot assembly at the time of PCT is less than 1 lbm/s; the Reynolds number (Re) based on film temperature is below the value for fully developed turbulent flow (Re = 10,000) throughout virtually all of the core uncovery transient, and it falls below 3000 near the time of minimum inventory. Moreover, for such low Re steam flows, the steam velocity is not sufficient to cause significant entrainment of droplets. For the 3-inch break case at Indian Point Unit 2, the entrained field flow is nonexistent for the core uncovery transient. In general, the small break LOCA transients show steam flow only above the mixture level for the smaller break sizes. At larger break sizes (8-inch break and greater), an entrained field is predicted, but the steam Re in the hot assembly for a 10-inch break transient for Indian Point Unit 2 is approximately 10,000 for much of the time that the core is uncovered.

12-2 Physical Processes

During the boiloff period, the fuel rods above the core mixture level are cooled by steam flowing (with or without entrained droplets) at a low rate. Review of the Indian Point Unit 2 cases emphasizes the importance of having heat transfer models that are valid for the laminar-turbulent transition range of Re, defined as [ ]^{a,c} in this work.

Therefore, the important physical processes are those associated with heat transfer in the single-phase vapor (SPV) and dispersed droplet regimes. In WCOBRA/TRAC modelling in the best estimate small break LOCA version of the code, validation is needed that the code provides reasonable predictions of the heat transfer coefficient (HTC) in low Re steam flows, with and without droplets, at high pressure conditions typical of the boiloff period in a small break LOCA.

The important physical processes in predicting heat transfer involving low Re flows, consisting of either SPV or a high quality [ ]^{a,c} dispersed droplet flow, are as follows:

- Convective HTC in the laminar-turbulent transition range dependence on the steam Re

- Drop-wall contact heat flux in the dispersed flow film boiling (DFFB) regime dependence on Re

  In the large break LOCA scenario, drop-wall contact depends solely on properties, local void fraction, and wall superheat because the effectiveness of drop-wall contact is comparable regardless of the mass flux. However, the drop-wall contact heat flux decreases to zero if the flow becomes laminar.

- Wall-to-steam thermal radiation in the DFFB and the SPV regimes

- Void fraction gradient defining a mixture level

  The hydraulics and the fluid condition at a sharp void fraction gradient differ markedly between the mixture and vapor phases.

12-3 WCOBRA/TRAC-SB Heat Transfer Model

The WCOBRA/TRAC heat transfer regime map presented as Figure 6-3 in Volume 1 of this document is repeated here as Figure 12-1 for ease of reference. Section 6 of this document provides the details of the models and correlations of the WCOBRA/TRAC-SB heat transfer package; some of the Section 6 equations are included in the discussion that follows.

12-3-1 Convective Heat Transfer

The SPV regime HTC is selected from among four correlations: Dittus-Boelter (Dittus and Boelter, 1930), Wong-Hochreiter (Wong and Hochreiter, 1981), laminar flow heat transfer (Nu = 10), and turbulent natural convection. The SPV HTC is used when the void fraction is [ ]^{a,c}.

The wall HTC $h_{wv,SPV}$ is selected according to: [

]^{a,c}

[ ]^{a,c}

In the SPV regime, liquid phase HTCs are set to zero:

$$h_{wl,SPV} = 0$$
$$h_{wb,SPV} = 0$$

The selection logic ensures a smooth and continuous transition in HTC from low Re (laminar flow) to high Re (turbulent). In ensuring that correlations are used within the range of Re that is appropriate for each, the convective HTC for vapor is calculated as:

$$h_{wv,FC} = (1 - R_{HTCV})h_{wv,low} + R_{HTCV}h_{wv,high} \tag{6-2-7}$$

where, R_{HTCV} acts to linearly ramp the HTC in the laminar-turbulent transition regime. This term is calculated as: [

]^{a,c} (6-2-8)

The low and high Re convective HTCs are selected as:

written

$$h_{wv,low} = maximum \left\{ \begin{array}{l} h_{w,v,lam} \\ h_{wv,nc} \end{array} \right. \quad (if\ Re < [\cancel{2000}]^{a,c}) \tag{6-2-9}$$

and

$$h_{wv,high} = maximum \left\{ \begin{array}{l} h_{wv,DB} \\ h_{wv,WH} \end{array} \right. \tag{6-2-10}$$

Thus, if Re_v < [ ]^{a,c}, the maximum of the HTC from a constant Nusselt number (Nu = 10) and turbulent natural convection is selected. For Re [ ]^{a,c}, the maximum of the Dittus-Boelter and Wong-Hochreiter correlations is used. (The Wong-Hochreiter predicts a larger value up to Re = 25,000.)

This selection logic retains the possibility of natural convection if flows are appropriately low (Regulatory Guide 1.157, 1989) and prohibits the use of turbulent flow correlations at Re below their validity.

12-3-2 Drop-Wall Contact

The direct contact heat transfer for the dispersed droplet field is calculated using a model originally proposed by Forslund and Rohsenow (Forslund and Rohsenow, 1968) with modifications suggested by Bajorek and Young (Bajorek and Young, 1998) to improve performance at low Re.

The direct wall contact term h_{dcht} is discussed in Section 6-2-8 of this document.

12-3-3 Radiation From Wall to Vapor

The SPV heat transfer includes the thermal radiation from wall to steam. Thermal radiation occurs at void fractions up to 1.0.

The SPV HTC is calculated as:

$$h_{wv,SPV} = F_{grid} h_{wv,FC} + h_{rwv} \tag{6-2-11}$$

where the radiation HTC from the wall to vapor is calculated by Equation 6-156 in Section 6 of this document.

The grid enhancement term F_{grid} applies only to the convective term. Likewise, the two-phase enhancement multiplier should not be applied to the thermal radiation term in the DFFB regime. Therefore, $F_{2\varphi}$ is restricted to the convective term and is not applied to the radiation term.

The HTCs for the DFFB regime are calculated as follows:

$$h_{wv,DFFB} = F_{grid}F_{2\varphi}h_{wv,FC} + h_{rwv} \tag{6-2-15}$$

$$h_{wl,DFFB} = h_{rwe} \tag{6-131}$$

$$h_{wb,DFFB} = h_{dcht} \tag{6-132}$$

where,

$h_{wv,FC}$ is the convective HTC as described in subsection 12-3-1
h_{rwv} is given by Equation 6-156
h_{rwe} is given by Equation 6-157
h_{dcht} is given by Equation 6-2-14

The two-phase enhancement term ($F_{2\varphi}$) is calculated by Equation 6-125 and is limited to values within the range $1.0 \leq F_{2\varphi} \leq$ [ ]^{a,c}

12-3-4 Mixture Level Sharpening

In a core uncovery situation during the boiloff period of a small break LOCA event, fuel rod heat transfer is orders of magnitude less in the SPV and/or DFFB regimes which prevail above the mixture level elevation than in the nucleate boiling regime which exists in the two-phase mixture region. Thus, for the calculation of fuel rod heatup, it is imperative that the mixture level interface be accurately defined. Section 11-2-4 of this document describes in detail the WCOBRA/TRAC-SB level sharpener coding.

The level sharpening logic is applied to void fractions from COBRA channel cells; it initially assumes that no sharp level exists. The parameter ISHARP is an indicator of where the mixture level is located. The void gradient is defined as being sharp when [ ]^{a,c}. If a sharp gradient is detected in the bottom half of the cell, ISHARP is set to 1; if the sharp gradient is in the top half of the cell, the value of ISHARP is set to 2.

The upper and lower limits of the void gradient search are [ ]^{a,c} respectively. [ ]^{a,c} corresponds to the void fraction for transition between the inverted annular dispersed flow (IADF) and DFFB heat transfer regimes. Thus, when ISHARP = 1, the physical picture of the cell is one in which a transition from inverted annular film boiling (IAFB) occurs in the bottom half of the cell and the transition from IADF to DFFB is at the top edge. Likewise, [ ]^{a,c} corresponds to the transition from inverted annular film boiling (IAFB) to IADF.

The coding of the level sharpener logic has been verified via a series of standalone calculations, which assume a uniform cell height.

12-4 Assessment of WCOBRA/TRAC-SB Heat Transfer Model for Small Break LOCA Application

A driver-plotter program (COBRAHT), similar to that used in large break LOCA heat transfer assessment, was used to examine the performance of WCOBRA/TRAC-SB in the SPV and DFFB regimes important to small break LOCA PCT determination and to determine the bias and uncertainty of these models. In COBRAHT, convective heat transfer correlations are selected per the Re dependence. In testing the performance, HTCs predicted from the WCOBRA/TRAC heat transfer package were compared to experimental test data. The test data for comparison contained a complete set of local measurements so that the HTC could be assessed without uncertainty due to compensating error. The HTC calculation in COBRAHT can be altered to perform assessments and investigate sensitivities. Figure 12-2 provides pictorially the calculational procedure used with COBRAHT.

The local conditions for each (steady-state) test-wall temperature, vapor temperature, quality, pressure, and total mass flux were used as input to the driver-plotter routine. This driver-plotter routine consisted of the WCOBRA/TRAC-SB heat transfer package, property routines, and drop size correlations. The input hydraulic conditions were used to estimate the film boiling HTCs (based on $\Delta T = T_w - T_{sat}$), which were then compared to the measured HTCs for each test.

The driver-plotter routine calculates an overall HTC in terms of the local heat flux and wall superheat, defined as:

$$h = \frac{q''}{(T_w - T_{sat})}$$

The SPV and/or DFFB HTCs are then compared with the HTC values reported by the experimenters to validate the performance of WCOBRA/TRAC-SB.

One of the problems in quantifying the accuracy of heat transfer relations in a large thermal-hydraulic systems code such as WCOBRA/TRAC is that few experimental tests provide a sufficient amount of simultaneous local information on void fraction, phasic flowrates, and phase temperatures. While modelling an entire separate effects test facility and simulating experiments can provide useful information on overall code performance, the predicted results are subject to compensating errors. That is, inaccuracies in one model package can compensate for the inaccuracies in another package producing a fortuitously correct result. An example is an accurate prediction of wall heat flux when HTCs are underpredicted, while (T_w-T_v) was overpredicted because of errors in the hydraulics package. If sufficient local information is available, it is possible to separate the calculation of the HTCs from the calculation of the fluid conditions and provide an assessment of the heat transfer prediction alone.

12-4-1 ORNL-THTF DFFB Test Simulations

The Oak Ridge National Laboratory Thermal Hydraulic Test Facility (ORNL-THTF) blowdown tests are one source of data for validating the heat transfer predictions of WCOBRA/TRAC-SB in the DFFB/SPV regimes of interest for small break LOCA. A series of high-pressure steady-state upward DFFB tests in a rod bundle was performed in the ORNL-THTF and is discussed by Yoder (Yoder, et al., 1982). Tests were conducted for pressures ranging from 23 bar (635 psia) to 132 bar (1908 psia) at flowrates from 226 kg/m^2-s (166,300 lbm/ft^2-hr) to 713 kg/m^2-s (525,300 lbm/ft^2-hr). The test section was composed of 64 full-length (3.66 m) rods in an 8x8 bundle geometry typical of PWR designs. A cross section of the ORNL-THTF bundle is shown in Figure 12-3. Sixty of the rods were electrically heated fuel rod simulators (that is, heated rods) with flat axial and radial power distributions. One rod (rod 32) failed to function properly during certain tests (B, C, D, and E). Four of the other rods (rods 19, 22, 36, and 46) were inactive (unheated rods). Six spacer grids were evenly spaced along the bundle. Because the axial power shape in the bundle was uniform, critical heat flux (CHF) occurred at the bundle exit first, then moved down the bundle.

There were two fluid flow and temperature measurement sites at both the bottom and top ends of the test section. The heated rod surface temperatures were measured by the thermocouples at 30 axial levels and different circumferential locations. Some of the thermocouples were installed to measure the in-bundle fluid temperature. Local information was provided at the bundle exit, which was designated "Level G." During steady-state operation of the ORNL-THTF, the inlet flow at the bottom of the test section was established and the loop was adjusted to provide the desired inlet fluid temperature and inlet quality. The bundle power was then increased until the dryout (CHF) point was obtained. The steady-state point was assumed to be reached when both pressure and rod surface temperatures stabilized. The results of both rod surface conditions and local equilibrium fluid conditions were then reported as cross-sectional average values for each level. Table 12-1 lists the thermal-hydraulic conditions of the 10 selected ORNL-THTF steady-state film boiling tests used to evaluate the WCOBRA/TRAC-SB heat transfer package.

An initial assessment was performed with a version of COBRAHT that used the Forslund and Rohsenow (Forslund and Rohsenow, 1968) drop-wall DFFB contact model used in the large break LOCA version of WCOBRA/TRAC (Bajorek, et al., 1998) in place of the modified correlation of Equation 6-133. Comparisons between predicted and experimental HTC values for the ORNL-THTF simulations are shown in Table 12-2 for this version of COBRAHT. The measured local heat flux and wall surface temperature were reported for each thermocouple at different levels for individual rods and as a cross-sectional average value of all thermocouples at each level. In this validation, the HTC data at Level G are used for comparisons to determine the spread of the data relative to the prediction. This level is at 143 inches above the beginning of the heated length, and 1 inch below the top of the active bundle. Each test was screened for HTC "outliers."

Figure 12-4 shows a comparison of the predicted and average measured HTCs for the ORNL-THTF DFFB tests. For each test, the COBRAHT film boiling calculation based on the large break LOCA code version underpredicted the bundle average experimental HTC. Figure 12-5 also compares the predicted and measured HTCs, but in this figure, all 235 valid thermocouples are shown. On average, the experimental HTCs are underpredicted by 21.7 percent. This bias in the predicted heat transfer led to the work performed by Bajorek and Young (Bajorek and Young, 1998).

12-4-2 INEL Single Tube Heat Transfer Experiments

The COBRAHT version with Forslund and Rohsenow (Forslund and Rohsenow, 1968) driver-plotter predictions of the ORNL-THTF film boiling data show that the heat transfer package tends to underpredict experimental data. Increasing the direct contact heat transfer improves the predictions, but simply increasing this term according to Equation 6-133 may cause the heat transfer package to overpredict the HTCs for a different range of thermal-hydraulic conditions.

Therefore, in validating the <u>W</u>COBRA/TRAC-SB heat transfer modelling for the small break LOCA regimes of importance (SPV and DFFB), an additional experiment that provides film boiling data, the Idaho National Engineering Laboratory (INEL) single tube test, was also simulated.

Post-CHF film boiling tests were performed at INEL and are reported by Gottula (Gottula, et al., 1985). Steady-state film boiling tests were conducted in a 15.7-mm inside diameter vertical tube for water flowing upward. The experiments included tests at pressures up to 7 Mpa at mass fluxes ranging from 12 to 70 kg/m^2-s. The test section inlet quality ranged from approximately 7 to 47 percent. Steam temperature, and thus the thermal nonequilibrium, was measured using differentially aspirated microthermocouple probes located at various axial positions.

Data points for the COBRAHT driver-plotter were selected at four different pressures: 7.0, 3.6, 0.5, and 0.3 Mpa. Of the tests conducted, information for 198 points was available which provided local conditions for pressure, mass flow, quality, and steam temperature at the tube exit. For the INEL film boiling test simulations, a version of COBRAHT containing the <u>W</u>COBRA/TRAC-SB code SPV and DFFB heat transfer package with the drop-wall contact term (per Equation 6-133), was used.

Figure 12-6 shows a comparison of predicted HTCs for the INEL film boiling tests using the COBRAHT version containing the heat transfer models in the small break LOCA version of <u>W</u>COBRA/TRAC. In this comparison, the positive values are underpredictions of the HTC; the negative values are overpredictions. The good agreement indicates the effectiveness of the Re-dependence in the convective and drop-wall contact heat transfer terms in predicting SPV and DFFB heat transfer.

Figure 12-7 shows a comparison of COBRAHT results using the <u>W</u>COBRA/TRAC-SB heat transfer model for both the ORNL DFFB and the INEL data. In this comparison, average bias in the HTC is small, with the predicted HTC for all data shown underpredicting the measured HTC by approximately 5 percent. The heat transfer multiplier E is defined as

$$E_i = \frac{q''_{i,\,exp}}{q''_{i,\,code}}$$

where

$q''_{i,\,exp}$ is the experimental heat flux at elevation i

$q''_{i,\,code}$ is the predicted heat flux at elevation i

in order to ascertain the predictive capability of the WCOBRA/TRAC-SB computer code. For each of these tests, the minimum and maximum values of E for any individual data point were determined, as were the average value and the standard deviation of the distribution for the experimental facility simulation results as a whole. For the ORNL DFFB tests, the values are: E_{min}=0.859, E_{max}=1.332, and E_{ave}=1.031 with standard deviation σ=0.09. For the INEL experiment, E_{min}=0.571, E_{max}=1.886, and E_{ave}=1.065 with σ=0.29.

12-4-3 ORNL Uncovered Bundle Heat Transfer Test Simulators

A series of experiments investigating small break LOCA phenomena were performed in the ORNL-THTF high pressure rod bundle thermal-hydraulics loop, as reported in NUREG/CR-2456 (Anklam, et al., 1982). The test facility and the WCOBRA/TRAC-SB representation of it are described in more detail in subsection 15-4-2 of this report.

The ORNL-THTF series of uncovered bundle heat transfer tests provide another set of heat transfer data for small break LOCA model validation. The six uncovered bundle tests (I through N) were simulated with WCOBRA/TRAC-SB. The uncovered bundle tests were steady-state experiments with electrically heated rods in which the inlet liquid mass flow was approximately equal to exiting steam mass flow. Rod temperatures and heat transfer coefficients in the steam-cooling region of the rod bundle were determined. Once the steady-state condition was established, thermal and hydrodynamic data were collected at several heights in the uncovered portion of the rod bundle. Table 12-3 summarizes the steady-state test conditions in terms of system pressure, linear rod power, and inlet mass flux. The tests were characterized by low (580-650 psia) or high (1010-1090 psia) pressure, and low (0.10 and 0.14 kW/ft), medium (0.31 and 0.33 kW/ft), or high (0.66 and 0.68 kW/ft) linear power.

The WCOBRA/TRAC-SB model described in Section 15 was used for these ORNL test simulations, using an appropriate value of the interfacial drag multiplier (YDRAG). This multiplier adjusts the interfacial shear calculated between rising bubbles and liquid, and its use allows the separation of WCOBRA/TRAC-SB's heat transfer and hydrodynamic packages. Values of YDRAG to alter WCOBRA/TRAC-SB's two-phase level to better match the experimental two-phase level were used in the WCOBRA/TRAC-SB input decks that simulated these tests. With this approach the difference between the predicted heat transfer and the data can be attributed to the WCOBRA/TRAC-SB heat transfer models alone.

Overall, rod temperatures were under-predicted for the uncovered bundle tests, while vapor temperatures were slightly over-predicted. WCOBRA/TRAC-SB vapor heat transfer coefficients were generally greater than the experimental values. With all 10 ORNL-THTF experimental levels included (the top 2' of the rod bundle), the average ratio of experimental to WCOBRA/TRAC-SB vapor heat transfer coefficients (E_i) was 0.7769, with a standard deviation of 0.18 (see Figure 12-8). The E_{max} and E_{min} values are 1.314 and 0.452, respectively.

The ORNL uncovered bundle data are in the same Reynolds number range and exhibit heat transfer coefficients of similar magnitude to the INEL test data. There appears to be a wide range on the WCOBRA/TRAC-SB heat transfer multipliers for these datasets, from 0.452 to 1.886, or over a factor of 4. However, this is not surprising. As noted by Anklam (Anklam et al., 1982), the flow regimes present in these tests can vary between forced, mixed and free convection. This uncertainty about flow regime means that a significant range of results may be expected to occur in the WCOBRA/TRAC-SB predictions of the ORNL-THTF uncovered bundle tests. Anklam further notes that convective heat transfer under the high pressure uncovered bundle conditions can be very complex because of the number of possible flow regimes and flow transitions that may occur.

12-5 Summary and Conclusions

The WCOBRA/TRAC-SB heat transfer modelling of the SPV and DFFB regimes important to small break LOCA analysis has been assessed. The effect of using the drop-wall contact expression of Bajorek and Young (Bajorek and Young, 1998) in place of that of Forslund and Rohsenow (Forslund and Rohsenow, 1968) is shown to markedly improve predictions of the ORNL film boiling tests. The implementation of the Bajorek and Young drop-wall contact term and a Re-dependent laminar/turbulent flow transition convective heat transfer term has allowed the WCOBRA/TRAC-SB heat transfer package to predict the ORNL DFFB and uncovered bundle tests and INEL film boiling test data well. The statistical treatment of core heat transfer in the Westinghouse uncertainty methodology is based on these results as described in Volume 4 of this document.

12-6 References

Anklam, T. M., et al., 1982, "Experimental Investigations of Uncovered Bundle Heat Transfer and Two-Phase Mixture Level Swell Under High Pressure Low Heat Flux Conditions," NUREG/CR-2456.

Bajorek, S. M., et al., 1998, "Code Qualification Document for Best Estimate LOCA Analysis, Volume I: Models and Correlations," WCAP-12945-P-A, Vol. 1.

Bajorek, S. M. and Young, M. Y., 1998, "Assessment and Quantification of WCOBRA/TRAC-MOD7A Heat Transfer Coefficients for Blowdown Dispersed Flow Film Boiling." Proc. International Conf. On Nuclear Engineering (ICONE-6), Paper 6184.

Dittus, F. W. and Boelter, L. M. K., 1930, "Heat Transfer in Automobile Radiators of the Tubular Type," Publications in Engineering, 2, Univ. of California, Berkeley, pp. 443-461.

Forslund, R. P. and Rohsenow, W. M., 1968, "Dispersed Flow Film Boiling," J. Heat Trans., Vol. 90, No. 6, pp. 399-407.

Gottula, et al., 1985, "Forced Convective, Non Equilibrium Post-CHF Heat Transfer Experiment Data and Correlation Comparison Report," NUREG/CR-3193.

U.S. NRC Regulatory Guide 1.157, 1989, "Best Estimate Calculations of Emergency Core Cooling System Performance."

Wong, S. and Hochreiter, L. E., 1981, "Analysis of the FLECHT-SEASET Unblocked Bundle Steam Cooling and Boiloff Tests," NRC/EPRI/Westinghouse-8.

Yoder, et al., 1982, "Dispersed Flow Film Boiling in Rod Bundle Geometry-Steady State Heat Transfer Data and Correlation Comparisons," NUREG/CR-2435, ORNL-5822.

Table 12-1
ORNL-THTF Steady-State DFFB Tests

Test	Pressure (bar)	Mass Flux (kg/m^2-s)	Inlet Temperature (°C)	Power (kW/m)
B	127.6	713	310	2.52
C	124.5	334	293	1.58
D	127.5	518	303	1.92
E	131.7	593	304	1.99
K	43.8	226	213	1.24
L	23.0	527	276	2.17
M	85.7	657	284	2.47
P	60.3	520	267	2.26
Q	65.3	325	261	1.58
X	60.1	344	268	1.64

Table 12-2
Summary of ORNL-THTF Driver-Plotter Comparison, Forslund/Rohsenow Model

Test	Data Samples	$HTC_{data,min}$	$HTC_{data,ave}$	$HTC_{data,max}$	HTC_{code}	$HTC_{data,ave}/HTC_{code}$
B	24	451.5	498.5	529.9	405.45	1.229
C	24	221.2	247.4	276.7	185.91	1.331
D	24	342.1	379.3	400.5	275.69	1.376
E	24	381.2	427.7	447.6	317.11	1.349
K	20	145.9	156.1	165.8	116.73	1.337
L	26	298.7	331.1	356.1	291.57	1.136
M	26	350.4	391.7	415.8	353.07	1.109
P	22	280.5	308.5	327.0	280.35	1.100
Q	26	196.0	213.1	232.3	192.00	1.110
X	19	205.4	221.1	236.3	200.47	1.103

Table 12-3
ORNL Uncovered Bundle Test Matrix

	I	J	K	L	M	N
System Pressure (psia)	650	610	580	1090	1010	1030
Linear Power (kW/ft)	0.68	0.33	0.10	0.66	0.31	0.14
Mass Flux (lbm/h ft^2)	2.19E-4	0.94E-4	0.23E-4	2.15E-4	0.93E-4	0.34E-4

a,c

Figure 12-1. Heat Transfer Regime Map for Vessel Component

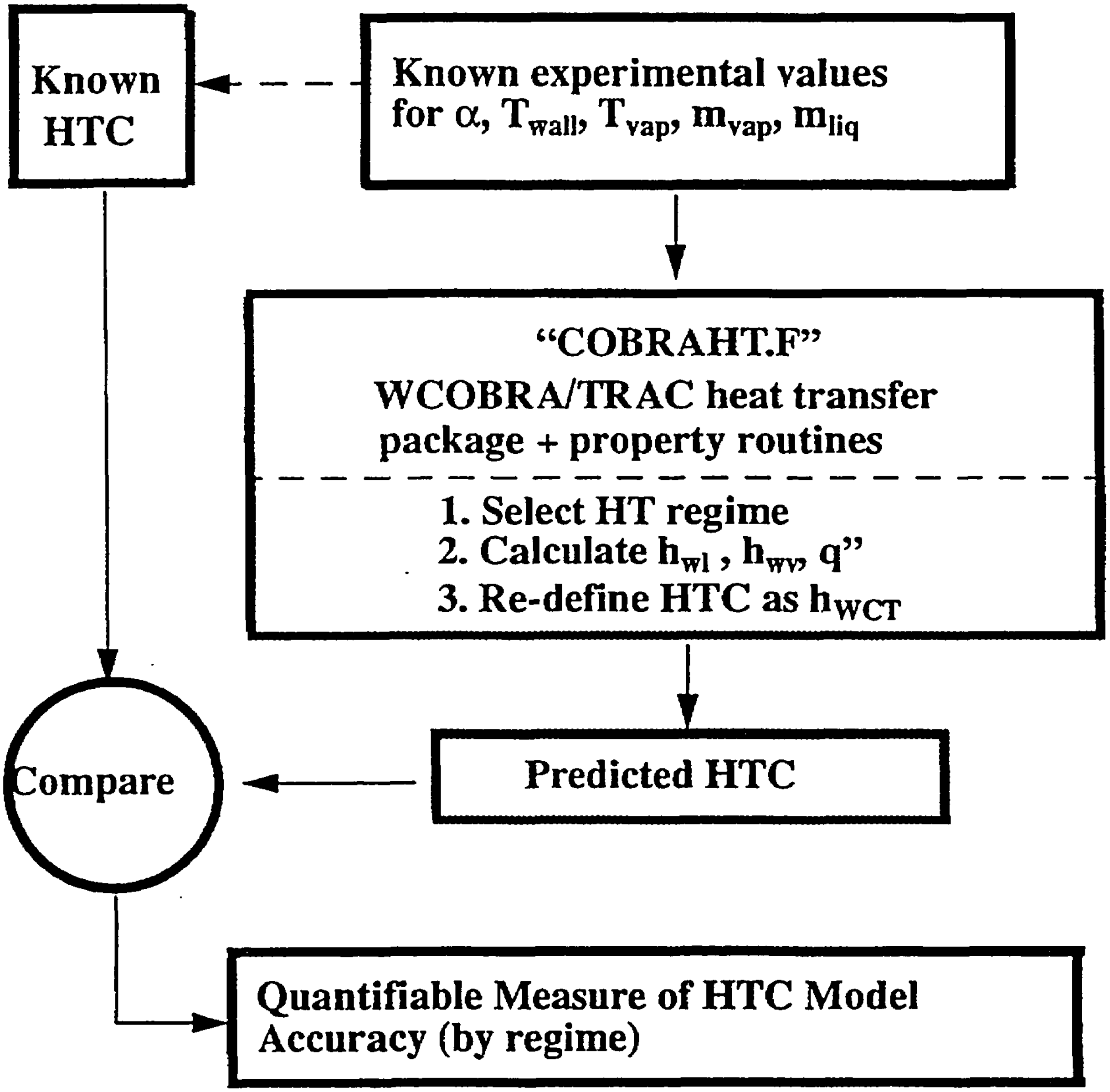

Figure 12-2. WCOBRA/TRAC Heat Transfer Driver-Plotter Routine

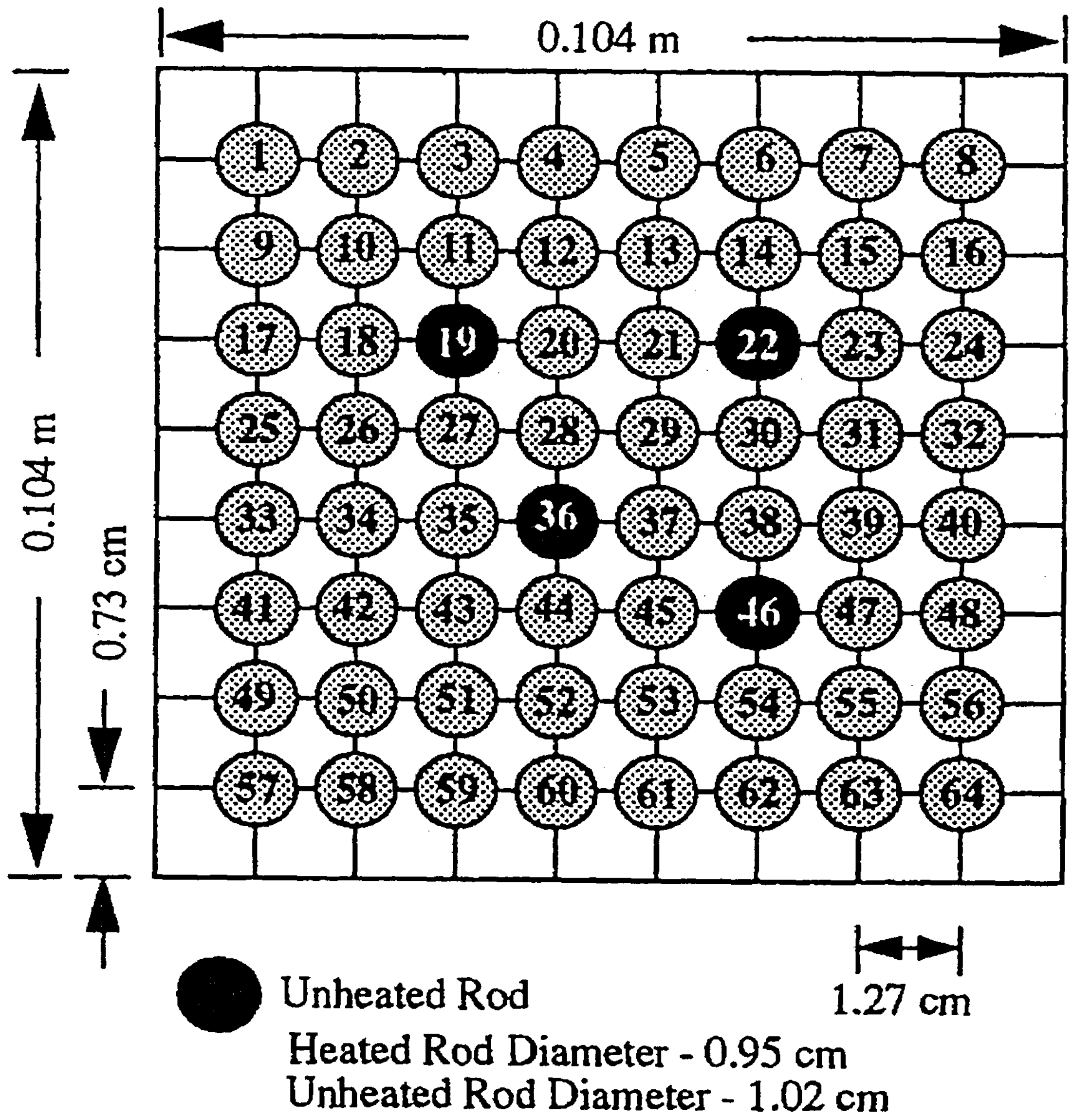

Figure 12-3. ORNL-THTF Rod Bundle Cross Section

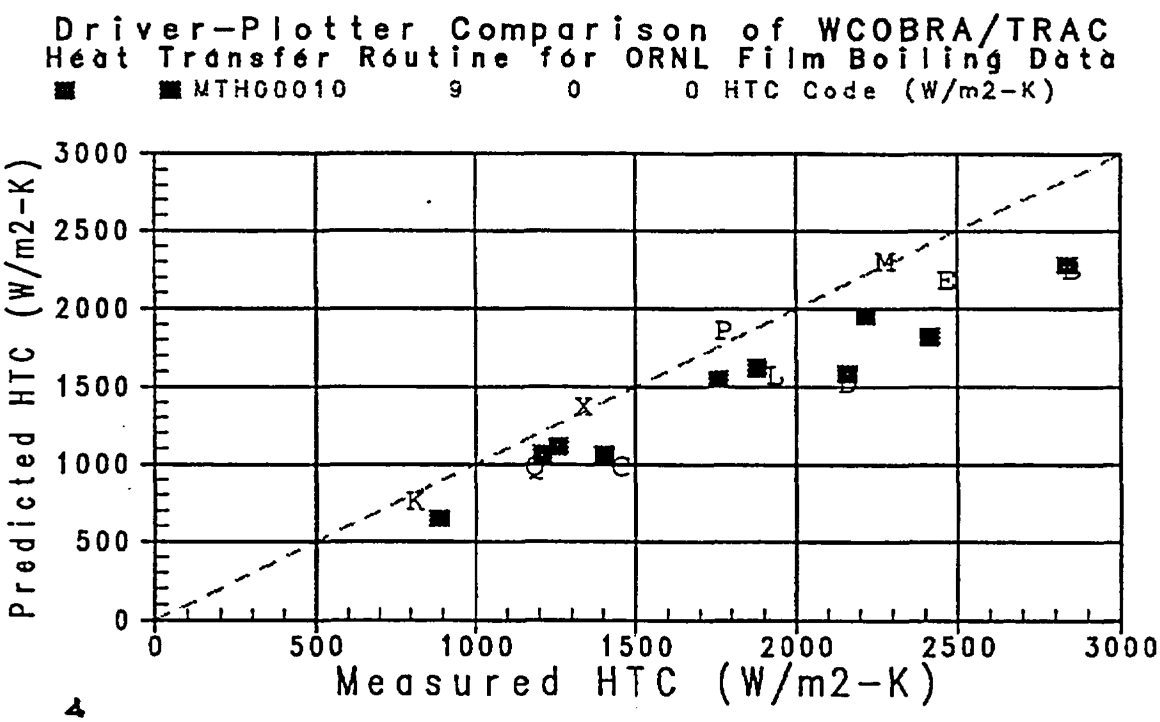

Figure 12-4. Comparison of Large Break LOCA WCOBRA/TRAC Code Logic Predicted and Measured HTCs for ORNL-THTF DFFB Tests – Bundle Average

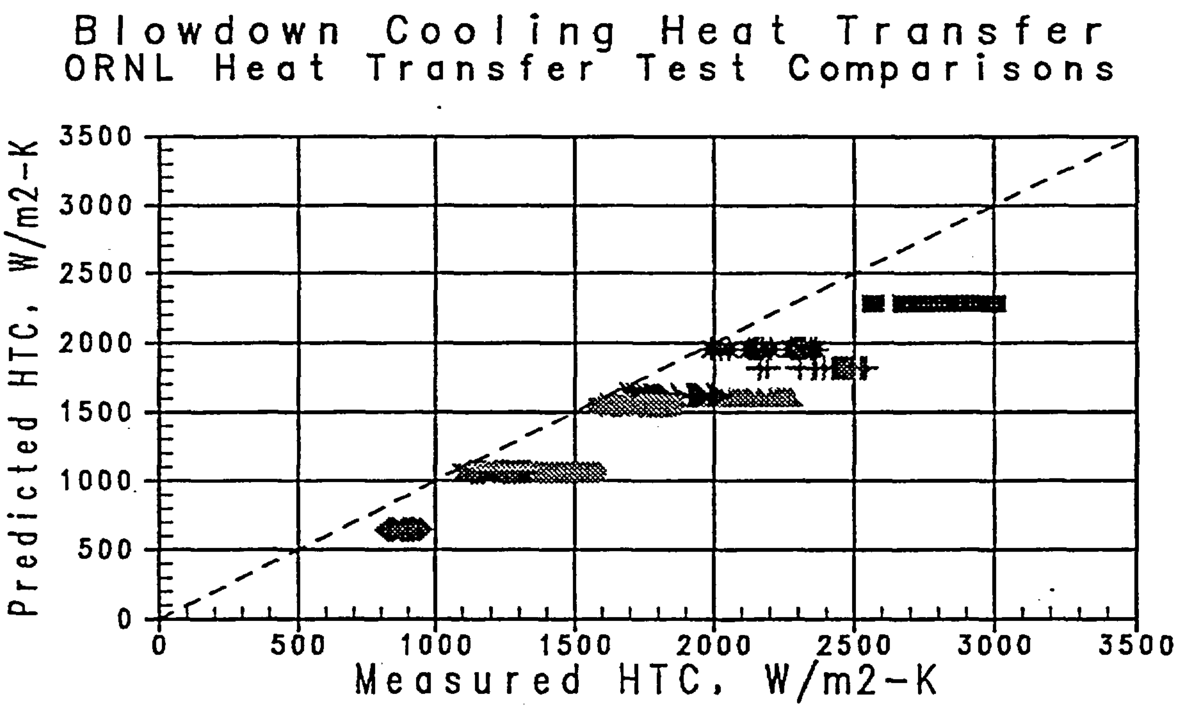

Figure 12-5. Comparison of Large Break LOCA WCOBRA/TRAC Code Logic Predicted and Measured HTCs for ORNL-THTF DFFB Tests – All Thermocouples

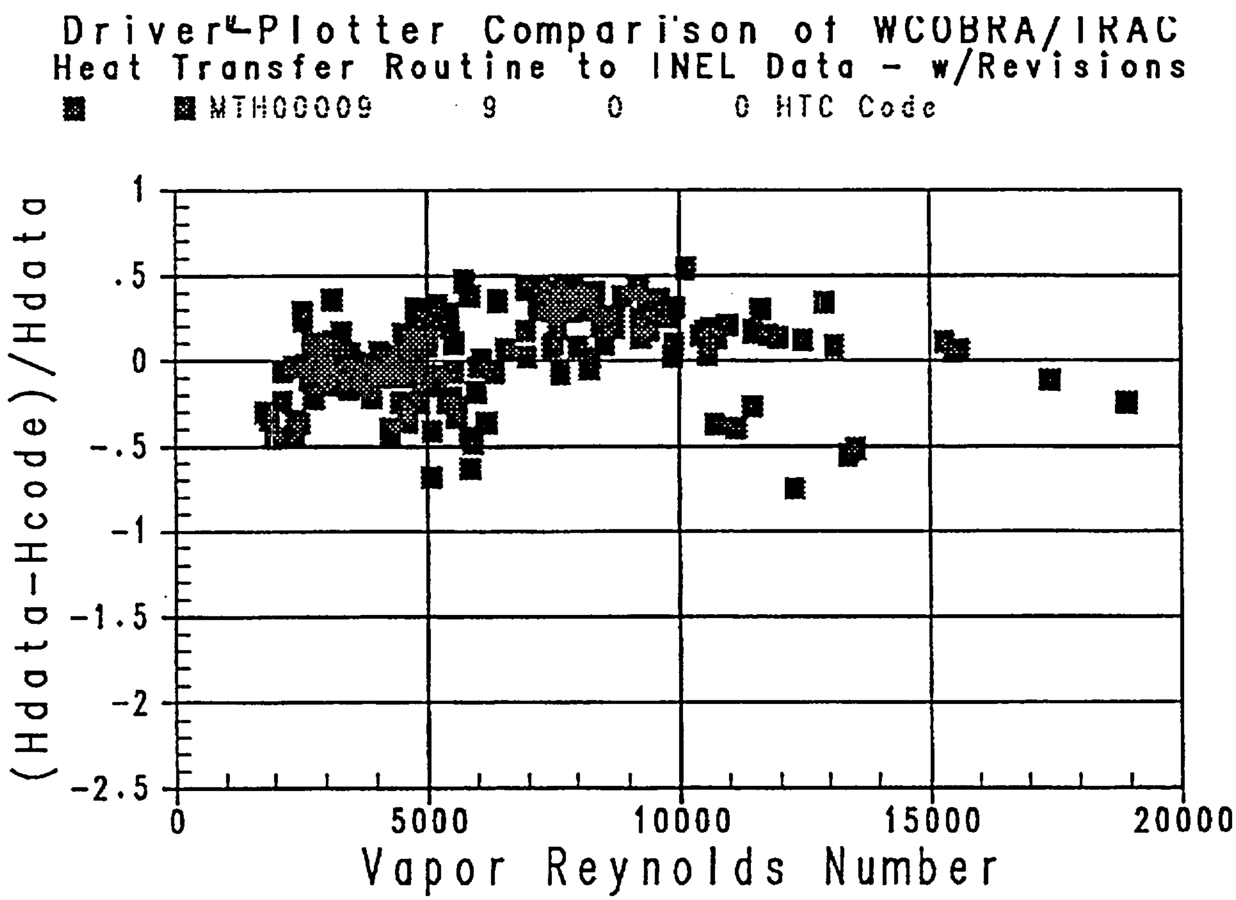

Figure 12-6. Comparison of Predicted and Measured INEL Film Boiling HTCs as a Function of Vapor Re Using WCOBRA/TRAC-SB Heat Transfer Models

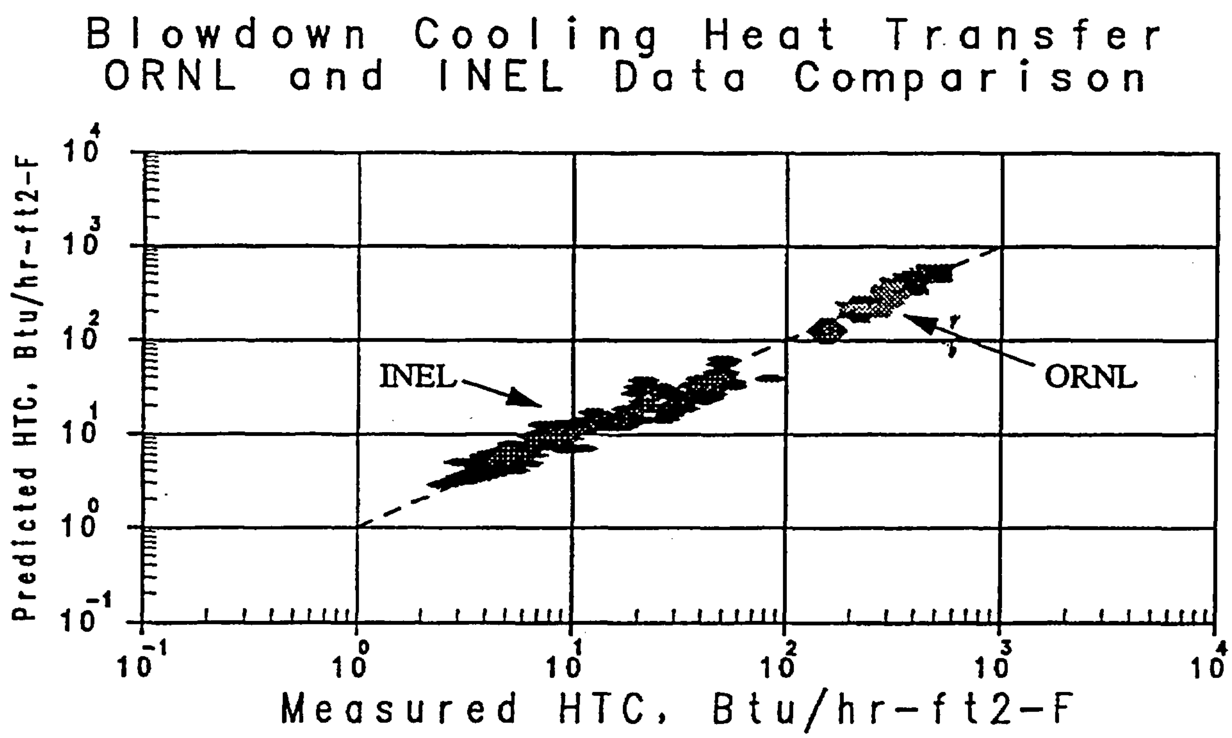

Figure 12-7. Comparison of Predicted and Measured HTCs for Combined ORNL DFFB and INEL Data Using WCOBRA/TRAC-SB Heat Transfer Models

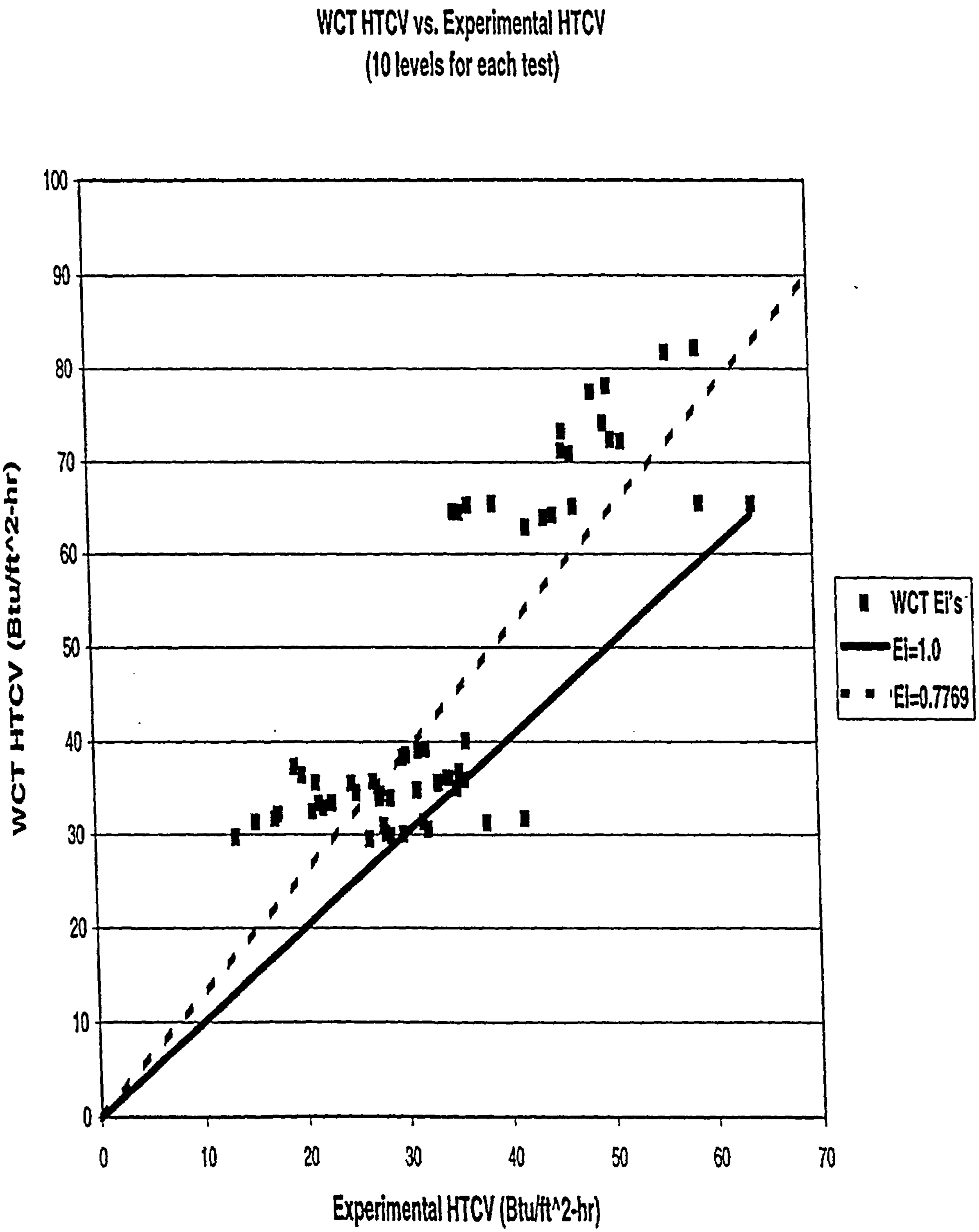

Figure 12-8. Comparison of Predicted and Measured HTCs for ORNL-THTF Uncovered Bundle Data Using WCOBRA/TRAC-SB

SECTION 13
ASSESSMENT OF BREAK FLOW MODEL

13-1 Introduction

During a small break LOCA, the break flowrate determines the depressurization rate as well as the mass inventory of the primary system of a PWR. These parameters in turn influence the timing of various engineered safeguard system responses, such as reactor trip and safety injection.

Early in a small break LOCA, the fluid condition upstream of the break location is subcooled. This results in a high discharge flowrate and a fast depressurization. As the pressure drops to the saturation pressure corresponding to the coolant liquid temperature upstream of the break, the discharge becomes two-phase and a relatively low discharge rate and a slow depressurization result. As the system mass depletes and the flow in the main pipe stratifies, the break location (typically a branch pipe) begins to uncover. This results in the void fraction upstream of the break changing from 0.0 (saturated liquid) to 1.0 (saturated vapor) as the liquid level in the main pipe drops. As the stratified surface lowers in the vicinity of the break, the quality at the break is greatly influenced by the entrainment of vapor/liquid off the stratified surface upstream of the break.

Although the size, location, and shape of the break are not known for the postulated small break LOCA, the best estimate code needs to predict consistent responses relative to experimental data over a range of pressure, subcooling, and upstream fluid states, as well as the break flow area variations, so that accurate sensitivity to small break LOCA responses can be obtained.

In this section, an assessment is made of the break flow model in the WCOBRA/TRAC-SB version described in Section 3, Volume 1, of this document. This version was created for the small break LOCA application from the WCOBRA/TRAC-MOD7A, Rev. 4.

13-2 Critical Flow in Small Break LOCA

A fluid system contained in a reactor vessel with a pipe break is in communication with the containment atmosphere, which is at a lower pressure through the break flow path. Under critical flow conditions, the discharge flowrate from the high pressure system becomes independent of the containment conditions, which are at the lower pressure.

13-2-1 Subcooled Liquid Discharge

Early in a small break LOCA, the fluid condition upstream of the break is subcooled. As the fluid accelerates through the path leading to the break, the static pressure decreases and the liquid flashes at the throat as seen in Figure 13-2-1. In subcooled liquid discharge, the degree of subcooling thus greatly influences the break flowrate. At the onset of a small break LOCA, $P_{sat}(T_l)$ is substantially lower than the primary system pressure. This results in a relatively high break flow. As the system depressurizes, the liquid subcooling decreases and the break flow lowers accordingly. Even slightly subcooled liquid going through a sudden depressurization does not flash at $P_{sat}(T_l)$ due to the underpressure at flashing inception (or nucleation delay). As a result, the throat pressure is lower than $P_{sat}(T_l)$ and the break flow is still higher than the two-phase break flowrate.

The nucleation delay (or nonequilibrium effect) dominates the break flowrate for the subcooled liquid in a geometry in which the fluid accelerates into a short flow path to an opening. The fluid going through a rapid expansion is not able to flash instantaneously; it remains as superheated liquid until at or near the throat, where the static pressure becomes lower than the underpressure required for the nucleation and the fluid becomes two-phase.

13-2-2 Stratified Entrainment at Break

As the system mass depletes, the break location becomes two-phase and eventually becomes stratified following an RCP trip. The two-phase break flowrate is a strong function of the upstream quality. Stratified flow conditions near the break may lead to vapor and liquid entrainment into the break path. The entrainment amount depends on the velocity of the fluid near the break and the height of the stratified liquid level in the pipe relative to the break elevation as seen in Figure 13-2-2.

The location of the branchline leading to the break, relative to the liquid level, determines the quality of the two-phase mixture in the branchline and at the break. In these conditions, the vapor pull-through and liquid entrainment may become important as seen in Figure 13-2-3.

13-2-3 Correlation for Onset of Liquid and Vapor Entrainment

A correlation for the onset of liquid and vapor entrainment to the branchline was suggested by Zuber (Zuber, 1980). This correlation is based on earlier investigations by Craya (Craya, 1949) and Lubin (Lubin, 1967). The liquid entrainment off the side orifice was derived by Craya as:

$$Fr_g = C_1 \cdot \left(\frac{h_{crit}}{d}\right)^{C_2}$$

where

$$Fr_g = \frac{U_g}{\sqrt{d \cdot g \cdot \dfrac{\Delta\rho}{\rho_g}}} \qquad (13\text{-}1)$$

Vapor pull-through off the bottom orifice was derived by Lubin as:

$$Fr_l = C_1 \cdot \left(\frac{h_{crit}}{d}\right)^{C_2}$$

where

$$Fr_l = \frac{U_l}{\sqrt{d \cdot g \cdot \dfrac{\Delta\rho}{\rho_l}}} \qquad (13\text{-}2)$$

where

Fr_g and Fr_l are the Froude numbers for vapor and liquid
U_g and U_l are phasic velocities in the break path
d is the break diameter
h_{crit} is the distance between the stratified level and the break elevation at the onset of entrainment
$\Delta\rho = \rho_l - \rho_g$
ρ_l, ρ_g are the liquid and vapor densities
g is the gravitational acceleration

In both cases, the constants are theoretically derived to be $C_1 = 3.23$ and $C_2 = 2.5$.

Other researchers have experimentally determined these constants, and the results are tabulated in Table 13-2-1.

The following are the selected correlation constants for WCOBRA/TRAC-SB:

[

]a,c

13-2-4 Correlation for Break/Branchline Quality

The following correlations were selected for WCOBRA/TRAC-SB:

- Upward-Vertical Branch

  Schrock (Schrock, et al., 1986) proposed the following correlation for this orientation:

$$x = R^{3.25 \cdot (1-R)^2} \tag{13-3}$$

where

$$R = \left| \frac{h}{h_{crit}} \right|$$

and where h is the distance between the break and the liquid surface.

- Downward-Vertical Branch

Smoglie and Reimann (Smoglie and Reimann, 1986) suggested the following correlation for the bottom branch:

$$x = x_0^{2.5 \cdot R} \cdot [1 - 0.5 \cdot R \cdot (1 + R) \cdot x_0^{(1 - R)}]^{0.5} \tag{13-4}$$

where

$$R = \left| \frac{h}{h_{crit}} \right|$$

$$x_0 = \frac{1.15}{1 + \sqrt{\frac{\rho_f}{\rho_g}}}$$

- Horizontal Side Branch

Smoglie and Reimann also suggested the following correlations for the side branch:

Horizontal above the midplane

$$x = x_0^{(1 + 1.09 \cdot R)} \cdot [1 - 0.5 \cdot R \cdot (1 + R) \cdot x_0^{(1 - R)}]^{0.5} \tag{13-5}$$

where

$$R = \frac{h}{h_{crit}}$$

$$x_0 = \frac{1.15}{1 + \sqrt{\frac{\rho_f}{\rho_g}}}$$

Horizontal below the midplane

$$x = x_0^{(1 + R)} \cdot [1 - 0.5 \cdot R \cdot (1 + R) \cdot x_0^{(1 - R)}]^{0.5} \tag{13-6}$$

where

$$R = \frac{h}{h_{crit}}$$

$$x_0 = \frac{1.15}{1 + \sqrt{\frac{\rho_f}{\rho_g}}}$$

Section 13-3 shows the result of an assessment of the ability of WCOBRA/TRAC to predict the branchline quality as a function of the mainline liquid level.

Table 13-2-1
Experimental Results of C_1 and C_2

Item	Yonomoto and Tasaka	Smoglie and Reimann	Schrock		Anderson	Maciaszek	Ardron and Bryce[a]
Maximum pressure (MPa)	0.7	0.5	1.1		6.0	2.0	–
Main pipe diameter (mm)	190 x 190 square	206	102	102	284	135	–
Branch pipe diameter (mm)	10, 20	6-20	3-10	3	34	20	–
Fluid	Air/water	Air/water	Air/ water	Steam/ water	Steam/water	Steam/water	–
Top break	3.22[b] 2.5[c]	0.35/ 2.5	0.4/2.5	0.4/2.5	–	2.17/1.5	0.35/2.5
Side break liquid entrainment	4.29/2.5	3.22/2.5	3.25/ 2.5	–	4.21/2.5	4.21/2.5	3.22/2.5
Side break vapor entrainment	2.61/2.5	2.61/2.5	2.2/2.0	1.19/2.0	2.09/2.5	4.21/2.5	2.61/2.5
Bottom break	1.27/2.5	0.94/2.5	1.47/ 2.0	0.78/2.0	1.27/2.5	1.27/2.5	0.46/2.5

a. No experiments were performed for this work.
b. Constant C_1
c. Constant C_2

References:
Yonomoto and Tasaka, 1988
Smoglie and Reimann, 1986
Schrock, et al., 1986
Anderson and Benedetti, 1985
Maciaszek and Memponteil, 1986
Ardron and Bryce, 1990

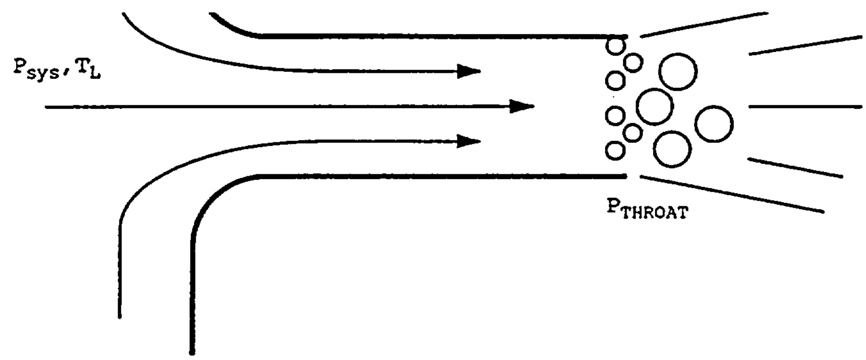

Figure 13-2-1. Diagram of Subcooled Break Flow

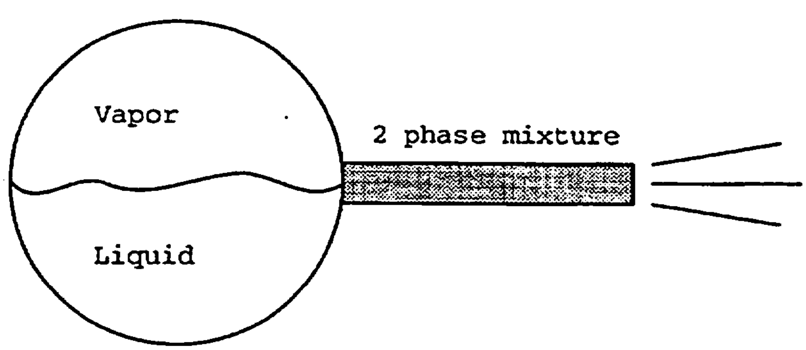

Figure 13-2-2. Diagram of Two-Phase Upstream Conditions

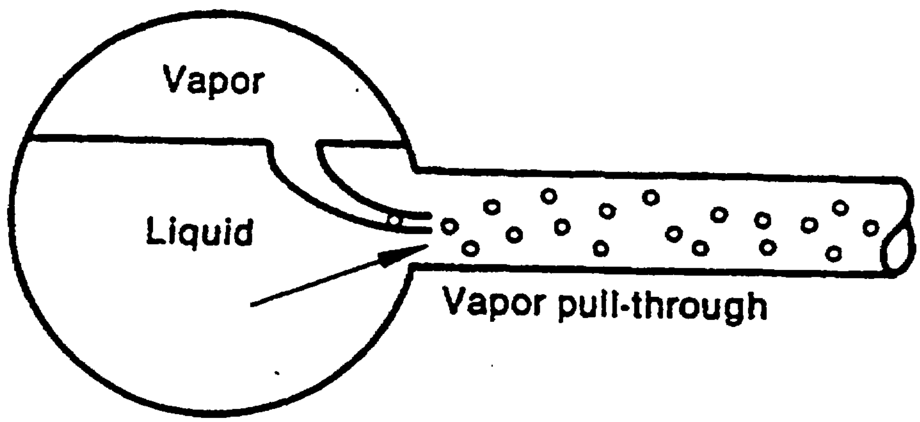

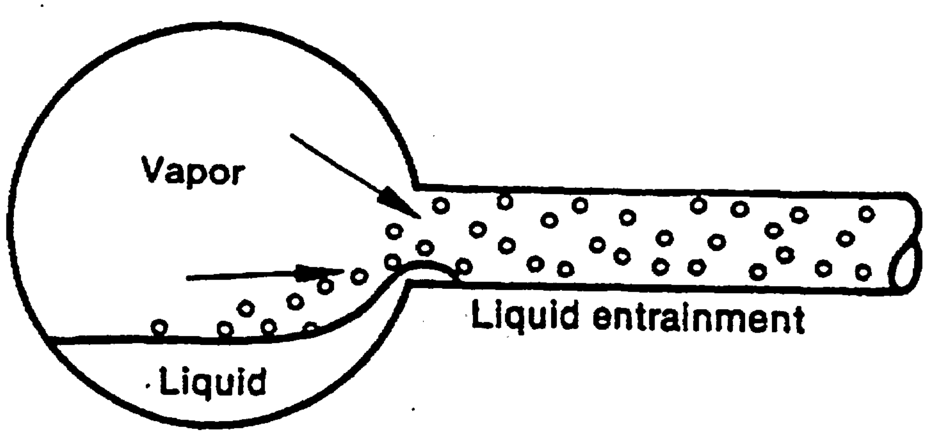

Figure 13-2-3. Vapor Pull-Through and Liquid Entrainment Phenomena

13-3 Assessment of the Horizontal Stratified Entrainment Model

13-3-1 Branchline Quality/Mainline Liquid Level Comparison Using TPFL

The break flowrate is a function of the pressure and the flow quality at the break and the size of the break. For two-phase fluid conditions encountered in a small break LOCA, this quality is, in turn, a function of the stratified level in the mainline and the liquid entrainment/vapor pull-through behavior. The break flow experiment performed at the two-phase flow loop (TPFL) in INEL specifically examined a break flow from the branchline off of a simulated hot/cold leg where the two-phase flow is horizontally stratified.

This experiment was motivated by the apparent inability to predict the break flow by RELAP5 and TRAC (Condie, 1980), when they were used to simulate LOFT test L3-5 (small break LOCA experiment) (Doa, 1980). The break flow predictions by the two codes were substantially higher than the experiment. The overprediction of the break flowrate and the depressurization rate was thought to be the consequence of the inability of the codes to pull through the vapor when the stratified level is above the branchline entrance.

The objective of the TPFL experiment is to develop a reliable and accurate experimental data base for critical flow through small pipe breaks in which stratified two-phase flow is prevalent. Recent experiments with an air-water mixture in small pipes have indicated that liquid entrainment and vapor pull-through significantly influence discharge rates and that these phenomena are functions of stratified level and break azimuthal location. The objective of these experiments is to obtain accurate data on critical discharge rates of steam-water mixtures as a function of break orientation and stratified level. More specifically, the objectives of the experiments are to establish the following:

- An experimental data base on critical flow through small breaks for two different break orientations: bottom and side
- A data base relating discharge rates to stratified level and thermal-hydraulic conditions in the mainline
- An experimentally measured data base relating the discharge rate and level in the mainline to the conditions in the branchline

13-3-1-1 Description of Test Facility

The tee/critical flow experiments were performed in the TPFL at the INEL Thermal Hydraulics Laboratory (Figure 13-3-1). The loop consists of 28.4-cm diameter mainline pipe which drains into a separator tank, and 3.44-cm diameter branchline which has a 1.62-cm diameter critical flow nozzle providing a known choke point. The mainline pipe is 7.9 meters long measured from the steam/water mixer to the separator. The branchline inlet tees off from the mainline pipe 2.7 meters from the separator. The branchline could be attached to the mainline either at the side (horizontal configuration) or at the bottom (vertical configuration). The schematic view of the facility is shown in Figure 13-3-2.

A six-beam gamma densitometer was used 0.4 meters upstream of the branchline entrance in the mainline to determine the level in the mainline. A single-beam gamma densitometer was used to measure the density 0.3 meters upstream of the nozzle in the branchline.

13-3-1-2 Test Ranges

In the experiment, for each configuration (horizontal and vertical), the mainline liquid level varied from 0 cm (all vapor) to 24 cm (85 percent of pipe diameter) at the system pressures of 900 psia, 640 psia, and 500 psia.

13-3-1-3 WCOBRA/TRAC Model

The vessel component of WCOBRA/TRAC uses the COBRA-TF formulation and can model multidimensional flows, such as the flow in the vessel of the RCS. Figure 13-3-3 shows the WCOBRA/TRAC noding diagram for TPFL simulation. This vessel component [

]^{a,c}

13-3-1-4 Comparison of WCOBRA/TRAC Prediction to Horizontal Data

Figure 13-3-4 shows the comparison of the WCOBRA/TRAC-SB prediction for the branchline quality as a function of the mainline liquid level for the horizontal configuration. WCOBRA/TRAC predicted the liquid level for the onset of vapor pull-through at D_H x 0.75, which compares well with the experimental observation. WCOBRA/TRAC predicted the onset of the liquid entrainment at D_H x 0.22, which also compares well with the experiment. WCOBRA/TRAC slightly overpredicted the vapor pull-through. In the TPFL horizontal configuration, the prediction and the data compared well. The trend of quality variation relative to the liquid level is also correct though higher than the data when the liquid level is above the mid-elevation in the mainline pipe.

13-3-1-5 Comparison of the WCOBRA/TRAC Prediction to Downward-Vertical Data

Figure 13-3-5 shows the comparison of the WCOBRA/TRAC-SB prediction and the experimental data of the branchline quality as a function of the mainline liquid level for the downward-vertical configuration. Predictions at 900 and 500 psia are plotted against the data taken at 900, 640, and 500 psia. Both an onset of vapor pull-through and the quality as a function of liquid level are well predicted by WCOBRA/TRAC-SB. The prediction did not show a significant trend relative to the pressure change, which is in agreement with the data.

13-3-1-6 Comparison of the WCOBRA/TRAC Prediction to Upward-Vertical Data

Figure 13-3-6 shows the comparison of the WCOBRA/TRAC-SB prediction for the branchline quality as a function of the mainline liquid level for the upward-vertical configuration.

Because there are no TPFL data for this configuration, the WCOBRA/TRAC prediction for this configuration with TPFL geometry and pressure was compared against data taken at much lower pressures. This set of data was used to benchmark the correlation given by Equation 13-3, in Ardron and Bryce (Ardron and Bryce, 1990).

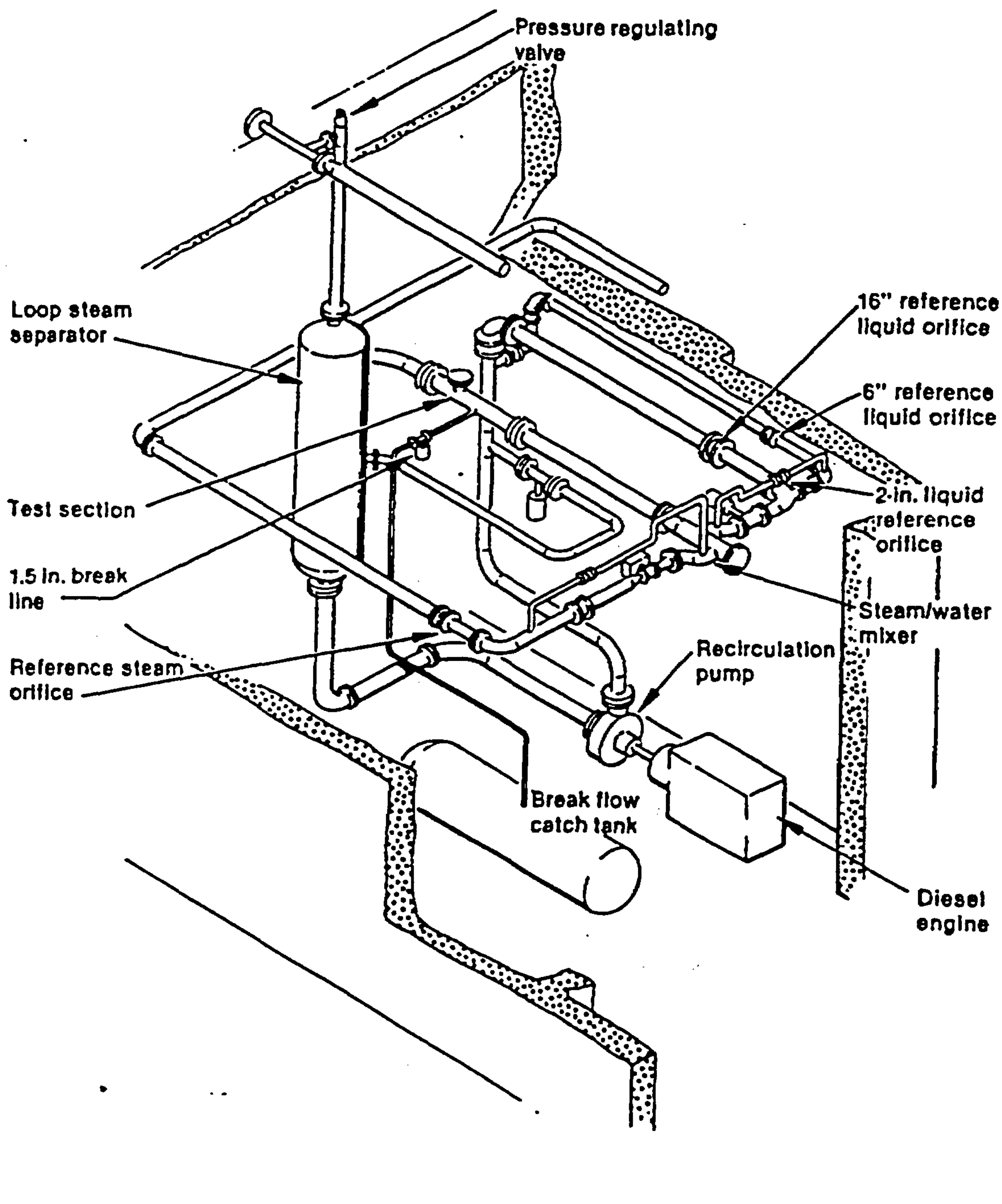

Figure 13-3-1. Diagram of TPFL

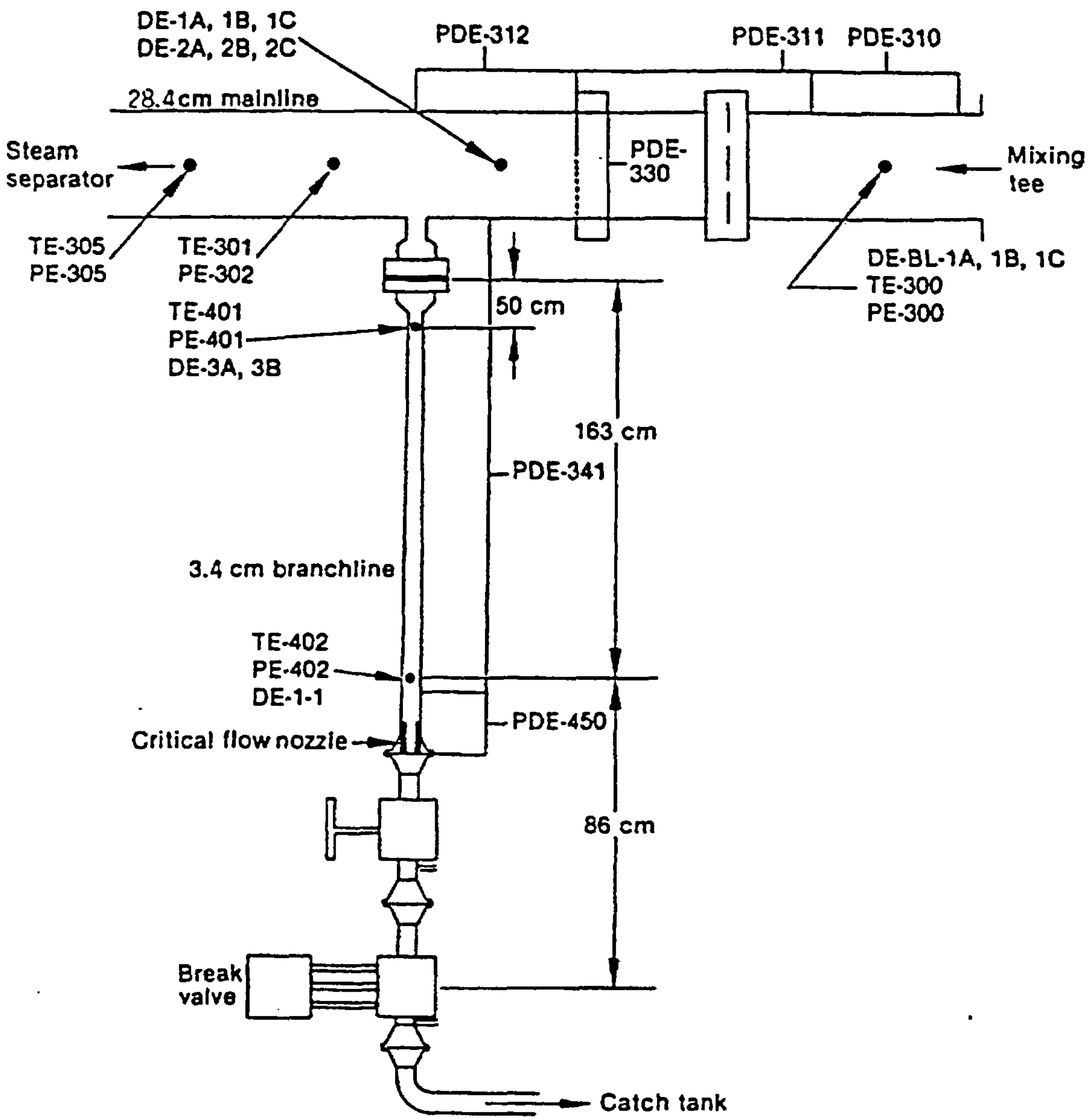

Figure 13-3-2. Schematic View of TPFL Test Section

a,c

Figure 13-3-3. WCOBRA/TRAC Noding for TPFL Branchline Quality Test Simulation

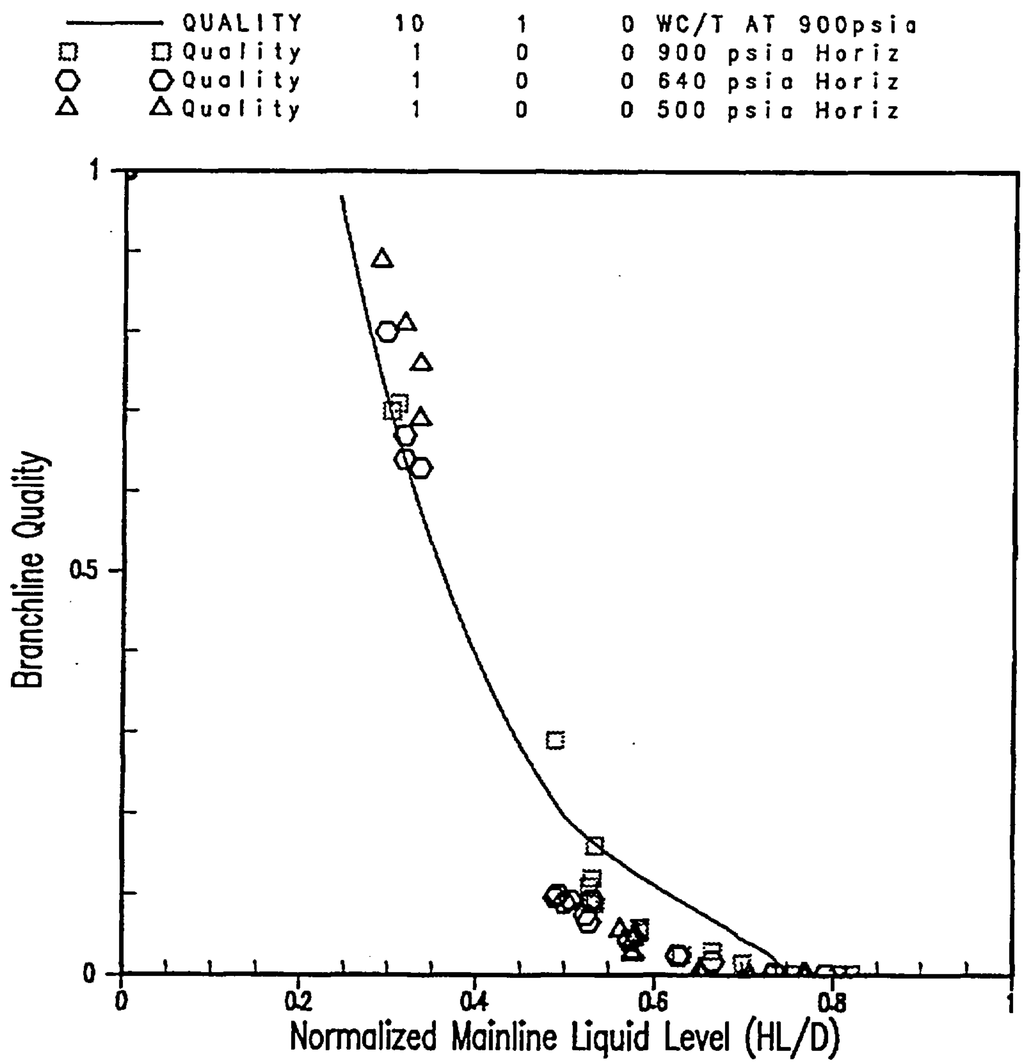

Figure 13-3-4. Branchline Quality Versus Mainline Liquid Level for Horizontal Configuration

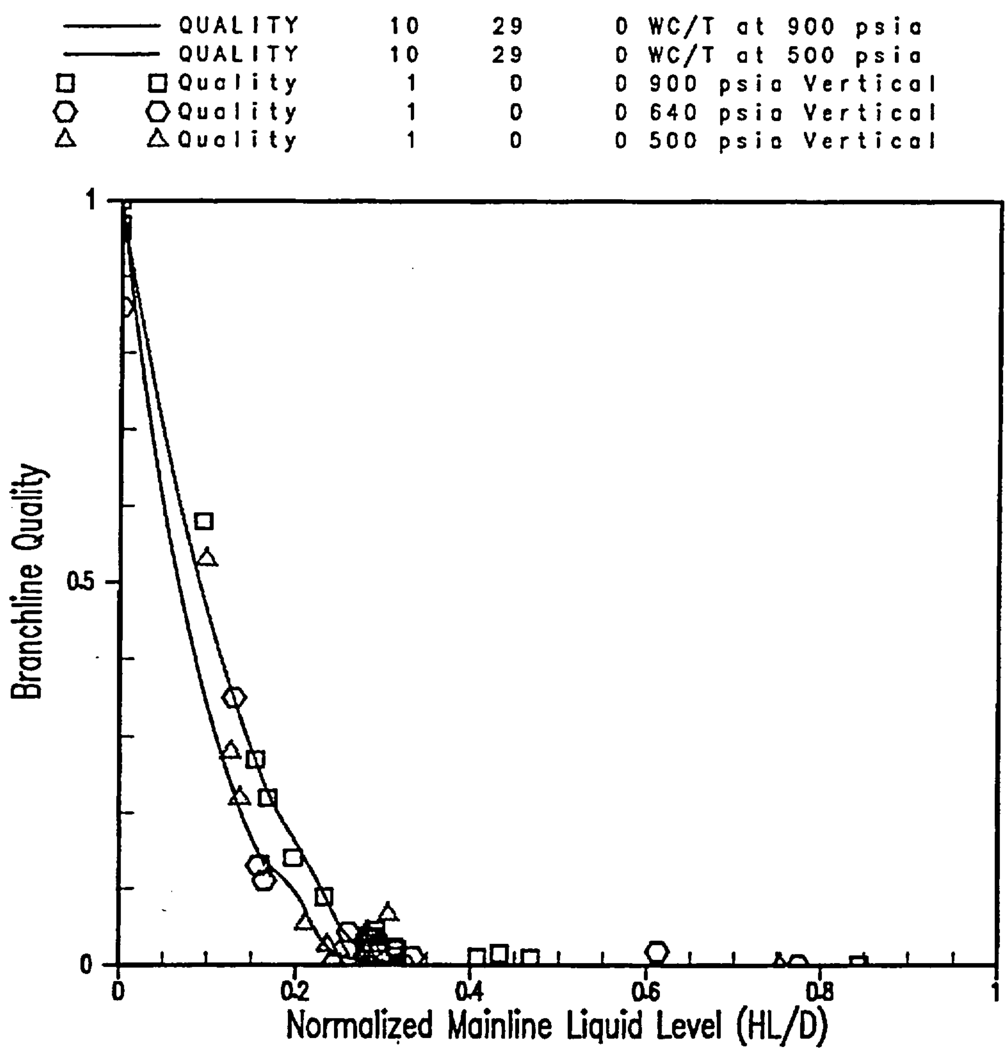

Figure 13-3-5. Branchline Quality Versus Mainline Liquid Level for Downward-Vertical Configuration

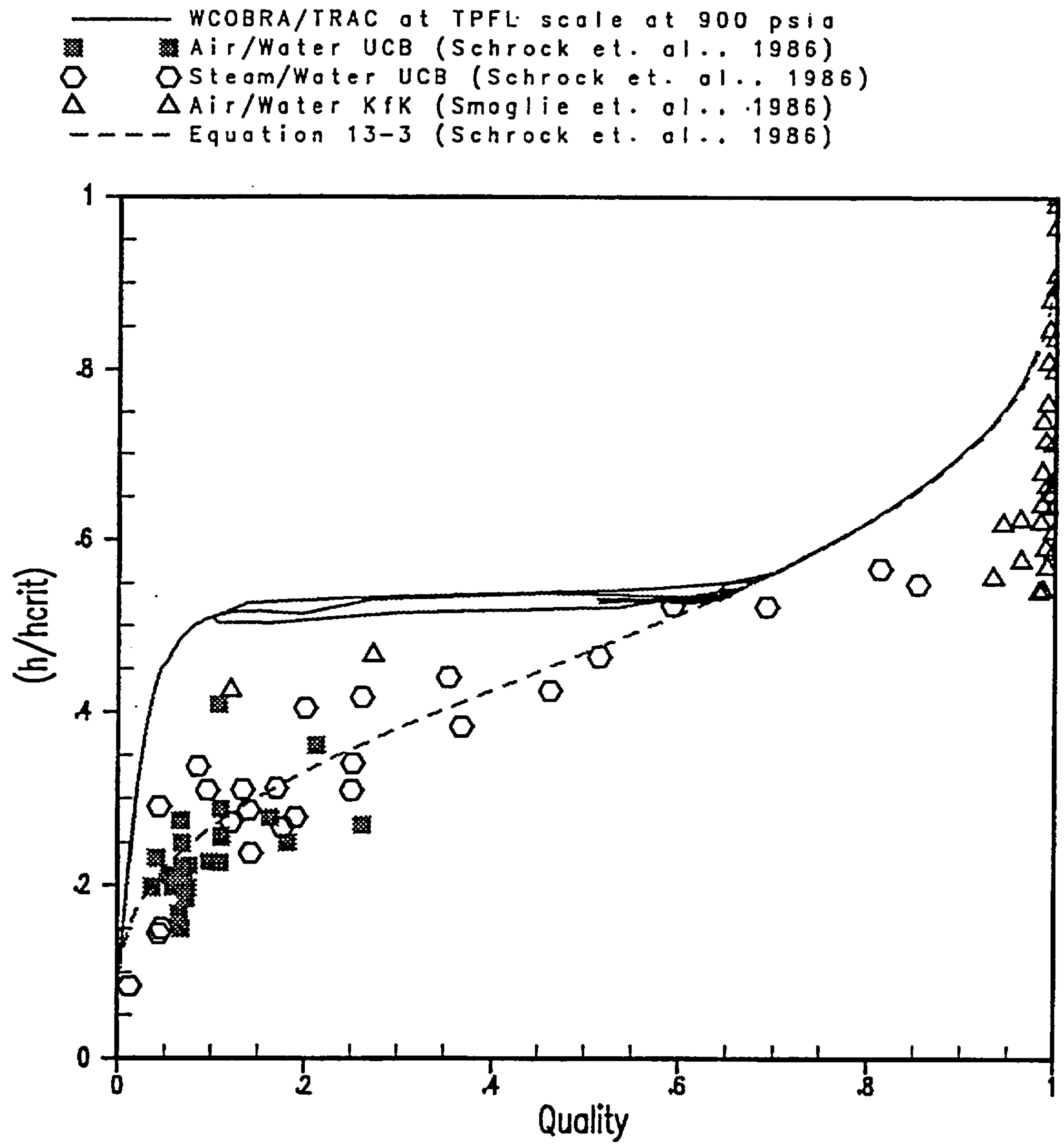

Figure 13-3-6. Branchline Quality Versus Mainline Liquid Level for Upward-Vertical Configuration

13-4 Assessment of the WCOBRA/TRAC Break Flow Model

13-4-1 Assessment Objective

In this section, the break flow model in WCOBRA/TRAC-SB is assessed relative to the following effects on the break flow:

- Break path length
- Break flow area variation
- Upstream pressure variation
- Variation in degree of subcooling during liquid discharge
- Upstream void fraction/quality variation
- Break entrance geometry

The critical flow model's bias and uncertainty will be determined by comparing the critical flow model prediction implemented in WCOBRA/TRAC-SB with selected data from the qualified break flow dataset by V. Illic et. al. (1986), the Marviken full scale critical flow test (EPRI-NP-2370, 1982, and Amos and Schrock, 1983) and the Two Phase Flow Loop (TPFL) (Anderson and Benedetti, 1985).

13-4-2 Assessment Test Matrix

Dataset mentioned in V. Illic (1986) was further examined for selection for comparison and bias/uncertainty evaluation. Data without well defined stagnation condition or upstream condition were excluded at this time. Dataset by Cruver (1963), Fauske (1962), Henry (1990), Isbin (1957) and Zaloudek (1964) do not report stagnation pressure. Dataset by Guizovarn (1975) contains superheated liquid upstream of the nozzle, which is contrary to the description in V. Illic (1986) which states subcooled inlet condition. Dataset by Bryers and Hsieh (1966) contains highly subcooled stagnation condition contrary to the description. The dataset by Ogasawara (1969) did not contain the reservoir temperature or the quality. Datasets by Danforth (1941) and Schrock (1977) are suspect with regard to achieving the critical condition according to Illic. Dataset by Morrison (1977) was felt to be inconsistent with other similar data.

The dataset mentioned above need to be further investigated for the use in the bias and uncertainty study since as-reported upstream condition is suspect. Table 13-4-1 is a summary of all selected dataset for this assessment. The dataset represents more than 1400 points from 40 geometries containing data from 13 to 2500 psia. The geometry ranges from $0 < L < 2300$mm, $0.464 < D_H < 500$mm.

Table 13-4-1
Selected Dataset and Input Variables

Data Set No.	Reference	Pressure (psia)	Upstream Condition	No. of Data Points	Length (mm)	Dhyd (mm)
1	Ardron (1978)	22-55	Subcooled	32	1015	26.3
2-4	Boivin (1979)	200-1500	Subcooled	21	500-1830	12-50
5	Fincke (1981)	13-45	Subcooled	92	79.72	18.28
6-7	Jeandey (1981)	100-2100	Subcooled	88	463	20.13
8-9	Neusen (1962)	100-600	Subcooled	37	0	6.4-11.125
10	Reocreux (1974)	30 50	Subcooled	28	2335	20
11-12	Seynhaeve (1980)	40-150	Subcooled	57	221-306	12.5
13-33	Sozzi (1975)	400-1100	Subcool and Saturated	667	4.7-1822.5	12.7
34-37	Marviken (1982)	400-750	Subcooled and Saturated	252	150-300	300-500
38-39	Amos (1983)	500-2300	Subcooled	44	63.5	0.464-0.748
40	Anderson (1985)	500-900	Saturated Liquid up to Saturated Vapor	109	54	16.2
TOTAL		13-2300	Subcooled Liquid to Saturated Vapor	1427	0-2335	0.418-500

The next table, Table 13-4-2, is the complete assessment test matrix used to evaluate the accuracy of the WCOBRA-TRAC break flow model; it describes in detail all 40 nozzle geometries and orientations.

Table 13-4-2
Critical Flow Data Considered for Model Evaluation

Data Set No.	Reference	L (mm)	D (mm)	cosθ	N-Data	Comments
1	Ardron, K. H. & Ackerman, M. C. (1978)	1015	26.3	0	33	One superheated upstream condition was not used
2	Boivin (1979)	500	12	0	10	D=50 (z<0); 0<z<50 rounded entrance; D=12 (50<z<500); D=12+19(z- 500) (500<z<700); D=50 (z>700 mm)
3	Boivin (1979)	1600	30	0	5	D=150 (z<0); 0<z<130 rounded entrance; D=30 (130<z<1730); D=30+0.12(z-1730) (1730<z<2305); D=100 (z>2305 mm)
4	Boivin (1979)	1700	50	0	6	D=150 (z<0); 0<z<130 rounded entrance; D=50 (130<z<1830); D=50+0.12(z-1830) (1830<z<2240); D=100 (z>2240 mm)
5	Fincke & Collins (1981)	13	44	0	92	D=18.28 (54.7<z<79.7); D=18.28+0.12(z-79.7), (z<215.9 mm)
6	Jeandey et al. (1981)	463	20	1	15	D=66.7-0.54z (0<z<86.9); D=20.1 (z>86.9 mm)
7	Jeandey et al. (1981)	463	20	1	73	see Appendix C.7.1 for (z<100); D=20.13 (100<z<463); D=20.13+0.12(z- 463) (z<900); D=737 (z>900 mm)
8	Neusen (1962)	0	11	0	7	D=11.12 mm at throat; D=11.12+0.425z (0<z<35.91 mm)
9	Neusen (1962)	0	6	0	5	D=16.4 mm at throat; D=6.4+0.425z (0<z<59.81 mm)
10	Reocreux (1974)	2335	20	1	28	D=20 (0<z<2335); D=20+0.12(z-2335) (z<2662 mm)
11	Seynhaeve (1980)	306	13	1	26	D=12.5 (0<z<306); D=12.5+0.245(z-306) (z>541); D=70 (z>541 mm)
12	Seynhaeve (1980)	306	13	1	31	D=12.5 (0<z<221); D=12.5+0.245(z-221) (z>541); D=70 (z>541 mm)
13	Sozzi & Sutherland (1975)	45	12.7	0	129	D=43.2 (z=0); rounded convergent (0<z<44.5); D=12.7+0.105(z-44.5) (z<158.5 mm) (Nozzle 1)
14	Sozzi & Sutherland (1975)	45	12.7	0	13	D=43.2 (z=0); rounded convergent (0<z<44.5 mm) (Nozzle 2)
15	Sozzi & Sutherland (1975)	57	12.7	0	47	D=43.2 (z=0); rounded convergent (0<z<44.5 mm) (Nozzle 2)
16	Sozzi & Sutherland (1975)	362	12.7	0	19	D=43.2 (z=0); rounded convergent (0<z<44.5 mm) (Nozzle 2)
17	Sozzi & Sutherland (1975)	83	12.7	0	17	D=43.2 (z=0); rounded convergent (0<z<44.5 mm) (Nozzle 2)
18	Sozzi & Sutherland (1975)	553	12.7	0	13	D=43.2 (z=0); rounded convergent (0<z<44.5 mm) (Nozzle 2)
19	Sozzi & Sutherland (1975)	108	12.7	0	23	D=43.2 (z=0); rounded convergent (0<z<44.5 mm) (Nozzle 2)
20	Sozzi & Sutherland (1975)	679	12.7	0	96	D=43.2 (z=0); rounded convergent (0<z<44.5 mm) (Nozzle 2)
21	Sozzi & Sutherland (1975)	159	12.7	0	15	D=43.2 (z=0); rounded convergent (0<z<44.5 mm) (Nozzle 2)
22	Sozzi & Sutherland (1975)	1823	12.7	0	81	D=43.2 (z=0); rounded convergent (0<z<44.5 mm) (Nozzle 2)
23	Sozzi & Sutherland (1975)	235	12.7	0	12	D=43.2 (z=0); rounded convergent (0<z<44.5 mm) (Nozzle 2)

Table 13-4-2 (Cont'd)
Critical Flow Data Considered for Model Evaluation

Data Set No.	Reference	L (mm)	D (mm)	cosθ	N-Data	Comments
24	Sozzi & Sutherland (1975)	273	12.7	0	22	D=43.2 (z=0); rounded convergent (0<z<44.5 mm) (Nozzle 2)
25	Sozzi & Sutherland (1975)	5	12.7	0	58	Nozzle No. 3 (Sharp entrance)
26	Sozzi & Sutherland (1975)	322	12.7	0	24	Nozzle No. 3 (Sharp entrance)
27	Sozzi & Sutherland (1975)	513	12.7	0	24	Nozzle No. 3 (Sharp entrance)
28	Sozzi & Sutherland (1975)	640	12.7	0	17	Nozzle No. 3 (Sharp entrance)
29	Sozzi & Sutherland (1975)	195	12.7	0	23	Nozzle No. 3 (Sharp entrance)
30	Sozzi & Sutherland (1975)	45	19	0	23	D=43.2 (z=0); rounded convergent (0<z<44.5 mm)
31	Sozzi & Sutherland (1975)	732	54	0	4	D=260-0.39(z-202) (202<z<732); D=54+0.263(z-732) (z<1112 mm)
32	Sozzi & Sutherland (1975)	696	76	0	3	D=260-0.39(z-223) (223<z<696); D=54+0.263(z-696) (z<1076 mm)
33	Sozzi & Sutherland (1975)	63	28	0	5	D=72.6 (z=0); rounded elliptical sec. (0<z<63.5); D=28+0.246(z-63.5) (z<228.5)
34	Marviken Test 6 (1982)	300	300	-1	84	Rounded entrance
35	Marviken Test 7 (1982)	300	300	-1	84	Rounded entrance
36	Marviken Test 23 (1982)	150	500	-1	44	Rounded entrance
37	Marviken Test 24 (1982)	150	500	-1	39	Rounded entrance
38	Amos & Schrock (1983)	63.5	0.747	-1	18	Rec. Slit 0.381x63.5 mm with known entrance losses
39	Amos & Schrock (1983)	63.5	0.418	-1	26	Rec. Slit 0.254x63.5 mm with known entrance losses
40	Anderson & Benedetti (1985)	31.9	16.2	0	109	Rounded entrance (at 500, 640 and 900 psia)

The following material contains a brief description and graphical presentation of the upstream conditions of experiments for selected data sources.

The stagnation condition of each dataset such as Pressure/Temperature and Pressure/Quality are shown graphically in the following figures. The Pressure/Temperature trajectories of the primary system of LOFT and ROSA during small break LOCA experiments along with the saturation line are shown for comparison.

Ardron and Ackerman

Ardron and Ackerman conducted critical flow experiments by discharging subcooled water from a pressure vessel through a horizontal test section. The test section consisted of a straight cylindrical pipe 0.0263 m in diameter and 1.015 m long. Instrumentation included measurement of stagnation pressure and temperature with reported uncertainties of 7.0 kPa and 0.1 °C, respectively, mass flux with uncertainty of 200 kg/m^2-s, and differential pressure measurements, the roughness of pipe was estimated to be 2.5E-06 m. As seen in Figures 13-4-1a and 13-4-1b, the range of stagnation pressure tested was from 150 to 370 kPa with subcooling from 0 to 7 °C. All tests were conducted with demineralized and degassed water.

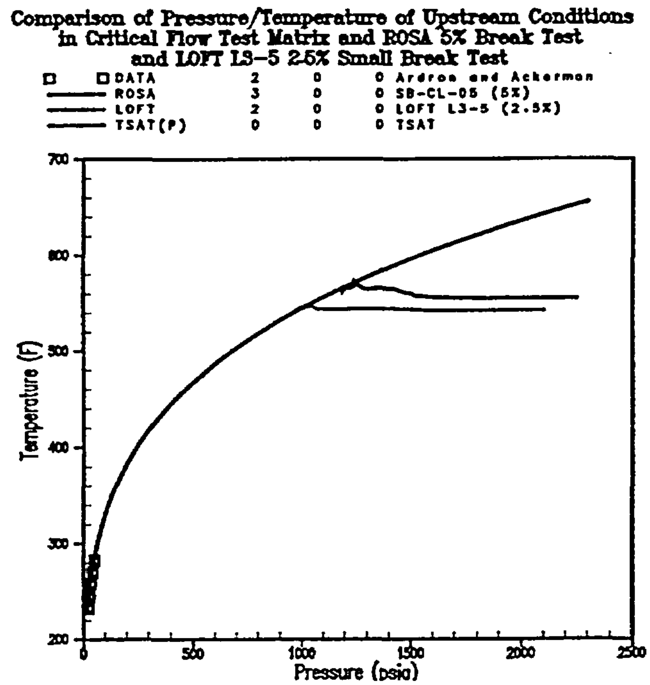

Figure 13-4-1a Upstream Condition in Ardron-Ackerman

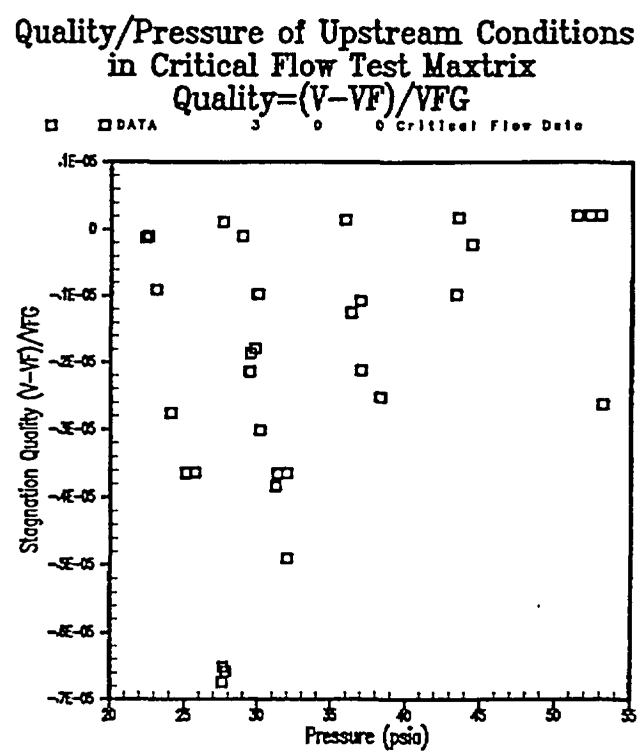

Figure 13-4-1b Upstream Condition in Ardron-Ackerman

Boivin

Boivin conducted critical flow experiments by discharging water through long, horizontal nozzles. Three nozzles were tested. Each nozzle had a rounded inlet, a long cylindrical smooth pipe, and a diffuser having a small expanding angle. In the three cases, the L/D ratio is greater than 30 to minimize 2-D effects. The first nozzle had a pipe diameter of 0.012 m, 0.45 m long with a diffuser angle of 11 degrees. The second nozzle had a pipe diameter of 0.030 m, 1.6 m long with a 7 degree diffuser. The diameter of the third nozzle was 0.050 m, 1.7 m long with a diffuser of 7.7 degree.

Measurements reported include inlet (stagnation) pressure and temperature, mass flux, and throat pressure. No measurement uncertainties were reported. Stagnation pressure conditions ranged from 1960 to 10100 KPa with inlet water somewhat subcooled.

The upstream conditions in Pressure/Temperature and Pressure/Quality planes, along with (P, T) trajectories observed in LOFT and ROSA small break tests, are shown in Figures 13-4-2a and 13-4-2b.

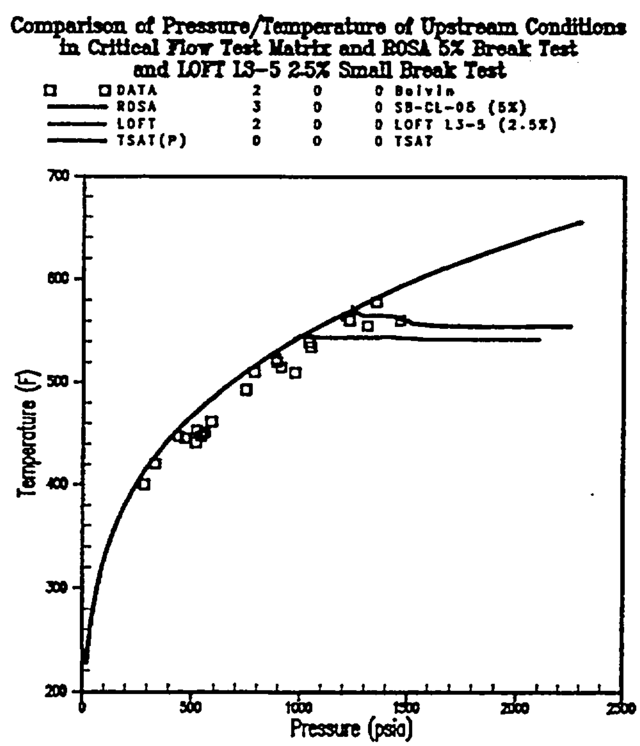

Figure 13-4-2a Upstream Conditions in Boivin

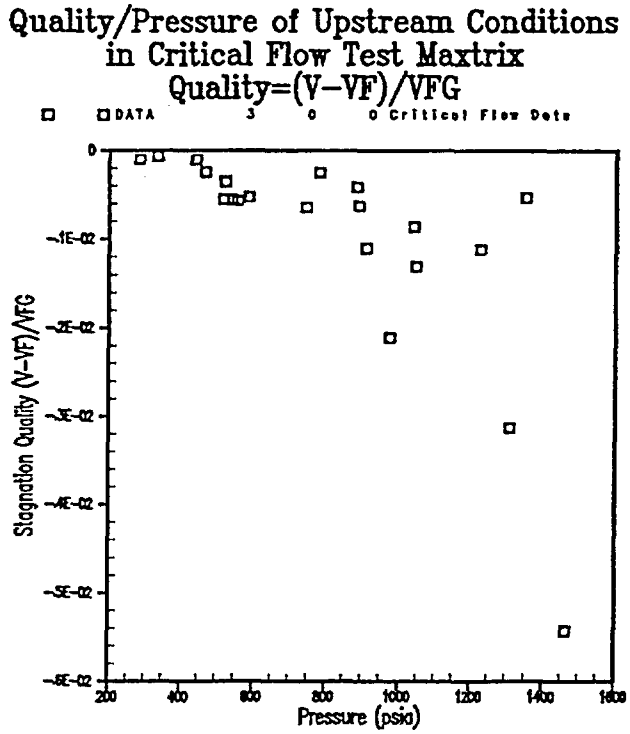

Figure 13-4-2b Upstream Condition in Boivin

Fincke and Collins

Fincke and Collins performed critical flow experiments by flowing subcooled water through a loop and test section. Mass flow rate was controlled by a flow control valve upstream of the test section and back pressure was controlled by a valve downstream of the test section. The test section consisted of a 1.8 m long, 0.0444 m diameter Lexan cylindrical tube followed by a convergent-divergent Lexan nozzle with a minimum diameter of 0.01828 m. Degassed water was used for all experiments. Instrumentation included upstream temperature (reported uncertainty of 0.1°C), volumetric flowrate (uncertainty of 0.1 l/s), pressure just upstream of the nozzle (no uncertainty given), and differential pressure measurements along the nozzle (uncertainty ranging from 0.5 to 2.5 kPa). The differential pressure measurements were used to determine the throat pressure that is included in this data base. The upstream pressure ranged from 90 to 300 kPa, inlet temperatures were 5° to 40°C subcooled.

The upstream conditions in Pressure/Temperature and Pressure/Quality planes, along with (P, T) trajectories from LOFT and ROSA small break tests, are shown in Figures 13-4-3a and 13-4-3b.

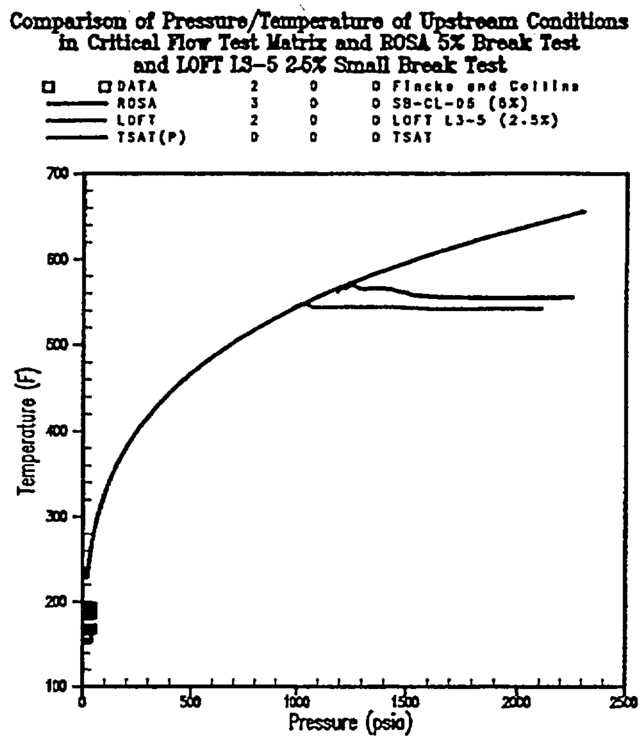

Figure 13-4-3a Upstream Condition in Fincke-Collins

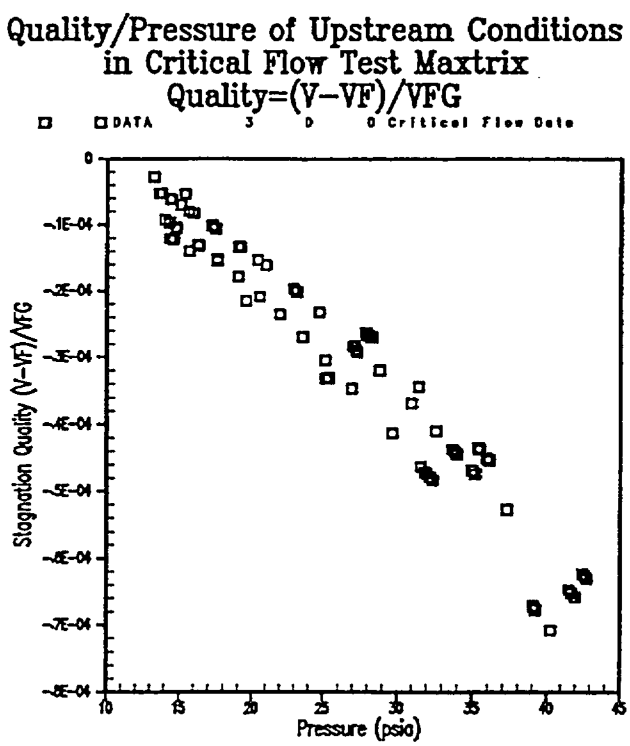

Figure 13-4-3b Upstream Condition in Fincke-Collins

Jeandey

Jeandey performed critical flow experiments by flowing subcooled, demineralized and degassed water through a vertical test section. The test section consisted of a smoothly convergent entrance followed by a straight cylindrical pipe 0.02013 m in diameter followed by a diverging section with a divergent angle of 7 degrees. Flow was vertically upward for all the experiments. Stagnation conditions ranged from pressures of 900 to 12000 kPa and temperatures of 148.5 to 324.6 C. The resulting critical mass fluxes ranged from 14500 to 62000 kg/m^2-s.

The throat pressure was measured along with many other pressures along the test section. In addition, for 21 of the experiments, axial and radial void fraction profiles were obtained using an X-ray densitometer.

The upstream conditions in Pressure/Temperature and Pressure/Quality planes, along with (P, T) trajectories observed in LOFT and ROSA small break tests, are shown in Figures 13-4-4a and 13-4-4b.

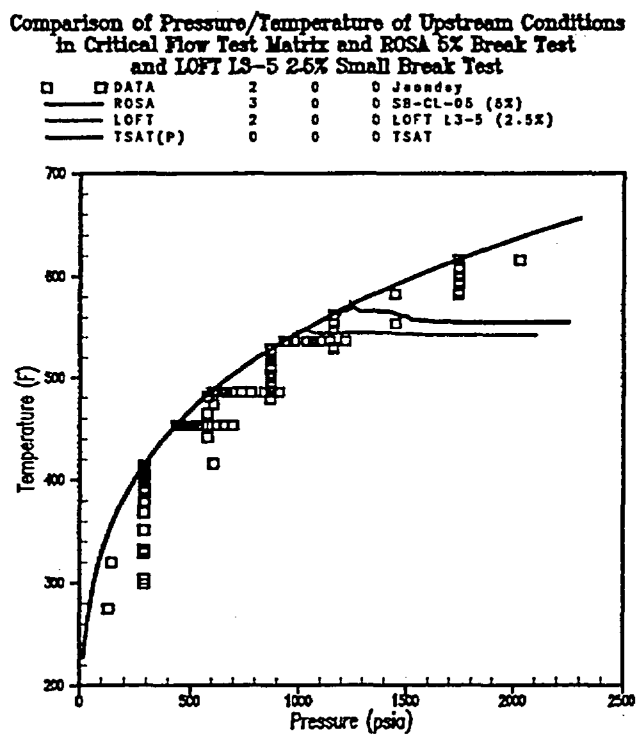

Figure 13-4-4a Upstream Condition in Jeandey

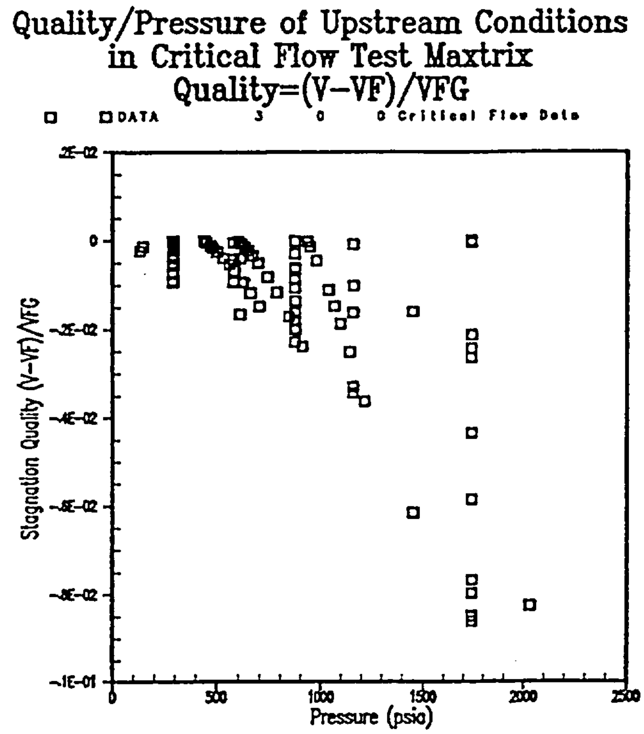

Figure 13-4-4b Upstream Condition in Jeandey

Neusen

Neusen performed experiments to determine design criteria for convergent-divergent nozzles. Critical flow occurred during these experiments, and the data are included in this data base. Neusen flowed saturated water through two convergent-divergent nozzles with minimum diameters of 0.0064 and 0.011 m. Reported stagnation conditions ranged from pressures of 840 to 5540 kPa and qualities of 0.0028 and 0.228.

Stagnation conditions for these experiments were determined by measuring subcooled temperature and pressure upstream of a throttling valve. The throttling process was assumed to be isentropic, and pressure was measured downstream of the throttling valve (reported uncertainty of 1%). Reported uncertainties for mass flux and calculated enthalpy were less than 2.5% and 0.5%, respectively.

The upstream conditions in Pressure/Temperature and Pressure/Quality planes, along with (P, T) trajectories observed in LOFT and ROSA small breaks, are shown in Figures 13-4-5a and 13-4-5b.

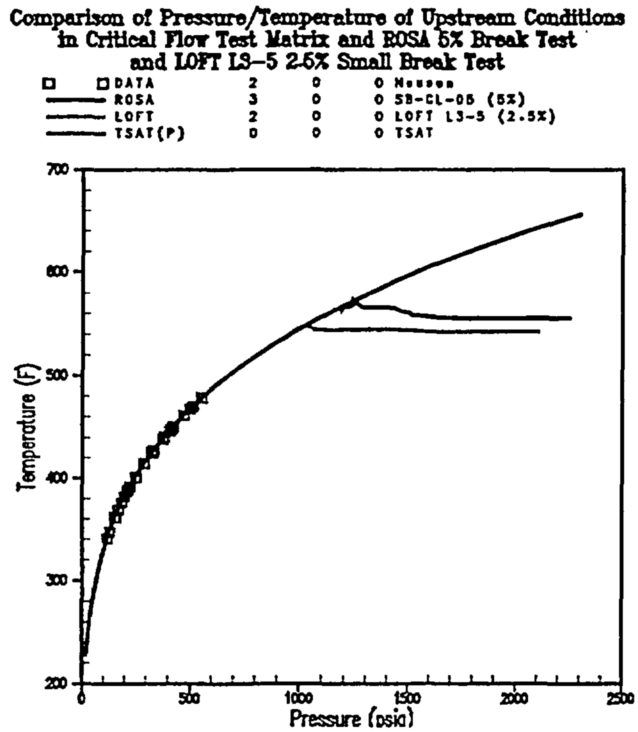

Figure 13-4-5a Upstream Condition in Neusen

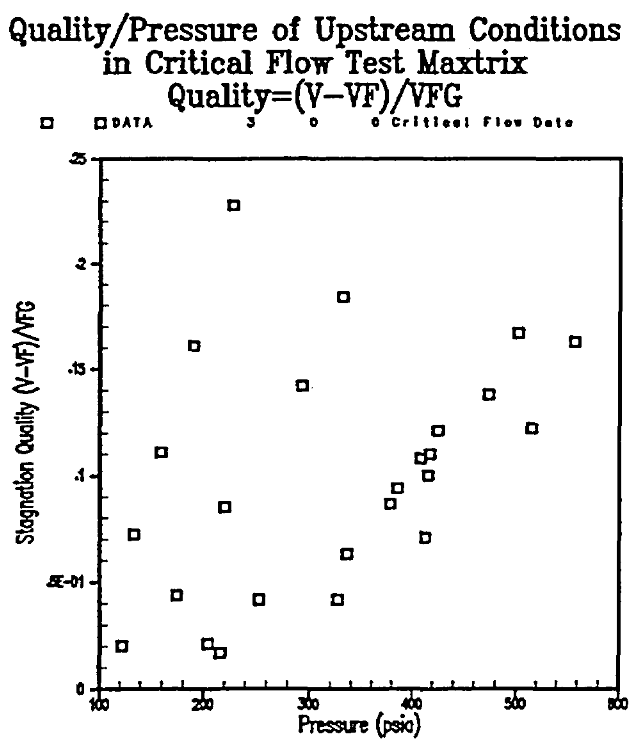

Figure 13-4-5b Upstream Condition in Neusen

Reocreux

Reocreux performed critical flow experiments by flowing subcooled degassed, demineralized water upwards through a vertical test section. The test section consisted of a straight, cylindrical section 2.335 m long and 0.020 m in diameter, followed by a divergent section 0.327 m long. Stagnation pressures ranged from 212 to 340 kPa, and stagnation temperatures ranged from 115.9 to 121.8 C. Pressure were measured along the test section at many locations, most concentrated near the choking point (at the entrance to the divergent section). The critical or throat pressures were determined from these measurements. In addition, the void fraction at the choking point was measured for most of the tests using X-ray attenuation method.

The upstream conditions in Pressure/Temperature and Pressure/Quality planes, along with (P, T) trajectories observed in LOFT and ROSA small break tests, are shown in Figures 13-4-6a and 13-4-6b.

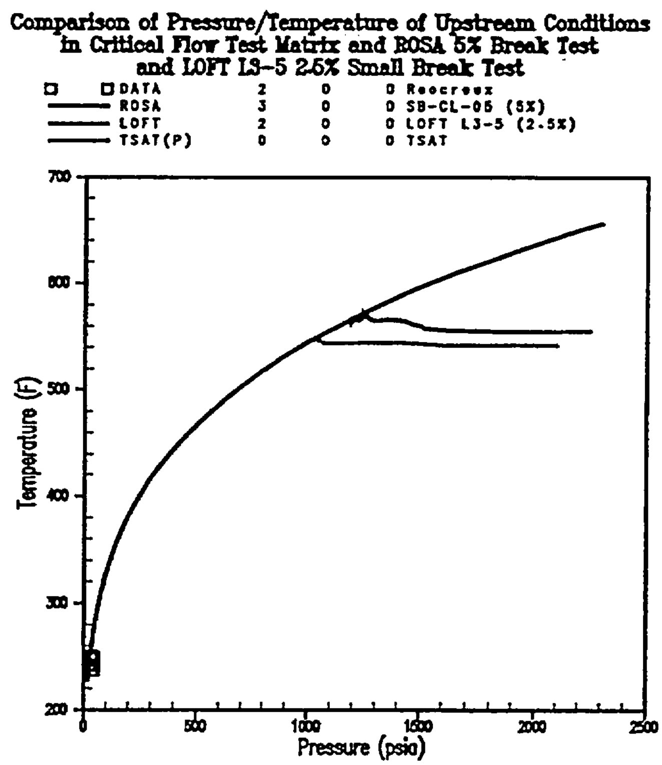

Figure 13-4-6a Upstream Condition in Reocreux

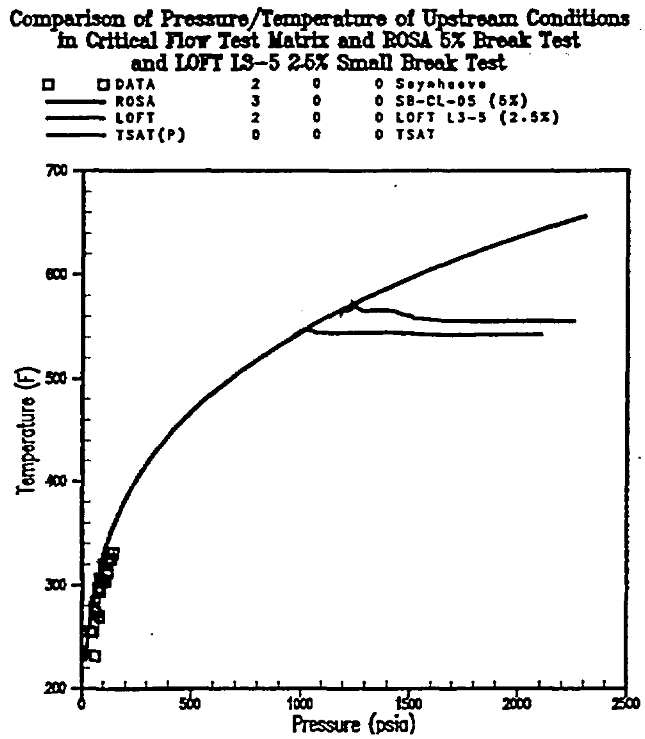

Figure 13-4-6b Upstream Condition in Reocreux

Seynhaeve

Seynhaeve performed critical flow experiments by flowing subcooled, demineralized water upwards in vertical test sections. Two test sections were employed. Each section consisted of a straight, cylindrical pipe 0.0125 m in diameter followed by a divergent section. One section had the straight pipe 0.306 m long, and the other 0.221 m long. Stagnation conditions for these experiments range from 280 to 1015 kPa in pressure and 1 to 166.8 C in temperature. Critical pressure was measured near the choking plane. Measurement uncertainties are not known.

The upstream conditions in Pressure/Temperature and Pressure/Quality planes, along with (P, T) trajectories observed in LOFT and ROSA small break tests, are shown in Figures 13-4-7a and 13-4-7b.

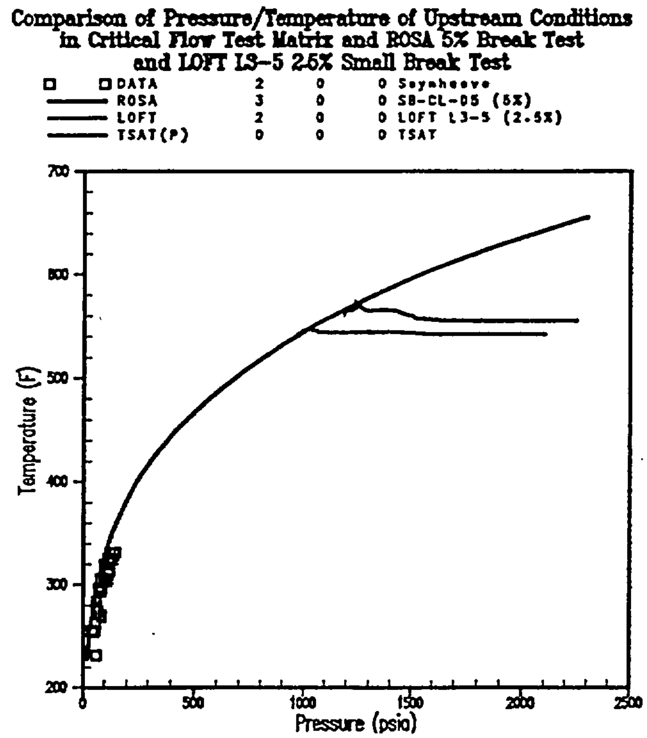

Figure 13-4-7a Upstream Condition in Seynhaeve

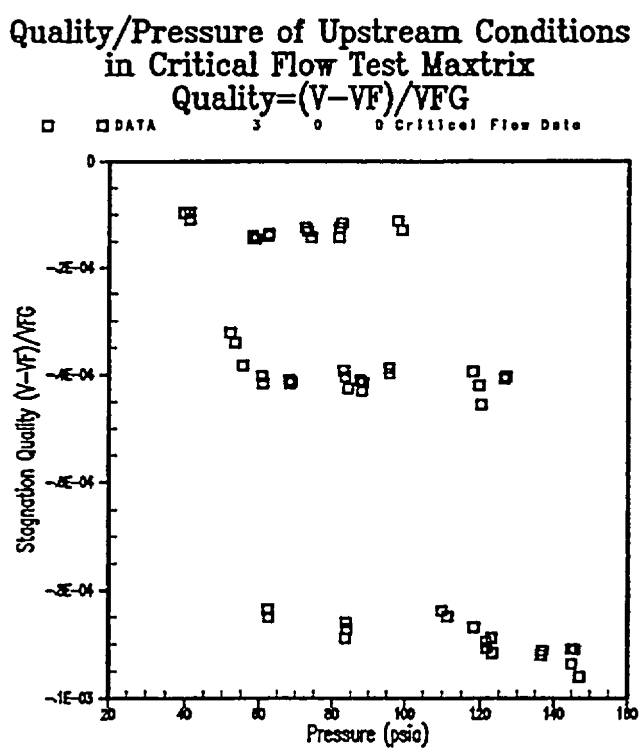

Figure 13-4-7b Upstream Condition in Seynhaeve

Sozzi and Sutherland

Sozzi and Sutherland conducted a series of critical flow experiments with subcooled and low quality water. The water for each experiment was demineralized and degassed. Water from a large vessel was blown-down through test nozzles. Data from 21 different nozzle shapes and configurations have been taken with more than 650 individual data points. Stagnation pressure ranged from 3000 to 7000 kPa, and stagnation qualities ranged from approximately -0.04 to 0.007 (based on the specific volume)

The upstream conditions in Pressure/Temperature and Pressure/Quality planes, along with (P, T) trajectories observed in LOFT and ROSA small break tests, are shown in Figures 13-4-8a and 13-4-8b.

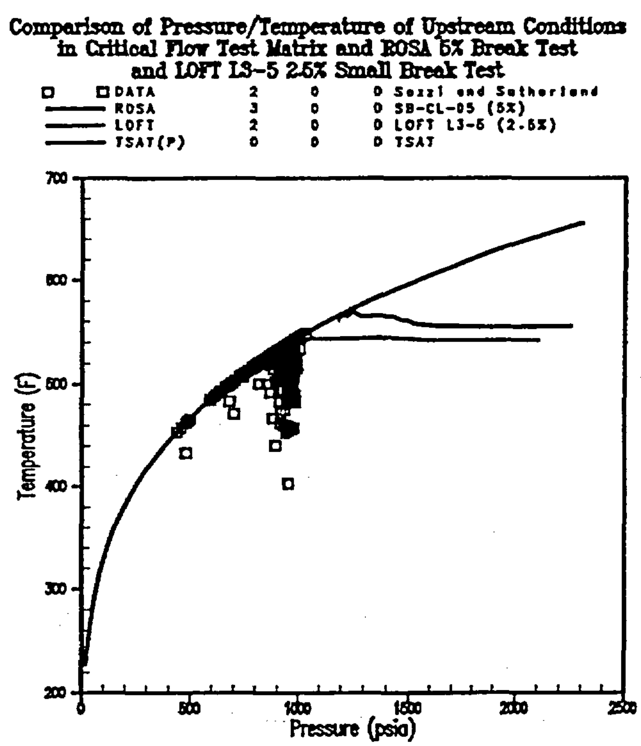

Figure 13-4-8a Upstream Condition in Sozzi-Sutherland

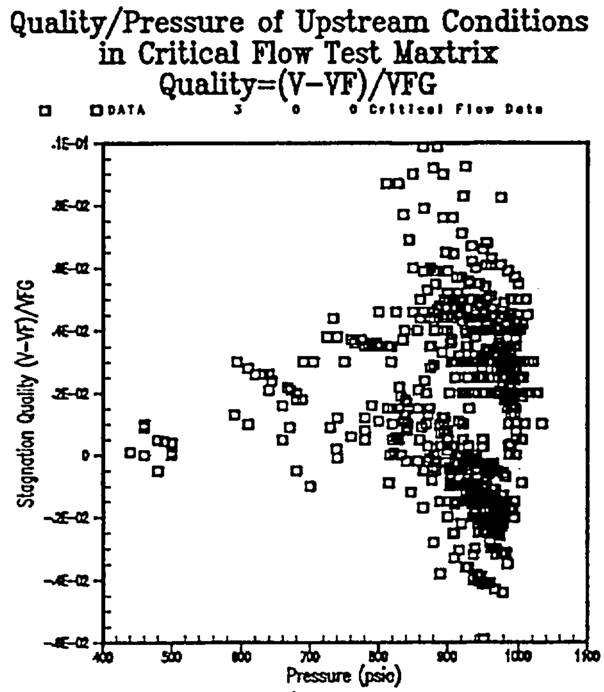

Figure 13-4-8b Upstream Condition in Sozzi-Sutherland

Marviken Tests 6, 7, 23 and 24

Marviken tests provide very large diameter downflow data typically considered full scale. The Marviken facility was used for full-scale critical flow tests between mid-1977 and December 1979. During this time, 27 tests were conducted by a downward discharge of water and steam mixtures from a full-sized reactor vessel through a large diameter vertical discharge pipe that supplied the flow to a test nozzle. There were 9 nozzles tested; all had rounded entrances followed by a nominal 20, 30 and 50 cm constant diameter straight section. Table 13-4-3 below shows the characteristic dimensions for the tests. As seen in the table, tests selected for the model evaluation are datasets taken with two of the shortest nozzles in the Marviken test series.

Table 13-4-3 Marviken Test Nozzles

Nozzle Number	Diameter (mm)	Length (mm)	Used in Tests
1	200	590	13, 14
2	300	300	6, 7
3	300	510	25, 26
4	300	895	1, 2, 12
5	300	1110	17, 18, 19
6	500	166	23, 24
7	500	730	20, 21, 22, 27
8	500	1809	15, 16
9	509	1589	3, 4, 5, 8, 9, 10, 11

The discharge pipe that connects the vessel to the nozzle is 6283 mm long and is geometrically complex. It is made up of several pieces: nozzle, permanently attached to the vessel with a 752 mm diameter, a 1980 mm long drift tube of the same diameter, a 1778 mm long global valve with a 780 mm diameter and a 1000 mm long with 752 mm diameter section to which the nozzle is attached. Besides these there were two 120 mm long instrument rings inserted on either end of the 1980 mm drift tube. It is quite clear that with this degree of geometric complexity, the question of establishing a consistent set of complete inlet conditions is not simple.

For this study, only the nozzle is modelled by the critical flow model. Thus the inlet condition to the nozzle was taken from 004M109 for pressure (0.7 m upstream) and 003M404 for temperature (2.8 m upstream).

Probable error Pressure - 7 kPa, Temperature - 0.6°C.

The upstream conditions in Pressure/Temperature and Pressure/Quality planes, along with (P, T) trajectories observed in LOFT and ROSA small break tests, are shown in Figures 13-4-9a and 13-4-9b.

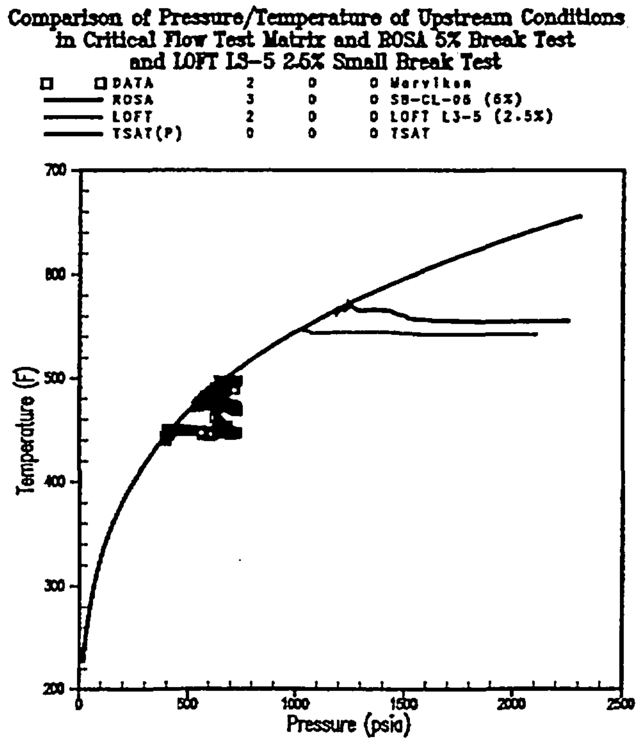

Figure 13-4-9a Upstream Condition in Marviken Tests 6, 7, 23 and 24

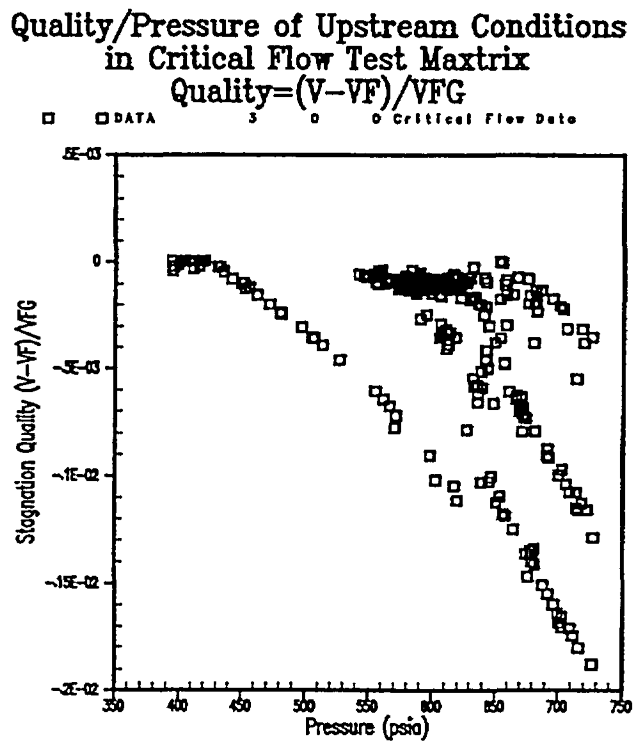

Figure 13-4-9b Upstream Condition in Marviken Tests 6, 7, 23 and 24

Amos and Schrock

Amos and Schrock's break flow data cover a wide range of pressure from 4000 to 15500 kPa, and subcooling from 0 to 60°C which is suited for evaluating a performance of the break model for small break LOCA analyses. The configuration of the break is thin rectangular slit with the nominal width of 0.381 and 0.254 mm. These set of tests are two of larger slit size of the three of their experiments. Although the break flow area is rectangular and small (equivalent hydraulic diameter = 0.748 and 0.464 mm), the data is valuable since the phenomena which governs the critical condition appeared to be the same for breaks of all sizes. This may be why the 1D flow model is sufficiently accurate to describe the break flows.

The upstream conditions in Pressure/Temperature and Pressure/Quality planes, along with (P, T) trajectories observed in LOFT and ROSA small break tests, are shown in Figures 13-4-10a and 13-4-10b.

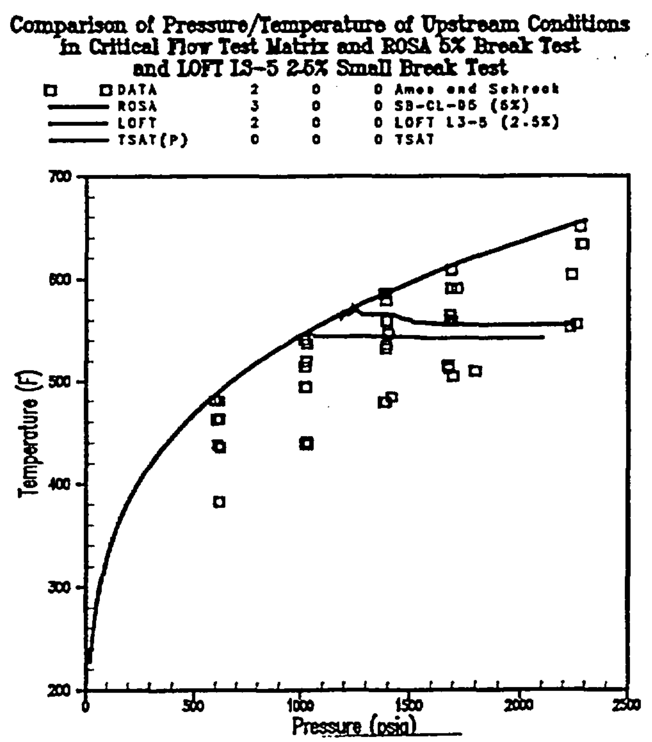

Figure 13-4-10a Upstream Condition in Amos-Schrock

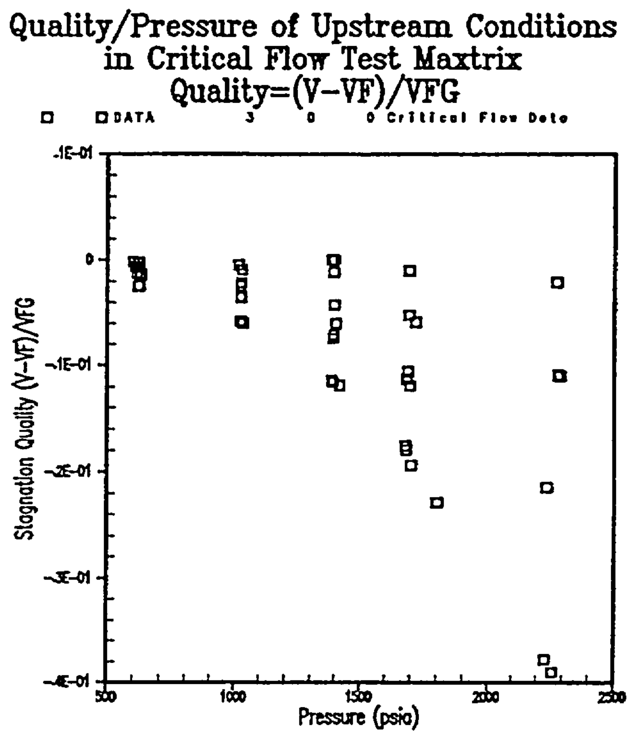

Figure 13-4-10b Upstream Condition in Amos-Schrock

Anderson and Benedetti (TPFL)

Anderson and Benedetti conducted critical flow tests at Two Phase Flow Loop (TPFL) located in INEL, for purpose of investigating the entrainment at the break off the stratified upstream flow under saturated condition. Two phase mixture of known phasic mass flow rate flowed through a branch line pipe of 1.63 m long, 34 mm diameter attached to a simulated cold leg pipe, to the nozzle which is 54 mm long and has a diameter of 16.2 mm. The pressure just upstream of the rounded entrance nozzle as well as the void fraction was measured by a gamma attenuation method. Their experiments are well instrumented critical flow tests with saturated upstream conditions at 900, 640 and 500 psia. The flow quality in the tests were varied from 0 to 1 at all three pressures.

The upstream conditions in Pressure/Temperature and Pressure/Quality planes, along with (P, T) trajectories observed in LOFT and ROSA small break tests, are shown in Figures 13-4-11a and 13-4-11b.

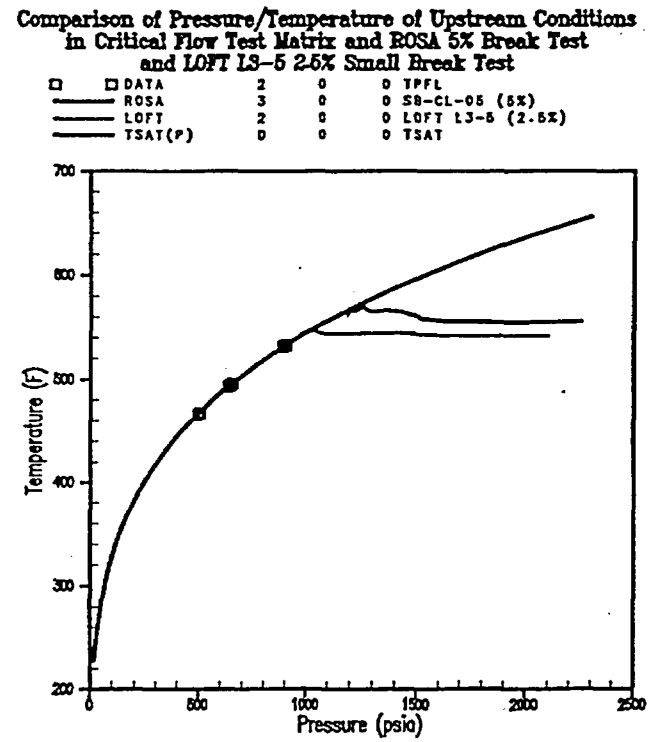

Figure 13-4-11a Upstream Condition in TPFL

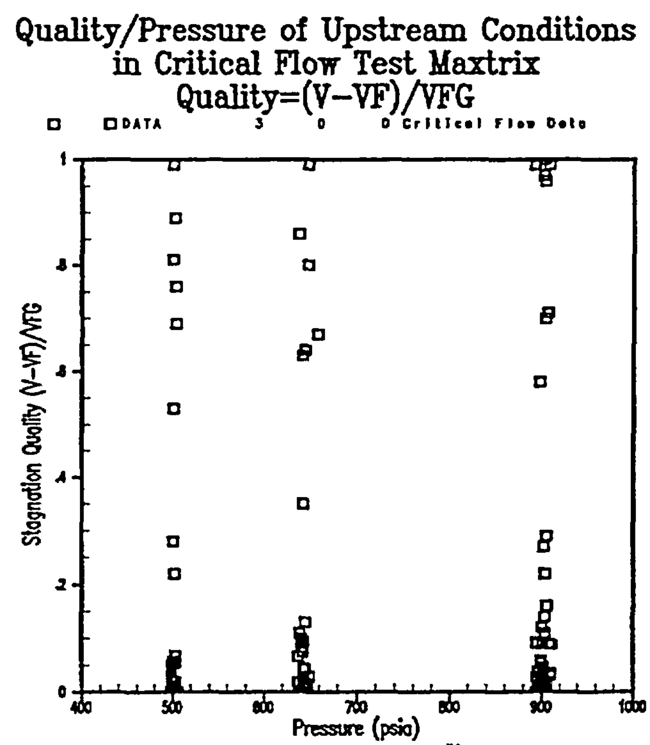

Figure 13-4-11b Upstream Condition in TPFL

Overall

The test matrix selected covers from 13 psia to 2300 psia, and quality of -0.039 to 1.0. The coverage of upstream condition is graphically shown in Figures 13-4-12a and Figure 13-4-12b below.

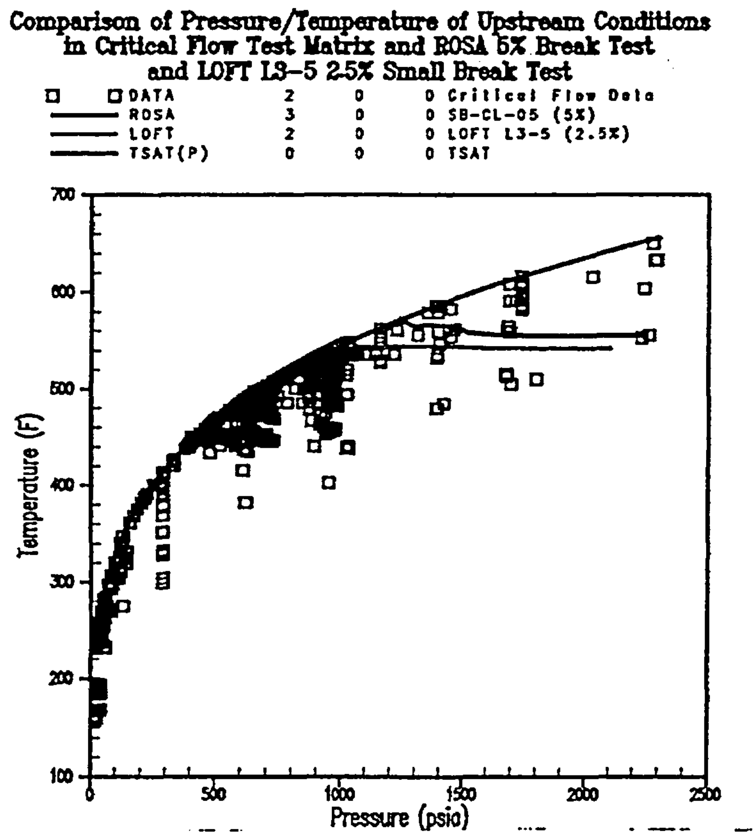

Figure 13-4-12a Upstream Condition in Test Matrix

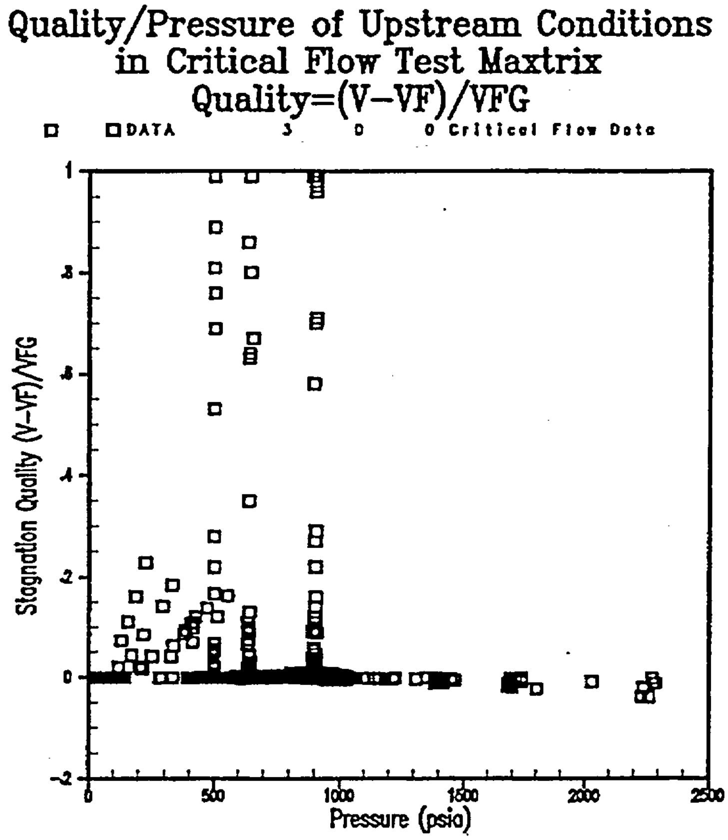

Figure 13-4-12b Upstream Condition in Test Matrix

13-4-3 Assessment Results

A total of 1427 data points from 40 nozzle geometries were used for the determination of bias and uncertainty associated with the critical flow model prediction used in WCOBRA/TRAC-SB. The following results were obtained through the comparison to data.

13-4-3-1 Bias and Uncertainty

A valid range of the bias and uncertainty estimate given here is based on selected experimental data. A comparison was made for $0 < L < 2335$ mm, and $0.418 < D_H < 500$ mm.

Overall (-0.039 < Quality < 1.0)

Predictions for all selected data are shown in Table 13-4.4. The mean error

$$\left(\bar{\varepsilon} = \frac{\sum_i^N \left(\frac{G_{calc} - G_{meas}}{G_{meas}} \right)_i}{N} \right)$$

was found to be -8.2% and the standard deviation

$$\left(\sigma(\varepsilon) = \sqrt{\frac{\sum_i^N (\varepsilon_i - \bar{\varepsilon})^2}{N-1}} \right)$$

was found to be 19.8%.

Subcooled Liquid Region (-0.039 < Quality < 0)

Bias = -4.3%
Standard Deviation = 14.9%

Saturated Two Phase Region (0 < Quality < 1.0)

Bias = -13.40%
Standard Deviation = 23.7%

Table 13-4-4
Critical Flow Data Comparison for WCOBRA/TRAC Critical Flow Model

Data Set No.	Reference	L (mm)	D (mm)	cosθ	N-Data	Mean Error ε (%) $\left(\frac{G_{calc} - G_{meas}}{G_{meas}}\right)$	σ(ε) (%)
1	Andron, K. H. & Ackerman, M.C. (1978) [10]	1015	26.3	0	32	1.1	12.7
2	Boivin (1979) [12]	500	12	0	10	9.2	2.8
3	Boivin (1979) [12]	1600	30	0	5	0.6	23.5
4	Boivin (1979) [12]	1700	50	0	6	-13.8	7.3
5	Fincke & Collins (1981) [15]	13	44	0	92	5.3	3.4
6	Jeandey et al. (1981) [20]	463	20	1	15	-1.0	9.2
7	Jeandey et al. (1981) [20]	463	20	1	73	-10.8	11.6
8	Neusen (1962) [22]	0	11	0	25	16.3	18.8
9	Neusen (1962) [22]	0	6	0	12	0.4	10.5
10	Reocreux (1974) [24]	2335	20	1	28	-2.6	6.5
11	Seybhaeve (1980) [25]	306	13	1	26	-11.0	1.9
12	Seybhaeve (1980) [25]	306	13	1	31	-9.4	4.2
13	Sozzi & Sutherland (1975) [27]	45	12.7	0	128	-34.6	11.8
14	Sozzi & Sutherland (1975) [27]	45	12.7	0	13	-45.8	6.5
15	Sozzi & Sutherland (1975) [27]	57	12.7	0	47	-37.1	6.6
16	Sozzi & Sutherland (1975) [27]	362	12.7	0	19	-5.1	9.9
17	Sozzi & Sutherland (1975) [27]	83	12.7	0	17	-23.4	12.5
18	Sozzi & Sutherland (1975) [27]	553	12.7	0	13	-2.9	7.7
19	Sozzi & Sutherland (1975) [27]	108	12.7	0	23	-2.4	6.4
20	Sozzi & Sutherland (1975) [27]	679	12.7	0	96	6.1	14.6
21	Sozzi & Sutherland (1975) [27]	159	12.7	0	15	-16.6	9.5
22	Sozzi & Sutherland (1975) [27]	1823	12.7	0	81	7.2	14.1
23	Sozzi & Sutherland (1975) [27]	235	12.7	0	12	-12.9	6.0
24	Sozzi & Sutherland (1975) [27]	273	12.7	0	22	-14.4	7.3
25	Sozzi & Sutherland (1975) [27]	5	12.7	0	58	-25.7	13.5
26	Sozzi & Sutherland (1975) [27]	322	12.7	0	24	-4.4	6.4
27	Sozzi & Sutherland (1975) [27]	513	12.7	0	24	-4.3	8.0
28	Sozzi & Sutherland (1975) [27]	640	12.7	0	17	-2.3	7.7
29	Sozzi & Sutherland (1975) [27]	195	12.7	0	23	-14.0	5.2
30	Sozzi & Sutherland (1975) [27]	45	19	0	23	-27.8	6.5
31	Sozzi & Sutherland (1975) [27]	732	54	0	4	-17.7	2.5
32	Sozzi & Sutherland (1975) [27]	696	76	0	3	-8.8	3.3
33	Sozzi & Sutherland (1975) [27]	63	28	0	5	-23.9	8.3
34	Marviken Test 6 (1982) [6]	300	300	-1	85	-10.3	9.0
35	Marviken Test 7 (1982) [6]	300	300	-1	84	-16.5	8.1
36	Marviken Test 23 (1982) [6]	150	500	-1	44	-2.1	11.1

Table 13-4-4 (Cont'd)
Critical Flow Data Comparison for WCOBRA/TRAC Critical Flow Model

Data Set No.	Reference	L (mm)	D (mm)	cosθ	N-Data	Mean Error ε (%) $(\frac{G_{calc} - G_{meas}}{G_{meas}})$	σ(ε) (%)
37	Marviken Test 24 (1982) [6]	150	500	-1	39	-19.2	14.3
38	Amos & Schrock (1983) [7	63.5	0.748	-1	18	0.7	7.2
39	Amos & Schrock (1983) [7]	63.5	0.464	-1	26	-0.3	9.5
40	Anderson & Benedetti (1985) [8]	31.9	16.2	0	109	15.2	26.9
TOTAL					1427	-8.2	19.8

Figure 13-4-13 below shows the comparison of all points in the test matrix with ±10% lines above and below the 45° line.

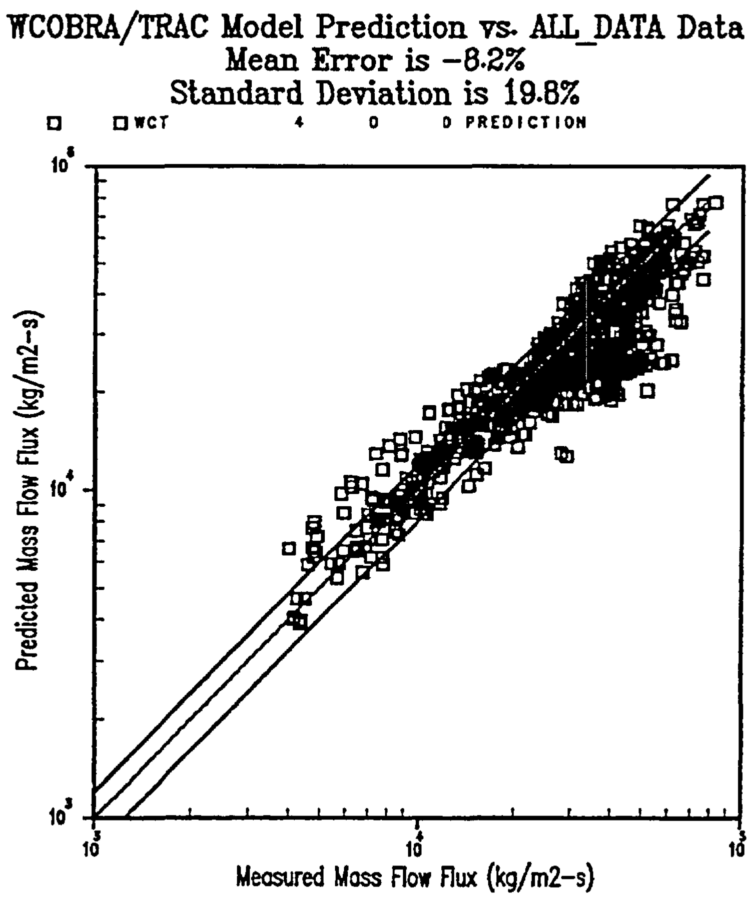

Figure 13-4-13 Comparison of Predicted and Measured Critical Flows

13-4-3-2 Model Prediction Trend with Respect to Pressure

In this section, a possible model trend with respect to the upstream pressure is examined. Figure 13-4-14 below shows the error vs. pressure of all data points. The figure does not show global trend relative to the upstream pressure, although it does show that there is a larger spread in the lower pressure points (p < 1000 psia).

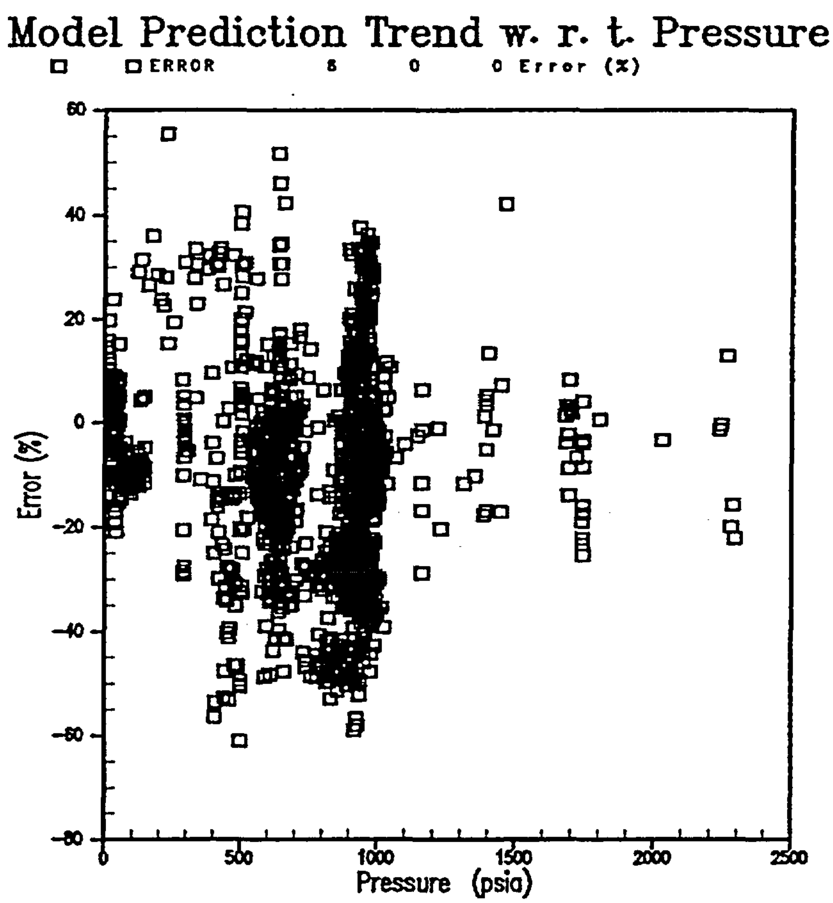

Figure 13-4-14 Prediction Trend in Pressure Variation

13-4-3-3 Model Prediction Trend with Respect to Quality

In this section, a possible model trend with respect to the upstream quality is examined. Figure 13-4-15 below shows the error vs. quality of all data points. The figure shows global trend relative to the upstream quality. The model tends to underpredict the critical mass flux for saurated liquid, X ≈0, and overpredict in the two-phase region. At or near single phase vapor region, the model's overprediction becomes substantially smaller.

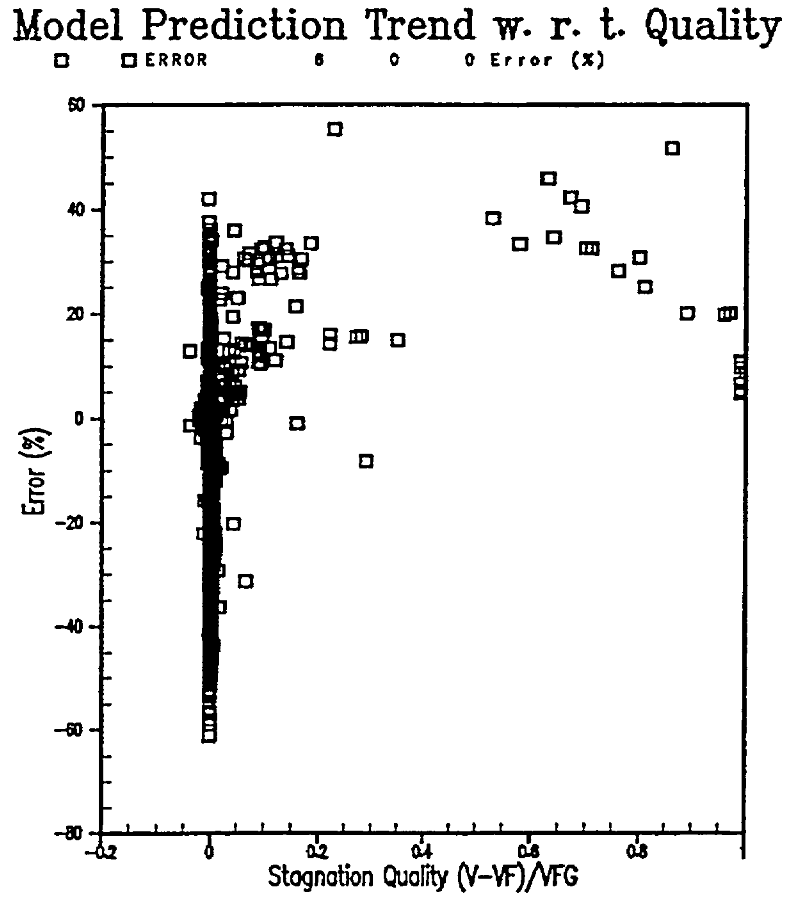

Figure 13-4-15a Prediction Trend in Quality Variation

A significant uncertainty is seen at or near the saturation. However, in the subcooled region no bias is seen whereas in the low quality two-phase region ($0 < X < 0.02$), a bias of about -20% is observed.

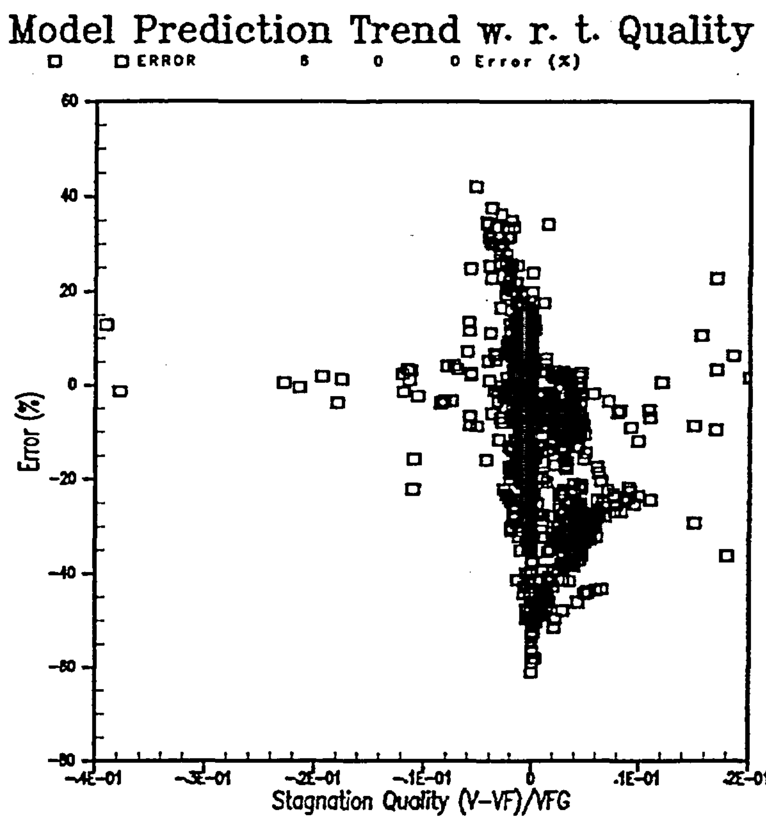

Figure 13-4-15b Prediction Trend in Quality Variation

13-4-3-4 Model Prediction Trend with Respect to Channel Length

In this section, a possible model trend with respect to the channel length is examined. Figures 13-4-16a and 13-4-16b below show the error vs. channel length of all data points. The figures do not show global trend relative to the channel length, although they do show that there is larger spread in the short length nozzle predictions.

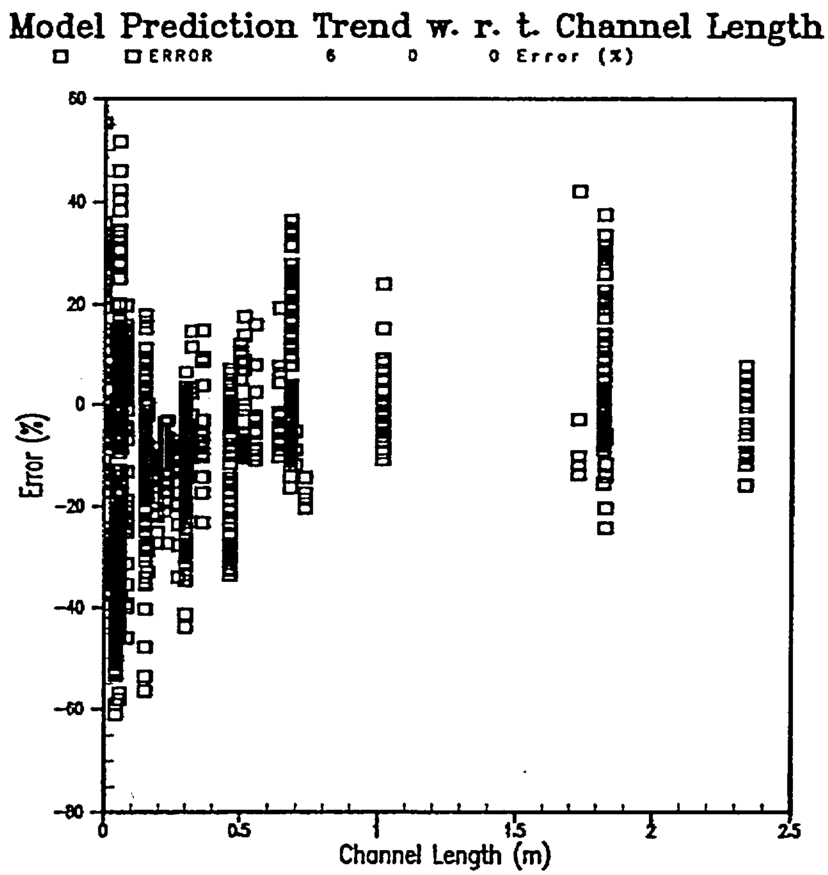

Figure 13-4-16a Prediction Trend in Channel Length Variation in Linear Scale

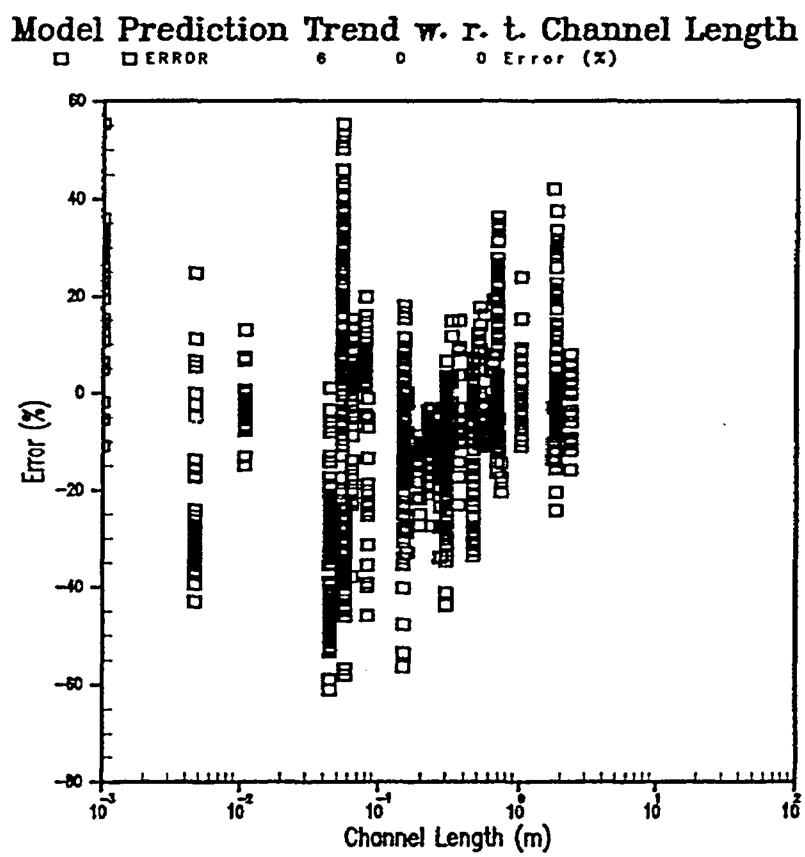

Figure 13-4-16b Prediction Trend in Channel Length Variation in Log Scale

13-4-3-5 Model Prediction Trend with Respect to Hydraulic Diameter

In this section, a possible model trend with respect to the hydraulic diameter is examined. Figure 13-4-17a below shows the error vs. hydraulic diameter of all data points. The figure does not show global trend relative to the hydraulic diameter variations.

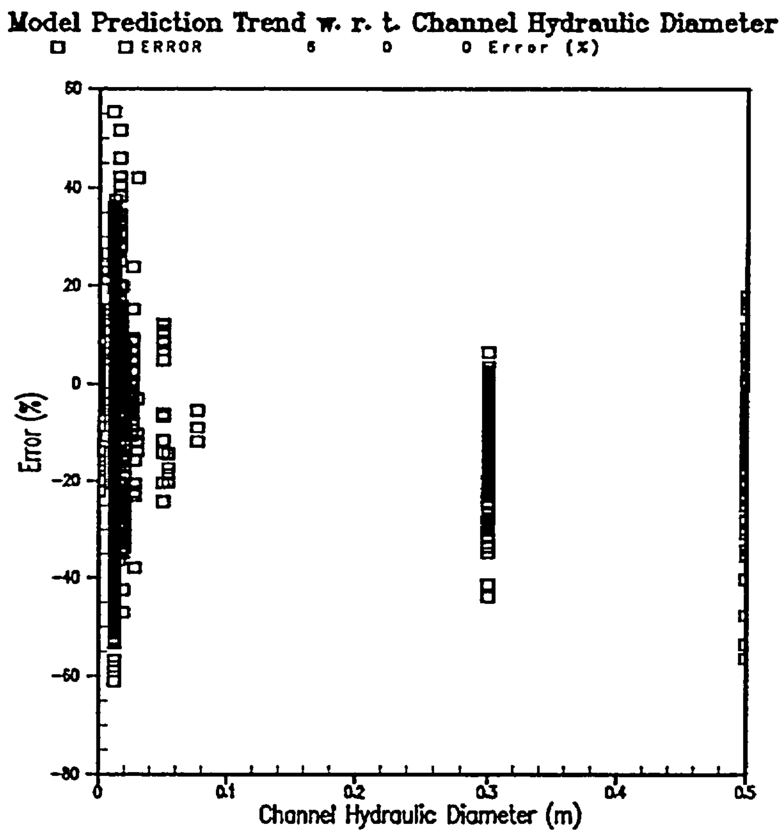

Figure 13-4-17a Prediction Trend in Channel Diameter in Linear Scale

There is a slight tendency to underpredict for large diameter nozzles, which can be seen in Figure 13-4-17b.

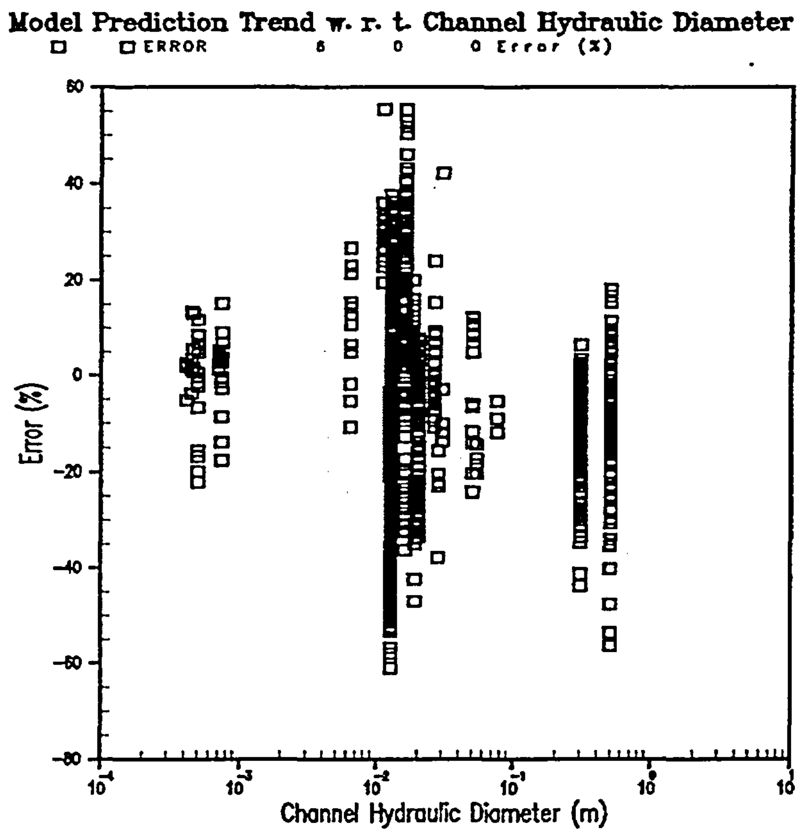

Figure 13-4-17b Prediction Trend in Channel Diameter in Log Scale

13-4-3-6 Model Prediction Trend with Respect to L/D

Figures 13-14-18a and 13-14-18b show the relative errors vs. L/D of the break path in linear and log scale. There is no global trend observed relative to L/D variations.

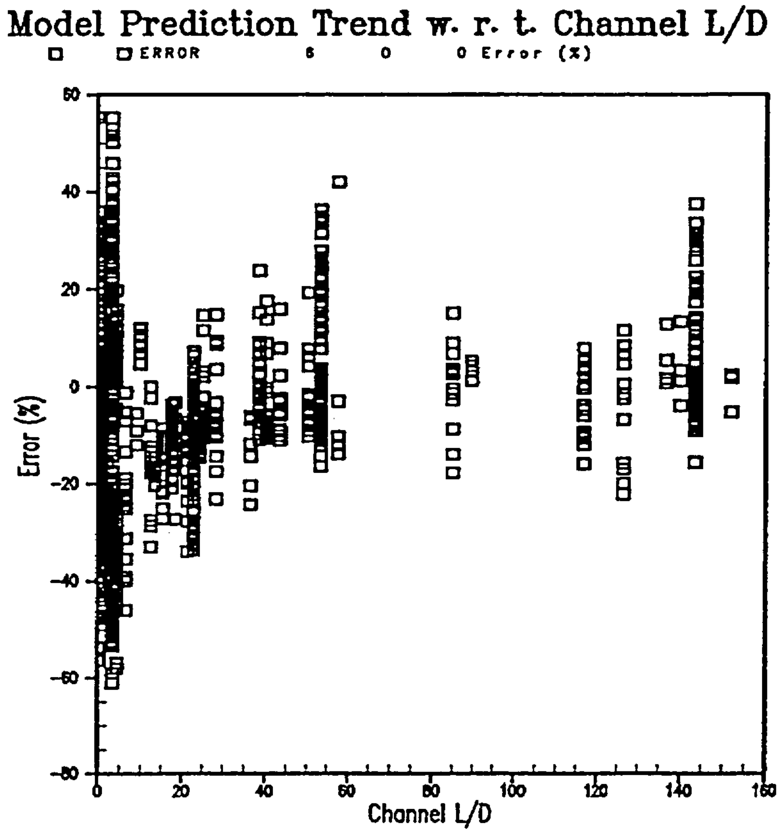

Figure 13-4-18a Prediction Trend in Channel L/D Variation - Linear Scale

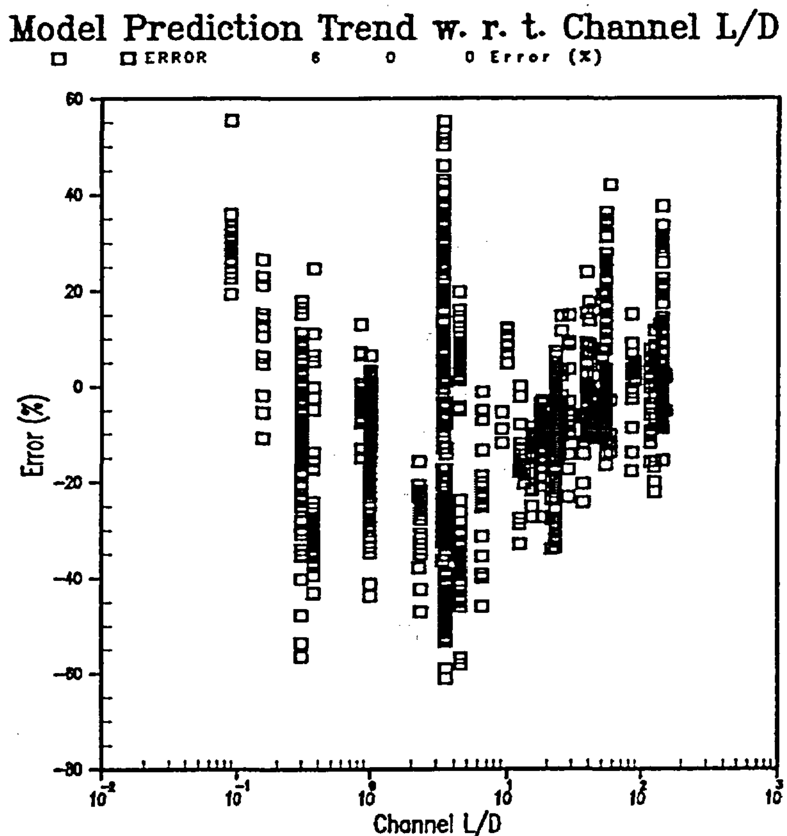

Figure 13-4-18b Prediction Trend in Channel L/D Variation - Log Scale

13-4-3-7 Influence of Upstream Void Fraction

The model prediction's sensitivity to the initial void fraction assumed in the critical flow module was investigated in this section. The minimum void fraction is set to ALMIN. The code [

]^{a,c} model prediction. The result is shown in Table 13-4-5 below.

Table 13-4-5
Prediction Sensitivity to the Initial Void Fraction

	Bias/Standard Deviation (%)		
ALMIN	Subcooled	Saturated	Total
1.0E-03	-4.6/14.9	-14.0/22.2	-8.7/19.0
1.0E-04	-4.3/14.9	-14.0/22.2	-8.5/19.0
1.0E-08	-4.0/15.0	-14.0/22.2	-8.4/19.1
1.0E-12	-4.0/15.0	-14.0/22.2	-8.3/19.1
1.0E-15	-2.8/18.7	-14.0/22.2	-7.6/21.0
0.0	-1.6/22.3	-14.0/22.2	-7.0/23.0

It is interesting to note that for subcooled regions, if [

]^{a,c} Judging from the ALMIN sensitivity results, the critical flow calculation is insensitive to the magnitude of residual void.

13-4-3-8 Influence of Two-Phase Multiplier

The current model uses Levy's model. For a sensitivity study, Richardson's model was used. The model is expressed as:

$$\Phi_{LO}^2 = \frac{1}{(1-\alpha)^{1.75}}$$

The results shown below indicated that the critical mass flow prediction was relatively insensitive to the choice of two-phase multiplier.

```
For 1427 Data Points, Average Error =          -8.59 %, STD =  19.04 %
For 807 Subcooled Data Points, Average Error =  -4.28 %, STD =  14.95 %
For 620 Saturated Data Points, Average Error = -14.20 %, STD =  22.09 %
```

13-4-3-9 Influence of Mesh Size

The model prediction's sensitivity to a number of axial nodes used in the critical flow module was investigated. The number of axial nodes, NMAX, is set [

]^{a,c} The result is shown in Table 13-4-6 below.

Table 13-4-6
Prediction Sensitivity to the Mesh Size

	Bias/Standard Deviation (%)		
NMAX	**Subcooled**	**Saturated**	**Total**
21	-3.6/15.1	-13.5/22.1	-7.9/19.1
51	-4.1/15.1	-13.8/22.2	-8.3/19.1
101	-4.3/15.0	-14.0/22.2	-8.5/19.0
401	-4.4/15.0	-14.0/22.2	-8.6/19.0
801	-4.4/14.9	-14.1/22.2	-8.6/19.0

As seen in the table, the model prediction is relatively insensitive to mesh size. [

]^{a,c}

13-4-3-10 Influence of Friction Factor/Entrance Effect

The entrance and friction factors were found to be very important for predicting the low pressure experiments such as those of Ardron and Ackerman (1978). This is the reason the reported friction factors were used for simulation of Ardron and Ackerman.

13-4-3-11 Critical Flow Predictions for Individual Dataset

The charts below show the comparison between the predicted and the measured data for individual datasets. A figure below each chart compares WCOBRA/TRACs predicted performance in relation to each data set.

Ardron and Ackerman

Run No.	Pressure (Pa)	Temperature (K)	Quality	Predicted Gc (Kg/m2-s)	Measured Gc (Kg/m2-s)	Error (Gp-Gm)/Gm (in %)	L (mm)	D (mm)
1	220500.0	391.75	-0.000005	13025.00	13300.00	-0.02	1015.0000	26.3000
2	216000.0	392.05	-0.000004	11910.00	10500.00	0.13	1015.0000	26.3000
3	207700.0	391.25	-0.000003	11207.00	10900.00	0.03	1015.0000	26.3000
4	205400.0	391.95	-0.000002	9797.90	9510.00	0.03	1015.0000	26.3000
5	203300.0	391.55	-0.000002	9869.60	9510.00	0.04	1015.0000	26.3000
6	199000.0	392.45	0.000000	7105.00	7080.00	0.00	1015.0000	26.3000
7	190000.0	391.65	0.000000	5359.10	5670.00	-0.05	1015.0000	26.3000
8	264000.0	399.85	-0.000003	10931.00	11800.00	-0.07	1015.0000	26.3000
9	255200.0	398.95	-0.000002	10492.00	10700.00	-0.02	1015.0000	26.3000
10	250000.0	398.85	-0.000001	9421.40	9300.00	0.01	1015.0000	26.3000
11	247300.0	399.65	0.000000	6719.20	6880.00	-0.02	1015.0000	26.3000
12	299000.0	405.05	-0.000001	9463.80	9980.00	-0.05	1015.0000	26.3000
13	299900.0	406.05	0.000000	7054.50	7740.00	-0.09	1015.0000	26.3000
14	203000.0	391.25	-0.000002	10220.00	9700.00	0.05	1015.0000	26.3000
15	354700.0	412.25	0.000000	5573.80	6760.00	-0.18	1015.0000	26.3000
16	206600.0	392.85	-0.000001	8684.50	9010.00	-0.04	1015.0000	26.3000
17	177000.0	385.15	-0.000004	11804.00	10800.00	0.09	1015.0000	26.3000
18	173000.0	384.35	-0.000004	11801.00	10900.00	0.08	1015.0000	26.3000
19	166000.0	383.95	-0.000003	10822.00	9160.00	0.18	1015.0000	26.3000
20	159000.0	384.75	-0.000001	8171.50	7740.00	0.06	1015.0000	26.3000
21	155400.0	385.05	0.000000	6480.50	6510.00	0.00	1015.0000	26.3000
22	154000.0	384.75	0.000000	6511.20	5900.00	0.10	1015.0000	26.3000
23	190200.0	384.55	-0.000007	14478.00	13800.00	0.05	1015.0000	26.3000
24	190600.0	384.85	-0.000007	14317.00	13600.00	0.05	1015.0000	26.3000
25	215100.0	391.75	-0.000004	12087.00	11600.00	0.04	1015.0000	26.3000
26	254400.0	399.55	-0.000001	9234.50	9610.00	-0.04	1015.0000	26.3000
27	306000.0	406.25	0.000000	8504.40	9630.00	-0.12	1015.0000	26.3000
28	365200.0	413.15	0.000000	6195.70	7730.00	-0.20	1015.0000	26.3000
29	360400.0	412.75	0.000000	5896.20	7790.00	-0.24	1015.0000	26.3000
30	191900.0	385.05	-0.000007	14363.00	13900.00	0.03	1015.0000	26.3000
31	220300.0	392.75	-0.000004	11898.00	11800.00	0.01	1015.0000	26.3000
32	366600.0	411.45	-0.000003	11530.00	7730.00	0.49	1015.0000	26.3000

For 32 Data Points, Average Error = 1.09 %, STD = 12.68 %
For 26 Subcooled Data Points, Average Error = 4.35 %, STD = 11.18 %
For 6 Saturated Data Points, Average Error = -13.06 %, STD = 8.75 %
Minimum quality is 0.0000, Maximum quality is 0.0000

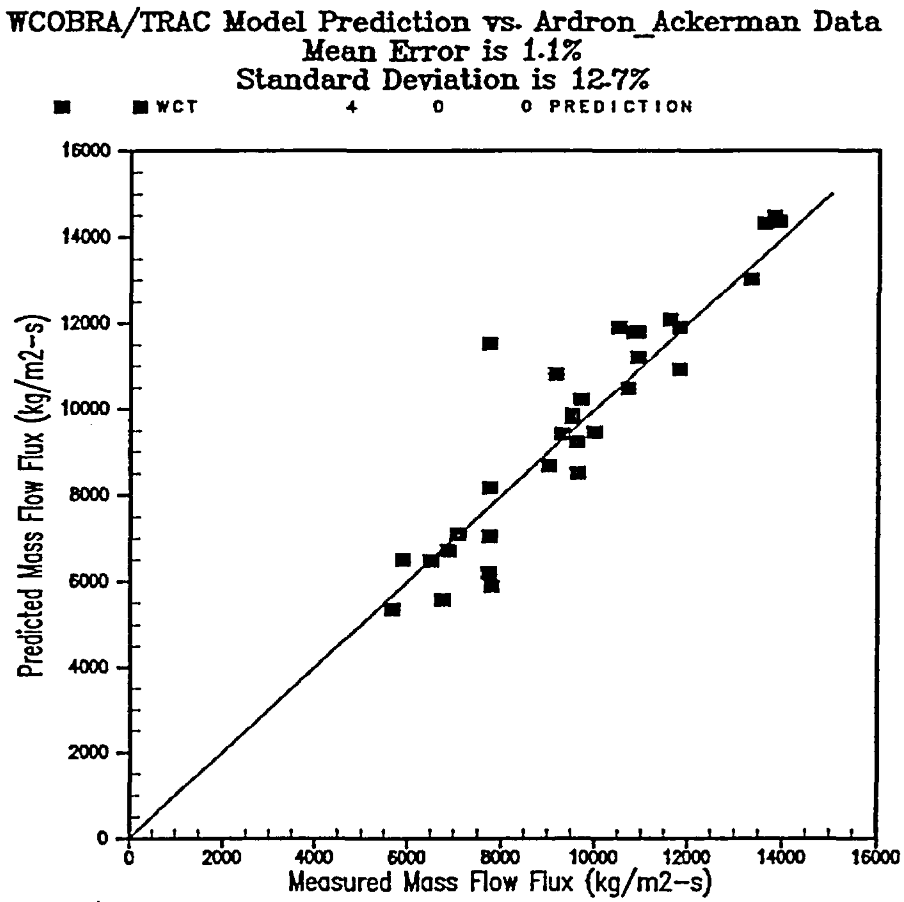

Figure 13-4-19 Prediction Comparison with Ardron-Ackerman Data

Boivin

Run No.	Pressure (Pa)	Temperature (K)	Quality	Predicted Gc (Kg/m2-s)	Measured Gc (Kg/m2-s)	Error (Gp-Gm)/Gm (in %)	L (mm)	D (mm)
1	2300000.0	489.15	-0.000063	17738.00	16900.00	4.96	500.0000	50.0000
2	1960000.0	477.95	-0.000099	21103.00	19500.00	8.22	500.0000	50.0000
3	6140000.0	544.45	-0.000629	30785.00	28800.00	6.89	500.0000	50.0000
4	3610000.0	507.35	-0.000351	32061.00	28600.00	12.10	500.0000	50.0000
5	7170000.0	555.05	-0.000865	31850.00	30300.00	5.12	500.0000	50.0000
6	4050000.0	512.05	-0.000525	36140.00	32600.00	10.86	500.0000	50.0000
7	5140000.0	529.25	-0.000644	35535.00	32700.00	8.67	500.0000	50.0000
8	7220000.0	552.55	-0.001313	37864.00	34200.00	10.71	500.0000	50.0000
9	3840000.0	505.95	-0.000566	38831.00	34700.00	11.90	500.0000	50.0000
10	3580000.0	500.85	-0.000550	38919.00	34700.00	12.16	500.0000	50.0000
11	6110000.0	546.15	-0.000414	23411.00	26600.00	-11.99	1730.0000	30.0000
12	10100000.0	567.15	-0.005431	49852.00	35100.00	42.03	1730.0000	30.0000
13	5400000.0	538.85	-0.000254	21124.00	24500.00	-13.78	1730.0000	30.0000
14	9320000.0	577.15	-0.000536	27822.00	31000.00	-10.25	1730.0000	30.0000
15	6280000.0	541.65	-0.001104	33478.00	34500.00	-2.96	1730.0000	30.0000
16	3740000.0	504.15	-0.000556	35526.00	37800.00	-6.02	1830.0000	50.0000
17	9040000.0	564.15	-0.003129	44200.00	50000.00	-11.60	1830.0000	50.0000
18	6730000.0	538.65	-0.002114	46664.00	50000.00	-6.67	1830.0000	50.0000
19	8460000.0	567.15	-0.001118	30307.00	38000.00	-20.24	1830.0000	50.0000
20	3240000.0	503.15	-0.000245	25573.00	29800.00	-14.18	1830.0000	50.0000
21	3050000.0	504.15	-0.000101	18061.00	23800.00	-24.11	1830.0000	50.0000

For 21 Data Points, Average Error = 0.56 %, STD = 15.04 %
For 21 Subcooled Data Points, Average Error = 0.56 %, STD = 15.04 %

WCOBRA/TRAC Model Prediction vs. Boivin Data
Mean Error is .56%
Standard Deviation is 15%

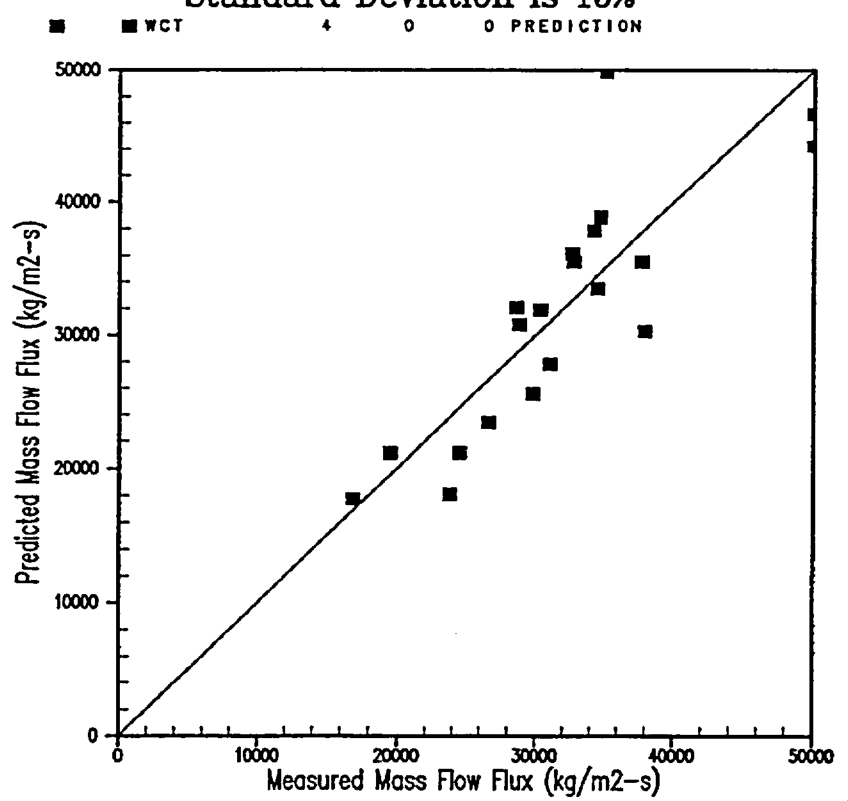

Figure 13-4-20 Prediction Comparison with Boivin Data

Fincke and Collins

Run No.	Pressure (Pa)	Temperature (K)	Quality	Predicted Gc (Kg/m2-s)	Measured Gc (Kg/m2-s)	Error (Gp-Gm)/Gm (in %)	L (mm)	D (mm)
1	99020.0	342.21	-0.000012	11908.00	9936.70	19.84	79.7200	18.2800
2	100510.0	342.68	-0.000012	11973.00	11038.00	8.47	79.7200	18.2800
3	134970.0	343.05	-0.000021	14400.00	13516.00	6.54	79.7200	18.2800
4	108150.0	343.37	-0.000014	12505.00	13072.00	-4.34	79.7200	18.2800
5	173570.0	344.47	-0.000033	16633.00	15572.00	6.81	79.7200	18.2800
6	173960.0	344.66	-0.000033	16621.00	15581.00	6.67	79.7200	18.2800
7	174080.0	344.74	-0.000033	16626.00	15564.00	6.82	79.7200	18.2800
8	174830.0	345.20	-0.000033	16658.00	15570.00	6.99	79.7200	18.2800
9	174830.0	345.55	-0.000033	16626.00	15579.00	6.72	79.7200	18.2800
10	217810.0	348.89	-0.000046	18654.00	18063.00	3.27	79.7200	18.2800
11	219620.0	348.77	-0.000047	18733.00	18176.00	3.06	79.7200	18.2800
12	220400.0	348.82	-0.000047	18798.00	18173.00	3.44	79.7200	18.2800
13	221900.0	348.88	-0.000048	18861.00	18230.00	3.46	79.7200	18.2800
14	223110.0	348.89	-0.000048	18913.00	18287.00	3.42	79.7200	18.2800
15	277580.0	349.00	-0.000071	21424.00	20647.00	3.76	79.7200	18.2800
16	269220.0	349.01	-0.000067	21062.00	20414.00	3.17	79.7200	18.2800
17	269100.0	349.01	-0.000067	21057.00	20394.00	3.25	79.7200	18.2800
18	270270.0	348.90	-0.000068	21104.00	20460.00	3.15	79.7200	18.2800
19	270460.0	349.01	-0.000068	21111.00	20430.00	3.33	79.7200	18.2800
20	94950.0	359.05	-0.000005	9145.50	8139.80	12.36	79.7200	18.2800
21	104030.0	358.69	-0.000007	10108.00	9541.80	5.93	79.7200	18.2800
22	131530.0	358.33	-0.000013	12447.00	12013.00	3.61	79.7200	18.2800
23	185940.0	358.10	-0.000028	16057.00	15443.00	3.98	79.7200	18.2800
24	187470.0	358.09	-0.000029	16124.00	15572.00	3.54	79.7200	18.2800
25	188010.0	357.90	-0.000029	16178.00	15592.00	3.76	79.7200	18.2800
26	187750.0	357.86	-0.000029	16167.00	15592.00	3.69	79.7200	18.2800
27	188040.0	357.74	-0.000029	16210.00	15667.00	3.47	79.7200	18.2800
28	242600.0	358.57	-0.000047	19007.00	18311.00	3.80	79.7200	18.2800
29	234200.0	358.46	-0.000044	18610.00	17907.00	3.93	79.7200	18.2800
30	234320.0	358.45	-0.000044	18615.00	17871.00	4.16	79.7200	18.2800
31	233270.0	358.51	-0.000044	18540.00	17833.00	3.96	79.7200	18.2800
32	232190.0	358.46	-0.000044	18498.00	17760.00	4.16	79.7200	18.2800
33	287670.0	358.45	-0.000065	21104.00	20339.00	3.76	79.7200	18.2800
34	287770.0	358.46	-0.000065	21107.00	20266.00	4.15	79.7200	18.2800
35	286350.0	358.48	-0.000065	21055.00	20155.00	4.47	79.7200	18.2800
36	287550.0	358.50	-0.000065	21099.00	20228.00	4.31	79.7200	18.2800
37	289320.0	358.57	-0.000066	21163.00	20301.00	4.25	79.7200	18.2800
38	91150.0	363.83	-0.000003	7501.80	6460.70	16.11	79.7200	18.2800
39	106030.0	363.50	-0.000005	9242.10	8775.40	5.32	79.7200	18.2800
40	194810.0	363.47	-0.000027	15843.00	15348.00	3.23	79.7200	18.2800
41	192230.0	363.35	-0.000026	15710.00	15356.00	2.31	79.7200	18.2800
42	194580.0	363.24	-0.000027	15866.00	15256.00	4.00	79.7200	18.2800
43	193190.0	363.11	-0.000027	15811.00	15213.00	3.93	79.7200	18.2800
44	192570.0	363.12	-0.000027	15756.00	15204.00	3.63	79.7200	18.2800
45	243920.0	363.11	-0.000043	18569.00	17942.00	3.49	79.7200	18.2800
46	244530.0	363.00	-0.000044	18594.00	17959.00	3.54	79.7200	18.2800
47	216830.0	362.88	-0.000034	17163.00	18052.00	-4.92	79.7200	18.2800
48	247730.0	362.87	-0.000045	18784.00	18074.00	3.93	79.7200	18.2800
49	248730.0	362.88	-0.000045	18822.00	18146.00	3.73	79.7200	18.2800
50	248690.0	362.87	-0.000045	18820.00	18146.00	3.71	79.7200	18.2800
51	294400.0	362.99	-0.000063	20956.00	20165.00	3.92	79.7200	18.2800
52	293350.0	362.90	-0.000063	20920.00	20130.00	3.92	79.7200	18.2800
53	292830.0	362.87	-0.000062	20902.00	20130.00	3.84	79.7200	18.2800
54	293000.0	362.87	-0.000062	20908.00	20057.00	4.24	79.7200	18.2800
55	294860.0	362.88	-0.000063	20974.00	20203.00	3.82	79.7200	18.2800
56	96420.0	348.90	-0.000009	10970.00	9936.00	10.41	79.7200	18.2800
57	98620.0	349.01	-0.000010	11157.00	10269.00	8.65	79.7200	18.2800
58	98770.0	348.89	-0.000010	11188.00	10752.00	4.06	79.7200	18.2800
59	101450.0	348.77	-0.000010	11426.00	11197.00	2.05	79.7200	18.2800
60	101940.0	348.72	-0.000011	11454.00	10753.00	6.52	79.7200	18.2800
61	112130.0	348.54	-0.000013	12288.00	11459.00	7.23	79.7200	18.2800
62	112140.0	348.42	-0.000013	12312.00	11904.00	3.43	79.7200	18.2800
63	112430.0	348.30	-0.000013	12328.00	12165.00	1.34	79.7200	18.2800
64	121160.0	348.06	-0.000015	13013.00	12389.00	5.04	79.7200	18.2800
65	121160.0	348.75	-0.000015	12937.00	12162.00	6.37	79.7200	18.2800
66	131130.0	348.66	-0.000018	13657.00	12681.00	7.70	79.7200	18.2800
67	141630.0	348.54	-0.000021	14374.00	13350.00	7.67	79.7200	18.2800
68	151540.0	349.01	-0.000024	14944.00	13902.00	7.50	79.7200	18.2800
69	162580.0	349.01	-0.000027	15617.00	14569.00	7.19	79.7200	18.2800
70	173260.0	348.90	-0.000030	16265.00	15238.00	6.74	79.7200	18.2800
71	204430.0	348.90	-0.000041	17978.00	17351.00	3.61	79.7200	18.2800
72	185490.0	348.79	-0.000035	16949.00	15980.00	6.06	79.7200	18.2800
73	93730.0	358.57	-0.000005	9130.60	7954.60	14.78	79.7200	18.2800
74	98900.0	358.69	-0.000006	9611.80	8815.60	9.03	79.7200	18.2800
75	109890.0	358.58	-0.000008	10647.00	9991.60	6.56	79.7200	18.2800
76	118730.0	358.56	-0.000010	11405.00	10827.00	5.34	79.7200	18.2800
77	131330.0	357.86	-0.000013	12490.00	11988.00	4.19	79.7200	18.2800
78	140650.0	358.45	-0.000015	13098.00	12115.00	8.11	79.7200	18.2800
79	132360.0	358.33	-0.000013	12511.00	11523.00	8.57	79.7200	18.2800
80	120370.0	358.33	-0.000011	11579.00	10617.00	9.06	79.7200	18.2800
81	107770.0	358.34	-0.000008	10512.00	9525.20	10.36	79.7200	18.2800
82	99560.0	358.81	-0.000006	9653.70	8656.90	11.51	79.7200	18.2800
83	144700.0	358.94	-0.000016	13307.00	12360.00	7.66	79.7200	18.2800
84	158190.0	358.93	-0.000020	14210.00	13302.00	6.83	79.7200	18.2800
85	159770.0	358.81	-0.000020	14336.00	13483.00	6.33	79.7200	18.2800
86	170500.0	358.81	-0.000023	15033.00	14309.00	5.06	79.7200	18.2800
87	186890.0	358.69	-0.000028	16034.00	15354.00	4.43	79.7200	18.2800
88	198590.0	358.70	-0.000032	16680.00	16028.00	4.07	79.7200	18.2800

89	213390.0	358.69	-0.000037	17510.00	16836.00	4.00	79.7200	18.2800
90	224860.0	358.57	-0.000041	18105.00	17381.00	4.17	79.7200	18.2800
91	241190.0	358.59	-0.000047	18952.00	18219.00	4.02	79.7200	18.2800
92	256940.0	358.70	-0.000053	19698.00	18938.00	4.01	79.7200	18.2800

For 92 Data Points, Average Error = 5.33 %, STD = 3.37 %
For 92 Subcooled Data Points, Average Error = 5.33 %, STD = 3.37 %

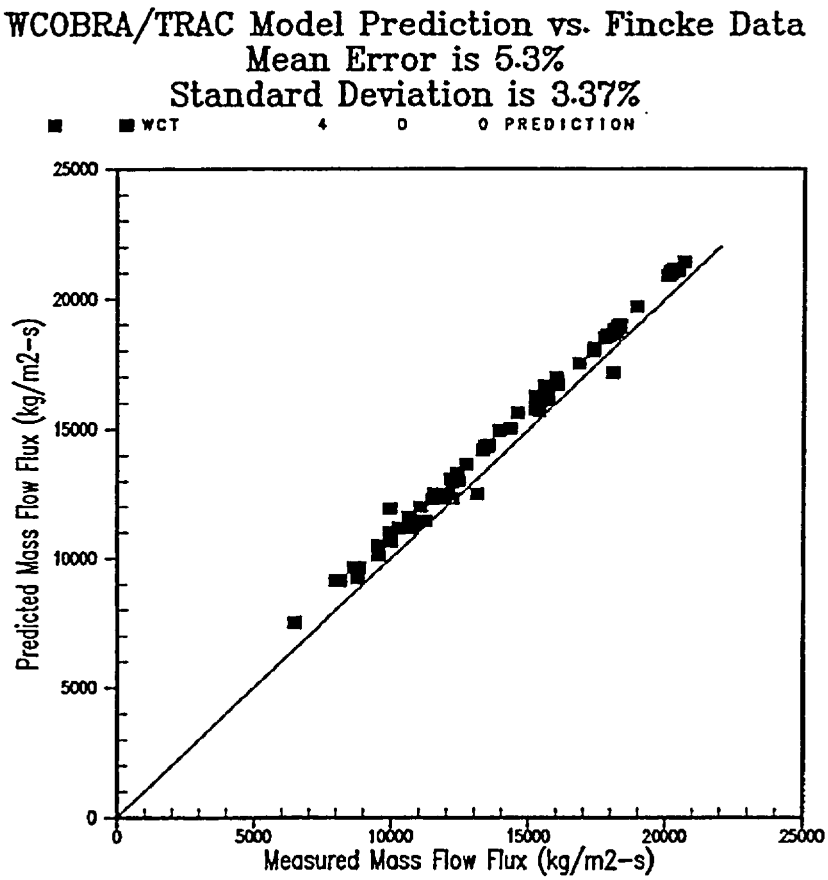

Figure 13-4-21 Prediction Comparison with Fincke Data

Jeandey

Run No.	Pressure (Pa)	Temperature (K)	Quality	Predicted Gc (Kg/m2-s)	Measured Gc (Kg/m2-s)	Error (Gp-Gm)/Gm (in %)	L (mm)	D (mm)
1	899000.0	408.15	-0.000233	30458.00	29200.00	4.31	463.0000	20.1300
2	1000000.0	433.15	-0.000136	24666.00	23500.00	4.96	463.0000	20.1300
3	1996000.0	438.15	-0.000715	44856.00	43300.00	3.59	463.0000	20.1300
4	2001000.0	473.15	-0.000199	26780.00	25500.00	5.02	463.0000	20.1300
5	4202000.0	486.35	-0.001658	57104.00	54900.00	4.01	463.0000	20.1300
6	4209000.0	518.35	-0.000400	30014.00	29400.00	2.09	463.0000	20.1300
7	6015000.0	525.15	-0.002002	53040.00	49900.00	6.29	463.0000	20.1300
8	6005000.0	542.55	-0.000640	30549.00	33300.00	-8.26	463.0000	20.1300
9	7999000.0	548.75	-0.003434	53684.00	50500.00	6.30	463.0000	20.1300
10	8006000.0	563.15	-0.001013	30998.00	37200.00	-16.67	463.0000	20.1300
11	10001000.0	563.15	-0.006150	59477.00	55500.00	7.17	463.0000	20.1300
12	9989000.0	579.15	-0.001601	33754.00	40700.00	-17.07	463.0000	20.1300
13	12001000.0	580.35	-0.007971	57579.00	55300.00	4.12	463.0000	20.1300
14	12010000.0	593.55	-0.002128	36432.00	44100.00	-17.39	463.0000	20.1300
15	13995000.0	597.55	-0.008258	50977.00	52700.00	-3.27	463.0000	20.1300
16	2003000.0	421.65	-0.000931	49142.00	48800.00	0.70	463.0000	20.1300
17	2000000.0	424.25	-0.000896	48514.00	48200.00	0.65	463.0000	20.1300
18	2001000.0	438.65	-0.000712	44796.00	44800.00	-0.01	463.0000	20.1300
19	2004000.0	440.25	-0.000693	44345.00	44100.00	0.56	463.0000	20.1300
20	2004000.0	450.75	-0.000545	40445.00	40400.00	0.11	463.0000	20.1300
21	2003000.0	460.25	-0.000403	35875.00	36100.00	-0.62	463.0000	20.1300
22	2006000.0	466.25	-0.000312	32266.00	32700.00	-1.33	463.0000	20.1300
23	2009000.0	471.65	-0.000227	28298.00	29000.00	-2.42	463.0000	20.1300
24	2008000.0	475.55	-0.000163	24701.00	25400.00	-2.75	463.0000	20.1300
25	2008000.0	477.55	-0.000130	22516.00	23400.00	-3.78	463.0000	20.1300
26	2004000.0	479.35	-0.000097	20180.00	21600.00	-6.57	463.0000	20.1300
27	2005000.0	481.65	-0.000059	16903.00	18800.00	-10.09	463.0000	20.1300
28	1997000.0	483.25	-0.000028	13753.00	17300.00	-20.50	463.0000	20.1300
29	2003000.0	484.55	-0.000008	11614.00	16200.00	-28.31	463.0000	20.1300
30	2003000.0	485.45	0.000001	10298.00	14500.00	-28.98	463.0000	20.1300
31	6004000.0	521.55	-0.002279	56069.00	55900.00	0.30	463.0000	20.1300
32	6005000.0	525.05	-0.001995	52987.00	52900.00	0.16	463.0000	20.1300
33	6001000.0	528.25	-0.001788	49866.00	50000.00	-0.27	463.0000	20.1300
34	6009000.0	530.95	-0.001615	47105.00	47500.00	-0.83	463.0000	20.1300
35	6009000.0	534.55	-0.001344	42863.00	43800.00	-2.14	463.0000	20.1300
36	5994000.0	537.85	-0.001052	38125.00	39700.00	-3.97	463.0000	20.1300
37	5999000.0	539.95	-0.000874	34979.00	37500.00	-6.72	463.0000	20.1300
38	6006000.0	542.95	-0.000603	29797.00	35100.00	-15.11	463.0000	20.1300
39	5998000.0	545.95	-0.000293	23865.00	33000.00	-27.68	463.0000	20.1300
40	6001000.0	548.65	-0.000011	21502.00	31000.00	-30.64	463.0000	20.1300
41	11999000.0	579.05	-0.008492	59503.00	62000.00	-4.03	463.0000	20.1300
42	12008000.0	581.15	-0.007670	56537.00	58400.00	-3.19	463.0000	20.1300
43	12003000.0	585.35	-0.005863	49573.00	54200.00	-8.54	463.0000	20.1300
44	12003000.0	588.75	-0.004347	43190.00	51300.00	-15.81	463.0000	20.1300
45	12000000.0	592.85	-0.002428	37004.00	48200.00	-23.23	463.0000	20.1300
46	12006000.0	597.75	-0.000050	33195.00	44500.00	-25.40	463.0000	20.1300
47	4820000.0	507.15	-0.001476	52050.00	52100.00	-0.10	463.0000	20.1300
48	4539000.0	507.15	-0.001174	48047.00	48200.00	-0.32	463.0000	20.1300
49	4292000.0	507.15	-0.000936	44210.00	44500.00	-0.65	463.0000	20.1300
50	4011000.0	507.15	-0.000680	39393.00	40100.00	-1.76	463.0000	20.1300
51	3850000.0	507.15	-0.000529	36280.00	37200.00	-2.47	463.0000	20.1300
52	3666000.0	507.15	-0.000397	32430.00	33500.00	-3.19	463.0000	20.1300
53	3460000.0	507.15	-0.000258	27447.00	29100.00	-5.68	463.0000	20.1300
54	3326000.0	507.15	-0.000174	23692.00	26300.00	-9.92	463.0000	20.1300
55	3246000.0	507.25	-0.000122	20949.00	24500.00	-14.49	463.0000	20.1300
56	3108000.0	507.15	-0.000046	16106.00	22200.00	-27.45	463.0000	20.1300
57	3070000.0	507.15	-0.000025	14777.00	21500.00	-31.27	463.0000	20.1300
58	3024000.0	507.25	0.000002	13568.00	20400.00	-33.49	463.0000	20.1300
59	6255000.0	525.15	-0.002379	56117.00	56000.00	0.21	463.0000	20.1300
60	5812000.0	525.15	-0.001707	50280.00	50100.00	0.36	463.0000	20.1300
61	5385000.0	525.15	-0.001151	43891.00	44300.00	-0.92	463.0000	20.1300
62	5087000.0	525.25	-0.000810	38756.00	39400.00	-1.63	463.0000	20.1300
63	4778000.0	525.15	-0.000509	32822.00	34300.00	-4.31	463.0000	20.1300
64	4594000.0	525.15	-0.000348	28594.00	31500.00	-9.23	463.0000	20.1300
65	4448000.0	525.15	-0.000230	24753.00	29300.00	-15.52	463.0000	20.1300
66	4334000.0	525.25	-0.000140	21239.00	27700.00	-23.32	463.0000	20.1300
67	4235000.0	525.15	-0.000075	18618.00	26400.00	-29.48	463.0000	20.1300
68	4151000.0	525.15	-0.000019	17098.00	25400.00	-32.69	463.0000	20.1300
69	8385000.0	553.25	-0.003631	52996.00	53600.00	-1.13	463.0000	20.1300
70	7885000.0	553.15	-0.002511	46380.00	47600.00	-2.56	463.0000	20.1300
71	7570000.0	553.15	-0.001871	41617.00	43400.00	-4.11	463.0000	20.1300
72	7357000.0	553.15	-0.001471	38052.00	40800.00	-6.74	463.0000	20.1300
73	7158000.0	553.25	-0.001106	34189.00	38700.00	-11.66	463.0000	20.1300
74	6732000.0	553.15	-0.000442	25883.00	34900.00	-25.84	463.0000	20.1300
75	6515000.0	553.15	-0.000134	23336.00	33100.00	-29.50	463.0000	20.1300
76	6429000.0	553.15	-0.000019	22536.00	31900.00	-29.35	463.0000	20.1300
77	2008000.0	465.45	-0.000326	32833.00	33300.00	-1.40	463.0000	20.1300
78	2005000.0	477.35	-0.000132	22675.00	23500.00	-3.51	463.0000	20.1300
79	2006000.0	484.95	-0.000003	11093.00	15300.00	-27.50	463.0000	20.1300
80	4003000.0	500.65	-0.000918	45012.00	45200.00	-0.42	463.0000	20.1300
81	4002000.0	513.65	-0.000418	31802.00	32800.00	-3.04	463.0000	20.1300
82	4003000.0	522.55	-0.000045	17100.00	25200.00	-32.14	463.0000	20.1300
83	8000000.0	549.65	-0.003302	52608.00	53400.00	-1.48	463.0000	20.1300
84	7995000.0	559.75	-0.001623	37469.00	42400.00	-11.63	463.0000	20.1300
85	8000000.0	567.75	-0.000091	26131.00	36700.00	-28.80	463.0000	20.1300
86	12006000.0	578.85	-0.008602	59878.00	62200.00	-3.73	463.0000	20.1300
87	11995000.0	592.35	-0.002648	37497.00	48200.00	-22.21	463.0000	20.1300
88	11992000.0	597.75	-0.000006	33142.00	40900.00	-18.97	463.0000	20.1300

For 88 Data Points, Average Error = -9.07 %, STD = 11.76 %
For 86 Subcooled Data Points, Average Error = -8.56 %, STD = 11.38 %
For 2 Saturated Data Points, Average Error = -31.23 %, STD = 3.19 %

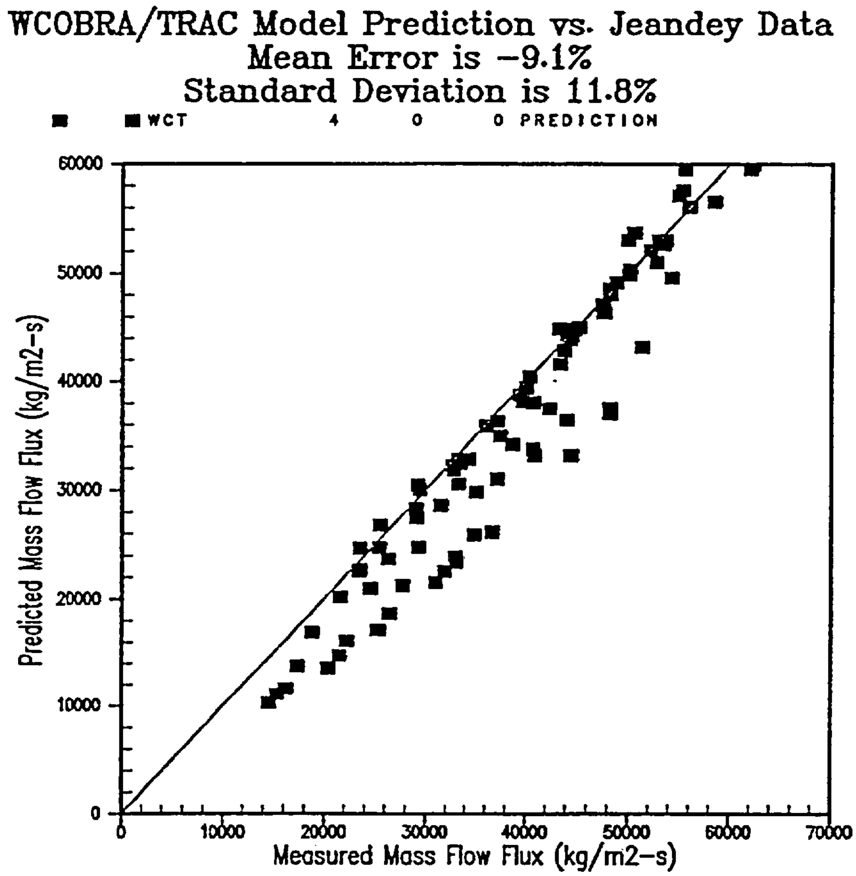

Figure 13-4-22 Prediction Comparison with Jeandey Data

Neusen

Run No.	Pressure (Pa)	Temperature (K)	Quality	Predicted Gc (Kg/m2-s)	Measured Gc (Kg/m2-s)	Error (Gp-Gm)/Gm (in %)	L (mm)	D (mm)
1	2654500.0	499.93	0.094000	12069.00	10265.00	17.57	1.0000	11.1250
2	2813000.0	503.12	0.108000	12304.00	10406.00	18.24	1.0000	11.1250
3	2875100.0	504.33	0.110000	12451.00	10546.00	18.06	1.0000	11.1250
4	2930200.0	505.39	0.121000	12420.00	10124.00	22.68	1.0000	11.1250
5	1744400.0	478.06	0.041700	9817.10	10617.00	-7.53	1.0000	11.1250
6	2606200.0	498.93	0.086400	12050.00	10617.00	13.50	1.0000	11.1250
7	2861300.0	504.06	0.100000	12586.00	10617.00	18.55	1.0000	11.1250
8	3461100.0	514.85	0.167000	13106.00	10617.00	23.44	1.0000	11.1250
9	1406500.0	467.61	0.021300	8713.40	10607.00	-17.85	1.0000	11.1250
10	2316600.0	492.61	0.063000	11514.00	10607.00	8.55	1.0000	11.1250
11	3261200.0	511.43	0.138000	13055.00	10617.00	22.96	1.0000	11.1250
12	1199700.0	460.21	0.043700	7669.10	6939.40	10.52	1.0000	11.1250
13	1516800.0	471.22	0.085100	8424.80	7030.80	19.83	1.0000	11.1250
14	2020100.0	485.47	0.142000	9314.10	7241.70	28.62	1.0000	11.1250
15	2282100.0	491.82	0.184000	9477.00	7171.40	32.15	1.0000	11.1250
16	841150.0	444.61	0.020400	6205.80	7171.40	-13.46	1.0000	11.1250
17	1489300.0	470.34	0.017000	9106.70	11741.00	-22.44	1.0000	11.1250
18	1096300.0	456.13	0.111000	6460.70	4865.30	32.79	1.0000	11.1250
19	1310000.0	464.27	0.161000	6607.50	4788.00	38.00	1.0000	11.1250
20	1572000.0	472.95	0.228000	6616.50	4009.10	65.04	1.0000	11.1250
21	2254600.0	491.18	0.041700	11648.00	11882.00	-1.97	1.0000	11.1250
22	2840600.0	503.66	0.070800	13050.00	11882.00	9.83	1.0000	11.1250
23	3550800.0	516.34	0.122000	14189.00	11812.00	20.12	1.0000	11.1250
24	3840300.0	520.94	0.163000	14199.00	11741.00	20.94	1.0000	11.1250
25	917000.0	448.29	0.072400	6191.60	4795.00	29.13	1.0000	11.1250
26	1599600.0	473.79	0.024600	9467.00	11952.00	-20.79	1.0000	6.4010
27	2330400.0	492.93	0.050300	11764.00	12023.00	-2.15	1.0000	6.4010
28	2985400.0	506.43	0.089800	13145.00	11812.00	11.29	1.0000	6.4010
29	3557700.0	516.45	0.157000	13543.00	11812.00	14.65	1.0000	6.4010
30	2109800.0	487.71	0.010900	19363.00	20460.00	-5.36	1.0000	6.4010
31	3240500.0	511.07	0.015600	22874.00	20671.00	10.66	1.0000	6.4010
32	4274700.0	527.37	0.034700	18359.00	20530.00	-10.57	1.0000	6.4010
33	5205500.0	539.59	0.058300	20323.00	20530.00	-1.01	1.0000	6.4010
34	2447600.0	495.55	0.002800	24324.00	27280.00	-10.84	1.0000	6.4010
35	3495600.0	515.43	0.005700	26635.00	27139.00	-1.86	1.0000	6.4010
36	5536400.0	543.53	0.018500	28625.00	26928.00	6.30	1.0000	6.4010
37	6515500.0	554.19	0.034200	28466.00	27139.00	4.89	1.0000	6.4010

For 37 Data Points, Average Error = 10.88 %, STD = 18.22 %
For 37 Saturated Data Points, Average Error = 10.88 %, STD = 18.22 %

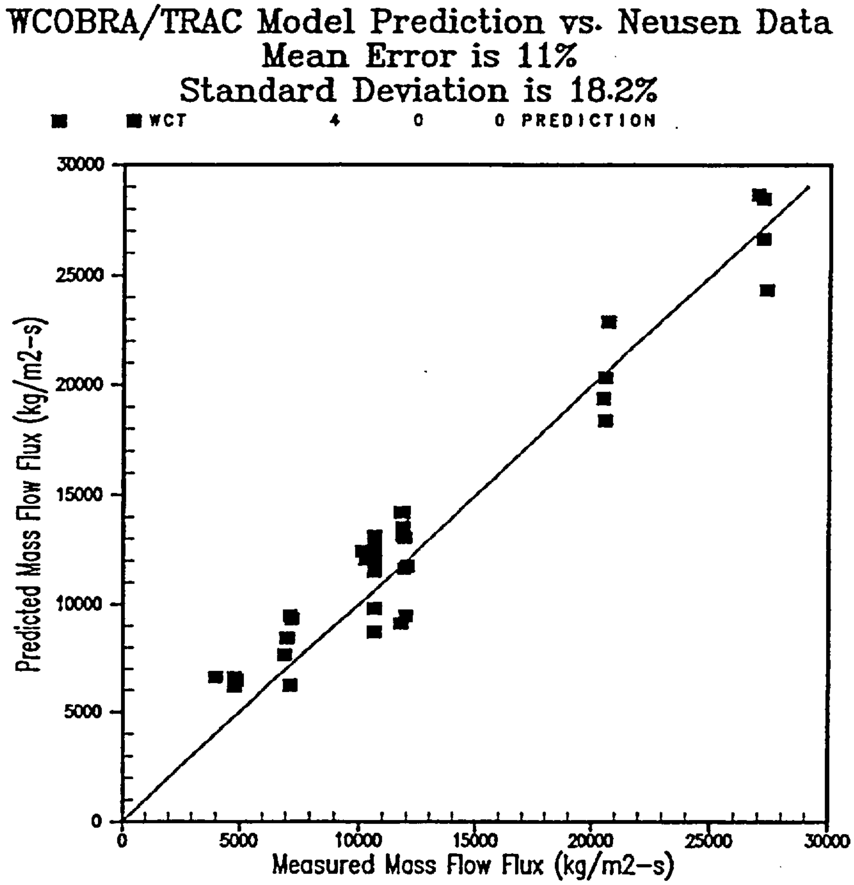

Figure 13-4-23 Prediction Comparison with Neusen Data

Reocreux

Run No.	Pressure (Pa)	Temperature (K)	Quality	Predicted Gc (Kg/m2-s)	Measured Gc (Kg/m2-s)	Error (Gp-Gm)/Gm (in %)	L (mm)	D (mm)
1	246500.0	389.86	-0.000013	6637.10	6526.00	1.70	2335.0000	20.0000
2	246700.0	389.75	-0.000013	6705.80	6465.00	3.72	2335.0000	20.0000
3	246100.0	389.82	-0.000013	6631.90	6495.50	2.10	2335.0000	20.0000
4	212300.0	389.87	-0.000005	4049.70	4192.50	-3.41	2335.0000	20.0000
5	211800.0	389.87	-0.000005	4007.00	4164.90	-3.79	2335.0000	20.0000
6	274100.0	389.43	-0.000021	8313.60	8708.90	-4.54	2335.0000	20.0000
7	289600.0	389.44	-0.000025	9078.20	8717.80	4.13	2335.0000	20.0000
8	253900.0	389.22	-0.000016	7312.80	8681.60	-15.77	2335.0000	20.0000
9	324100.0	387.02	-0.000039	11093.00	10291.00	7.79	2335.0000	20.0000
10	330400.0	389.09	-0.000038	10915.00	10309.00	5.88	2335.0000	20.0000
11	329700.0	389.07	-0.000038	10885.00	10311.00	5.57	2335.0000	20.0000
12	329900.0	389.20	-0.000037	10868.00	10324.00	5.27	2335.0000	20.0000
13	273200.0	394.47	-0.000013	6548.10	6518.60	0.45	2335.0000	20.0000
14	273200.0	394.14	-0.000013	6687.30	6558.90	1.96	2335.0000	20.0000
15	272700.0	394.23	-0.000013	6612.10	6499.20	1.74	2335.0000	20.0000
16	243300.0	395.05	-0.000005	3960.30	4382.70	-9.64	2335.0000	20.0000
17	242400.0	394.91	-0.000005	3969.60	4356.90	-8.89	2335.0000	20.0000
18	241800.0	394.84	-0.000005	3948.80	4355.40	-9.34	2335.0000	20.0000
19	241700.0	394.91	-0.000005	3899.40	4359.70	-10.56	2335.0000	20.0000
20	241900.0	394.91	-0.000005	3901.00	4345.40	-10.23	2335.0000	20.0000
21	242000.0	394.95	-0.000005	3901.70	4330.80	-9.91	2335.0000	20.0000
22	287200.0	394.25	-0.000017	7471.80	8474.20	-11.83	2335.0000	20.0000
23	313700.0	394.21	-0.000024	8858.10	8529.30	3.85	2335.0000	20.0000
24	298300.0	394.04	-0.000020	8136.50	8537.60	-4.70	2335.0000	20.0000
25	298600.0	394.12	-0.000020	8140.10	8508.20	-4.33	2335.0000	20.0000
26	298900.0	393.90	-0.000020	8217.60	8536.80	-3.74	2335.0000	20.0000
27	339500.0	394.00	-0.000032	10079.00	10111.00	-0.32	2335.0000	20.0000
28	327000.0	394.01	-0.000028	9534.40	10131.00	-5.89	2335.0000	20.0000

For 28 Data Points, Average Error = -2.60 %, STD = 6.45 %
For 28 Subcooled Data Points, Average Error = -2.60 %, STD = 6.45 %

WCOBRA/TRAC Model Prediction vs. REOCREUX Data
Mean Error is −2.6%
Standard Deviation is 6.45%

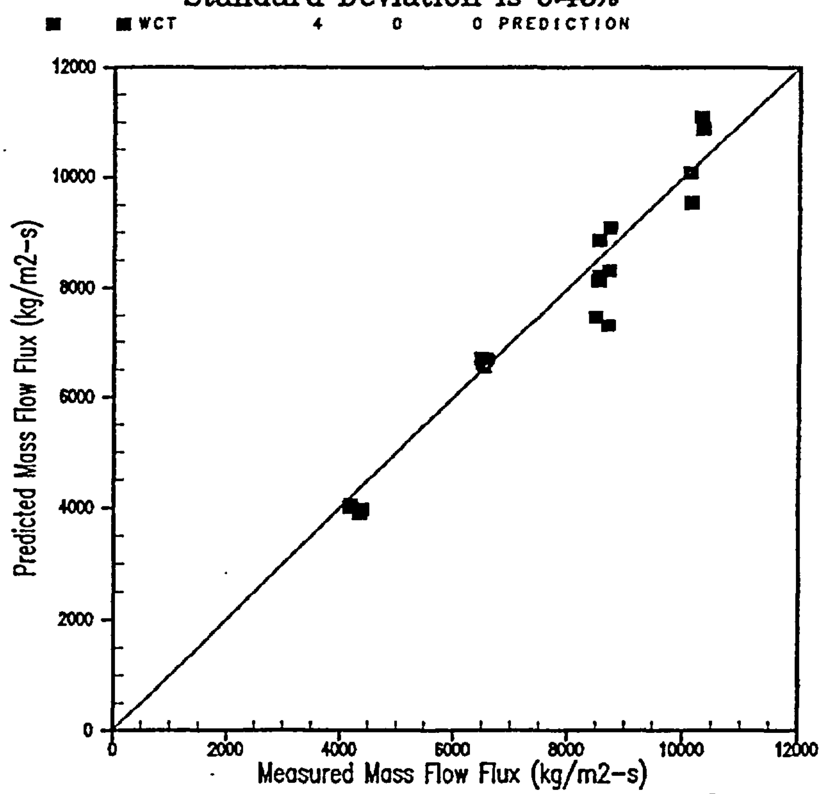

Figure 13-4-24 Prediction Comparison with Reocreux Data

Seynhaeve

Run No.	Pressure (Pa)	Temperature (K)	Quality	Predicted Gc (Kg/m2-s)	Measured Gc (Kg/m2-s)	Error (Gp-Gm)/Gm (in %)	L (mm)	D (mm)
1	674900.0	433.17	-0.000011	8750.30	10105.00	-13.41	306.0000	12.5000
2	683200.0	433.34	-0.000013	9089.30	10103.00	-10.03	306.0000	12.5000
3	431200.0	413.52	-0.000013	9098.20	10138.00	-10.26	306.0000	12.5000
4	430200.0	413.26	-0.000014	9195.70	10182.00	-9.69	306.0000	12.5000
5	471400.0	407.72	-0.000042	13712.00	15266.00	-10.18	306.0000	12.5000
6	470400.0	407.81	-0.000041	13629.00	15328.00	-11.08	306.0000	12.5000
7	474400.0	408.14	-0.000041	13683.00	15098.00	-9.37	306.0000	12.5000
8	608900.0	421.34	-0.000041	13475.00	15277.00	-11.80	306.0000	12.5000
9	602900.0	420.94	-0.000041	13414.00	15221.00	-11.87	306.0000	12.5000
10	606600.0	420.76	-0.000043	13657.00	15230.00	-10.33	306.0000	12.5000
11	418400.0	401.60	-0.000040	13625.00	15472.00	-11.94	306.0000	12.5000
12	420400.0	401.36	-0.000042	13788.00	15367.00	-10.28	306.0000	12.5000
13	874600.0	439.91	-0.000040	13080.00	14851.00	-11.93	306.0000	12.5000
14	871200.0	439.65	-0.000041	13117.00	14912.00	-12.04	306.0000	12.5000
15	873000.0	439.83	-0.000040	13069.00	14683.00	-10.99	306.0000	12.5000
16	431500.0	384.15	-0.000085	17867.00	20770.00	-13.98	306.0000	12.5000
17	430000.0	384.53	-0.000084	17765.00	20775.00	-14.49	306.0000	12.5000
18	575500.0	404.92	-0.000089	18111.00	20499.00	-11.65	306.0000	12.5000
19	578200.0	405.73	-0.000087	17991.00	20509.00	-12.28	306.0000	12.5000
20	577000.0	405.92	-0.000086	17895.00	20507.00	-12.74	306.0000	12.5000
21	1005500.0	439.93	-0.000091	17656.00	19908.00	-11.31	306.0000	12.5000
22	998500.0	439.53	-0.000091	17634.00	19653.00	-10.27	306.0000	12.5000
23	1014200.0	439.72	-0.000096	18021.00	19751.00	-8.76	306.0000	12.5000
24	999500.0	439.19	-0.000094	17869.00	18736.00	-4.63	306.0000	12.5000
25	847000.0	430.01	-0.000089	17702.00	19836.00	-10.76	306.0000	12.5000
26	838400.0	429.27	-0.000090	17772.00	19780.00	-10.15	306.0000	12.5000
27	563000.0	424.67	-0.000014	9632.60	10236.00	-5.89	221.0000	12.5000
28	563700.0	425.19	-0.000012	9274.50	10235.00	-9.38	221.0000	12.5000
29	568400.0	425.77	-0.000012	9103.30	10348.00	-12.03	221.0000	12.5000
30	407200.0	410.68	-0.000015	9670.20	10170.00	-4.91	221.0000	12.5000
31	401200.0	410.30	-0.000014	9530.40	10081.00	-5.46	221.0000	12.5000
32	400200.0	409.95	-0.000014	9665.00	10131.00	-4.60	221.0000	12.5000
33	274500.0	396.73	-0.000010	8461.90	10481.00	-19.26	221.0000	12.5000
34	283700.0	397.32	-0.000011	8798.60	10584.00	-16.87	221.0000	12.5000
35	282700.0	397.93	-0.000010	8456.50	10674.00	-20.77	221.0000	12.5000
36	510700.0	420.47	-0.000014	9615.00	9963.00	-3.49	221.0000	12.5000
37	504700.0	420.30	-0.000013	9378.00	10016.00	-6.37	221.0000	12.5000
38	500200.0	420.13	-0.000012	9235.80	10114.00	-8.68	221.0000	12.5000
39	580400.0	418.57	-0.000042	14000.00	15137.00	-7.51	221.0000	12.5000
40	571400.0	418.65	-0.000039	13599.00	15032.00	-9.53	221.0000	12.5000
41	574900.0	418.64	-0.000040	13738.00	14875.00	-7.64	221.0000	12.5000
42	381700.0	397.29	-0.000038	13792.00	15366.00	-10.24	221.0000	12.5000
43	367400.0	397.15	-0.000034	13215.00	15325.00	-13.77	221.0000	12.5000
44	358600.0	396.72	-0.000032	12962.00	15267.00	-15.10	221.0000	12.5000
45	828600.0	436.31	-0.000046	14102.00	14889.00	-5.29	221.0000	12.5000
46	824900.0	436.70	-0.000042	13692.00	14785.00	-7.39	221.0000	12.5000
47	812900.0	436.40	-0.000039	13398.00	14691.00	-8.80	221.0000	12.5000
48	657900.0	425.90	-0.000039	13448.00	14800.00	-9.14	221.0000	12.5000
49	659400.0	425.81	-0.000040	13568.00	14733.00	-7.91	221.0000	12.5000
50	659700.0	426.06	-0.000039	13438.00	14771.00	-9.02	221.0000	12.5000
51	943800.0	436.13	-0.000091	18160.00	19718.00	-7.90	221.0000	12.5000
52	942000.0	435.89	-0.000092	18239.00	19743.00	-7.62	221.0000	12.5000
53	768000.0	424.77	-0.000085	17931.00	20180.00	-11.14	221.0000	12.5000
54	758500.0	424.22	-0.000084	17858.00	20281.00	-11.95	221.0000	12.5000
55	849200.0	429.68	-0.000092	18346.00	19726.00	-7.00	221.0000	12.5000
56	839500.0	429.14	-0.000091	18280.00	19463.00	-6.08	221.0000	12.5000
57	815500.0	428.05	-0.000087	18039.00	19901.00	-9.36	221.0000	12.5000

For 57 Data Points, Average Error = -10.11 %, STD = 3.40 %
For 57 Subcooled Data Points, Average Error = -10.11 %, STD = 3.40 %

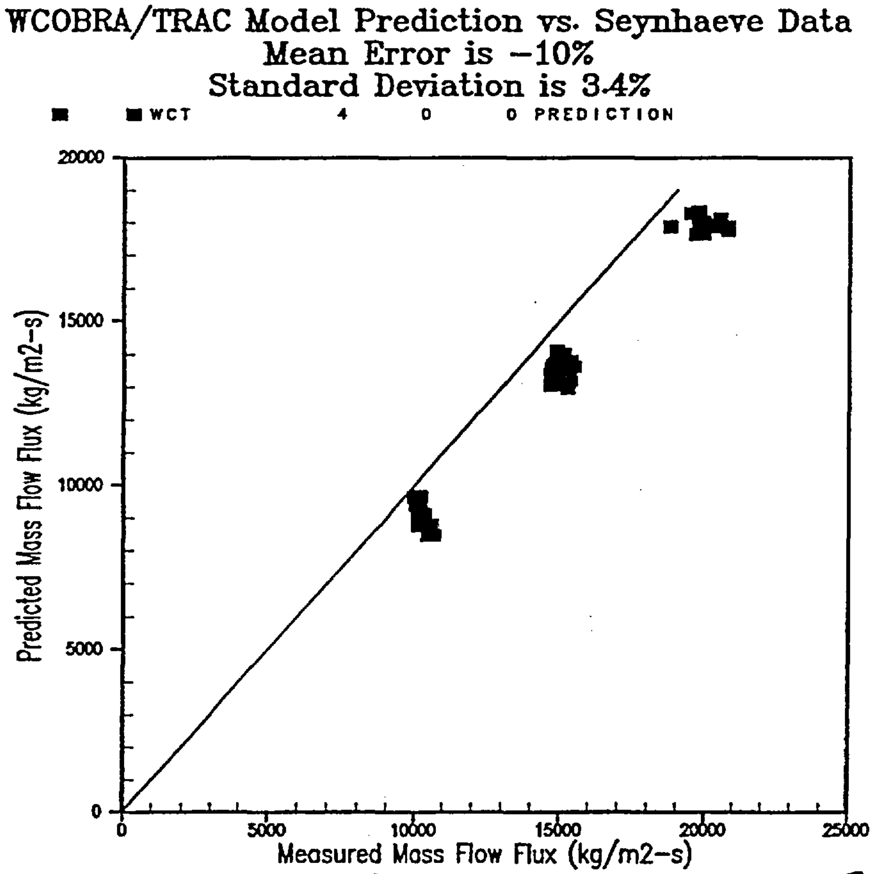

Figure 13-4-25 Prediction Comparison with Seynhaeve Data

Sozzi and Sutherland

Run No.	Pressure (Pa)	Temperature (K)	Quality	Predicted Gc (Kg/m2-s)	Measured Gc (Kg/m2-s)	Error (Gp-Gm)/Gm (in %)	L (mm)	D (mm)
1	5377900.0	541.66	0.003500	22225.00	32371.00	-31.34	44.5000	12.7000
2	5274400.0	540.43	0.003600	21986.00	31034.00	-29.16	44.5000	12.7000
3	5963900.0	528.77	-0.001700	53730.00	65030.00	-17.38	44.5000	12.7000
4	5839800.0	533.41	-0.001200	46511.00	54191.00	-14.17	44.5000	12.7000
5	5619200.0	533.64	-0.000900	42351.00	53581.00	-20.96	44.5000	12.7000
6	5102100.0	536.96	-0.000100	25617.00	48322.00	-46.99	44.5000	12.7000
7	4095200.0	524.78	0.003000	19652.00	32190.00	-38.95	44.5000	12.7000
8	4860800.0	535.28	0.003000	21258.00	30438.00	-30.16	44.5000	12.7000
9	4757300.0	533.94	0.003000	21037.00	30691.00	-31.46	44.5000	12.7000
10	6756800.0	540.25	-0.002000	52283.00	69390.00	-24.65	44.5000	12.7000
11	6894700.0	557.98	0.003000	25345.00	36521.00	-30.60	44.5000	12.7000
12	6825800.0	557.31	0.004000	25088.00	36521.00	-31.31	44.5000	12.7000
13	6791300.0	556.97	0.004200	25004.00	36521.00	-31.54	44.5000	12.7000
14	6722300.0	556.28	0.004400	24848.00	36521.00	-31.96	44.5000	12.7000
15	6653400.0	555.59	0.004700	24669.00	36521.00	-32.45	44.5000	12.7000
16	6446500.0	553.48	0.005000	24218.00	35300.00	-31.39	44.5000	12.7000
17	6274200.0	551.68	0.005000	23868.00	35300.00	-32.39	44.5000	12.7000
18	6170800.0	550.59	0.005000	23640.00	35300.00	-33.03	44.5000	12.7000
19	6963600.0	558.66	0.005000	25290.00	36131.00	-30.00	44.5000	12.7000
20	6894700.0	557.98	0.005500	25105.00	36131.00	-30.52	44.5000	12.7000
21	6860200.0	557.65	0.005700	24995.00	35447.00	-29.49	44.5000	12.7000
22	6791300.0	556.97	0.005900	24836.00	35447.00	-29.93	44.5000	12.7000
23	6722300.0	556.28	0.006100	24676.00	34422.00	-28.31	44.5000	12.7000
24	6584400.0	554.89	0.006800	24318.00	33689.00	-27.82	44.5000	12.7000
25	4619400.0	532.12	0.000900	21371.00	36619.00	-41.64	44.5000	12.7000
26	4550500.0	531.19	0.001600	21016.00	35794.00	-41.29	44.5000	12.7000
27	4412600.0	529.30	0.002100	20579.00	34080.00	-39.62	44.5000	12.7000
28	4205800.0	526.38	0.002800	19901.00	30272.00	-34.26	44.5000	12.7000
29	6618900.0	510.38	-0.004100	76434.00	75671.00	1.01	44.5000	12.7000
30	6274200.0	512.64	-0.003300	71165.00	73726.00	-3.47	44.5000	12.7000
31	6136300.0	534.89	-0.001500	49414.00	66832.00	-26.06	44.5000	12.7000
32	5998300.0	546.85	-0.000200	27904.00	49802.00	-43.97	44.5000	12.7000
33	5688100.0	545.27	0.000600	23497.00	44333.00	-47.00	44.5000	12.7000
34	5377900.0	541.66	0.000800	22878.00	43357.00	-47.23	44.5000	12.7000
35	5102100.0	538.32	0.001200	22214.00	40915.00	-45.71	44.5000	12.7000
36	6481000.0	522.39	-0.003001	66302.00	71284.00	-6.99	44.5000	12.7000
37	6343100.0	529.97	-0.002200	57808.00	66402.00	-12.94	44.5000	12.7000
38	6274200.0	536.17	-0.001600	50039.00	66402.00	-24.64	44.5000	12.7000
39	5929400.0	547.97	0.000500	23987.00	46530.00	-48.45	44.5000	12.7000
40	5791500.0	546.44	0.000900	23565.00	45603.00	-48.33	44.5000	12.7000
41	5653700.0	544.88	0.001000	23280.00	43747.00	-46.78	44.5000	12.7000
42	5515800.0	543.29	0.001100	22990.00	42478.00	-45.88	44.5000	12.7000
43	5377100.0	541.66	0.001200	22725.00	40915.00	-44.46	44.5000	12.7000
44	6274200.0	551.68	0.000300	24665.00	48469.00	-49.11	44.5000	12.7000
45	6136300.0	550.22	0.000300	24424.00	47141.00	-48.19	44.5000	12.7000
46	5977700.0	548.50	0.002400	23608.00	33802.00	-30.16	44.5000	12.7000
47	5060500.0	537.81	0.004400	21406.00	32029.00	-33.17	44.5000	12.7000
48	5777800.0	546.28	0.004000	22950.00	32029.00	-28.35	44.5000	12.7000
49	5757100.0	546.05	0.003700	22973.00	32337.00	-28.96	44.5000	12.7000
50	5639900.0	544.72	0.003500	22741.00	32337.00	-29.67	44.5000	12.7000
51	5536400.0	543.53	0.003500	22536.00	32029.00	-29.64	44.5000	12.7000
52	5495100.0	543.05	0.003600	22432.00	30940.00	-27.50	44.5000	12.7000
53	5446800.0	542.48	0.003600	22355.00	30940.00	-27.75	44.5000	12.7000
54	5343400.0	541.25	0.003700	22117.00	30940.00	-28.52	44.5000	12.7000
55	5240000.0	540.01	0.003700	21905.00	30940.00	-29.20	44.5000	12.7000
56	5171000.0	539.17	0.003000	21865.00	30940.00	-29.33	44.5000	12.7000
57	5102100.0	538.32	0.003800	21608.00	29866.00	-27.65	44.5000	12.7000
58	4998700.0	537.03	0.003800	21386.00	29329.00	-27.08	44.5000	12.7000
59	6756800.0	556.62	0.002700	25101.00	36814.00	-31.82	44.5000	12.7000
60	6550000.0	554.54	0.004000	24540.00	34178.00	-28.20	44.5000	12.7000
61	6412100.0	553.12	0.004400	24216.00	33494.00	-27.70	44.5000	12.7000
62	6170800.0	550.59	0.004500	23698.00	33494.00	-29.25	44.5000	12.7000
63	5929400.0	547.97	0.004400	23214.00	33006.00	-29.67	44.5000	12.7000
64	5688100.0	545.27	0.004600	22701.00	31240.00	-27.33	44.5000	12.7000
65	5515800.0	543.29	0.004600	22331.00	30320.00	-26.35	44.5000	12.7000
66	6770600.0	556.76	0.003100	25096.00	33640.00	-25.40	44.5000	12.7000
67	6674100.0	555.80	0.004100	24785.00	33396.00	-25.78	44.5000	12.7000
68	6584400.0	554.89	0.004400	24557.00	33299.00	-26.25	44.5000	12.7000
69	6481000.0	553.84	0.004400	24364.00	33152.00	-26.51	44.5000	12.7000
70	6446500.0	553.48	0.004400	24290.00	33152.00	-26.73	44.5000	12.7000
71	6329300.0	552.26	0.004500	24022.00	32029.00	-25.00	44.5000	12.7000
72	6253500.0	551.47	0.004400	23868.00	32029.00	-25.48	44.5000	12.7000
73	6170800.0	550.59	0.004400	23720.00	30125.00	-21.26	44.5000	12.7000
74	6067300.0	549.48	0.004600	23474.00	30125.00	-22.08	44.5000	12.7000
75	5963900.0	548.35	0.004600	23271.00	29539.00	-21.22	44.5000	12.7000
76	5860500.0	547.21	0.004600	23039.00	29539.00	-22.00	44.5000	12.7000
77	6288000.0	547.53	-0.000500	33013.00	62955.00	-47.56	44.5000	12.7000
78	6088000.0	547.89	-0.000200	27898.00	55084.00	-49.35	44.5000	12.7000
79	5743200.0	545.89	0.000000	24061.00	51149.00	-52.96	44.5000	12.7000
80	5626000.0	544.56	0.000004	23890.00	47575.00	-49.78	44.5000	12.7000
81	5722600.0	545.66	0.001500	23312.00	39704.00	-41.29	44.5000	12.7000
82	5639100.0	544.71	0.003000	22845.00	31477.00	-27.42	44.5000	12.7000
83	5605400.0	544.32	0.003500	22691.00	32190.00	-29.51	44.5000	12.7000
84	5515800.0	543.29	0.003500	22511.00	33089.00	-31.97	44.5000	12.7000
85	5446800.0	542.48	0.003500	22354.00	32371.00	-30.94	44.5000	12.7000
86	5412300.0	542.07	0.003500	22276.00	30760.00	-27.58	44.5000	12.7000
87	6136300.0	500.23	-0.003800	77294.00	82270.00	-6.05	44.5000	12.7000
88	6067300.0	514.93	-0.002800	67212.00	72993.00	-7.92	44.5000	12.7000
89	5653700.0	544.88	0.000500	23485.00	45896.00	-48.83	44.5000	12.7000
90	5377900.0	541.66	0.000500	23003.00	44968.00	-48.85	44.5000	12.7000
91	5033100.0	537.46	0.000900	22194.00	39646.00	-44.02	44.5000	12.7000
92	5240000.0	540.01	0.000600	22710.00	44187.00	-48.60	44.5000	12.7000
93	6481000.0	543.64	-0.001200	43290.00	63814.00	-32.16	44.5000	12.7000

94	6205200.0	550.95	0.000500	24449.00	47751.00	-48.80	44.5000	12.7000
95	5791500.0	546.44	0.001300	23454.00	42917.00	-45.35	44.5000	12.7000
96	5653700.0	544.88	0.001500	23166.00	39792.00	-41.78	44.5000	12.7000
97	5446000.0	542.47	0.001600	22753.00	38328.00	-40.64	44.5000	12.7000
98	4826300.0	517.33	-0.001000	47925.00	59078.00	-18.88	44.5000	12.7000
99	4688400.0	524.01	-0.000500	37541.00	56149.00	-33.14	44.5000	12.7000
100	4550500.0	531.19	0.000500	21455.00	41111.00	-47.81	44.5000	12.7000
101	4205800.0	526.38	0.001000	20557.00	39792.00	-48.34	44.5000	12.7000
102	4067900.0	524.37	0.001300	20147.00	39402.00	-48.87	44.5000	12.7000
103	3447400.0	514.62	0.000002	20165.00	51755.00	-61.04	44.5000	12.7000
104	3309500.0	496.25	-0.000500	40683.00	47311.00	-14.01	44.5000	12.7000
105	3171600.0	509.84	0.000002	19605.00	41990.00	-53.31	44.5000	12.7000
106	3033700.0	507.33	0.000100	18897.00	39988.00	-52.74	44.5000	12.7000
107	3447400.0	514.62	0.000002	20165.00	40818.00	-50.60	44.5000	12.7000
108	3447400.0	514.62	0.000100	19787.00	39744.00	-50.21	44.5000	12.7000
109	3447400.0	514.62	0.000400	19391.00	38328.00	-49.41	44.5000	12.7000
110	3378400.0	513.45	0.000450	19203.00	35935.00	-46.56	44.5000	12.7000
111	3309500.0	512.27	0.000500	19011.00	35545.00	-46.52	44.5000	12.7000
112	3171600.0	509.84	0.000900	18394.00	31248.00	-41.14	44.5000	12.7000
113	3171600.0	509.84	0.001000	18330.00	30272.00	-39.45	44.5000	12.7000
114	6150100.0	550.37	0.000300	24445.00	49313.00	-50.43	44.5000	12.7000
115	5805300.0	546.59	0.000800	23645.00	45310.00	-47.82	44.5000	12.7000
116	6715400.0	544.29	-0.001500	46322.00	65426.00	-29.20	44.5000	12.7000
117	6467200.0	553.69	0.000004	25205.00	52863.00	-52.32	44.5000	12.7000
118	6225900.0	551.17	0.002000	24181.00	42282.00	-42.81	44.5000	12.7000
119	5908800.0	547.74	0.001500	23639.00	41208.00	-42.63	44.5000	12.7000
120	6749900.0	542.06	-0.001800	49895.00	68843.00	-27.52	44.5000	12.7000
121	6501700.0	548.40	-0.000700	35879.00	62740.00	-42.81	44.5000	12.7000
122	6356900.0	552.55	0.000500	24741.00	49802.00	-50.32	44.5000	12.7000
123	6177700.0	550.66	0.001200	24227.00	44919.00	-46.07	44.5000	12.7000
124	5784700.0	546.36	0.001800	23350.00	40051.00	-41.70	44.5000	12.7000
125	7074000.0	559.72	0.002000	25825.00	42478.00	-39.20	44.5000	12.7000
126	6998100.0	558.99	0.003000	25552.00	39548.00	-35.39	44.5000	12.7000
127	6481000.0	553.84	0.004000	24395.00	36570.00	-33.29	44.5000	12.7000
128	6219000.0	551.10	0.005000	23742.00	34910.00	-31.99	44.5000	12.7000
129	6743000.0	556.49	0.002900	25064.00	48044.00	-47.83	44.5000	12.7000
130	6584400.0	554.89	0.004300	24578.00	45607.00	-46.11	44.5000	12.7000
131	6300700.0	551.96	0.005200	23902.00	42590.00	-43.88	44.5000	12.7000
132	5998300.0	548.73	0.005300	23241.00	41667.00	-44.22	44.5000	12.7000
133	6687100.0	539.06	-0.002000	52713.00	75825.00	-30.48	44.5000	12.7000
134	6550000.0	543.70	-0.001300	44437.00	75825.00	-41.40	44.5000	12.7000
135	6481000.0	549.83	-0.000500	32716.00	64937.00	-49.62	44.5000	12.7000
136	6343100.0	552.41	0.000004	25020.00	61031.00	-59.00	44.5000	12.7000
137	5915700.0	547.82	0.002100	23536.00	48473.00	-51.45	44.5000	12.7000
138	5722600.0	545.66	0.002200	23149.00	45993.00	-49.67	44.5000	12.7000
139	6756000.0	556.62	0.004900	24875.00	44709.00	-44.36	44.5000	12.7000
140	6481000.0	553.84	0.006000	24194.00	42859.00	-43.55	44.5000	12.7000
141	6190300.0	550.80	0.006500	23527.00	41540.00	-43.36	44.5000	12.7000
142	6653400.0	538.47	-0.002000	52408.00	75010.00	-30.13	57.2000	12.7000
143	6618900.0	539.93	-0.001800	50114.00	67847.00	-26.14	57.2000	12.7000
144	6481000.0	545.49	-0.001000	39799.00	61368.00	-35.15	57.2000	12.7000
145	6412100.0	553.12	0.000300	24407.00	58195.00	-58.06	57.2000	12.7000
146	6839500.0	557.44	0.002000	25014.00	43698.00	-42.76	57.2000	12.7000
147	6777500.0	556.83	0.002500	24829.00	40720.00	-39.03	57.2000	12.7000
148	6743000.0	556.49	0.002800	24726.00	39890.00	-38.01	57.2000	12.7000
149	6722300.0	556.28	0.003000	24666.00	39890.00	-38.16	57.2000	12.7000
150	6504400.0	554.08	0.003000	24189.00	39250.00	-38.37	57.2000	12.7000
151	6481000.0	553.84	0.003800	24057.00	38035.00	-36.75	57.2000	12.7000
152	6446500.0	553.48	0.004400	23914.00	38035.00	-37.13	57.2000	12.7000
153	6329300.0	552.26	0.004500	23673.00	36492.00	-35.13	57.2000	12.7000
154	6239700.0	551.32	0.004500	23473.00	36687.00	-36.02	57.2000	12.7000
155	6205200.0	550.95	0.004500	23398.00	36004.00	-35.01	57.2000	12.7000
156	6122500.0	550.07	0.004800	23183.00	34617.00	-33.03	57.2000	12.7000
157	5904600.0	547.70	0.004000	22797.00	34265.00	-33.47	57.2000	12.7000
158	6025800.0	549.02	0.003500	23109.00	39592.00	-41.63	57.2000	12.7000
159	6812000.0	557.17	0.004000	24742.00	39709.00	-37.69	57.2000	12.7000
160	6756800.0	556.62	0.004000	24622.00	39021.00	-36.90	57.2000	12.7000
161	6722300.0	556.28	0.004000	24550.00	38035.00	-35.45	57.2000	12.7000
162	6632700.0	555.38	0.004700	24300.00	38088.00	-36.20	57.2000	12.7000
163	6584400.0	554.89	0.005000	24171.00	36101.00	-33.05	57.2000	12.7000
164	6515500.0	554.19	0.005000	24022.00	36101.00	-33.46	57.2000	12.7000
165	6412100.0	553.12	0.005500	23751.00	35344.00	-32.80	57.2000	12.7000
166	6329300.0	552.26	0.005000	23623.00	35344.00	-33.16	57.2000	12.7000
167	6308700.0	552.05	0.005200	23558.00	34885.00	-32.47	57.2000	12.7000
168	6205200.0	550.95	0.005200	23329.00	34441.00	-32.26	57.2000	12.7000
169	6081100.0	549.62	0.005500	23009.00	33011.00	-30.30	57.2000	12.7000
170	6032900.0	549.10	0.006000	22851.00	33753.00	-32.30	57.2000	12.7000
171	6067100.0	549.47	0.002900	23265.00	39744.00	-41.46	57.2000	12.7000
172	6818900.0	557.24	0.003300	24820.00	39744.00	-37.55	57.2000	12.7000
173	6777500.0	556.83	0.003500	24713.00	39744.00	-37.82	57.2000	12.7000
174	6681000.0	555.87	0.004000	24480.00	39744.00	-38.41	57.2000	12.7000
175	6543100.0	554.47	0.004000	24163.00	37839.00	-36.14	57.2000	12.7000
176	6300700.0	551.96	0.004500	23598.00	36497.00	-35.34	57.2000	12.7000
177	6067300.0	549.48	0.004300	23111.00	35764.00	-35.38	57.2000	12.7000
178	6770600.0	541.44	-0.001900	50451.00	72993.00	-30.88	57.2000	12.7000
179	6667200.0	545.37	-0.001300	43313.00	62740.00	-30.96	57.2000	12.7000
180	6577500.0	549.33	-0.000700	34968.00	62740.00	-44.27	57.2000	12.7000
181	6150100.0	550.37	0.001200	23693.00	43088.00	-45.01	57.2000	12.7000
182	6012200.0	548.88	0.001300	23386.00	42331.00	-44.75	57.2000	12.7000
183	5798400.0	546.52	0.001700	22884.00	42331.00	-45.94	57.2000	12.7000
184	6701600.0	537.24	-0.002200	54504.00	71529.00	-23.80	57.2000	12.7000
185	6591300.0	541.46	-0.001600	47639.00	66500.00	-28.36	57.2000	12.7000
186	6391300.0	552.91	0.000004	24519.00	56783.00	-56.82	57.2000	12.7000
187	5770900.0	546.21	0.001300	22884.00	40891.00	-44.04	57.2000	12.7000
188	5605400.0	544.32	0.001500	22520.00	40891.00	-44.93	57.2000	12.7000
189	6694800.0	556.00	0.004000	22318.00	23802.00	-6.23	362.0000	12.7000
190	6577500.0	554.82	0.004000	22048.00	23802.00	-7.37	362.0000	12.7000
191	6460300.0	553.62	0.004000	21775.00	23802.00	-8.52	362.0000	12.7000
192	6350000.0	552.48	0.004300	21505.00	23802.00	-9.65	362.0000	12.7000
193	6867100.0	557.71	0.003500	22727.00	25291.00	-10.14	362.0000	12.7000
194	6832600.0	557.38	0.003000	22705.00	25291.00	-10.22	362.0000	12.7000

195	6694800.0	556.00	0.003000	22393.00	23802.00	-5.92	362.0000	12.7000
196	6556900.0	554.61	0.003000	22105.00	23802.00	-7.13	362.0000	12.7000
197	6412100.0	553.12	0.003000	21761.00	23802.00	-8.57	362.0000	12.7000
198	6274200.0	551.68	0.003000	21441.00	23802.00	-9.92	362.0000	12.7000
199	6577500.0	533.71	-0.002300	51293.00	46872.00	9.43	362.0000	12.7000
200	6474100.0	537.45	-0.001800	45776.00	41990.00	9.02	362.0000	12.7000
201	6411000.0	540.63	-0.001400	40848.00	37595.00	8.65	362.0000	12.7000
202	6370700.0	543.98	-0.001000	35173.00	33933.00	3.65	362.0000	12.7000
203	6329300.0	543.40	-0.001000	35338.00	30760.00	14.88	362.0000	12.7000
204	6253500.0	547.11	-0.000500	27129.00	28026.00	-3.20	362.0000	12.7000
205	6074200.0	549.55	0.000004	21306.00	25780.00	-17.35	362.0000	12.7000
206	5095000.0	538.23	0.000200	18959.00	24657.00	-23.11	362.0000	12.7000
207	5715700.0	545.58	0.000500	20406.00	23802.00	-14.27	362.0000	12.7000
208	6674100.0	534.50	-0.002400	56455.00	57125.00	-1.17	82.6000	12.7000
209	6598200.0	536.40	-0.002100	53236.00	57208.00	-6.94	82.6000	12.7000
210	6481000.0	536.46	-0.001900	51501.00	54293.00	-5.14	82.6000	12.7000
211	6425900.0	542.84	-0.001200	42036.00	52609.00	-20.10	82.6000	12.7000
212	6288000.0	551.83	0.000004	23669.00	43762.00	-45.91	82.6000	12.7000
213	6853300.0	557.58	0.002700	24593.00	31936.00	-22.99	82.6000	12.7000
214	6784400.0	556.90	0.002700	24427.00	31936.00	-23.51	82.6000	12.7000
215	6701600.0	556.07	0.003700	24154.00	31936.00	-24.37	82.6000	12.7000
216	6584400.0	554.89	0.003400	23919.00	31936.00	-25.10	82.6000	12.7000
217	6391400.0	552.91	0.003900	23434.00	29686.00	-21.06	82.6000	12.7000
218	6198300.0	550.88	0.004000	22992.00	29686.00	-22.55	82.6000	12.7000
219	6853300.0	541.85	-0.002000	50354.00	58102.00	-13.34	82.6000	12.7000
220	6777500.0	543.41	-0.001700	47149.00	58102.00	-18.85	82.6000	12.7000
221	6618900.0	551.43	-0.000500	30639.00	51022.00	-39.95	82.6000	12.7000
222	6315500.0	552.12	0.001090	23527.00	38669.00	-39.16	82.6000	12.7000
223	6026000.0	549.03	0.001500	22843.00	35398.00	-35.47	82.6000	12.7000
224	5736400.0	545.82	0.001900	22140.00	32225.00	-31.30	82.6000	12.7000
225	6790200.0	556.96	0.001500	21917.00	23241.00	-5.70	552.5000	12.7000
226	6687100.0	555.93	0.002000	21632.00	22313.00	-3.05	552.5000	12.7000
227	6577500.0	554.82	0.002000	21393.00	22704.00	-5.77	552.5000	12.7000
228	6467200.0	553.69	0.002000	21153.00	22313.00	-5.20	552.5000	12.7000
229	6350000.0	552.48	0.002000	20913.00	21483.00	-2.65	552.5000	12.7000
230	6715400.0	539.55	-0.002000	44382.00	41111.00	7.96	552.5000	12.7000
231	6694800.0	539.19	-0.002000	44474.00	38328.00	16.04	552.5000	12.7000
232	6563800.0	546.60	-0.001000	32634.00	35740.00	-8.69	552.5000	12.7000
233	6508600.0	545.86	-0.001000	32808.00	33592.00	-2.33	552.5000	12.7000
234	6460300.0	545.21	-0.001000	32976.00	32225.00	2.33	552.5000	12.7000
235	6419000.0	549.10	-0.000500	25487.00	28319.00	-10.00	552.5000	12.7000
236	5991500.0	548.65	0.001000	20218.00	22704.00	-10.95	552.5000	12.7000
237	5812200.0	546.67	0.001000	19796.00	21776.00	-9.09	552.5000	12.7000
238	6812000.0	557.17	0.002300	29447.00	31492.00	-6.49	10.8000	12.7000
239	6777500.0	556.83	0.002500	29295.00	31492.00	-6.98	10.8000	12.7000
240	6729100.0	556.35	0.002900	29092.00	31492.00	-7.62	10.8000	12.7000
241	6667200.0	555.73	0.003200	28948.00	30418.00	-4.83	10.8000	12.7000
242	6563800.0	554.68	0.003200	28768.00	30418.00	-5.42	10.8000	12.7000
243	6391400.0	552.91	0.003500	28437.00	28465.00	-0.10	10.8000	12.7000
244	6232800.0	551.25	0.003600	28152.00	28465.00	-1.10	10.8000	12.7000
245	6039800.0	549.18	0.003500	27881.00	28465.00	-2.05	10.8000	12.7000
246	6867100.0	557.71	0.003700	29089.00	29881.00	-2.65	10.8000	12.7000
247	6805100.0	557.10	0.004400	28788.00	29881.00	-3.66	10.8000	12.7000
248	6708500.0	556.14	0.004500	28600.00	29881.00	-4.29	10.8000	12.7000
249	6639600.0	555.45	0.004500	28510.00	28953.00	-1.53	10.8000	12.7000
250	6570600.0	554.75	0.004500	28420.00	28953.00	-1.84	10.8000	12.7000
251	6474100.0	553.76	0.004500	28281.00	28953.00	-2.32	10.8000	12.7000
252	6301800.0	551.97	0.004500	27995.00	27830.00	0.59	10.8000	12.7000
253	6736100.0	536.81	-0.002300	59147.00	55172.00	7.20	10.8000	12.7000
254	6660300.0	537.54	-0.002100	57399.00	50778.00	13.04	10.8000	12.7000
255	6584400.0	539.35	-0.001800	54312.00	50778.00	6.96	10.8000	12.7000
256	6508600.0	541.15	-0.001500	51059.00	47849.00	6.71	10.8000	12.7000
257	6432800.0	545.11	-0.000970	44576.00	47849.00	-6.84	10.8000	12.7000
258	6363000.0	544.16	-0.000970	44790.00	46304.00	-3.27	10.8000	12.7000
259	6225900.0	547.59	-0.000410	37000.00	43454.00	-14.85	10.8000	12.7000
260	5708800.0	545.51	0.000600	28827.00	33201.00	-13.17	10.8000	12.7000
261	6722300.0	556.28	0.003000	21091.00	22362.00	-5.68	679.5000	12.7000
262	6460300.0	553.62	0.004000	20423.00	22362.00	-8.67	679.5000	12.7000
263	6743000.0	556.49	0.003000	21140.00	22557.00	-6.28	679.5000	12.7000
264	6501700.0	554.05	0.004000	20523.00	22557.00	-9.02	679.5000	12.7000
265	6867100.0	557.71	0.003000	21404.00	22557.00	-5.11	679.5000	12.7000
266	6474100.0	535.19	-0.002000	44324.00	41111.00	7.82	679.5000	12.7000
267	6260400.0	542.42	-0.001000	32572.00	27391.00	18.91	679.5000	12.7000
268	6956800.0	558.59	0.001000	21796.00	25438.00	-14.32	679.5000	12.7000
269	6515500.0	554.19	0.002500	20698.00	22826.00	-9.32	679.5000	12.7000
270	6246600.0	551.39	0.003000	20064.00	22582.00	-11.15	679.5000	12.7000
271	6874000.0	557.78	0.004000	21331.00	21971.00	-2.91	679.5000	12.7000
272	6798200.0	557.03	0.004000	21160.00	21971.00	-3.69	679.5000	12.7000
273	6687900.0	555.94	0.004000	20916.00	21971.00	-4.80	679.5000	12.7000
274	6453400.0	553.55	0.004000	20424.00	21971.00	-7.04	679.5000	12.7000
275	6660300.0	526.40	-0.003000	54114.00	46481.00	16.42	679.5000	12.7000
276	6515500.0	529.82	-0.002500	49780.00	41745.00	19.25	679.5000	12.7000
277	6274200.0	542.62	-0.001000	32498.00	27098.00	19.93	679.5000	12.7000
278	6094900.0	545.13	-0.000500	25119.00	22948.00	9.46	679.5000	12.7000
279	5908800.0	545.80	-0.000200	21232.00	20995.00	1.13	679.5000	12.7000
280	7129100.0	560.25	0.001000	22138.00	23485.00	-5.74	679.5000	12.7000
281	7080100.0	559.78	0.002000	21950.00	23485.00	-6.54	679.5000	12.7000
282	6936100.0	558.39	0.002500	21609.00	23485.00	-7.99	679.5000	12.7000
283	6704400.0	556.10	0.003000	21069.00	22948.00	-8.19	679.5000	12.7000
284	6639600.0	555.45	0.003000	20923.00	22948.00	-8.82	679.5000	12.7000
285	6487900.0	553.91	0.003000	20608.00	22948.00	-10.20	679.5000	12.7000
286	7018800.0	559.19	0.002000	21808.00	22826.00	-4.46	679.5000	12.7000
287	6977400.0	558.79	0.002000	21741.00	22826.00	-4.75	679.5000	12.7000
288	6832600.0	557.38	0.002000	21435.00	22626.00	-5.26	679.5000	12.7000
289	6694800.0	556.00	0.002500	21084.00	22626.00	-6.82	679.5000	12.7000
290	6556900.0	554.61	0.002500	20796.00	22826.00	-8.89	679.5000	12.7000
291	6412100.0	553.12	0.003000	20436.00	22826.00	-10.47	679.5000	12.7000
292	6260400.0	551.54	0.003000	20088.00	22826.00	-12.00	679.5000	12.7000
293	7039500.0	559.39	0.003000	21759.00	23924.00	-9.05	679.5000	12.7000
294	6998100.0	558.99	0.003000	21663.00	23924.00	-9.45	679.5000	12.7000
295	6308700.0	549.53	-0.000300	22659.00	22118.00	2.45	679.5000	12.7000

296	6681000.0	524.24	-0.003200	55937.00	42527.00	31.53	679.5000	12.7000
297	6632700.0	525.64	-0.003000	54422.00	39939.00	36.26	679.5000	12.7000
298	6570600.0	531.08	-0.002500	49369.00	38669.00	27.67	679.5000	12.7000
299	6508600.0	535.84	-0.002000	44148.00	35252.00	25.24	679.5000	12.7000
300	6460300.0	540.38	-0.001500	38385.00	32078.00	19.66	679.5000	12.7000
301	6425900.0	541.86	-0.001300	36016.00	32078.00	12.28	679.5000	12.7000
302	6743000.0	509.69	-0.004400	65374.00	48581.00	34.57	679.5000	12.7000
303	6667200.0	508.84	-0.004300	65195.00	48581.00	34.20	679.5000	12.7000
304	6584400.0	509.34	-0.004100	64242.00	51266.00	25.31	679.5000	12.7000
305	6536200.0	510.94	-0.003900	62931.00	51266.00	22.75	679.5000	12.7000
306	6460300.0	519.37	-0.003200	57068.00	45505.00	25.41	679.5000	12.7000
307	6749900.0	552.24	-0.000590	25624.00	27147.00	-5.61	679.5000	12.7000
308	6701600.0	552.14	-0.000530	25007.00	24168.00	3.47	679.5000	12.7000
309	6646500.0	552.06	-0.000460	24330.00	23582.00	3.17	679.5000	12.7000
310	6584400.0	551.99	-0.000380	23592.00	22752.00	3.69	679.5000	12.7000
311	6522400.0	552.09	-0.000280	22726.00	21971.00	3.44	679.5000	12.7000
312	6474100.0	552.27	-0.000190	22003.00	21971.00	0.15	679.5000	12.7000
313	6439600.0	552.54	-0.000110	21455.00	21971.00	-2.35	679.5000	12.7000
314	6825800.0	557.31	0.001300	21504.00	20897.00	2.90	679.5000	12.7000
315	6805100.0	557.10	0.001800	21389.00	20897.00	2.35	679.5000	12.7000
316	6701600.0	532.72	-0.002600	49424.00	39060.00	26.53	679.5000	12.7000
317	6715400.0	533.01	-0.002600	49337.00	39060.00	26.31	679.5000	12.7000
318	6667200.0	533.18	-0.002500	48578.00	38035.00	27.72	679.5000	12.7000
319	6584400.0	532.64	-0.002400	48124.00	36668.00	31.24	679.5000	12.7000
320	6515500.0	534.83	-0.002100	45219.00	36375.00	24.31	679.5000	12.7000
321	6446500.0	539.12	-0.001600	39706.00	34910.00	13.74	679.5000	12.7000
322	6384500.0	542.23	-0.001200	34894.00	30516.00	14.35	679.5000	12.7000
323	6805100.0	557.10	0.001000	21470.00	25682.00	-16.40	679.5000	12.7000
324	6818900.0	557.24	0.002800	21335.00	23338.00	-8.58	679.5000	12.7000
325	6805100.0	557.10	0.003500	21222.00	21044.00	0.85	679.5000	12.7000
326	6777500.0	556.83	0.003400	21160.00	21044.00	0.55	679.5000	12.7000
327	6743000.0	556.49	0.003300	21101.00	21044.00	0.27	679.5000	12.7000
328	6708500.0	556.14	0.003600	21017.00	21044.00	-0.13	679.5000	12.7000
329	6853300.0	557.58	0.001500	21522.00	22167.00	-2.91	679.5000	12.7000
330	6825800.0	557.31	0.001900	21423.00	22167.00	-3.36	679.5000	12.7000
331	6874000.0	557.78	0.000520	21668.00	22167.00	-2.25	679.5000	12.7000
332	6874000.0	557.78	0.000790	21640.00	22167.00	-2.38	679.5000	12.7000
333	6805100.0	557.10	0.002000	21362.00	22167.00	-3.63	679.5000	12.7000
334	6770600.0	556.76	0.002000	21291.00	20897.00	1.89	679.5000	12.7000
335	6743000.0	556.49	0.002200	21219.00	20897.00	1.54	679.5000	12.7000
336	6715400.0	538.53	-0.002100	43989.00	35935.00	22.41	679.5000	12.7000
337	6749900.0	538.12	-0.002200	44824.00	35935.00	24.74	679.5000	12.7000
338	6722300.0	538.65	-0.002100	43917.00	34910.00	25.80	679.5000	12.7000
339	6646500.0	538.35	-0.002000	43267.00	32078.00	34.88	679.5000	12.7000
340	6570600.0	539.12	-0.001800	41423.00	31004.00	33.61	679.5000	12.7000
341	6501700.0	541.04	-0.001500	38212.00	30467.00	25.42	679.5000	12.7000
342	6446500.0	544.09	-0.001100	33304.00	29686.00	12.19	679.5000	12.7000
343	6391400.0	545.48	-0.000870	30188.00	25731.00	17.32	679.5000	12.7000
344	6350000.0	548.63	-0.000460	24293.00	23680.00	2.59	679.5000	12.7000
345	6736100.0	542.77	-0.001700	39475.00	34861.00	13.24	679.5000	12.7000
346	6708500.0	542.34	-0.001700	39571.00	32957.00	20.07	679.5000	12.7000
347	6646500.0	542.32	-0.001600	38720.00	31785.00	21.82	679.5000	12.7000
348	6584400.0	542.32	-0.001500	37807.00	31004.00	21.94	679.5000	12.7000
349	6515500.0	543.19	-0.001300	35613.00	30516.00	16.70	679.5000	12.7000
350	6460300.0	545.21	-0.001000	31835.00	28660.00	11.08	679.5000	12.7000
351	6405200.0	547.90	-0.000620	26429.00	27879.00	-5.20	679.5000	12.7000
352	6074000.0	549.55	0.004000	19595.00	22069.00	-11.21	679.5000	12.7000
353	6756000.0	556.62	0.004000	21062.00	22069.00	-4.56	679.5000	12.7000
354	6625800.0	555.31	0.004000	20794.00	22069.00	-5.78	679.5000	12.7000
355	6508600.0	554.12	0.004000	20549.00	22069.00	-6.89	679.5000	12.7000
356	6377600.0	552.77	0.004000	20249.00	22069.00	-8.25	679.5000	12.7000
357	6756800.0	556.62	0.002700	23746.00	27342.00	-13.15	158.8000	12.7000
358	6722300.0	556.28	0.002700	23676.00	27342.00	-13.41	158.8000	12.7000
359	6632700.0	555.38	0.003000	23431.00	27342.00	-14.30	158.8000	12.7000
360	6536200.0	554.40	0.003100	23195.00	28074.00	-17.38	158.8000	12.7000
361	6474100.0	553.76	0.003200	23058.00	28074.00	-17.87	158.8000	12.7000
362	6315500.0	552.12	0.003200	22690.00	27342.00	-17.01	158.8000	12.7000
363	6150100.0	550.37	0.003300	22272.00	26610.00	-16.30	158.8000	12.7000
364	6839500.0	543.46	-0.001800	46547.00	47604.00	-2.22	158.8000	12.7000
365	6770600.0	545.09	-0.001500	43114.00	46872.00	-8.02	158.8000	12.7000
366	6701600.0	544.08	-0.001500	43450.00	43454.00	-0.01	158.8000	12.7000
367	6639600.0	546.74	-0.001100	38137.00	43454.00	-12.24	158.8000	12.7000
368	6536200.0	552.08	-0.000300	25856.00	38572.00	-32.97	158.8000	12.7000
369	6205200.0	550.95	0.000800	22629.00	31248.00	-27.58	158.8000	12.7000
370	5991500.0	548.65	0.001000	22106.00	31004.00	-28.70	158.8000	12.7000
371	5764000.0	546.13	0.001100	21572.00	29783.00	-27.57	158.8000	12.7000
372	6800900.0	557.06	0.000300	18501.00	20165.00	-8.25	1822.5000	12.7000
373	6867100.0	557.71	0.002000	18401.00	19286.00	-4.59	1822.5000	12.7000
374	6032600.0	549.10	0.002800	16721.00	18358.00	-8.92	1822.5000	12.7000
375	6791300.0	556.97	0.003100	18124.00	17919.00	1.14	1822.5000	12.7000
376	6756000.0	556.62	0.002500	18149.00	17919.00	1.28	1822.5000	12.7000
377	6722300.0	556.28	0.003500	17948.00	17528.00	2.40	1822.5000	12.7000
378	6681000.0	555.87	0.003300	17918.00	17528.00	2.23	1822.5000	12.7000
379	6646500.0	555.52	0.003400	17836.00	17528.00	1.76	1822.5000	12.7000
380	6605100.0	555.10	0.003300	17771.00	17528.00	1.39	1822.5000	12.7000
381	6743000.0	543.79	-0.001600	30276.00	29441.00	2.84	1822.5000	12.7000
382	6736100.0	543.14	-0.001660	30804.00	29441.00	4.63	1822.5000	12.7000
383	6708500.0	542.90	-0.001640	30759.00	29441.00	4.48	1822.5000	12.7000
384	6625800.0	543.42	-0.001450	29268.00	24559.00	19.17	1822.5000	12.7000
385	6584400.0	544.20	-0.001300	27916.00	24559.00	13.67	1822.5000	12.7000
386	6550000.0	545.53	-0.001100	25994.00	23875.00	8.88	1822.5000	12.7000
387	6508600.0	546.67	-0.000910	24214.00	23875.00	1.42	1822.5000	12.7000
388	6674100.0	543.12	-0.001560	30137.00	25682.00	17.35	1822.5000	12.7000
389	6777500.0	527.53	-0.003140	43450.00	33933.00	28.05	1822.5000	12.7000
390	6756800.0	526.39	-0.003180	43959.00	33933.00	29.55	1822.5000	12.7000
391	6729200.0	526.37	-0.003130	43710.00	33933.00	28.81	1822.5000	12.7000
392	6681000.0	526.67	-0.003020	43126.00	32810.00	31.44	1822.5000	12.7000
393	6618900.0	528.06	-0.002810	41724.00	32078.00	30.07	1822.5000	12.7000
394	6570600.0	531.85	-0.002440	38677.00	32078.00	20.57	1822.5000	12.7000
395	6522400.0	535.76	-0.002030	35203.00	31541.00	11.61	1822.5000	12.7000
396	6474100.0	539.27	-0.001630	31599.00	28856.00	9.51	1822.5000	12.7000

397	6591300.0	508.94	-0.004140	51579.00	39304.00	31.23	1822.5000	12.7000
398	6556900.0	508.03	-0.004130	51711.00	39304.00	31.57	1822.5000	12.7000
399	6460300.0	508.50	-0.003910	50705.00	36863.00	37.55	1822.5000	12.7000
400	6384500.0	511.25	-0.003590	48956.00	36668.00	33.51	1822.5000	12.7000
401	6515500.0	508.15	-0.004040	51313.00	39304.00	30.55	1822.5000	12.7000
402	6322400.0	517.74	-0.003060	45242.00	35935.00	25.90	1822.5000	12.7000
403	6260300.0	523.42	-0.002530	41401.00	34226.00	20.96	1822.5000	12.7000
404	6212100.0	530.12	-0.001980	36414.00	30320.00	20.10	1822.5000	12.7000
405	6936100.0	558.39	0.001880	18532.00	19335.00	-4.15	1822.5000	12.7000
406	6915300.0	558.19	0.003010	18369.00	19335.00	-5.00	1822.5000	12.7000
407	6901600.0	558.05	0.004050	18238.00	19335.00	-5.67	1822.5000	12.7000
408	6880900.0	557.85	0.004280	18165.00	18309.00	-0.79	1822.5000	12.7000
409	6853300.0	557.58	0.004300	18110.00	17772.00	1.90	1822.5000	12.7000
410	6825800.0	557.31	0.004550	18032.00	17577.00	2.59	1822.5000	12.7000
411	6598200.0	552.53	-0.000330	20079.00	21385.00	-6.11	1822.5000	12.7000
412	6550000.0	554.54	0.000270	18044.00	21385.00	-15.62	1822.5000	12.7000
413	6407900.0	551.64	-0.000180	18847.00	20458.00	-7.87	1822.5000	12.7000
414	6653400.0	553.44	-0.000290	19885.00	21385.00	-7.01	1822.5000	12.7000
415	6432800.0	552.39	-0.000120	18515.00	20067.00	-7.73	1822.5000	12.7000
416	6377600.0	552.28	-0.000060	18075.00	19237.00	-6.04	1822.5000	12.7000
417	6336200.0	552.01	-0.000040	17909.00	19237.00	-6.90	1822.5000	12.7000
418	6208000.0	550.98	0.000150	17420.00	18846.00	-7.57	1822.5000	12.7000
419	6246600.0	551.39	0.000290	17466.00	18846.00	-7.32	1822.5000	12.7000
420	6212100.0	551.03	0.000510	17365.00	18358.00	-5.41	1822.5000	12.7000
421	6170800.0	550.59	0.000790	17272.00	17577.00	-1.74	1822.5000	12.7000
422	6129300.0	550.14	0.000980	17156.00	17577.00	-2.40	1822.5000	12.7000
423	6674100.0	535.63	-0.002300	36818.00	30320.00	21.43	1822.5000	12.7000
424	6694800.0	536.03	-0.002300	36730.00	30320.00	21.14	1822.5000	12.7000
425	6681000.0	535.76	-0.002300	36809.00	30320.00	21.40	1822.5000	12.7000
426	6610900.0	535.53	-0.002200	36269.00	29588.00	22.58	1822.5000	12.7000
427	6556100.0	533.26	-0.002300	37468.00	28056.00	33.55	1822.5000	12.7000
428	6501700.0	533.36	-0.002200	36903.00	28074.00	31.45	1822.5000	12.7000
429	6453400.0	541.29	-0.001400	29367.00	27537.00	6.65	1822.5000	12.7000
430	6825800.0	557.31	0.000370	18522.00	20067.00	-7.70	1822.5000	12.7000
431	6874000.0	557.78	0.000770	18584.00	20067.00	-7.39	1822.5000	12.7000
432	6860200.0	557.65	0.001310	18480.00	19401.00	-4.75	1822.5000	12.7000
433	6832600.0	557.38	0.001620	18380.00	18944.00	-2.98	1822.5000	12.7000
434	6812000.0	557.17	0.001720	18351.00	18944.00	-3.13	1822.5000	12.7000
435	6784400.0	556.90	0.001780	18283.00	18554.00	-1.46	1822.5000	12.7000
436	6756000.0	556.62	0.001770	18240.00	18554.00	-1.69	1822.5000	12.7000
437	6708500.0	556.14	0.001970	18129.00	18554.00	-2.29	1822.5000	12.7000
438	6708500.0	556.14	0.002090	18114.00	18554.00	-2.37	1822.5000	12.7000
439	6749900.0	546.53	-0.001300	27443.00	27879.00	-1.56	1822.5000	12.7000
440	6743000.0	544.24	-0.001550	29822.00	27879.00	6.97	1822.5000	12.7000
441	6729200.0	544.31	-0.001520	29576.00	26707.00	10.74	1822.5000	12.7000
442	6687900.0	544.24	-0.001460	29156.00	25504.00	14.32	1822.5000	12.7000
443	6639600.0	544.35	-0.001370	28452.00	25243.00	12.71	1822.5000	12.7000
444	6591300.0	544.66	-0.001260	27495.00	24559.00	11.95	1822.5000	12.7000
445	6550000.0	546.06	-0.001040	25391.00	24120.00	5.27	1822.5000	12.7000
446	6501700.0	510.83	-0.003840	50018.00	38474.00	30.00	1822.5000	12.7000
447	6007800.0	548.83	0.000290	17006.00	20116.00	-15.46	1822.5000	12.7000
448	6880900.0	557.85	0.001000	18555.00	20116.00	-7.76	1822.5000	12.7000
449	6860200.0	557.65	0.002400	18347.00	19335.00	-5.11	1822.5000	12.7000
450	6825800.0	557.31	0.002400	18274.00	17870.00	2.26	1822.5000	12.7000
451	6791300.0	556.97	0.002800	18173.00	17870.00	1.70	1822.5000	12.7000
452	6756800.0	556.62	0.002900	18092.00	17577.00	2.93	1822.5000	12.7000
453	6825800.0	557.31	0.002200	23446.00	28231.00	-16.95	235.0000	12.7000
454	6687900.0	555.94	0.003000	23055.00	26795.00	-13.96	235.0000	12.7000
455	6543100.0	554.47	0.003000	22716.00	26795.00	-15.22	235.0000	12.7000
456	6908400.0	558.12	0.004000	23476.00	26224.00	-10.48	235.0000	12.7000
457	6812000.0	557.17	0.004400	23221.00	26224.00	-11.45	235.0000	12.7000
458	6632700.0	555.38	0.004400	22805.00	26224.00	-13.04	235.0000	12.7000
459	6501700.0	554.05	0.004900	22477.00	25150.00	-10.63	235.0000	12.7000
460	6336200.0	552.33	0.004800	22091.00	26224.00	-15.76	235.0000	12.7000
461	6618900.0	543.78	-0.001400	41362.00	42722.00	-3.18	235.0000	12.7000
462	6584400.0	548.58	-0.000800	32712.00	36585.00	-10.59	235.0000	12.7000
463	6812000.0	543.93	-0.001700	44321.00	47390.00	-6.48	235.0000	12.7000
464	6377600.0	552.77	0.000004	22643.00	31150.00	-27.31	235.0000	12.7000
465	6867100.0	557.71	0.000005	23551.00	35642.00	-33.92	273.1000	12.7000
466	6770600.0	551.63	-0.000700	30221.00	35642.00	-15.21	273.1000	12.7000
467	6674100.0	552.06	-0.000500	27285.00	35642.00	-23.45	273.1000	12.7000
468	6632700.0	552.37	-0.000400	25931.00	33933.00	-23.58	273.1000	12.7000
469	6550000.0	554.54	0.000500	22773.00	31492.00	-27.69	273.1000	12.7000
470	6356900.0	552.55	0.001000	22284.00	27830.00	-19.93	273.1000	12.7000
471	6170800.0	550.59	0.001000	21850.00	27098.00	-19.37	273.1000	12.7000
472	5991500.0	548.65	0.002000	21320.00	24657.00	-13.53	273.1000	12.7000
473	6922300.0	558.25	0.002000	23467.00	26854.00	-12.61	273.1000	12.7000
474	6874000.0	557.78	0.002700	23288.00	25877.00	-10.01	273.1000	12.7000
475	6784400.0	556.90	0.003000	23078.00	25877.00	-10.82	273.1000	12.7000
476	6722300.0	556.28	0.003000	22934.00	26121.00	-12.20	273.1000	12.7000
477	6563800.0	554.68	0.003000	22571.00	25145.00	-10.24	273.1000	12.7000
478	6405200.0	553.05	0.003500	22172.00	24901.00	-10.96	273.1000	12.7000
479	6246600.0	551.39	0.003700	21763.00	24266.00	-10.31	273.1000	12.7000
480	6984300.0	558.86	0.004500	23379.00	25145.00	-7.02	273.1000	12.7000
481	6936100.0	558.39	0.004200	23303.00	26854.00	-13.22	273.1000	12.7000
482	6887800.0	557.92	0.004500	23161.00	25145.00	-7.89	273.1000	12.7000
483	6805100.0	557.10	0.004500	22993.00	25145.00	-8.56	273.1000	12.7000
484	6667200.0	555.73	0.004500	22674.00	25145.00	-9.83	273.1000	12.7000
485	6529300.0	554.33	0.004800	22330.00	24413.00	-8.53	273.1000	12.7000
486	6391400.0	552.91	0.004700	22021.00	23729.00	-7.20	273.1000	12.7000
487	6894700.0	557.98	0.003000	28581.00	45075.00	-36.59	4.7000	12.7000
488	6825800.0	557.31	0.003500	28342.00	43737.00	-35.20	4.7000	12.7000
489	6756800.0	556.62	0.004000	28101.00	42970.00	-34.60	4.7000	12.7000
490	6687900.0	555.94	0.004000	28014.00	42600.00	-34.24	4.7000	12.7000
491	6584400.0	554.89	0.004300	27828.00	41872.00	-33.54	4.7000	12.7000
492	6550000.0	554.54	0.004500	27729.00	40271.00	-31.14	4.7000	12.7000
493	6481000.0	553.84	0.004600	27583.00	40271.00	-31.51	4.7000	12.7000
494	6260400.0	551.54	0.004700	27248.00	39836.00	-31.60	4.7000	12.7000
495	6274200.0	551.68	0.004700	27299.00	39836.00	-31.47	4.7000	12.7000
496	6205200.0	550.95	0.004700	27149.00	39304.00	-30.93	4.7000	12.7000
497	6101800.0	549.85	0.004700	27003.00	38787.00	-30.38	4.7000	12.7000

498	6607900.0	537.66	-0.002000	48396.00	58492.00	-17.26	4.7000	12.7000
499	6618900.0	537.86	-0.002000	48378.00	58492.00	-17.29	4.7000	12.7000
500	6584400.0	539.35	-0.001800	46701.00	54191.00	-13.82	4.7000	12.7000
501	6550000.0	544.62	-0.001200	41393.00	54586.00	-24.17	4.7000	12.7000
502	6377600.0	552.77	0.000004	29739.00	52267.00	-43.10	4.7000	12.7000
503	6791300.0	523.24	-0.003500	60194.00	57130.00	5.36	4.7000	12.7000
504	6687900.0	527.14	-0.003000	56859.00	56930.00	-0.12	4.7000	12.7000
505	6618900.0	528.20	-0.002800	55516.00	56930.00	-2.48	4.7000	12.7000
506	6584400.0	539.86	-0.001750	46285.00	55831.00	-17.10	4.7000	12.7000
507	6412100.0	539.61	-0.001500	44589.00	53795.00	-17.11	4.7000	12.7000
508	6308700.0	552.05	0.000004	29674.00	48971.00	-39.40	4.7000	12.7000
509	6825800.0	557.31	0.005000	27991.00	39621.00	-29.35	4.7000	12.7000
510	6805100.0	557.10	0.004500	28093.00	39836.00	-29.48	4.7000	12.7000
511	6756000.0	556.62	0.004500	28000.00	41404.00	-32.37	4.7000	12.7000
512	6722300.0	556.28	0.004500	27955.00	44397.00	-37.03	4.7000	12.7000
513	6618900.0	555.24	0.005100	27663.00	39206.00	-29.44	4.7000	12.7000
514	6570600.0	554.75	0.005400	27567.00	38689.00	-28.75	4.7000	12.7000
515	6515500.0	554.19	0.005500	27417.00	38689.00	-29.13	4.7000	12.7000
516	6412100.0	553.12	0.005600	27271.00	38181.00	-28.57	4.7000	12.7000
517	6343100.0	552.41	0.005700	27171.00	38181.00	-28.84	4.7000	12.7000
518	6294900.0	551.90	0.005700	27069.00	38181.00	-29.10	4.7000	12.7000
519	6205200.0	550.95	0.005900	26914.00	38186.00	-29.52	4.7000	12.7000
520	6088000.0	549.70	0.005900	26706.00	38181.00	-30.05	4.7000	12.7000
521	6067300.0	549.48	0.005900	26706.00	36668.00	-27.17	4.7000	12.7000
522	5963900.0	548.35	0.005900	26496.00	36668.00	-27.74	4.7000	12.7000
523	5860500.0	547.21	0.006000	26332.00	36668.00	-28.19	4.7000	12.7000
524	6563800.0	479.18	-0.005900	76335.00	61227.00	24.68	4.7000	12.7000
525	6460300.0	507.08	-0.004000	65607.00	59029.00	11.14	4.7000	12.7000
526	6412100.0	511.90	-0.003600	62893.00	59029.00	6.55	4.7000	12.7000
527	6274200.0	524.06	-0.002500	54862.00	57662.00	-4.86	4.7000	12.7000
528	6205200.0	536.12	-0.001500	45259.00	53600.00	-15.56	4.7000	12.7000
529	6053500.0	541.54	-0.000800	38310.00	51359.00	-25.41	4.7000	12.7000
530	5963900.0	543.46	-0.000500	35060.00	49460.00	-29.11	4.7000	12.7000
531	5791500.0	544.40	-0.000200	31482.00	47243.00	-33.36	4.7000	12.7000
532	5667400.0	545.03	0.000100	28532.00	45632.00	-37.47	4.7000	12.7000
533	6515500.0	554.19	0.004400	27683.00	42966.00	-35.57	4.7000	12.7000
534	6205200.0	550.95	0.005200	27032.00	40266.00	-32.87	4.7000	12.7000
535	4743600.0	533.76	0.001800	25720.00	39499.00	-34.88	4.7000	12.7000
536	4743600.0	533.76	0.001800	25720.00	39499.00	-34.88	4.7000	12.7000
537	4688400.0	533.03	0.001800	25640.00	39499.00	-35.09	4.7000	12.7000
538	4688400.0	533.03	0.002000	25542.00	38323.00	-33.35	4.7000	12.7000
539	4633200.0	532.30	0.002100	25380.00	37585.00	-32.47	4.7000	12.7000
540	4598800.0	531.84	0.002200	25270.00	37585.00	-32.77	4.7000	12.7000
541	4440200.0	529.68	0.002400	24856.00	36961.00	-32.75	4.7000	12.7000
542	4412600.0	529.30	0.002600	24730.00	36961.00	-33.09	4.7000	12.7000
543	4357500.0	528.53	0.002600	24577.00	34636.00	-29.04	4.7000	12.7000
544	4274700.0	527.37	0.002600	24448.00	33162.00	-26.28	4.7000	12.7000
545	6887800.0	557.92	0.001000	21915.00	24046.00	-8.86	322.2000	12.7000
546	6846400.0	557.51	0.002000	21765.00	24046.00	-9.49	322.2000	12.7000
547	6853300.0	557.58	0.002500	21722.00	23045.00	-5.74	322.2000	12.7000
548	6860200.0	557.65	0.003000	21708.00	22704.00	-4.39	322.2000	12.7000
549	6453400.0	553.55	0.003000	20839.00	22704.00	-8.21	322.2000	12.7000
550	6322400.0	552.19	0.003200	20540.00	22704.00	-9.53	322.2000	12.7000
551	6681000.0	555.87	0.002000	21410.00	22948.00	-6.70	322.2000	12.7000
552	6550000.0	554.54	0.002000	21122.00	22948.00	-7.96	322.2000	12.7000
553	6419000.0	553.20	0.002000	20860.00	22948.00	-9.10	322.2000	12.7000
554	6281100.0	551.76	0.002500	20520.00	22948.00	-10.58	322.2000	12.7000
555	6880900.0	557.85	0.003000	21756.00	22826.00	-4.69	322.2000	12.7000
556	6846400.0	557.51	0.003000	21685.00	22826.00	-5.00	322.2000	12.7000
557	6777500.0	556.83	0.003000	21514.00	22826.00	-5.75	322.2000	12.7000
558	6729200.0	556.35	0.003000	21419.00	22826.00	-6.16	322.2000	12.7000
559	6612000.0	555.17	0.003000	21179.00	22826.00	-7.22	322.2000	12.7000
560	6384500.0	552.84	0.003500	20645.00	22826.00	-9.55	322.2000	12.7000
561	6687900.0	539.07	-0.002000	39671.00	40525.00	-2.11	322.2000	12.7000
562	6639600.0	542.22	-0.001600	35764.00	34666.00	3.17	322.2000	12.7000
563	6598200.0	542.53	-0.001500	34888.00	31248.00	11.65	322.2000	12.7000
564	6563800.0	546.60	-0.001000	29191.00	28563.00	2.20	322.2000	12.7000
565	6501700.0	545.77	-0.001000	29395.00	25633.00	14.68	322.2000	12.7000
566	6350000.0	549.14	-0.000400	22952.00	23924.00	-4.06	322.2000	12.7000
567	6191400.0	548.62	-0.000250	21783.00	22948.00	-5.08	322.2000	12.7000
568	6026000.0	548.11	-0.000100	20670.00	22215.00	-6.95	322.2000	12.7000
569	6943000.0	558.46	0.002000	21140.00	22752.00	-7.09	512.7000	12.7000
570	6894700.0	557.98	0.002000	21047.00	22752.00	-7.49	512.7000	12.7000
571	6756800.0	556.62	0.002500	20730.00	22752.00	-8.89	512.7000	12.7000
572	6610900.0	555.16	0.002500	20417.00	22069.00	-7.49	512.7000	12.7000
573	6401000.0	553.01	0.003000	19942.00	22069.00	-9.64	512.7000	12.7000
574	6343100.0	552.41	0.003000	19819.00	22069.00	-10.20	512.7000	12.7000
575	6904300.0	558.08	0.002500	21012.00	22362.00	-6.04	512.7000	12.7000
576	6943000.0	558.46	0.002500	21109.00	22362.00	-5.60	512.7000	12.7000
577	6825800.0	557.31	0.003500	20781.00	22362.00	-7.07	512.7000	12.7000
578	6694800.0	556.00	0.003500	20516.00	22362.00	-8.26	512.7000	12.7000
579	6570600.0	554.75	0.004000	20212.00	22362.00	-9.61	512.7000	12.7000
580	6439600.0	553.41	0.004000	19940.00	22069.00	-9.65	512.7000	12.7000
581	6556900.0	530.77	-0.002500	43824.00	41013.00	6.85	512.7000	12.7000
582	6453400.0	534.80	-0.002000	39380.00	39792.00	-1.04	512.7000	12.7000
583	6343100.0	538.48	-0.001500	34569.00	31736.00	8.93	512.7000	12.7000
584	6301800.0	537.78	-0.001500	34738.00	29539.00	17.60	512.7000	12.7000
585	6232800.0	542.02	-0.001000	29031.00	25487.00	13.91	512.7000	12.7000
586	6060400.0	545.67	-0.000400	21937.00	21971.00	-0.15	512.7000	12.7000
587	6867100.0	557.71	0.001000	21070.00	23045.00	-8.57	512.7000	12.7000
588	6825800.0	557.31	0.001500	20940.00	23045.00	-9.13	512.7000	12.7000
589	6687900.0	555.94	0.002000	20622.00	23045.00	-10.51	512.7000	12.7000
590	6543100.0	554.47	0.002500	20271.00	21776.00	-6.91	512.7000	12.7000
591	6405200.0	553.05	0.002500	20007.00	21776.00	-8.12	512.7000	12.7000
592	6253500.0	551.47	0.003000	19620.00	21776.00	-9.90	512.7000	12.7000
593	6556900.0	536.74	-0.002000	37892.00	38816.00	-2.38	639.7000	12.7000
594	6460300.0	534.93	-0.002000	38387.00	35642.00	7.70	639.7000	12.7000
595	6288000.0	542.81	-0.001000	28107.00	23558.00	19.31	639.7000	12.7000
596	6239700.0	546.01	-0.000600	23367.00	22411.00	4.27	639.7000	12.7000
597	5977700.0	543.64	-0.000500	22431.00	21117.00	6.22	639.7000	12.7000
598	6901600.0	558.05	0.003000	20515.00	21776.00	-5.79	639.7000	12.7000

599	6687900.0	555.94	0.003000	20084.00	21776.00	-7.77	639.7000	12.7000
600	6474100.0	553.76	0.004000	19555.00	21776.00	-10.20	639.7000	12.7000
601	6929200.0	558.32	0.000500	20786.00	21117.00	-1.57	639.7000	12.7000
602	6887800.0	557.92	0.001000	20661.00	21117.00	-2.16	639.7000	12.7000
603	6632700.0	555.38	0.002000	20052.00	21117.00	-5.04	639.7000	12.7000
604	6377600.0	552.77	0.002000	19549.00	21117.00	-7.43	639.7000	12.7000
605	6901600.0	558.05	0.002000	20598.00	21776.00	-5.41	639.7000	12.7000
606	6887800.0	557.92	0.002000	20575.00	21776.00	-5.52	639.7000	12.7000
607	6763700.0	556.69	0.002000	20313.00	21776.00	-6.72	639.7000	12.7000
608	6632700.0	555.38	0.002000	20052.00	21776.00	-7.92	639.7000	12.7000
609	6384500.0	552.84	0.002000	19547.00	21483.00	-9.01	639.7000	12.7000
610	6867100.0	557.71	0.001500	22476.00	26121.00	-13.95	195.2000	12.7000
611	6818900.0	557.24	0.002000	22336.00	25389.00	-12.02	195.2000	12.7000
612	6736100.0	556.42	0.002500	22125.00	24657.00	-10.27	195.2000	12.7000
613	6681000.0	555.87	0.002700	21975.00	24657.00	-10.88	195.2000	12.7000
614	6543100.0	554.47	0.002800	21672.00	24657.00	-12.11	195.2000	12.7000
615	6398300.0	552.98	0.003000	21351.00	24168.00	-11.66	195.2000	12.7000
616	6253500.0	551.47	0.003000	21031.00	23436.00	-10.26	195.2000	12.7000
617	6846400.0	557.51	0.004000	22253.00	24901.00	-10.63	195.2000	12.7000
618	6812000.0	557.17	0.003000	22245.00	24901.00	-10.67	195.2000	12.7000
619	6694800.0	556.00	0.004000	21913.00	24412.00	-10.24	195.2000	12.7000
620	6577500.0	554.82	0.004000	21669.00	24412.00	-11.24	195.2000	12.7000
621	6460300.0	553.62	0.004000	21424.00	23436.00	-8.59	195.2000	12.7000
622	6336200.0	552.33	0.004500	21099.00	23436.00	-9.97	195.2000	12.7000
623	6853300.0	546.27	-0.001500	34904.00	42722.00	-18.30	195.2000	12.7000
624	6784400.0	545.29	-0.001500	35161.00	40036.00	-12.18	195.2000	12.7000
625	6729200.0	546.24	-0.001300	33156.00	38816.00	-14.58	195.2000	12.7000
626	6667200.0	547.11	-0.001100	31106.00	36619.00	-15.06	195.2000	12.7000
627	6612000.0	550.56	-0.000600	25374.00	34861.00	-27.21	195.2000	12.7000
628	6570600.0	550.88	-0.000500	24491.00	31346.00	-21.87	195.2000	12.7000
629	6529300.0	552.00	-0.000300	23204.00	29539.00	-21.45	195.2000	12.7000
630	6494800.0	553.98	0.000004	21811.00	29100.00	-25.05	195.2000	12.7000
631	6136300.0	550.22	0.000700	20965.00	24022.00	-12.73	195.2000	12.7000
632	5950100.0	548.20	0.000900	20515.00	23094.00	-11.17	195.2000	12.7000
633	6625800.0	555.31	0.006100	24554.00	32469.00	-24.38	44.5000	19.0000
634	6439600.0	553.41	0.006700	24107.00	32469.00	-25.75	44.5000	19.0000
635	6343100.0	552.41	0.007100	23871.00	30760.00	-22.40	44.5000	19.0000
636	6253500.0	551.47	0.007600	23636.00	30760.00	-23.16	44.5000	19.0000
637	6157000.0	550.44	0.007600	23423.00	30760.00	-23.85	44.5000	19.0000
638	5963900.0	548.35	0.007900	22977.00	30760.00	-25.30	44.5000	19.0000
639	5757100.0	546.05	0.007700	22526.00	30760.00	-26.77	44.5000	19.0000
640	6632700.0	555.38	0.006300	24541.00	33933.00	-27.68	44.5000	19.0000
641	6550000.0	554.54	0.006600	24357.00	32469.00	-24.98	44.5000	19.0000
642	6356900.0	552.55	0.008300	23787.00	32469.00	-26.74	44.5000	19.0000
643	6157000.0	550.44	0.009000	23290.00	29783.00	-21.80	44.5000	19.0000
644	6060400.0	549.40	0.009200	23053.00	29783.00	-22.60	44.5000	19.0000
645	5957000.0	548.27	0.009900	22759.00	29783.00	-23.58	44.5000	19.0000
646	5853600.0	547.13	0.009000	22618.00	29783.00	-24.06	44.5000	19.0000
647	6577500.0	552.54	-0.000300	29542.00	51266.00	-42.38	44.5000	19.0000
648	6419000.0	553.20	0.001500	24698.00	46628.00	-47.03	44.5000	19.0000
649	6288000.0	551.83	0.003000	24203.00	36619.00	-33.91	44.5000	19.0000
650	6157000.0	550.44	0.004000	23813.00	36619.00	-34.97	44.5000	19.0000
651	6032900.0	549.10	0.004400	23498.00	33933.00	-30.75	44.5000	19.0000
652	5929400.0	547.97	0.005000	23207.00	33933.00	-31.61	44.5000	19.0000
653	5819100.0	546.75	0.006900	22766.00	30760.00	-25.99	44.5000	19.0000
654	5708800.0	545.51	0.008700	22318.00	29295.00	-23.82	44.5000	19.0000
655	5590500.0	544.15	0.008700	22057.00	29295.00	-24.71	44.5000	19.0000
656	6894700.0	557.98	0.005000	23771.00	27781.00	-14.43	732.0000	54.0000
657	6584400.0	554.89	0.006100	22948.00	27781.00	-17.40	732.0000	54.0000
658	6446500.0	553.48	0.006200	22601.00	27781.00	-18.65	732.0000	54.0000
659	6260400.0	551.54	0.006450	22133.00	27781.00	-20.33	732.0000	54.0000
660	6722300.0	556.28	0.008250	23472.00	24803.00	-5.37	696.0000	76.2000
661	6377600.0	552.77	0.009250	22569.00	24803.00	-9.01	696.0000	76.2000
662	6101800.0	549.85	0.009900	21844.00	24803.00	-11.93	696.0000	76.2000
663	6929500.0	552.01	-0.000900	36884.00	43757.00	-15.71	63.5000	28.0000
664	6232800.0	545.46	-0.000650	34857.00	43923.00	-20.64	63.5000	28.0000
665	6812000.0	557.17	0.000005	25274.00	40671.00	-37.86	63.5000	28.0000
666	6798200.0	557.03	0.003000	24859.00	32298.00	-23.03	63.5000	28.0000
667	6770600.0	556.76	0.003000	24814.00	31932.00	-22.29	63.5000	28.0000

For 667 Data Points, Average Error = -14.71 %, STD = 20.32 %
For 212 Subcooled Data Points, Average Error = 0.54 %, STD = 21.06 %
For 455 Saturated Data Points, Average Error = -21.81 %, STD = 15.51 %

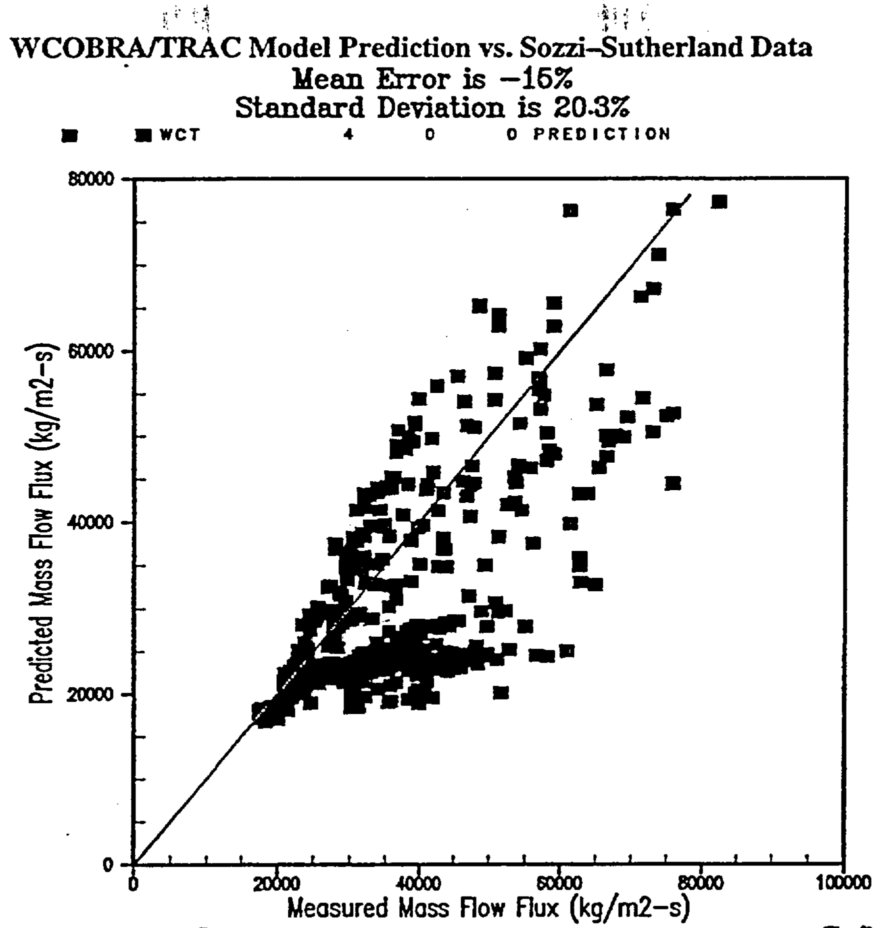

Figure 13-4-26 Prediction Comparison with Sozzi-Sutherland Data

Marviken Tests 6, 7, 23 and 24

Run No.	Pressure (Pa)	Temperature (K)	Quality	Predicted Gc (Kg/m2-s)	Measured Gc (Kg/m2-s)	Error (Gp-Gm)/Gm (in %)	L (mm)	D (mm)
1	4664000.0	503.45	-0.001469	56961.00	57833.00	-1.51	300.0000	300.0000
2	4847000.0	502.85	-0.001706	60041.00	59828.00	0.36	300.0000	300.0000
3	4830000.0	502.85	-0.001686	59808.00	60451.00	-1.06	300.0000	300.0000
4	5009000.0	503.45	-0.001878	61843.00	59800.00	3.42	300.0000	300.0000
5	4907000.0	503.55	-0.001746	60353.00	59107.00	2.11	300.0000	300.0000
6	4938000.0	503.15	-0.001803	61095.00	59955.00	1.90	300.0000	300.0000
7	4822000.0	503.65	-0.001640	59116.00	58498.00	1.06	300.0000	300.0000
8	4889000.0	503.85	-0.001711	59895.00	58442.00	2.49	300.0000	300.0000
9	4800000.0	503.95	-0.001601	58510.00	58852.00	-0.58	300.0000	300.0000
10	4847000.0	503.95	-0.001656	59244.00	57749.00	2.59	300.0000	300.0000
11	4742000.0	504.55	-0.001507	57221.00	57324.00	-0.18	300.0000	300.0000
12	4772000.0	504.35	-0.001550	57799.00	56306.00	2.65	300.0000	300.0000
13	4683000.0	505.45	-0.001401	55599.00	56037.00	-0.78	300.0000	300.0000
14	4654000.0	505.55	-0.001365	55106.00	57409.00	-4.01	300.0000	300.0000
15	4702000.0	505.65	-0.001413	55759.00	56829.00	-1.88	300.0000	300.0000
16	4689000.0	506.35	-0.001367	54938.00	55103.00	-0.30	300.0000	300.0000
17	4677000.0	506.45	-0.001349	54672.00	54410.00	0.48	300.0000	300.0000
18	4582000.0	506.45	-0.001248	53185.00	54382.00	-2.20	300.0000	300.0000
19	4540000.0	506.85	-0.001188	52172.00	54551.00	-4.36	300.0000	300.0000
20	4699000.0	507.15	-0.001342	54433.00	54268.00	0.30	300.0000	300.0000
21	4526000.0	506.75	-0.001178	52037.00	54127.00	-3.86	300.0000	300.0000
22	4487000.0	507.15	-0.001122	51049.00	52061.00	-1.94	300.0000	300.0000
23	4409000.0	507.55	-0.001028	49424.00	54325.00	-9.02	300.0000	300.0000
24	4507000.0	508.25	-0.001094	50410.00	52514.00	-4.01	300.0000	300.0000
25	4446000.0	508.45	-0.001026	49203.00	52415.00	-6.13	300.0000	300.0000
26	4460000.0	509.25	-0.001004	48617.00	52557.00	-7.50	300.0000	300.0000
27	4326000.0	511.45	-0.000787	43978.00	52458.00	-16.17	300.0000	300.0000
28	4385000.0	515.65	-0.000658	40200.00	50449.00	-20.32	300.0000	300.0000
29	4386000.0	516.55	-0.000620	39082.00	49458.00	-20.98	300.0000	300.0000
30	4472000.0	517.25	-0.000663	40022.00	47690.00	-16.08	300.0000	300.0000
31	4407000.0	517.65	-0.000589	38102.00	46332.00	-17.76	300.0000	300.0000
32	4405000.0	519.35	-0.000512	35688.00	45780.00	-22.04	300.0000	300.0000
33	4184000.0	519.65	-0.000326	29691.00	44733.00	-33.63	300.0000	300.0000
34	4260000.0	520.35	-0.000353	30567.00	44323.00	-31.04	300.0000	300.0000
35	4364000.0	516.95	-0.000584	38132.00	46714.00	-18.37	300.0000	300.0000
36	4383000.0	517.55	-0.000573	37708.00	44521.00	-15.30	300.0000	300.0000
37	4213000.0	518.25	-0.000407	32753.00	44677.00	-26.69	300.0000	300.0000
38	4175000.0	518.85	-0.000353	30789.00	44097.00	-30.18	300.0000	300.0000
39	4360000.0	517.75	-0.000545	36947.00	40093.00	-7.85	300.0000	300.0000
40	4071000.0	518.95	-0.000266	27752.00	32850.00	-15.52	300.0000	300.0000
41	4225000.0	518.95	-0.000386	31954.00	29964.00	6.64	300.0000	300.0000
42	4208000.0	520.35	-0.000314	29110.00	32411.00	-10.18	300.0000	300.0000
43	4181000.0	519.25	-0.000341	30274.00	30063.00	0.70	300.0000	300.0000
44	4102000.0	520.05	-0.000247	26644.00	31859.00	-16.37	300.0000	300.0000
45	4230000.0	520.35	-0.000330	29707.00	31746.00	-6.42	300.0000	300.0000
46	4180000.0	520.45	-0.000289	28174.00	30331.00	-7.11	300.0000	300.0000
47	4183000.0	523.05	-0.000156	23098.00	29737.00	-22.33	300.0000	300.0000
48	4175000.0	523.05	-0.000151	22819.00	29384.00	-22.34	300.0000	300.0000
49	4109000.0	522.85	-0.000115	21058.00	29186.00	-27.85	300.0000	300.0000
50	4064000.0	523.35	-0.000052	18696.00	26427.00	-29.25	300.0000	300.0000
51	4077000.0	522.65	-0.000099	20419.00	25309.00	-19.32	300.0000	300.0000
52	4068000.0	522.95	-0.000076	19509.00	25337.00	-23.00	300.0000	300.0000
53	4132000.0	522.65	-0.000143	22263.00	25295.00	-11.99	300.0000	300.0000
54	4116000.0	522.75	-0.000127	21506.00	24856.00	-13.48	300.0000	300.0000
55	4097000.0	522.45	-0.000127	21525.00	25295.00	-14.90	300.0000	300.0000
56	4028000.0	522.35	-0.000075	19436.00	23626.00	-17.73	300.0000	300.0000
57	4066000.0	522.35	-0.000106	20685.00	24319.00	-14.94	300.0000	300.0000
58	4042000.0	521.95	-0.000108	20753.00	24956.00	-16.84	300.0000	300.0000
59	4042000.0	521.55	-0.000129	21615.00	24022.00	-10.02	300.0000	300.0000
60	4039000.0	521.75	-0.000116	21063.00	24234.00	-13.08	300.0000	300.0000
61	4008000.0	521.55	-0.000102	20457.00	24687.00	-17.13	300.0000	300.0000
62	3994000.0	521.05	-0.000116	21058.00	24404.00	-13.71	300.0000	300.0000
63	3955000.0	521.05	-0.000084	19726.00	23696.00	-16.75	300.0000	300.0000
64	3967000.0	520.95	-0.000098	20346.00	23484.00	-13.36	300.0000	300.0000
65	3956000.0	520.65	-0.000101	20606.00	22876.00	-9.92	300.0000	300.0000
66	3954000.0	521.15	-0.000079	19497.00	23017.00	-15.29	300.0000	300.0000
67	3967000.0	520.95	-0.000098	20346.00	22621.00	-10.06	300.0000	300.0000
68	3954000.0	520.35	-0.000111	21197.00	23230.00	-8.75	300.0000	300.0000
69	3954000.0	520.35	-0.000111	21197.00	23215.00	-8.69	300.0000	300.0000
70	3910000.0	520.35	-0.000076	19689.00	22494.00	-12.47	300.0000	300.0000
71	3895000.0	519.75	-0.000088	20446.00	22692.00	-9.90	300.0000	300.0000
72	3898000.0	519.95	-0.000082	20115.00	21772.00	-7.61	300.0000	300.0000
73	3890000.0	519.75	-0.000084	20267.00	21051.00	-3.72	300.0000	300.0000
74	3889000.0	519.75	-0.000083	20236.00	22466.00	-9.93	300.0000	300.0000
75	3883000.0	519.45	-0.000090	20674.00	22338.00	-7.45	300.0000	300.0000
76	3847000.0	519.65	-0.000054	19026.00	21574.00	-11.81	300.0000	300.0000
77	3837000.0	519.45	-0.000056	19090.00	21985.00	-13.17	300.0000	300.0000
78	3826000.0	519.25	-0.000057	19123.00	21136.00	-9.52	300.0000	300.0000
79	3830000.0	519.05	-0.000067	19690.00	21546.00	-8.61	300.0000	300.0000
80	3827000.0	518.35	-0.000092	21081.00	21192.00	-0.52	300.0000	300.0000
81	3790000.0	518.45	-0.000065	19549.00	21376.00	-8.55	300.0000	300.0000
82	3809000.0	518.65	-0.000069	19812.00	20952.00	-5.44	300.0000	300.0000
83	3780000.0	518.15	-0.000071	19861.00	22169.00	-10.41	300.0000	300.0000
84	3765000.0	518.15	-0.000061	19329.00	21192.00	-8.79	300.0000	300.0000
85	3737000.0	517.85	-0.000056	18966.00	21150.00	-10.33	300.0000	300.0000
86	4630000.0	517.55	-0.000794	42779.00	52698.00	-18.82	300.0000	300.0000
87	4934000.0	516.45	-0.001158	49473.00	53632.00	-7.75	300.0000	300.0000
88	5014000.0	515.65	-0.001288	51581.00	54141.00	-4.73	300.0000	300.0000
89	4980000.0	517.45	-0.001159	49188.00	54127.00	-9.12	300.0000	300.0000
90	4827000.0	517.45	-0.000995	46554.00	56122.00	-17.05	300.0000	300.0000
91	4926000.0	516.45	-0.001149	49307.00	54622.00	-9.73	300.0000	300.0000
92	4868000.0	517.45	-0.001038	47252.00	53080.00	-10.98	300.0000	300.0000
93	4888000.0	517.15	-0.001074	47935.00	52401.00	-8.52	300.0000	300.0000

94	4951000.0	517.45	-0.001127	48665.00	52443.00	-7.20	300.0000	300.0000
95	4921000.0	517.85	-0.001075	47734.00	52825.00	-9.64	300.0000	300.0000
96	4767000.0	518.05	-0.000904	44738.00	51255.00	-12.71	300.0000	300.0000
97	4775000.0	517.95	-0.000917	45029.00	51255.00	-12.15	300.0000	300.0000
98	4847000.0	518.35	-0.000972	45903.00	50477.00	-9.06	300.0000	300.0000
99	4653000.0	519.35	-0.000732	41005.00	51326.00	-20.11	300.0000	300.0000
100	4768000.0	518.65	-0.000877	44085.00	49897.00	-11.65	300.0000	300.0000
101	4702000.0	519.05	-0.000793	42342.00	49501.00	-14.46	300.0000	300.0000
102	4637000.0	519.15	-0.000726	40946.00	50519.00	-18.95	300.0000	300.0000
103	4647000.0	519.25	-0.000731	40984.00	49472.00	-17.16	300.0000	300.0000
104	4613000.0	519.25	-0.000699	40288.00	50562.00	-20.32	300.0000	300.0000
105	4633000.0	519.35	-0.000713	40612.00	49600.00	-18.12	300.0000	300.0000
106	4637000.0	519.85	-0.000693	39992.00	48454.00	-17.46	300.0000	300.0000
107	4633000.0	519.95	-0.000685	39787.00	49331.00	-19.35	300.0000	300.0000
108	4596000.0	520.15	-0.000642	38769.00	49034.00	-20.93	300.0000	300.0000
109	4437000.0	520.25	-0.000498	35117.00	47605.00	-26.23	300.0000	300.0000
110	4558000.0	520.15	-0.000607	37946.00	47251.00	-19.69	300.0000	300.0000
111	4600000.0	520.55	-0.000626	38280.00	47379.00	-19.20	300.0000	300.0000
112	4623000.0	520.85	-0.000633	38358.00	46233.00	-17.03	300.0000	300.0000
113	4427000.0	520.85	-0.000463	33921.00	47251.00	-28.21	300.0000	300.0000
114	4429000.0	521.75	-0.000415	32572.00	47605.00	-31.58	300.0000	300.0000
115	4532000.0	522.15	-0.000477	34417.00	45426.00	-24.24	300.0000	300.0000
116	4482000.0	523.15	-0.000375	31550.00	44365.00	-28.89	300.0000	300.0000
117	4509000.0	523.85	-0.000356	31068.00	45271.00	-31.37	300.0000	300.0000
118	4445000.0	523.95	-0.000299	29190.00	44648.00	-34.62	300.0000	300.0000
119	4290000.0	524.25	-0.000165	23974.00	42654.00	-43.79	300.0000	300.0000
120	4417000.0	524.45	-0.000248	27456.00	41225.00	-33.40	300.0000	300.0000
121	4339000.0	524.65	-0.000178	24702.00	42003.00	-41.19	300.0000	300.0000
122	4541000.0	525.35	-0.000295	29218.00	37065.00	-21.17	300.0000	300.0000
123	4424000.0	525.25	-0.000207	26058.00	33034.00	-21.12	300.0000	300.0000
124	4369000.0	525.25	-0.000166	24352.00	27941.00	-12.84	300.0000	300.0000
125	4388000.0	524.95	-0.000196	25586.00	26993.00	-5.21	300.0000	300.0000
126	4344000.0	525.05	-0.000158	24000.00	29171.00	-17.73	300.0000	300.0000
127	4346000.0	524.95	-0.000165	24271.00	30855.00	-21.34	300.0000	300.0000
128	4400000.0	525.05	-0.000200	25733.00	29638.00	-13.18	300.0000	300.0000
129	4362000.0	525.25	-0.000161	24128.00	29865.00	-19.21	300.0000	300.0000
130	4322000.0	526.05	-0.000095	21124.00	29086.00	-27.37	300.0000	300.0000
131	4304000.0	525.85	-0.000092	20971.00	28549.00	-26.54	300.0000	300.0000
132	4307000.0	525.85	-0.000094	21065.00	26681.00	-21.05	300.0000	300.0000
133	4305000.0	525.75	-0.000097	21237.00	26144.00	-18.77	300.0000	300.0000
134	4294000.0	525.85	-0.000084	20658.00	25790.00	-19.90	300.0000	300.0000
135	4273000.0	525.85	-0.000070	20032.00	25408.00	-21.16	300.0000	300.0000
136	4267000.0	525.05	-0.000103	21512.00	25960.00	-17.13	300.0000	300.0000
137	4221000.0	525.05	-0.000071	20050.00	24757.00	-19.01	300.0000	300.0000
138	4246000.0	524.75	-0.000106	21471.00	24927.00	-13.86	300.0000	300.0000
139	4231000.0	524.65	-0.000101	21208.00	24927.00	-14.92	300.0000	300.0000
140	4234000.0	524.35	-0.000120	21946.00	24475.00	-10.33	300.0000	300.0000
141	4219000.0	524.75	-0.000087	20601.00	24319.00	-15.29	300.0000	300.0000
142	4243000.0	524.55	-0.000115	21817.00	24687.00	-11.63	300.0000	300.0000
143	4208000.0	524.75	-0.000080	20259.00	24291.00	-16.60	300.0000	300.0000
144	4212000.0	523.95	-0.000127	22078.00	23838.00	-7.38	300.0000	300.0000
145	4154000.0	524.05	-0.000082	19986.00	24050.00	-16.90	300.0000	300.0000
146	4161000.0	524.05	-0.000087	20202.00	23074.00	-12.45	300.0000	300.0000
147	4158000.0	523.65	-0.000107	20951.00	23513.00	-10.90	300.0000	300.0000
148	4163000.0	523.65	-0.000110	21106.00	23484.00	-10.13	300.0000	300.0000
149	4150000.0	523.75	-0.000096	20471.00	23583.00	-13.20	300.0000	300.0000
150	4142000.0	523.85	-0.000085	20021.00	23696.00	-15.51	300.0000	300.0000
151	4119000.0	523.25	-0.000102	20528.00	23668.00	-13.27	300.0000	300.0000
152	4139000.0	523.45	-0.000105	20769.00	23626.00	-12.09	300.0000	300.0000
153	4092000.0	523.35	-0.000074	19467.00	23795.00	-18.19	300.0000	300.0000
154	4092000.0	523.05	-0.000090	20072.00	22593.00	-11.16	300.0000	300.0000
155	4065000.0	523.05	-0.000068	19245.00	22451.00	-14.28	300.0000	300.0000
156	4103000.0	522.85	-0.000110	20844.00	21475.00	-2.94	300.0000	300.0000
157	4022000.0	522.95	-0.000039	18276.00	23456.00	-22.08	300.0000	300.0000
158	4056000.0	522.75	-0.000077	19545.00	23046.00	-15.19	300.0000	300.0000
159	4042000.0	522.35	-0.000087	19892.00	23385.00	-14.94	300.0000	300.0000
160	4050000.0	521.95	-0.000115	20999.00	23187.00	-9.44	300.0000	300.0000
161	4016000.0	521.95	-0.000087	19871.00	22947.00	-13.40	300.0000	300.0000
162	4022000.0	521.55	-0.000113	20915.00	22352.00	-6.43	300.0000	300.0000
163	3989000.0	521.95	-0.000065	19021.00	21956.00	-13.37	300.0000	300.0000
164	3989000.0	521.65	-0.000081	19620.00	21589.00	-9.12	300.0000	300.0000
165	3973000.0	521.35	-0.000084	19704.00	22395.00	-12.02	300.0000	300.0000
166	3965000.0	521.05	-0.000092	20058.00	22239.00	-9.81	300.0000	300.0000
167	3935000.0	520.55	-0.000088	20109.00	22635.00	-11.16	300.0000	300.0000
168	3949000.0	519.95	-0.000123	21895.00	21857.00	0.17	300.0000	300.0000
169	3859000.0	520.25	-0.000039	18265.00	19268.00	-5.21	300.0000	300.0000
170	4693000.0	526.25	-0.000379	32227.00	28948.00	11.33	150.0000	500.0000
171	4926000.0	527.15	-0.000547	36124.00	30986.00	16.58	150.0000	500.0000
172	4872000.0	530.45	-0.000311	29287.00	35085.00	-16.53	150.0000	500.0000
173	4964000.0	530.75	-0.000379	31058.00	33639.00	-7.67	150.0000	500.0000
174	4731000.0	531.45	-0.000129	23345.00	30670.00	-23.88	150.0000	500.0000
175	5005000.0	531.85	-0.000351	30093.00	29081.00	3.48	150.0000	500.0000
176	4503000.0	531.85	0.000003	16860.00	26107.00	-35.42	150.0000	500.0000
177	4953000.0	531.65	-0.000314	29132.00	24675.00	18.06	150.0000	500.0000
178	4832000.0	531.65	-0.000204	25830.00	24584.00	5.07	150.0000	500.0000
179	4850000.0	531.65	-0.000220	26334.00	24080.00	9.36	150.0000	500.0000
180	4794000.0	531.65	-0.000171	24731.00	24706.00	0.10	150.0000	500.0000
181	4661000.0	531.35	-0.000077	21597.00	25164.00	-14.18	150.0000	500.0000
182	4703000.0	531.05	-0.000129	23382.00	24523.00	-4.65	150.0000	500.0000
183	4603000.0	530.65	-0.000071	21340.00	24706.00	-13.62	150.0000	500.0000
184	4519000.0	530.65	-0.000006	19440.00	23871.00	-18.56	150.0000	500.0000
185	4704000.0	530.55	-0.000159	24454.00	24375.00	0.32	150.0000	500.0000
186	4670000.0	530.15	-0.000153	24292.00	25460.00	-4.59	150.0000	500.0000
187	4704000.0	530.05	-0.000187	25465.00	24278.00	4.89	150.0000	500.0000
188	4693000.0	529.75	-0.000194	25777.00	23779.00	8.40	150.0000	500.0000
189	4541000.0	529.55	-0.000083	21736.00	23723.00	-8.38	150.0000	500.0000
190	4664000.0	529.35	-0.000192	25744.00	23703.00	8.61	150.0000	500.0000
191	4710000.0	529.35	-0.000231	27044.00	23448.00	15.34	150.0000	500.0000
192	4532000.0	529.05	-0.000102	22499.00	22898.00	-1.74	150.0000	500.0000
193	4578000.0	528.85	-0.000149	24281.00	23591.00	2.92	150.0000	500.0000
194	4541000.0	528.65	-0.000130	23600.00	23570.00	0.13	150.0000	500.0000

195	4541000.0	528.25	-0.000151	24413.00	23540.00	3.71	150.0000	500.0000
196	4358000.0	528.05	-0.000025	19580.00	23815.00	-17.78	150.0000	500.0000
197	4419000.0	527.95	-0.000074	21382.00	23901.00	-10.54	150.0000	500.0000
198	4430000.0	527.75	-0.000092	22116.00	23489.00	-5.85	150.0000	500.0000
199	4508000.0	527.35	-0.000171	25274.00	23596.00	7.11	150.0000	500.0000
200	4343000.0	526.85	-0.000072	21350.00	24288.00	-12.10	150.0000	500.0000
201	4325000.0	526.25	-0.000088	22020.00	22241.00	-0.99	150.0000	500.0000
202	4249000.0	525.75	-0.000058	20724.00	23204.00	-10.69	150.0000	500.0000
203	4292000.0	525.25	-0.000110	23067.00	23041.00	0.11	150.0000	500.0000
204	4284000.0	524.85	-0.000126	23639.00	22322.00	5.90	150.0000	500.0000
205	4139000.0	523.95	-0.000078	20947.00	21635.00	-3.18	150.0000	500.0000
206	4139000.0	523.55	-0.000099	21759.00	22384.00	-2.79	150.0000	500.0000
207	4142000.0	523.15	-0.000123	22666.00	22710.00	-0.19	150.0000	500.0000
208	4003000.0	522.05	-0.000071	20479.00	21762.00	-5.90	150.0000	500.0000
209	4046000.0	521.35	-0.000143	23299.00	23056.00	1.05	150.0000	500.0000
210	4003000.0	520.85	-0.000131	22942.00	22414.00	2.36	150.0000	500.0000
211	3845000.0	519.95	-0.000041	19591.00	22221.00	-11.84	150.0000	500.0000
212	3881000.0	519.25	-0.000096	22199.00	21217.00	4.63	150.0000	500.0000
213	3842000.0	518.35	-0.000101	22725.00	20418.00	11.30	150.0000	500.0000
214	4157000.0	502.05	-0.001019	50025.00	56491.00	-11.45	150.0000	500.0000
215	4273000.0	502.35	-0.001114	51658.00	55798.00	-7.42	150.0000	500.0000
216	3932000.0	502.55	-0.000776	45682.00	53639.00	-14.83	150.0000	500.0000
217	4256000.0	503.65	-0.001046	50264.00	52738.00	-4.69	150.0000	500.0000
218	4124000.0	504.25	-0.000904	47554.00	52850.00	-10.02	150.0000	500.0000
219	3938000.0	504.25	-0.000719	44172.00	51510.00	-14.25	150.0000	500.0000
220	3871000.0	504.55	-0.000644	42639.00	49717.00	-14.24	150.0000	500.0000
221	3905000.0	504.55	-0.000676	43282.00	47691.00	-9.24	150.0000	500.0000
222	3829000.0	504.65	-0.000605	41722.00	47023.00	-11.27	150.0000	500.0000
223	3495000.0	504.85	-0.000357	34295.00	45587.00	-24.77	150.0000	500.0000
224	3632000.0	504.65	-0.000460	37609.00	45944.00	-18.14	150.0000	500.0000
225	3537000.0	504.75	-0.000389	35373.00	44360.00	-20.26	150.0000	500.0000
226	3311000.0	504.85	-0.000237	29554.00	42664.00	-30.73	150.0000	500.0000
227	3483000.0	504.75	-0.000353	34080.00	42745.00	-20.27	150.0000	500.0000
228	3317000.0	504.75	-0.000244	29847.00	45974.00	-35.08	150.0000	500.0000
229	3051000.0	504.95	-0.000078	21204.00	40474.00	-47.61	150.0000	500.0000
230	3121000.0	504.85	-0.000121	23837.00	39832.00	-40.16	150.0000	500.0000
231	3253000.0	504.95	-0.000198	27784.00	38676.00	-28.16	150.0000	500.0000
232	3426000.0	505.05	-0.000305	32346.00	37337.00	-13.37	150.0000	500.0000
233	3186000.0	505.15	-0.000151	25434.00	35259.00	-27.87	150.0000	500.0000
234	3103000.0	505.25	-0.000099	22514.00	34113.00	-34.00	150.0000	500.0000
235	2792000.0	505.25	0.000002	12664.00	28979.00	-56.30	150.0000	500.0000
236	2812000.0	505.25	0.000002	12943.00	27894.00	-53.60	150.0000	500.0000
237	3115000.0	505.55	-0.000097	22395.00	25862.00	-13.41	150.0000	500.0000
238	2984000.0	505.55	-0.000024	17478.00	22786.00	-23.30	150.0000	500.0000
239	3143000.0	505.45	-0.000116	23544.00	22898.00	2.82	150.0000	500.0000
240	2900000.0	505.35	0.000002	14800.00	21059.00	-29.72	150.0000	500.0000
241	2970000.0	505.25	-0.000025	17519.00	20464.00	-14.39	150.0000	500.0000
242	2895000.0	504.85	0.000002	15425.00	19486.00	-20.84	150.0000	500.0000
243	3004000.0	505.15	-0.000046	19041.00	18966.00	0.40	150.0000	500.0000
244	2880000.0	504.75	0.000002	15074.00	17953.00	-16.04	150.0000	500.0000
245	2868000.0	504.35	0.000002	15315.00	17820.00	-14.06	150.0000	500.0000
246	2870000.0	503.45	-0.000021	17095.00	20122.00	-15.04	150.0000	500.0000
247	2782000.0	503.05	0.000002	14496.00	19328.00	-25.00	150.0000	500.0000
248	2838000.0	502.45	-0.000031	17729.00	19027.00	-6.82	150.0000	500.0000
249	2718000.0	501.75	0.000002	14378.00	17647.00	-18.52	150.0000	500.0000
250	2756000.0	501.45	-0.000014	16369.00	18406.00	-11.07	150.0000	500.0000
251	2730000.0	500.55	-0.000023	17054.00	17708.00	-3.69	150.0000	500.0000
252	2722000.0	499.65	-0.000042	18461.00	16848.00	9.57	150.0000	500.0000

For 252 Data Points, Average Error = -12.24 %, STD = 11.56 %
For 243 Subcooled Data Points, Average Error = -11.58 %, STD = 10.87 %
For 9 Saturated Data Points, Average Error = -29.94 %, STD = 15.68 %

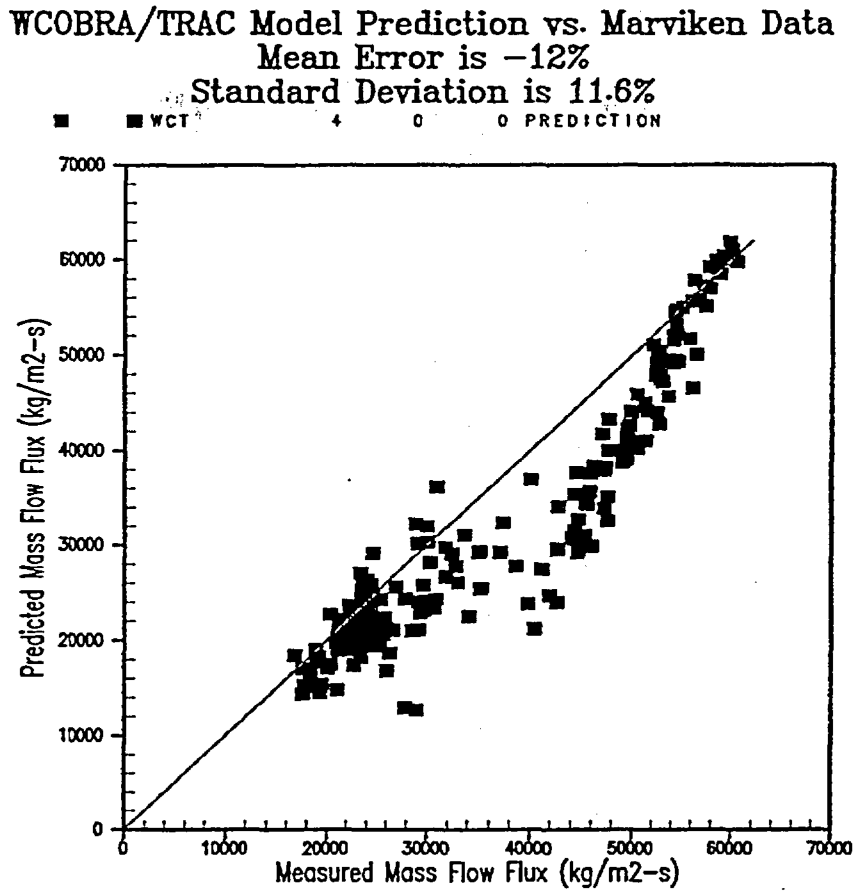

Figure 13-4-27 Prediction Comparison with Marviken Data

Amos and Schrock

Run No.	Pressure (Pa)	Temperature (K)	Quality	Predicted Gc (Kg/m2-s)	Measured Gc (Kg/m2-s)	Error (Gp-Gm)/Gm (in %)	L (mm)	D (mm)
1	7073000.0	530.11	-0.003522	47138.00	44160.00	6.74	63.5000	0.7480
2	7077000.0	544.15	-0.002142	37030.00	33980.00	8.98	63.5000	0.7480
3	7091000.0	553.69	-0.000931	24547.00	25220.00	-2.67	63.5000	0.7480
4	7093000.0	500.31	-0.005817	59298.00	57810.00	2.57	63.5000	0.7480
5	9595000.0	521.74	-0.011554	59922.00	57920.00	3.46	63.5000	0.7080
6	11580000.0	541.80	-0.017580	58551.00	57830.00	1.25	63.5000	0.7080
7	9584000.0	551.16	-0.007416	45819.00	43940.00	4.28	63.5000	0.7080
8	9619000.0	566.22	-0.004212	34961.00	33230.00	5.21	63.5000	0.7080
9	11608000.0	566.68	-0.011275	45903.00	44480.00	3.20	63.5000	0.7080
10	4220000.0	498.59	-0.001212	33778.00	32560.00	3.74	63.5000	0.7470
11	4187000.0	512.21	-0.000638	26058.00	25260.00	3.16	63.5000	0.7470
12	4271000.0	468.02	-0.002387	40811.00	40990.00	-0.44	63.5000	0.7470
13	4134000.0	522.54	-0.000151	16499.00	14330.00	15.14	63.5000	0.7470
14	15398000.0	562.80	-0.037795	68735.00	69690.00	-1.37	63.5000	0.7470
15	9542000.0	580.74	0.000008	21910.00	26630.00	-17.72	63.5000	0.7470
16	11672000.0	583.90	-0.005217	35246.00	38600.00	-8.69	63.5000	0.7470
17	15452000.0	591.18	-0.021448	52698.00	52960.00	-0.49	63.5000	0.7470
18	11672000.0	593.60	-0.000980	26333.00	30580.00	-13.89	63.5000	0.7470
19	4289000.0	467.97	-0.002411	35559.00	35000.00	1.60	63.5000	0.4640
20	4320000.0	497.31	-0.001362	28951.00	28460.00	1.73	63.5000	0.4640
21	4281000.0	512.56	-0.000702	22778.00	21600.00	5.45	63.5000	0.4640
22	4272000.0	522.53	-0.000249	17007.00	16870.00	0.81	63.5000	0.4640
23	7117000.0	498.94	-0.005968	47691.00	42710.00	11.66	63.5000	0.5020
24	7050000.0	499.19	-0.005790	41809.00	40910.00	2.20	63.5000	0.4180
25	7055000.0	530.34	-0.003467	38811.00	36410.00	6.59	63.5000	0.5020
26	7055000.0	541.34	-0.002420	33988.00	31310.00	8.55	63.5000	0.5020
27	7000000.0	555.71	-0.000494	21242.00	20270.00	4.80	63.5000	0.5020
28	9553000.0	521.72	-0.011399	44577.00	44050.00	1.20	63.5000	0.4530
29	9600000.0	553.08	-0.007095	33601.00	32470.00	3.48	63.5000	0.4530
30	9667000.0	559.29	-0.005999	31164.00	27480.00	13.41	63.5000	0.4530
31	9602000.0	577.30	-0.001168	20847.00	21980.00	-5.15	63.5000	0.4180
32	9774000.0	524.49	-0.011858	48123.00	48830.00	-1.45	63.5000	0.5020
33	9609000.0	581.25	0.000008	18729.00	22540.00	-16.91	63.5000	0.5020
34	11728000.0	536.16	-0.019396	50162.00	49240.00	1.87	63.5000	0.4180
35	11601000.0	540.34	-0.017970	42448.00	44130.00	-3.81	63.5000	0.4530
36	11696000.0	565.86	-0.011934	39474.00	38520.00	2.48	63.5000	0.4180
37	12420000.0	538.95	-0.022870	51640.00	51370.00	0.53	63.5000	0.5020
38	11642000.0	569.11	-0.010627	38094.00	39010.00	-2.35	63.5000	0.5020
39	11838000.0	583.88	-0.005855	30077.00	32240.00	-6.71	63.5000	0.5020
40	11675000.0	593.52	-0.001027	22281.00	20580.00	8.27	63.5000	0.5020
41	15601000.0	564.26	-0.038999	56678.00	50190.00	12.93	63.5000	0.4640
42	15798000.0	607.48	-0.011009	32940.00	42310.00	-22.15	63.5000	0.5020
43	15747000.0	607.22	-0.010916	31214.00	37030.00	-15.71	63.5000	0.5020
44	15703000.0	616.79	-0.002074	26350.00	32920.00	-19.96	63.5000	0.5020

For 44 Data Points, Average Error = 0.13 %, STD = 8.78 %
For 42 Subcooled Data Points, Average Error = 0.96 %, STD = 8.08 %
For 2 Saturated Data Points, Average Error = -17.32 %, STD = 0.58 %

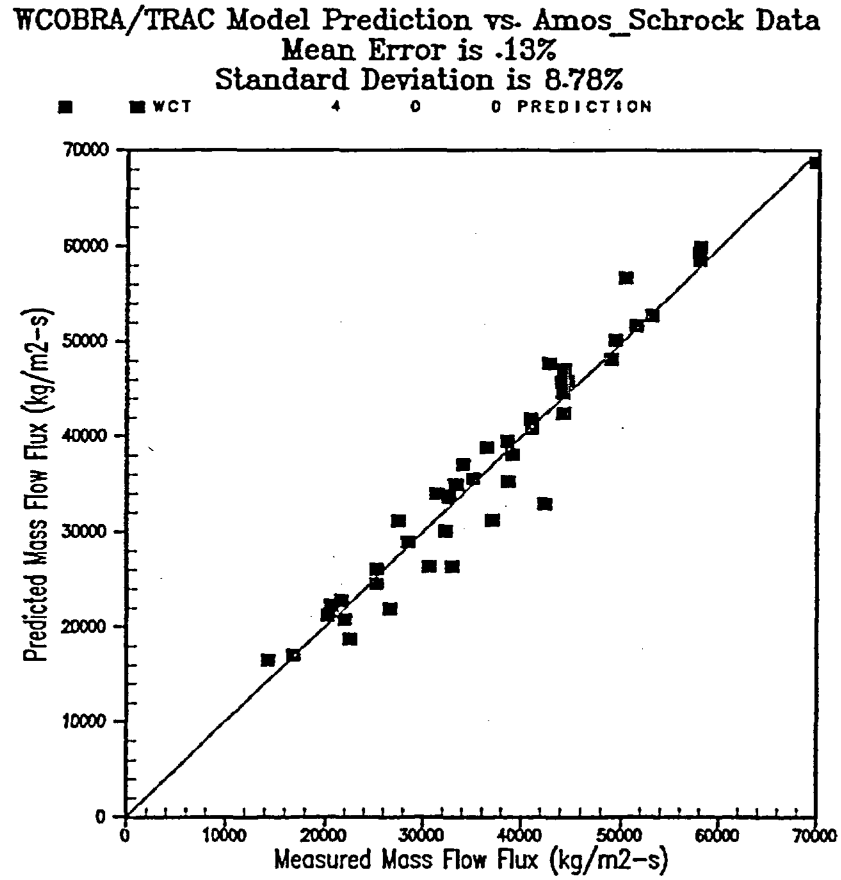

Figure 13-4-28 Prediction Comparison with Amos-Schrock Data

TPFL (Anderson and Benedetti)

Run No.	Pressure (Pa)	Temperature (K)	Quality	Predicted Gc (Kg/m2-s)	Measured Gc (Kg/m2-s)	Error (Gp-Gm)/Gm (in %)	L (mm)	D (mm)
1	3450000.0	514.67	0.990000	4723.60	4269.40	10.64	54.0000	16.2000
2	3450000.0	514.67	0.990000	4723.60	4511.90	4.69	54.0000	16.2000
3	3490000.0	515.33	0.000002	19951.00	29012.00	-31.23	54.0000	16.2000
4	3450000.0	514.67	0.001100	18656.00	27072.00	-31.09	54.0000	16.2000
5	3430000.0	514.33	0.001400	18462.00	22899.00	-19.38	54.0000	16.2000
6	3460000.0	514.83	0.007100	17107.00	17466.00	-2.06	54.0000	16.2000
7	3460000.0	514.83	0.002000	18292.00	17466.00	4.73	54.0000	16.2000
8	3440000.0	514.50	0.029000	15910.00	13778.00	15.47	54.0000	16.2000
9	3440000.0	514.50	0.026000	16001.00	13439.00	19.06	54.0000	16.2000
10	3440000.0	514.50	0.050000	15353.00	12954.00	18.52	54.0000	16.2000
11	3440000.0	514.50	0.045000	15475.00	12177.00	27.08	54.0000	16.2000
12	3450000.0	514.67	0.056000	15249.00	12663.00	20.42	54.0000	16.2000
13	3450000.0	514.67	0.810000	5946.90	4754.50	25.08	54.0000	16.2000
14	3470000.0	515.00	0.760000	6281.80	4900.10	28.20	54.0000	16.2000
15	3470000.0	515.00	0.690000	6752.90	4803.00	40.60	54.0000	16.2000
16	3460000.0	514.83	0.890000	5533.50	4609.00	20.06	54.0000	16.2000
17	3450000.0	514.67	0.001200	18600.00	27072.00	-31.29	54.0000	16.2000
18	3450000.0	514.67	0.001100	18656.00	15622.00	19.42	54.0000	16.2000
19	3440000.0	514.50	0.044000	15500.00	17320.00	-10.51	54.0000	16.2000
20	3450000.0	514.67	0.021000	16196.00	16883.00	-4.07	54.0000	16.2000
21	3470000.0	515.00	0.001300	18596.00	17320.00	7.37	54.0000	16.2000
22	3470000.0	515.00	0.067000	15062.00	18824.00	-19.99	54.0000	16.2000
23	3470000.0	515.00	0.001300	18596.00	17514.00	6.18	54.0000	16.2000
24	3450000.0	514.67	0.001300	18569.00	19164.00	-3.10	54.0000	16.2000
25	3440000.0	514.50	0.008000	16908.00	17708.00	-4.52	54.0000	16.2000
26	3470000.0	515.00	0.020000	15605.00	15185.00	2.77	54.0000	16.2000
27	3440000.0	514.50	0.026000	16001.00	14361.00	11.42	54.0000	16.2000
28	3470000.0	515.00	0.054000	15351.00	12954.00	18.50	54.0000	16.2000
29	3450000.0	514.67	0.280000	11190.00	7374.40	51.74	54.0000	16.2000
30	3450000.0	514.67	0.530000	8052.90	5821.90	38.32	54.0000	16.2000
31	3460000.0	514.83	0.220000	12179.00	8102.10	50.32	54.0000	16.2000
32	4470000.0	530.09	0.990000	6030.40	5724.80	5.34	54.0000	16.2000
33	4470000.0	530.09	0.990000	6030.40	5433.70	10.98	54.0000	16.2000
34	4450000.0	529.82	0.000003	21705.00	30856.00	-29.66	54.0000	16.2000
35	4410000.0	529.27	0.002600	20221.00	26101.00	-22.53	54.0000	16.2000
36	4440000.0	529.68	0.017000	18416.00	20134.00	-8.53	54.0000	16.2000
37	4440000.0	529.68	0.025000	17783.00	17369.00	2.38	54.0000	16.2000
38	4440000.0	529.68	0.023000	17943.00	17417.00	3.02	54.0000	16.2000
39	4440000.0	529.68	0.045000	18524.00	14652.00	26.43	54.0000	16.2000
40	4440000.0	529.68	0.042000	18618.00	15331.00	21.44	54.0000	16.2000
41	4420000.0	529.40	0.093000	17211.00	12517.00	37.50	54.0000	16.2000
42	4420000.0	529.40	0.089000	17304.00	12614.00	37.18	54.0000	16.2000
43	4420000.0	529.40	0.100000	17050.00	12371.00	37.82	54.0000	16.2000
44	4420000.0	529.40	0.096000	17141.00	12614.00	35.89	54.0000	16.2000
45	4430000.0	529.54	0.074000	17696.00	13390.00	32.16	54.0000	16.2000
46	4430000.0	529.54	0.630000	9064.80	6210.00	45.97	54.0000	16.2000
47	4400000.0	529.13	0.066000	17817.00	13633.00	30.69	54.0000	16.2000
48	4440000.0	529.68	0.094000	17242.00	13293.00	29.71	54.0000	16.2000
49	4470000.0	530.09	0.800000	7734.80	5918.90	30.68	54.0000	16.2000
50	4540000.0	531.05	0.670000	8902.80	6258.50	42.25	54.0000	16.2000
51	4450000.0	529.82	0.640000	9008.80	6695.10	34.56	54.0000	16.2000
52	4400000.0	529.13	0.860000	7212.10	4754.50	51.69	54.0000	16.2000
53	4440000.0	529.68	0.000450	21072.00	27848.00	-24.33	54.0000	16.2000
54	4400000.0	529.13	0.018000	18228.00	28285.00	-35.56	54.0000	16.2000
55	4470000.0	530.09	0.011000	19057.00	20231.00	-5.80	54.0000	16.2000
56	4420000.0	529.40	0.000230	21220.00	18339.00	15.71	54.0000	16.2000
57	4480000.0	530.23	0.030000	19147.00	17902.00	6.95	54.0000	16.2000
58	4410000.0	529.27	0.000260	21178.00	18630.00	13.68	54.0000	16.2000
59	4450000.0	529.82	0.017000	18431.00	17660.00	4.37	54.0000	16.2000
60	4400000.0	529.13	0.001400	20556.00	15088.00	36.24	54.0000	16.2000
61	4450000.0	529.82	0.043000	18616.00	16059.00	15.92	54.0000	16.2000
62	4410000.0	529.27	0.110000	16799.00	10819.00	55.27	54.0000	16.2000
63	4450000.0	529.82	0.130000	16479.00	10770.00	53.01	54.0000	16.2000
64	4430000.0	529.54	0.350000	12491.00	8732.80	43.04	54.0000	16.2000
65	6150000.0	550.36	0.990000	8142.60	7422.90	9.70	54.0000	16.2000
66	6260000.0	551.53	0.990000	8279.40	7762.50	6.66	54.0000	16.2000
67	6260000.0	551.53	0.990000	8279.40	7908.00	4.70	54.0000	16.2000
68	6260000.0	551.53	0.990000	8279.40	7859.50	5.34	54.0000	16.2000
69	6160000.0	550.47	0.000004	24575.00	33379.00	-26.38	54.0000	16.2000
70	6170000.0	550.58	0.000004	24599.00	32942.00	-25.33	54.0000	16.2000
71	6210000.0	551.00	0.001900	24070.00	32991.00	-27.04	54.0000	16.2000
72	6240000.0	551.32	0.000004	24703.00	29546.00	-16.39	54.0000	16.2000
73	6200000.0	550.90	0.000068	24544.00	27848.00	-11.86	54.0000	16.2000
74	6240000.0	551.32	0.015000	22915.00	24888.00	-7.93	54.0000	16.2000
75	6270000.0	551.64	0.030000	22098.00	22075.00	0.10	54.0000	16.2000
76	6220000.0	551.11	0.025000	22269.00	20037.00	11.14	54.0000	16.2000
77	6200000.0	550.90	0.058000	23041.00	18533.00	24.32	54.0000	16.2000
78	6200000.0	550.90	0.054000	23184.00	18921.00	22.53	54.0000	16.2000
79	6170000.0	550.58	0.091000	21916.00	17223.00	27.25	54.0000	16.2000
80	6170000.0	550.58	0.093000	21858.00	17029.00	28.36	54.0000	16.2000
81	6210000.0	551.00	0.120000	21227.00	16689.00	27.19	54.0000	16.2000
82	6280000.0	551.74	0.088000	22284.00	17320.00	28.66	54.0000	16.2000
83	6260000.0	551.53	0.090000	22175.00	17417.00	27.32	54.0000	16.2000
84	6230000.0	551.22	0.110000	21540.00	16641.00	29.44	54.0000	16.2000
85	6230000.0	551.22	0.700000	11699.00	8829.80	32.49	54.0000	16.2000
86	6250000.0	551.43	0.710000	11630.00	8781.30	32.44	54.0000	16.2000
87	6240000.0	551.32	0.160000	20292.00	17805.00	13.97	54.0000	16.2000
88	6240000.0	551.32	0.290000	17603.00	16544.00	6.40	54.0000	16.2000
89	6230000.0	551.22	0.960000	9413.90	7859.50	19.78	54.0000	16.2000
90	6220000.0	551.11	0.970000	9326.10	7762.50	20.14	54.0000	16.2000
91	6220000.0	551.11	0.999990	8229.70	7568.40	8.74	54.0000	16.2000
92	6190000.0	550.79	0.000550	24313.00	32117.00	-24.30	54.0000	16.2000
93	6220000.0	551.11	0.046000	23526.00	19843.00	18.56	54.0000	16.2000

94	6180000.0	550.69	0.009500	23222.00	30759.00	-24.50	54.0000	16.2000
95	6170000.0	550.58	0.028000	21968.00	19891.00	10.44	54.0000	16.2000
96	6220000.0	551.11	0.011000	23192.00	30371.00	-23.64	54.0000	16.2000
97	6220000.0	551.11	0.024000	22328.00	21347.00	4.60	54.0000	16.2000
98	6230000.0	551.22	0.015000	22909.00	32117.00	-28.67	54.0000	16.2000
99	6220000.0	551.11	0.036000	21686.00	20522.00	5.67	54.0000	16.2000
100	6270000.0	551.64	0.036000	21792.00	20279.00	7.46	54.0000	16.2000
101	6180000.0	550.69	0.038000	21478.00	19940.00	7.71	54.0000	16.2000
102	6200000.0	550.90	0.021000	22456.00	22317.00	0.62	54.0000	16.2000
103	6190000.0	550.79	0.012000	23045.00	22705.00	1.50	54.0000	16.2000
104	6210000.0	551.00	0.038000	21555.00	21056.00	2.37	54.0000	16.2000
105	6210000.0	551.00	0.089000	22075.00	17563.00	25.69	54.0000	16.2000
106	6230000.0	551.22	0.140000	20775.00	15768.00	31.75	54.0000	16.2000
107	6230000.0	551.22	0.220000	18964.00	14312.00	32.50	54.0000	16.2000
108	6220000.0	551.11	0.270000	17939.00	13390.00	33.97	54.0000	16.2000
109	6190000.0	550.79	0.580000	13003.00	9751.60	33.34	54.0000	16.2000

For 109 Data Points, Average Error = 11.96 %, STD = 22.20 %
For 109 Saturated Data Points, Average Error = 11.96 %, STD = 22.20 %

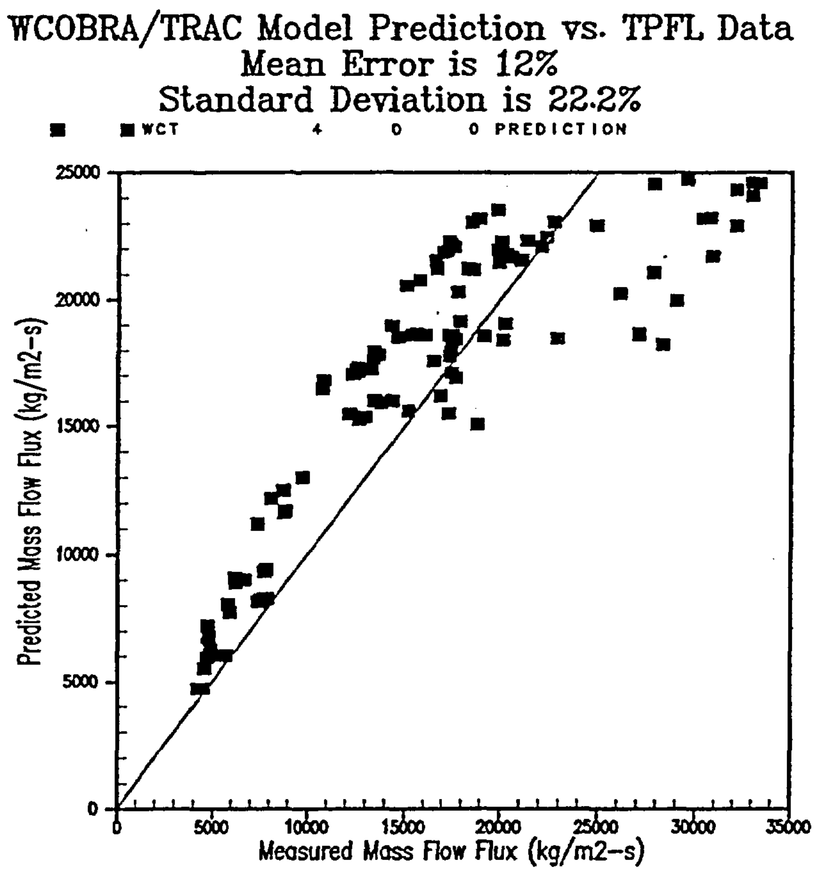

Figure 13-4-29 Prediction Comparison with TPFL Data

13-5 Scaling Consideration

An observation relative to the scalability of the model is addressed in this section.

13-5-1 Pressure, Subcooling, and Quality

For the subcooled break flow model, a pressure range of 13 to 2300 psia and a quality range of -0.039 to 1.0 were examined. The results indicated that the model is scalable relative to pressure and subcooling with reasonable accuracy. The results showed that the model adequately accounts for the pressure and the quality variations.

13-5-2 Break Flow Area

The break flow comparisons showed that the present model predicted both small diameter tests such as Amos and Schrock for 0.0295 inch (Amos and Schrock, 1983), and Sozzi and Sutherland for 0.5-inch (Sozzi and Sutherland, 1975), as well as the large diameter (19.7-inch) data obtained in the Marviken tests (EPRI-NP-2370, 1982) with adequate accuracy.

The WCOBRA/TRAC break model was able to simulate both small and large diameter nozzles adequately.

13-5-3 Break Geometry

The entrance effects, such as the roundness/sharpness of the orifice are accounted for in the present model although the flow area variation along the axis is neglected.

13-5-4 Pressure Effect on the Onset of Entrainment and Branchline Quality

The horizontal stratified entrainment model was validated from 500 up to 900 psia, close to the full pressure at which the entrainment is an important factor in small break LOCAs. Thus, no significant distortion in the PWR calculation is expected relative to the pressure.

13-5-5 Mainline Pipe Diameter Variation on the Onset of Entrainment and Branchline Quality

This parameter may be important for stratified entrainment behavior. The correlation used in WCOBRA/TRAC is validated up to 28.4 cm. This is roughly one-third of the cold leg diameter, where a postulated small break LOCA is assumed to occur. There may be a scale distortion at a full PWR diameter of 99 cm. However, the original correlations were derived by assuming an infinite diameter tank; it is likely that the size distortion is small.

13-6 Conclusions

The break flow comparisons showed that the present model predicted both small diameter tests such as Amos and Schrock at 0.0295 inch, and Sozzi and Sutherland at 0.5-inch as well as the large diameter (19.7-inch) data obtained in the Marviken tests (EPRI-NP-2370, 1982) with acceptable accuracy.

The onset of vapor pull-through and liquid entrainment, in addition to break quality, are well simulated by WCOBRA/TRAC-SB. However, it is possible that the entrainment is strongly influenced by the presence of waves and vortex; the uncertainty may be higher than estimated in this assessment in other applications.

13-7 References

Alamgir, M. D. and Lienhard, J. H., 1981, "Correlation of Pressure Undershoot During Hot-Water Depressurization," Trans. ASME, J. Heat Transfer, Vol. 103, pp. 52-55.

Amos, C. N. and Schrock, V. E., 1983, "Critical Discharge of Initially Subcooled Water Through Slits," NUREG/CR-3475.

Anderson, J. L. and Benedetti, R. L., 1985, "Critical Flow Through Small Pipe Break," NUREG/CR-4532.

Ardron, K. H. & Ackerman, M. C., "Studies of the Critical Flow of Subcooled Water in a Pipe," CEGB Report: RD/B/N4299, 1978.

Ardron, K. H. and Bryce, W. M., 1990, "Assessment of Horizontal Stratification Entrainment Model in RELAP5/MOD2 by Comparison With Separate Effects Experiment," Nuclear Engineering and Design 122, pp. 263-271.

Bajorek, S. M., et al., 1992, "Westinghouse Code Qualification Document for Best Estimate Loss of Coolant Accident Analysis Volume 1: Models and Correlations," WCAP-12945-P-A, Vol. 1, pp. 4-124.

Boivin, J. V., "Two-phase Critical Flow in Long Nozzles," Nuclear Technology, 46, pages 540-545, 1979.

Bryers, R. W., Hsieh, W. W., Hunter, J. A. & Sieder, E. N., "Study of Two-phase Metastable Flow," U. S. Department of Interior, Office of Saline Water, R&D Progress Report No. 234, November, 1966.

Condie, K. G., 1980, "LOFT LOCE L3-5/L3-5A Results and Analysis." Paper presented at the LOFT Review Group Meeting, Idaho Falls, Idaho.

Craya, A., 1949, "Experimental Research on the Flow of Nonhomogeneous Fluids," LeHouille Blanche, January-February, pp. 56-64.

Cruver, J. E., "Metastable Critical Flow of Steam Water Mixtures," Ph.D. Dissertation, Department of Chemical Engineering, University of Washington, 1963 (University Microfilms Inc., Ann Arbor, Michigan).

Danforth, J. L., "Flow of Hot Water Through a Rounded Orifice," M. S. Dissertation, Department of Mechanical Engineering, Massachusetts Institute of Technology, 1941.

Doa, L. T. C and Carpenter, J. M., 1980, "Experiment Data Report for LOFT Nuclear Small-Break Experiment L3-5/L3-5A," NUREG/CR-1695, EGG-2060.

EPRI-NP-2370, 1982, "The Marviken Full-Scale Critical Flow Tests," Vol. 1, Summary Report.

Fauske, H. K., "Contribution to the Theory of Two-phase, One Component Critical Flow," Argonne National Laboratory Report ANL-6633, 1962.

Fincke, J. R. & Collins, D. R., "The Correlation of Two-dimension and Non-equilibrium Effects in Subcooled Choked Nozzle Flow," NUREG/CR-1907, EGG-2081.

Guizovarn, L., Pinet, B., Barriere, G. & Pietri, D., "Etude Expermentale des Debits Critiques en Ecoulement Diphasiques eau Vapeur a Faible Titre Dans un Canal Avec Divergent de 7° a des Transports Thermiques," Note TT No. 501, 1975.

Henry, R. E., "An Experimental Study of Low Quality, Steam-Water Critical Flow at Moderate Pressures," Argonne National Laboratory Report ANL-7740, 1970.

Illic, V., Banerjee S. and Behling S., "A Qualified Database for the Critical Flow of Water," EPRI-NP-4556, May, 1986.

Jeandey, C., Gros D'Aillon, L., Bourgin, R. & Barriere, G., "Auto Vaporisation d'Ecoulements Eau/Vapeur," Departement des Reacteurs a Eau Service des Transferts Thermiques (Centre D'Etudes Nucleaires de Grenoble) Report T. T. No. 163, 1981.

Jones, O. C., Jr., 1980, "Flashing Inception in Flowing Liquids," Trans. ASME, J. Heat Transfer, Vol. 102, pp. 439-444.

Lubin, B. T. and Springer, G. S., 1967, "The Formation of a Dip on the Surface of a Liquid Draining from a Tank," Journal of Fluid Mechanics, 29, pp. 385-390.

Maciaszek, T. and Memponteil, A., 1986, "Experimental Study on Phase Separation in a Tee Junction for Steam-Water Stratified Inlet Flow," Paper C2 presented at European Two-phase Flow Group Meeting, Munich, June 10-13.

Morrison, A. F., "Blowdown Flow in the BWR BDHT Test Apparatus," GEAP-21656, 1977.

Neusen, K. F., "Optimizing of Flow Parameters for the Expansion of Very Low-quality Steam," University of California, Lawrence Radiation Laboratory, UCRL-6152, 1969.

Reocreux, M., 1974, "Contributions a l'Etude das Debits Critique en Econlement Diphasique Eau-Vapeur," Ph.D. Thesis, Universite Scientifique et Medicale de Grenoble, France.

Schrock, V. E., et al., 1986, "Small Break Critical Discharge - The Roles of Vapor and Liquid Entrainment in a Stratified Two-phase Region Upstream of the Break," NUREG/CR-4761.

Schrock, V. E., Starkman, E. S. & Brown, R. A., "Flashing Flow of Initially Subcooled Water in Convergent-divergent Nozzles," Journal of Heat Transfer 99 (2), 1977.

Seynhaeve, J. M., "Etude Experimentale des Ecoulements Diphasiques Critiques a Faible Titre," Doctoral thesis, Department Thermodynamique et Turbomachines, Universite Catholique de Louvain, 1980.

Seynhaeve, J. M., et al., 1976, "Nonequilibrium Effects on Critical Flow Rates at Low Qualities," Vol. 2, pp. 672-688, Proceedings of the CSNI Specialist Meeting on Transient Two-phase Flow, Toronto, August 3-4.

Smoglie, C. and Reimann, J., 1986, "Two-phase Flow Through Small Branches in a Horizontal Pipe with Stratified Flow," International Journal of Multi-Phase Flow, pp. 609-626.

Sozzi, G. L. and Sutherland, W. A., 1975, "Critical Flow of Saturated and Subcooled Water at High Pressure," NEDO-13418.

Yonomoto, T. and Tasaka, K., 1988, "New Theoretical Model for Two-phase Flow Discharge from Stratified Two-phase Region Through Small Break," Journal of Nuclear Science and Technology, 25[5], pp. 441-455.

Zaloudek, F. R., 1964, "Steam-Water Critical Flow From High Pressure Systems," HW-80535.

Zuber, N., 1980, "Problem in Modelling of Small Break LOCA," NUREG-724.

SECTION 14
SAFETY INJECTION JET CONDENSATION: COSI EXPERIMENTS

14-1 Introduction

The phenomenon of direct-contact condensation, the condensation of vapor by subcooled liquid, takes place in the cold leg piping during a small break LOCA transient once any voiding has occurred and the relatively cold safety injection water is being injected. Steam condensation results in volume shrinkage, and this in turn affects the pressure globally throughout the RCS, with ultimate implications for how much water the centrifugal safety injection pumps can inject against the RCS backpressure. If left within the RCS indefinitely, the injected cold water eventually mixes with the hot liquid and steam and reaches equilibrium conditions; a simple mass and energy balance should be adequate to describe and predict the process. However, because the water is injected into the cold leg piping, many more complex effects can occur from the localized condensation process. In the broken loop cold leg, the degree of condensation affects the enthalpy of fluid at the break plane. This can affect the break flowrate and thus the system pressure and mass loss. Also, the volume reduction from the steam condensed in the cold leg tends to be replaced by steam flowing from other parts of the RCS, and this generates flow pressure drops that affect coolant distribution. Finally, the degree to which complete mixing and condensation occur in the cold leg affects the water conditions in the vessel downcomer, which in turn can affect the gravity head for coolant distribution in the reactor vessel.

To investigate the ability of the WCOBRA/TRAC-SB code to correctly predict condensation phenomena, a model was constructed of a series of experiments which were performed in the Condensation On Safety Injection (COSI) facility. The COSI facility is an approximately 1:100 scale model of the cold leg and safety injection lines of a Westinghouse-type nuclear power plant (NPP), constructed specifically for investigating the interaction of steam and cold safety injection water in a prototypical NPP configuration and at typical NPP fluid conditions encountered during a small break LOCA. A description of the facility, the experiments, and the modelling follow.

14-2 Description of COSI

14-2-1 Facility Description

The COSI facility is a 1:100 scale model of the cold leg and safety injection ports of a Westinghouse-type NPP. It is capable of operating at pressures [ ]^{a,c} and at appropriately scaled flowrates to cover nearly the full range of injection conditions expected in an NPP transient, during which condensation on the safety injection water is an identified phenomenon. The main scaling philosophy followed in designing the system was [

]^{a,c}.

Figure 14-1 illustrates the arrangement of the main components of the test facility. The main pipe (cold leg simulator) is [ ]^{a,c} as seen in Figure 14-2. The experiments simulated herein [

]^{a,c} Instrumentation in the facility was state-of-the-art in the mid-1980s, and measurement accuracies are extremely good. Measurements are available for steam and liquid flowrates in and out of the test assembly, for temperatures of all fluid entering and exiting, for pressures, and for differential pressures. Within the test section, a series of thermocouple rakes provides information concerning stratification of the liquid.

14-2-2 Key Phenomena

Information obtained from the tests provides a data base for assessing models for steam condensation on cold safety injection jets and with varying levels of water in the main pipe simulating the cold leg. Previous evaluations of the data (Shimeck, 1988 and Jonicot and Bestion, 1993) concluded that there was significant condensation for nearly all test conditions which, when measured in terms of condensation efficiency, approached values of 100 percent in some cases. Condensation efficiency is defined as the ratio of the steam mass condensation which occurs to the mass of the steam condensation that would raise the enthalpy of the injected safety injection water to saturation. There was clear evidence of stratification in the main pipe, and other evidence pointed to the conclusion that the majority of the condensation was occurring directly within the relatively small jet mixing zone. The jet mixing zone is defined as encompassing the jet of water flowing out of the injection port together with the area a short distance immediately upstream and downstream of the injection point in which water in the cold leg is turbulently mixed by the impact and spreading of the jet. Investigations were conducted for a range of pressures, injection rates, and weir heights to determine to what degree any of these affected the results.

14-2-3 Applicable Tests and Parameter Ranges

A large matrix of tests was conducted over the course of the program by both Westinghouse and Framatome, and some reconfiguration of the facility test section was performed with regard to the length of the main pipe in the test assembly and the angle and size of the injection piping. The experiments of most interest and applicability to code validation for small break LOCA transients were the steady-state points with flows simulating pumped high head injection.

A core series of 11 tests, with 55 individual data points, is identified in WCAP-11767 (Shimeck, 1988). The key parameters of interest from these tests, which are useful for sensitivity studies, are shown in Table 14-1.

14-3 Description of WCOBRA/TRAC Model

Figure 14-3 shows the component layout of the WCOBRA/TRAC-SB model of the COSI facility. The main test section, which consists here of the cold leg pipe and the downcomer, is modelled [

]^{a,c}. The test points to be simulated were established to be steady-state with constant pressure and constant flowrates of steam and water. The two BREAK components on either end of the assembly allow for controlling the system at a given pressure. The FILL component provides a constant source of safety injection water.

[

]^{a,c} Figure 14-4 shows more detail

concerning the modelling of the test section [ ],[a,c] and Figure 14-5 is a cross-sectional view of [

]^{a,c} so that tests with the weir, which was one-half of the pipe diameter, can be more properly simulated. The [channel size was selected to provide a reasonable degree of detail, but without an excessive number of channels.] a,c

14-4 Simulations

14-4-1 Summary of Experimental Results

A set of test points, as obtained from the experiments, corresponds to a given configuration of injection line size and weir installation (in or out). Two injection line diameters (d) were tested [

]^{a,c}

Information from measurements made with the thermocouple rakes was reviewed to deduce the phenomena involved in the condensation process along the cold leg when a weir is present. Significant amounts of temperature stratification were observed, and combined with examination of the actual temperatures, the conclusion was that the overall behavior depicted in Figure 14-6 was taking place. Fluid temperatures upstream and downstream of the injection point were stable and indicated that a countercurrent flow pattern was in place on the upstream side. On the downstream side, it is not clear whether the flow pattern was cocurrent or countercurrent, but again stratification was noted. In the immediate vicinity of the injection port, the thermocouple measurements exhibited a significant standard deviation, indicating turbulent conditions. The downward impingement of the safety injection jet, combined with the significant influx of steam to this point, supported a turbulent jet mixing zone, with rather complex flow and heat transfer patterns. Any safety injection water that leaves the jet mixing zone and is not saturated will support further condensation on the pool surface both upstream and downstream. Additionally, the small waterfall that occurs in the downcomer region accentuated the condensation in this region. Although this waterfall effect may be argued to possibly be somewhat prototypical of water in an NPP falling into the downcomer from the cold leg, it was not the intent of the experiment to simulate this effect. Therefore, a set of experiments was conducted in the facility in which the downcomer water level was varied to obtain an adjustment to the data that removed this factor. The conclusion from analysis of the data was that there is a strong condensation mechanism in the jet mixing zone which must be modelled in a small break LOCA simulation. Any nonsaturated water that exits this zone will then simply interact in a more quiescent fashion. Condensation beyond the jet mixing zone is calculated with other models (see Section 18).

The experimental results are best described in terms of the condensation efficiency, which is defined as the ratio of the mass flowrate of steam to the mass flowrate of steam that raises all of the safety injection water to saturation. The black symbols in Figures 14-7, 14-8, and 14-9 show the experimental results for various configurations. The results are presented in Tables 14-2, 14-3, and 14-4 as well. The presented condensation efficiencies were corrected so that condensation in the downcomer region is not taken into account. [

]a,c In general, condensation efficiencies were high for all conditions that were examined at all pressures, injection rates, and injection configurations. [

]a,c

14-4-2 WCOBRA/TRAC-SB Results

The calculations with the WCOBRA/TRAC-SB model were performed [

]a,c In this model, no attempt is made to modify or increase the heat transfer due to the entrainment or droplet production.

The effects of condensation in the downcomer region were not taken into account (by deactivating condensation in that region) to make the code results comparable with the corrected experimental results. Only condensation on the water-steam interfacial surface in the horizontal pipe and condensation due to the presence of the subcooled jet water were applied in the model.

The condensation due to the jet presence was [

]a,c in agreement with the analysis of the experiments.

[ ]a,c Figure 14-7 shows calculated condensation efficiency (white symbols). The results are presented in Table 14-2 as well. The comparison of numerical and experimental results (white and black symbols) shows that calculated condensation efficiency is in good agreement with the measured results for the [

]a,c Comparison of the calculated condensation efficiencies for various pressures leads to the conclusion that they have similar values regardless of the pressure. That could be expected because the developed correlation for the subcooled liquid condensation heat transfer coefficient does not take into account pressure effects. Calculated condensation efficiencies have a range of the possible numerical values (presented as variation bars in the Figure 14-7 or in the last column in Table 14-2) due to small oscillations of the calculated results.

The results for the case [

]a,c

The case [

]a,c As for the previous cases, the smallest difference is for the lowest injection water flowrates.

The WCOBRA/TRAC-SB small break LOCA computer code contains a safety injection condensation model to simulate that phenomenon. The condensation in the jet mixing zone is dominant, and an increase of the condensation due to the jet presence is necessary to achieve better agreement with the experimental results, particularly at high safety injection flows. The present model does not take into account detailed effects of the entrainment, disturbance of the water surface due to the jet impingement, droplet formation, and consequently, the increase of heat transfer area with the increased jet Reynolds number. Agreement between experimental and numerical results is closest at the lowest COSI safety injection water flowrate. This flowrate is the closest to the scaled injection rate that corresponds to the analyzed single failure condition for the PWR. For instance, [

]a,c

14-5 Conclusions

A W̲COBRA/TRAC-SB model of the COSI safety injection condensation separate-effects experiments has been used to simulate the phenomena. The comparison with experimental results shows that the code was able to predict condensation rates within a reasonable range for the lower safety injection flowrates. In the range of the higher safety injection flowrates, the code underpredicts the condensation efficiencies. The lowest COSI injection flowrate is the most representative of the as-analyzed PWR flowrates during the pressure range of interest for small break LOCA events. Therefore, the jet condensation efficiency in the W̲COBRA/TRAC-SB predictions is judged to be acceptable for integral test facility and PWR simulations.

14-6 References

Jonicot, A. and Bestion, D., 1993, "Condensation Modelling for ECC Injection," Nuclear Engineering and Design, 145, pp. 37-45.

Shimeck, D. J., 1988, "COSI SI/Steam Condensation Experiment Analysis," WCAP-11767, Proprietary.

Table 14-1
Summary of Applicable COSI Experiments

Item	Parameter	
Pressures	[ ]^{a,c}	
	COSI	**Full-Scale**
Flowrates	[	
Safety injection line diameters		
Safety injection temperature		
Simulated pump weir	]^{a,c}	

a,c

Table 14-2

a,c

Table 14-3

a,c

Table 14-4

a,c

Figure 14-1. COSI Facility Arrangement

a,c

Figure 14-2. Test Section Arrangement

a,c

Figure 14-3. COSI WCOBRA/TRAC Model Component Layout

a,c

Figure 14-4. COSI Main Test Section and Downcomer WCOBRA/TRAC Model

a,c

Figure 14-5. COSI Cold Leg Pipe Vertical Cell Nodalization

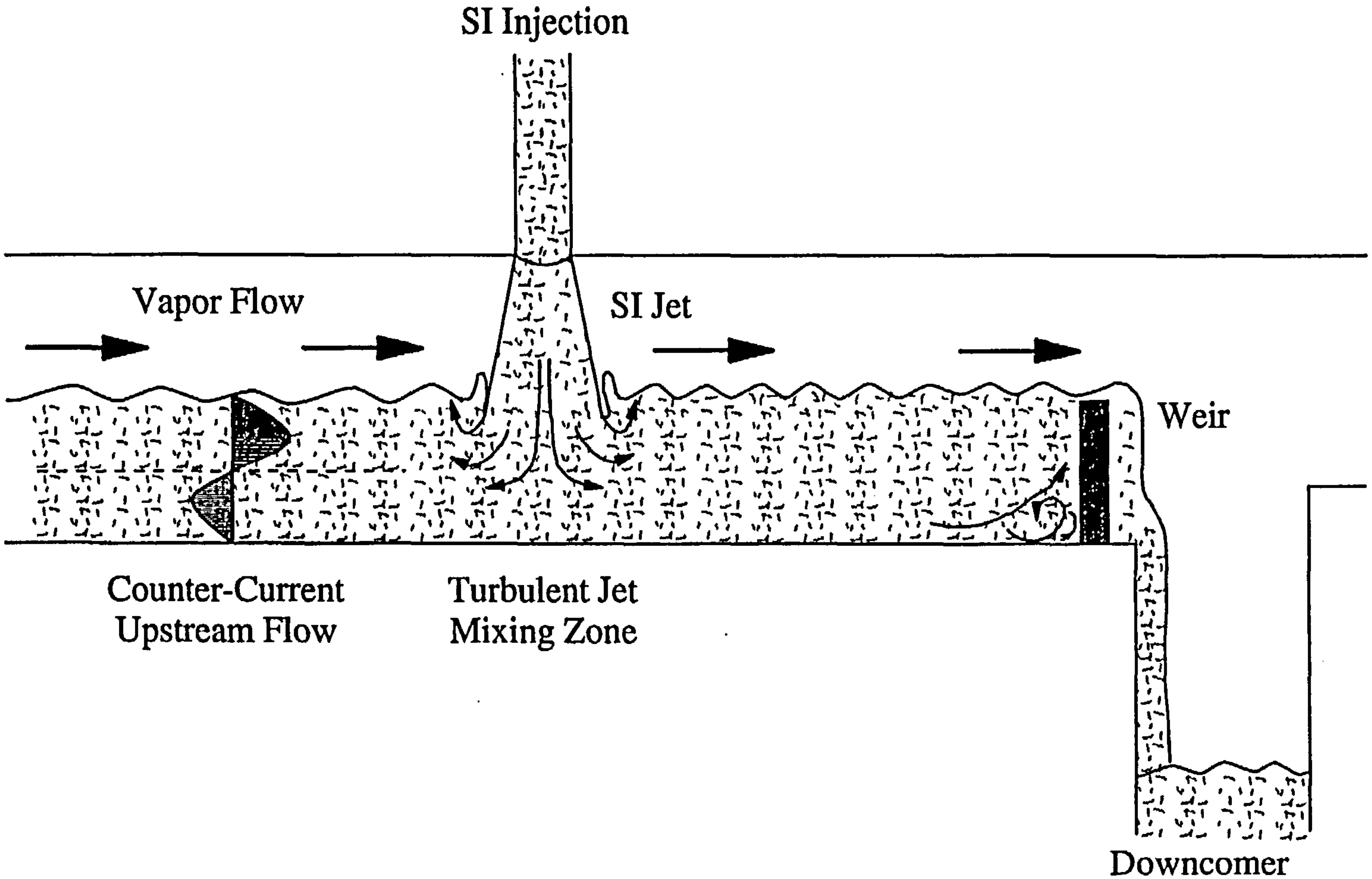

Figure 14-6. Depiction of Flow Patterns in the Test Section as Deduced From Data

a,c

Figure 14-7. Condensation Efficiency for Small Injection Pipe (d = 0.22 Inches) and Weir (H/D = 0.5)

a,c

Figure 14-8. Condensation Efficiency for Large Injection Pipe (d = 0.90 Inches) and Weir (H/D = 0.5)

a,c

Figure 14-9. Condensation Efficiency for Large Injection Pipe (d = 0.90 Inches) and Without Weir (H/D =0)

SECTION 15
MIXTURE LEVEL SWELL

15-1 Introduction

Early in a small break LOCA, voids are generated in the primary RCS by flashing and boiling in the core. Because of the small break size, flows in the RCS are primarily gravity-driven. Following the initial rapid depressurization stage of the LOCA, distinct liquid levels are formed at several locations. Below this liquid or two-phase mixture level, the fluid is a low quality two-phase mixture; while above the level, it is primarily single-phase vapor. Liquid levels initially occur in the pressurizer, in the upper head, and in the uphill and downhill steam generator tubing. Eventually, the RCS drains so that the level in the reactor vessel reaches the hot leg. At this point, the rate of system depressurization is low and vapor generation results from boiling in the core, from power produced by decay heat. Because the vapor generated by this decay heat can be high, regions in the vessel can achieve a significant void fraction. The two-phase mixture level depends on the interfacial shear exerted by the vapor on the liquid, and as a result, the mixture level can be significantly higher than the collapsed liquid level. The difference between the two-phase mixture level and the collapsed level is a measure of the "mixture level swell," which is defined as:

$$S = \frac{Z_{2\Phi} - Z_{CLL}}{Z_{CLL}} \tag{15-1}$$

where Z_{CLL} is the collapsed liquid level and $Z_{2\Phi}$ is the two-phase mixture level.

Prediction of the mixture level swell and tracking of the mixture level are important in the later stages of a small break LOCA. As more liquid is boiled away, the mixture level can eventually drop into the core. While good cooling can be maintained below the mixture level, dryout occurs above the mixture level. Heat transfer above the mixture level is by convection and thermal radiation to steam. These relatively poor modes of heat transfer cause the cladding temperature above the mixture level to increase rapidly. Thus, prediction of the two-phase mixture level in the active core is vital to an accurate prediction of the PCT in a small break LOCA.

15-2 Physical Processes

As described in Section 15-1, mixture level swell is the process that determines the vertical position of the two-phase interfaces in the system; below the interface the mixture is low quality and above the interface the mixture is essentially single-phase vapor. The mixture level swell depends on several processes: the interfacial drag between the vapor and liquid (film), wall drag, bubble rise velocity and bubble size, entrainment of droplets at the two-phase interface, and transition point between bubbly and other vertical flow regimes. In general, the liquid and vapor flowrates are low, which make wall drag due to form and friction losses negligible compared to the interfacial drag. In small break LOCA scenarios, the steam velocities are too low to entrain droplets at the two-phase interface, and thus entrainment is negligible. Therefore, mixture level swell is most directly affected by processes that determine the interfacial shear and the relative velocity between the phases.

Several experimental tests have been run under small break LOCA thermal-hydraulic conditions to measure the effects of various parameters on mixture level swell. Bundle power, or more accurately the vapor generation rate, had the most dominant effect on the measured mixture level and void fraction distributions. Transition to dryout did not occur until the void fraction exceeded a value of approximately 0.85.

Based on these observations, factors considered important in the assessment of predictions of mixture level swell include:

- Mixture level as a function of bundle power and inlet flowrate
- Collapsed liquid level as a function of bundle power and inlet flowrate
- Void fraction distribution

15-3 WCOBRA/TRAC Determination of the Mixture Level

The models and correlations for wall and interfacial drag are described in Section 4, Volume 1, of this document. Flow regime transitions are described in Section 3 of this document. These models are used to determine the void fraction distribution within a region.

WCOBRA/TRAC-SB does not include a specific model or pointer to identify the mixture level. Thus, mixture level tracking is accomplished [

]a,c

[

]a,c

While the WCOBRA/TRAC interface logic prevents the use of an unrealistically low void fraction in a cell, it does not uniquely determine the mixture level elevation.

Therefore, the ability of WCOBRA/TRAC to track a mixture level is dependent upon the axial noding. In the core, [

]a,c

15-4 Assessment of WCOBRA/TRAC Mixture Level Predictions

15-4-1 Introduction

There are several separate effects experimental tests that provide data on the mixture level and mass inventory distribution in a rod bundle under small break LOCA thermal-hydraulic conditions. Three such experimental facilities were modelled with WCOBRA/TRAC-SB, and several experimental tests were simulated to determine the predictive capability of the code. The tests were as follows:

- The ORNL-THTF Uncovered Bundle Tests by Anklam (Anklam, et al., 1982)
- The Westinghouse G-1 Core Uncovery Tests, WCAP-9764 (WCAP-9764, 1980)
- The General Electric (GE) Vessel Blowdown Tests by Findlay and Sozzi (Findlay and Sozzi, 1981)

Each of these tests, run at pressures typical of those in a small break LOCA (1100 to 400 psia), provides information on the mass distribution in a vessel for various thermal-hydraulic conditions. The ORNL-THTF and G-1 tests provide mixture level and mass inventories for uncovered rod bundles, and the GE tests provide mass inventory in a vessel during a rapid depressurization.

The following sections discuss each test, the WCOBRA/TRAC-SB simulation, and the comparisons between the measured and predicted results.

15-4-2 ORNL-THTF Small Break Tests

15-4-2-1 Introduction

The ORNL-THTF performed a series of experimental tests pertinent to small break LOCA model validation. The ORNL-THTF was a high pressure rod bundle thermal-hydraulics loop. The bundle was full height and contained 64 electrically heated rods with internal dimensions typical of a 17x17 PWR fuel bundle.

Figure 15-4-2-1 shows a cross section of the ORNL-THTF test bundle. Four of the rods were unheated to represent control rod guide tubes in a nuclear fuel assembly. Figure 15-4-2-2 shows an axial profile of the ORNL-THTF bundle. The bundle had a heated length of 12 feet (3.66 m) and contained six spacer grids. Thermocouples were located at 25 different axial elevations.

Two types of experiments were conducted in the ORNL-THTF. One series consisted of several uncovered bundle heat transfer tests. In these tests, the experiment was continued until a steady-state condition was reached in the uncovered part of the bundle and rods were heated to a high temperature. The second type of tests did not have bundle uncovery. The bundle remained covered, and a void profile over the entire axial length was obtained.

Additional information on the ORNL-THTF test bundle, and on the tests conducted in the facility, is in NUREG/CR-2456 (Anklam, et al., 1982).

15-4-2-2 WCOBRA/TRAC Model of the ORNL-THTF

Figure 15-4-2-3 shows the WCOBRA/TRAC model of the ORNL-THTF. The heated length is modelled [

]^{a,c}

15-4-2-3 Test Matrix for ORNL-THTF Simulations

Simulations of small break LOCAs in PWRs generally show that there are two periods in which the core can possibly be uncovered. The first occurs during the loop seal clearance period. During this uncovery, the primary system pressure is high (approximately 1150 psia) and the two-phased mixture level can drop below the top of the core. The second uncovery occurs if the break flow exceeds the pumped SI flow during the boil-off period. The system pressure during this uncovery is low, typically 600 to 650 psia, which is just below the accumulator gas pressure.

Table 15-4-2-1 lists tests selected for simulation by WCOBRA/TRAC-SB. Six of the tests are bundle uncovery tests. Three are at relatively low pressure (580 to 650 psia), and three are at high pressure (1010 to 1090 psia). All six had roughly one-half the bundle uncovered. Six other tests are from the level swell test series. Again, three were at low pressure (520 to 590 psia), and three were at high pressure (1090 to 1170 psia). These tests span the expected range of conditions for uncovery in PWR calculations leading to the most limiting PCTs.

15-4-2-4 Simulation of ORNL-THTF Tests

Each test was simulated by imposing a flow and enthalpy boundary condition at the bottom of channel 1, and a constant pressure boundary condition at the top of channel 3. The simulation was continued until the calculation reached a steady-state condition. The parameter YDRAG and the tests are discussed below.

- Interfacial Drag Multiplier YDRAG

  The parameter YDRAG has been introduced to facilitate WCOBRA/TRAC-SB ranging of interfacial drag. YDRAG is a multiplier on the interfacial drag value that is computed according to the vertical flow regime map. It is specified on an individual cell basis, and 1.0 is the default value. The results obtained for some of the ORNL-THTF tests with a value of 1.0 are presented in Table 15-4-2-2.

  The series of ORNL-THTF tests was executed using a variety of YDRAG values in the simulated core region. Table 15-4-2-3 contains the results obtained when a YDRAG value of 0.8 is specified. With YDRAG equal to 0.8, the amount of level swell is reduced. In order to quantify the appropriate YDRAG for each test level swell prediction to match the data, further simulations were performed at YDRAG values of 1.2, 0.65, and 0.5. Based on these results, the YDRAG value for each test that enables the prediction to match the data is shown in Table 15-4-2-4. The average YDRAG for the set is 0.79.

- Bundle Uncovery Tests (YDRAG = 0.8)

  Figures 15-4-2-4 to 15-4-2-9 show the results of WCOBRA/TRAC-SB simulations with YDRAG set to 0.8 of the bundle uncovery tests, I to N, in which one-third to one-half of the core is uncovered. Results for the bundle uncovery tests are shown in comparison with the predicted values of axial void fraction profiles; in the predictions, some variation in the void fractions was observed. In general, WCOBRA/TRAC predicts the void fraction reasonably well in the lower half of the bundle. In the upper half, the void fraction tends to be overpredicted. The cladding temperatures predicted and the heat transfer/void fraction relationship as modelled in WCOBRA/TRAC-SB are discussed in Volume 4 of this document.

- Level Swell Tests (YDRAG = 0.8)

  Figures 15-4-2-10 to 15-4-2-15 show the results of WCOBRA/TRAC simulations with YDRAG set to 0.8 of the six level swell tests, AA to FF, in which the mixture level is at the top of the bundle. Because these tests had no uncovery, a cladding heatup did not occur.

  In general, the predicted and measured void profiles were in good agreement for this test series. As in the bundle uncovery test simulations, WCOBRA/TRAC-SB tends at times to overpredict the void fraction in the upper half of the bundle. Also, at times the void fraction profile is not smooth in the upper part of the bundle (tests AA and BB). Overall, however, agreement between the predictions and the measured profiles is reasonable.

15-4-2-5 Summary and Conclusions

A WCOBRA/TRAC-SB mixture level was determined for each of the 12 ORNL-THTF steady-state tests simulated. The mixture level was defined as the elevation where $\alpha = 0.9$ at a sharp gradient in the predicted void fractions, based on a linear interpolation between two continuity cells. Table 15-4-2-3 lists the mixture level and the collapsed liquid level at steady-state for each test with YDRAG = 0.8.

Figure 15-4-2-16 shows a comparison of the predicted and measured mixture level at YDRAG = 0.8; Figure 15-4-2-17 compares the collapsed liquid level. In general, the agreement for two-phase mixture level is good. The poorest agreement is for test 3.09.10N, which is a test at the lowest power at high pressure.

Taken together, the summary figures show that WCOBRA/TRAC-SB tends to predict mass in the rod bundle (at YDRAG = 0.8) well compared with the experimental data. The average misprediction is small, and there is not a great deal of scatter. This indicates that the correlations affecting mixture level have a small bias and the uncertainty is also small. The predicted and measured void profiles are in reasonable agreement for both the uncovery test series and the level swell series. This supports the premise that the models for interfacial drag and bubble rise are well behaved.

The simulation of ORNL tests at different values of YDRAG was conducted to produce a set of results that could be used to determine heated core interfacial drag multipliers for a small LOCA calculation in a PWR. The range of YDRAG values was sufficient to bound the data for low mixture level swell values. No modification to the core interfacial drag (YDRAG = 1.0) was found to overpredict the level swell; the multiplier of YDRAG = 0.8 produced improved results on average. YDRAG = 0.8 is the reference value for PWR core calculations. The set of multipliers that forces the code to match the data level swell was also identified. The minimum value for this set is $YDRAG_{min} = 0.503$, and the maximum is $YDRAG_{max} = 1.169$; the average value was $YDRAG_{ave} = 0.79$.

Because the number of tests simulated is low (12), the multipliers in these simulations are combined with those from other level swell tests (G-1) to obtain a YDRAG distribution for application to the core region in the small break LOCA analysis of a PWR.

Table 15-4-2-1
ORNL-THTF Test Simulation Matrix

Test No.	Pressure (psia)	Rod Power (kW/ft)	Data Mixture Level (ft)	Data Collapsed Liquid Level (ft)
Bundle uncovery tests				
3.09.10I	650	0.68	8.60	4.39
3.09.10J	610	0.33	8.10	5.31
3.09.10K	580	0.10	6.98	5.31
3.09.10L	1090	0.66	9.02	5.77
3.09.10M	1010	0.31	8.60	6.20
3.09.10N	1030	0.14	6.98	6.10
Level swell tests				
3.09.10AA	590	0.39	11.23	6.56
3.09.10BB	560	0.20	10.85	7.61
3.09.10CC	520	0.10	11.80	9.45
3.09.10DD	1170	0.39	10.61	7.84
3.09.10EE	1120	0.19	11.40	9.35
3.09.10FF	1090	0.098	10.61	9.51

Table 15-4-2-2
Summary of ORNL-THTF Simulation Results

Test No.	Pressure (psia)	Rod Power (kW/ft)	Data Mixture Level (ft)	Code Mixture Level (ft)	Data Collapsed Liquid Level (ft)	Code Collapsed Liquid Level (ft)
3.09.10J	610	0.33	8.10	7.62	5.31	4.92
3.09.10K	580	0.10	6.98	6.97	5.31	5.23
3.09.10AA	590	0.39	11.23	11.54	6.56	6.12
3.09.10BB	560	0.20	10.85	10.10	7.61	6.88
3.09.10DD	1170	0.39	10.61	10.11	7.84	7.35

Table 15-4-2-3
Summary of ORNL-THTF Simulation Results With YDRAG = 0.8

Test No.	Pressure (psia)	Rod Power (kW/ft)	Data Mixture Level (ft)	Code Mixture Level (ft)	Data Collapsed Liquid Level (ft)	Code Collapsed Liquid Level (ft)
3.09.10I	650	0.68	8.60	8.61	4.39	4.36
3.09.10J	610	0.33	8.10	7.70	5.31	5.07
3.09.10K	580	0.10	6.98	6.97	5.31	5.34
3.09.10L	1090	0.66	9.02	9.42	5.77	5.58
3.09.10M	1010	0.31	8.60	8.42	6.20	6.52
3.09.10N	1030	0.14	6.98	6.16	6.10	5.21
3.09.10AA	590	0.39	11.23	10.97	6.56	6.51
3.09.10BB	560	0.20	10.85	10.11	7.61	7.34
3.09.10CC	520	0.10	11.80	>12.0	9.45	9.40
3.09.10DD	1170	0.39	10.61	10.21	7.84	7.64
3.09.10EE	1120	0.19	11.40	>12.0	9.35	9.73
3.09.10FF	1090	0.098	10.61	>12.0	9.51	10.33

Table 15-4-2-4
YDRAG Values to Match ORNL-THTF Data

Test Number	Pressure (psia)	Rod Power (kW/ft)	YDRAG
3.09.10AA	590	0.390	0.827
3.09.10BB	560	0.200	0.908
3.09.10CC	520	0.100	0.698
3.09.10DD	1170	0.390	0.881
3.09.10EE	1120	0.190	0.752
3.09.10FF	1090	0.098	0.635
3.09.10I	650	0.680	0.779
3.09.10J	610	0.330	0.840
3.09.10K	580	0.100	0.871
3.09.10L	1090	0.660	0.503
3.09.10M	1010	0.310	1.169
3.09.10N	1030	0.140	0.61

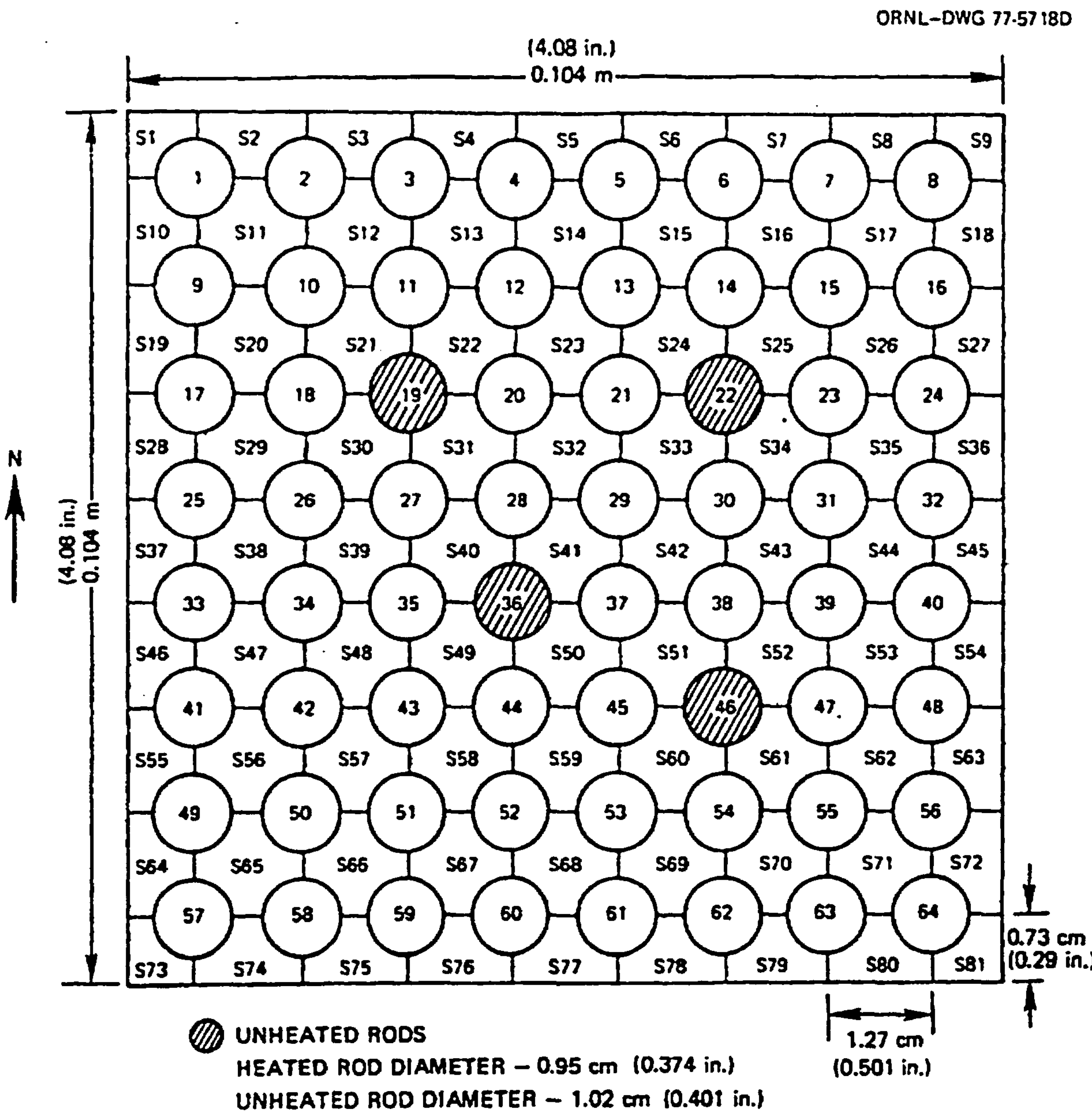

Figure 15-4-2-1. Cross Section of the ORNL-THTF Test Bundle

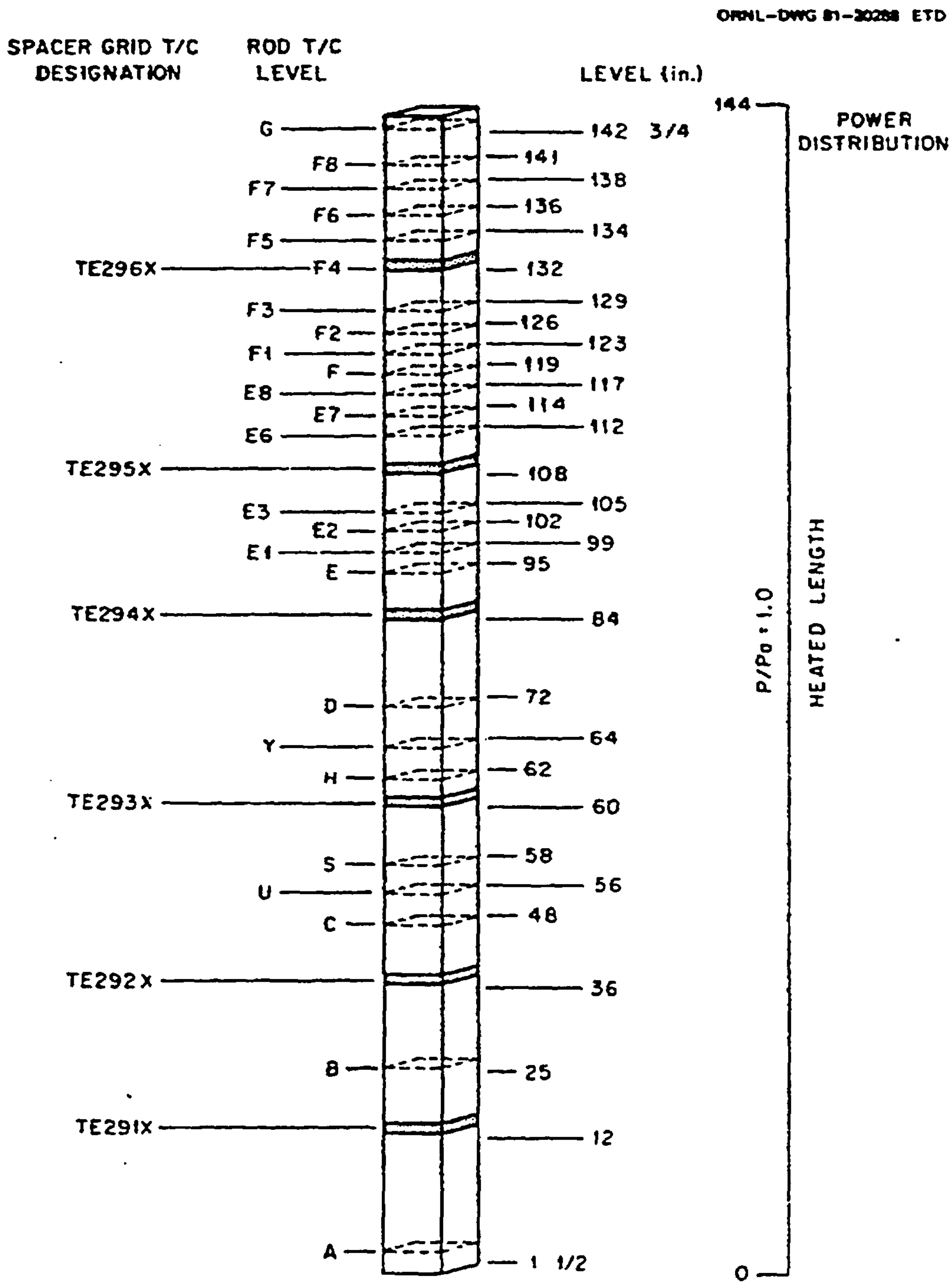

Figure 15-4-2-2. Axial View of the ORNL-THTF Test Bundle

a,c

Figure 15-4-2-3. WCOBRA/TRAC Model of the ORNL-THTF

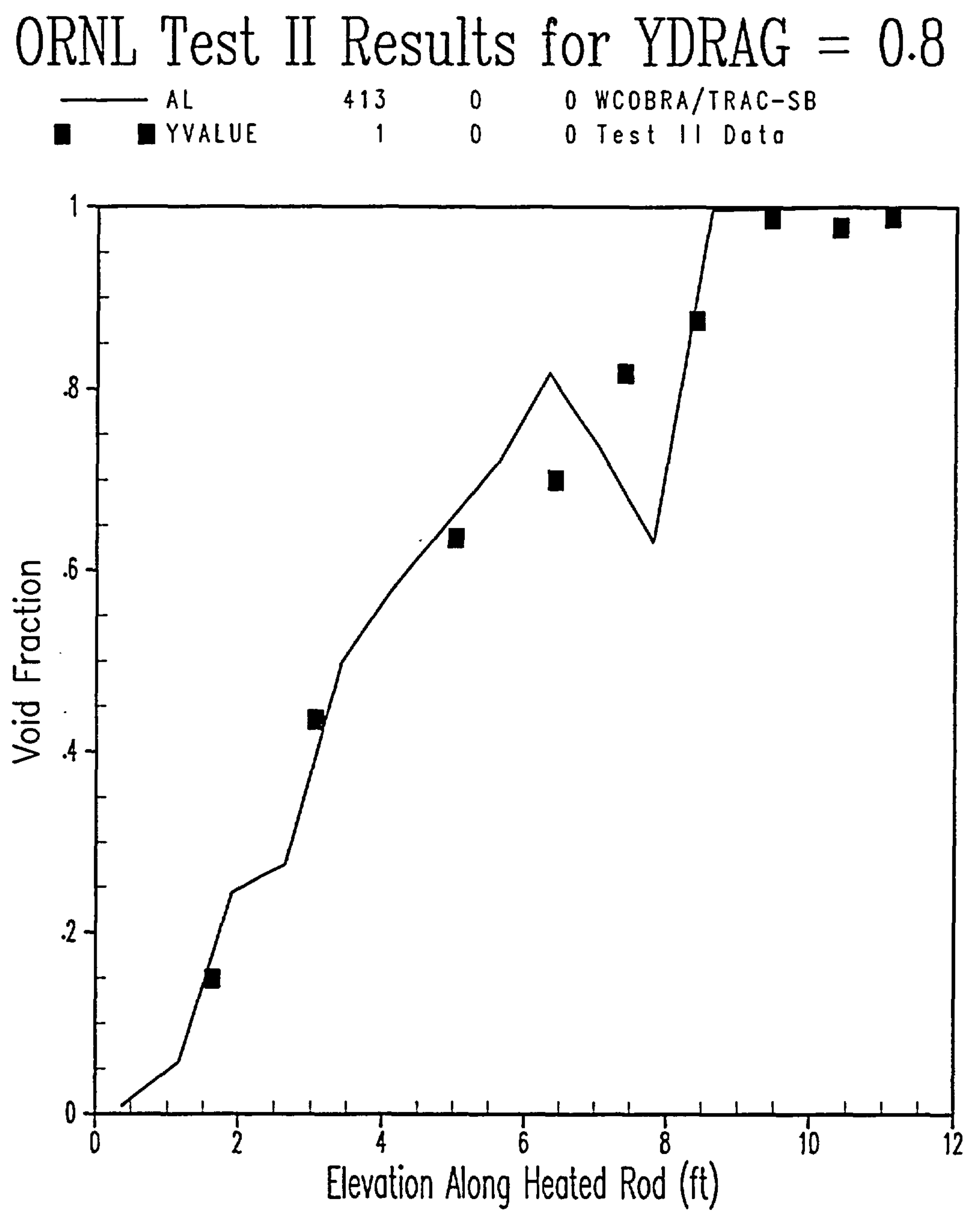

Figure 15-4-2-4. Comparison of Predicted and Measured Void Profiles for ORNL-THTF Test 3.09.10I

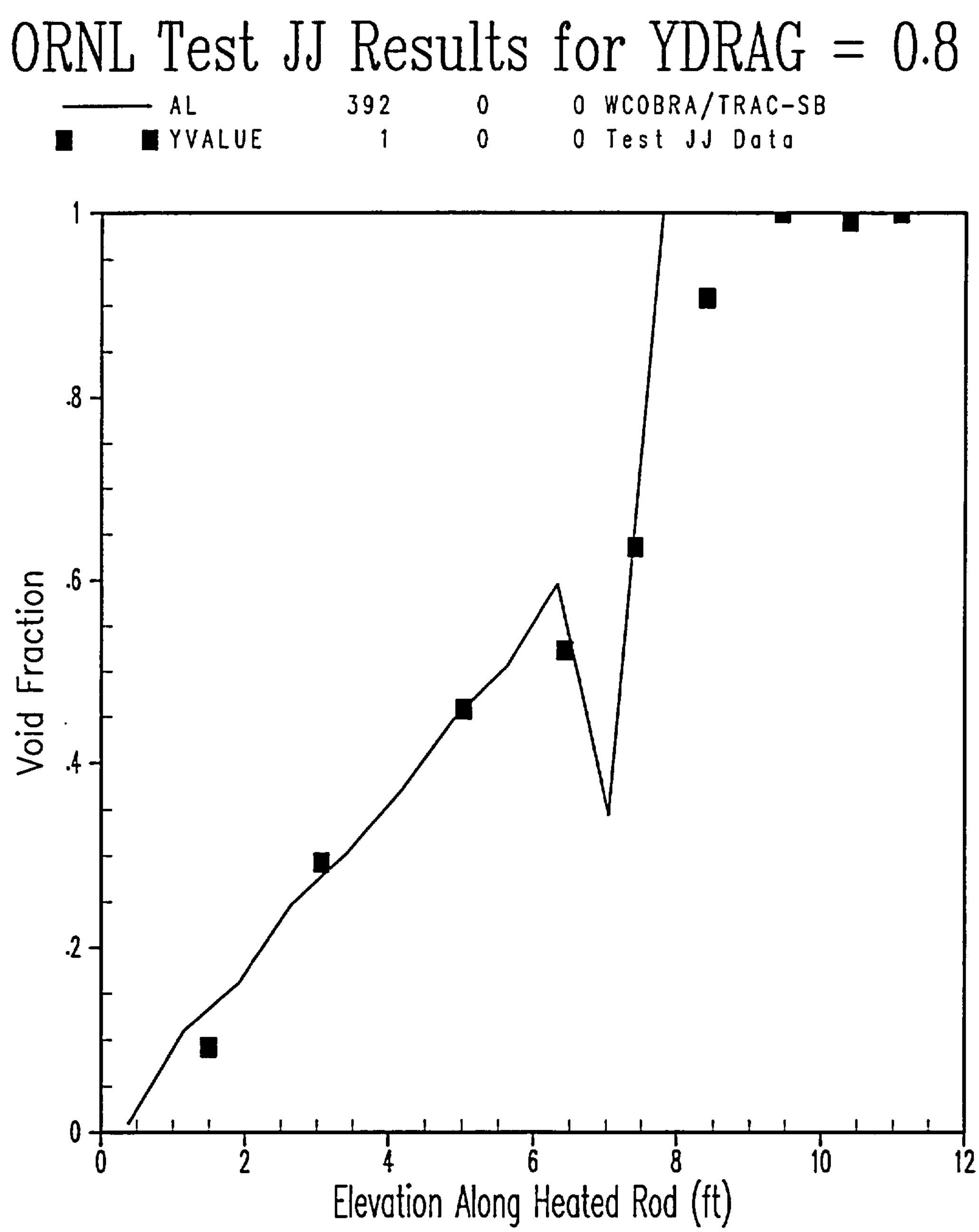

Figure 15-4-2-5. Comparison of Predicted and Measured Void Profiles for ORNL-THTF Test 3.09.10J

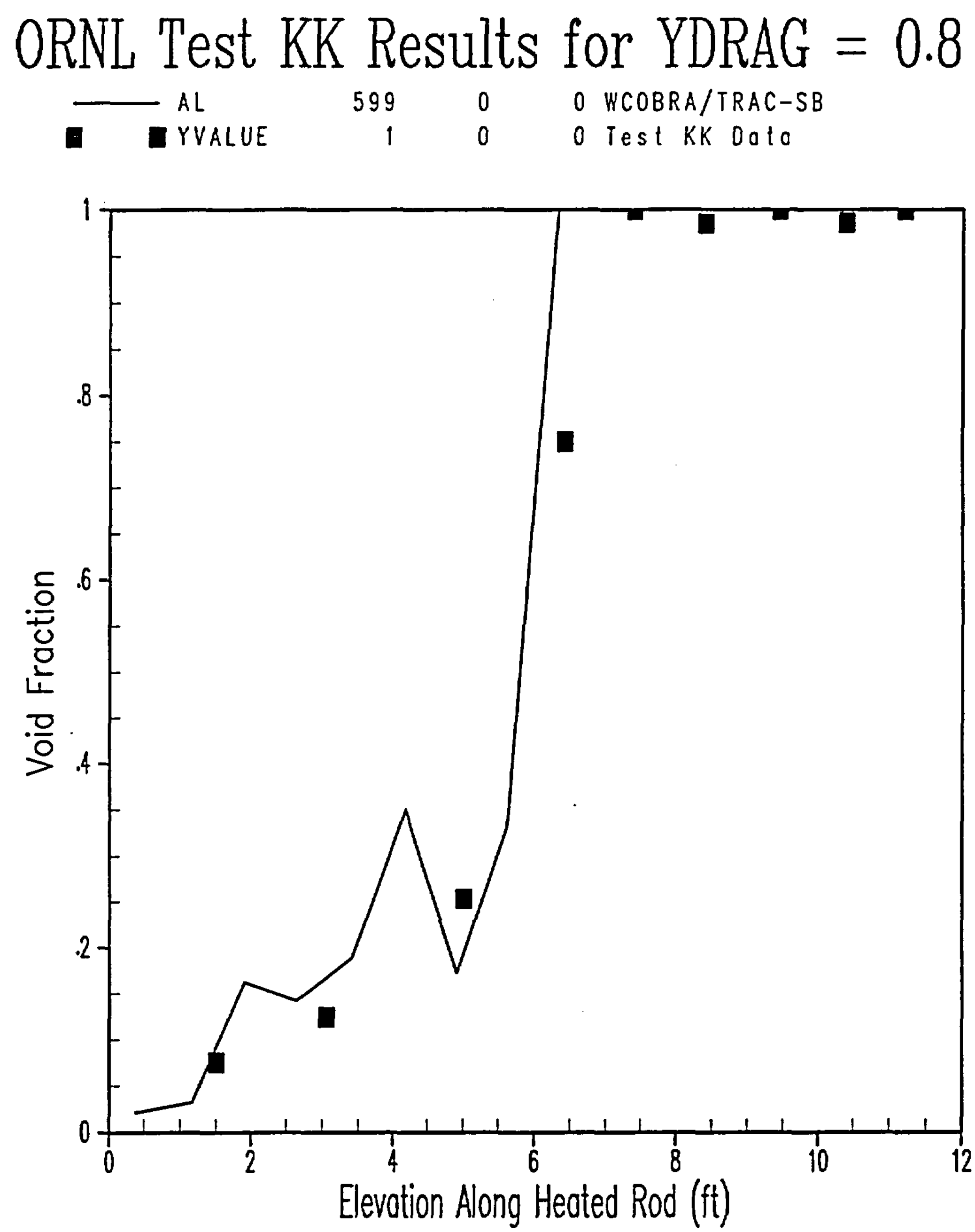

Figure 15-4-2-6. Comparison of Predicted and Measured Void Profiles for ORNL-THTF Test 3.09.10K

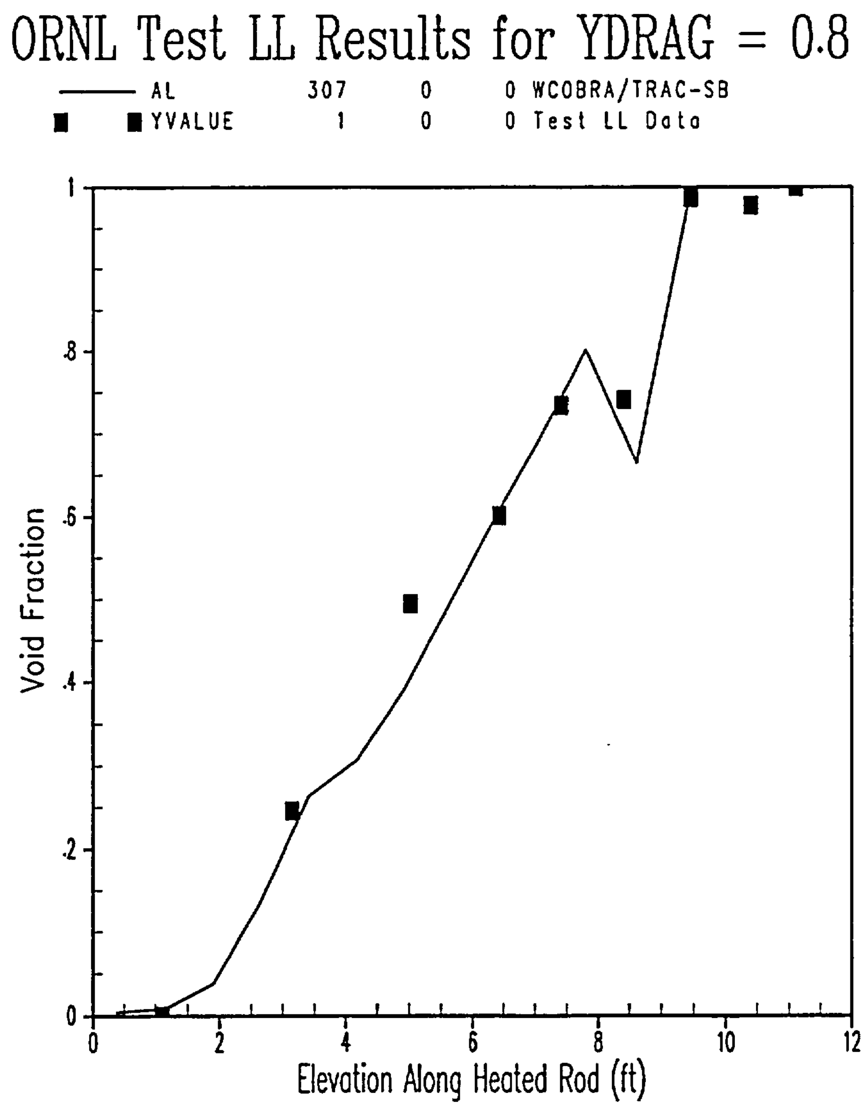

Figure 15-4-2-7. Comparison of Predicted and Measured Void Profiles for ORNL-THTF Test 3.09.10L

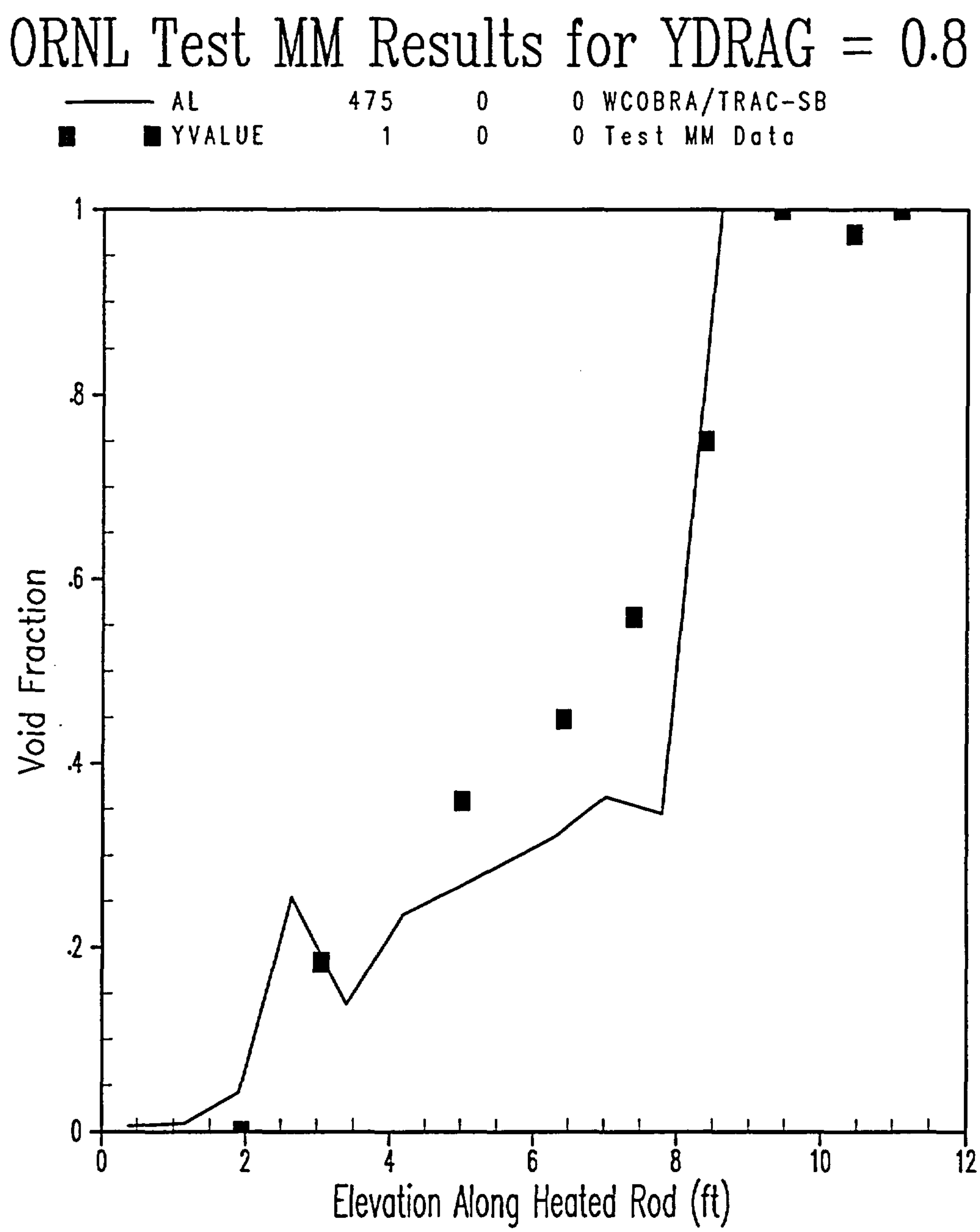

Figure 15-4-2-8. Comparison of Predicted and Measured Void Profiles for ORNL-THTF Test 3.09.10M

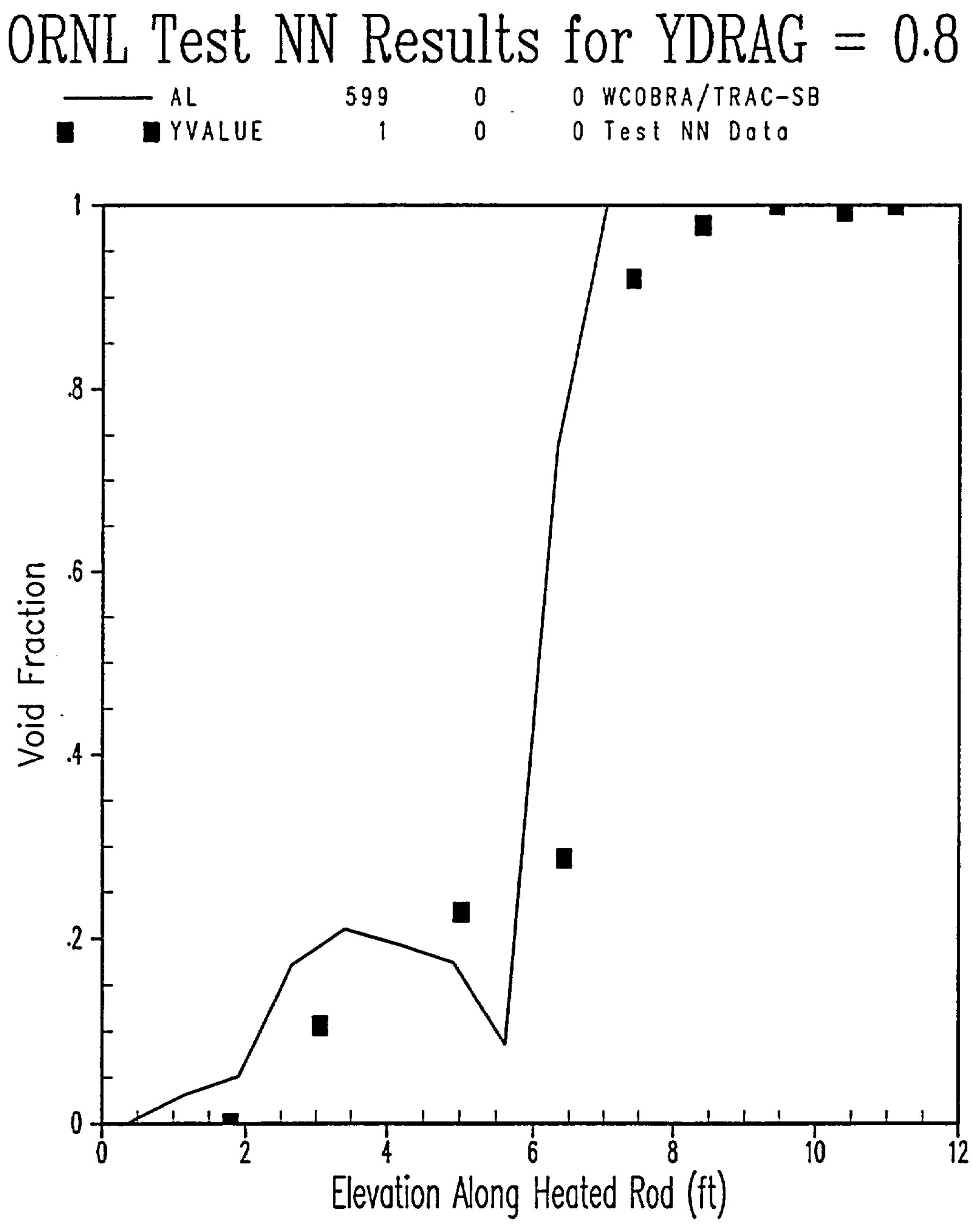

Figure 15-4-2-9. Comparison of Predicted and Measured Void Profiles for ORNL-THTF Test 3.09.10N

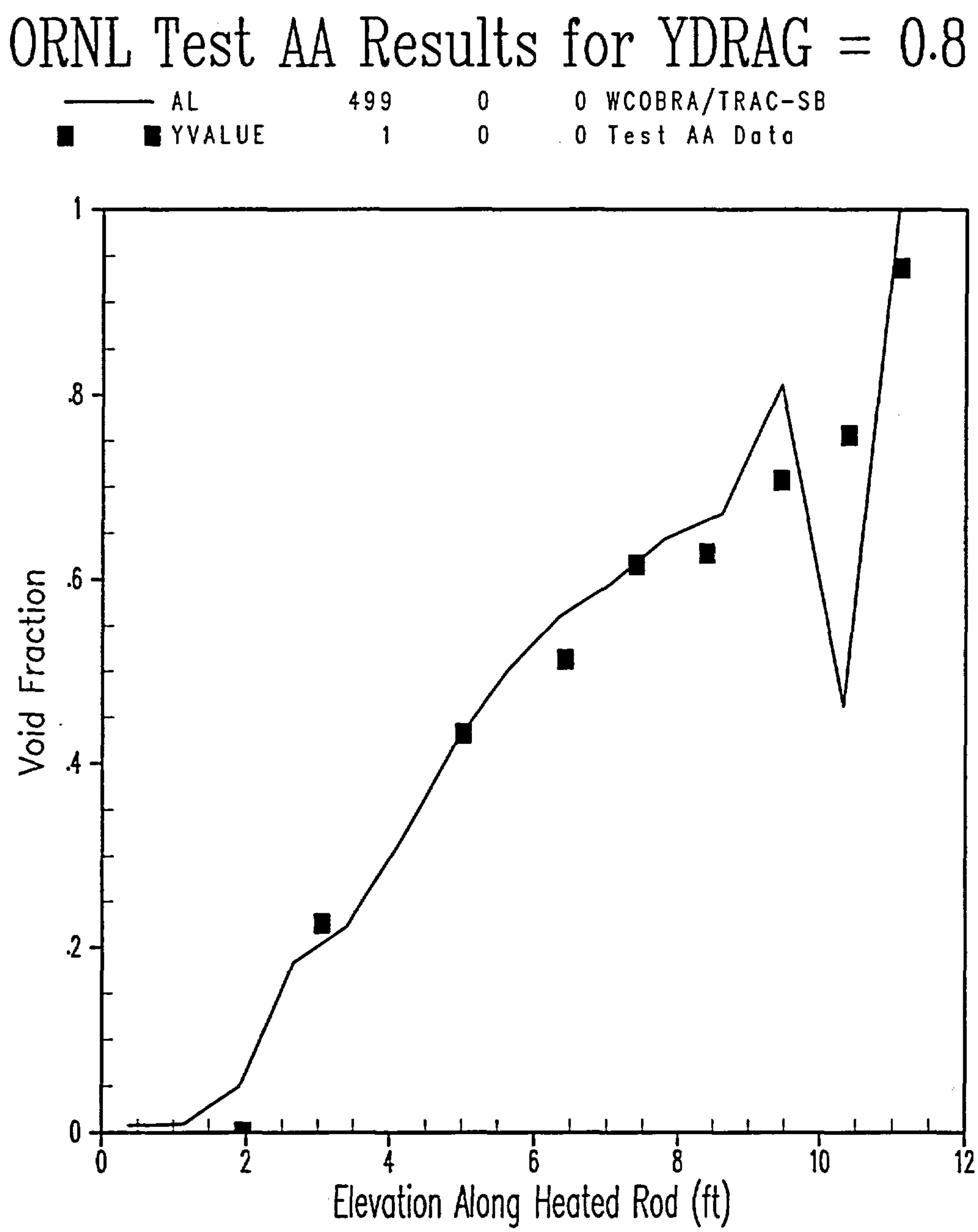

Figure 15-4-2-10. Comparison of Predicted and Measured Void Profiles for ORNL-THTF Test 3.09.10AA

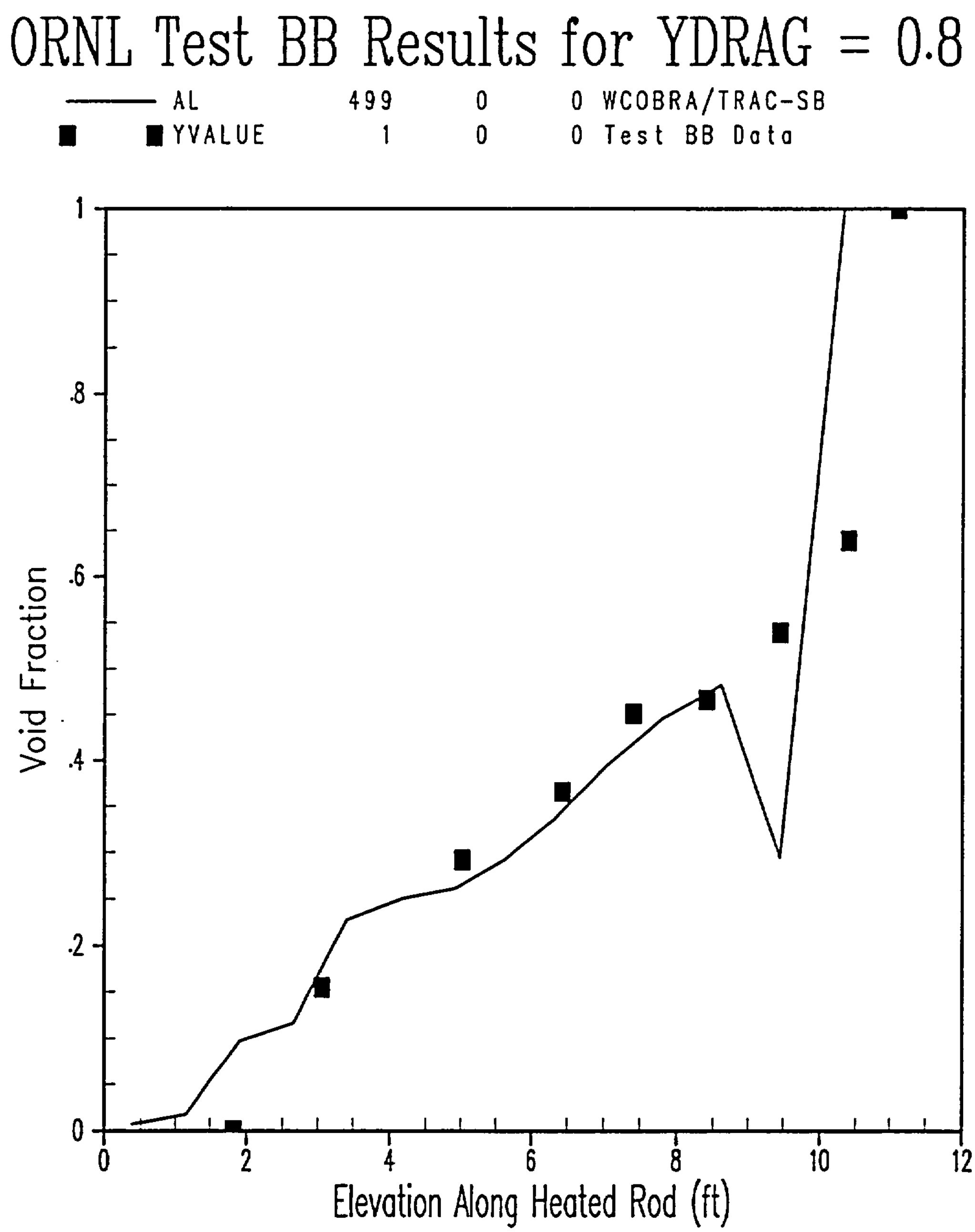

Figure 15-4-2-11. Comparison of Predicted and Measured Void Profiles for ORNL-THTF Test 3.09.10BB

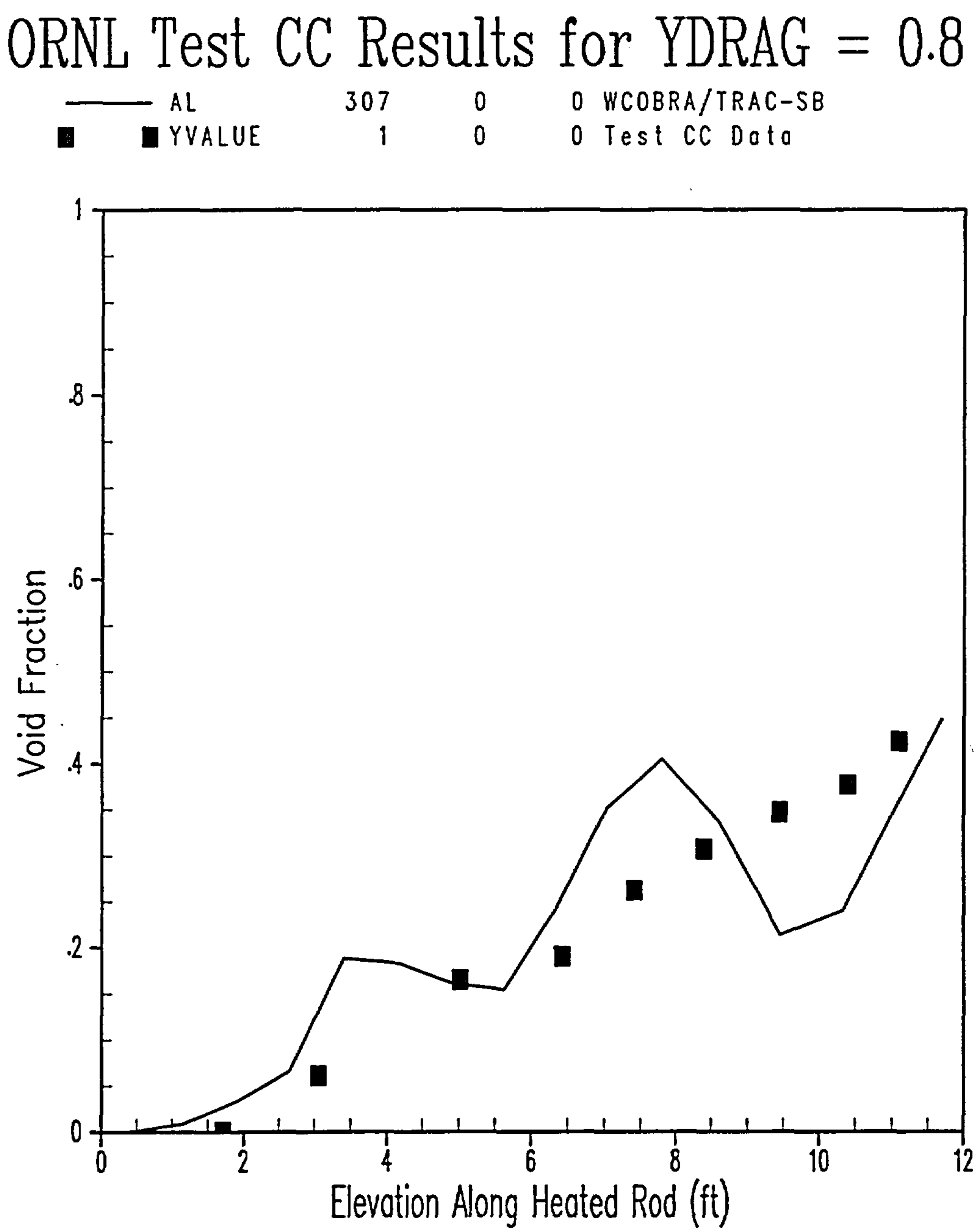

Figure 15-4-2-12. Comparison of Predicted and Measured Void Profiles for ORNL-THTF Test 3.09.10CC

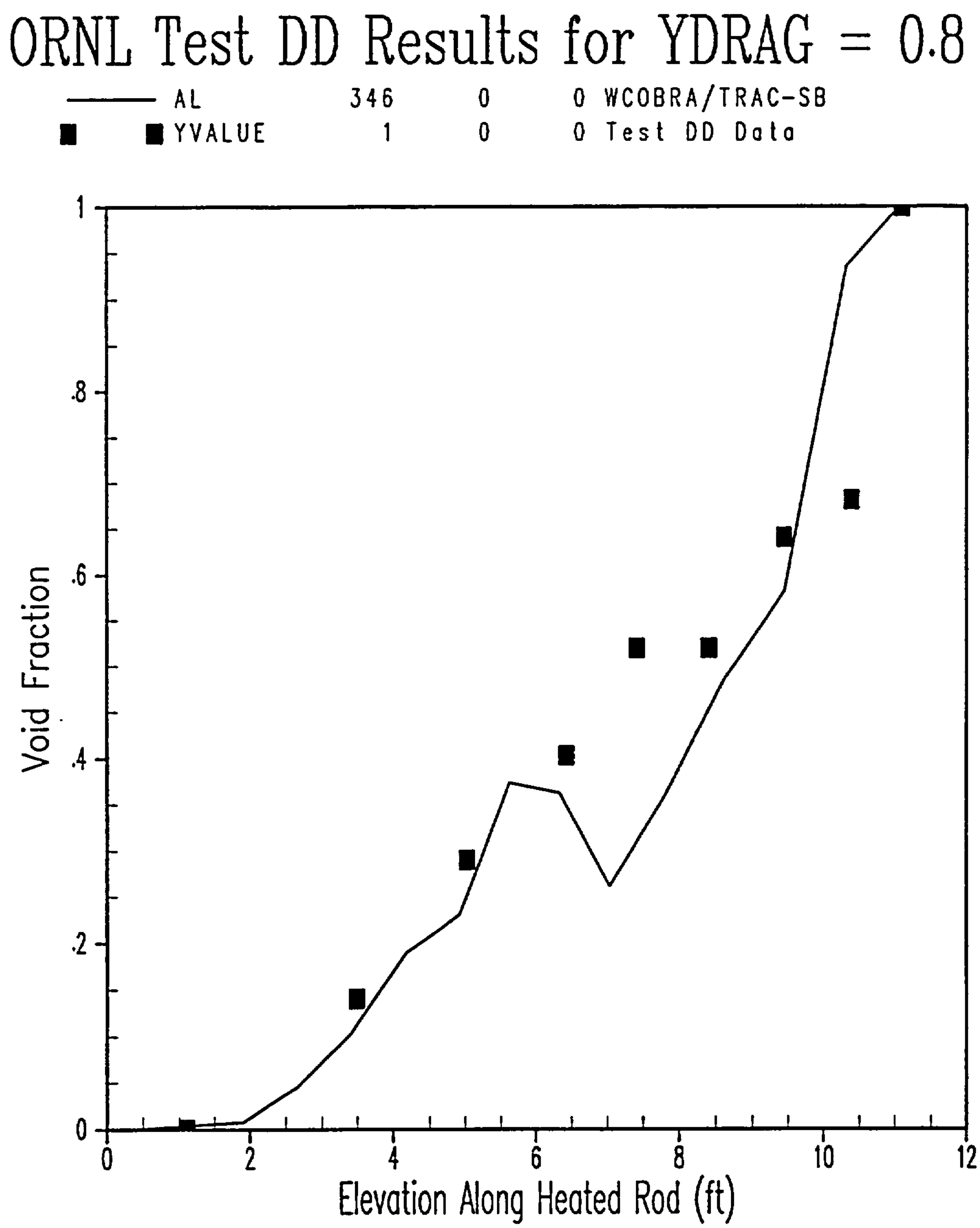

Figure 15-4-2-13. Comparison of Predicted and Measured Void Profiles for ORNL-THTF Test 3.09.10DD

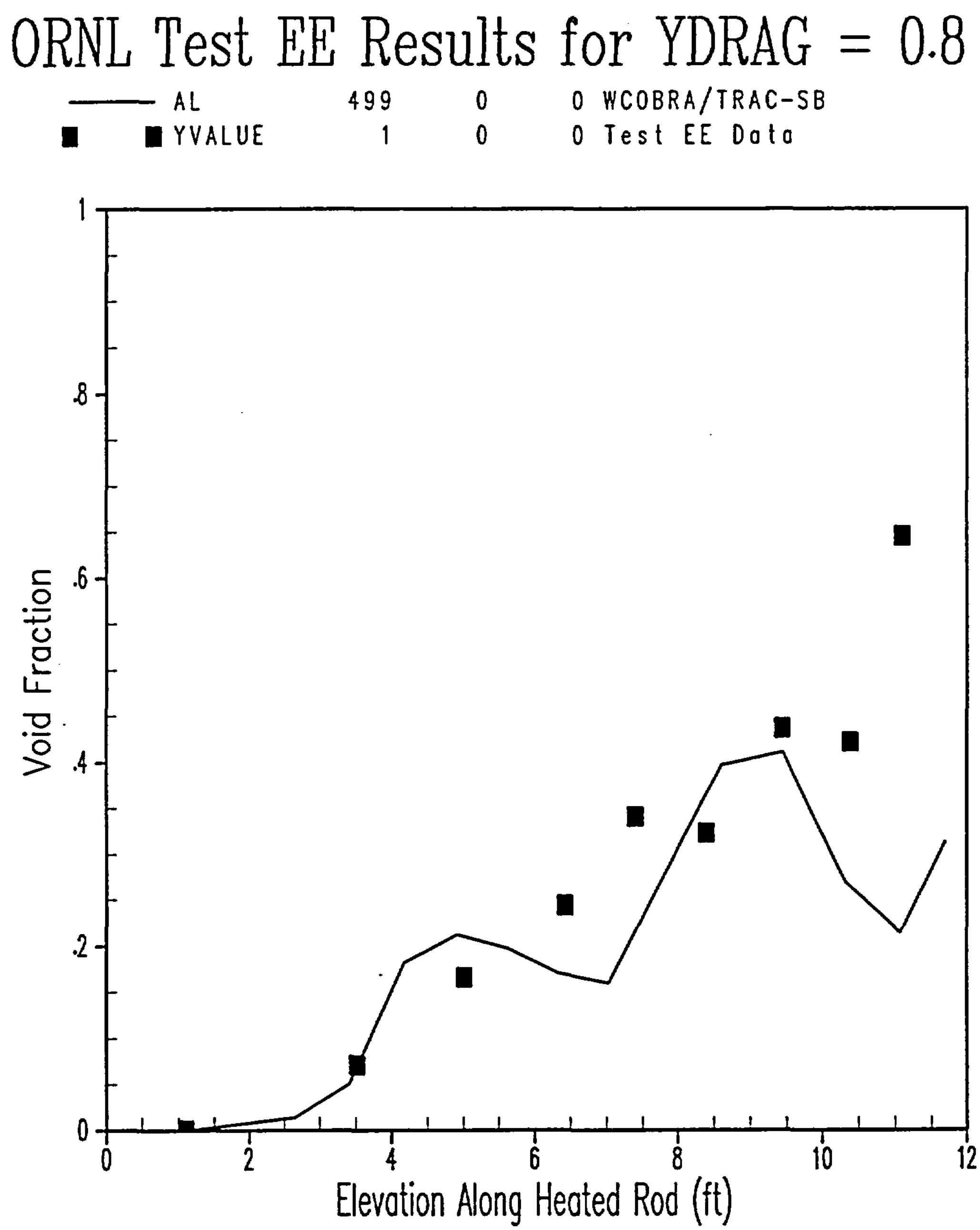

Figure 15-4-2-14. Comparison of Predicted and Measured Void Profiles for ORNL-THTF Test 3.09.10EE

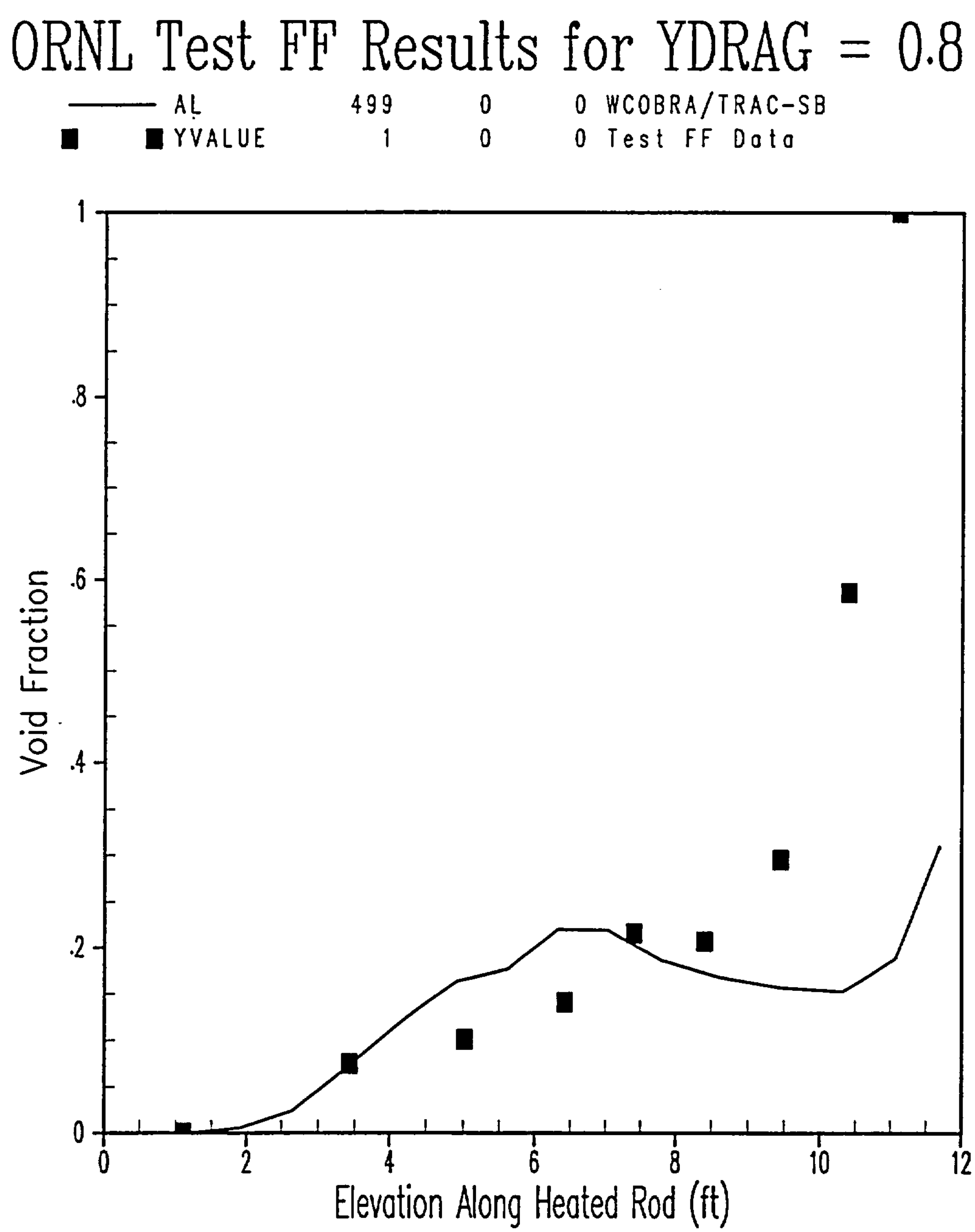

Figure 15-4-2-15. Comparison of Predicted and Measured Void Profiles for ORNL-THTF Test 3.09.10FF

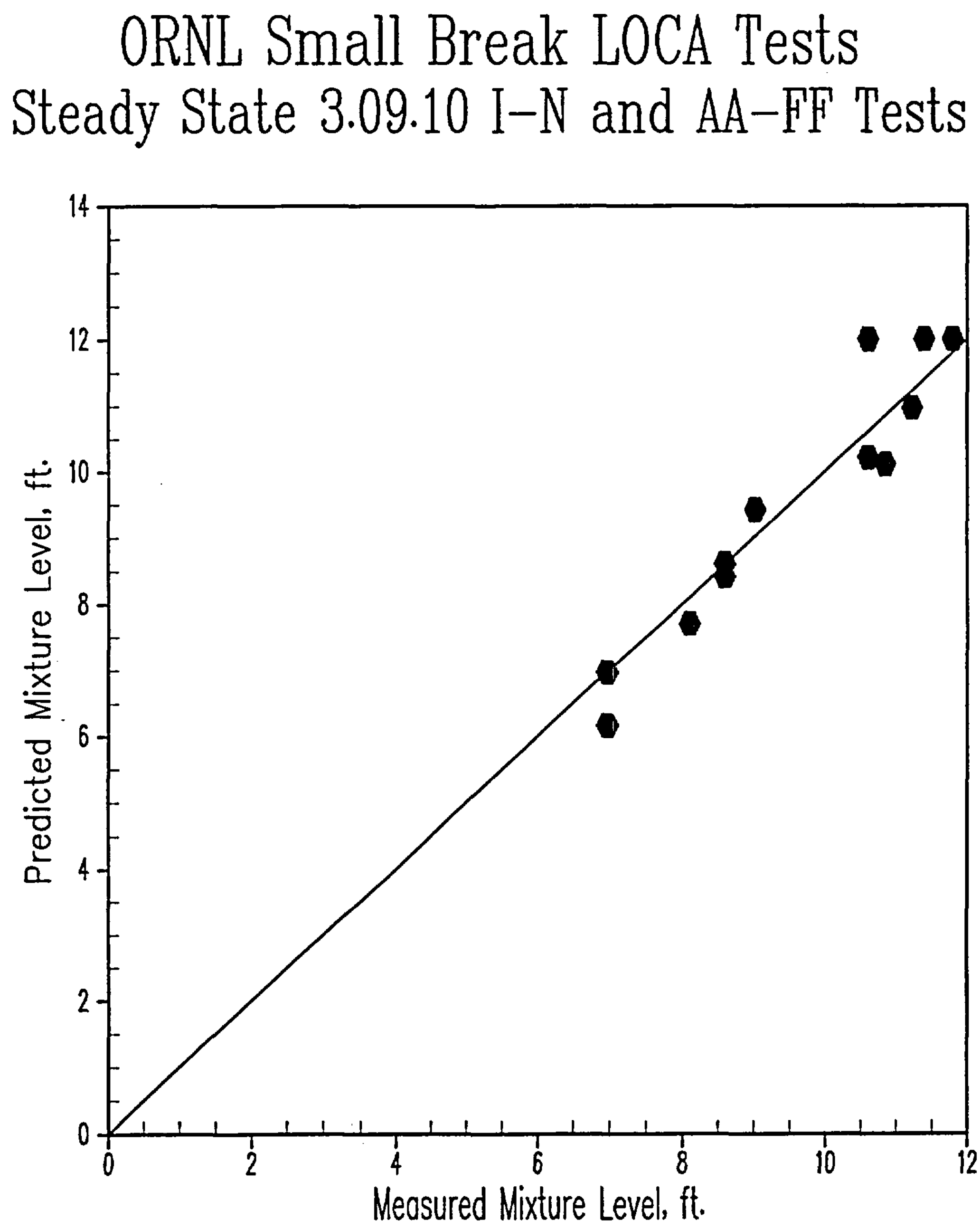

Figure 15-4-2-16. Comparison of Predicted and Measured Mixture Levels for ORNL-THTF Tests, YDRAG=0.8

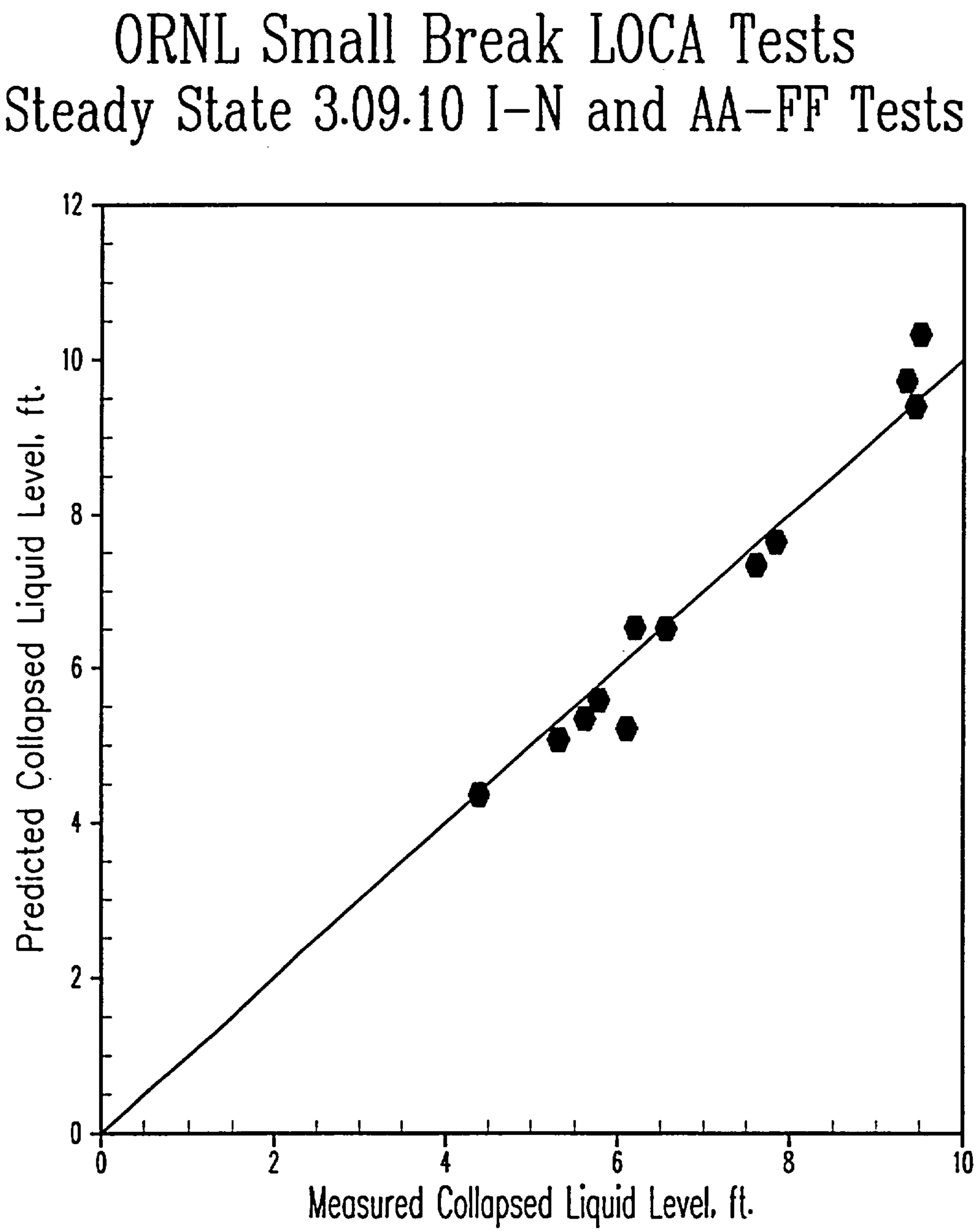

Figure 15-4-2-17. Comparison of Predicted and Measured Collapsed Liquid Levels for ORNL-THTF Tests, YDRAG=0.8

15-4-3 Simulation of G-1 Core Uncovery Tests

15-4-3-1 Introduction

A series of core uncovery experiments was conducted in the Westinghouse Emergency Core Cooling System (ECCS) High Pressure Test Facility. Figure 15-4-3-1 shows a schematic of this facility. [

]a,c Figure 15-4-3-2 shows a schematic of the heater rod bundle.

The bundle was instrumented [

]a,c

The tests were performed for a range [

]a,c

Additional information on the test facility and the data for the G-1 Core Uncovery Tests are in WCAP-9764 (1980).

15-4-3-2 WCOBRA/TRAC Model of G-1 Test Facility

Figure 15-4-3-3 shows the WCOBRA/TRAC model for the G-1 test bundle and loop. The heated bundle is modelled with [

]a,c

[

]a,c

15-4-3-3 Test Matrix for G-1 Uncovery Tests

Eight of the tests run in the G-1 Uncovery Test series fall into the range of conditions expected in a small break LOCA in a typical PWR. Table 15-4-3-1 lists these tests. The tests selected [

]a,c.

15-4-3-4 Simulation of G-1 Core Uncovery Tests

Each simulation was started with the initial water level covering the top of the test bundle (i.e., the initial liquid fraction in the test section was 1.0); channels above the top elevation of the test bundle were initiated as void. The initial water temperature was based on available fluid temperature measurements and was generally a few degrees subcooled in core and downcomer channels at the start of the test. The test was started when the power to the bundle was turned on at 0.0 seconds and simulation continued for several hundred seconds, depending on the length of the experiment.

The main parameters of interest in the simulations are the uncovery times of both the 10-foot and the 8-foot elevations, and the amount of water present in the bundle when the uncovery occurred. The uncovery time is readily identified in the test data as the time when the thermocouples at a particular elevation began to rapidly increase in temperature. The test report listed the average void fraction below the measurement elevation as the parameter representative of the amount of mass in the bundle. This value was deduced from DP cell measurements.

15-4-3-5 Discussion of Results

Typical simulation results are shown for run 63 in Figure 15-4-3-4. Run 63 [

]^{a,c}

The predicted void fraction in the test bundle increased rapidly at the start of the (YDRAG = 1.0) WCOBRA/TRAC-SB run. While the lower half of the bundle was predicted to remain at relatively low void fraction, boiloff at the top of the bundle progressively caused the void fractions to increase and eventually become single-phase vapor. Early in the simulation, the [

]^{a,c} The collapsed liquid level predicted in the test section falls as indicated in Figure 15-4-3-4.

After 210 seconds, the void fraction in the channel at the 10-foot bundle elevation became single-phase vapor. The predicted cladding temperature at the 10-foot elevation for run 63, as shown in Figure 15-4-3-4, increases rapidly at this time. At the end of the simulation, the mixture level approaches the 6-foot elevation. The uncovery times at the 8- and 10-foot elevations are easily identifiable in Figure 15-4-3-4; uncovery at the 10-foot elevation occurs at 210 seconds and at the 8-foot elevation, 320 seconds. The heatup rate is greater at the 8-foot elevation because of the higher local power. The summary of results and the comparison to the data for run 63 and the other G-1 simulations are listed in Table 15-4-3-2. The uncovery times in the WCOBRA/TRAC-SB predictions executed with YDRAG = 0.8 in the test bundle are gleaned from the review of the cladding temperature figures, as described above.

Table 15-4-3-2 compares the predicted and measured uncovery times for the eight G-1 test simulations. The predicted uncovery time is less than that measured for some points, but the prediction is greater for others. The trend is for the low pressure cases to exhibit predicted uncovery times beyond the measured values and for the high pressure cases to underpredict the uncovery times. The table also compares the level swell predictions to the data at the time of core uncovery for the 10-foot and 8-foot elevations. Figures 15-4-3-5 and 15-4-3-6 present the data in Table 15-4-3-2 graphically.

The level swell is both overpredicted and underpredicted by WCOBRA/TRAC-SB with YDRAG = 0.8 specified for the test bundle. Therefore, cases with increased and reduced interfacial drag were investigated by analyzing the tests using YDRAG values of 1.0, 1.2, 0.65, 0.5, 0.4, and 0.3. WCOBRA/TRAC-SB predictions of uncovery time and level swell decrease as YDRAG is decreased. The YDRAG values at which WCOBRA/TRAC-SB matches the G-1 test data level swell are shown in Table 15-4-3-3. Figure 15-4-3-7 compares the YDRAG values to match the measured level swell as a function of total bundle power for the tests. Consistent with the data, WCOBRA/TRAC-SB shows [

]^{a,c}

15-4-3-6 Summary and Conclusions

In general, WCOBRA/TRAC-SB predicted the uncovery times and major trends in the G-1 Core Uncovery Test data with reasonable accuracy; predicted level swell values were both greater and less than the test data. The effect of variations in YDRAG were explored, and the set of multipliers that forces the code to match the G-1 test data level swell was identified. The minimum value for this set is $YDRAG_{min}$ = 0.353, and the maximum is $YDRAG_{max}$ = 1.121. The average value is $YDRAG_{ave}$ = 0.693.

The bias observed in the WCOBRA/TRAC-SB prediction of the G-1 tests is similar but somewhat higher than that observed in the ORNL-THTF simulations. Taken together, the ORNL-THTF and G-1 simulations provide the YDRAG distribution for the core region level swell in the small break LOCA uncertainty analysis of a PWR.

Table 15-4-3-1
Core Uncovery Test Matrix

a,c

Table 15-4-3-2

G-1 Simulation Results Summary, YDRAG = 0.8

a,c

(a) The specific elevations reported in the WCOBRA/TRAC-SB runs are 10.03 ft. and 7.90 ft., respectively.

Table 15-4-3-3

YDRAG Values to Match G-1 Level Swell Data

a,c

a,c

Figure 15-4-3-1. Westinghouse ECCS High Pressure Test Facility (G-1 Loop)

a,c

[ ]

Figure 15-4-3-2. G-1 Core Uncovery Test Heater Rod Bundle

a,c

Figure 15-4-3-3. WCOBRA/TRAC Model of the G-1 Test Bundle

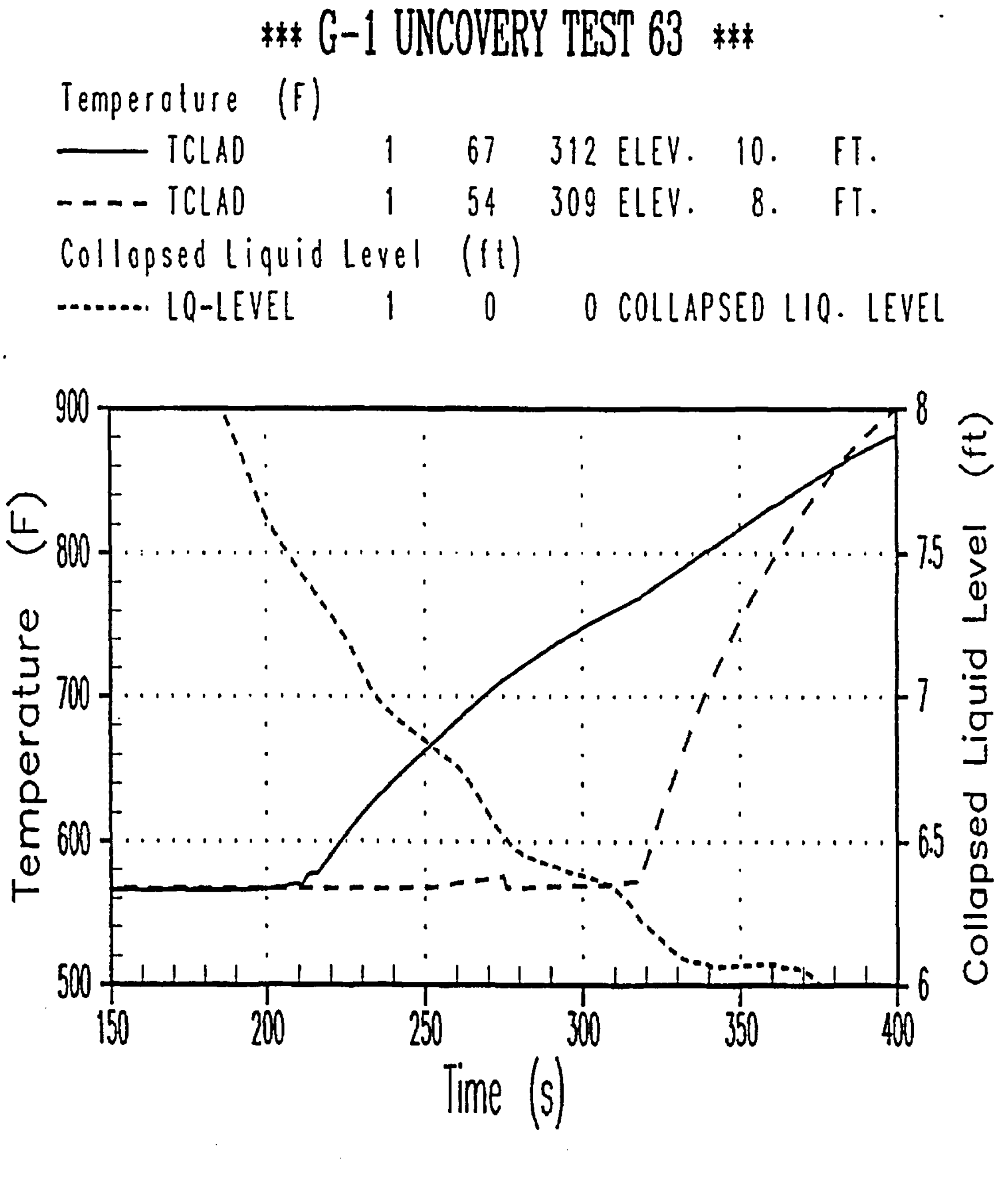

Figure 15-4-3-4. Collapsed Liquid Level and Predicted Cladding Temperatures at the 8- and 10-Foot Elevations, G-1 Run 63

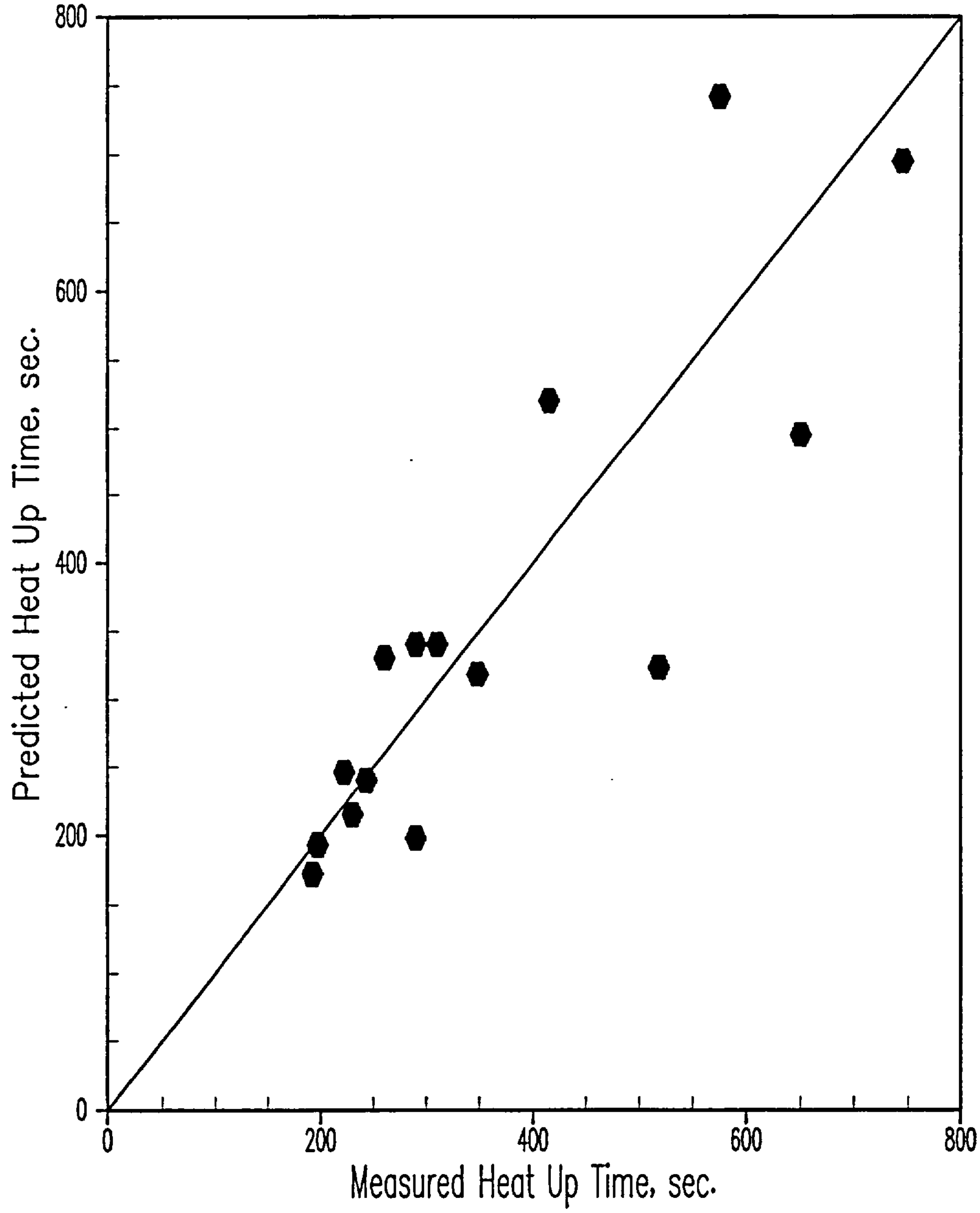

Figure 15-4-3-5. Comparison of Predicted and Measured Uncovery Times, YDRAG=0.8

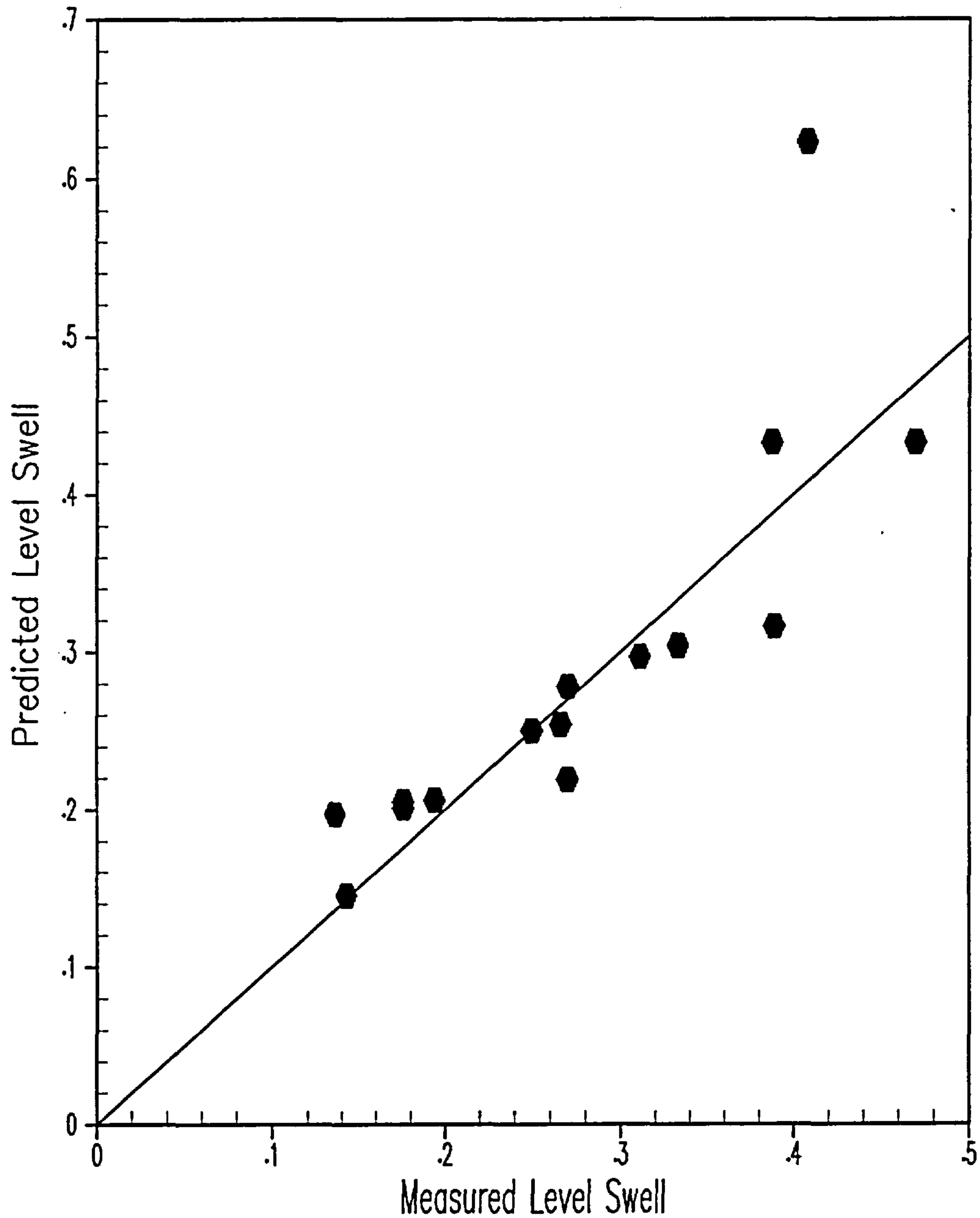

Figure 15-4-3-6. Comparison of Predicted and Measured Level Swells at Uncovery, YDRAG=0.8

a,c

Figure 15-4-3-7. **WCOBRA/TRAC-SB YDRAG Value to Match Measured Level Swell Versus Bundle Power**

a,c

[ ]

Figure 15-4-3-8. WCOBRA/TRAC-SB YDRAG Value to Match Measured Level Swell Versus Pressure

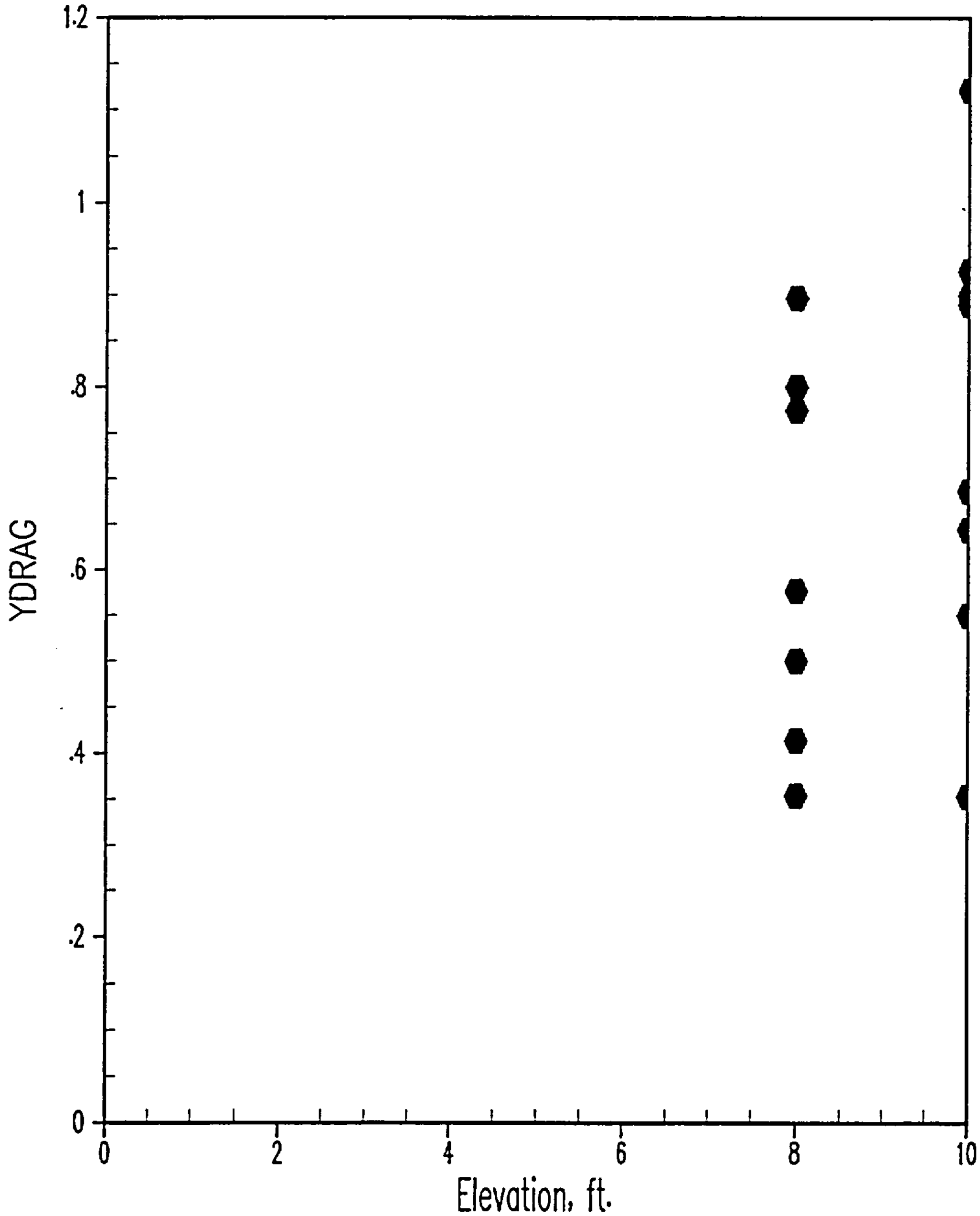

Figure 15-4-3-9. WCOBRA/TRAC-SB YDRAG Value to Match Measured Level Swell Versus Bundle Elevation

15-4-4 GE Vessel Blowdown Tests

15-4-4-1 Introduction

The GE Vessel Blowdown Facility is designed to study basic phenomena such as void fraction distribution and transient liquid-vapor level swell during blowdown. A description of all the tests performed is given in NUREG/CR-1899 (Findlay and Sozzi, 1981).

The blowdown tests were performed in a cylindrical carbon steel vessel. The vessel was a two-piece unit that could be separated at a pair of flanges located near the center of the vessel. The cylindrical portion of the vessel was constructed from Schedule 80 pipe, 12 feet long with an inside diameter of 1 foot. Elliptical heads were welded onto the ends of the pipe to create the vessel. The total vessel volume was 10 cubic feet, and the total height was 14 feet. There were five calorimetric heater rods, 1 inch in diameter and 2 feet high, in the bottom of the vessel to heat the water. The steam exhaust was located at the 13-foot elevation with an orifice that was captured in a flange. The orifices used to control the tank blowdown rate were plates with the prescribed hole machined without a chamber. The orifice was located close to the vessel in a 2-inch Schedule 80 pipe. Figure 15-4-4-1 is a scaled drawing that shows the vessel, its penetrations, the blowdown line, and a suppression pool where the blowdown effluent was discharged.

A 3/4-inch thick perforated plate (containing 109 holes, 9/16-inch diameter), designed to provide an internal flow restriction, was installed between the main vessel flanges at the mid-elevation during some of the tests. The resistance of the plate was varied by plugging a selected number of holes. Orifice plates with different flow areas were used in the blowdown line to limit the blowdown flowrate and vary the vessel depressurization rate.

Figure 15-4-4-2 shows the instrumentation arrangement used to measure three basic parameters: pressures, pressure differences, and temperatures. Vessel pressure and differential pressures were measured using strain-gauge pressure transducers, and temperatures were measured using Iron-Constantan thermocouples. The transient void fraction and the mixture level were calculated from differential pressure measurements.

The vessel was initially filled with demineralized water and boiled at atmospheric pressure for approximately 30 minutes to liberate any dissolved gas in the supply water. A vent at the top of the vessel was then closed, and the water was heated to establish the initial conditions (which were a nominal pressure of 1000 psi and 545°F). Actual initial conditions for each test are given in the test matrix in Table 15-4-4-1.

With the facility initially heated and pressurized, several top-break blowdown tests were conducted using different-sized orifice plates to vary the blowdown transient. The tests also varied the open area of the resistance plate at the vessel mid-plane.

15-4-4-2 WCOBRA/TRAC Model for GE Vessel Blowdown Tests

The WCOBRA/TRAC model of the GE Vessel Blowdown Facility is shown in Figure 15-4-4-3. The test vessel itself is modelled [

]^{a,c} Actual dimensions of the orifice were used in the modelling of the flowpath to the break.

15-4-4-3 Test Matrix for Simulations

Table 15-4-4-1 lists the seven tests in the small break test series. Each was simulated with WCOBRA/TRAC-SB.

15-4-4-4 Simulation of GE Vessel Blowdown Tests

The results of the WCOBRA/TRAC-SB simulations of the Vessel Blowdown Tests are compared to experimental data in Figures 15-4-4-4 to 15-4-4-17. For each test, a comparison between the predicted and measured vessel pressure is presented; the two-phase level predicted and measured values are also presented. For the WCOBRA/TRAC-SB prediction, the two-phase level was defined as the elevation where a void fraction of 0.95 defines a sharp gradient between adjacent hydraulic cells.

In general, the comparison between predicted and measured vessel pressure shows the code underpredicted the measured pressures. Table 15-4-4-2 compares the WCOBRA/TRAC-SB model prediction of several parameters with test data.

The predicted mixture levels for the tests vary from being overpredicted to being underpredicted. The variation of mixture level with time is generally well predicted. Overall, the void fraction in the two-phase mixture tends to be overpredicted by WCOBRA/TRAC-SB.

15-4-4-5 Effect of Interfacial Drag Multiplier

The simulations of the GE Vessel Blowdown Tests were also rerun with WCOBRA/TRAC-SB to investigate the impact of the interfacial drag multiplier (YDRAG) on the prediction of the two-phase level and pressure. Simulations were made with YDRAG = 0.65 to compare the effect of interfacial drag on the results using WCOBRA/TRAC-SB. The results indicate a small pressure effect of using a lower YDRAG value. Figures 15-4-4-18, -19, and -20 compare the YDRAG = 1.0 (solid curve) to YDRAG = 0.65 (dashed curve) results. In all cases, the depressurization to 400 psi is quicker with YDRAG = 0.65 because steam is passing to the exit BREAK more efficiently. These effects are expected because with a lower interfacial drag coefficient, there is less force acting to raise the two-phase level in the vessel. For void fraction predictions, the difference is again small; in some cases, the void fraction is shifted lower with a YDRAG = 0.65 at a given elevation, and in others, it shifts higher. Overall, there is little difference between the simulation results of void fraction for a given test caused by varying YDRAG.

15-4-4-6 Summary and Conclusions

The results of the GE Vessel Blowdown Test simulations tend to confirm the results for the ORNL-THTF Uncovered Bundle Tests and the G-1 Core Uncovery Test simulations, which showed that WCOBRA/TRAC tends to underpredict the amount of mass present in a given test. The results of the GE Vessel Blowdown Tests using WCOBRA/TRAC-SB indicate that varying YDRAG appears to make little difference relative to the pressure and void fraction predicted. Therefore, the blowdown flashing behavior predicted by the code as YDRAG is varied within the core during plant sensitivity studies is judged to be minimally affected; the YDRAG values in the core may be specified based on the effect on the fluid condition at the time of core uncovery during the boiloff phase of a small break LOCA, in the knowledge that the blowdown phase behavior is not significantly impacted by the selection. In particular, a core YDRAG value of 0.8 is employed for both the integral test and PWR simulations.

Table 15-4-4-1

Summary of Test Parameters for Small Blowdown Vessel Steam Blowdown Tests

Test No.	Orifice Size (in.)	Restriction Plate (9/16 in. diameter holes)	Initial Conditions	
			Pressure (psia)	Level (ft)
8-21-1	3/8	109 holes	1015	8.89
8-25-1	½	109 holes	1020	8.82
8-28-1	1	109 holes	1015	8.76
9-1-1	3/8	77 holes	1014	8.75
9-15-1	3/8	55 holes	1015	8.74
1004-3	3/8	No plate	1011	10.4
1004-2	7/8	No plate	1011	10.5

Table 15-4-4-2
Characterization of WCOBRA/TRAC-SB Results Versus Test Data

Test	P(t)	L(t)	ALP(1)	ALP(2)	ALP(3)	ALP(4)	ALP(5)	ALP(6)
8-21-1	Low	High	High	OK	High	NC	OK	OK
8-25-1	Low	OK	Low	OK	High	NC	OK	OK
8-28-1	Low	NC	OK	High	High	Low	High	OK
9-1-1	OK	High	High	OK	Low	None	High	OK
9-15-1	OK	Low	High	Low	High	NC	High	OK
1004-3	Low	Low	High	OK	OK	High	High	OK
1004-2	Low	Low	Low	High	High	High	OK	OK

Key:

High = Code overpredicts data.
Low = Code underpredicts data.
OK = Prediction agrees well with data for most of the transient.
NC = Not clear. No consistent trend found in the comparison.
None = No comparison. Data are not available.
P(t) = Pressure transient prediction
L(t) = Mixture level transient prediction
ALP(N) = Void fraction prediction at elevation N of Figure 15-4-4-3

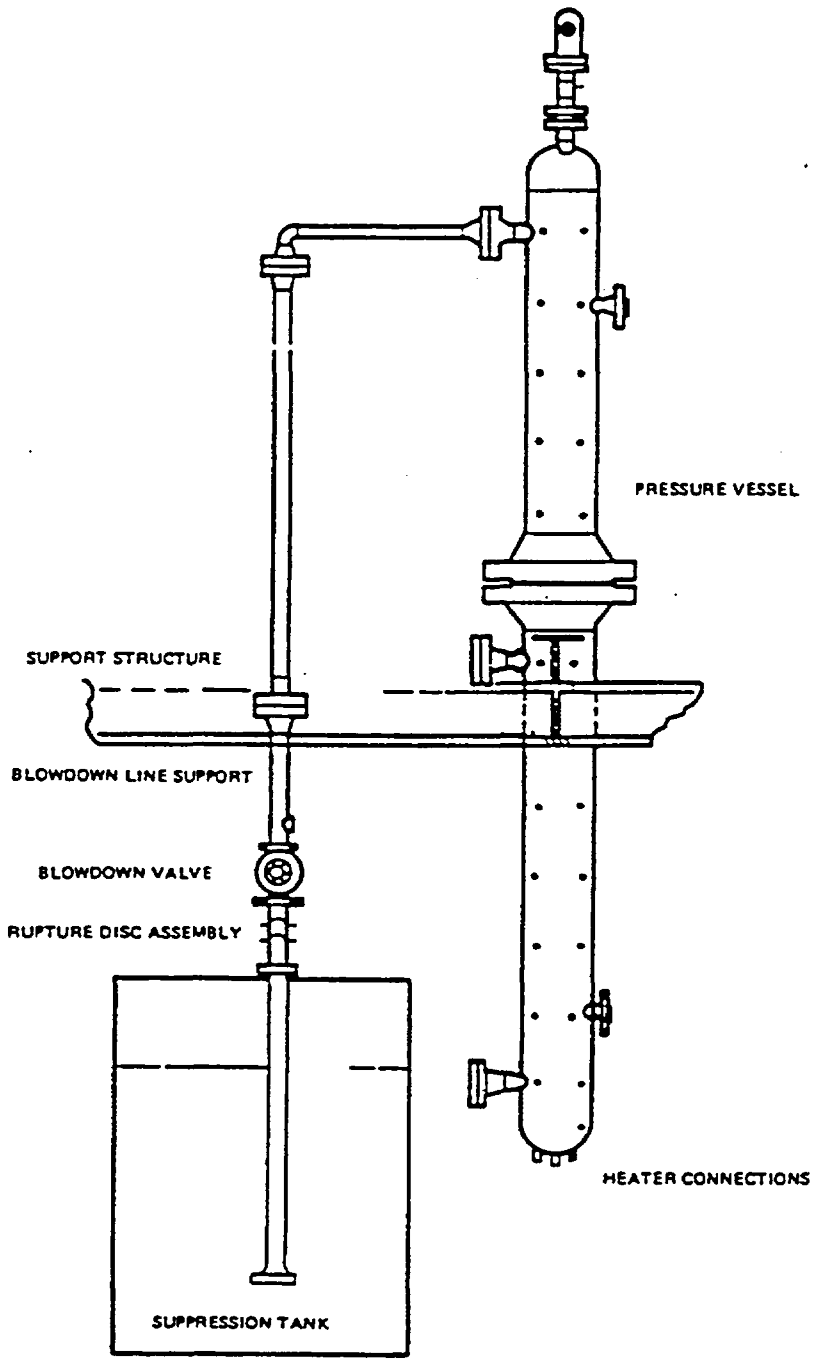

Figure 15-4-4-1. Small Blowdown Vessel

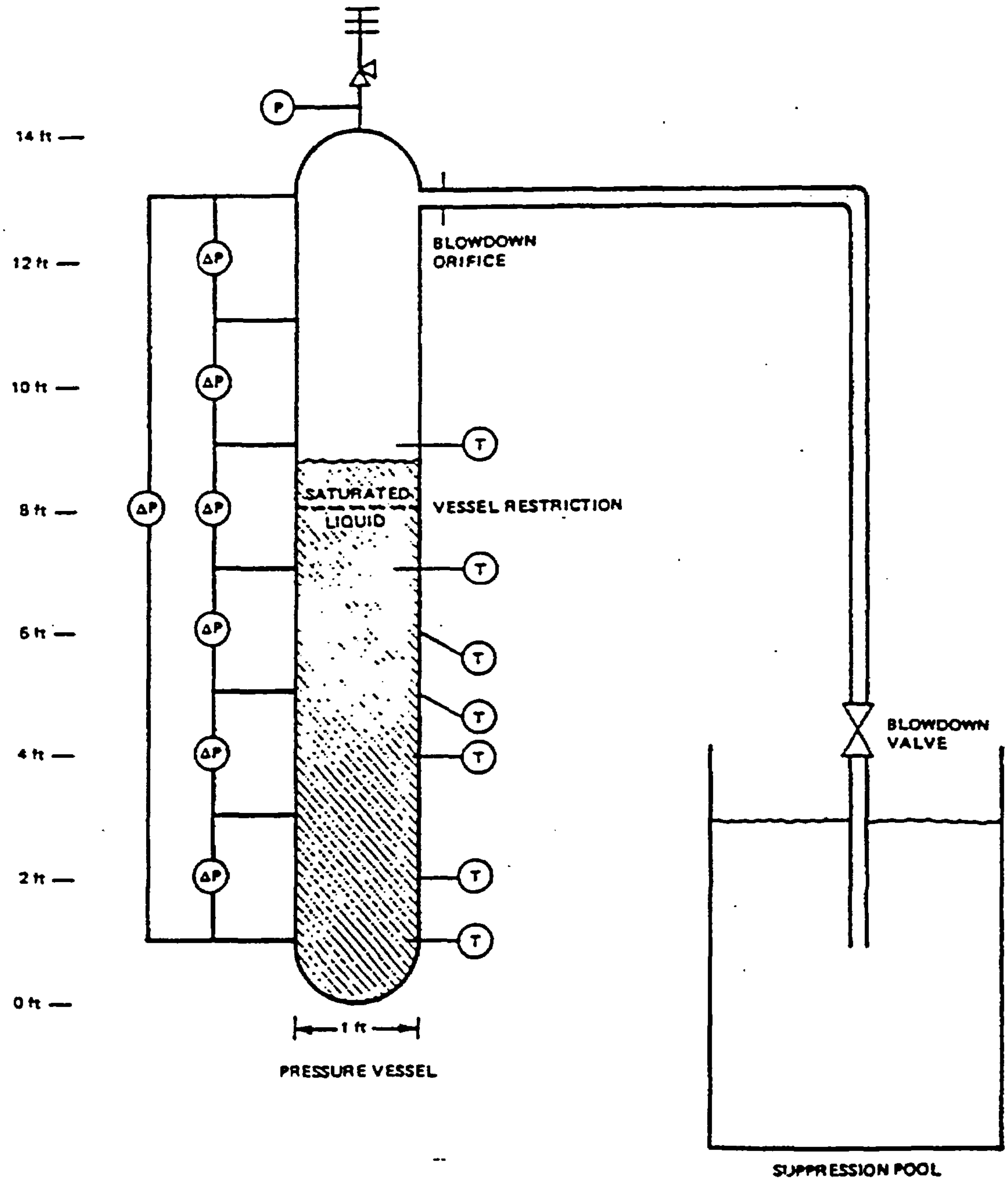

Figure 15-4-4-2. Small Blowdown Vessel Instrumentation

a,c

Figure 15-4-4-3. WCOBRA/TRAC Model of the GE Vessel Blowdown Facility

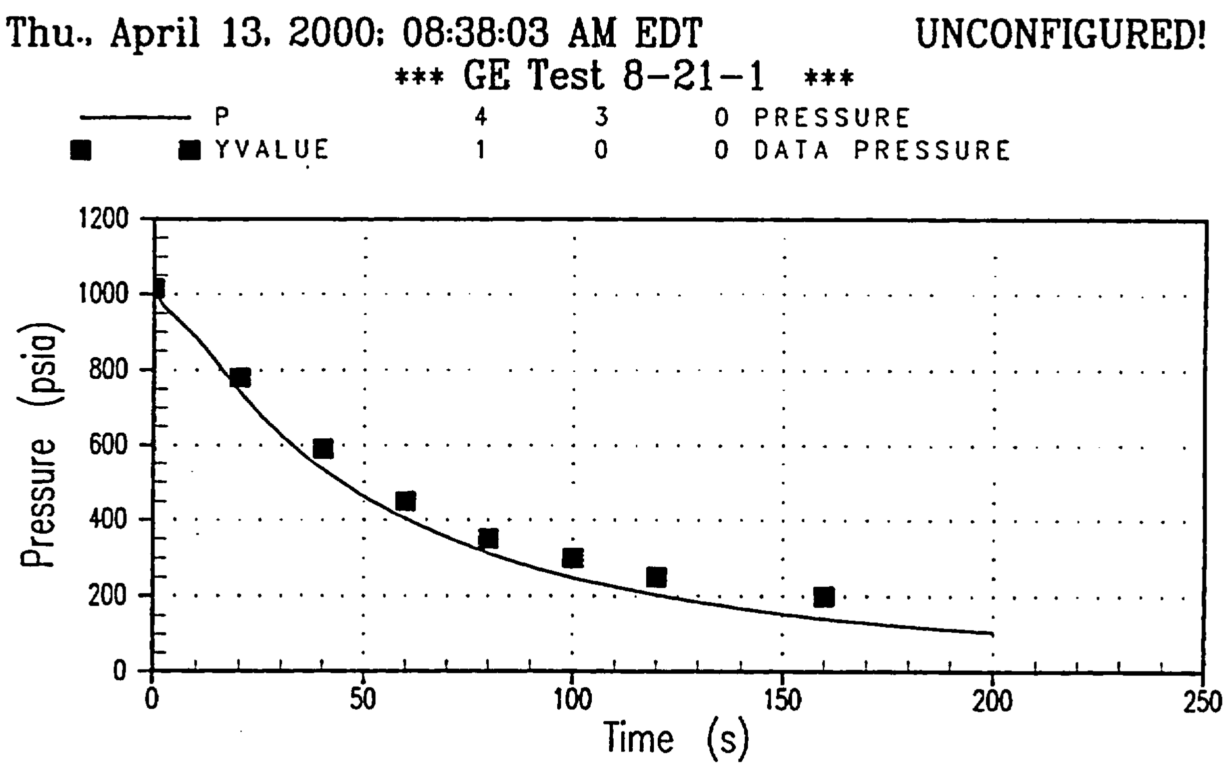

Figure 15-4-4-4. Comparison of Predicted and Measured Vessel Pressure, Test 8-21-1

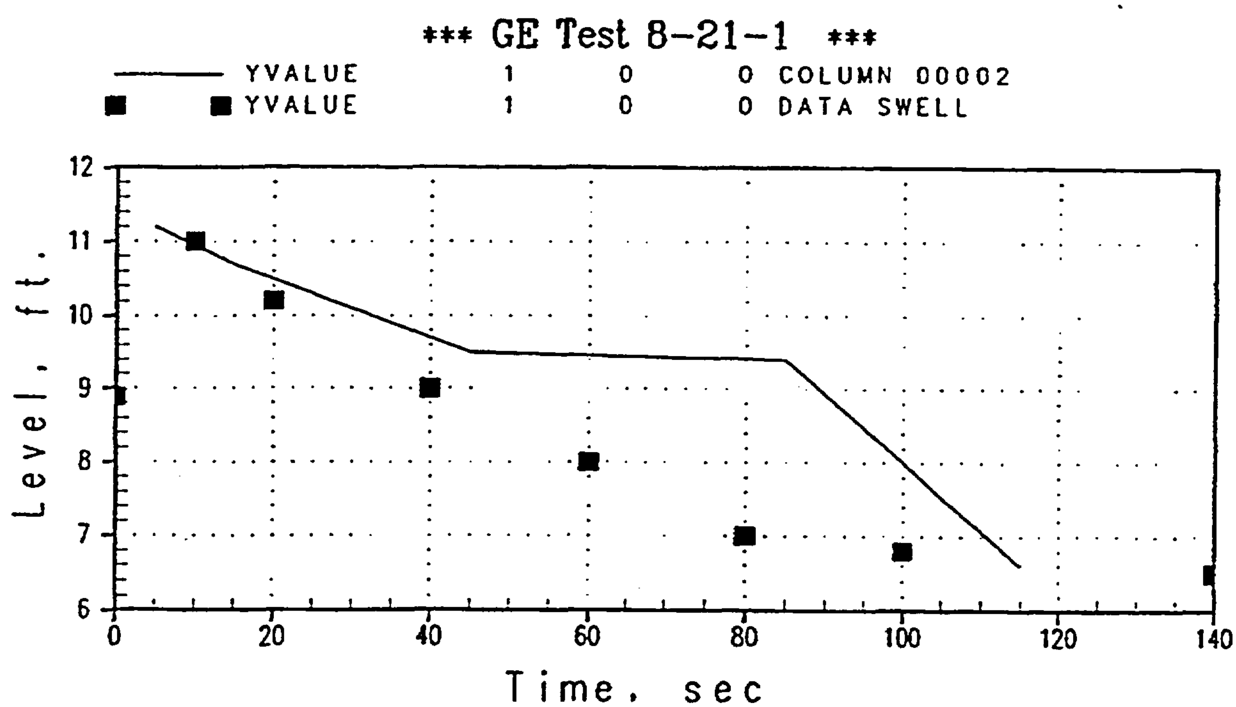

Figure 15-4-4-5. Comparison of Predicted and Measured Vessel Level, Test 8-21-1

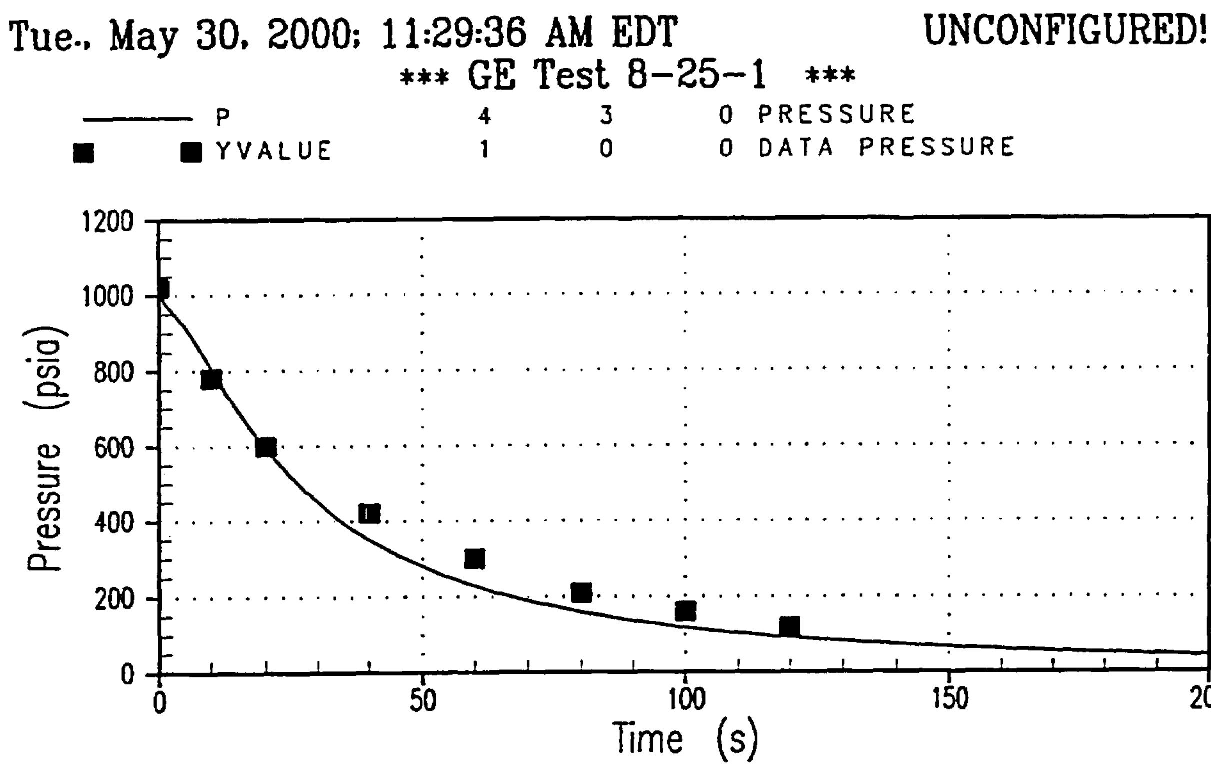

Figure 15-4-4-6. Comparison of Predicted and Measured Vessel Pressure, Test 8-25-1

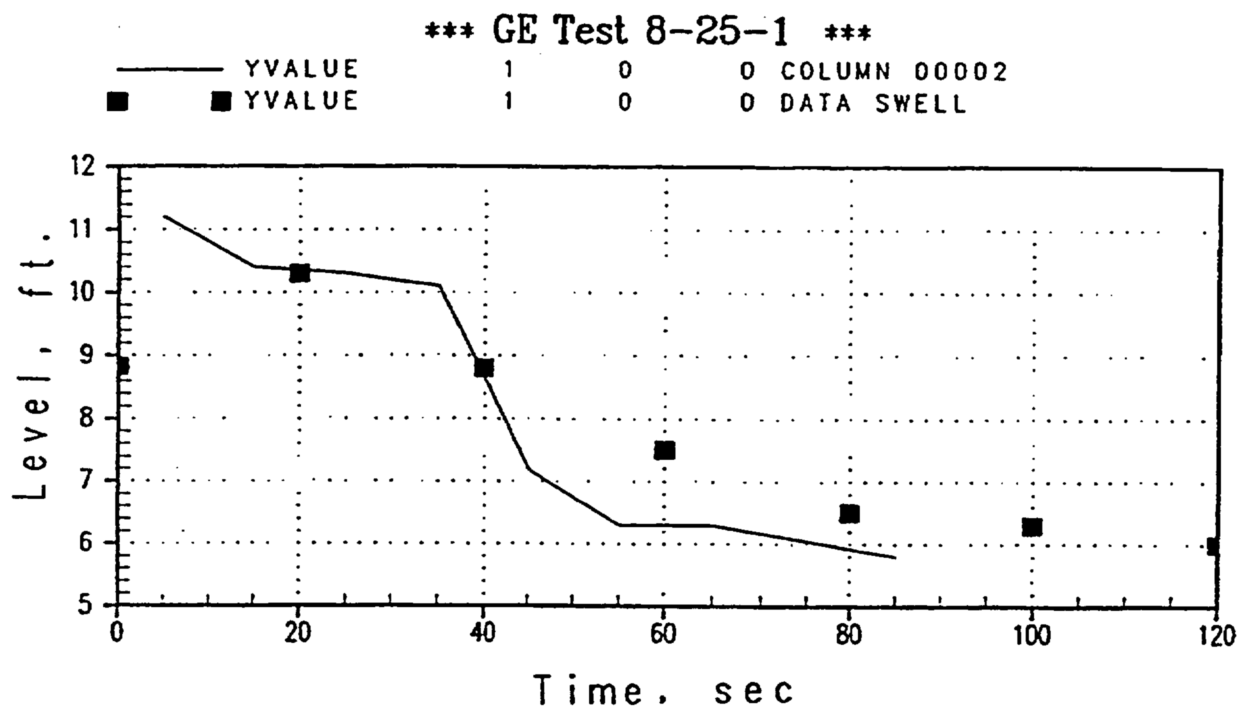

Figure 15-4-4-7. Comparison of Predicted and Measured Vessel Level, Test 8-25-1

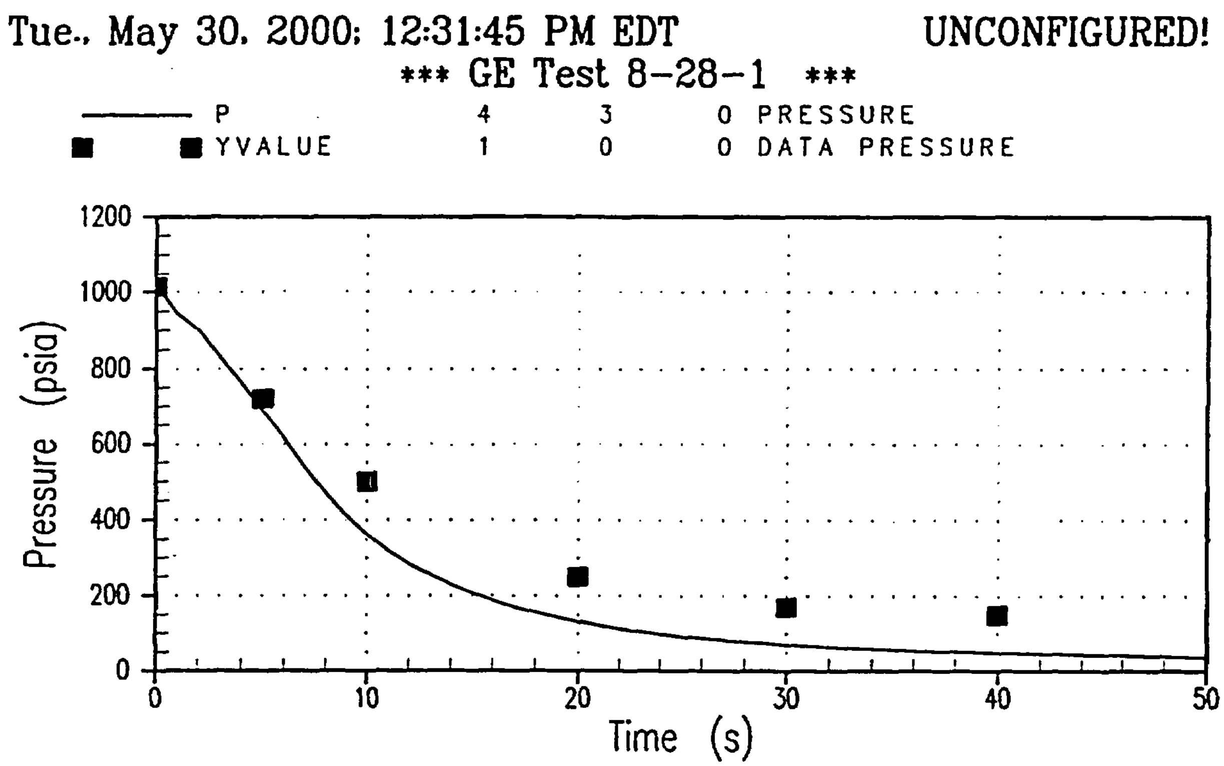

Figure 15-4-4-8. Comparison of Predicted and Measured Vessel Pressure, Test 8-28-1

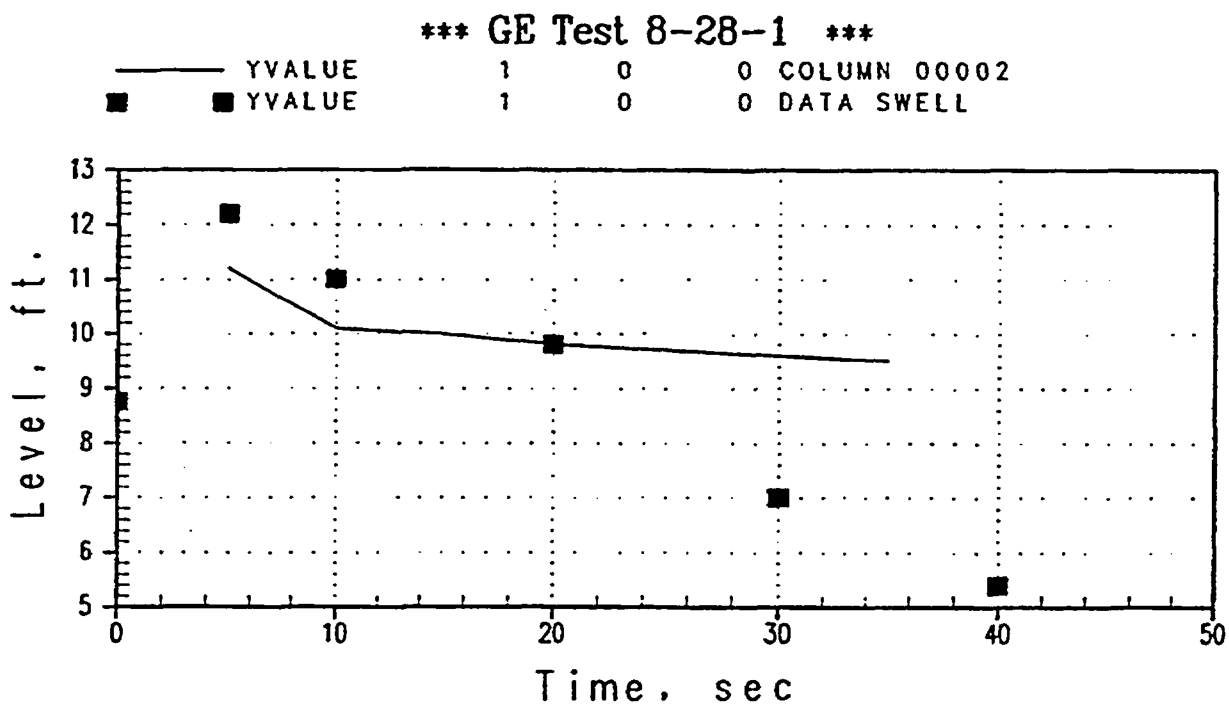

Figure 15-4-4-9. Comparison of Predicted and Measured Vessel Level, Test 8-28-1

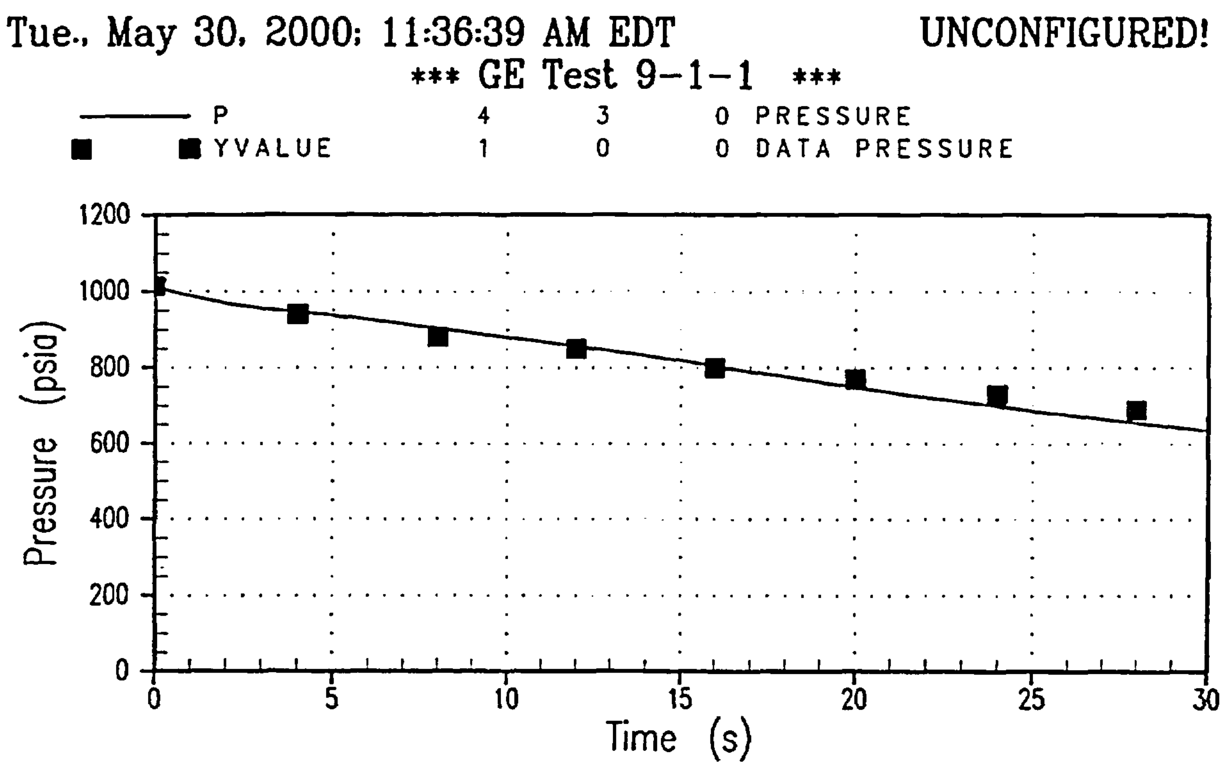

Figure 15-4-4-10. Comparison of Predicted and Measured Vessel Pressure, Test 9-1-1

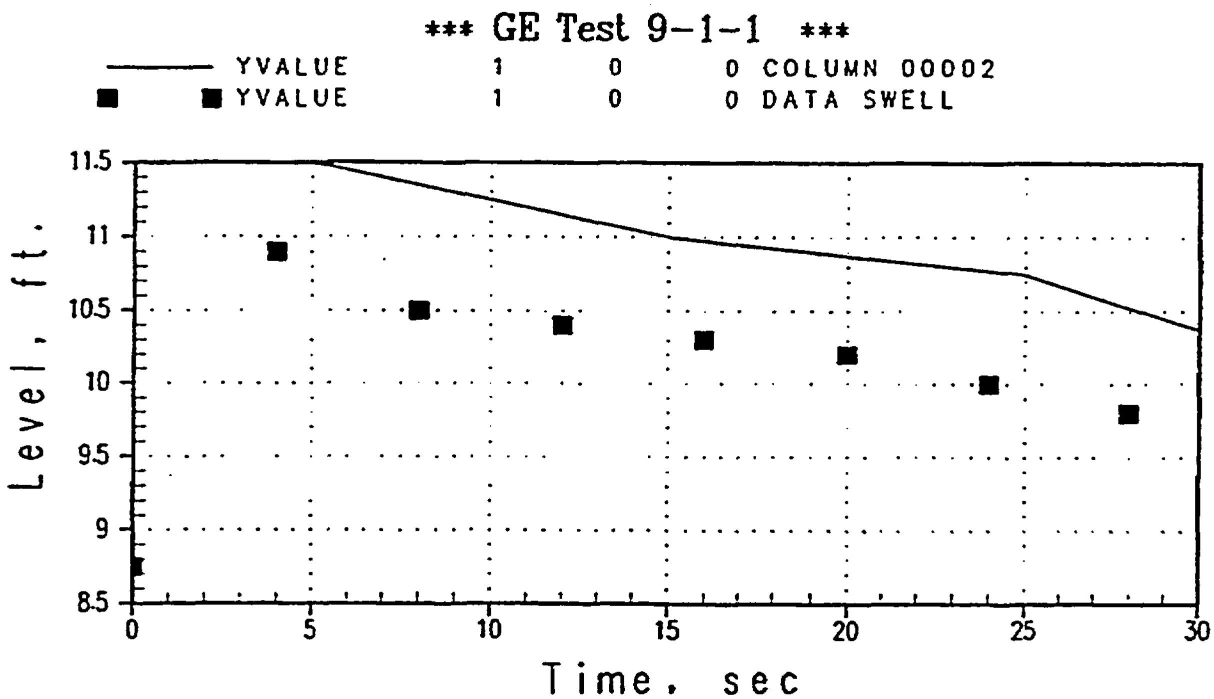

Figure 15-4-4-11. Comparison of Predicted and Measured Vessel Level, Test 9-1-1

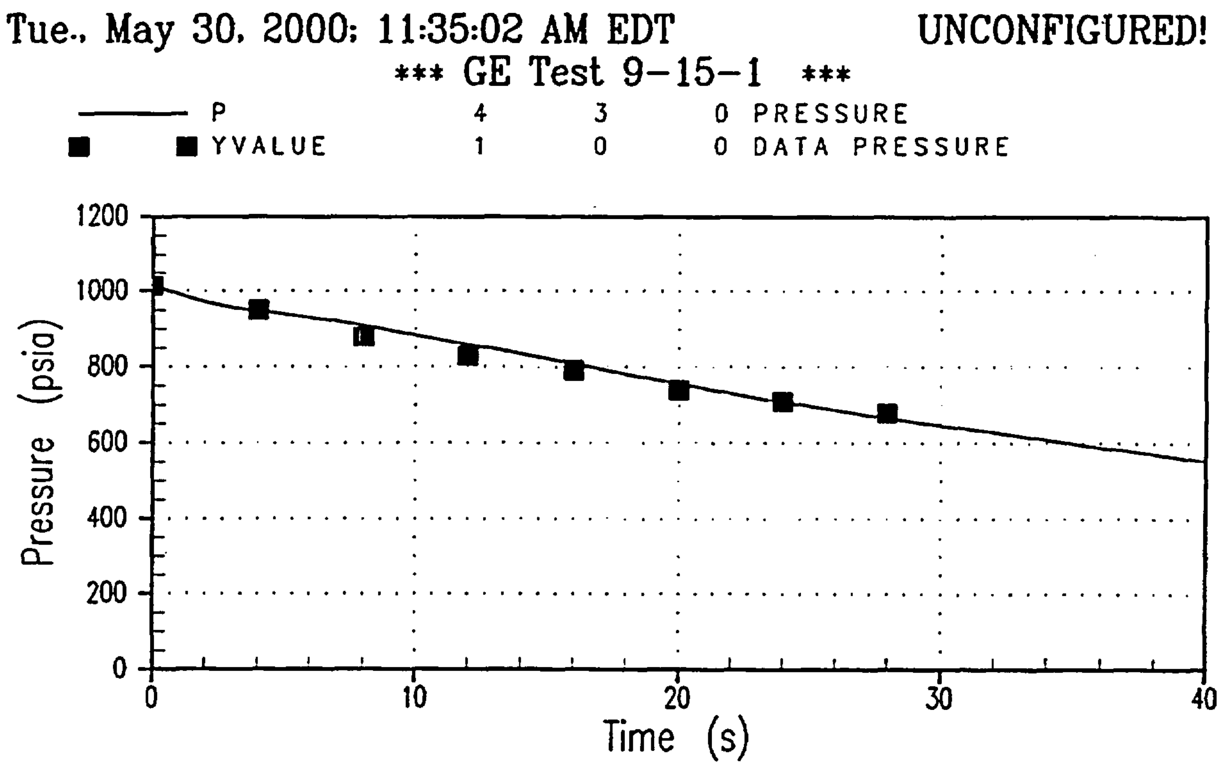

Figure 15-4-4-12. Comparison of Predicted and Measured Vessel Pressure, Test 9-15-1

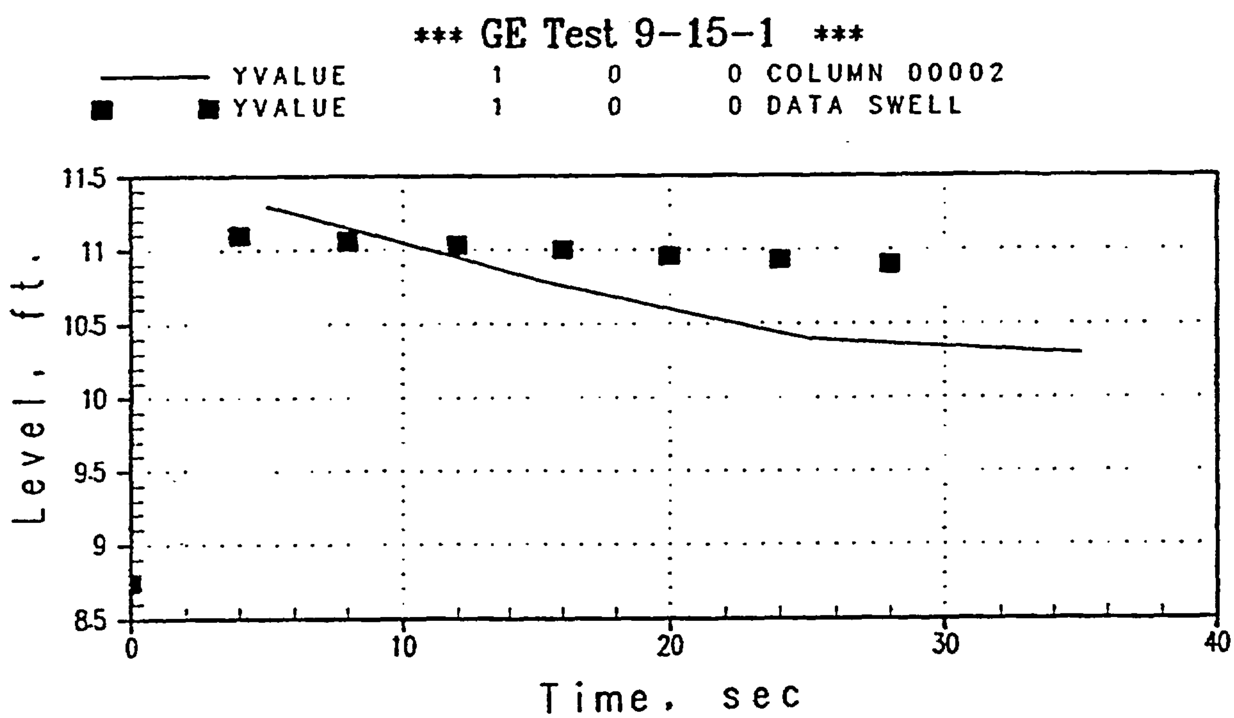

Figure 15-4-4-13. Comparison of Predicted and Measured Vessel Level, Test 9-15-1

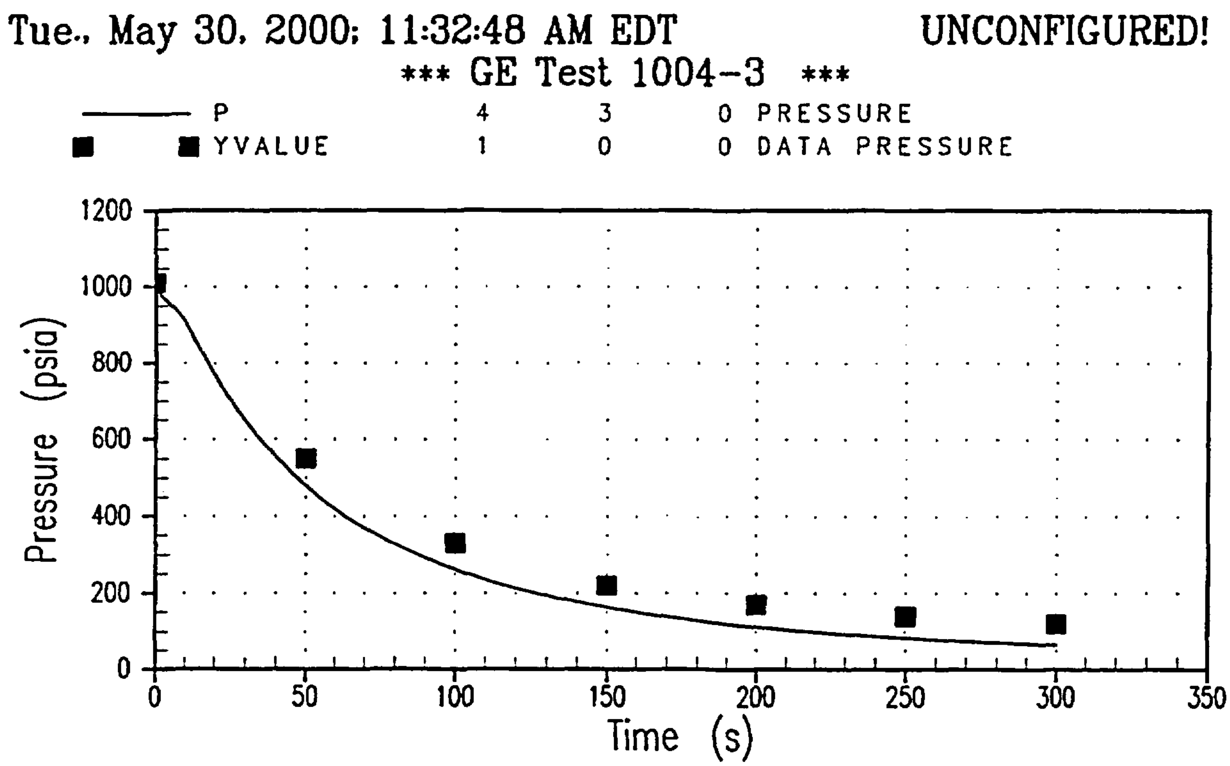

Figure 15-4-4-14. Comparison of Predicted and Measured Vessel Pressure, Test 1004-3

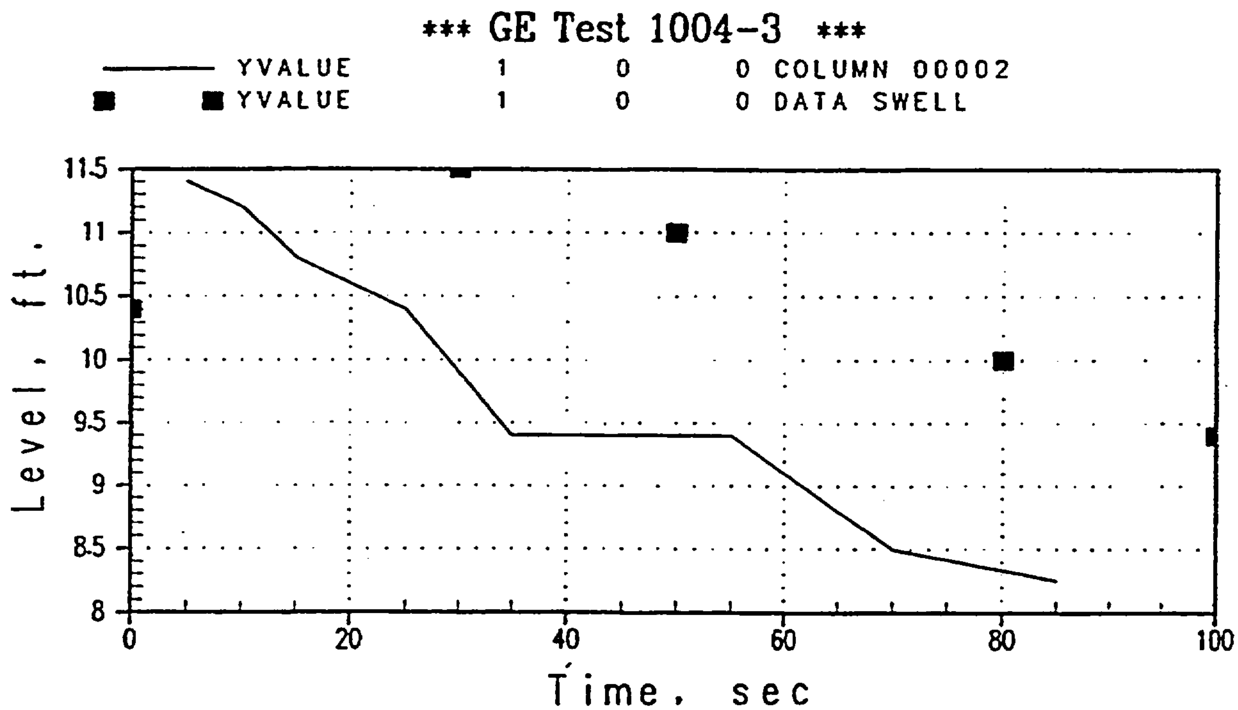

Figure 15-4-4-15. Comparison of Predicted and Measured Vessel Level, Test 1004-3

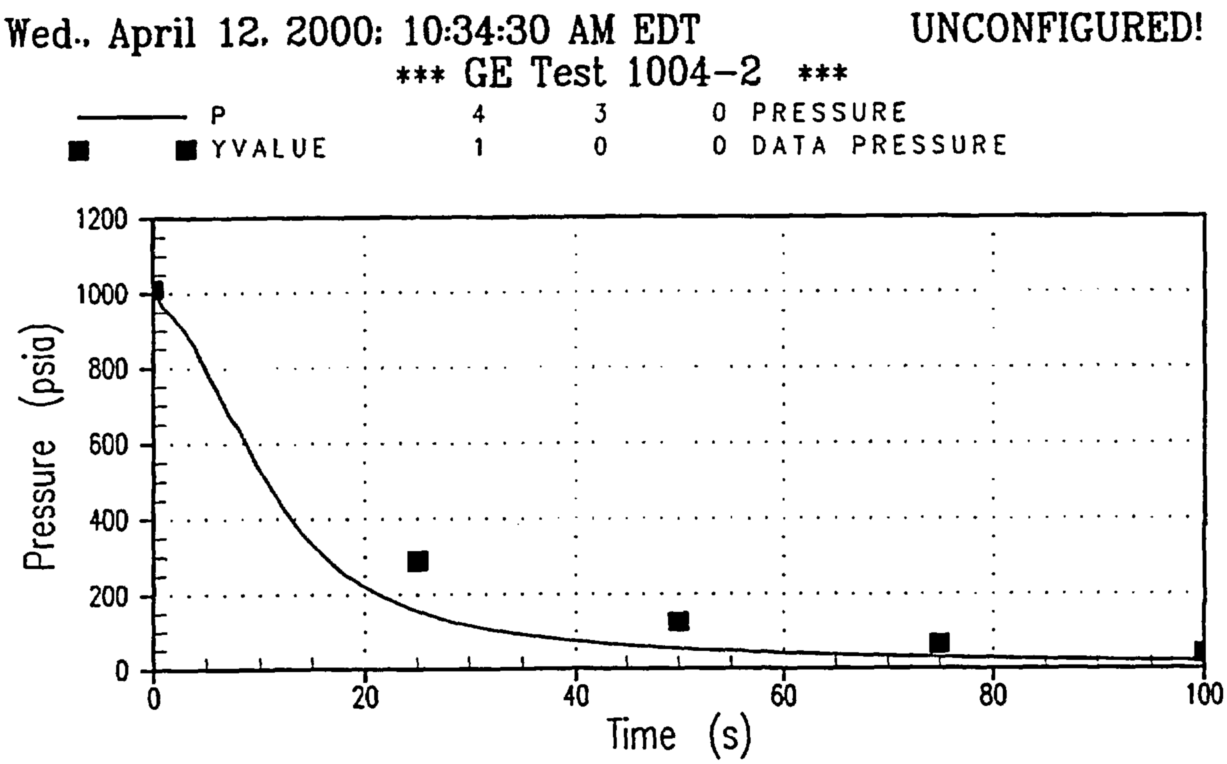

Figure 15-4-4-16. Comparison of Predicted and Measured Vessel Pressure, Test 1004-2

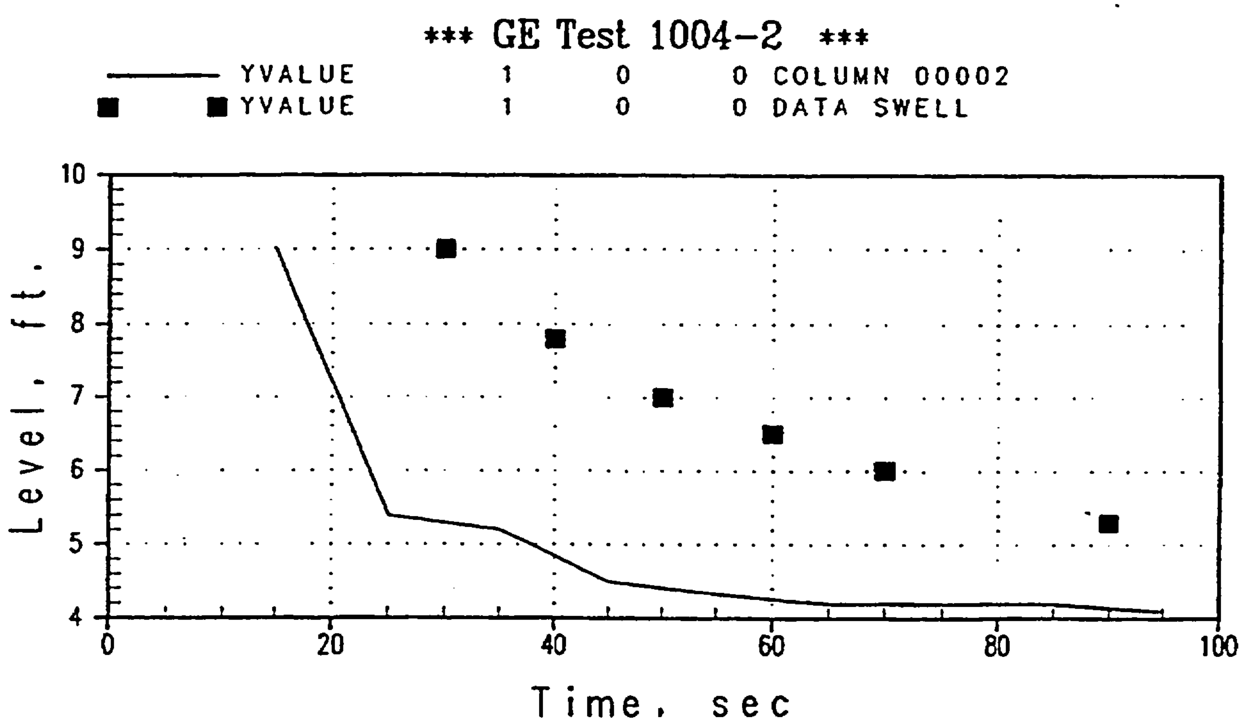

Figure 15-4-4-17. Comparison of Predicted and Measured Vessel Level, Test 1004-2

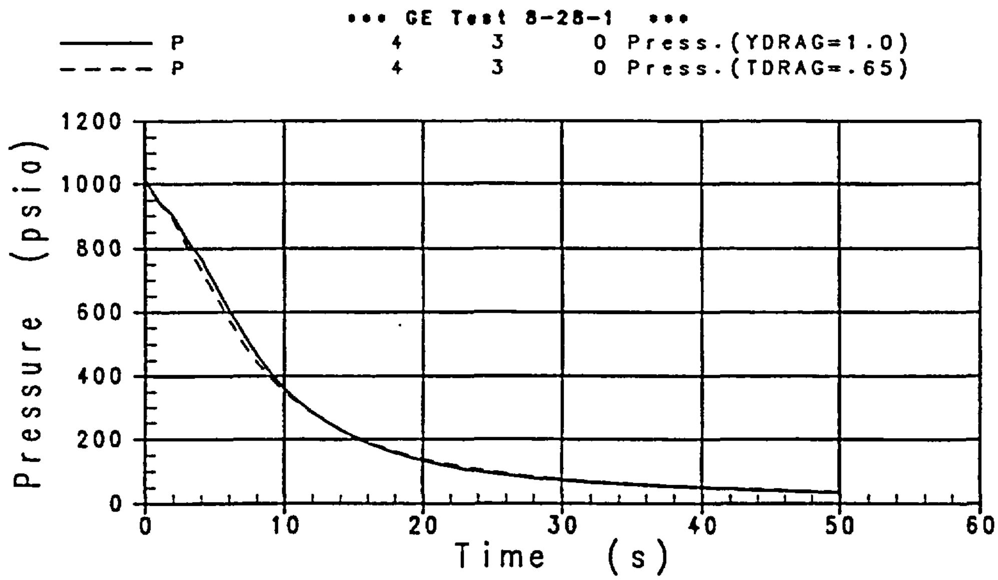

Figure 15-4-4-18. Effect of YDRAG Multiplier on the Pressure Prediction, Test 8-28-1

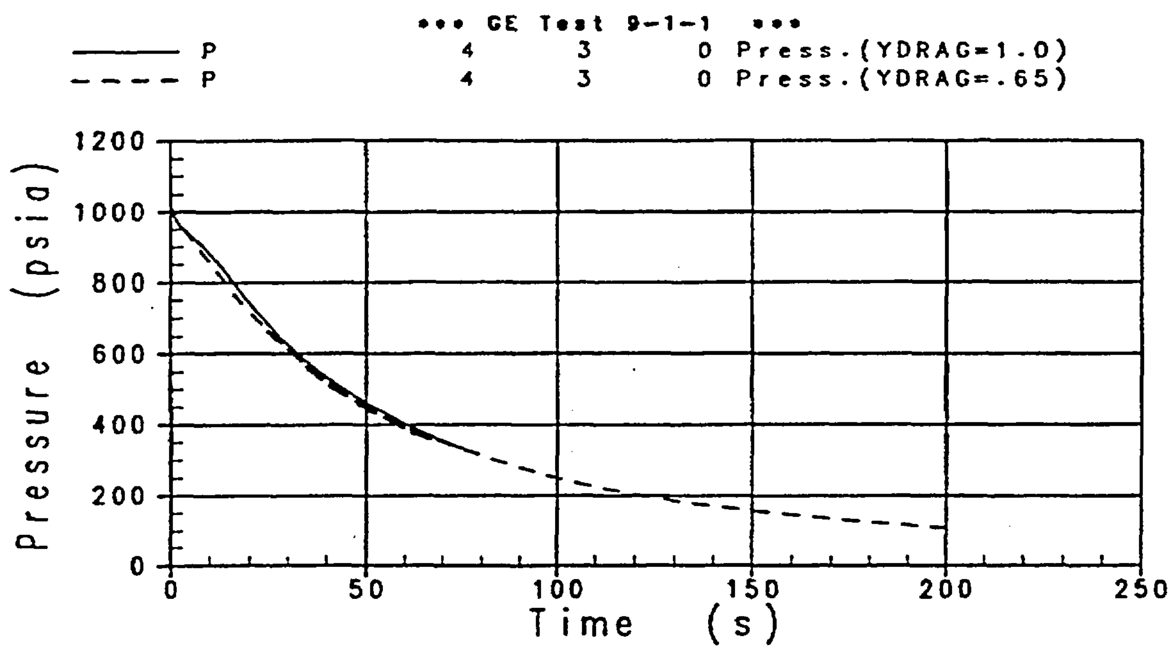

Figure 15-4-4-19. Effect of YDRAG Multiplier on the Pressure Prediction, Test 9-1-1

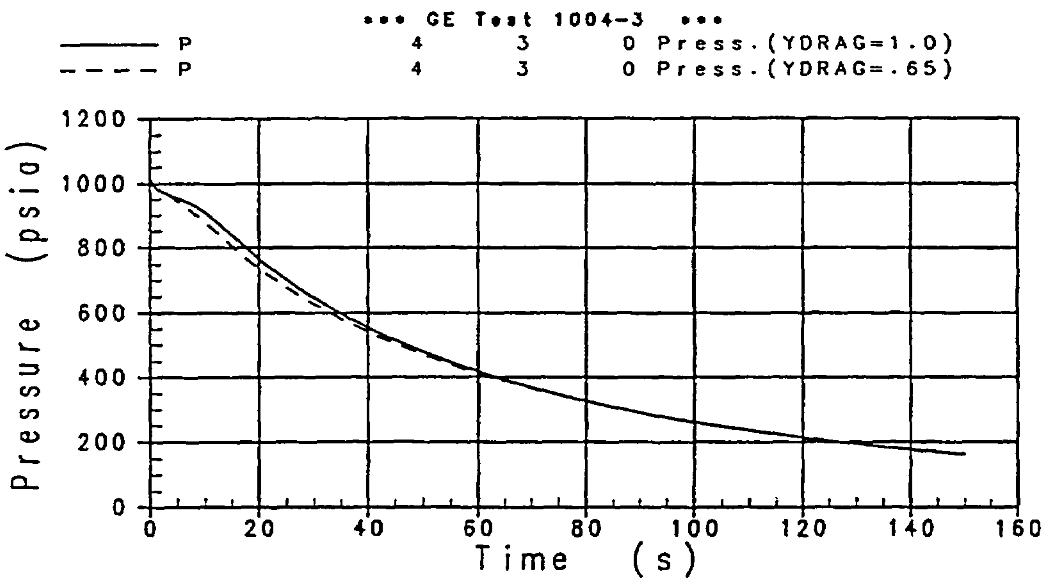

Figure 15-4-4-20. Effect of YDRAG Multiplier on the Pressure Prediction, Test 1004-3

15-5 Summary and Conclusions

This section considers mixture level swell tests in three different facilities. The ORNL-THTF simulations showed that WCOBRA/TRAC-SB tends to predict both the collapsed liquid level in the test bundle and the mixture level fairly well but in general overpredicts the level swell. The G-1 Core Uncovery Tests simulations showed the WCOBRA/TRAC-SB predictions of boiloff to a given elevation ranged both earlier than and later than the data. The code predictions of bundle level swell are both less and greater than that reported in the data, but most often are overstated. Finally, the simulations of the GE Vessel Blowdown Tests showed WCOBRA/TRAC-SB, in general, overpredicts the reported voiding in the test vessel.

The interfacial drag model contains a bias so that the mixture level is not "frothed" to the appropriate level. The simulated test facilities, on the average, overpredicted the void fraction in the bundle during flashing and/or boiloff, suggesting that the interfacial drag is too high.
[

]a,c

The use of a nominal value for YDRAG of 0.8 in the integral test facility simulations and in PWR calculations is supported by the WCOBRA/TRAC-SB predictions of G-1 and ORNL-THTF.

15-6 References

Anklam, T. M., et al., 1982, "Experimental Investigations of Uncovered Bundle Heat Transfer and Two-Phase Mixture Level Swell Under High Pressure Low Heat Flux Conditions," NUREG/CR-2456.

Bajorek, S. M., et al., 1998, "Code Qualification Document for Best Estimate LOCA Analyses Volume I: Models and Correlations," WCAP-12945-P-A, Vol. 1, Proprietary.

Findlay, J. A. and Sozzi, G. L., 1981, "BWR Refill-Reflood Program – Model Qualification Task Plan, NUREG/CR-1899.

WCAP-9764, 1980, "Documentation of the Westinghouse Core Uncovery Tests and the Small Break Evaluation Model Core Mixture Level Model," Proprietary.

SECTION 16
LOOP SEAL CLEARANCE

16-1 Introduction

The small break LOCA PIRT in Volume 1 of this document identifies the loop seal behavior as an important process affecting the evolution of the transient. This component, and its effect on the transient, is discussed in more detail below. The following sections assess the important phenomena occurring in the loop seal, the available experiments which quantify the phenomena, and the performance of WCOBRA/TRAC-SB in predicting the phenomena.

During a small break LOCA, mass is slowly depleted from the system. Early in the transient, the pumps continue to run and the flow through the pump suction piping remains single-phase. After generation of a trip signal, the reactor automatically trips and subsequently the pumps. The system then enters a natural circulation phase. Pressures have fallen sufficiently to cause boiling in the fluid entering the hot leg, but the steam generator acts as a heat sink and the fluid entering the pump suction pipe is still nearly single-phase. Any bubbles that enter the pump suction pipe are carried through by natural circulation as illustrated in Figure 16-1(a).

When the primary pressure approaches the secondary pressure, voids remain in the fluid as it enters the steam generator. As the loop mass flowrate decreases further, liquid begins to drain down both the uphill and downhill sides of the steam generator tubes. Natural circulation is terminated, and mixture levels form on both the uphill and downhill sides of the tubes. The levels then move downward as liquid drains and vapor rises as shown in Figure 16-1(b).

Because there is no escape path for the steam generated in the core, except for some small bypass paths such as the upper head, the pressure in the region above the core (the upper plenum, the hot legs, and the steam generator tubes) rises and depresses the level in both the core and the downhill sides of the pump suction pipe. Eventually, the downhill side level reaches the top of the horizontal portion of the pump suction pipe, as shown in Figure 16-1(c), and vapor begins to escape into the pump and flow toward the break.

At the onset of clearing, the fluid pressure in the downhill leg of the loop seal is about 3 psi higher than on the uphill side, due to the column of water from the horizontal leg to the pump outlet as shown in Figure 16-1(c). Because the volume of steam at this pressure is significant – in the steam generator tubes, hot legs, vessel upper plenum, and upper head – the steam flowing through the pump suction becomes significantly greater than the core steam generation rate for a period of time (Kukita, 1990). This causes the loop seal to clear completely, not resealing until much later in the transient.

As the steam flows through the pump suction, the flow regime is first a slug regime with significant amounts of water being entrained from the pump suction pipe as seen in Figure 16-2 and described by Tuomisto and Kajanto (Tuomisto and Kajanto, 1988). Eventually, a residual level of water will remain in the pump suction pipe.

As the pressure in the system is relieved, the steam flow decreases to the core steam generation level. If this steam flow is low enough, water in the cold leg may begin to drain back through the pump and begin to fill the pump suction again as shown in Figure 16-1(d). Another potential source of loop seal refilling is the draining of condensed steam from the downhill side of the steam generators. Because there is no pressure driving force, the steam flow through the loop seal is quickly terminated when the water level reaches the top of the horizontal section and plugs the loop seal. The system pressure increases, and core and loop seal levels change once again as the loop seal plugging and clearing cycle is repeated (Kukita, 1990).

16-2 Important Physical Processes and Scaling Laws

The onset of loop seal clearing is a function of the pressure difference across the loop seal, which depresses the level to the bottom of the loop seal and depends on the following factors:

- Core steam generation rate
- Bypass steam flow rate through vent paths
- Rate of accumulation of water in the pump suction pipe

These factors are the result of processes that occur elsewhere in the system and are accounted for in other components (for example, the core steam generation rate is accounted for by ranging core power and core mixture level).

The loop seal clearing and refilling process is a function of the interfacial drag between the vapor and the water. The initial steam flow surge and the interfacial drag determine the rate at which water is expelled. The steam flowrate, in turn, depends on the loop pressure drop, of which the loop seal is a part. This determines how quickly the venting process takes place and the final water level in the horizontal section. The residual water and degree to which water is held up by steam flowing out of the pump suction pipe determine the rate at which the pump suction refills and replugs. Based on these considerations, the following factors are considered to be important in the assessment of predictions of loop seal behavior:

- Overall loop seal pressure drop as a function of steam flow
- Liquid distribution in the loop seal as a function of steam flow

Various experiments have shown that the basic physical process is controlled by two factors: the extent to which a stratified flow regime can be maintained in the horizontal leg of the loop seal and the degree to which liquid pushed into the downstream vertical leg can be entrained out of the loop seal. Figure 16-2 illustrates these processes.

Scaled loop seal experiments are discussed in the following sections to gain a better understanding of the loop seal behavior. These tests are used to highlight important physical and scaling features and are then compared with larger scale tests to confirm the indicated scaling trends. Finally, these tests are predicted using WCOBRA/TRAC-SB to assess the models and correlations in the code.

16-2-1 Westinghouse Loop Seal Tests

Westinghouse performed scaled U-tube experiments designed to examine the hydraulic behavior of a U-tube under conditions similar to those encountered during a small break LOCA. The vapor flow required to "clear" the U-tube was a specific focus of the tests.

16-2-1-1 Test Facility Description

The tests were run in a plexiglass facility with air and water at atmospheric pressure. The facility, illustrated schematically in Figure 16-3, consists of a blower, a run of horizontal piping from the blower, a U-tube, and a catch tank.

The pipe diameter chosen for the facility was 25 cm or 0.82 feet. This corresponds to approximately 1/3-geometric scale compared with a PWR, which has a pipe diameter of 2.58 feet. The air and water flowrates were scaled so that approximate similitude was maintained for the Froude number, shown to define the flow regime transition from stratified to intermittent and annular flow by Taitel and Dukler (Taitel and Dukler, 1976). Figure 16-4 shows the predicted flow regime transition using the Taitel and Dukler flow regime map for atmospheric pressure, 1/3-scale geometry, compared with the transition for 1000 psia, full-scale geometry. This figure indicates that the transition occurs at a higher vapor flux in the air-water tests. While better similitude could have been obtained with a smaller pipe, the chosen diameter also assures that the vertical pipes of the U-tube are sufficiently large so that any countercurrent flow limits (CCFL) that occur will not be affected by the pipe diameter. According to Richter (Richter, 1981), the critical vapor flux for CCFL in pipes larger than approximately 2 inches in diameter depends only on pressure, not on pipe diameter.

Pressure drop across the U-tube was measured. In the horizontal and in the downstream vertical sections, several independent measurements of void fraction were made using pressure drops, optical probes, and gamma densitometers.

16-2-1-2 Test Procedures

Several tests series were performed, as described below:

- Limit Line Tests

  These tests were designed to obtain the water level in the horizontal portion of the U-tube, which produces significant water entrainment for a given air flowrate. This is equivalent in some ways to the CCFL limit and is termed the U-tube limit line. The tests were performed as follows:

  1. Begin with an empty U-tube.
  2. Start the air flow at the desired value.
  3. Add water at the bottom of the horizontal pipe until significant entrainment into the catch tank is observed.
  4. Terminate the water flow, and continue the test until the entrainment becomes negligible.
  5. Measure flows and pressure drops.
  6. Stop the air flow and measure the quiescent water level remaining in the pipe.

- Within Limit Line Tests

  These tests were performed at air and water flows inside the limit line established in the first phase with little or no entrainment. The tests primarily examined the interaction, if any, between the gas and the liquid at nonlimiting flows. The tests were run as follows:

  1. Set the desired water level in the horizontal pipe with the air flow at zero.

  2. Incrementally increase the air flow and take measurements.

  3. Confirm that final level is approximately the same as the initial level.

  In addition to flow and delta-p measurements, the appearance of the water level was observed. At low air flows, the water was either quiescent or small ripples were observed. At higher flows, the water began to drop near the upstream side of the U-tube. Next, droplets were observed forming and reaching the downstream elbow of the U-tube. At still higher flows, droplets began to reach the top of the downstream pipe, and finally, water was observed to stream upward in the downstream pipe.

- Optical Probe Tests

  These tests were performed similarly to the test series at conditions inside the limit line. Optical probes were used to measure the water level. These tests confirmed the delta-p measurements, later used to derive vapor fraction.

- Complementary Tests

  In some of the tests with high initial water level, oscillatory flow was observed. These oscillations consisted of movements of water back and forth between the upstream and downstream elbows. Slugs of water momentarily filled the pipe, increasing the pressure drop across the U-tube. These slugs were then ejected from the U-tube. The tests were similar to the limit line tests except that continuous readings were taken during the oscillations and until steady-state was reached.

- Gamma Densitometer Tests

  These tests used a gamma densitometer to measure the mixture density inside the horizontal portion of the U-tube. The tests confirmed void fraction measurements based on delta-P.

16-2-1-3 Analysis of 1/3-Scale Test Results

Figure 16-5 plots the normalized residual water level in the loop seal (*H/D*) as a function of the vapor volumetric flux (j_g). The loop seal was completely cleared when gas velocities exceeded about 70 ft/s. At low gas flows, some hysteresis was observed; i.e., the residual water level remaining after the test depended on how the test was performed. The lower levels shown in Figure 16-5 were obtained when the test was started with an initial water level above the top of the horizontal leg. This configuration introduced level oscillations between both vertical legs. These oscillations caused additional water to be entrained from the loop seal.

Figure 16-6 shows the results of tests performed under the limit line. The water level in the horizontal leg was relatively unaffected by gas flow until flows near the limit line were reached.

The residual water level is an indication of the overall liquid mass contained in the loop seal as a function of gas flow, but does not represent the liquid distribution within the U tube during the tests. Figure 16-7 shows the average void fraction at the midpoint of the horizontal leg and in the downstream vertical leg during the test. At low gas flowrates, there is wide scatter in the measured void fraction in the horizontal leg and indications of significant liquid content in the downstream vertical leg. The void fraction in the vertical leg was inferred from a delta-P cell spanning the vertical leg (ΔP_{15} in Figure 16-3). The flow regime in the vertical leg is, therefore, likely to be that depicted in Figure 16-2C with a low void fraction region at the bottom of the pipe, and a high void fraction at the top of the pipe. The measured void fraction in the horizontal leg is more representative of the void fraction in the elbow and bottom of the vertical leg. Figure 16-8 compares the measured void fraction in the horizontal leg with the void fraction calculated from the residual water level. This plot shows that at higher gas flows, nearly all the water retained in the loop seal resides in the horizontal leg. At lower gas flows, the same is still generally true, although the storage in the vertical leg is more evident due to the higher measured void fraction during the test.

Figure 16-9 shows the measured pressure difference between the upstream and downstream exits of the U-tube. As water collects in the downstream vertical leg, the pressure difference increases. The basic processes occurring during these tests can be explained in terms of several hydrodynamic limits applied to both the horizontal and vertical legs. Figure 16-10 shows the horizontal leg average void fraction as a function of j_g^*, defined as:

$$j_g^* = \frac{j_g}{\sqrt{\frac{(\rho_l - \rho_g) g D}{\rho_g}}} \tag{16-1}$$

where D is the pipe diameter.

The loop seal behavior can be explained in terms of three regimes, bounded by the limit lines shown in Figure 16-10. These regimes are described in the following paragraphs.

Regime III: Droplet Entrainment

Ishii and Grolmes (Ishii and Grolmes, 1975) describe entrainment in horizontal cocurrent flow as the stripping of drops from the tops of waves. They describe four mechanisms: 1) the shearing off of the top of roll waves by the turbulent gas flow, 2) the undercutting of the liquid film by the gas flow, 3) the gas bubbles bursting at the liquid-vapor interface, and 4) the liquid impingement on the liquid-vapor interface. The only mechanism of the four expected to be of significance to loop seal clearing is the shearing off of the tops of the waves, which Ishii and Grolmes state is valid for liquid Reynolds numbers greater that 160 in horizontal cocurrent flow.

Assuming for the moment that the WCOBRA/TRAC-SB calculations reported herein are reasonably valid, the horizontal (GAP) liquid velocities during entrainment vary from less than 1 ft/s to several ft/s. The liquid film thickness is then estimated to be from about 0.5 inch at 1000 psia to about 1 inch at 43 psia, and about 1.5 inches for air-water at atmospheric pressure. For roll wave entrainment, Ishii and Grolmes provide two correlations based on the Reynolds number.

For Reynolds numbers greater than [ ]^{a,c} the following applies:

$$\frac{\mu_l u_{gt}}{\sigma}\sqrt{\frac{\rho_g}{\rho_l}} \geq N_\mu^{0.8} \; for \; N_\mu < \frac{1}{15}$$

$$\frac{\mu_l u_{gt}}{\sigma}\sqrt{\frac{\rho_g}{\rho_l}} \geq 0.1146 \; for \; N_\mu > \frac{1}{15} \tag{16-2}$$

Inequality 16-2 is valid in the rough turbulent regime. For Reynolds numbers below [ ]^{a,c} (laminar-turbulent transition regime), Ishii suggests the following correlation:

$$\frac{\mu_l u_g}{\sigma}\sqrt{\frac{\rho_g}{\rho_l}} \geq 11.78 N_\mu^{0.8} Re_l^{-\frac{1}{3}} \; for \; N_\mu \leq \frac{1}{15}$$

$$\frac{\mu_l u_g}{\sigma}\sqrt{\frac{\rho_g}{\rho_l}} \geq 1.35 Re_l^{-\frac{1}{3}} \; for \; N_\mu > \frac{1}{15} \tag{16-3}$$

The Reynolds number is calculated based on the liquid film thickness where u_g is the minimum gas velocity for entrainment to occur.

The gas velocity can be represented in terms of a more easily measured velocity, the superficial gas velocity (j_g):

$$j_g = \alpha u_g \tag{16-4}$$

As droplets are entrained into the downstream vertical leg, they are ejected out of the loop seal because the gas flow exceeds the CCFL in the vertical pipe. This limit is described further in Regime II.

Regime II: Wave Instability and Vertical CCFL Regime

In this regime, the water level in the horizontal leg is governed by the stability of waves on the stratified interface. If these waves grow, they could span the pipe, as illustrated in Figure 16-2(b), and cause a slug of water to be pushed into the downstream vertical leg as seen in Figure 16-2(c).

The water level or void fraction at the onset of wave instability was characterized by Taitel and Dukler (Taitel and Dukler, 1976). They proposed the following criterion:

$$
\begin{aligned}
j_g^{*2} &= \frac{(1-\tilde{h})^2\alpha^3}{-d\alpha/d\tilde{h}} \\
\tilde{h} &= \frac{H_L}{D} \\
\alpha &= \frac{1}{\pi}\left[\cos^{-1}(2\tilde{h}-1)-(2\tilde{h}-1)\sqrt{1-(2\tilde{h}-1)^2}\right]
\end{aligned}
\qquad (16\text{-}5)
$$

where the relationship between void fraction and level is determined by the pipe geometry.

The third line of Equation 16-5 describes the relationship for a circular pipe. The limit line shown in Figure 16-10 is Equation 16-5, solved for α as a function of j_g^*. The data follow this limit in Region II.

If the gas flow in the downstream vertical leg still exceeds the flooding limit, then any water pushed into the vertical leg by wave instabilities will be ejected from the loop seal. The CCFL limit line shown in Figure 16-10 is based on the critical velocity for liquid holdup (known as the Kutateladze number) developed by Pushkina and Sorokin (Pushkina and Sorokin, 1969) for large diameter pipes:

$$
U_{CCFL} = 3.2\left[\frac{\sigma(\rho_l-\rho_g)g}{\rho_g^2}\right]^{0.25} \qquad (16\text{-}6)
$$

The j_g versus α relationship is determined as in Equation 16-4.

Regime I: Slug/Oscillatory Regime

When gas velocities are reduced below the CCFL, water pushed into the vertical leg collects there and can fall back. This leads to a low void fraction, chaotic regime in which there is wide scatter in measured void fraction at constant gas flow as seen in Figure 16-11. Hysteresis is also observed in this regime with variations in residual water level depending on how the tests are performed. This hysteresis is caused by U-tube oscillations, which are the result of intermittent holdup and fallback in the vertical leg as the flow regime changes from slug to churn-turbulent.

16-2-1-4 Effect of Scale

An important question which must be answered is what distortions the scaled geometry and low pressure used in these tests has introduced relative to the PWR. Having explained the data in terms of the limit lines above, we can examine the effect of scale by seeing how these limit lines change with scale (Figure 16-12). Here, the limit lines at 1/3-scale are compared to the limit lines at full-scale at the same (atmospheric) pressure and with air-water. The wave limit line is constant with respect to j_g^*. For the same j_g^*, however, the entraining and CCFL limit lines move to the left, and flow regime III becomes more important over a wider range of j_g^*.

Figure 16-13 shows what happens when the full-scale pressure of 1000 psia is also introduced. Although it is expected that both the critical entrainment and critical CCFL velocities will decrease with pressure, the entrainment velocity calculated from Equation 6-2 becomes very small (less than 1 ft/s), indicating this correlation may not be valid at high pressure. In Figure 16-13, it has been assumed that the entrainment limit is the same as the CCFL limit, calculated by Equation 16-5. The limit line has moved even further to the left, and the droplet and CCFL lines have effectively merged. This would indicate that a full pressure and full-scale, the most dominant regimes are I and III. This implies that over a fairly narrow range of steam flows, the liquid in the loop seal will be almost completely expelled, and that the wave instability limit does not play an important role in determining the amount of water contained in the loop seal.

Full-scale air/water experiments were carried out at the IVO test facility simulating PWRs of Russian design (Tuomisto, 1988). These tests were performed in a manner similar to the Westinghouse tests. It was found that the Taitel-Dukler unstable wave theory predicted the onset of slugging in the U-tube (in the Westinghouse tests, this would correspond to the point at which significant water entrainment occurred; that is, at the limit line), particularly when the water level was adjusted to account for the increased level at the downstream elbow of the U-tube.

Figure 16-14 plots the full-scale U-Tube data against the corresponding limit lines. It can be seen that the data lies entirely to the left of the CCFL limit line. This behavior is different from the 1/3-scale test, and is believed due to the large U-tube oscillations which occurred in most of the large scale tests. These oscillations, which were attributed to undesirable air blower operating characteristics (see next section), pushed water into the downstream vertical leg, which was then ejected from the loop seal. This process continued until sufficient water was ejected to allow the gas velocity to fall below the CCFL limit, at which point the oscillations stopped and no more mass was lost out of the loop seal. These results indicate that if the loop seal behavior is oscillatory, the dominant mechanism controlling the amount of water in the loop seal is vertical leg CCFL.

16-2-1-5 Full-Scale Steam-Water Tests

Tests were performed at full-scale for a typical four-loop PWR in the Upper Plenum Test Facility (UPTF) at pressures of 3 bar (43.5 psia) and 15 bar (217.5 psia). The separate effects tests (Liebert and Emmerling, 1998) were conducted by blocking three of the four loops as seen in Figure 16-15, partially filling the loop seal in the open loop, injecting steam into the reactor vessel simulator, and measuring the residual level once entrainment had completed, but before the steam flow was terminated. The published data from the two test series are shown in Figure 16-16 (Liebert and Emmerling, 1998 and Ohvo, et al., 1998).

A line is drawn through the data that represents a constant average gas velocity as seen in Figure 16-16. This velocity is the best estimate of the minimum velocity at which entrainment from the liquid surface will take place within the horizontal section of the loop seal and is independent of the level in the horizontal run. Also shown is the Taitel-Dukler line for transition from slug to entrained flow. Liebert and Emmerling note that slugging was observed only at the lowest Froude number in each test series. Otherwise, the flow was observed to be stratified. The calculated critical gas velocities are 60 ft/s and 32 ft/s for the 3-bar and 15-bar test series, respectively.

Using the above critical velocities and calculated viscosity numbers and the critical velocity from the Westinghouse air-water tests (Figure 16-10), the results can be compared to Ishii's correlation as shown in Figure 16-17 (Ishii and Grolmes, 1975). The UPTF and Westinghouse data lie well below the data base upon which Ishii's correlation was constructed. While the loop seal data lie close to the correlation, the data do not quite fit. If Ishii's correlation is used to determine the critical gas velocity, the lines of constant velocity are as shown in Figure 16-16. For this case, the lines of constant velocity collapse to what is in effect a single line and are not representative of the data. However, as shown in Figure 16-17, the UPTF data lie on approximately a line of constant Ishii parameter equal to 0.0033. The deviation in the UPTF data from the Ishii and Grolmes correlation might be explained as a scale effect that is not included in the correlation. Because the UPTF data are at full geometric scale, these data are believed to be more reliable. The viscosity number (6.3×10^{-4}) for full pressure (about 70 bar) lies between the viscosity numbers at 3 bar and 15 bar. Therefore, the Ishii correlation is modified to become constant for viscosity numbers less than [ ]^{a,c}.

Using [

]^{a,c}. The UPTF data may lie in the transition regime and not the rough turbulent regime. This may point to the reason for the wider spread in the data for the 3-bar test series as compared to the spread in the 15-bar test series.

16-3 WCOBRA/TRAC Modelling of Loop Seal Clearing Process

The objective of this assessment is to confirm that the WCOBRA/TRAC-SB loop seal model adequately calculates the loop seal clearing process for a PWR. The assessment will be performed as follows:

- Model-scaled experiments to confirm that the interfacial drag models adequately predict the liquid distribution in the loop seal for various flowrates

- Examination of the effect of changes in scale on the predicted results

16-4 WCOBRA/TRAC Simulation of the UPTF 3-Bar and 15-Bar Tests

The two UPTF full-scale steam-water tests are worthy of simulation. The separate effects tests were conducted by blocking three of the four loops and injecting steam into the reactor vessel simulator as shown in Figure 16-15 (Liebert and Emmerling, 1998). The WCOBRA/TRAC model for the simulations has [

]^{a,c}. The noding in this model is sufficient for simulation of the UPTF tests.

Initial conditions for the tests appear to have been subcooled liquid in the loop seal and a superheated steam supply (Ohvo, et al., 1998). It is expected that [

]^{a,c}.

Each of the test simulations is run separately, starting from the same initial conditions. The steam flowrate is increased from zero to the specified flowrate [

]^{a,c}.

The results of the 3-bar simulations are shown in Figure 16-19. The solid squares are the data values. At low vapor velocities, WCOBRA/TRAC-SB over predicts the residual level. While there is a tendency to under predict the residual level at $j_g^* > 0.1$. The calculations for the solid square cases to the left of the Ishii's entrainment limit line predict a sudden blowout of fluid from the pump suction leg as shown in Figures 16-20 and 16-21 at approximately 270 seconds. This behavior appears to result from the oscillation in the pump suction by building sufficient momentum to clear the liquid into the hot leg.

The results of the 3-bar calculations are summarized in Figure 16-22. WCOBRA/TRAC seriously over predicts the residual level for $j_g^* < 0.1$ and under predict the residual level for $j_g^* > 0.1$.

The predicted behavior for the 15-bar tests compared to the data and limit line is shown in Figure 16-23. As with the 3-bar tests, WCOBRA/TRAC-SB over predicts the data $j_g^* < 0.1$ and under predicts the data for $j_g^* > 0.1$ with some variance in the transition region.

However, there is less variance in the trend of both the data and calculations for 15-bar than for the 3-bar tests and calculations, as shown in both Figures 16-23 and 16-24.

Although no data are known to exist for full-scale and approximately 1000 psia, WCOBRA/TRAC-SB calculations were made using the UPTF model. As shown in Figure 16-24, the calculations follow the trend of the 15-bar calculations. It is reasonable to conclude that for 1000 psia WCOBRA/TRAC-SB will over predict residual level for j_g^* less than approximately 0.1 and underpredict residual levels for j_g^* >0.1.

Measured pressure drops across the UPTF loop seal are shown in Figure 16-26a. The highest pressure drops occur for j_g^* <0.1 and then become approximately constant with increasing steam velocity. Also the magnitude of the observed differential pressure oscillations is significantly greater for j_g^* <0.1. The pressure drop calculated by WCOBRA/TRAC-SB is shown in Figure 16-26b. The calculated pressure drops shown in Figure 16-26b represent averages over a 300 second slice of the transient. The calculations generally show the same trend with the pressure drops increasing below j_g^* = 0.1 and approximately constant above j_g^* 0.1. However there are several significant exceptions to the general trend. The 3-bar calculations (open squares) designated 1, 2 and 3 represent cells where the liquid in the loop seal was overpredicted at low steam velocity and correspond to cases where the liquid level was underpredicted by WCOBRA/TRAC-SB. Calculations for 15-bar (solid triangles) marked 4 and 5 represent cases where significant liquid is retrained in the pump suction leg, which increases the flow resistance. Solid triangles designated 6 and 7 represent single phase steam flow. As with points 4 and 5 the calculated resistance is greater than implied by the data. The described variances in the calculations may well be attributed to [

]^{a,c}. The calculations for 1000 psia (open diamonds) do not exhibit the variances noted for the 3-bar and 15-bar calculations. As shown in the data there is little effect of system pressure on the pressure drop, and that trend is observed in the calculations.

16-5 Conclusions

Assessment of the experimental data indicates the following:

- Hysteresis and flow oscillations are likely to occur during the clearing process. These oscillations will result in continued inventory loss from the loop seal until conditions fall below the CCFL in the vertical leg. Uncertainty in the remaining mass inventory of liquid in the loop seal will result in a corresponding uncertainty in the time at which the loop seal will possibly replug.

- Full-scale low pressure steam-water test data are consistent in trend with low pressure air-water test data, both for residual water level and pressure drop.

Assessment of WCOBRA/TRAC-SB relative to the experiments indicates the following:

- WCOBRA/TRAC-SB does not reproduce the observed flow oscillations or residual water level exactly. This deficiency can be accounted [

  ]a,c.

- WCOBRA/TRAC-SB overpredicts the quantity of liquid cleared from the loop seal for high vapor flows. This may be attributed to [

  ]a,c.

- WCOBRA/TRAC-SB adequately predicts the trend of the residual level data in full-scale tests.

- WCOBRA/TRAC-SB adequately predicts the trend of the pressure difference data.

16-6 References

Ishii, M. and Grolmes, M. A., 1975, "Inception Criteria for Droplet Entrainment In Two-Phase Concurrent Film Flow," AIChE J., Vol. 21, No 2.

Kukita, Y. et al., 1990, "Loop Seal Clearing and Refilling During a PWR Small Break LOCA," Nuclear Eng. and Design, 121, 431-440.

Liebert, J. and Emmerling, R., 1998, UPTF Experiment Flow Phenomena During Full-Scale Loop Seal Clearing of a PWR, Nuclear Engineering and Design, Vol. 179, pp. 51-64.

Ohvo, J., et al., 1998, Simulation of Full-Scale UPTF Loop Seal Experiments with APROS, CATHARE and RELAP, 6th International Conference on Nuclear Engineering, ICONE6-6090.

Pushkina, O. L. and Sorokin, Y. L., 1969, "Breakdown of Liquid Film Motion in Vertical Tubes," Heat Transfer-Soviet Research, Vol. 1, No. 5.

Richter, H. J., 1981, "Flooding in Tubes and Annuli," Int. J. Multiphase Flow, Vol. 7, No. 6, pp. 647-658.

Taitel, Y. and Dukler, A. E., 1976, "A Model for Predicting Flow Regime Transitions in Horizontal and Near Horizontal Gas-Liquid Flow," AIChE J., Vol. 22, No 1.

Tuomisto, H. and Kajanto, P., 1988, "Two Phase Flow in a Full Scale Loop Seal Facility," Nuclear Eng. and Design, 107, 295-305.

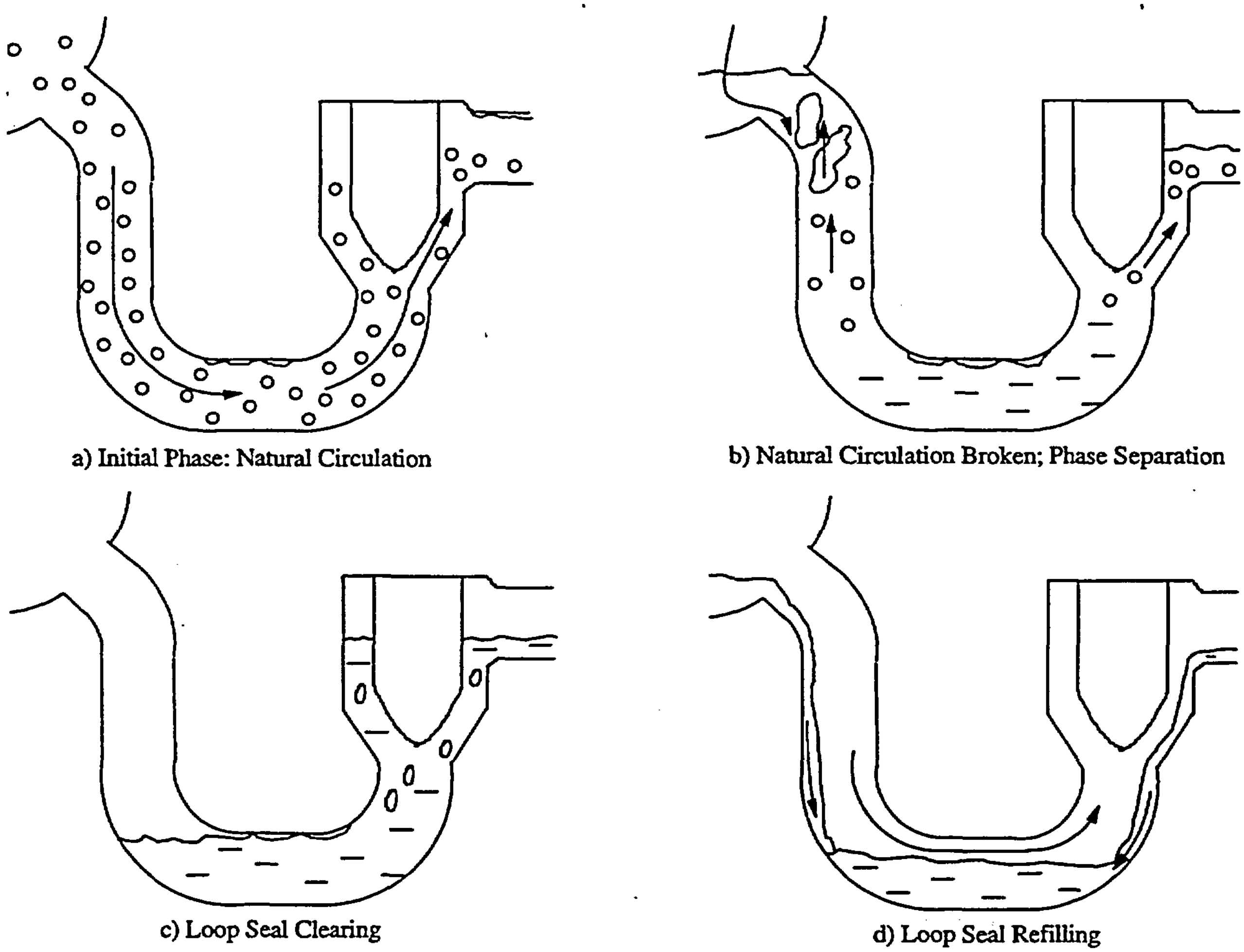

Figure 16-1. Loop Seal Clearing and Refilling

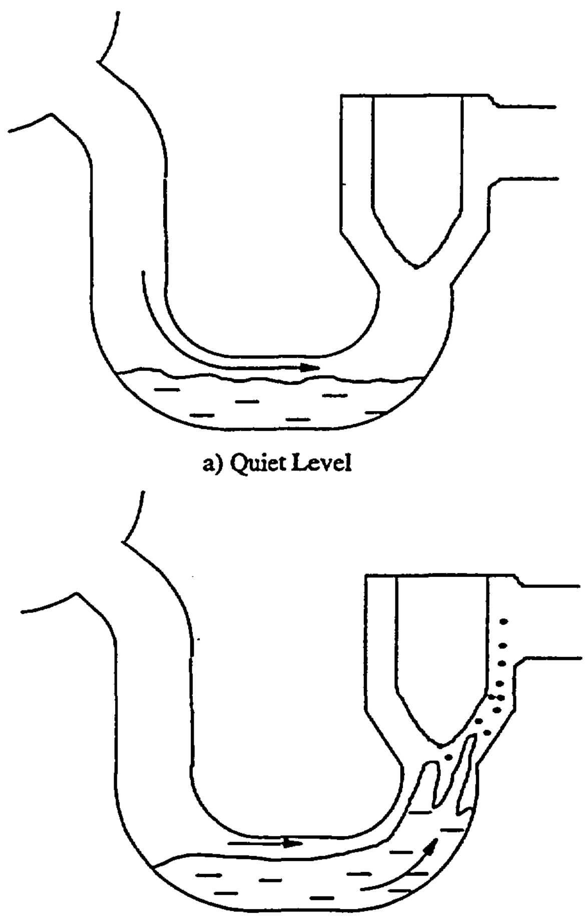

a) Quiet Level

b) Plug Formation

c) CCFL in Vertical Pipe

d) Drop Entrainment

Figure 16-2. Loop Seal Clearing Process

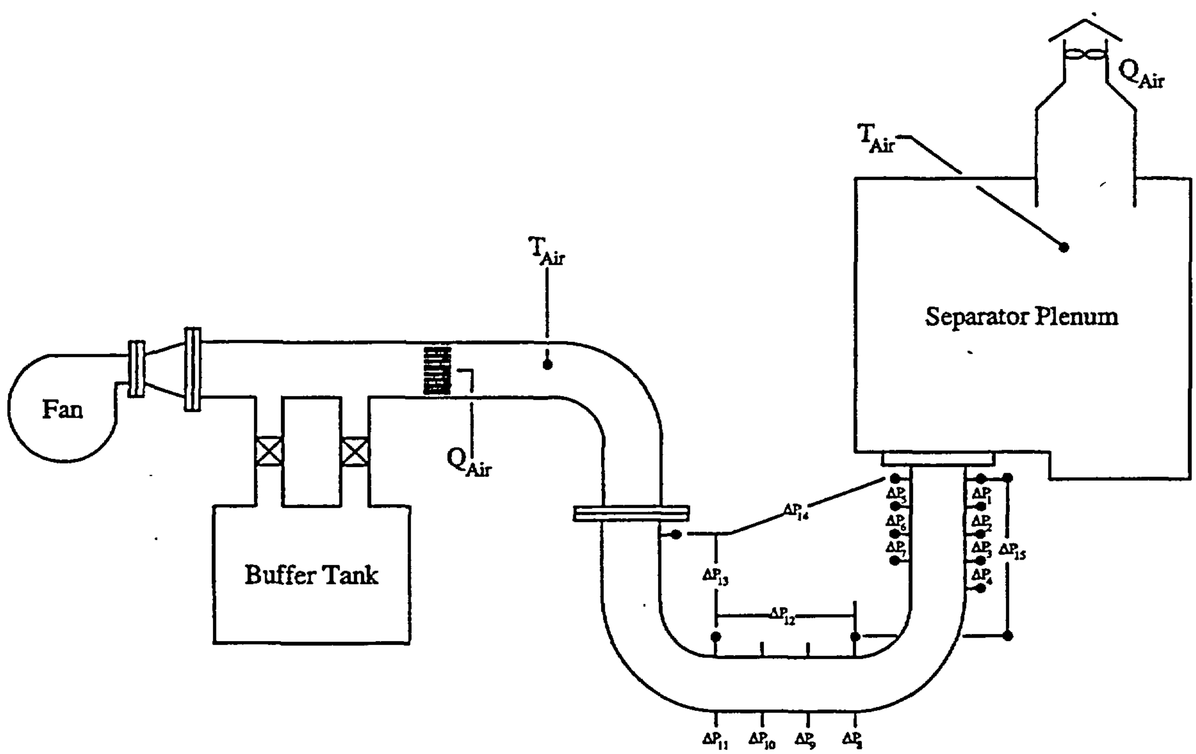

Figure 16-3. 1/3-Scale U-Tube Test Facility

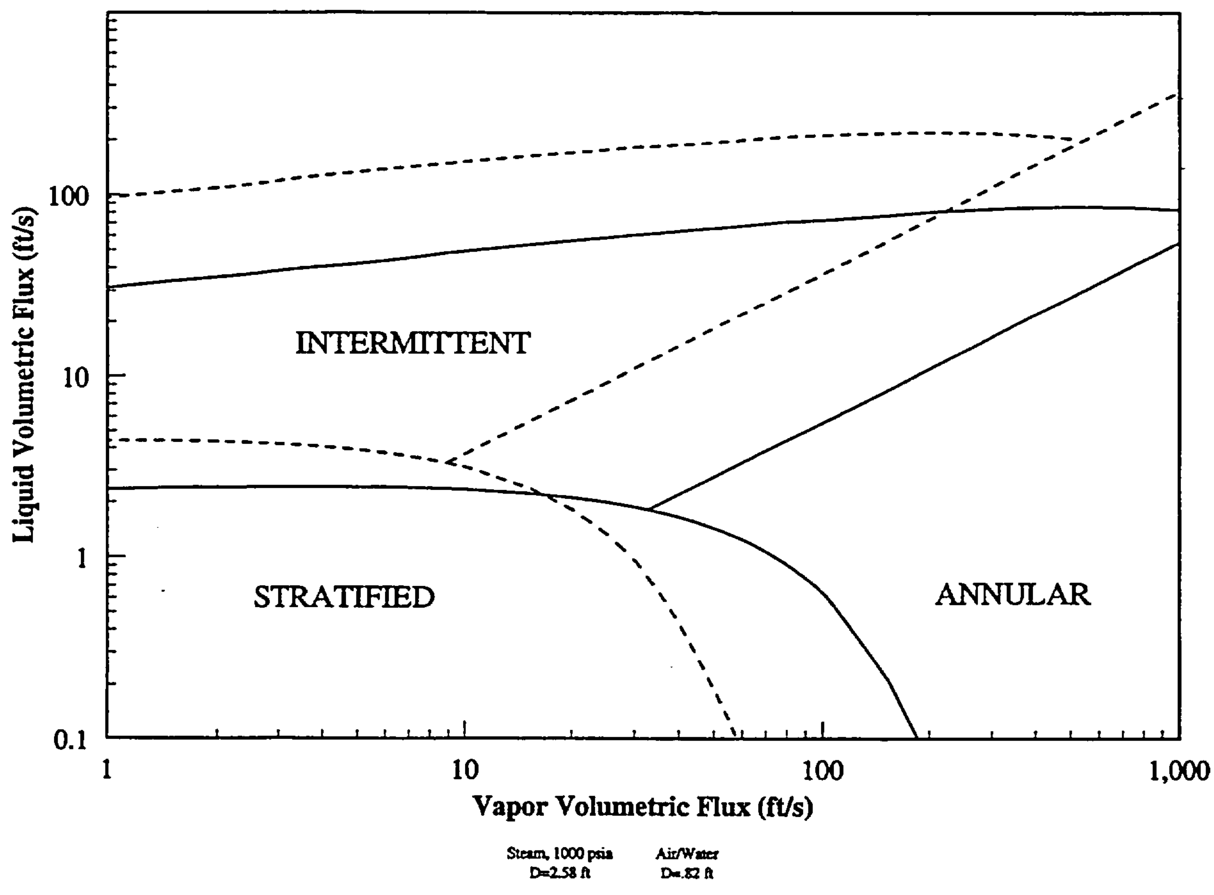

Figure 16-4. Taitel-Dukler Flow Regime Map, Comparing 1/3-Scale Pipe at 14.7 psia and Full-Scale Pipe at 1000 psia (Taitel and Dukler, 1976)

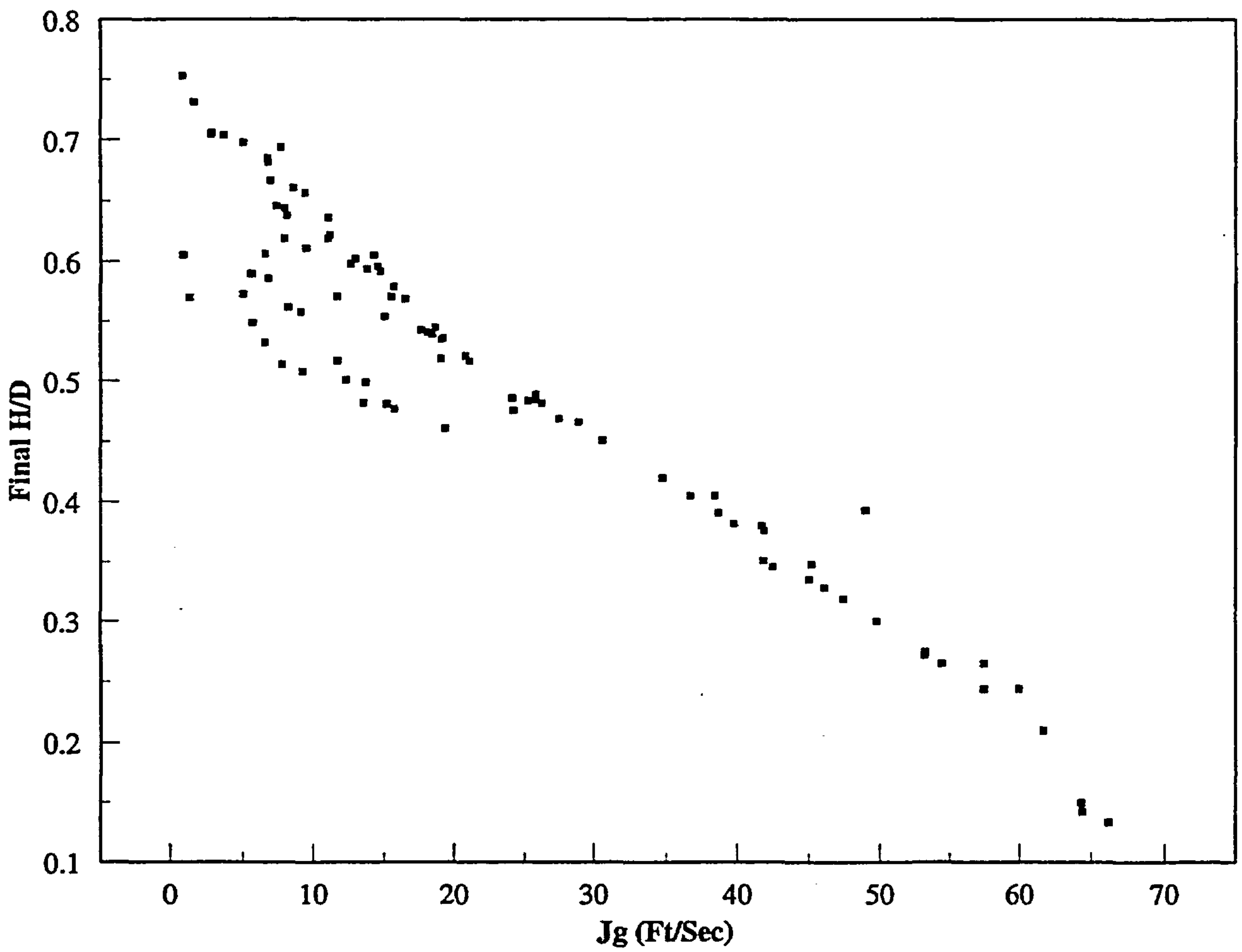

Figure 16-5. 1/3-Scale U-Tube Residual Water Level Remaining After Test as a Function of Test Gas Flowrate

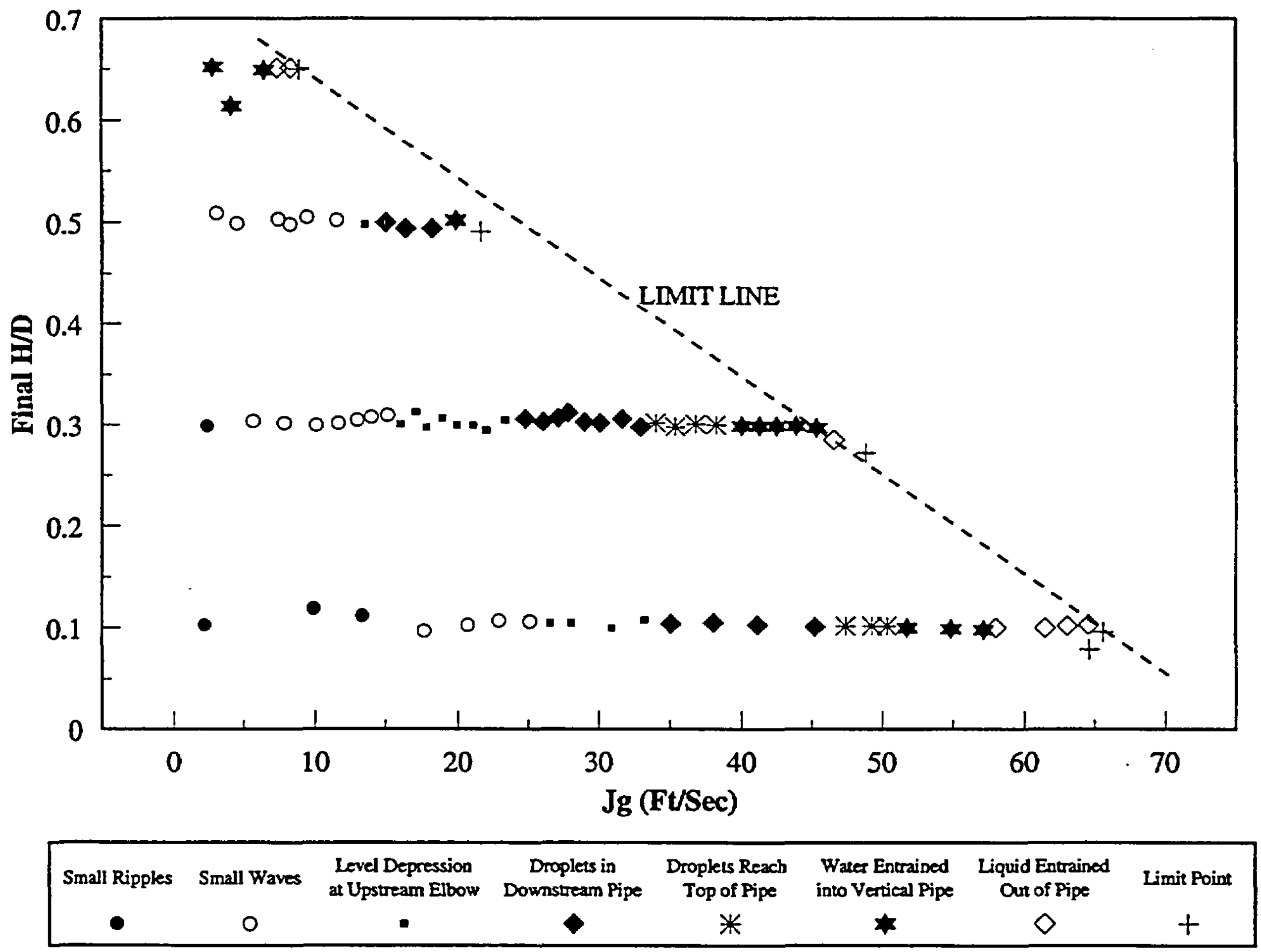

Figure 16-6. 1/3-Scale U-Tube Flow Regimes Observed Under the Limit Line

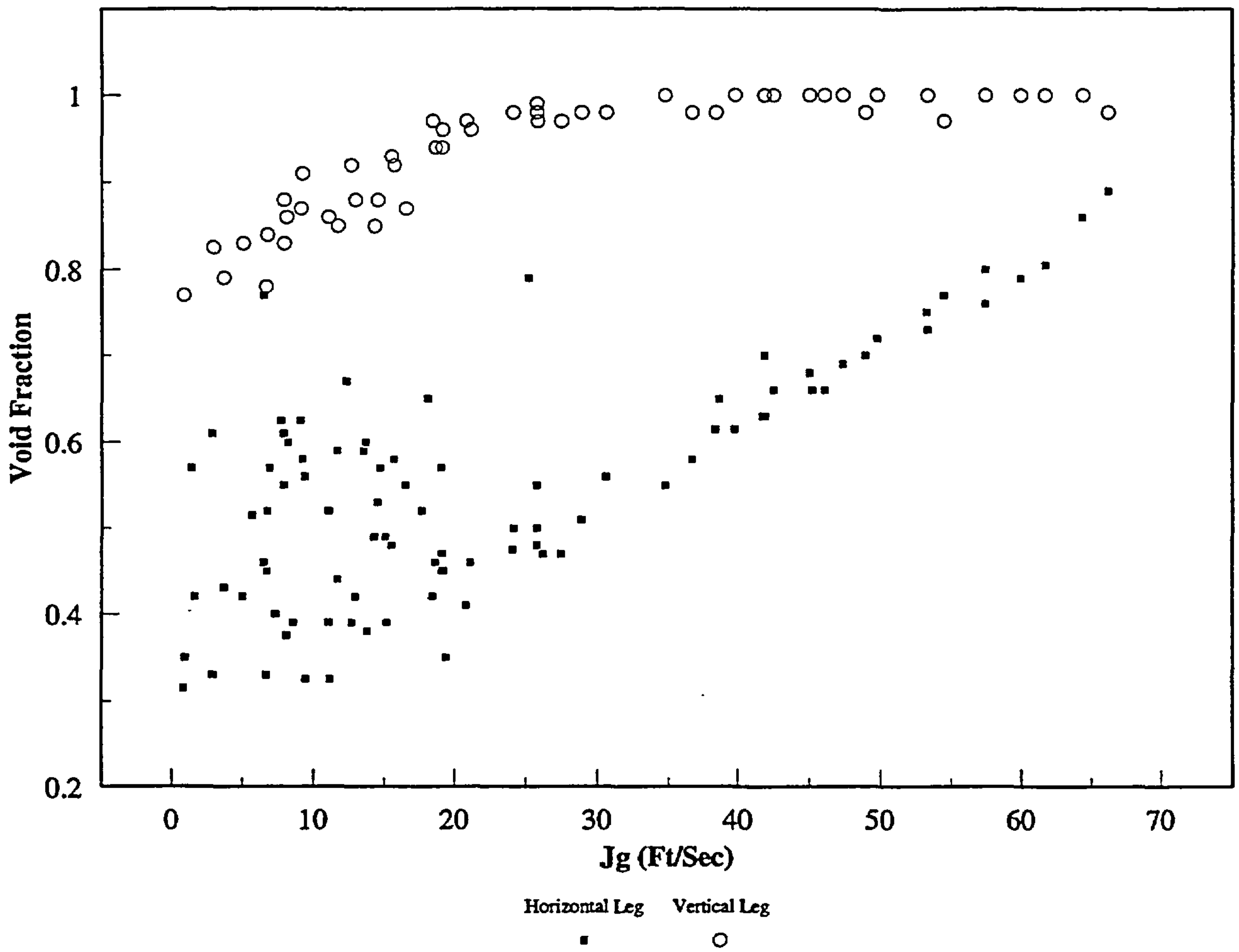

Figure 16-7. 1/3-Scale U-Tube Horizontal and Vertical Leg Average Void Fractions During Test

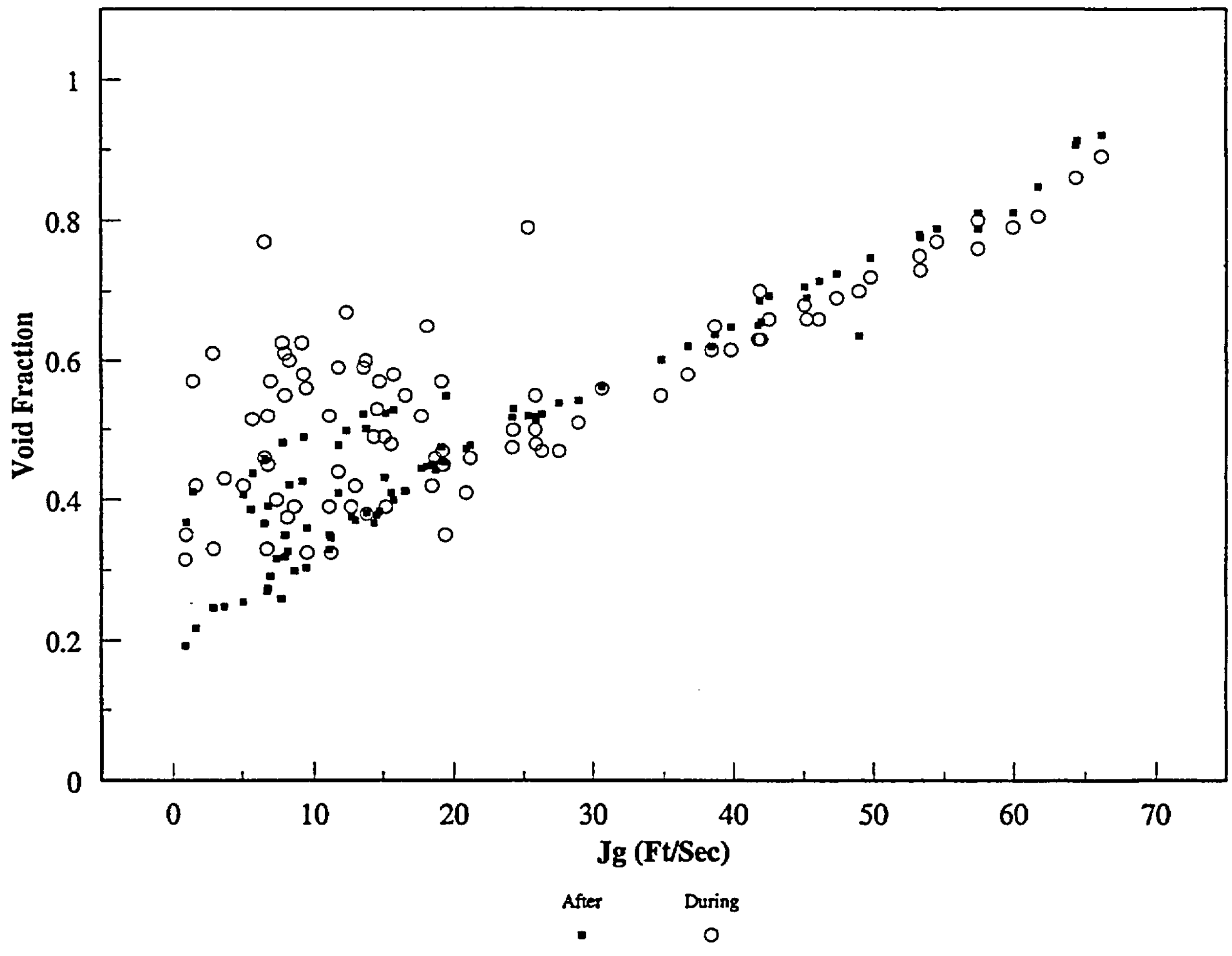

Figure 16-8. 1/3-Scale U-Tube Horizontal Average Void Fraction During Test Compared With Average Void Fraction After Test

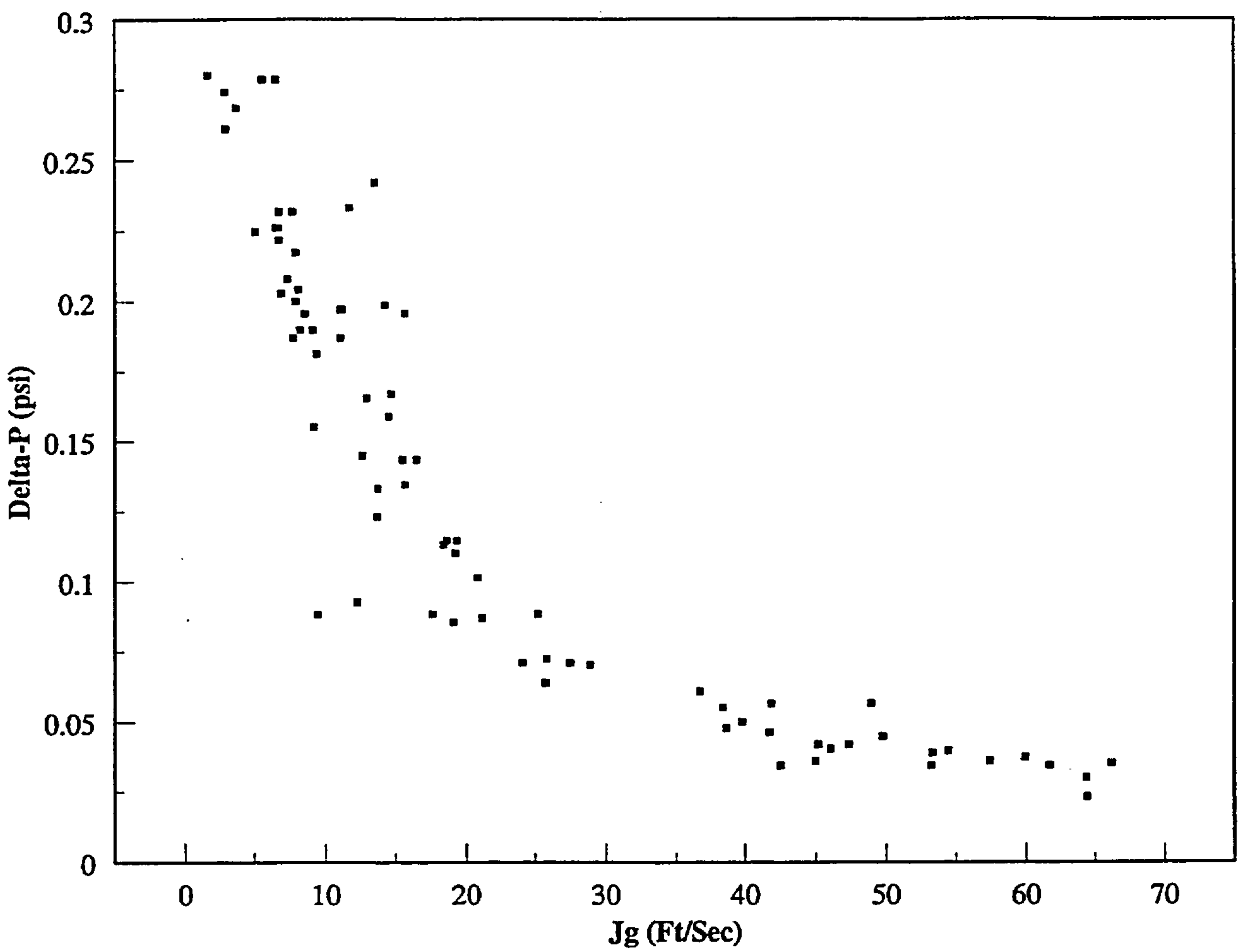

Figure 16-9. Pressure Difference Across the 1/3-Scale U-Tube

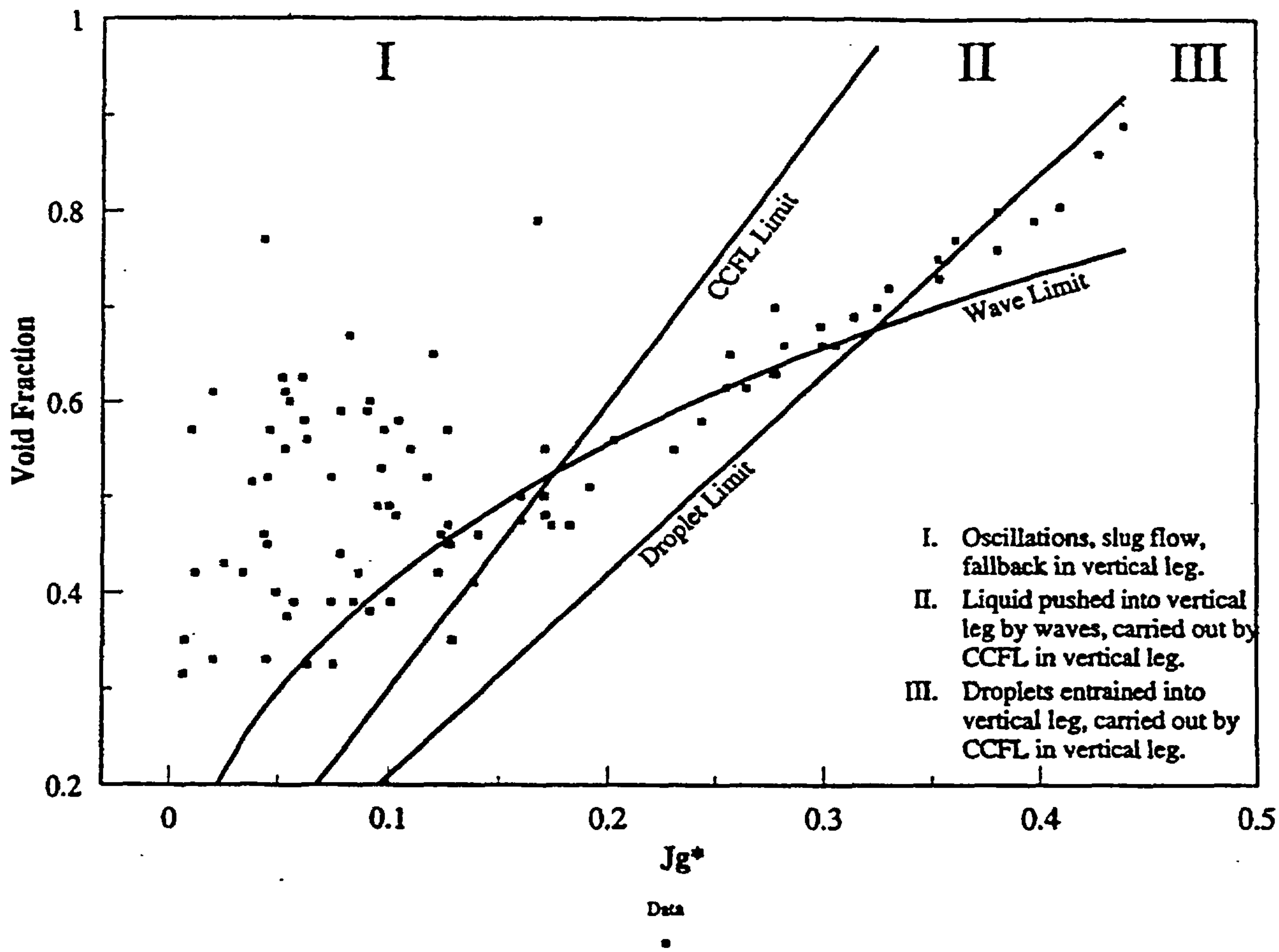

Figure 16-10. 1/3-Scale U-Tube Normalized Level and Limit Lines

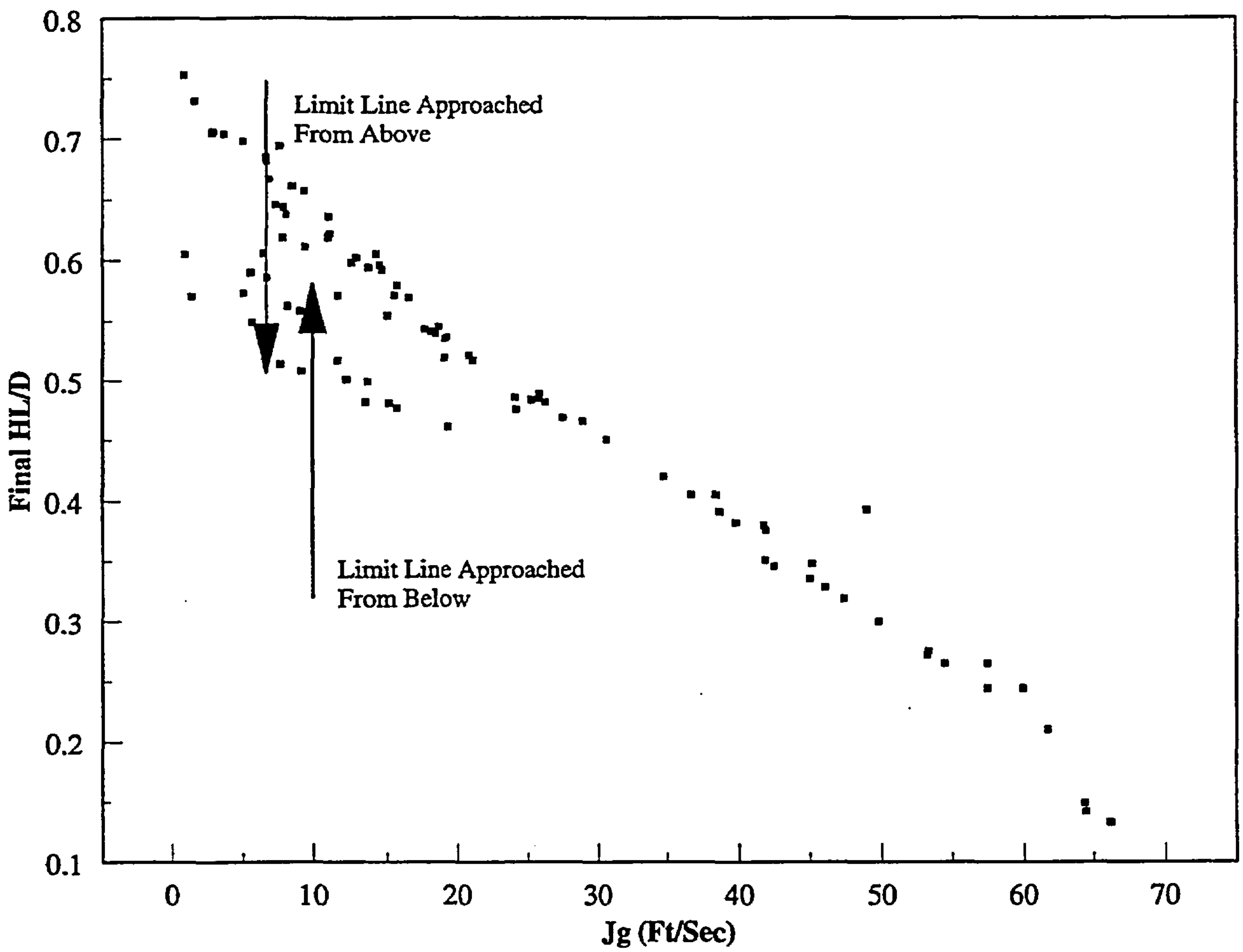

Figure 16-11. Hysteresis in Loop Seal Limit Line

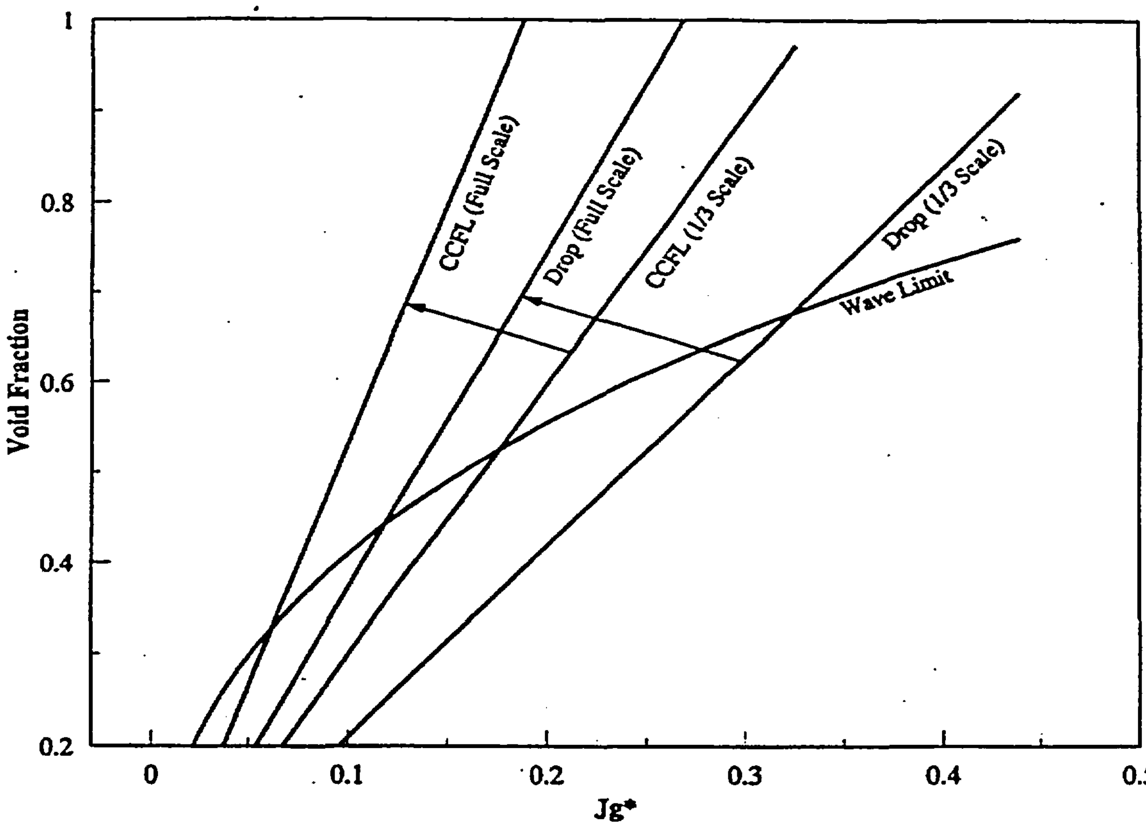

Figure 16-12. Effect of Increased Geometric Scale on Limit Lines

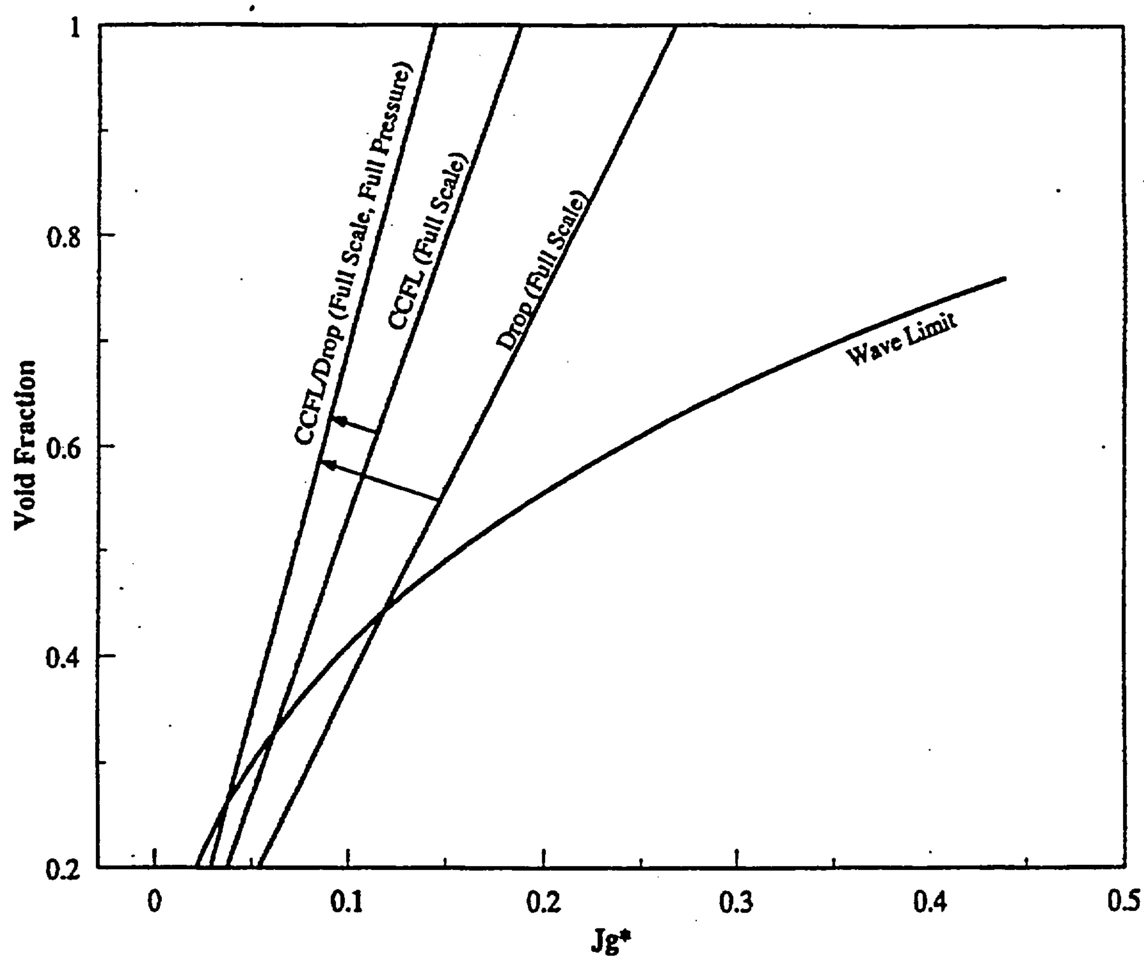

Figure 16-13. Effect of Increased Pressure and Scale on Limit Lines

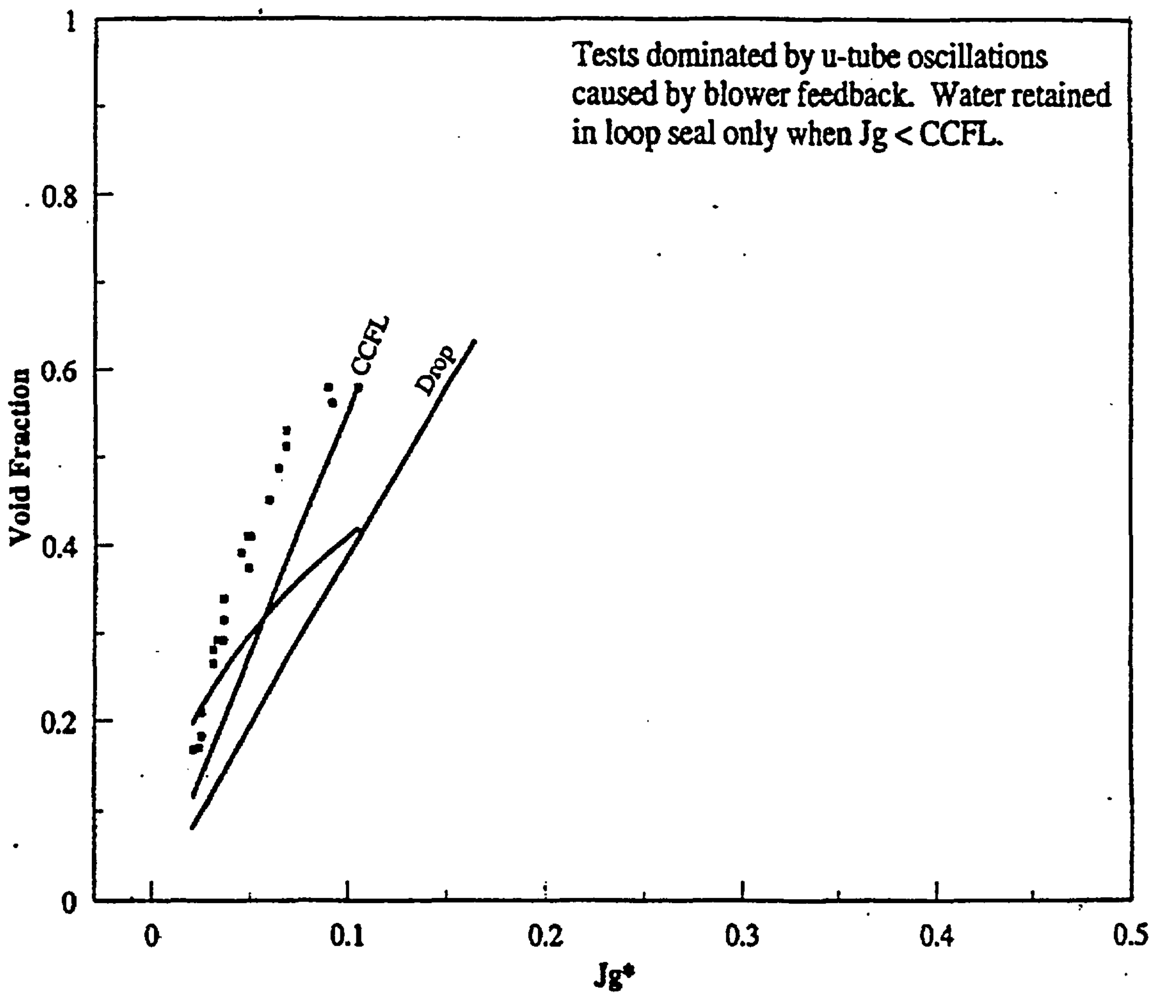

Figure 16-14. IVO Full-Scale Final Void Fraction and Limit Lines

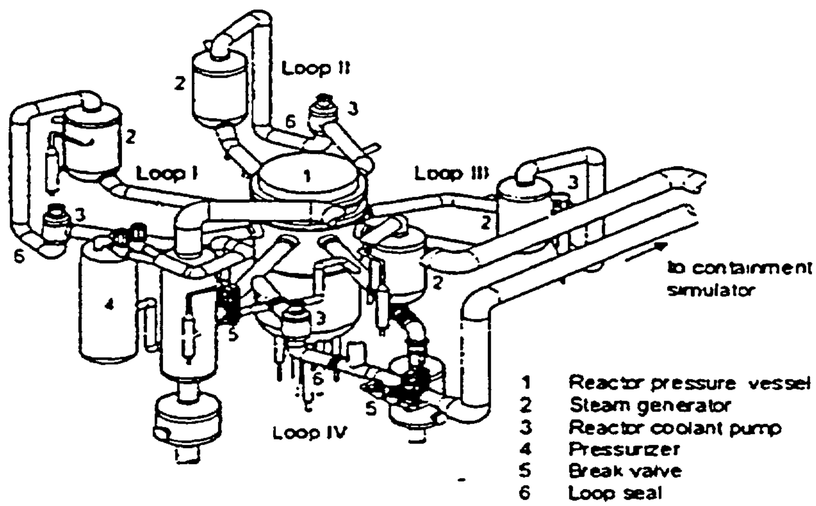

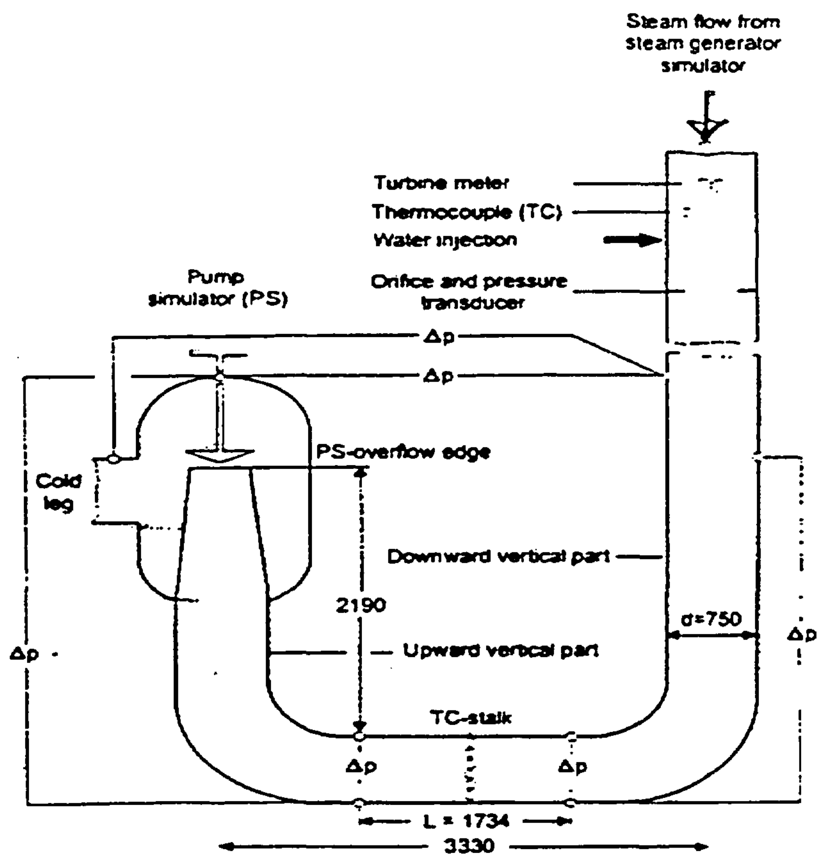

Figure 16-15. UPTF Facility and Single Loop Seal (Liebert and Emmerling, 1998)

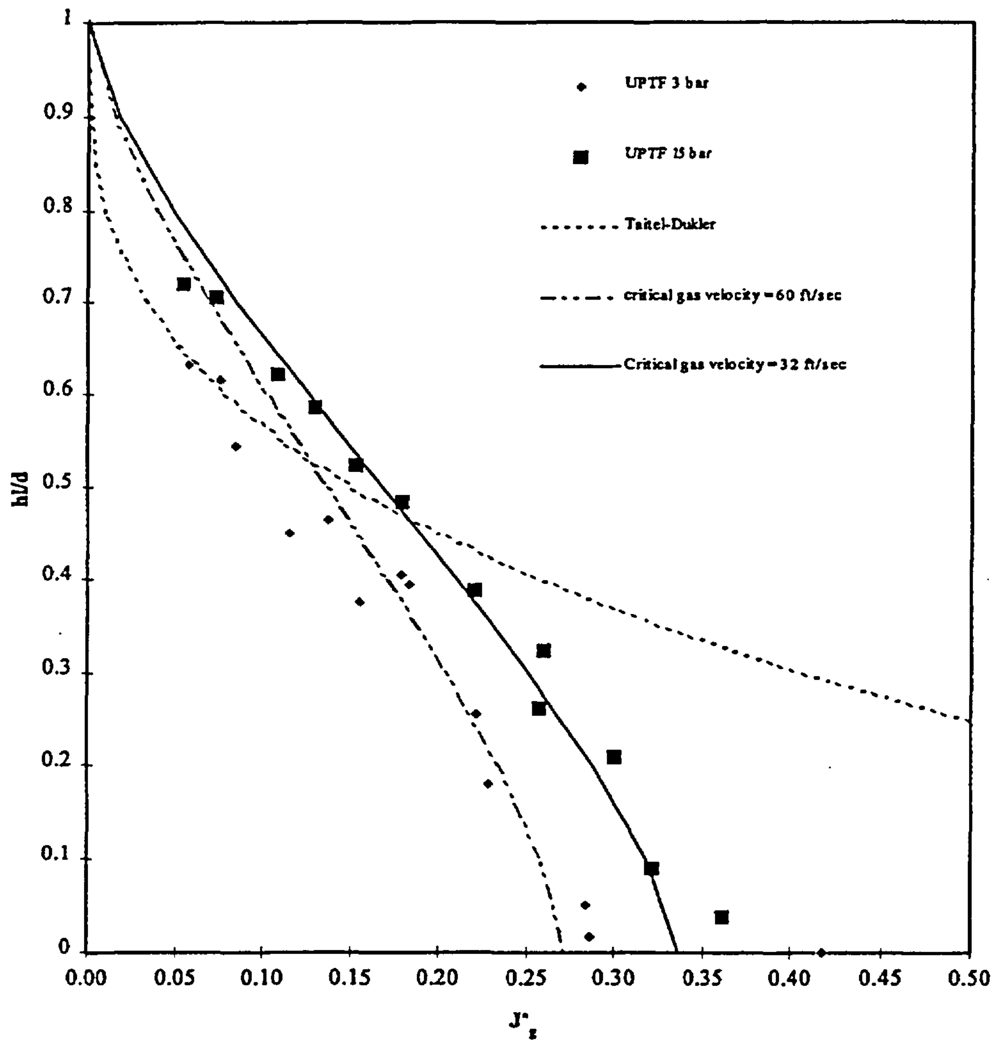

Figure 16-16. Lines of Constant Gas Velocity Compared to UPTF Data for 3-Bar and 15-Bar Loop Seal Tests (Liebert and Emmerling, 1998)

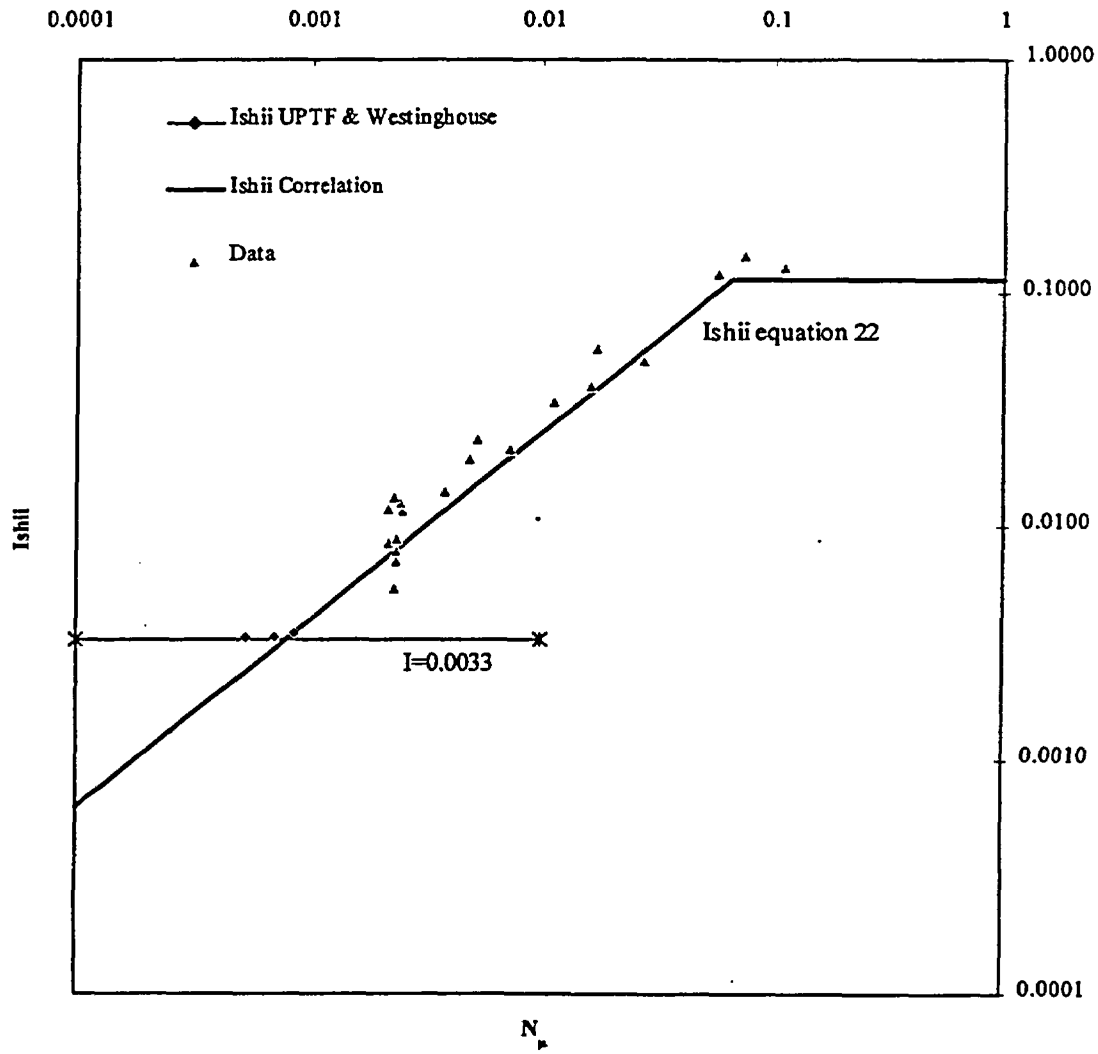

Figure 16-17. UPTF and PWS Compared to the Ishii Correlation and Data Base (Ishii and Grolmes, 1975)

a,c

[redacted]

Figure 16-18. WCOBRA/TRAC Model of the UPTF Separate Effects Loop Seal Clearing Tests

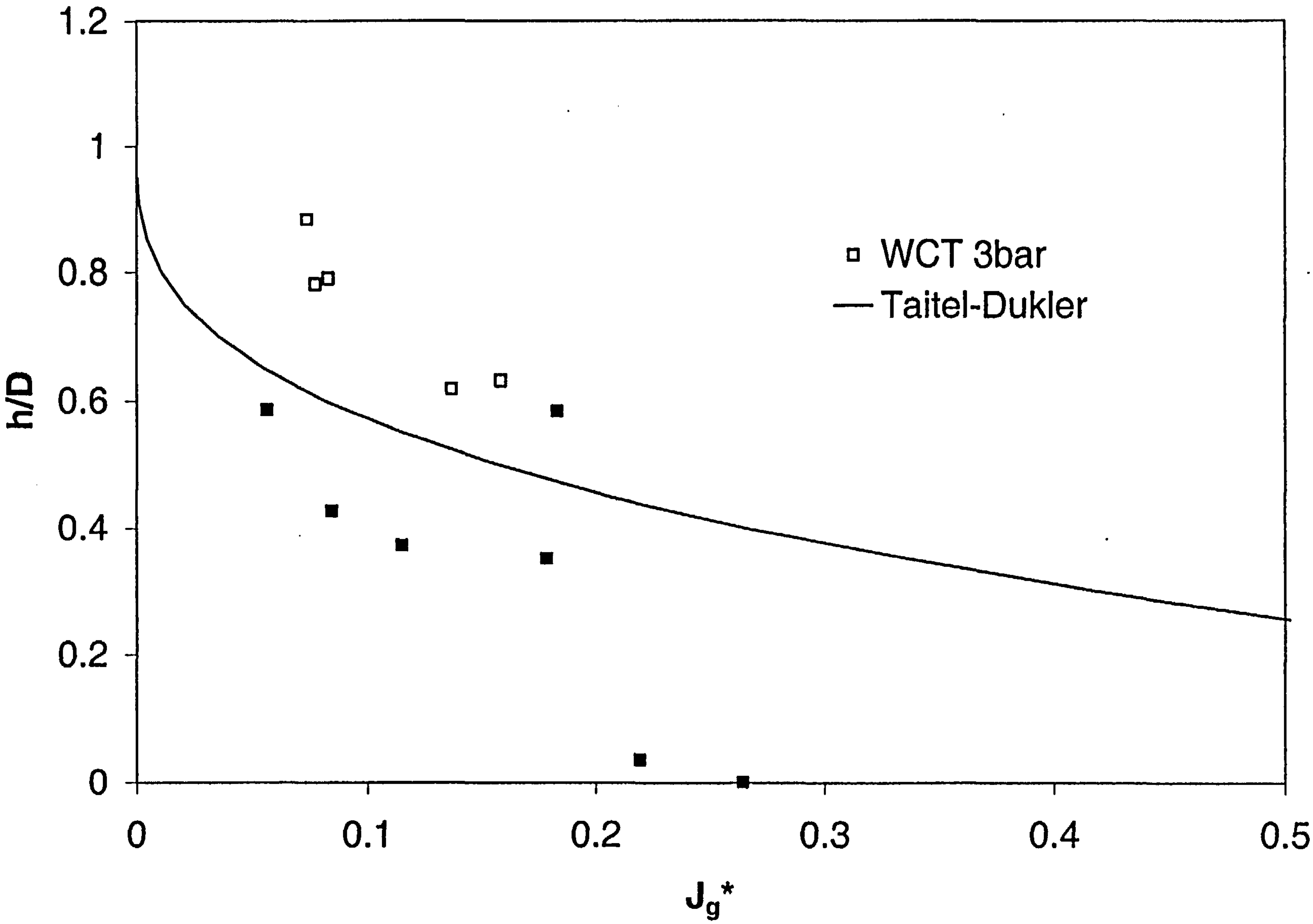

Figure 16-19. Calculated Residual Levels versus UPTF 3-Bar Data

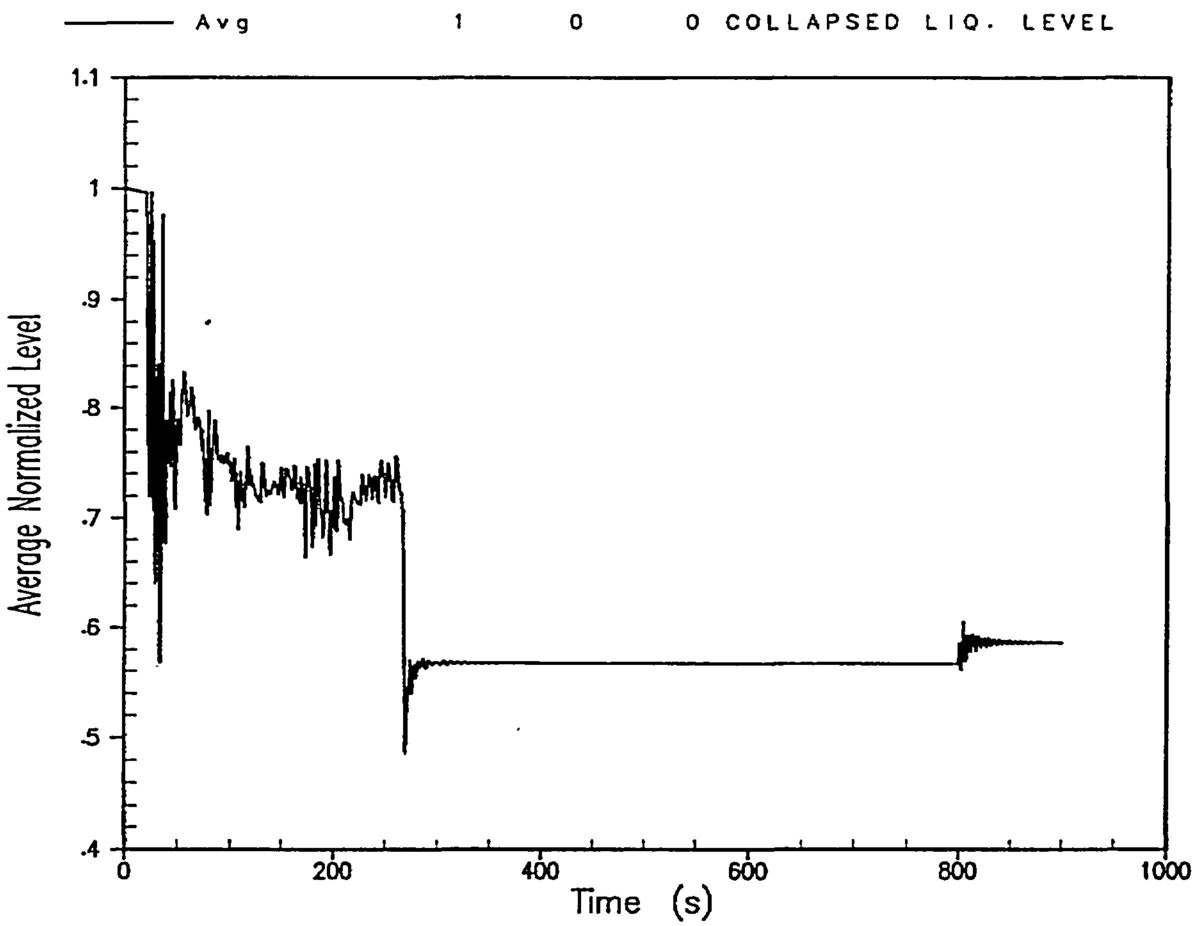

Figure 16-20. Calculated Level for 3-Bar Test at a Superficial Gas Velocity of 5.7 ft/s

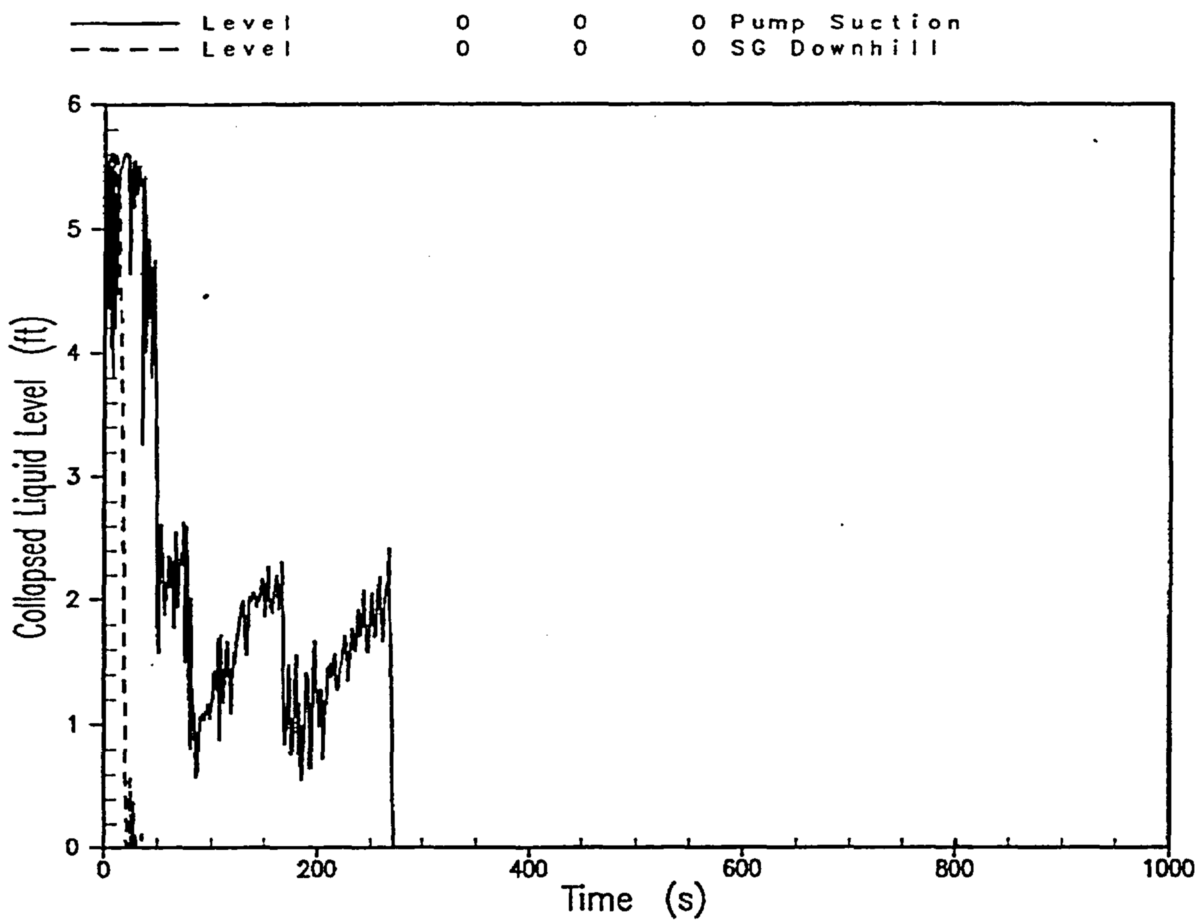

Figure 16-21. Calculated Liquid Level in Steam Generator Downhill Pipe and Pump Suction Pipe for a Superficial Gas Velocity of 5.7 ft/s

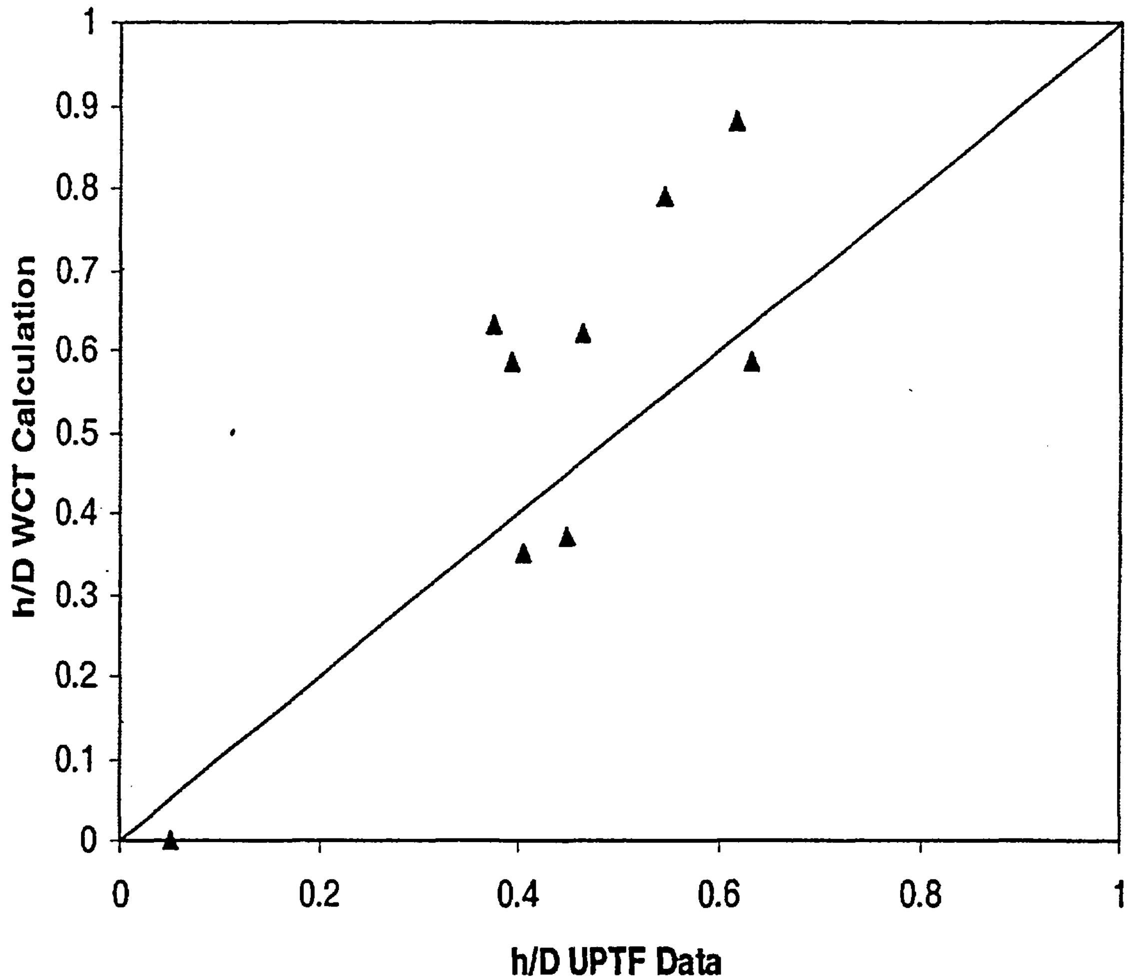

Figure 16-22. Comparison of WCOBRA/TRAC-SB Calculations and UPTF Data for the 3-Bar Tests

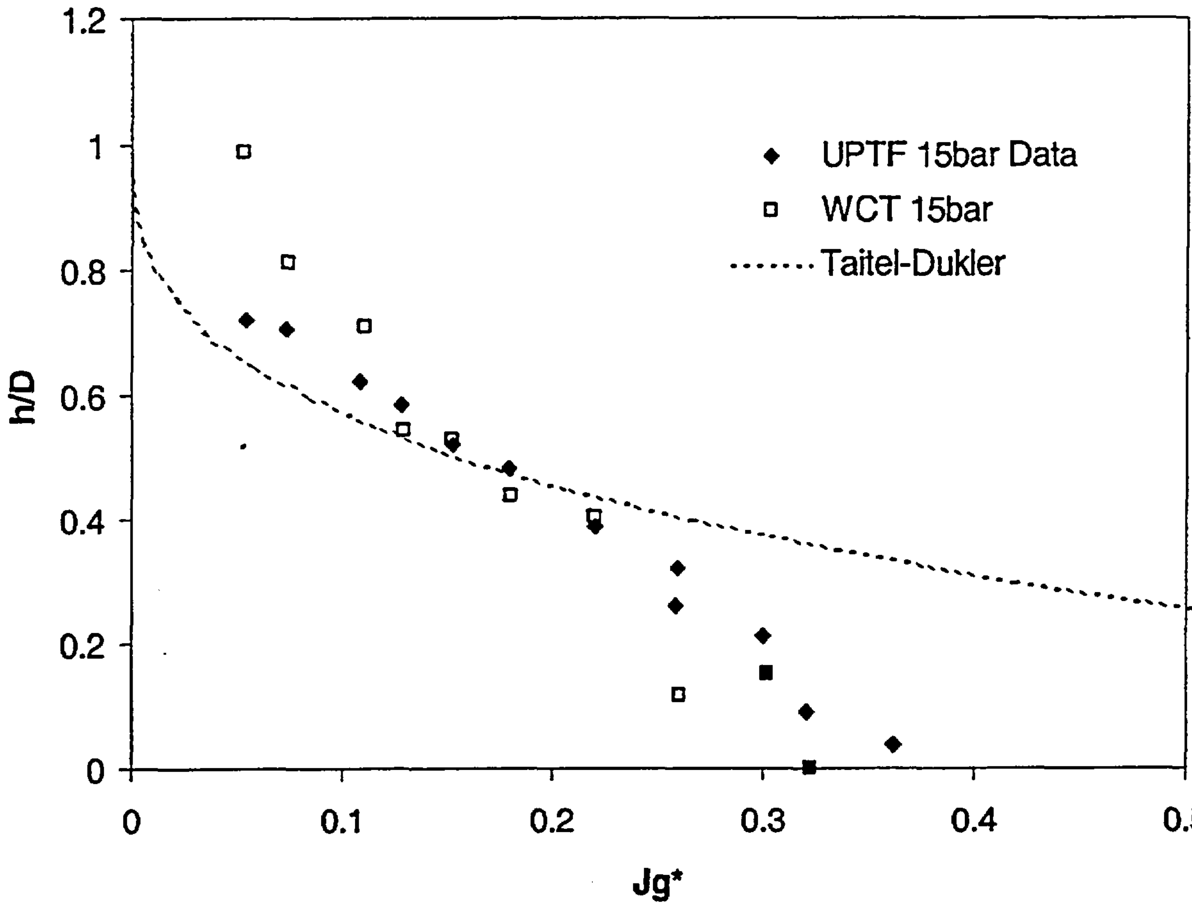

Figure 16-23. Calculated Residual Levels versus UPTF 15-Bar Data

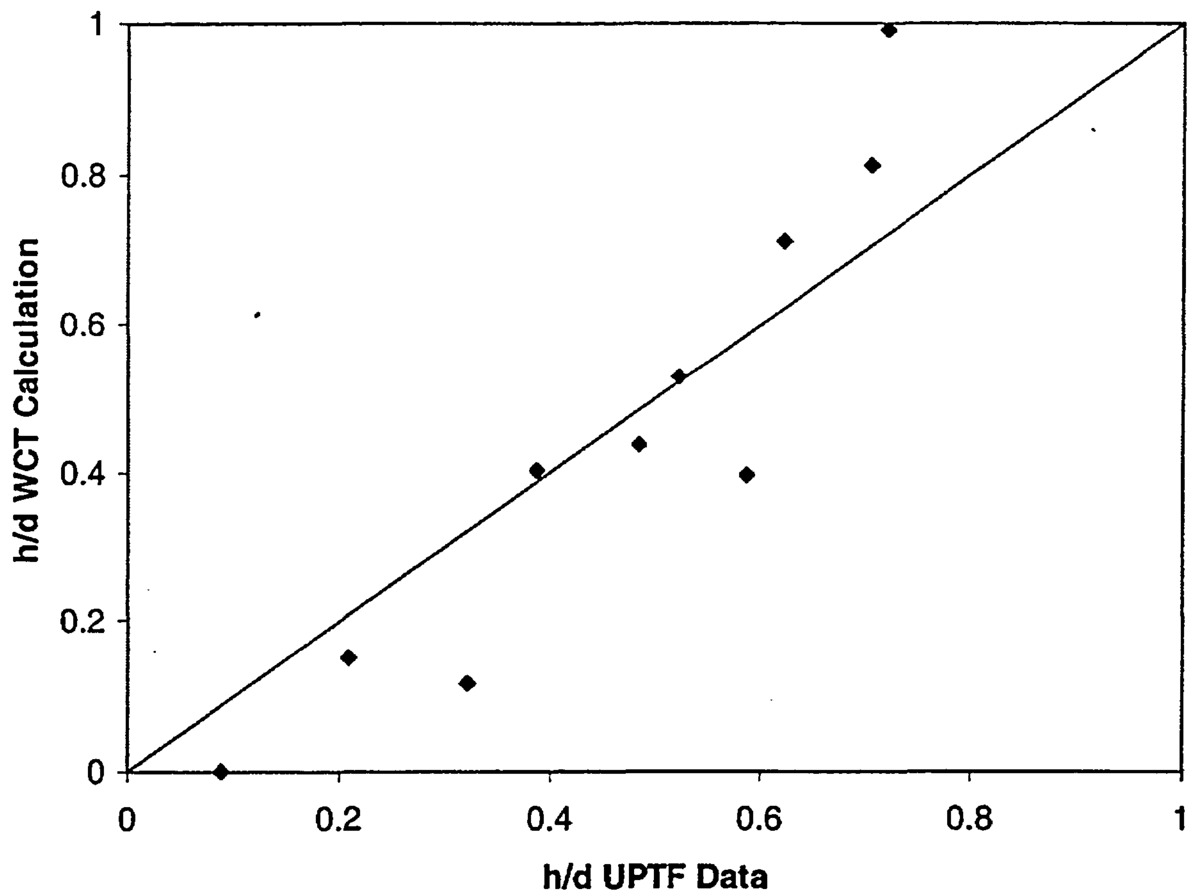

Figure 16-24. Comparison of WCOBRA/TRAC-SB Calculations and UPTF Data for the 15-Bar Tests

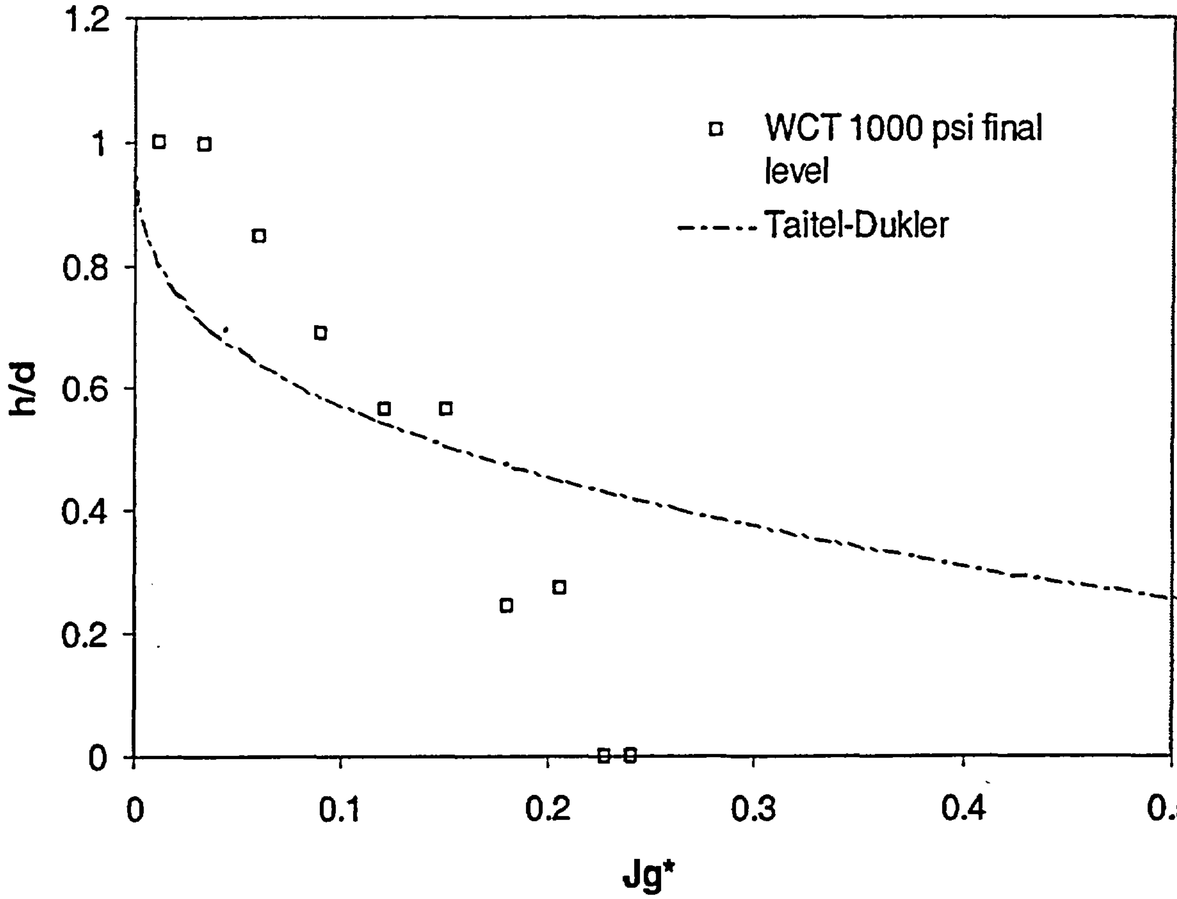

Figure 16-25. Calculated Residual Levels for 1015 psia

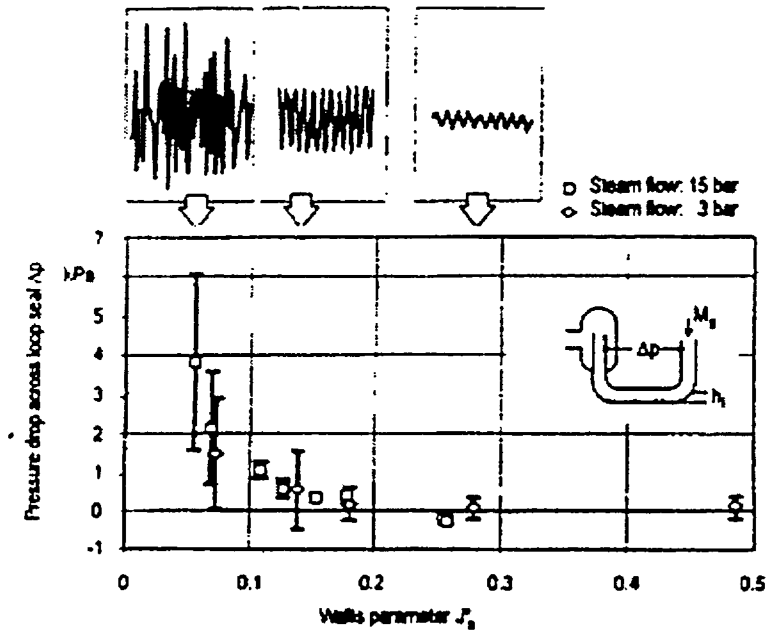

Figure 16-26a. Measured Pressure Drop for UPTF 3-Bar and 15-Bar Loop Seal Tests (from Liebert and Emmerling, 1998)

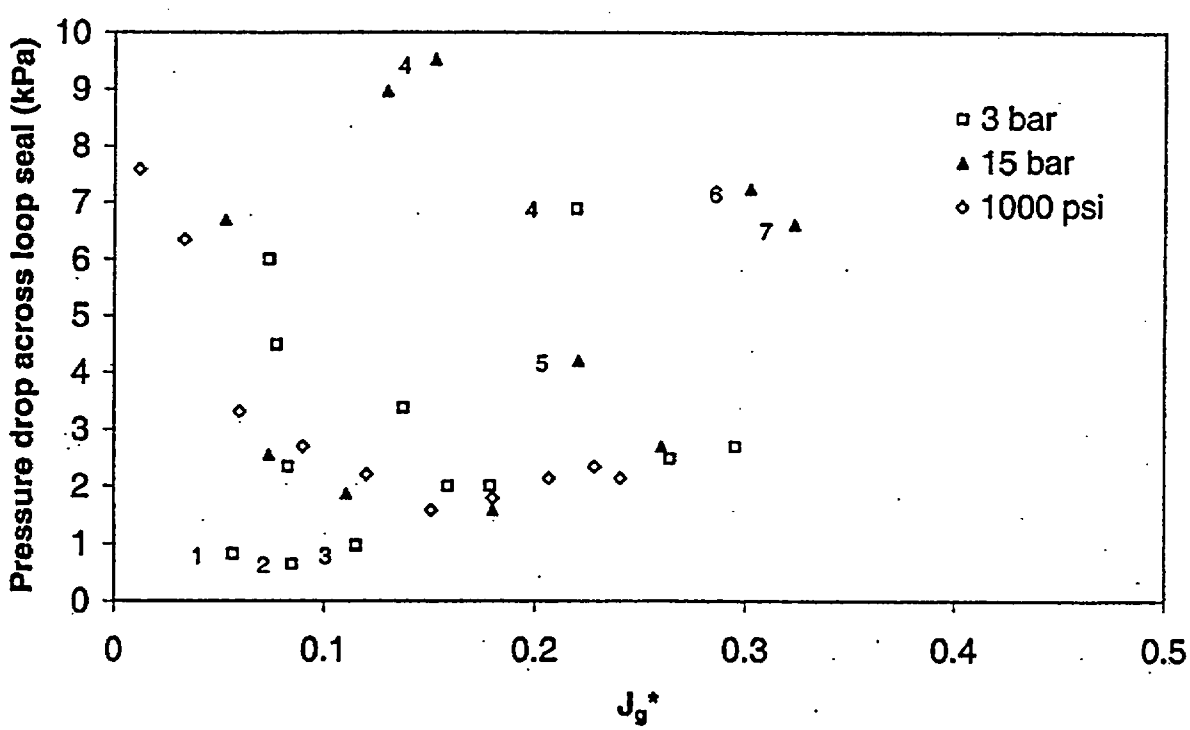

Figure 16-26b. Calculated Loop Seal Pressure Drop for 3-Bar, 15-Bar, and 1000 psia

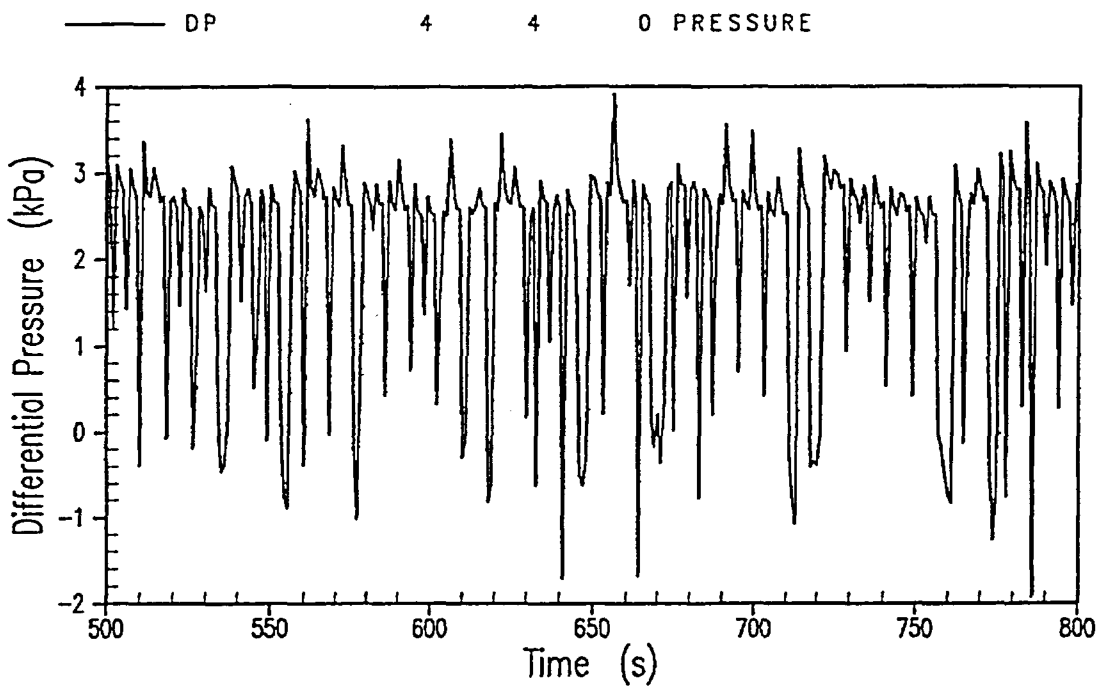

Figure 16-27. Calculated Pressure Drop for 15-Bar and Vapor Superficial Gas Velocity of 7 ft/s

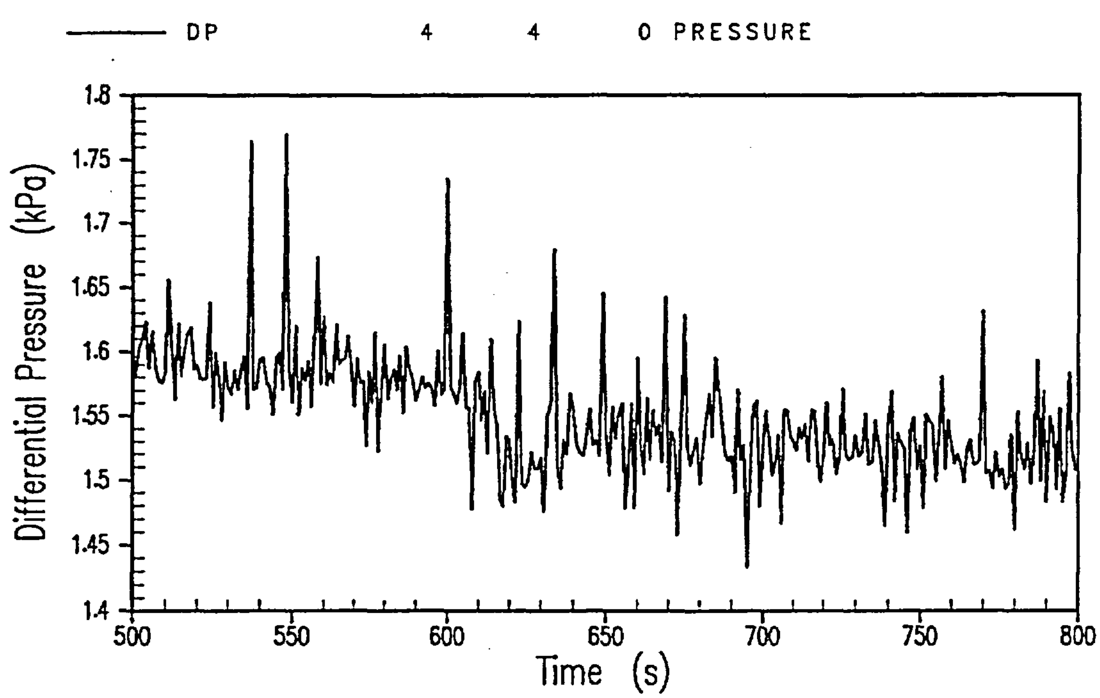

Figure 16-28. Calculated Loop Seal Pressure Drop for 15-Bar and Superficial Gas Velocity of 17 ft/s

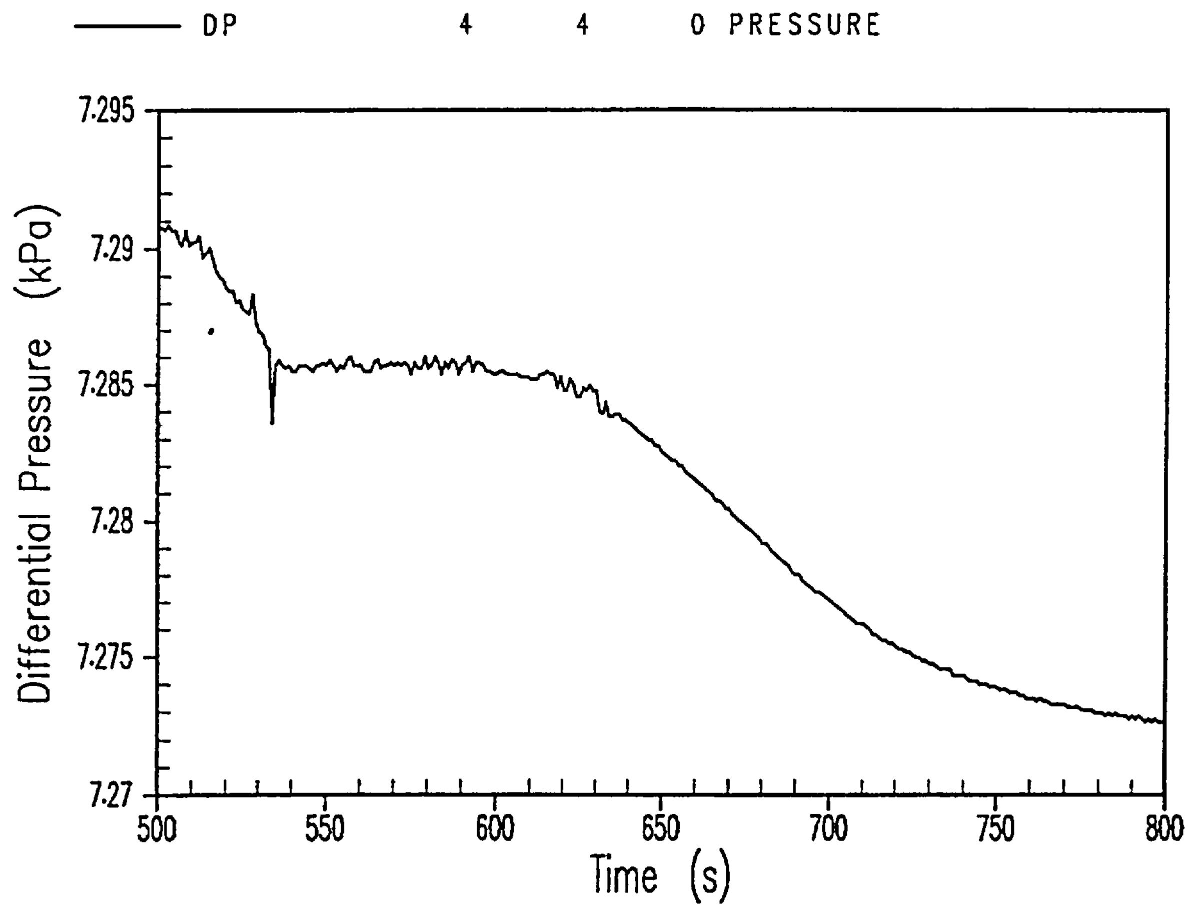

Figure 16-29. **Calculated Loop Seal Pressure Drop for 15-Bar and Superficial Gas Velocity of 29 ft/s**

SECTION 17
STEAM GENERATOR REGION HYDRAULICS MODELLING

17-1 Introduction

Steam generator hydraulics is identified as one of the major processes affecting the small break LOCA transient (See Section 1, Volume 1, of this document). Early in a postulated small break LOCA event, the power generated in the core is removed to the secondary systems by heat transfer through the steam generator tubes. This primary to secondary heat transfer initiates several processes that occur in the steam generator and which are ranked high in the PIRT because they affect the small break LOCA transient. These important processes include steam generator primary side heat transfer; steam generator tube voiding and CCFL, which may occur in the tubes themselves and/or in the steam generator inlet plenum and hot leg piping; and primary side pressure drop associated with the two-phase mixture in the tubes. Validation of the WCOBRA/TRAC-SB computer code for the small break LOCA application should include a demonstration that the code adequately predicts steam generator hydraulic phenomena as follows:

- Flooding in the vertical tubes and horizontal tubes
- Possible flooding in the hot leg steam generator inlet plenum connection
- Condensation within the steam generator tubes for primary to secondary heat transfer
- Steam generator primary mass inventory
- Associated pressure drop as the RCS inventory decreases during a small break LOCA event

Therefore, in this section, the performance of WCOBRA/TRAC-SB is qualified against pertinent single-effects experimental data and analytic solutions for benchmark problems, and against the Natural Circulation (NC) test series experiments performed in the Semiscale facility.

17-2 Physical Processes

The natural circulation period of small break LOCA scenarios is in large measure determined by the steam generator hydraulics. The steam generator processes affect the rate of RCS depressurization, particularly for the smaller small break LOCAs, which in turn affects the break flowrate, the rate of safety injection flow into the RCS, the state of the RCS at the time of loop seal clearance, and ultimately the core mixture level depression.

Condensation in the steam generator tubes not only removes the core decay power but also generates liquid mass within tubes. For the smaller small break LOCAs, an extended quasi-steady-state condition of nearly constant pressure occurs during which the core power is closely matched by the steam generator heat transfer to the secondary side. As system inventory decreases, eventually the steam generator tubes drain and the steam generator heat transfer reverses.

During the natural circulation period, condensate in the uphill portion of the steam generator tubes may possibly be carried into the steam generator outlet plenum in cocurrent flow or drain countercurrently into the steam generator inlet plenum. The prediction of CCFL in the vertical steam generator tubes determines whether any liquid from the steam generator uphill can proceed to drain into the steam generator inlet plenum. Furthermore, CCFL in the hot leg connection at the steam generator inlet could potentially prevent the steam generator liquid from drawing back into the hot legs, where it may contribute to the vessel upper plenum inventory.

The steam generator hydraulic behavior affects not only the pressure drop in the steam generator but also the timing and nature of the loop seal clearing. Consideration of steam generator hydraulics in the context of the overall mass distribution in the RCS is important. The Semiscale NC test series experiments are similar in design and execution to those conducted in other test facilities; they covered a range of single- and two-phase conditions with a regulated system coolant inventory. Predictions of test results from the Semiscale NC series are compared to such parameters as flow versus system mass inventory as the RCS is drained and transitions between two-phase flow and heat transfer modes.

17-3 CCFL Modelling in WCOBRA/TRAC-SB

17-3-1 Introduction

The CCFL is associated with the process of restricting liquid flow by counterflowing vapor due to interphasic drag forces. For example, liquid downflow in a pipe under the influence of gravity becomes unstable with increasing vapor upflow and eventually flows together with the vapor. Thus, stable countercurrent conditions can exist only within a certain range. The boundary of this range is recognized as the CCFL. This type of phenomenon can also exist in a horizontal stratified flow.

CCFL can occur in several locations in the PWR during the small break LOCA. CCFL may occur in the U-tubes of a steam generator. Inside the reactor vessel, the liquid inside the upper head can be prevented from downflow by steam flow inside the guide tubes. The liquid in the upper plenum may be held up at the upper core plate or upper fuel tie plates by upflowing steam from the core.

The focus of this section is the predictive capability of the multidimensional vessel hydrodynamics models for CCFL. In Section 17-3-2, the CCFL in a vertical pipe is evaluated with saturated liquid and steam at 1000 psia. In Section 17-3-3, the CCFL on a perforated plate is evaluated with saturated liquid and steam at 1000 and 35 psia. The geometry of the plate (perforation ratio and thickness) simulates, at small scale, the upper tie plates in a PWR. The computed results are compared with Northwestern test data (Hsieh, et al., 1980). In Section 17-3-4, CCFL of horizontal stratified flow is computed and the results are compared with available correlations.

17-3-2 CCFL in a Vertical Channel

17-3-2-1 Vertical WCOBRA/TRAC Channel Model

Flooding in a pipe has been studied with a TRAC 1-D component (Takeuchi and Young, 1983 and Takeuchi, et al., 1992). In this section, the prediction of pipe flooding with the WCOBRA/TRAC 3-D vessel fluid models is assessed. The purpose is to evaluate the interphase flow model, which is applied to several locations in the vessel such as support columns and guide tubes, and to compare predictions to classical flooding relationships.

Figure 17-1 illustrates the WCOBRA/TRAC model for pipe flooding computations. [

]^{a,c} All of the computations use saturated steam/water mixtures and saturated steam/subcooled water.

The computational experiment to generate the flooding curve proceeds as follows. Liquid is injected into channel 9 at a constant rate. After a steady liquid downflow into the bottom tank is established, steam is injected from channel 4 at a gradually increasing rate. At the beginning, a countercurrent condition is observed with steam flowing up through channels 4, 5, and 6, and separated via channel 7 into the pressure boundary condition in channel 8. By increasing steam flowrate and by maintaining a constant liquid injection rate, the magnitude of the liquid downflow through channels 5 and 4 is reduced. Eventually, liquid downflow is prevented by steam upflow. This experiment is repeated for several constant liquid flowrates.

The cases studied included the following conditions:

- Liquid is injected from the top of the test section at constant flowrates as shown in Table 17-1.

- For each case in Table 17-1, after a steady-state was established for 80 seconds with falling water but no vapor counterflow, vapor is injected and gradually increased to maintain quasi-steady conditions. Vapor is injected from the bottom of the test section with a linearly increasing rate as shown in Table 17-2.

Computed steam (g) flowrates and liquid (f) flowrates through channel 5 are plotted in a $(j_g^*)^{1/2}$ *versus* $(j_f^*)^{1/2}$ coordinate system, where the dimensionless volumetric fluxes are defined by:

$$j_g^* = j_g \left[\rho_g / g \; D_h \, \Delta\rho\right]^{1/2} \tag{17-1}$$

and j_f^* is similarly defined with subscript g replaced by f.

All the calculations exhibited similar behavior. A typical calculation (Case 3 in Table 17-1) is described as follows.

[

]a,c

Figure 17-5 shows the vapor versus liquid mass flows at several time intervals. These flows are then converted to j_g^* *and* j_f^*, using Equation 17-1, and plotted along with the Wallis flooding curve (Wallis, 1969), Equation 17-5 in Figure 17-6. This comparison shows that the flooding limit is not violated even in the presence of flow oscillations.

The results for several cases at high pressure are shown in Figure 17-7a, which plots the square root of the fluxes. Each symbol represents a j_f, j_g pair taken from the WCOBRA/TRAC run. The family of symbols (Figure 17-7b) indicates how the liquid downflow is reduced as the vapor upflow is increased (some of the oscillatory points have been removed for clarity). A straight line drawn through the upper bound of these points is regarded as the CCFL predicted by WCOBRA/TRAC.

17-3-2-2 Predicted CCFL at High Pressure

For the pipe model evaluation, the system pressure is 1000 psia, a representative pressure for the draining of steam generator tubes during a small break LOCA event. Both liquid and steam are assumed to be saturated. The countercurrent flow conditions at various points are plotted as:

$$y = [j_g^*]^{1/2} / C \tag{17-2}$$

$$x = [j_f^*]^{1/2} / C \tag{17-3}$$

in Figure 17-7b. In this coordinate system, the Wallis flooding correlation (Wallis, 1969) becomes:

$$x + y = 1 \tag{17-4}$$

the straight line shown in the plots. The figures clearly indicate the existence of a flooding limit approximately defined by:

$$(j_f^*)^{1/2} + (j_g^*)^{1/2} = C \tag{17-5}$$

with $C = 1$.

In the case of the TRAC 1-D pipe model, which was previously studied by Takeuchi and Young (Takeuchi and Young, 1983), the predicted flooding curve was at $C = 0.726$. In the vessel component pipe model, the interphasic drag force is somewhat weaker and leads to a higher flooding limit. However, pipe flooding data typically lie between $0.9 < C < 1.0$ (Wallis, 1969).

17-3-3 CCFL in a Perforated Plate

CCFL in a perforated plate has been tested and analyzed by Hsieh (Hsieh, et al., 1980). The geometry of the perforated plates approximately simulated the geometry of a fuel assembly top nozzle (or upper tie plate). The tests were conducted with air/water and steam/water systems. The air/water experiment was designed to investigate the effects of geometric factors on CCFL. The steam/water tests investigated subcooling effects on the CCFL. Air/water test data are analyzed in this section with a 15-hole perforated plate that most closely simulated the upper tie plate. The analyses were performed with the WCOBRA/TRAC code for a saturated steam/ saturated water system at high pressure (1000 psia) and at low pressure (35 psia). The low pressure condition approximates the vapor density in the air/water test at atmospheric conditions so that the computed results can be compared with the test data. In Section 17-3-3-1, the CCFL at a perforated plate is described. The computed CCFL at high pressure is developed in Section 17-3-3-2. The computed CCFL at 35 psia is compared with the test data in Section 17-3-3-3.

17-3-3-1 Correlations and Scaling for CCFL in a Perforated Plate

Various scaling methods and the correlations associated with them are described below:

- Northwestern (H^*) Scaling

  Hsieh (Hsieh, et al., 1980) developed a scaling parameter similar to the one used by Wallis (Wallis, 1969) to define a nondimensional volumetric flux, which is referred to here as Northwestern scaling:

$$h_g^* = j_g[\rho_g / g \ W_8 \ \Delta\rho]^{1/2} \qquad (17\text{-}6)$$

where:

$$W_8 \equiv D_h^{1-\alpha} [\sigma / g \ \Delta\rho]^{\alpha/2} \qquad (17\text{-}7)$$

and where D_h is the hole diameter and α is defined as:

$$\alpha \equiv \tanh\{k \ D_h \ A_h \ / A_T\} \qquad (17\text{-}8)$$

for the perforation ratio $A_h \ / A_T$ (hole area divided by total plate area) and a wave number defined by:

$$k \equiv 2\pi/t \qquad (17\text{-}9)$$

where t is the thickness of the plate and h_f^* for the liquid phase is similarly defined.

With these dimensionless volumetric fluxes, the test data for CCFL in the perforated plates were correlated by Hsieh to yield:

$$h_g^{*1/2} + h_f^{*1/2} = C \tag{17-10}$$

where:

$$C = \min\,(2.0,\ 1.07 + 0.004332\ L_1)$$

$$L_1 = n\ \pi\ D_h\,[\,g\,\Delta\rho/\sigma]^{1/2}$$

and n is the number of holes.

One way to examine Northwestern scaling is to compare it to other scaling methods as discussed below.

- Wallis (J^*) Scaling

$$j_g^* = j_g\,[\rho_g/g\ D_h\ \Delta\rho]^{1/2} \tag{17-11}$$

- Kutateladze (K^*) Scaling

$$\begin{aligned} k_g^* &= j_g\,[\rho_g^{\,2}/g\ \sigma\ \Delta\rho]^{1/4} \\ &= j_g^*\,[D^*]^{1/2} \end{aligned} \tag{17-12}$$

where use has been made of the dimensionless diameter:

$$D^* \equiv D_h\,[g\ \Delta\rho/\ \sigma]^{1/2} \tag{17-13}$$

- Westinghouse (L^*) Scaling

Takeuchi and Young (Takeuchi and Young, 1983) proposed a generalized scaling approach that combined J^* and K^* scaling as follows:

$$l_g^* \equiv j_g^* (D^*/K^2)^{1/2} \tag{17-14}$$

where K is the critical Kutateladze number that approaches $K_0\sqrt{D^*}$ at small diameters, and K_1, at large diameters, respectively. That is:

$$\begin{aligned} l_g^* &\rightarrow j_g^*/K_0 \quad as\ D^* \rightarrow 0 \\ &\rightarrow k_g^*/K_1 \quad as\ D^* \rightarrow \infty \end{aligned} \tag{17-15}$$

where $K_0 = 0.645$ and $K_1 = 3.2$. Similar relationships hold for the liquid phase.

For a given plate thickness (t), the Northwestern scaling approaches the following limits:

- For $D_h \rightarrow 0$, it approaches the Wallis number:

$$\begin{aligned} h_g^* &\rightarrow j_g^* \\ h_f^* &\rightarrow j_f^* \end{aligned} \tag{17-16}$$

- For $D_h \rightarrow \infty$, on the other hand:

$$h_f^* \rightarrow k_f^* \tag{17-17}$$

17-3-3-2 WCOBRA/TRAC Results

A WCOBRA/TRAC analysis of the test data was performed; the test case selected was the 15-hole plate with the following dimensions (WCOBRA/TRAC-SB produces approximately the same results):

D_h = 0.413 in.
t = 0.787 in.
A_T = 4.726 in^2
A_h = 2.013 in^2
A_h/A_T = 0.4260

The WCOBRA/TRAC analysis was initially performed for the large break LOCA application (Bajorek, et al., 1992). Given these dimensions, C ≈ 2.0 is used for both 1000 and 35 psia. This approximates the typical dimensions in a PWR or LOFT fuel assembly (tie plate). The WCOBRA/TRAC model used to predict the CCFL for the perforated plate is shown in Figure 17-8. Channels 1 through 3 simulate a large tank receiving falling water. Channel 4 is a large diameter pipe section where vapor is injected. Channel 5, representing the region directly above the plate holes, has the area of the holes in the plate, the hydraulic diameter of the hole, and the gap geometry obtained by assuming that the holes are projected as channels into the space above the plate. This modelling is similar to that used in the CCFL and upper plenum regions of the PWR. Channel 6 is the space above the solid portion of the plate. Channel 7 is a bridge for the countercurrent flow carried into the constant pressure boundary condition in channel 8. Cells 2 and 3 of channel 7 are isolated and inactive. Channel 9 is the top of the test section where liquid is uniformly injected. Gaps for lateral flow are also indicated with numbers enclosed by circles. The lower half of gaps 4 and 5 are blocked.

The computational experiment is performed in the same manner as the previous study. The saturated liquid is injected at a constant rate over an entire transient. After 30 seconds or so, when a steady-state is reached, steam is gradually injected at a linearly increasing rate. When the steam injection rate is low, all the falling liquid passes through the perforated plate and settles in the large tank at the bottom. The injected steam flows up through the perforated plate channel 5, and then through channels 6 to 8 into the constant pressure sink. As the steam injection rate increases, the amount of falling liquid becomes less and the residual liquid accumulates in channel 6, which then overflows into channel 8. Eventually, falling liquid is shut off, and the accumulated liquid flows into channel 8 together with injected steam. The computed liquid and steam flowrates are expressed in terms of the Northwestern dimensionless flowrates (h_g^* and h_f^*), and then the values are plotted in the coordinate system:

$$\frac{\sqrt{h_g^*}}{C} \; versus \; \frac{\sqrt{h_f^*}}{C}$$

The results are shown in Figures 17-9 and 17-10 for different liquid injection rates under a system pressure of 35 psia. Saturated steam and liquid in 35 psia simulate air/water under the atmospheric condition. For both cases, the computed flow states are bounded by the Northwestern flooding limit. For a higher system pressure, such as 1000 psia, similar results can be seen in Figure 17-11, but the flooding limit seems to be slightly more severe than lower pressure.

[

]^{a,c}

In the comparisons that follow, the results are presented in terms of the Northwestern scaling parameters.

17-3-3-3 WCOBRA/TRAC MOD7 Results

The predicted countercurrent fluxes are shown in Figure 17-14 in nondimensional form for 1000 psia as calculated using WCOBRA/TRAC MOD7. Similarly, the results at 35 psia are shown in Figure 17-15. The countercurrent flow conditions at various points are plotted in an x-y coordinate system as:

$$
\begin{aligned}
y &= [h_g^*]^{1/2}/C \\
x &= [h_f^*]^{1/2}/C
\end{aligned}
\tag{17-18}
$$

As described previously, each point on the figure represents conditions at a point in time as steam flow is gradually increased. The CCFL predicted by WCOBRA/TRAC is approximately located by the tangent drawn as the dashed line.

[

]^{a,c}

17-3-3-4 Comparison with Data

The MOD7 and MOD7A results can be compared with the test data (Hsieh, et al., 1980) for air/water at 14.7 psia (Figure 17-16). The Northwestern flooding curve represents the midpoints of all the test data of all the cases. For the 17-hole case studied here (*n = 15*), the test data lie above the flooding curve as shown by the open squares in Figure 17-16. In conclusion, the WCOBRA/TRAC MOD7A predicted CCFL is slightly conservative relative to the test data. The WCOBRA/TRAC MOD7A method is included in the WCOBRA/TRAC-SB version.

17-3-4 CCFL in a Horizontal Channel

In a small break LOCA, substantial stratification of two-phase flows occurs. These and other problems in predicting two-phase flow phenomena have been summarized by Zuber (Zuber, 1980). Entrainment of liquid and/or vapor pull-through at a break located at the top, the side, or the bottom of a horizontal pipe cannot be determined without a stratification model. The same problem exists in the hot leg at the pressurizer surgeline junction and at the steam generator inlet elbow, where flow stratification and CCFL in the hot leg must be predicted. In a large break LOCA, conditions in the loops are much more homogeneous due to the high fluid velocities. However, some stratification is likely in some regions of the reactor vessel, such as the upper core plate. In this section, the vessel model capability to predict liquid levels and flow transitions in horizontal flow is compared against flow regime transition correlations and weir flow models.

17-3-4-1 WCOBRA/TRAC Simulation of Horizontal Flow

A horizontal 18-foot long pipe of a 3x3-foot square cross section was modelled with six horizontal channels and three cells in each channel, as illustrated in Figure 17-17. These dimensions approximate a PWR hot leg. The channels are connected laterally by gaps. Channel 10 has a dead-end at the left and a constant pressure boundary condition at the top. A pipe component is connected at the bottom of channel 9 to supply liquid. Steam is injected at the top of channel 5. The right end of channel 5, as shown in Figure 17-17, is connected to a large volume simulating a vessel region.

The CCFL is obtained with saturated steam and liquid flowing initially in a countercurrent state. As steam flowrate is gradually increased, the liquid flow direction (initially from the injection point to the vessel) is eventually reversed.

17-3-4-2 Relation of Flooding Correlations to Slug Flow Regime Transition Models

The CCFL in a horizontal pipe was originally considered by Wallis (Wallis, 1969). He defined the flooding curve as a bounding condition of Long's equation for existence of a solitary wave (Long, 1956). Using a similar basis of an instability condition of a solitary wave, Taitel and Dukler (Taitel and Dukler, 1976) and also Wallis and Dobson (Wallis and Dobson, 1973) studied the flow regime transition from a stratified flow to a slug flow. The conditions for these two events are mathematically the same, but the expressions given for the phase transition are different from those used to define the flooding curves. In this section, the two events are related and the formula for the flow regime transitions are translated to the flooding curves for the stratified flow in a circular pipe and a square channel. These translated flooding curves and the Long-Wallis flooding curve are also compared in the next section. The predicted CCFL transitions computed with the WCOBRA/TRAC-SB horizontal pipe model are developed and compared in Section 17-3-4-3. The predicted water levels in the channel are also compared with results from the weir flow model (Wallis and Dobson, 1973) in Section 17-3-4-4.

Wallis derived a flooding model for a horizontal stratified flow by identifying the bounding condition of Long's equation for a stratified wave in a channel. In accommodating other correlations and theories, the more general form is assumed:

$$\frac{j_f^{*2}}{(1-\alpha)^\nu} + \frac{j_g^{*2}}{\alpha^\nu} = c^2 \tag{17-19}$$

as the drift flux relation, where dimensionless volumetric flux for steam is defined by:

$$j_g^* = j_g\,[\rho_g/g\; D_h\; \Delta\rho]^{1/2} \tag{17-20}$$

where j_g is the volumetric flux, D_h is the hydraulic diameter, g is the acceleration of gravity, ρ_g is the steam density, and $\Delta\rho = \rho_f - \rho_g$. The dimensionless volumetric flux (j_f^*) for liquid is similarly defined with the liquid density (ρ_f). Equation 17-19 with $c = 1$ and $\nu = 3$ becomes the Long-Wallis equation which represents a family of ellipses in the (j_f^*, j_g^*)-plane. The derivative of this equation with respect to void fraction α:

$$\frac{j_f^{*2}}{(1-\alpha)^{\nu+1}} - \frac{j_g^{*2}}{\alpha^{\nu+1}} = 0 \tag{17-21}$$

yields a family of curves tangent to the above family of ellipses.

The flooding curves are obtained from these two equations by eliminating the void fraction (α). Eliminating j_f^* from Equations 17-19 and 17-21 yields the expression:

$$j_g^* = c\;\alpha^{(\nu+1)/2} \tag{17-22}$$

The flooding curve is:

$$(j_f^*)^{2/(\nu+1)} + (j_g^*)^{2/(\nu+1)} = c^{2/(\nu+1)} \tag{17-23}$$

The drift flux relation for a vertical flow in the (j_g^*, j_f^*) coordinate system is a straight line for a given void fraction. Equation 17-19 gives the drift flux relation for a horizontal flow, which forms a family of ellipses as α is varied, as shown in Figure 17-18. The first quadrant is for the cocurrent flow, and the second quadrant, for countercurrent flow. The envelope in the first quadrant defines the flow regime transition. The flow regime outside the envelope can no longer be a horizontal stratified flow but a slug, intermittent, or annular dispersed flow. The envelope in the second quadrant is the flooding limit beyond which no countercurrent flow state exists. Both conditions for the flow regime transition and the flooding point have been derived mathematically based on the same process of wave instability. The flow regime transitions are expressed in the form of Equation 17-22. Once the flow regime transition is identified, the coefficients c and ν are determined for the flooding relationship of Equation 17-21. Specific applications of the above equations are described in the following examples:

- Taitel-Dukler Flow Regime Transition in a Circular Pipe

  The Taitel-Dukler transition from horizontal stratified flow to intermittent and annular dispersed liquid flow regimes (Taitel and Dukler, 1976, Equation 23) can be expressed as:

$$j_g^* > C_2 \, \alpha^{3/2} \left[\frac{4}{\pi D_h} \frac{dA_L}{dh_L} \right]^{-1/2} \tag{17-24}$$

  where $C_2 = 1 - h_L/D$ and A_L and h_L are the liquid flow area and the liquid level, respectively. For a circular pipe, this is a complicated expression of α, which can be approximated to yield: [

]^{a,c} (17-25)

Therefore, in Equation 17-22, $c = 1$ and $\nu = 5$. The flooding curve of Equation 17-21 becomes:

$$(j_f^*)^{1/3} + (j_g^*)^{1/3} = 1 \tag{17-26}$$

- Taitel-Dukler Flow Regime Transition in a Circular Pipe with $C_2 = 0.5$

  In the Taitel-Dukler transition formula, the factor C_2 can be set to 0.5 as in Wallis and Dobson (Wallis and Dobson, 1973), which is discussed below. In this case, the transition condition can be approximated by:

$$j_g^* = 0.55\,\alpha^2 \ . \tag{17-27}$$

  therefore, $c = 0.55$ and $\nu = 3$, and the flooding curve of Equation 17-23 becomes:

$$(j_f^*)^{1/2} + (j_g^*)^{1/2} = 0.742 \tag{17-28}$$

- Wallis-Dobson Transition in a Square Channel

  After a series of tests, Wallis and Dobson derived the flow regime transition formula in a similar expression:

$$j_g^* = 0.5\,\alpha^{1.5} \tag{17-29}$$

  In this case, therefore, $c = 0.5$ and $\nu = 2$ and the flooding curve of Equation 17-23 becomes:

$$(j_f^*)^{2/3} + (j_g^*)^{2/3} = 0.707 \tag{17-30}$$

These flooding curves are shown in Figure 17-19. The three flooding curves are approximately the same, especially at the middle point, $\alpha = 0.5$.

The transition and the flooding curves are symmetric, consistent with the Taitel-Dukler approximation that the interfacial force is dependent only on the steam velocity, ignoring the interface velocity.

The Long-Wallis flooding curve (Wallis, 1969) is shown as curve 4 in Figure 17-19. Their flooding curve is derived from Long's wave equation, which is based on the velocity potential theory for a stratified flow. The Taitel-Dukler phase transition correlations takes into account the interphasic forces as well as fluid wall forces. Therefore, the two phases are more strongly coupled in the Taitel-Dukler correlation than they are in the Long-Wallis correlation. The Wallis-Dobson correlation in curve 3 is derived from the test data, and obviously, these forces are in effect.

17-3-4-3 Predicted Horizontal CCFL at High Pressure

The CCFL predicted by WCOBRA/TRAC-SB for the model shown in Figure 17-17 was obtained as follows.

Initially, the entire system is filled with saturated steam at 1000 psia. A transient calculation begins with injection of saturated liquid at a constant rate. After a steady-state of liquid flowing into the container is established, saturated steam is injected. The injected steam flows out of the system at the pressure boundary. This forms a countercurrent state. The steam injection rate is gradually increased so that a quasi-steady-state is maintained throughout the computation.

With a constant liquid injection rate ranging from 70 to 650 lb_m/sec, the predicted countercurrent conditions are shown by circles in Figure 17-20. For a given liquid injection flowrate, the predicted conditions are linked by lines as steam flow is increased. Although the lowest point shows a finite steam flowrate, the steam injection rate is zero; the steam flow shown is the steam in the large vessel volume displaced by the liquid flowing into the vessel. As the steam injection rate increases, the circles move upward and turn along the flooding curve. Eventually, the liquid flow direction is reversed, and both liquid and steam flow out of the system through the pressure boundary at the top of channel 10. The predicted flow states agree well with the flooding constraints defined by the transition curves. At low values of j_f (high void fraction), the flooding limit is underpredicted, possibly because the 3-cell model cannot resolve the liquid level accurately.

A sensitivity study was conducted to find stability in the above results by varying the number of cells per channel, by changing the length of the pipe, and then by changing the channel length. The computed results were quite stable as long as the number of cells is greater than one and the channel length (or horizontal cell spacings) remains approximately the size of the pipe diameter.

17-3-4-4 Predicted Water Level

Before steam was injected in the computational experiments described in the previous section, a steady-state liquid flow was established through the square channel into the vessel. The liquid fractions computed in each cell are shown in Table 17-3. The equivalent water levels are also shown. It is evident that realization of horizontal stratified flow is predicted. The predicted water levels are compared with the weir flow level (Shames, 1982), n_0, given by:

$$q_T = D\, g^{1/2}\, (2/3\ n_0)^{3/2} \tag{17-31}$$

for the total volumetric flowrate (q_T), the width of the crest (D), and the acceleration of gravity (g). The weir flow level calculations and results for each flowrate are shown in Table 17-3. The water levels predicted with the WCOBRA/TRAC code agree reasonably well near the channel exit (channel 6) with the weir flow calculations over the entire range of flowrates considered.

17-4 CCFL in Hot Leg-to-Steam Generator Flow Path

17-4-1 Introduction

During a small break LOCA, the amount of countercurrent flow in the hot legs of a PWR is important in determining the inner reactor vessel mixture level response. One factor influencing the countercurrent flow in the hot leg is the potential for countercurrent flow at the hot leg-to-steam generator inlet plenum connection. If the amount of steam generated in the core by decay heat is large enough, liquid flow from the steam generator inlet plenum to the hot leg may be inhibited. The potential for liquid holdup (flooding) in the hot leg-to-steam generator inlet plenum connection during a small break LOCA is considered in this section.

17-4-2 Physical Processes

Figure 17-21 depicts the PWR geometry in the hot leg-to-steam generator inlet plenum connection region. Countercurrent flow at the steam generator tube inlet due to reflux condensation results in liquid falling from the tubes to the bottom of the steam generator inlet plenum where it will collect. The liquid then attempts to flow down the 45-degree incline which joins the steam generator inlet plenum to the horizontal section of the hot leg. Steam flow in the hot leg impinges upon the 45-degree incline and must change direction to flow into the steam generator inlet plenum. The interaction between the steam and liquid tends to restrict countercurrent flow for some steam flow conditions.

The specific geometry of the hot leg and the steam generator inlet plenum can influence the countercurrent flow and flooding phenomenon. For instance, the inclination of the hot leg-to-steam generator inlet plenum connection has a complicated effect on flooding, as indicated by Tien and Liu (Tien and Liu, 1979), Hewitt (Hewitt, 1977), and Lee and Bankoff (Lee and Bankoff, 1982). Moreover, liquid entry effects described by Dukler and Smith (Dukler and Smith, 1979) in the steam generator inlet plenum may also influence the flooding phenomena in this region of a PWR.

17-4-2-1 Small-Scale Tests

There have been several small-scale experiments (Wongwises, 1996; Ghiaasiaan, et al., 1994; Ohnuki, 1986; Ohnuki, et al., 1988; Wan, 1986; Siddiqui, et al., 1986; Kroleswki, 1980; and Richter, et al., 1978) that have studied countercurrent flow phenomena and flooding in geometric configurations, consisting of horizontal pipes connected to inclined (at various angles) vertical pipes or elbows as in the hot leg-to-steam generator geometry of a PWR. In these small-scale tests, the onset of flooding appears to coincide with interfacial wave instability and growth, which leads to water slug formation in the horizontal piping section, usually near the bend or elbow region. At lower liquid flowrates, the slugging occurs simultaneously with formation of a hydraulic jump near the bend or inclined region where the liquid flow transitions from super-critical to subcritical. At higher liquid flowrates, the water slug formation moves away from the bend (in the horizontal section) and the hydraulic jump is usually weaker or not present at all. This flooding pheonema has also been confirmed by Choi and No (Choi and No, 1995) in experimental studies of nearly horizontal pipes and Kawaji (Kawaji, et al., 1991) in experimental studies of flooding in vertical to inclined pipes. It was observed in these small-scale tests that the geometric configuration of the bend and vertical pipe section strongly influences the location of the hydraulic jump and the water slugging. Gas velocities associated with flooding in these small-scale geometric configurations were also found to be well below those expected for countercurrent flow in vertical pipes alone.

Based upon the small-scale test experience, a special CCFL model would seem to be needed for the hot leg-to-steam generator geometry. However, as discussed in the next section, this is not the case for the full-scale PWR geometry based upon the experimental results from full-scale (geometric) tests.

17-4-2-2 Large-Scale Tests

There have been few large- or full-scale experiments for studying countercurrent flow and flooding in hot leg-to-steam generator geometries. While the experimental facility used by Richter was of a larger scale than the numerous small-scale experimental facilities, the UPTF is the only full-scale (geometric) experiment to study the countercurrent flow and flooding prototypic of the hot leg-to-steam generator geometry. The results of the full-scale UPTF test run 37, which is prototypical of PWR steam and liquid flowrates during reflux condensation during a small break LOCA, indicate that CCFL does not occur in the hot leg-to-steam generator flow path. All the water injected in the steam generator drained back into the hot leg unimpeded by the steam injected via the hot leg. Test run 38 of UPTF, which has twice the steam flowrate and three times the liquid injection rate as test run 37, also shows virtually no impedence of water drainback either because 98 percent of the water injected in the steam generator during this test run drains into the hot leg. It takes test run 39, which has nearly three times the steam and three times the liquid injection rate as test run 37, to approach the flooding limit (84 percent of the water drains into the hot leg).

Analysis performed by Wang and Mayinger (Wang and Mayinger, 1995) for UPTF test results also supports that no CCFL occurs during reflux conditions in the PWR, as margin to the flooding limit is shown when data from test runs 37 and 38 are plotted against the Richter flooding correlation for the hot leg-to-steam generator geometry. Work by de Bertodano (de Bertodano, 1994), in which a flooding correlation was developed from scaled test data, further supports that flooding is precluded in the hot leg-to-steam generator flow path for a less than 4-percent decay heat power condition in a four-loop PWR.

17-4-3 Conclusion

Based upon the full-scale UPTF test results, CCFL is not expected to occur in the hot leg-to-steam generator geometry during the reflux condensation phase of a small break LOCA, when it might possibly be important. Therefore, no special flooding models (beyond those discussed in this section for horizontal and vertical piping flooding) are needed to handle the hot leg-to-steam generator geometry in WCOBRA/TRAC-SB.

17-5 WCOBRA/TRAC-SB Modelling of Wall Condensation

The WCOBRA/TRAC-SB code calculates wall condensation heat transfer, based on the void fraction of the fluid cell in contact with the wall, as discussed in Section 4 of this document. The correlation of Shah (Shah, 1979) is applied at void fractions [ ]^{a,c}. For void fractions [ ]^{a,c}, the heat transfer coefficient computed using Shah is ramped into the heat transfer coefficient from the EPRI correlation (EPRI, 1988). At void fractions exceeding [ ]^{a,c}.

17-6 Steam Generator Tube Condensation

During a smaller size small break LOCA event, the RCS primary depressurizes to an equilibrium pressure slightly above the steam generator secondary side pressure. The primary RCS pressure equilibrates for a time at the pressure at which the primary fluid volume swells due to decay heat and pumped safety injection equals the primary fluid volume shrinkage due to mass lost through the break and through primary to secondary heat transfer. Initially, a small cold leg break is incapable of compensating for the safety injection and decay heat induced fluid volume swell. Primary to secondary heat transfer results and the steam generator secondary side conditions determine the equilibration pressure. Three modes of primary to secondary heat transfer that occur depending on the primary fluid conditions are as follows:

- Subcooled convection heat transfer, which could be forced convection heat transfer or natural circulation convection heat transfer

- Two-phase condensation heat transfer

- Steam condensation heat transfer

Condensation will occur at the steam generator tube walls when the tube walls are at a lower temperature than the primary side vapor. Condensation heat transfer as calculated by WCOBRA/TRAC-SB during two-phase flow conditions has been validated by simulation of the Semiscale Mod-2A NC tests, as discussed in Section 17-7.

The Semiscale NC 60-kW power test is a suitable experiment to simulate to validate the performance of the WCOBRA/TRAC-SB computer code in predicting condensation in the steam generator tubes over the void fraction range for small break LOCA conditions. In the high void fraction range, the EPRI correlation (EPRI, 1988) for cocurrent/countercurrent flow film condensation heat transfer is used as described in Section 6, Volume 1, of this document. At low void fractions, the Shah correlation (Shah, 1979) two-phase multiplier to liquid heat transfer coefficients is used. The mass inventory of the primary is continuously reduced during the Semiscale NC tests; therefore, the effect of steam generator tube condensation is observed over a wide range of fluid qualities. In the latter stages of the NC test simulation, a high void fraction (α>0.980) condition exists in the steam generator tube primary fluid. This provides the opportunity to assess the performance of WCOBRA/TRAC-SB in predicting condensation heat transfer coefficients in the high void fraction range. The WCOBRA/TRAC-SB predicted heat transfer coefficients for the high void fraction condition at the top of the SG tubes are found to be in the range of 2500 to 25,000 Btu/hr/ft^2, which is in agreement with the values predicted by the Nusselt film condensation theory.

17-7 Simulation of Semiscale Mod-2A NC Test Series Experiments

17-7-1 Introduction

The Semiscale facility is a small scale (1:1700) replica of a Westinghouse RCS including all of the major components. Figure 17-22 shows the layout of the major components, as configured for the NC tests. Although there are two loops in the facility, the one scaled as a single loop was blocked during these tests; the reactor vessel upper head was also blocked. The Mod-2A facility modifications focused on small break LOCA phenomena, and extensive instrumentation was installed to measure key phenomena. The Semiscale reactor vessel houses an electrically heated bundle consisting of 25 heater rods; the tests simulated herein are at a power of 60 kW. The overall scaling philosophy used in designing the facility is the maintenance of the power-to-volume ratio, coupled with a 1:1 elevation scaling criteria (Larson, et al., 1980 and Loomis, 1987).

17-7-1-1 Natural Circulation Phenomena

The Semiscale NC test series experiments provided information concerning the overall flow and the qualitative interaction of phenomena that occur throughout the various stages of a small break LOCA in a simulated integral RCS. The NC test series consisted of three individual (30-kW, 60-kW, and 100-kW core power) experiments with multiple points each. In all, approximately

15 discrete data points were available at given primary system inventories that were established for a fixed core power and secondary mass by draining fluid from the reactor vessel lower plenum. Each discrete inventory was maintained until steady-state (or nearly steady-state) conditions were established. The NC tests were tabulated by Loomis and Soda (Loomis and Soda, 1982), and they provide valuable data for validating the predictive capability of WCOBRA/TRAC-SB for the single-phase, two-phase, and reflux condensation natural circulation modes.

One important phenomenon that influences the severity of small break LOCA transients is steam generator tube liquid holdup. This holdup phenomenon was first identified experimentally in a Semiscale small break LOCA experiment (Leonard, 1982). It has since been duplicated in other facilities such as ROSA (Osakabe, et al., 1987) and has been discussed extensively in the open literature (Leonard, 1983 and Loomis, 1985a). Steam generator liquid holdup is the result of condensation due to natural circulation flow in the upflow side of the tubes relatively early during a small break LOCA transient. This holdup is unable to gravity-drain back through the hot leg because it is impeded by high upward steam flowrates; the pressure drop induced by this holdup affects the hydrostatic head balances throughout the RCS. Therefore, the liquid present in the steam generator tubes as a function of total system inventory is an important phenomenon in small break LOCA performance.

17-7-1-2 Applicable Tests

Information from the 60-kW core power test conducted in the NC test series at the Semiscale Mod-2A configuration is available in the literature (Loomis, 1985b and Loomis, 1987). Among the NC experiments, the 60-kW experiment is chosen for simulation because its core power, corresponding to 3-percent full power, is closest to the decay power during the natural circulation period for a PWR 3-inch break event. A series of individual test points was generated at various inventories while heat generated in the core was being removed by heat transfer to the steam generator secondary side. Temperatures and pressures are typical of PWR conditions during small break LOCA events.

17-7-2 Description of WCOBRA/TRAC-SB Model

The WCOBRA/TRAC-SB model used to simulate the Semiscale NC tests is described in detail in Section 21 of this document. The same nodalization was used in the NC test prediction with these exceptions: [

]^{a,c}

17-7-3 Simulation Results

A series of inventory points in the 60-kW NC test (at mass inventories decreasing from 100 percent of nominal until the reflux condensation heat transfer mode was established) were simulated with WCOBRA/TRAC-SB. The results are presented in several ways.

Figure 17-23 shows the system inventory percentage as a function of time to which the WCOBRA/TRAC-SB simulation was set. During the first 50 seconds of each time interval, the inventory was reset downward using a boundary condition. The code was run long enough at each inventory to reach a steady-state prediction of loop flow at that inventory condition. Figure 17-24 shows the natural circulation mass flow rate predicted as a function of system inventory by WCOBRA/TRAC-SB compared with the data as reported by the experimenters (Loomis and Soda, 1982). The code prediction of peak flowrate agrees well with the data. However, drain of the steam generator tubes occurs earlier in the prediction than in the test.

Figures 17-25 and 17-26 show the void fraction in the uppermost nodes of the steam generator tube uphill and downhill, respectively. The draining predicted by WCOBRA/TRAC-SB as mass inventory decreases takes place when the void fraction exceeds 0.5 in these nodes. At this point, [

]^{a,c}. Figures 17-27 and 17-28 present condensation rate as a function of time in the upper nodes of the steam generator tube uphill and downhill sides. Condensation is almost constant at inventory levels approaching the draining; therefore, draining is not triggered by a lack of condensation. This is true even though the condensation is underpredicted by WCOBRA/TRAC-SB; not quite all of the steam entering the steam generator is predicted to condense in the code, as it did in the experiment.

Because the draining predicted by WCOBRA/TRAC-SB is a function of void fraction in the steam generator tubes, [

]^{a,c}

[

]^{a,c}.

Overall, the qualitative prediction of WCOBRA/TRAC-SB shows fair agreement with the Semiscale Mod-2A NC test data. The peak flowrate is matched closely, and the characteristic shape is predicted by the code. The data are similar to that observed in comparable experimental facilities. Figure 17-29 compares the 30-kW Semiscale natural circulation result with that obtained in the PKL facility at a similar power level. The PKL facility (Hein, et al., 1980) is similar to the Semiscale facility except the scaling factor is approximately 134:1 compared with the Semiscale scaling factor of 1705.5:1.

As reported in Loomis and Soda (Loomis and Soda, 1982), PKL conducted natural circulation experiments similar to those in Semiscale, but at lower pressure (approximately 3 to 4 MPa versus 6.9 MPa). The results of the experiments were similar. Figure 17-29 compares the loop mass flowrate versus primary system mass inventory for the two systems, indicating similar trends. (The PKL mass flowrate shown was reduced by the ratio of the volume scaling factors used for each facility, and both experiments represent core decay powers of approximately 1.5 percent.) Not only is the overall trend between the two experiments similar, but also the peak two-phase mass flowrate agrees well quantitatively. Furthermore, Loomis and Soda state that the fact that PKL entered the reflux mode at about 80-percent system mass inventory and Semiscale, at about 70-percent inventory constitutes only a slight difference (the uncertainty is +5 percent). The variance between the WCOBRA/TRAC-SB prediction and the Semiscale Mod-2A data for natural circulation and for the time at which the reflux mode begins is similar to that observed between the two comparable test facilities and is characterized as slight by the Semiscale experimenters. Therefore, the WCOBRA/TRAC-SB prediction is judged to be acceptably accurate for small break LOCA analysis.

17-7-4 Conclusions

The following conclusions about WCOBRA/TRAC-SB are drawn from the Semiscale NC tests simulations:

- The peak natural circulation flowrate is well predicted.

- Draining is a function of the void fraction predicted in the steam generator tubes.

- The difference between the code prediction and the Semiscale data is similar to the difference observed between the Semiscale and PKL data.

Therefore, the two-phase natural circulation and steam generator drain phenomena are adequately predicted.

17-8 References

Bajorek, S. M., et al., 1992, "Code Qualification Document for Best Estimate LOCA Analysis Volume I: Models and Correlations," WCAP-12945-P, Vol. 1.

Choi, K. and No, H., 1995, "Experimental Studies of Flooding In Nearly Horizontal Pipes," Int. Journal of Multiphase Flow, Vol. 21, pp. 419-436.

de Bertodano, M., 1994, "Countercurrent Gas-Liquid Flow in a Pressurized Water Reactor Hot Leg," Nuclear Science and Engineering, Vol. 117, pp. 126-133.

Dukler, A. E. and Smith, L., 1979, "Two-Phase Interactions in Countercurrent Flow: Studies of the Flooding Mechanism," NUREG/CR-0617.

EPRI Report NP-5700, 1988, "Condensation Inside Tubes," Research Project 1160-3 Final Report.

Ghiaasiaan, S., et al., 1994, "Countercurrent Flow Limitation in Inclined Channels with Bends," Nuclear Engineering and Design, Vol. 152, pp. 379-388.

Hein, D., et al., 1980, "PKL Experiment Data Report," Report Number R 513/58/80, KWV.

Hewitt, G. F., 1977, "Influence of End Conditions, Tube Inclination and Fluid Physical Properties on Flooding in Gas-Liquid Flows," HTFS-RS222, Heat Transfer and Fluid Flow Service.

Hsieh, C., et al., 1980, "Countercurrent Air/Water and Steam/Water Flow Above a Perforated Plate," NUREG/CR-1808.

Kawaji, M., et al., 1991, "Countercurrent Flooding in Vertical to Inclined Pipes," Exp. Heat Transfer 4, pp. 95-110.

Krowlewski, S., 1980, "Flooding Limits in a Simulated Nuclear Hot-Leg," B.Sc. Thesis, MIT.

Larson, T. K., et al., 1980, "Scaling Criteria and an Assessment of Semiscale Mod-3 Scaling for Small Break Loss Of Coolant Transients," EGG-SEMI-5121.

Lee, S. C. and Bankoff, S. G., 1982, "Stability of Steam-Water Countercurrent Flow In An Inclined Channel," ASME Paper No. 82-WA/HT-6.

Leonard, M. T., 1982, "Vessel Coolant Mass Depletion During a Small Break LOCA," EGG-SEMI-6010.

Leonard, M. T., 1983, "An Analytical Study of a Small Break Loss-Of-Coolant Accident with Upper Head Injection," Nuclear Technology, Vol. 62.

Long, R. R., 1956, "Solitary Wave in the One- and Two-Fluid Systems," Tellus, Vol. 8.

Loomis, G. G. and Soda, K., 1982, "Results of the Semiscale Mod-2A Natural Circulation Experiments," NUREG/CR-2335 (EGG-2200).

Loomis, G. G., 1985a, "Semiscale Liquid Holdup Investigations: A Comparison of Small Break LOCA Tests Performed in the Semiscale Mod-2A and Mod-2C Facilities," 13th Annual Water Reactor Safety Research Information Meeting, Gaithersburg, MD.

Loomis, G. G., 1985b, "Summary of Semiscale Small Break Loss-of-Coolant Accident Experiments (1979 to 1985)," NUREG/CR-4393 (EGG-2419).

Loomis, G. G., 1987, "Summary of the Semiscale Program (1965-1986)," NUREG/CR-4945 (EGG-2509).

Ohnuki, A., 1986, "Experimental Study of Counter-Current Two-Phase Flow in Horizontal Tube Connected to Inclined Riser," Journal of Nuclear Science and Technology, Vol. 23, pp. 219-232.

Ohnuki, A., et al., 1988, "Scale Effects on Countercurrent Gas-liquid Flow in a Horizontal Tube Connected to an Inclined Riser," Nuclear Engineering and Design, Vol. 107, pp. 283-294.

Osakabe, M., et al., 1987, "Core Liquid Level Depression due to Manometric Effect during PWR Small Break LOCA," J. of Nuclear Science and Technology 24(2), pp. 103-110.

Richter, H., et al., 1978, "De-entrainment and Countercurrent Air-Water Flow in a Model PWR Hot-leg," USNRC Report NRC-0193-9.

Shah, M. M., 1979, "A General Correlation for Heat Transfer During Film Condensation Inside Pipes," Int. J. Heat and Mass Transfer, V22 N4.

Shames, I. H., 1982, "Mechanics of Fluids," McGraw-Hill, New York, N. Y.

Siddiqui, H., et al., 1986, "Flooding in an Elbow Between a Vertical and a Horizontal or Near-horizontal Pipe," Int. Journal of Multiphase Flow, Vol. 12, pp. 531-541.

Taitel, Y. and Dukler, A. E., 1976, "A Model for Predicting Flow Regime Transitions in Horizontal and Near Horizontal Gas-Liquid Flow," AIChE Journal, 22.

Takeuchi, K. and Young, M.Y., 1983, "Generalized Drift Flux Correlation for Steam Generators," First Proceedings of Nuclear Thermal Hydraulics, American Nuclear Society, p. 102.

Takeuchi, K., et al., 1992, "Generalized Drift Flux Correlation for Vertical Flow," Nuclear Science & Engineering, 112, 170.

Tien, C. L. and Liu, C. P., 1979, "Survey on Vertical Two-Phase Countercurrent Flooding," EPRI NP-984.

Wallis, G. B., 1969, One Dimensional Two Phase Flow, McGraw-Hill.

Wallis, G. B. and Dobson, J. E., 1973, "The Onset of Slugging in Horizontal Stratified Air-Water Flow," Int. J. Multiphase Flow, Vol. 1.

Wan, P., 1986, "Countercurrent Steam-Water Flow in an Upright 90° Elbow," Proc. 8th International Heat Transfer Conference, pp. 2313-2318.

Wang, M. and Mayinger, F., 1995, "Simulation and Analysis of Thermal-Hydraulic Phenomena in a PWR Hot Leg Related to SBLOCA," Nuclear Engineering and Design, Vol. 155, pp. 643-652.

Wongwises, S., 1996, "Two-Phase Countercurrent Flow in a Model of a Pressurized Water Reactor Hot Leg," Nuclear Engineering and Design, Vol. 166, pp. 121-133.

Zuber, N., 1980, "Problems in Modelling of Small Break LOCA," NUREG-0724.

Table 17-1
Water Injection Rates

Case	Liquid Flow j_f (ft/s)	
	1000 (psia)	**35 (psia)**
1	0.0239	0.0238
2	0.0718	0.0713
3	0.1196	0.1188
4	0.1675	0.1664
5	0.2153	0.2139
6	0.248	-

Table 17-2
Steam Injection Rates

Time (sec)	1000 psia j_g(ft/s)	35 psia j_g(ft/s)
0-80	0.0	0.0
80-300	0-7.123	0-74.02

Table 17-3
Predicted Water Levels in WCOBRA/TRAC Horizontal Channel Compared With Weir Flow Theory

Channel		10	9	8	7	6	5
W_L=70 lb_m/sec		(j_l = 0.168 ft/s)					
α_L	Cell 2	0.0	0.0	0.0	0.0	0.0	0.0
	Cell 1	0.674	0.617	0.494	0.424	0.359	0.160
Water level (ft.)		0.674	0.617	0.494	0.424	0.359	0.160
						Weir flow level = 0.30 ft.	
W_L=170 lb_m/sec		(j_l = 0.408 ft/s)					
α_L	Cell 2	0.0	0.0	0.0	0.0	0.0	0.0
	Cell 1	0.993	0.923	0.988	0.876	0.763	0.321
Water level (ft.)		0.993	0.923	0.988	0.876	0.763	0.321
						Weir flow level = 0.54 ft.	
W_L=325 lb_m/sec		(j_l = 0.780 ft/s)					
α_L	Cell 2	0.030	0.104	0.030	0.0	0.0	0.0
	Cell 1	0.992	0.992	0.994	0.942	0.892	0.499
Water level (ft.)		1.022	1.096	1.024	0.942	0.892	0.499
						Weir flow level = 0.83 ft.	
W_L=650 lb_m/sec		(j_l = 1.559 ft/s)					
α_L	Cell 2	0.733	0.988	0.525	0.351	0.222	0.0
	Cell 1	0.992	0.999	0.989	0.991	0.980	0.581
Water level (ft.)		1.725	1.987	1.514	1.342	1.202	0.581
						Weir flow level = 1.32 ft.	
W_L=975 lb_m/sec		(j_l = 2.339 ft/s)					
α_L	Cell 3	0.134	0.016	0.040	0.023	0.0	0.0
	Cell 2	0.992	0.990	0.846	0.683	0.528	0.296
	Cell 1	0.995	1.0	0.993	0.992	0.998	0.746
Water level (ft.)		2.121	2.006	1.879	1.698	1.520	1.042
						Weir flow level = 1.72 ft.	

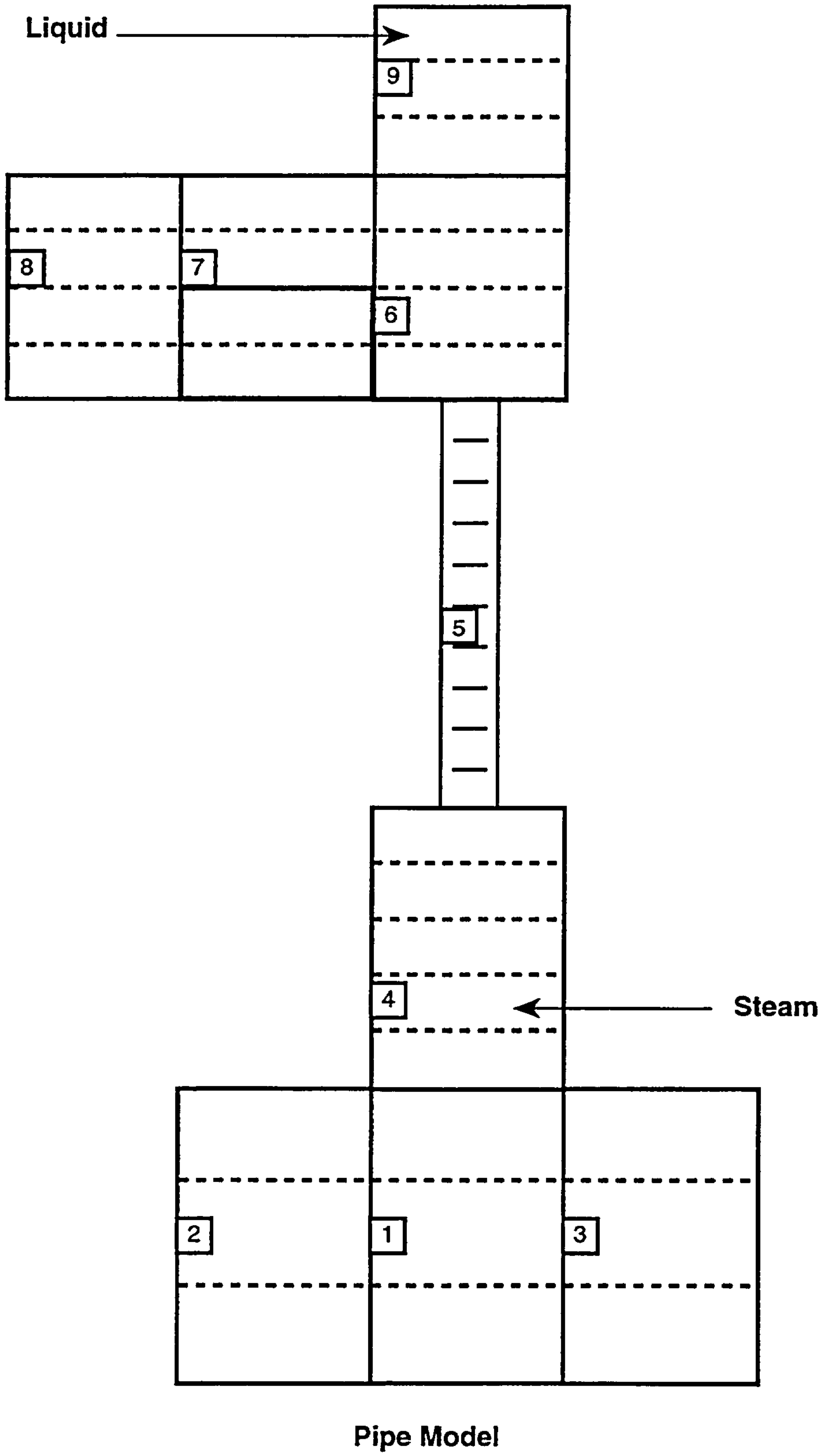

Figure 17-1. Flooding Model for a Vertical WCOBRA/TRAC Channel

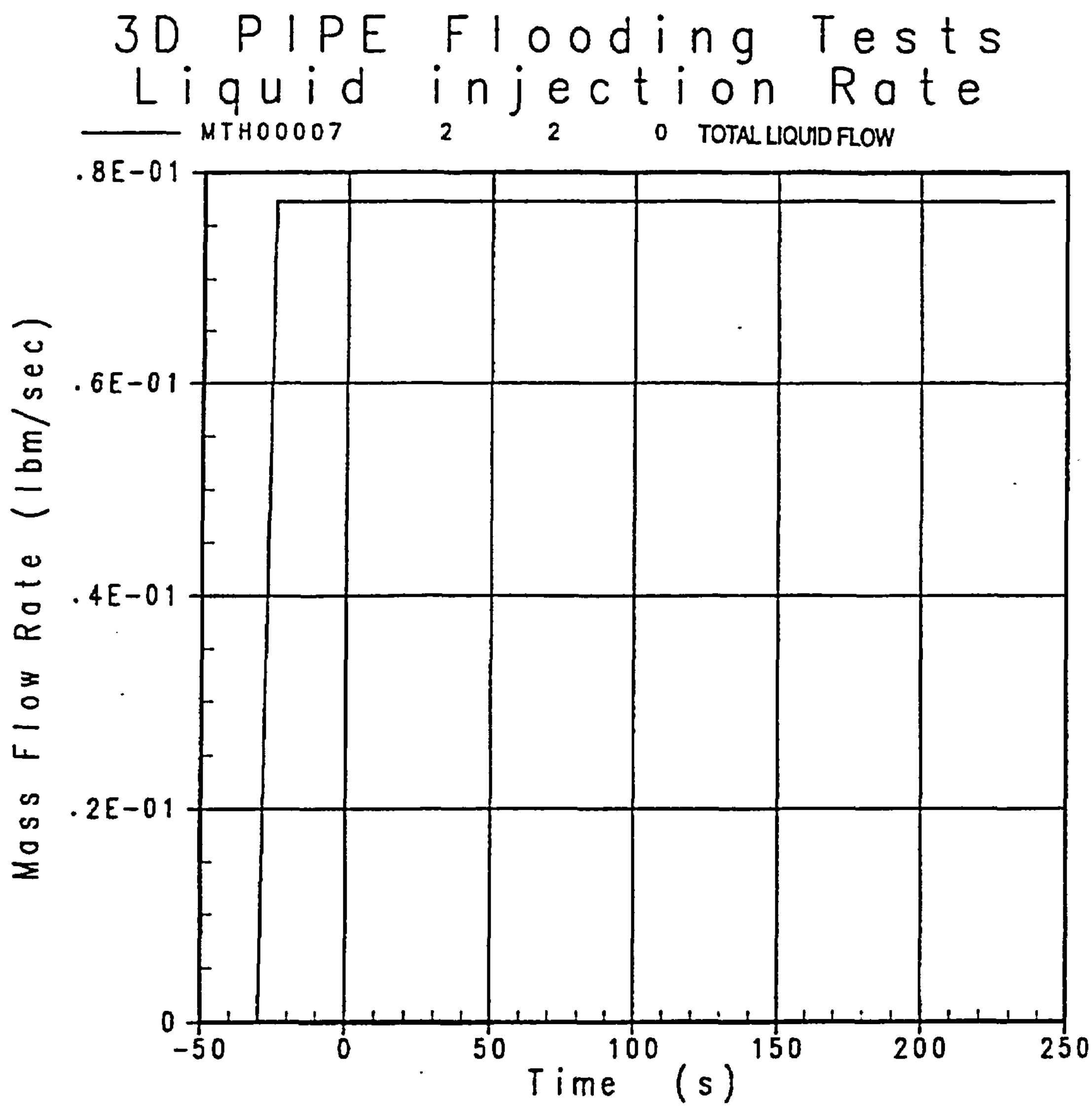

Figure 17-2. Liquid Injection Rate for Case 3 (1000 psi)

a,c

Figure 17-3. Vapor Mass Flowrate at Middle of Pipe for Case 3 (1000 psi)

a,c

Figure 17-4. Liquid Mass Flowrate at Middle of Pipe for Case 3 (1000 psi)

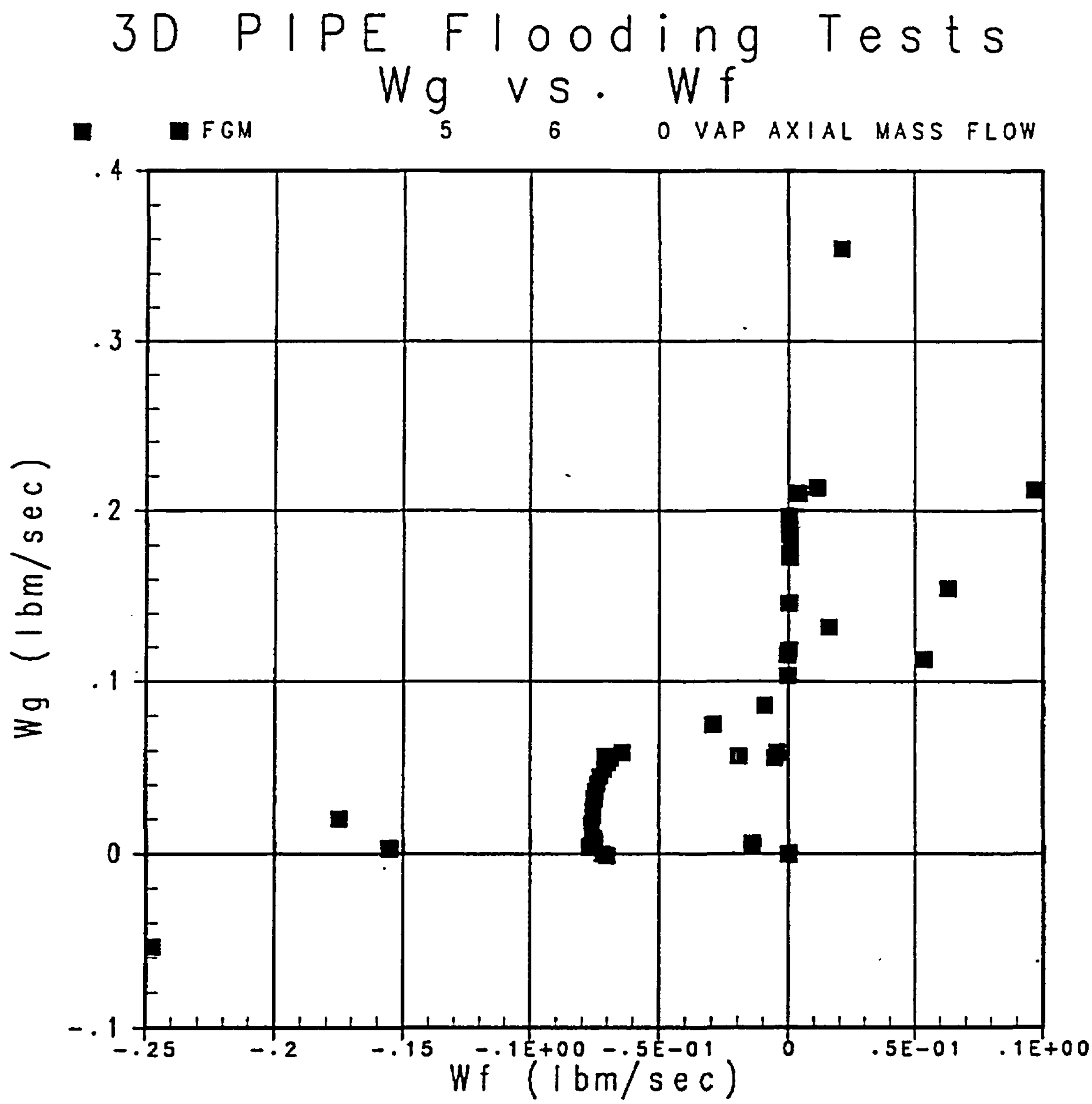

Figure 17-5. Vapor Flow (Wg) Versus Liquid Flow (Wf) for Case 3 (1000 psi)

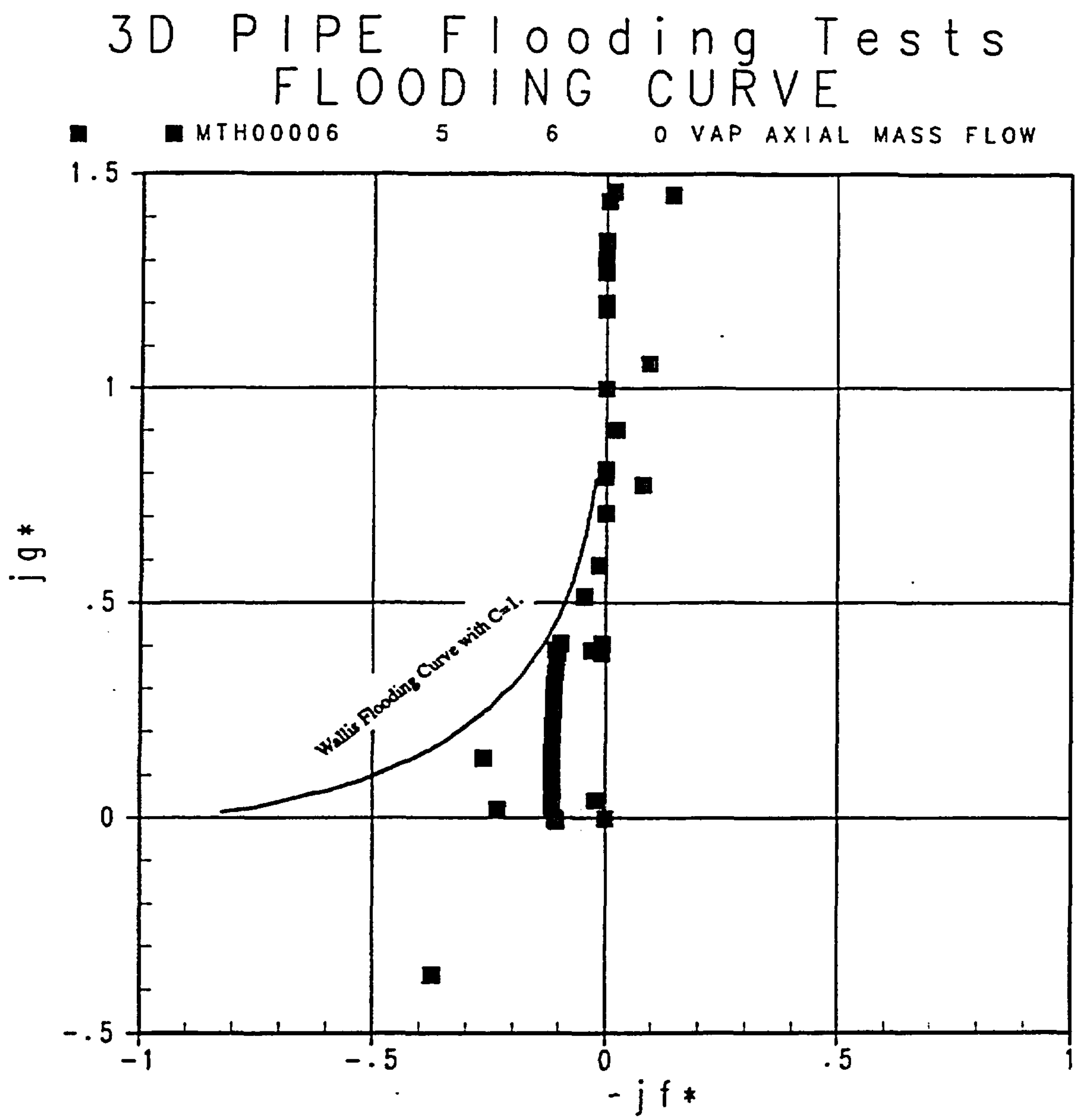

Figure 17-6. j_g^* Versus j_f^* for Case 3 (1000 psi)

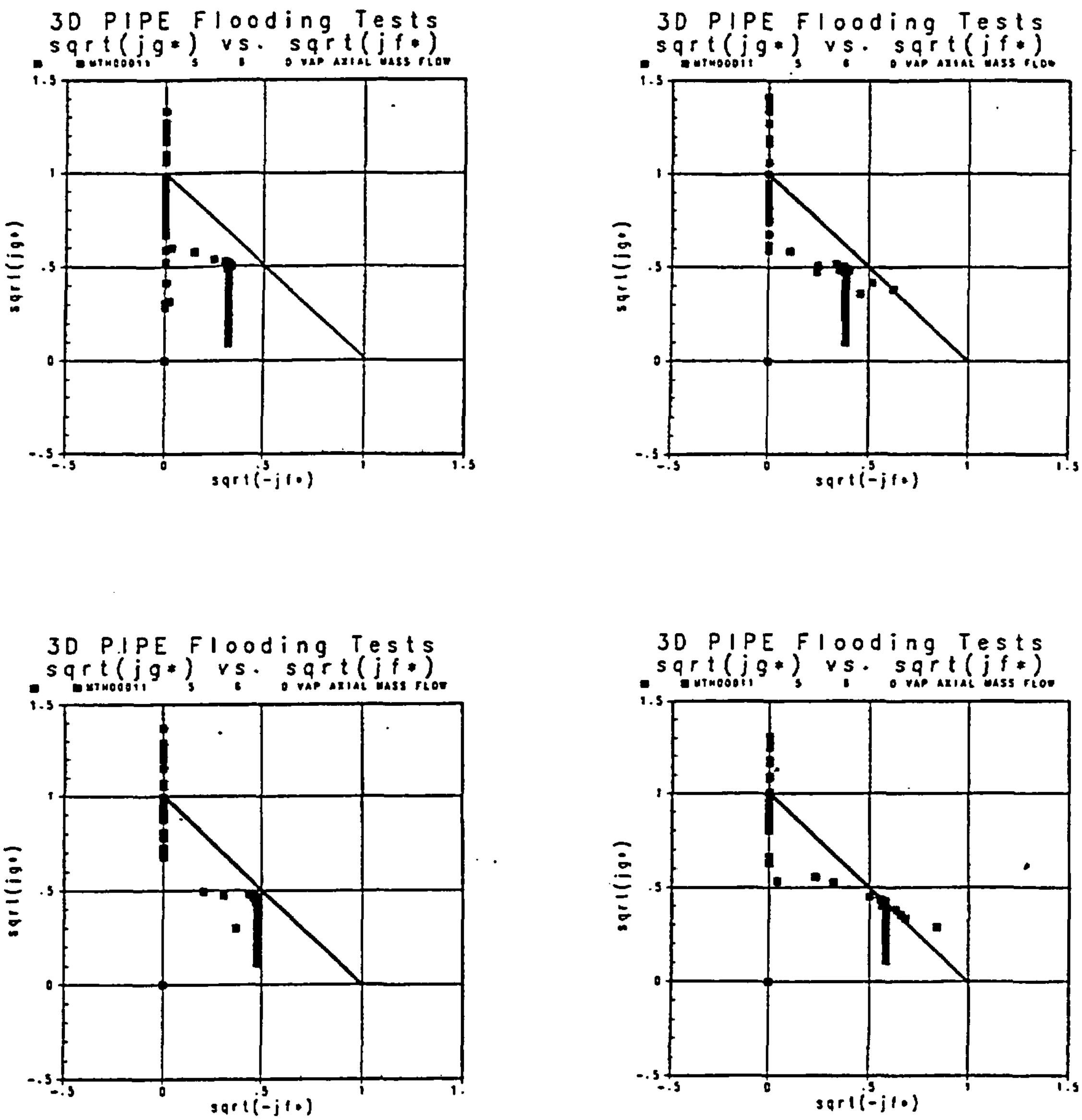

Figure 17-7a. Typical Flooding Results for Vertical Pipe (ID = 1.6 inches)

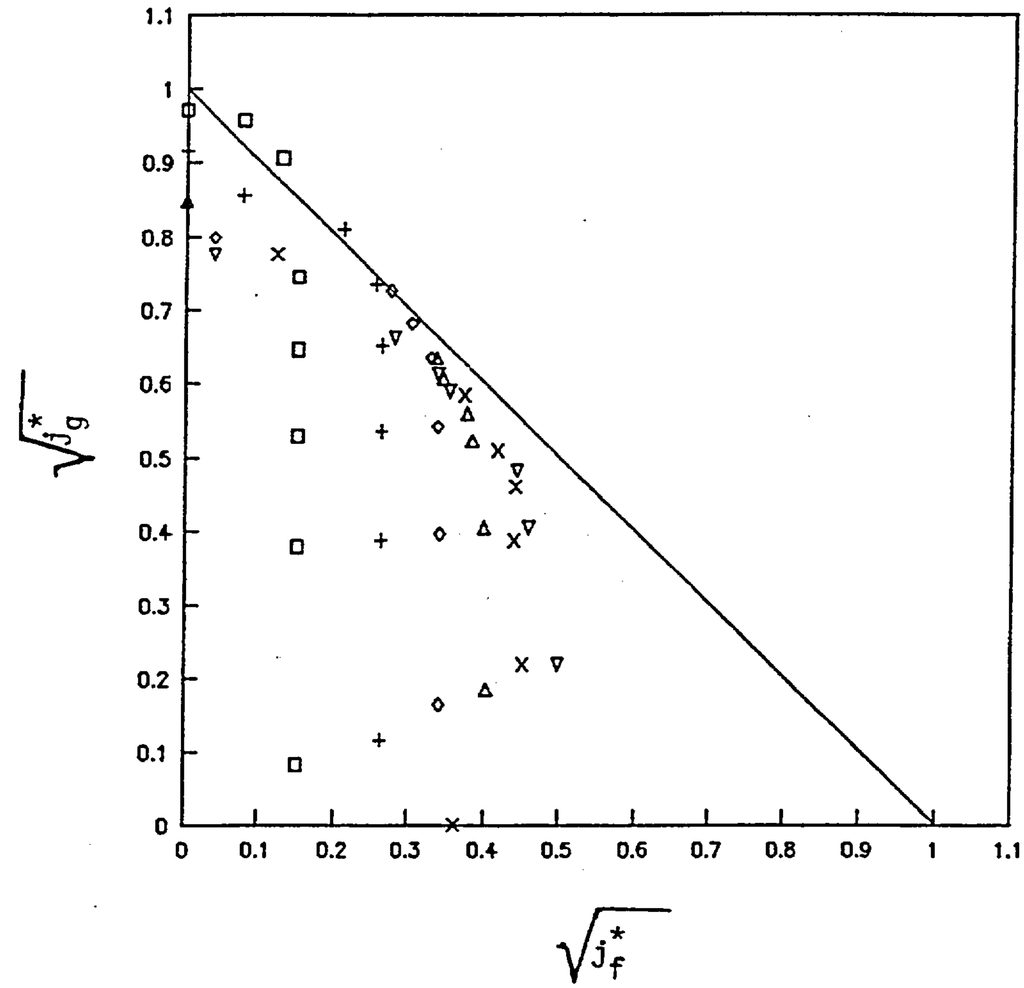

□	$j_{f,in} = 0.0239$	△	$j_{f,in} = 0.1675$
+	$j_{f,in} = 0.0718$	x	$j_{f,in} = 0.2153$
◇	$j_{f,in} = 0.1196$	▽	$j_{f,in} = 0.248$

Figure 17-7b. Countercurrent Flow Map Predicted by WCOBRA/TRAC

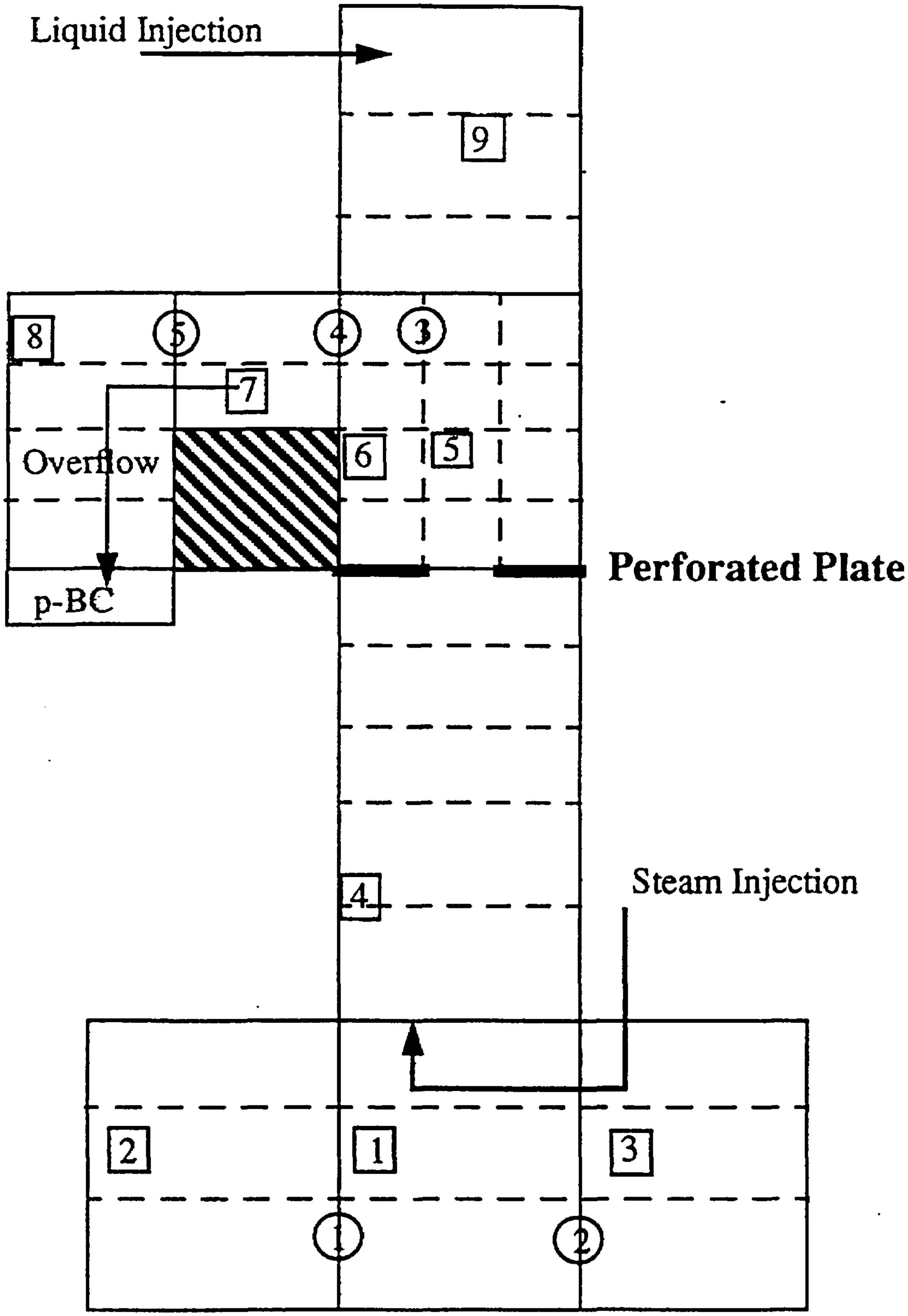

Figure 17-8. Flooding Model 1 for a Perforated Plate

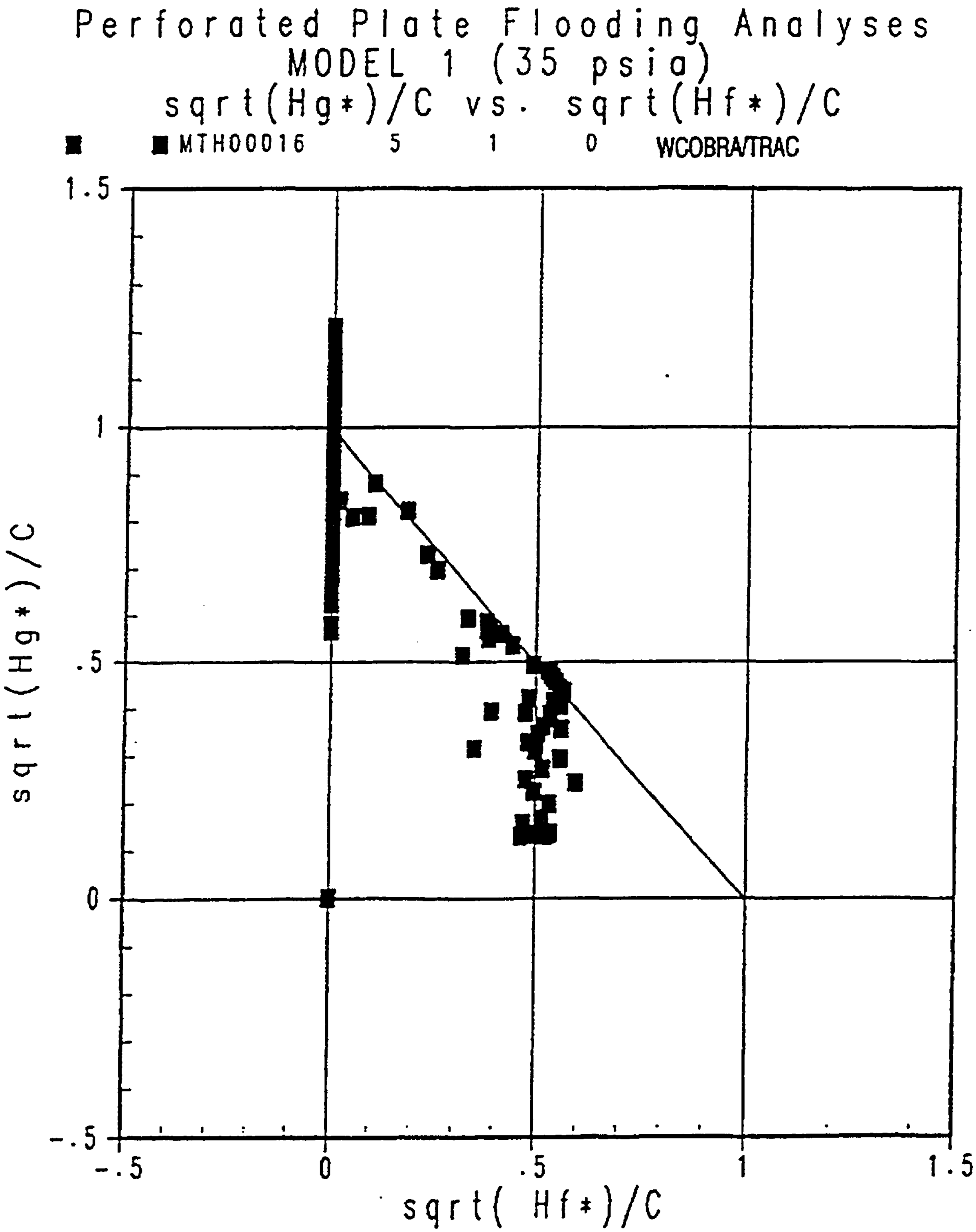

Figure 17-9. Flooding Velocities for Saturated Liquid and Vapor at 35 psia and j_f = 3.3 ft/s Compared With Northwestern Flooding Limit (WCOBRA/TRAC MOD7A)

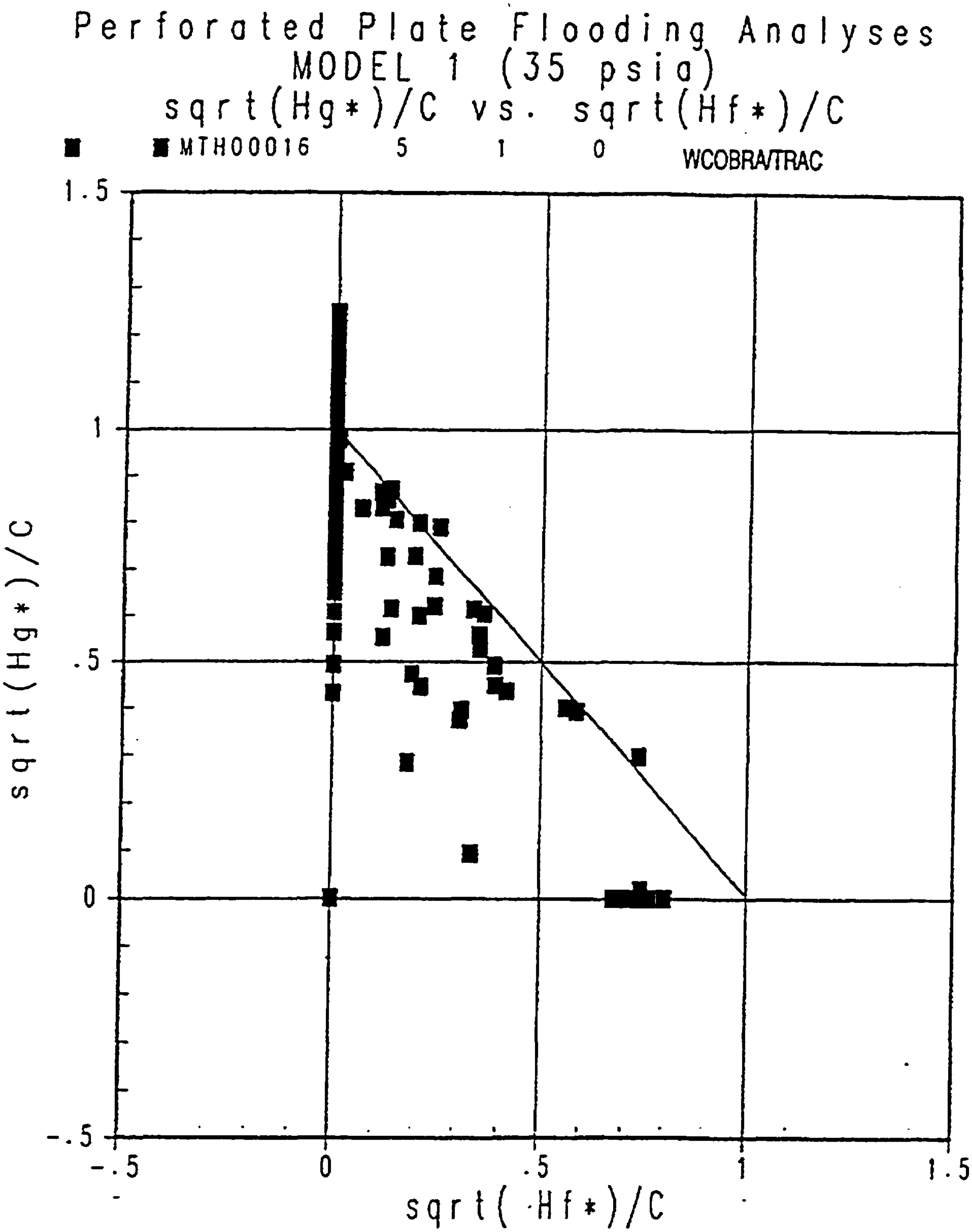

Figure 17-10. Flooding Velocities for Saturated Liquid and Vapor at 35 psia and j_f = 8.0 ft/s Compared With Northwestern Flooding Limit (WCOBRA/TRAC MOD7A)

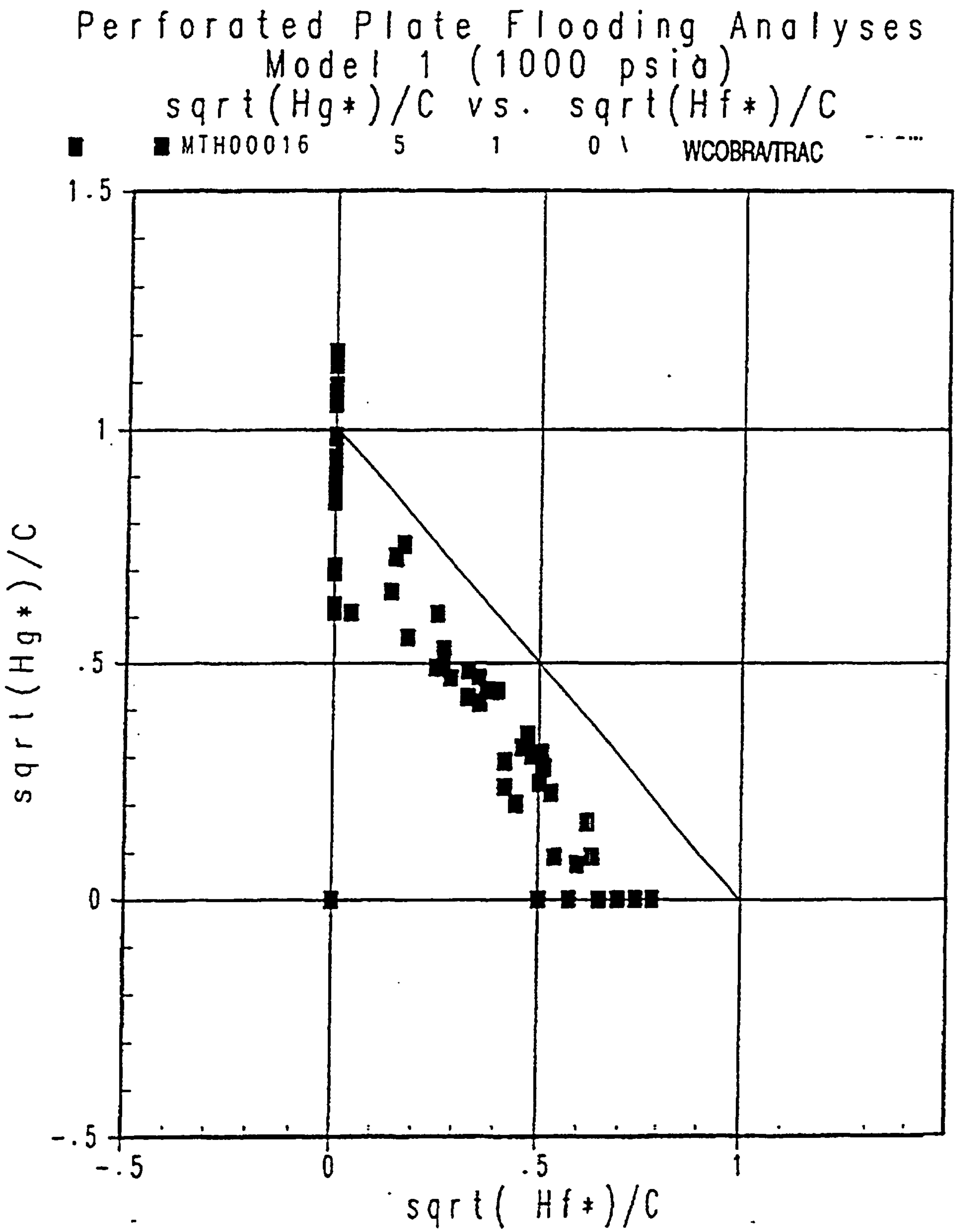

Figure 17-11. Flooding Velocities for Saturated Liquid and Vapor at 1000 psia and j_ℓ = 3.3 ft/s Compared With Northwestern Flooding Limit (WCOBRA/TRAC MOD7A)

a,c

Figure 17-12. Liquid Mass Flowrates Through Perforated Plate at 35 psia and $j_\ell = 8.0$ ft/s (WCOBRA/TRAC MOD7A)

a,c

Figure 17-13. Vapor Mass Flowrates Through Perforated Plate at 35 psia and $j_\ell = 8.0$ ft/s (WCOBRA/TRAC MOD7A)

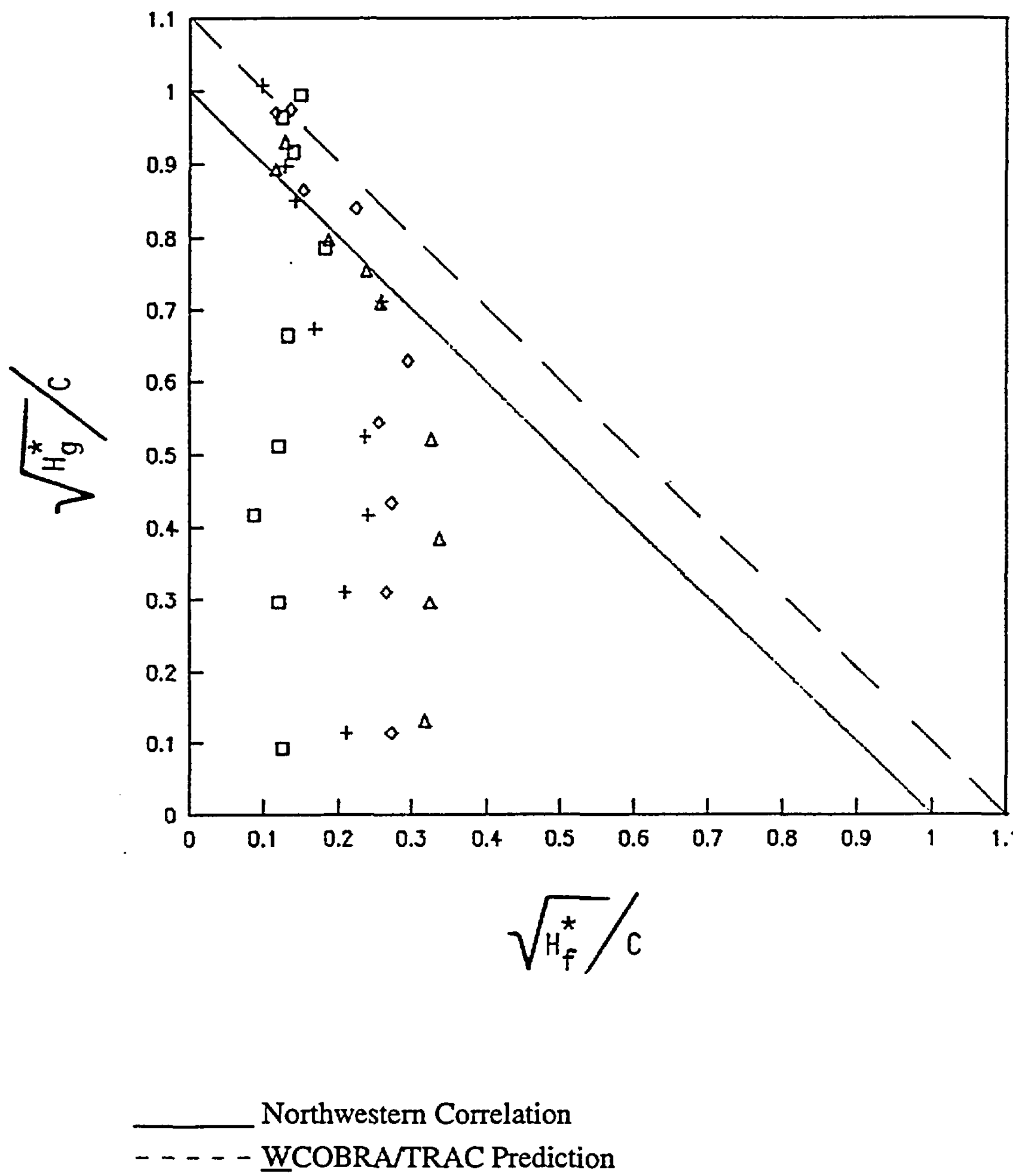

Figure 17-14. Predicted Flow Conditions and CCFL for Perforated Plate at High Pressure

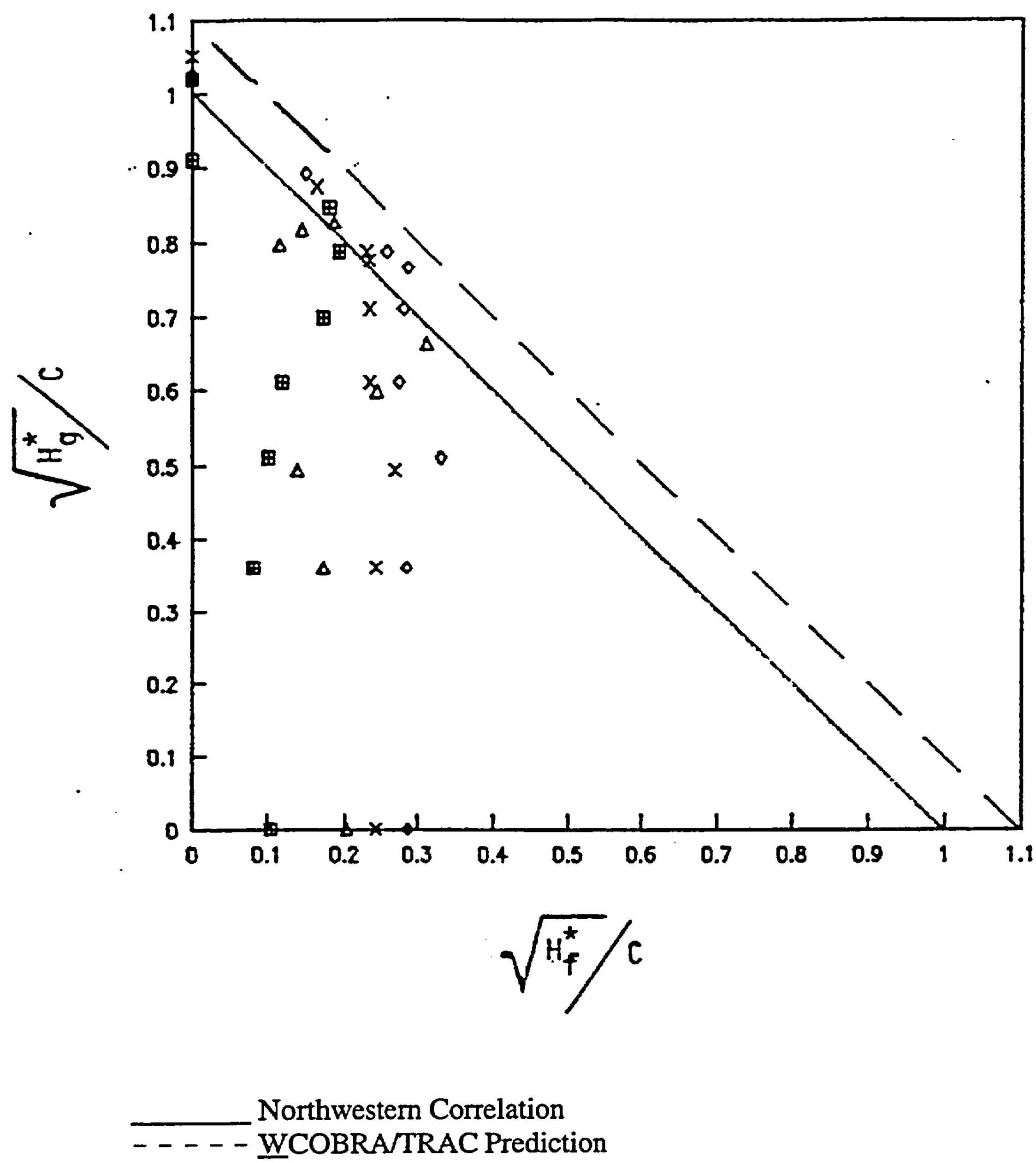

Figure 17-15. Predicted Flow Conditions and CCFL of a Perforated Plate at Low Pressure

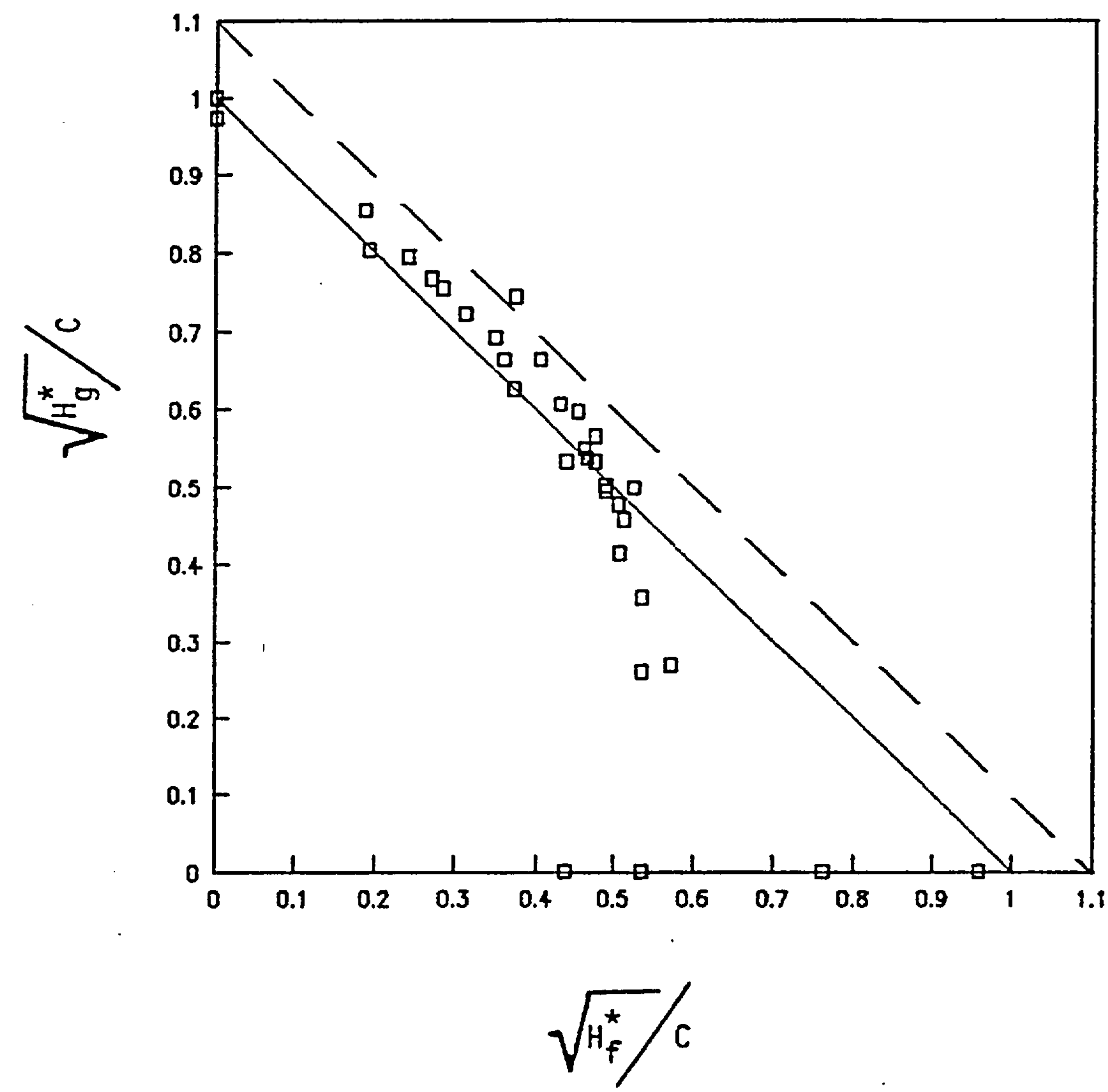

________ Northwestern Correlation
\- - - - - WCOBRA/TRAC Prediction

Figure 17-16. CCFL Data for Perforated Plate and Air/Water at Atmospheric Conditions (Hsieh, 1980)

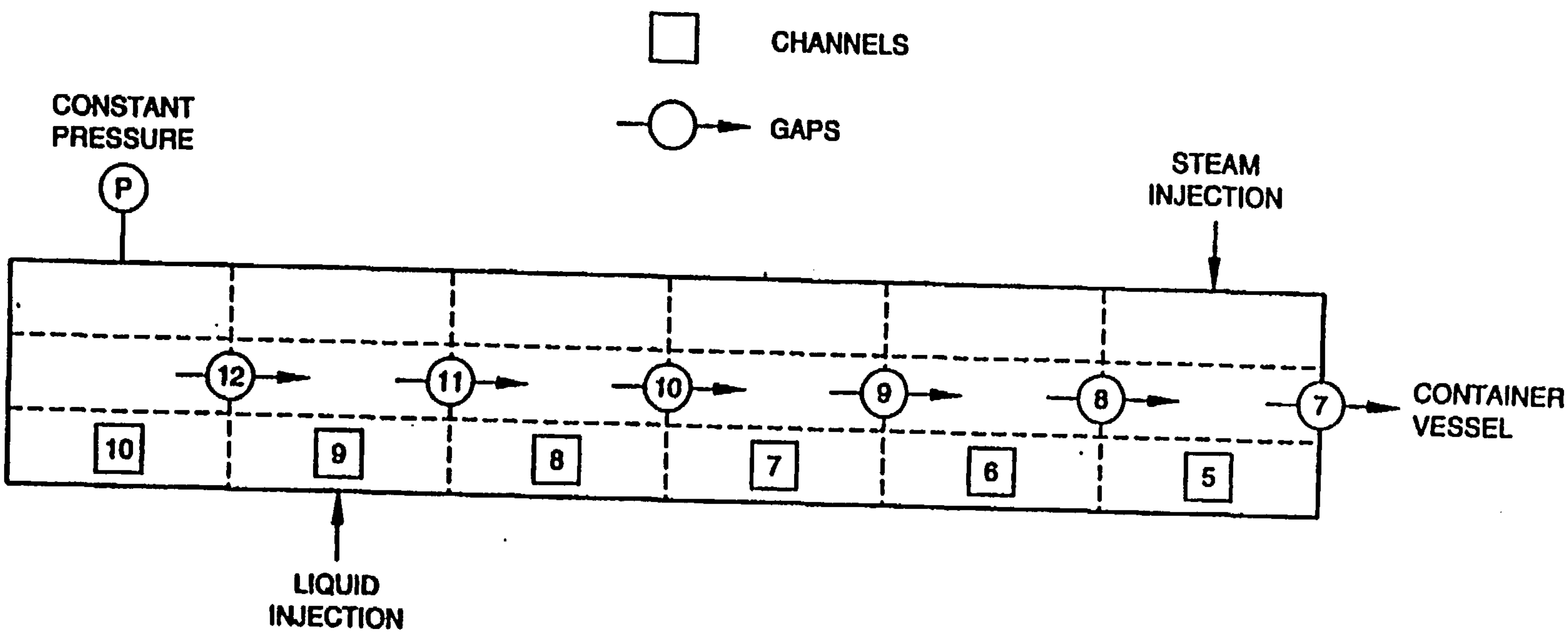

Figure 17-17. A 3-D Model for a Horizontal Pipe

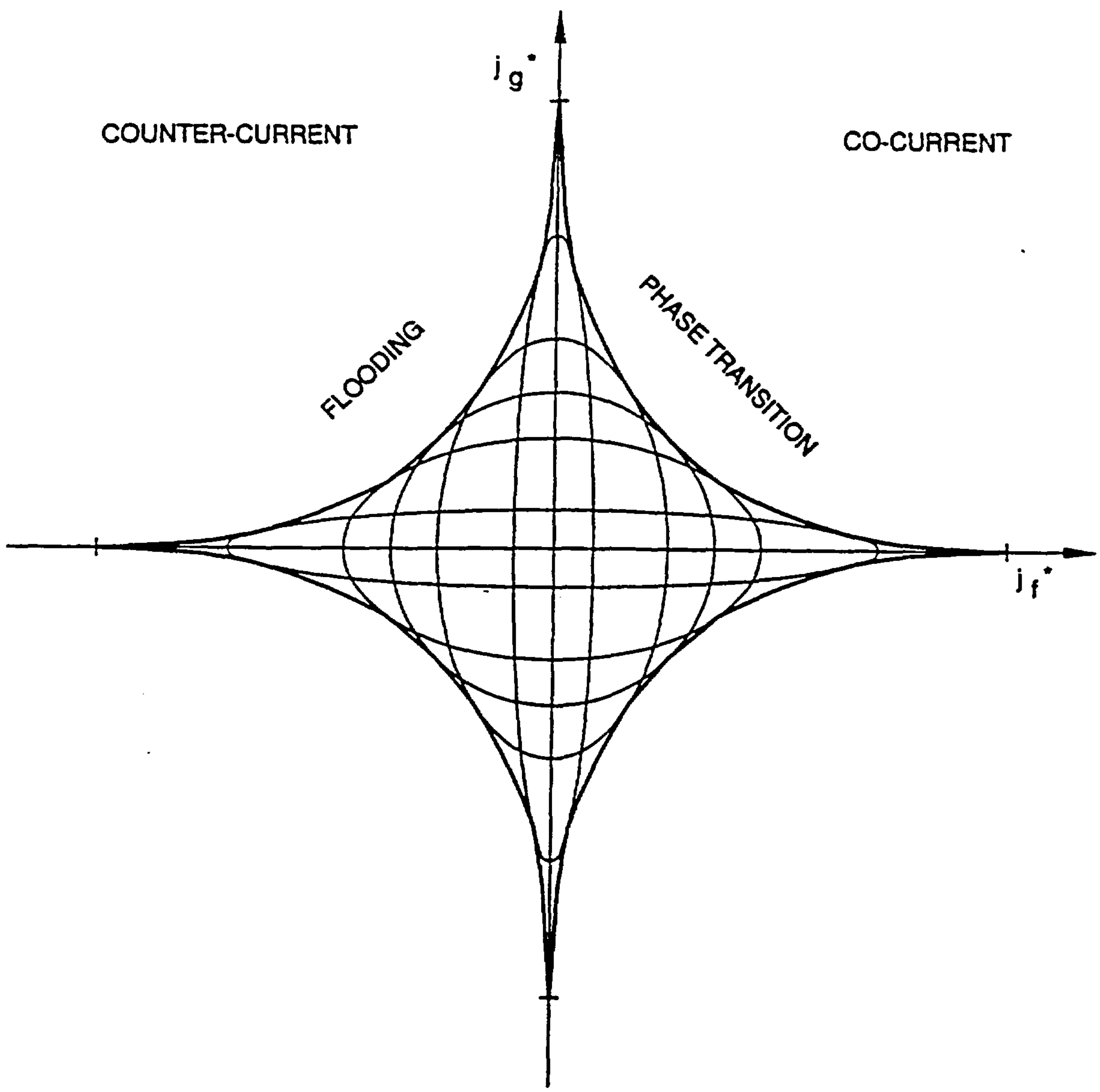

Figure 17-18. Drift Flux in a Horizontal Stratified Flow and Flooding Curves

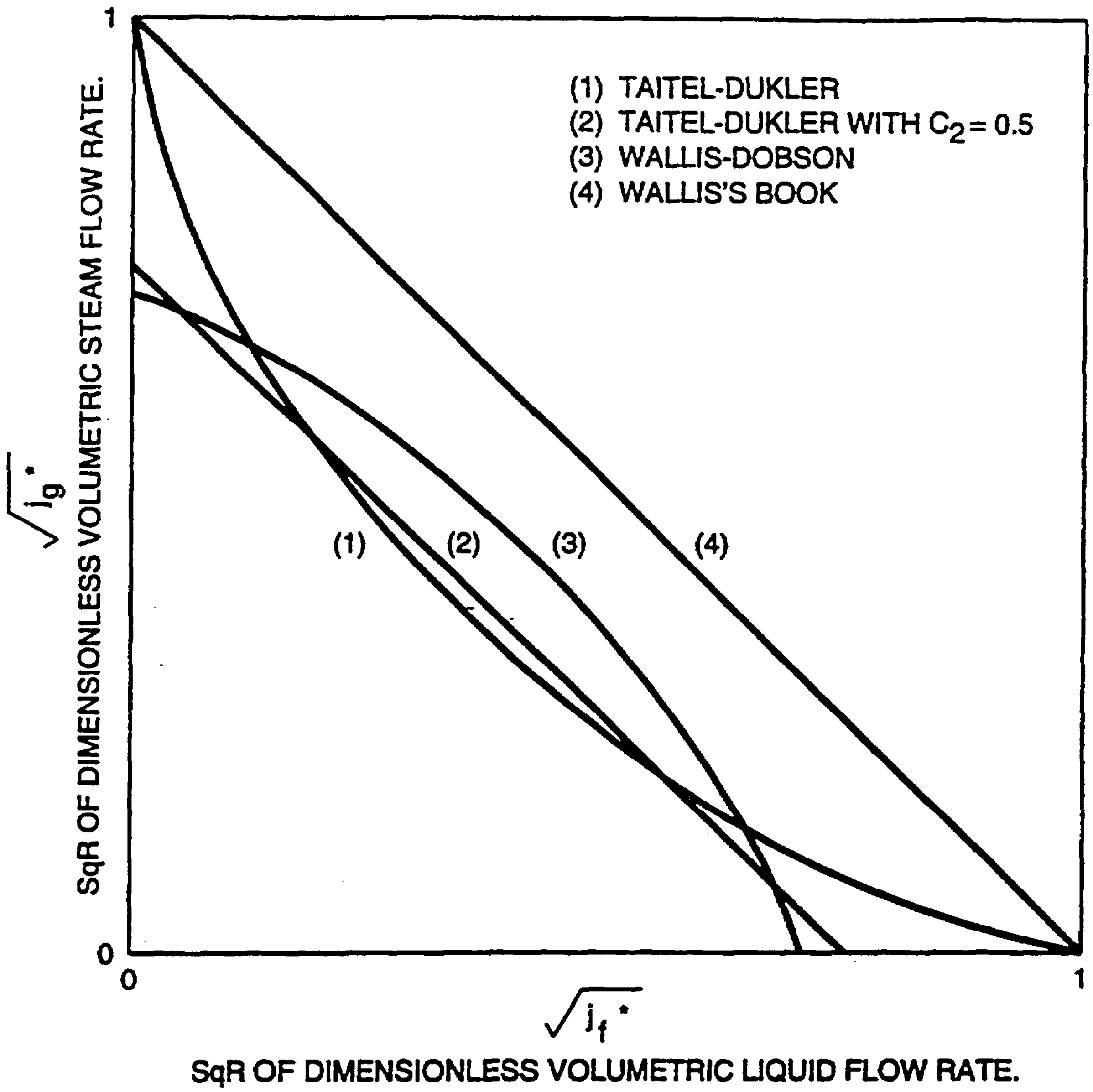

Figure 17-19. Flooding Curves for Horizontal Stratified Flow

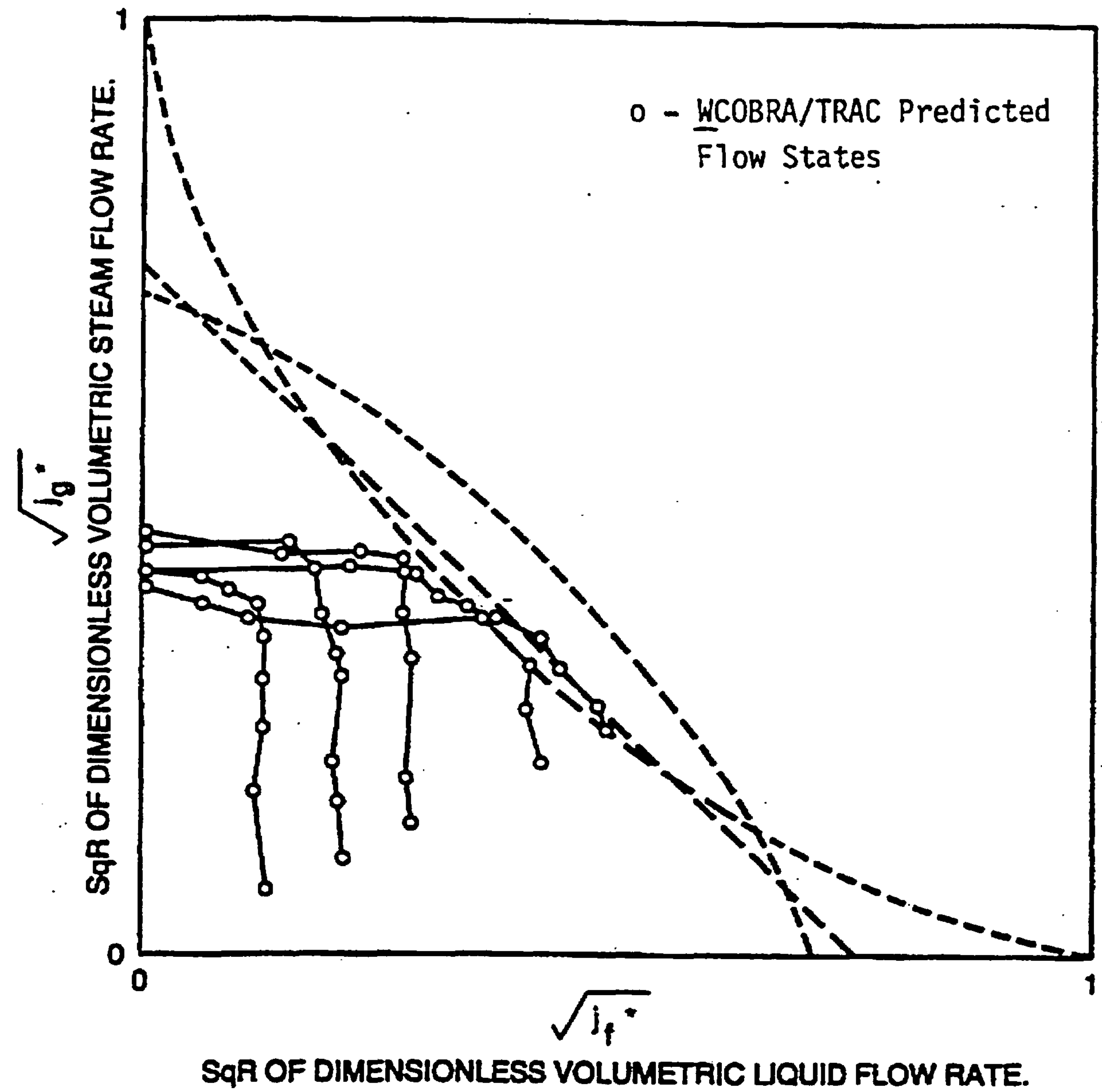

Figure 17-20. Computed Horizontal Flow State and Flooding Curves

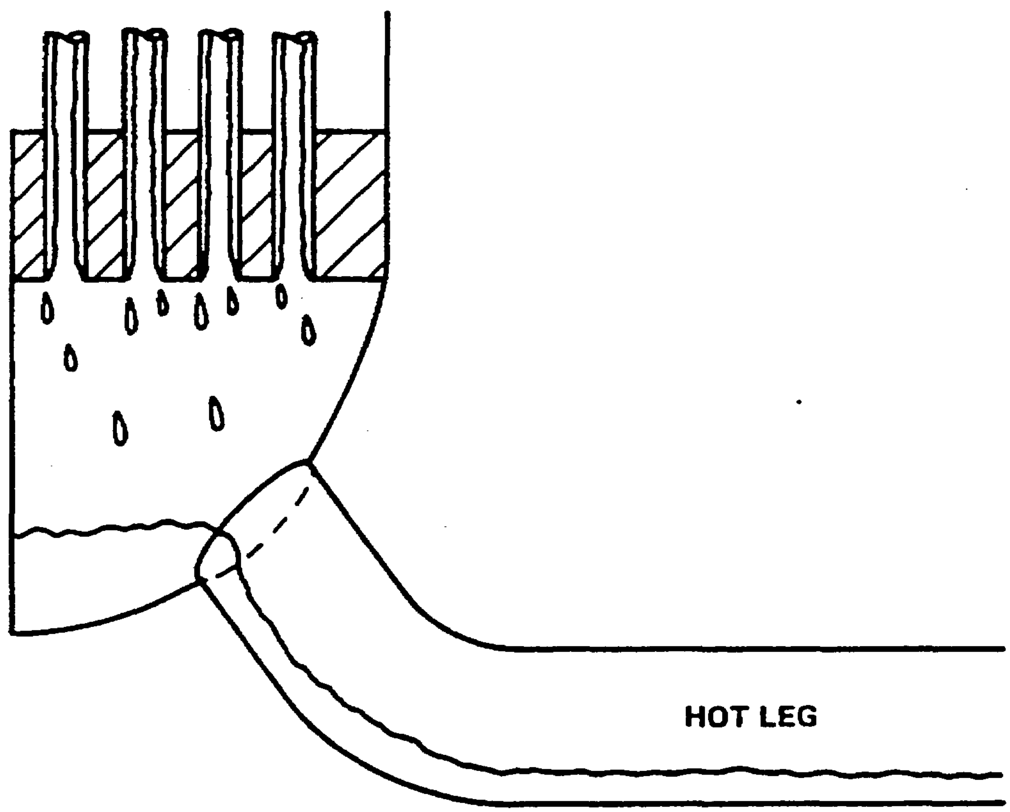

Figure 17-21. PWR Hot Leg-to-Steam Generator Inlet Plenum Connection

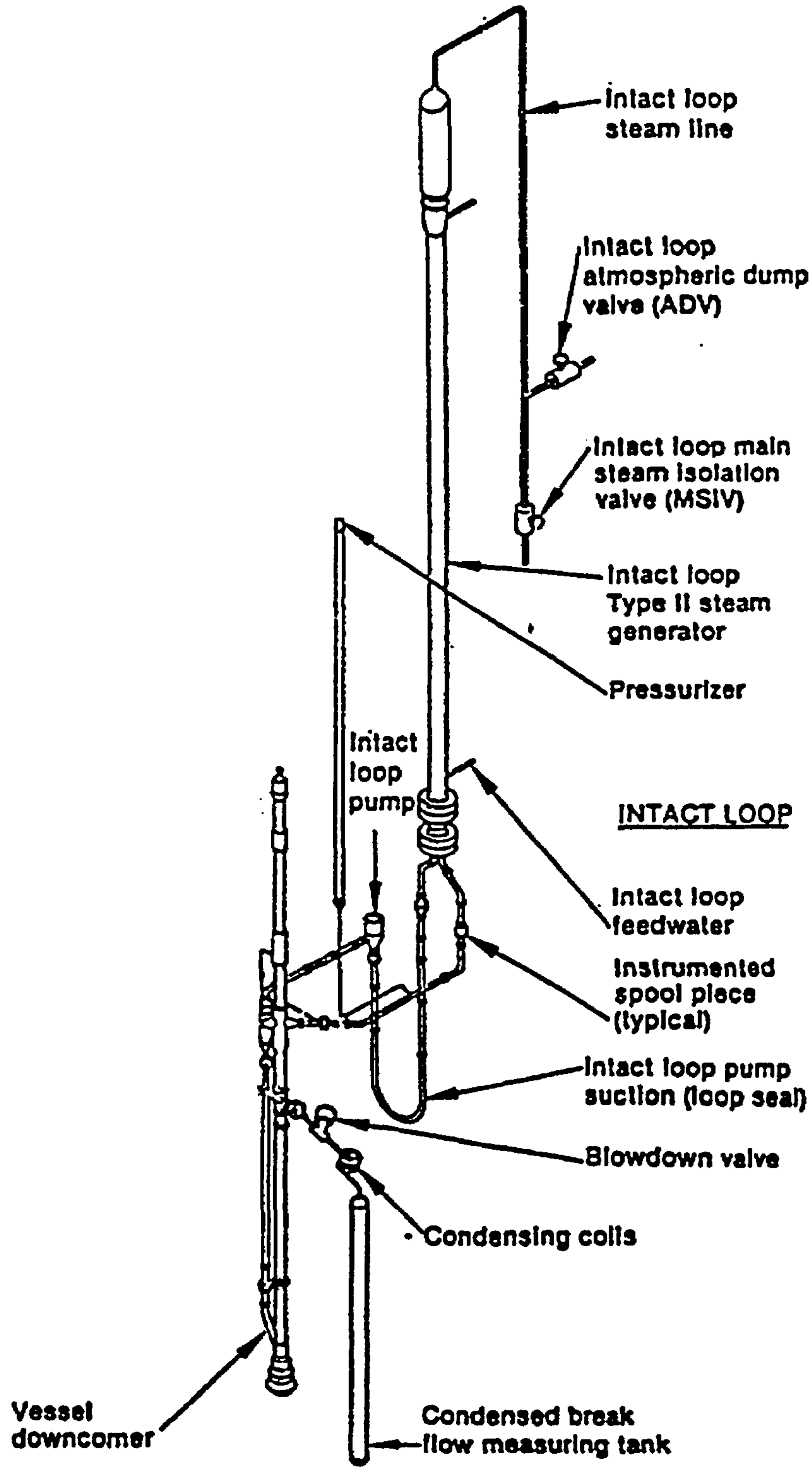

Figure 17-22. Semiscale Mod-2A System for NC Tests

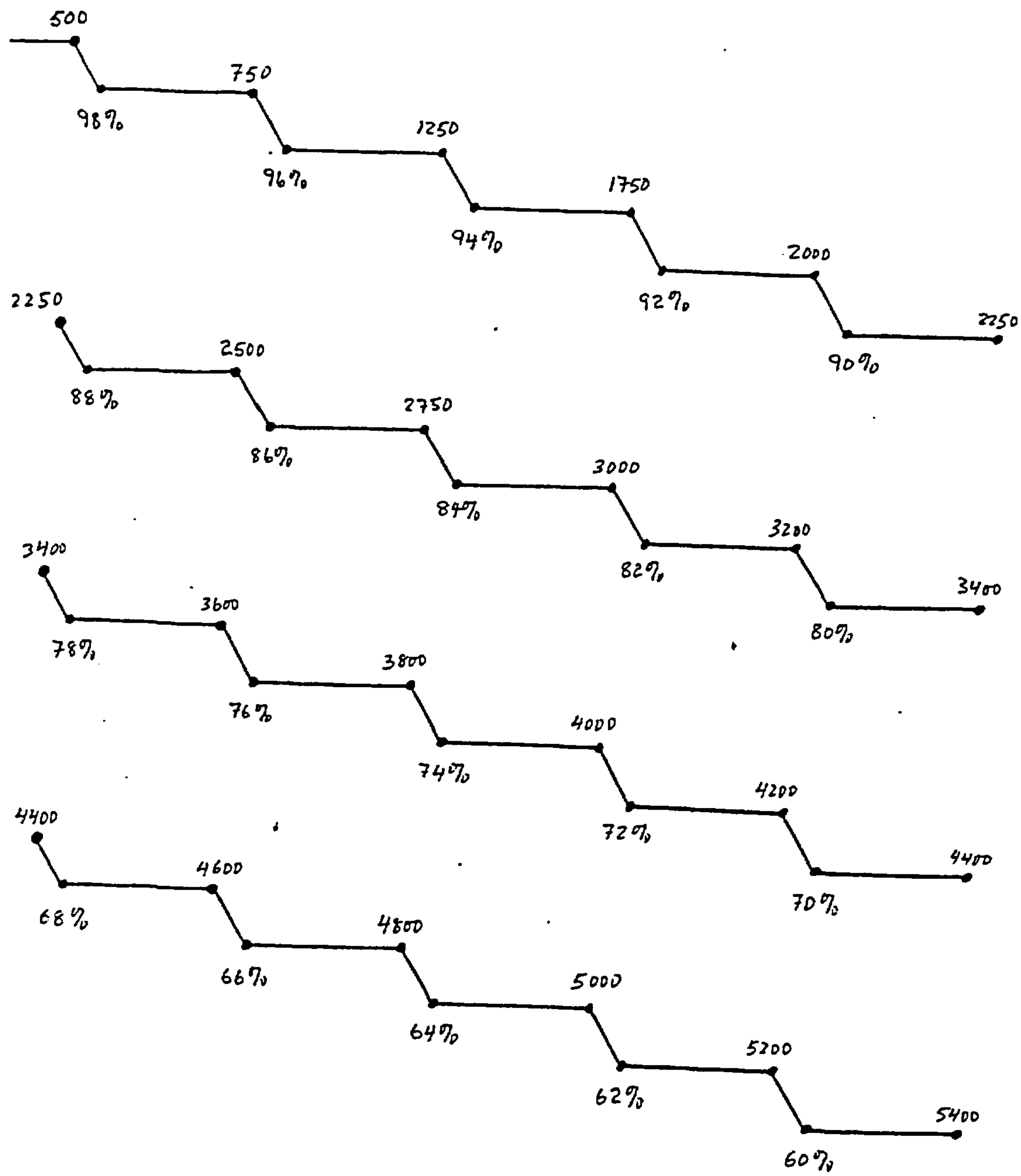

Figure 17-23. W̲COBRA/TRAC-SB Inventory Versus Time, Semiscale Mod-2A NC Test

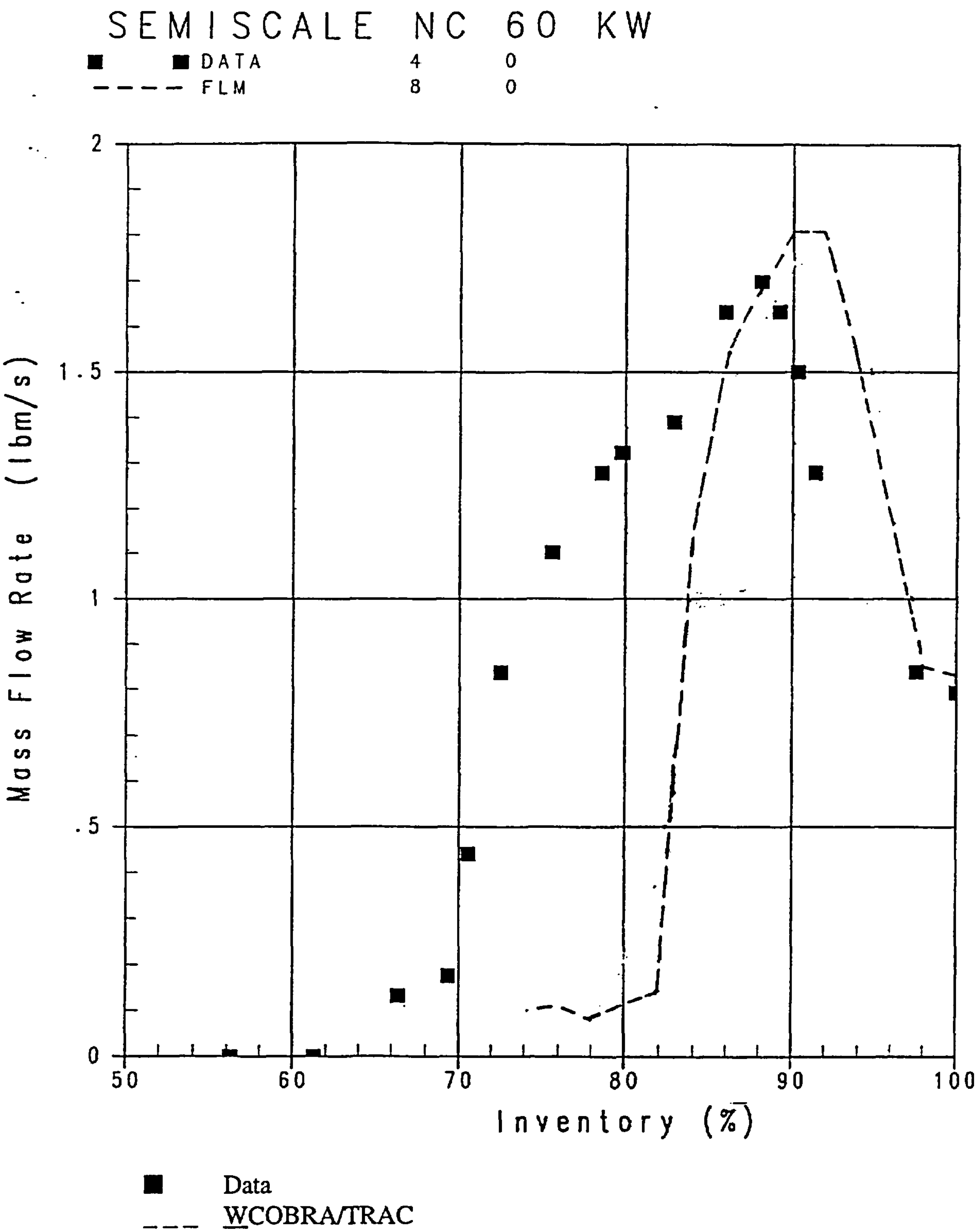

Figure 17-24. Comparison of WCOBRA/TRAC-SB Prediction and Semiscale NC 60-kW (3-Percent Power) Data

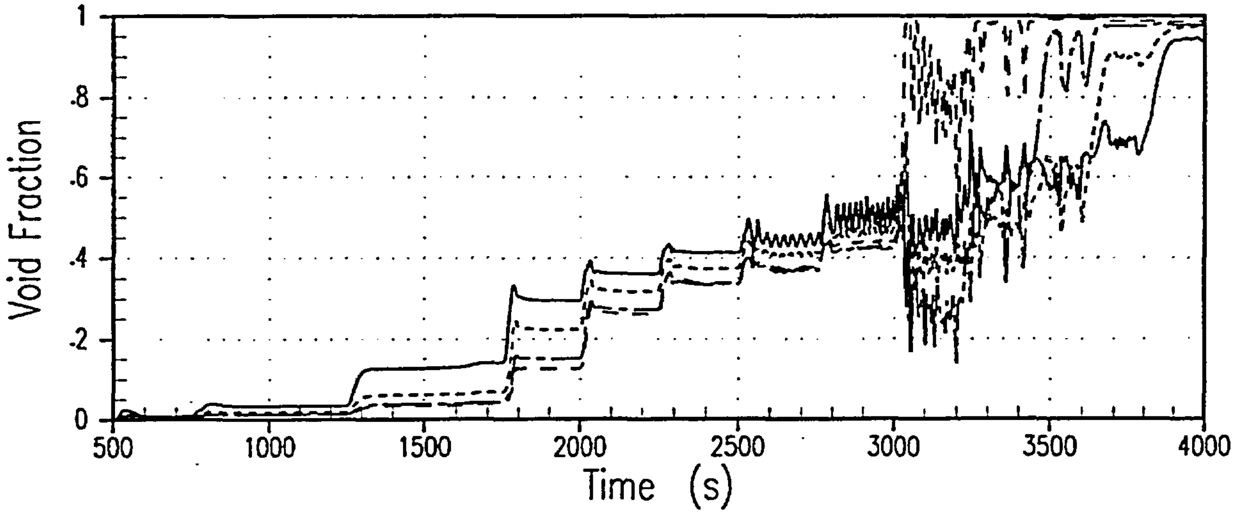

________	Vapor fraction, lower middle elevation
- - - - - - - -	Vapor fraction, middle elevation
-·-·-·-·-·-·-·-	Vapor fraction, upper middle elevation
– – – – – –	Vapor fraction, top elevation

Figure 17-25. Predicted Void Fraction in the Steam Generator Tubes Uphill Region, Semiscale NC 60-kW Test

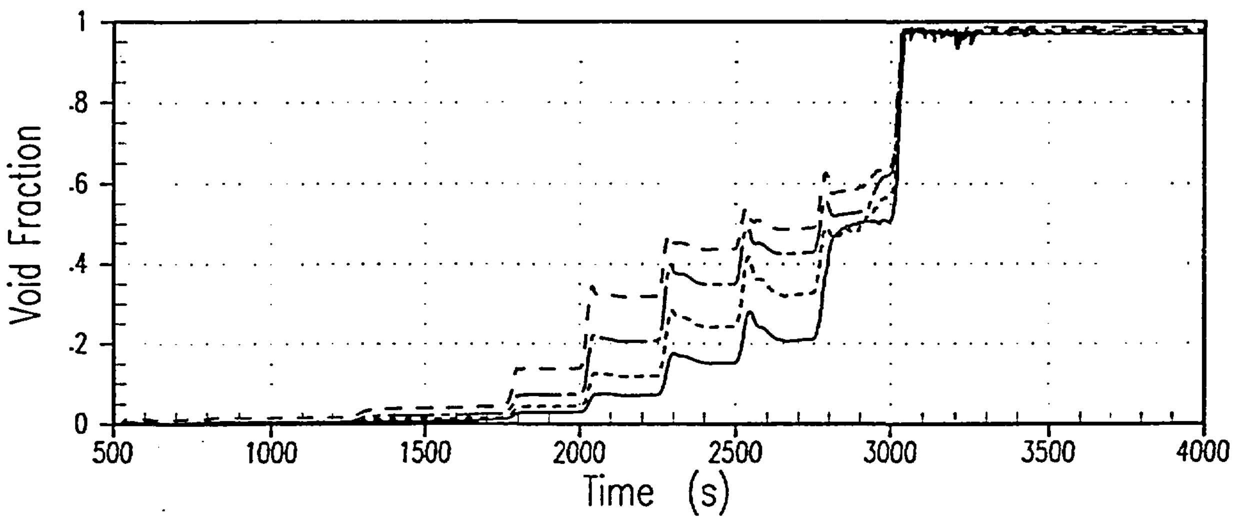

————	Vapor fraction, lower middle elevation
- - - - - - - -	Vapor fraction, middle elevation
-·-·-·-·-·-·-·-	Vapor fraction, upper middle elevation
— — — — — —	Vapor fraction, top elevation

Figure 17-26. Predicted Void Fraction in the Steam Generator Tubes Downhill Region, Semiscale NC 60-kW Test

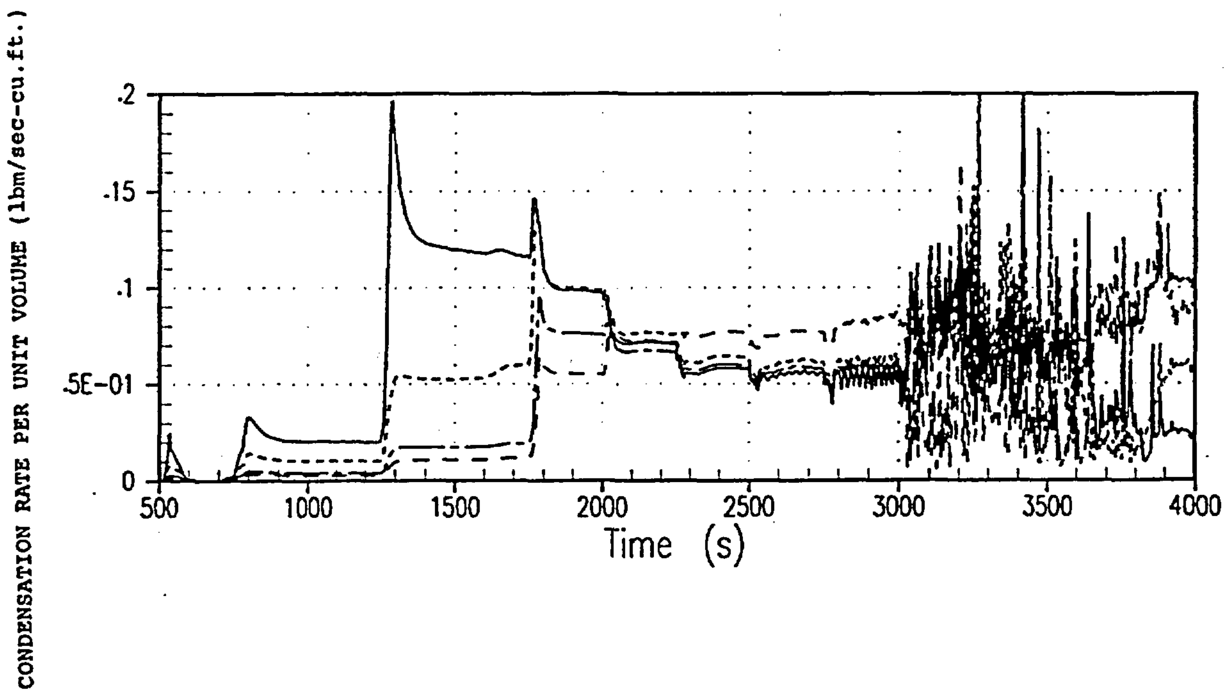

________	Lower middle elevation rate
- - - - - - - -	Middle elevation rate
-·-·-·-·-·-·-·-	Upper middle elevation rate
– – – – – –	Top elevation rate

Figure 17-27. Predicted Condensation Rate in the Steam Generator Tubes Uphill Region, Semiscale NC 60-kW Test

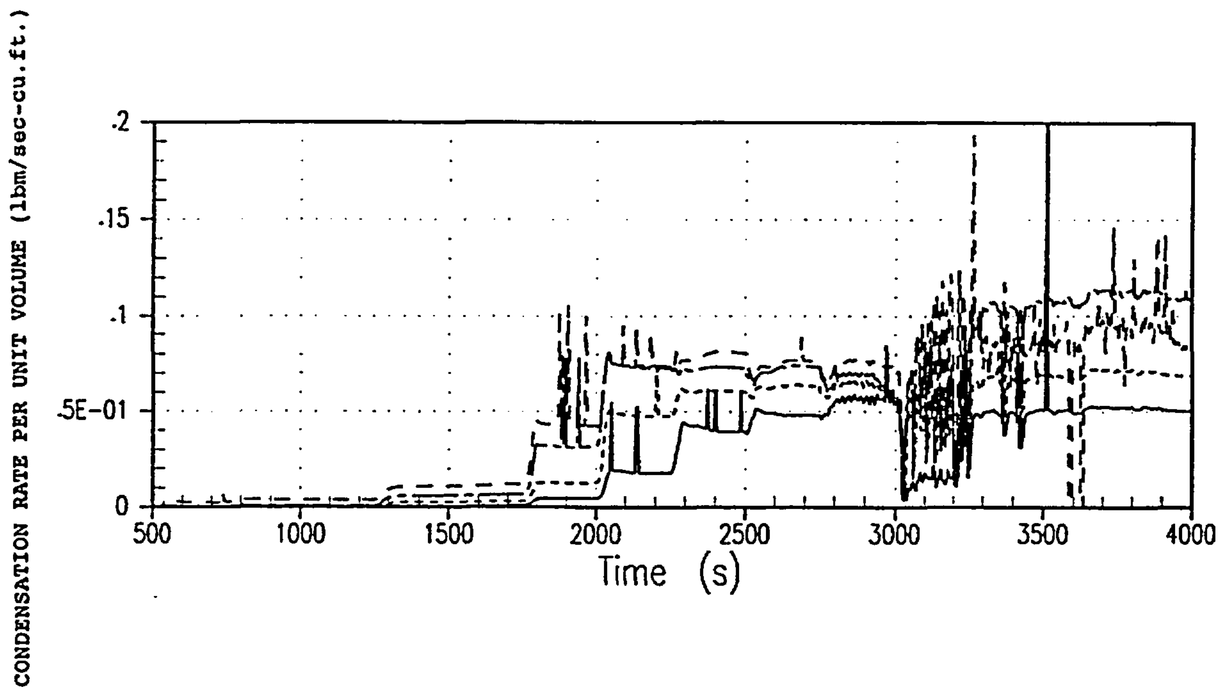

________	Lower middle elevation rate
- - - - - - - -	Middle elevation rate
-·-·-·-·-·-·-·-	Upper middle elevation rate
— — — — — —	Top elevation rate

Figure 17-28. Predicted Condensation Rate in the Steam Generator Tubes Downhill Region, Semiscale NC 60-kW Test

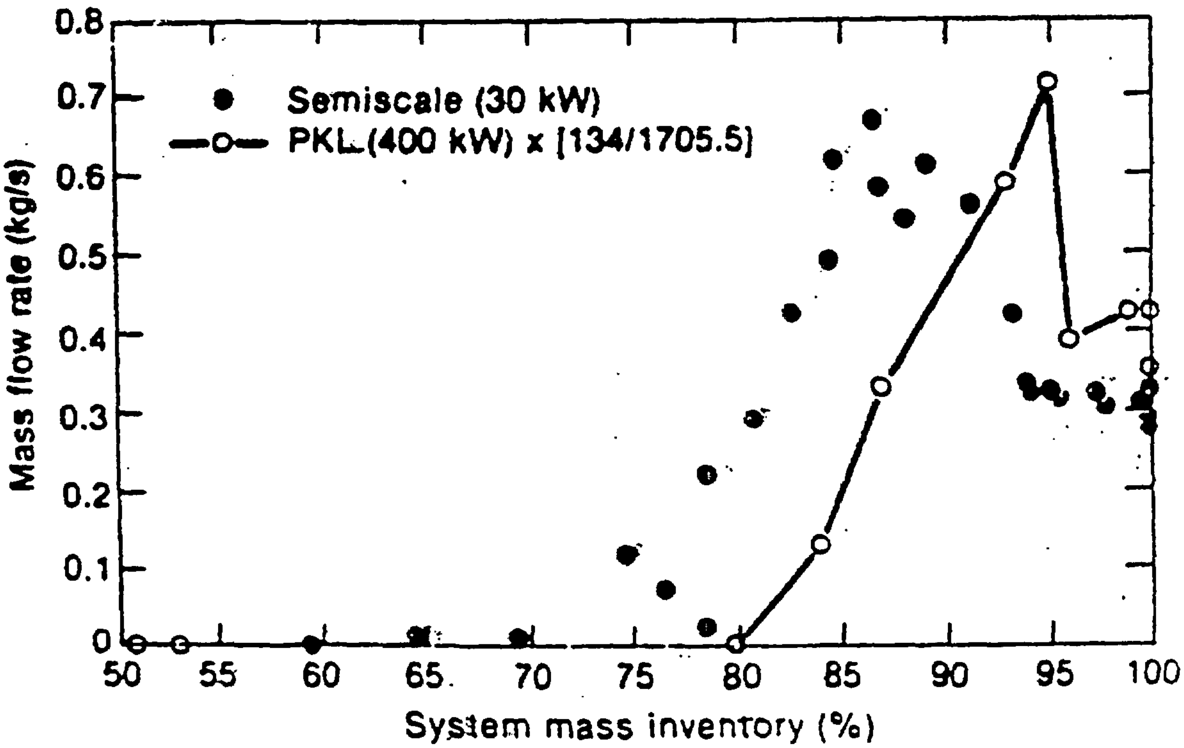

Figure 17-29. Comparison of Semiscale and PKL Natural Circulation Flowrates

SECTION 18
HORIZONTAL STRATIFIED FLOW BENCHMARKS

18-1 Introduction

The predicted performance of a PWR during a small break LOCA transient is to a large extent determined by the two-phase flow regime present in the horizontal pipes of the RCS. The duration of the natural circulation period, the loop seal clearing process, and the break flow composition are a consequence of the flow regime(s) in the hot leg, pump suction leg, and cold leg horizontal sections, respectively. In the WCOBRA/TRAC-SB computer code, the Taitel and Dukler flow regime map (Taitel and Dukler, 1976) is used to define the horizontal pipe flow regime. At the relatively low flowrates associated with the break size range of small break LOCA, the horizontal two-phase flow is in the stratified wavy and/or stratified smooth flow regimes most of the time. Therefore, the prediction of small break LOCA phenomena in the stratified flow regimes is of central importance for the horizontal RCS piping.

Within WCOBRA/TRAC-SB logic, the horizontal flow regime is identified [ ]^{a,c} using the Taitel and Dukler regime map. If the path is determined to be stratified, the Jensen and Yuen model (Jensen and Yuen, 1982) is applied to calculate the interfacial drag and condensation that occurs; entrainment at the interface between gas and liquid is calculated according to the Kataoka and Ishii model (Kataoka and Ishii, 1983). Because the interfacial drag, condensation, and entrainment modelling for horizontal stratified flow are basic processes that are directly related to high-ranked items in the small break LOCA PIRT in Volume 1 of this document, individual validation of each of these models is needed to confirm their accuracy. This is accomplished using the experimental WCOBRA/TRAC-SB simulations presented in the following sections.

18-2 Physical Processes

In the condition of a smooth, equilibrium-stratified flow, the wall resistance of the liquid is similar to that for open-channel flow and that of the gas is similar to closed-duct flow. Because the gas phase velocity is much larger than the velocity at the gas-liquid interface, the gas side interfacial shear stress is evaluated using the equation for gas wall shear. The interfacial drag is thus easily defined theoretically.

Entrainment from the liquid film at the stratified flow two-phase interface is important in determining the mass distribution in the RCS during a small break LOCA. This is particularly true in establishing the liquid fraction of flow through the break once the break location is uncovered. Liquid that exits the RCS through the break is no longer available to possibly contribute to core liquid inventory and to maintain the core in a covered state. Also, entrainment from the stratified two-phase interface in the hot leg affects the natural circulation period in the small break LOCA, and entrainment from the residual liquid in the horizontal leg of the pump suction leg affects the loop seal clearing.

Condensation of steam by the subcooled water of the safety injection jet has been separately addressed in Section 14 in this volume. Condensation of steam in the cold leg remains important in the depressurization of the RCS to the point where safety injection exceeds break flow and the recovery period of the small break LOCA begins.

18-3 WCOBRA/TRAC-SB Horizontal Stratified Flow Models

Important phenomena in the production of horizontal, stratified flow during a small break LOCA – the interfacial drag, entrainment, and condensation – are discussed in this section.

18-3-1 Interfacial Drag

The models and correlations used to calculate interfacial drag in horizontal stratified flow are described in Section 4-6 in Volume 1 of this document. In particular, the work reported by Jensen and Yuen (Jensen and Yuen, 1982) is used.

18-3-2 Entrainment

Section 4-6 describes the models and correlations in WCOBRA/TRAC-SB that are used to calculate the entrainment and de-entrainment processes. Entrainment is the result of interfacial shear between vapor and liquid film. In WCOBRA/TRAC-SB, liquid is moved from the continuous liquid field to the entrained field when the interfacial shear forces acting on the liquid are sufficient. In de-entrainment, liquid is moved from the entrained field to the continuous liquid field. A summary of the applicable models in WCOBRA/TRAC-SB is as follows:

- Entrainment in Film Flow

  WCOBRA/TRAC determines film entrainment rates by comparing the entrainment rate based on a stable film flow to an empirical entrainment rate based on the work of Walley (Walley, et al., 1973).

- Entrainment in Bottom Reflood

  The model for entrainment in the core near the quench front is based on a model by Kataoka and Ishii (Kataoka and Ishii, 1983) assuming vapor bubbling through a liquid pool.

- Entrainment at a Horizontally Stratified Surface

  In small break LOCA events, if the vapor velocity is sufficient, entrainment can occur from a horizontal interface of vapor and liquid.

- De-entrainment in Film Flow

  The model to estimate the de-entrainment of entrained drops into the continuous liquid field uses an empirical model by Cousins (Cousins, et al., 1965).

- Crossflow De-entrainment

  Entrained liquid in the upper plenum can de-entrain on structures there as the two-phase mixture flows from the vessel into the hot legs. WCOBRA/TRAC uses a model based on experiments by Dallman and Kirchner (Dallman and Kirchner, 1980) to determine the amount of de-entrainment in the upper plenum and other regions of the reactor vessel.

- De-entrainment at Area Changes

  De-entrainment occurs as a two-phase mixture encounters a flow restriction such as a tie plate. WCOBRA/TRAC uses a simple area ratio to de-entrain a fraction of the droplet field where an area reduction occurs in the reactor vessel.

- De-entrainment at Solid Surfaces and Liquid Pools

  Drops are assumed to de-entrain when the drops flow into a cell with a solid surface at the opposite face or when the drops flow into a cell which is in a bubbly flow regime.

The small break LOCA PIRT presented in Volume 1 identified entrainment as a high-ranked phenomenon only during loop seal clearing. Therefore, WCOBRA/TRAC-SB simulations of loop seal clearing in small break LOCA scenarios presented in Section 16 in this volume provide the necessary validation for code prediction of the entrainment from a stratified interface.

18-3-3 Condensation

Section 14 in this volume presents the validation of the model for condensation on the safety injection jet in a small break LOCA transient. When this location is not being modelled, WCOBRA/TRAC-SB uses a model for interfacial heat and mass transfer similar to other best estimate codes. As described in Section 5 in Volume 1 of this document, four components are evaluated to calculate interfacial heat and mass transfer; they may be described as

$$\begin{aligned}
\Gamma_{SCL} &= \frac{HA_{SCL}(T_l - T_i)}{H_v - H_f} \\
\Gamma_{SHL} &= \frac{HA_{SHL}(T_l - T_i)}{H_g - H_l} \\
\Gamma_{SCV} &= \frac{HA_{SCV}(T_v - T_i)}{H_v - H_f} \\
\Gamma_{SHV} &= \frac{HA_{SHV}(T_v - T_i)}{H_g - H_l}
\end{aligned} \qquad (18\text{-}1)$$

where:

Γ_{SCL} = condensation to subcooled liquid
Γ_{SHL} = evaporation from superheated liquid
Γ_{SCV} = condensation from subcooled vapor
Γ_{SHV} = evaporation to superheated vapor

Figure 18-1 provides a pictorial representation of the WCOBRA/TRAC-SB approach. [

]^{a,c} This term is described in Section 6-4 of this document.

Overall, condensation of vapor in WCOBRA/TRAC-SB [

]^{a,c}

Table 18-1 is a summary, according to the Equation 18-1 terminology, of the interfacial heat transfer models used in the vessel component of WCOBRA/TRAC-SB. [

]^{a,c}

[

]a,c

In the following sections, an additional set of experiments is examined which focuses on condensation in a geometry similar to the PWR cold leg.

18-4 Assessment of WCOBRA/TRAC-SB Horizontal Stratified Flow Models

The performance of the horizontal stratified flow models in WCOBRA/TRAC-SB must be established in predicting interfacial drag and condensation heat transfer for a pertinent single-effect test to demonstrate that the models are adequate for small break LOCA applications. The interfacial drag predictive capability is validated against relevant experimental data (Lim, et al., 1981); these data are also used to validate the interfacial condensation heat transfer.

18-4-1 Test Facility Description and Modelling

The test facility of Lim (Lim, et al., 1981) used a rectangular channel to measure condensation of steam in cocurrent, horizontal flow. The channel was constructed of stainless steel with pyrex glass windows; its dimensions were 160.1 cm long, 6.35 cm high, and 30.48 cm wide. Data were taken in the course of 35 runs. Controlled parameters in the experiments included water and steam inlet temperatures, mass flowrates, and water layer thickness at the inlet. The range of steam (maximum velocity 18 m/s) and water (maximum velocity 41 cm/s) flowrates were restricted by either the initiation of bridging phenomena or the occurrence of a hydraulic jump. Inlet steam pressure was approximately 1 atmosphere. Steam velocity, static pressure (for some experiments), and water layer thickness were measured at five locations along the channel. The water inlet temperature was also measured. Figure 18-2 is a schematic diagram of the experimental system.

Figure 18-3 presents the WCOBRA/TRAC noding of the test facility. [

]a,c

[

]a,c

As shown in Figure 18-3, the experimental channel is modeled axially [

]a,c. This was considered sufficient to provide enough resolution to compare with experimental measurements, which are available at only five axial locations.

The experimental channel is divided [

]a,c

The experimental report (Lim, et al., 1981) offers no data on liquid level in the discharge tank during the experiments and on the tank dimensions. Because it is impractical to simulate a constant liquid level in the tank due to condensation in the channel, the liquid level in the tank was allowed to rise during the simulation, but it was always kept below the liquid level in the channel. Condensation was turned off [

]a,c to minimize the effect of the discharge tank on the channel flow.

[

]a,c

The liquid level at the channel inlet [

]a,c As shown in Figures 18-4 and 18-5, the liquid profile away from the channel inlet is determined only by the steam and water flowrates. The "line" in Figure 18-5 is a linear correlation plane oriented in parallel to the reader's line of sight. Because essentially all of the variation in the liquid water thickness in the experimental channel can be attributed to the variations in steam and water flowrates, the effect of the initial water layer thickness on the flow pattern away from the inlet can be ignored.

The experimental results used in this analysis are reported to be at steady-state. That is, the water level, pressure, temperature, and steam flow in the channel were stable and not varying significantly.

The WCOBRA/TRAC-SB simulations were run [

]^{a,c}.

18-4-2 Calculational Results

A total of 35 tests are reported in Lim (Lim, et al., 1981). Those tests in which the horizontal two-phase flow is fully within the wavy or stratified flow regimes (32 in number) were simulated. The experimental results and test conditions for the tests simulated with WCOBRA/TRAC-SB are shown in Table 18-2. Steam density and steam and water velocities were input as boundary conditions in the model's steam and liquid fill components, respectively.

In Table 18-2, steam flowrate and water layer thickness data at locations 1, 2, 3, 4, and 5 correspond to 6.18, 12.05, 23.08, 34.18, and 48.14 inches from the experimental channel inlet. Static pressure difference measurements at 4.88, 10.75, 21.77, 32.87, and 47.24 inches are listed as being at locations 1 through 5. Nomenclature is provided on the table.

Steam density input is calculated using NIST/ASME steam properties for given values of the steam inlet temperature and constant pressure of 16 psi. Due to small variations in the liquid temperature and density among the tests and along the experimental channel, a constant liquid density corresponding to the average liquid temperature of 148.6°F is assumed. Steam and water inlet velocities in the model fill components (Figure 18-3) are calculated using a constant flow area of 0.2083 ft^2.

Figures 18-6 through 18-11 provide, for a typical case (run 275), the predicted results and the comparison between experimental data and the WCOBRA/TRAC-SB predictions. For calculated quantities, stable or periodic (at one or two axial locations) behavior is observed over the duration of the test (Figures 18-6, 18-8, and 18-10). There is a reasonably good agreement between the measured and predicted average values of liquid level and pressure drop[1] in the channel as seen in Figures 18-7 and 18-9. While the liquid level at 47.27 inches is significantly underpredicted, the observed trend of the liquid level to recover toward the channel outlet is well

[1] Note that the pressure actually increases as the steam flow proceeds through the channel.

reproduced by WCOBRA/TRAC-SB (Figure 18-7). WCOBRA/TRAC-SB overpredicted the steam flowrate axially as seen in Figure 18-11; underpredicting the steam condensation rate is the cause. This matter was investigated further; condensation heat transfer correlations used in WCOBRA/TRAC-SB (Jensen and Yuen, 1982), and one derived from the experimental data, were compared to each other for typical flow conditions in the channel. This comparison is presented in Figure 18-12.

The alternative correlation for a smooth interface based on this test data (Lim, et al., 1981) is given by:

$$Nu_{xAs} := 0.631 \cdot (Re_g)^{0.58} \cdot (Re_1)^{0.09} \cdot (Pr_1)^{0.3} \qquad (18\text{-}1)$$

where:

Nu_{xAs} = is the Nusselt number (Nu), *equals* 1344 *for case* 275

The principal difference between the correlations is that the Nu value in WCOBRA/TRAC-SB is [

]^{a,c}

The cumulative results of all tests simulated are shown in Figures 18-13 through 18-16, which show scatter plots of predicted versus measured quantities of the liquid level, steam mass flowrate, liquid temperature at the channel exit, and the pressure drop in the channel, respectively. For most of the cases, liquid level predictions are within ± 0.2 inches of the measurements. The steam flowrate is overestimated almost everywhere in the test section, particularly near the channel exit. As a result, the liquid temperature at the channel exit is underpredicted by 20° to 40°F. The large majority (approximately 80%) of the pressure drop predictions are within ± 33 percent of the experimental data, as shown in Figure 18-16.

18-5 Conclusions

WCOBRA/TRAC-SB predictions of two-phase flow in a horizontal channel were verified against data of steam condensation in a rectangular channel with cocurrent water flow at atmospheric pressure. A model of the experimental channel, consisting of [ ][a,c] was developed. The pertinent cases among the 35 test cases reported in Lim (Lim et al., 1981) were simulated. For most of the cases, liquid level predictions are within ± 0.2 inches of the measurements. Depending on the axial position, steam flowrate can be overestimated by a factor of 2 or more (near the channel exit). As a result, the liquid temperature at the channel exit is underpredicted by 20 to 40°F. To address this, values of the condensation heat transfer coefficient calculated by the code were compared with those given by the correlation used in WCOBRA/TRAC-SB and one derived from the experimental data. The difference in the condensation heat transfer coefficient is determined to be due to the correlation used in the code. Condensation heat transfer in horizontal stratified flow will be ranged in the PWR sensitivity study to address this discrepancy and considered in the uncertainty methodology.

Most of the pressure drop predictions are within ± 33 percent of the experimental data, and the number of points for which the pressure drop is underpredicted is approximately the same as the number for which it is overpredicted. Inasmuch as steam velocities are low when horizontal stratified flow conditions exist in PWR loop pipes during a small break LOCA event, the pressure drop prediction uncertainties of this model are judged to be unimportant relative to the total hydraulic pressure drop of the RCS. Nevertheless, interfacial drag variations in the horizontal stratified flow regime are considered in the uncertainty methodology.

18-6 References

Cousins, L. B., et al., 1965, "Liquid Mass Transfer in Annular Two-Phase Flow," Paper C4, Symposium on Two-Phase Flow, Vol. 2, Exeter, England.

Dallman, J. C. and Kirchner, W. L., 1980, "De-Entrainment Phenomena on Vertical Tubes in Droplet Cross Flow," NUREG/CR-1421.

Lim, I. S., et al., 1981, "Cocurrent Steam-water Flow in a Horizontal Channel," NUREG/CR-2289.

Jensen, R. J. and Yuen M. C., 1982, "Interphase Transport in Horizontal Stratified Cocurrent Flow," NUREG/CR-2334.

Kataoka, I. and Ishii, M., 1983, "Mechanistic Modelling and Correlations for Pool Entrainment Phenomena," NUREG/CR-3304.

Taitel, Y. and Dukler, A. E., 1976, "A Model for Predicting Flow Regime Transitions in Horizontal and Near Horizontal Gas-Liquid," AIChE Journal, Vol. 22.

Walley, P. B., et al., 1973, "Experimental Wave and Entrainment Measurements in Vertical Annular Two-Phase Flow," AERE-R7521, Atomic Energy Research Establishment, Harwell, England.

Table 18-1
WCOBRA/TRAC-SB 3-D Interfacial Heat Transfer Models

[				

]a,c

Table 18-2
Test Matrix Parameters

No.	Units[a]	Location: Inlet	1	2	3	4	5	W_L^{in} (lb/s)	T_G^{in} (°F)	T_L^{in} (°F)	T_L^{ex} (°F)
211	W_G (lb/s)	0.09	0.083	0.077	0.069	0.065	0.064	0.866	281	76.7	160
	δ_L (in)	0.623	0.534	0.393	0.223	0.222	0.241				
	ΔP(psi)	0	7E-05	1E-04	2E-04	3E-04	3E-04				
231	W_G (lb/s)	0.09	0.082	0.074	0.063	0.06	0.059	0.896	271	33.8	118
	δ_L (in)	0.623	0.626	0.487	0.317	0.293	0.317				
	ΔP(psi)	0	1E-04	2E-04	3E-04	4E-04	5E-04				
251	W_G (lb/s)	0.09	0.077	0.072	0.06	0.055	0.054	1.17	272	33.8	98.1
	δ_L (in)	0.623	0.624	0.55	0.349	0.403	0.436				
	ΔP(psi)	0	3E-04	5E-04	7E-04	7E-04	7E-04				
253	W_G (lb/s)	0.143	0.129	0.12	0.086	0.063	0.039	1.447	281	70.88	156
	δ_L (in)	0.623	0.569	0.444	0.3	0.417	0.484				
	ΔP(psi)	0	7E-04	1E-03	0.002	0.002	0.002				
255	W_G (lb/s)	0.204	0.188	0.167	0.113	0.081	0.061	1.57	278	72.68	175
	δ_L (in)	0.623	0.411	0.291	0.208	0.218	0.433				
	ΔP(psi)	0	0.001	0.002	0.004	0.004	0.004				
257	W_G (lb/s)	0.275	0.248	0.222	0.163	0.128	0.101	1.573	287	72.86	190
	δ_L (in)	0.623	0.298	0.208	0.173	0.178	0.23				
	ΔP(psi)	0	0.002	0.004	0.006	0.007	0.007				
273	W_G (lb/s)	0.144	0.119	0.096	0.061	0.042	0.025	2.253	280	77.54	144
	δ_L (in)	0.623	0.783	0.643	0.525	0.591	0.642				
	ΔP(psi)	0	7E-04	0.001	0.002	0.002	0.002				
275	W_G (lb/s)	0.202	0.169	0.14	0.097	0.069	0.047	2.244	285	79.7	163
	δ_L (in)	0.623	0.623	0.51	0.403	0.352	0.622				
	ΔP(psi)	0	0.001	0.002	0.004	0.004	0.005				

a. Definitions for all units are listed at the end of this table.

Table 18-2 (Cont'd)
Test Matrix Parameters

No.	Units	Location: Inlet	1	2	3	4	5	W_L^{in} (lb/s)	T_G^{in} (°F)	T_L^{in} (°F)	T_L^{ex} (°F)
277	W_G (lb/s)	0.277	0.24	0.212	0.156	0.117	0.08	2.289	287	76.1	175
	δ_L (in)	0.623	0.427	0.334	0.307	0.283	0.314				
	ΔP(psi)	0	0.002	0.004	0.006	0.007	0.008				
293	W_G (lb/s)	0.144	0.106	0.084	0.05	0.033	0.019	3.17	279	76.82	126
	δ_L (in)	0.623	0.956	0.819	0.658	0.702	0.754				
	ΔP(psi)	0	7E-04	0.002	0.002	0.002	0.003				
295	W_G (lb/s)	0.199	0.155	0.127	0.08	0.055	0.034	3.148	284	78.44	144
	δ_L (in)	0.623	0.869	0.693	0.551	0.652	0.726				
	ΔP(psi)	0	5E-04	0.002	0.004	0.004	0.005				
297	W_G (lb/s)	0.276	0.224	0.193	0.141	0.101	0.064	3.165	287	79.34	161
	δ_L (in)	0.623	0.605	0.444	0.446	0.389	0.419				
	ΔP(psi)	0	0.001	0.004	0.006	0.007	0.008				
353	W_G (lb/s)	0.144	0.132	0.127	0.09	0.067	0.043	1.5	281	76.73	160
	δ_L (in)	0.873	0.653	0.528	0.309	0.242	0.451				
357	W_G (lb/s)	0.274	0.255	0.231	0.173	0.138	0.109	1.489	288	77	192
	δ_L (in)	0.873	0.493	0.303	0.203	0.173	0.213				
373	W_G (lb/s)	0.141	0.125	0.114	0.077	0.049	0.03	2.233	281	75.92	139
	δ_L (in)	0.873	0.828	0.665	0.453	0.363	0.585				
377	W_G (lb/s)	0.272	0.246	0.218	0.155	0.112	0.074	2.236	288	76.1	175
	δ_L (in)	0.873	0.653	0.456	0.316	0.282	0.302				
393	W_G (lb/s)	0.141	0.118	0.102	0.06	0.042	0.024	3.143	280	78.62	127
	δ_L (in)	0.873	0.931	0.776	0.562	0.606	0.711				

Table 18-2 (Cont'd)
Test Matrix Parameters

No.	Units	Location						W_L^{in}	T_G^{in}	T_L^{in}	T_L^{ex}
		Inlet	1	2	3	4	5	(lb/s)	(°F)	(°F)	(°F)
	W_G (lb/s)	0.277	0.233	0.201	0.144	0.104	0.067				
397	δ_L (in)	0.873	0.688	0.638	0.441	0.367	0.393	3.095	288	77.36	161
	W_G (lb/s)	0.146	0.13	0.117	0.071	0.05	0.031				
153	δ_L (in)	0.375	0.568	0.524	0.414	0.541	0.573	1.5	221	73.04	165
	W_G (lb/s)	0.285	0.254	0.227	0.169	0.135	0.124				
157	δ_L (in)	0.375	0.306	0.279	0.196	0.241	0.484	1.463	241	75.74	194
	W_G (lb/s)	0.147	0.128	0.105	0.063	0.043	0.041				
173	δ_L (in)	0.375	0.779	0.71	0.546	0.663	0.681	2.311	220	73.4	144
	W_G (lb/s)	0.285	0.262	0.217	0.159	0.115	0.086				
177	δ_L (in)	0.375	0.503	0.438	0.335	0.36	0.381	2.315	241	80.06	177
	W_G (lb/s)	0.142	0.131	0.123	0.099	0.08	0.063				
453	δ_L (in)	0.623	0.6	0.544	0.43	0.535	0.567	1.504	280	122.2	182
	W_G (lb/s)	0.207	0.193	0.176	0.138	0.119	0.108				
455	δ_L (in)	0.623	0.445	0.361	0.299	0.305	0.507	1.5	284	119.5	190
	W_G (lb/s)	0.282	0.261	0.238	0.199	0.179	0.165				
457	δ_L (in)	0.623	0.407	0.293	0.257	0.252	0.263	1.496	287	118.4	197
	W_G (lb/s)	0.344	0.315	0.294	0.254	0.236	0.223				
459	δ_L (in)	0.623	0.329	0.257	0.227	0.214	0.249	1.562	288	125.8	201
	W_G (lb/s)	0.141	0.125	0.112	0.084	0.064	0.045				
473	δ_L (in)	0.623	0.766	0.663	0.526	0.61	0.675	2.344	280	123.8	172
	W_G (lb/s)	0.199	0.176	0.156	0.119	0.094	0.079				
475	δ_L (in)	0.623	0.635	0.53	0.444	0.367	0.632	2.286	284	119.5	180
	W_G (lb/s)	0.285	0.256	0.233	0.187	0.158	0.132				
477	δ_L (in)	0.623	0.491	0.367	0.336	0.298	0.333	2.337	287	117.9	189

Table 18-2 (Cont'd)
Test Matrix Parameters

No.	Units	Location						W_L^{in}	T_G^{in}	T_L^{in}	T_L^{ex}
		Inlet	1	2	3	4	5	(lb/s)	(°F)	(°F)	(°F)
	W_G (lb/s)	0.143	0.118	0.102	0.072	0.056	0.037				
493	δ_L (in)	0.623	0.906	0.825	0.665	0.728	0.77	3.002	278	119.7	164
	W_G (lb/s)	0.2	0.17	0.149	0.109	0.083	0.064				
495	δ_L (in)	0.623	0.812	0.735	0.546	0.451	0.721	3.007	285	119.8	172
	W_G (lb/s)	0.282	0.252	0.225	0.178	0.142	0.11				
497	δ_L (in)	0.623	0.622	0.458	0.426	0.392	0.426	3.156	287	119.3	181

W_G = steam mass flowrate
δ_L = water layer thickness
ΔP = differential pressure
W_L^{in} = inlet liquid mass flowrate
T_G^{in} = inlet vapor temperature
T_L^{in} = inlet liquid temperature
T_L^{ex} = outlet liquid temperature

a,c

Figure 18-1. WCOBRA/TRAC-SB Representation of Interfacial Heat Transfer

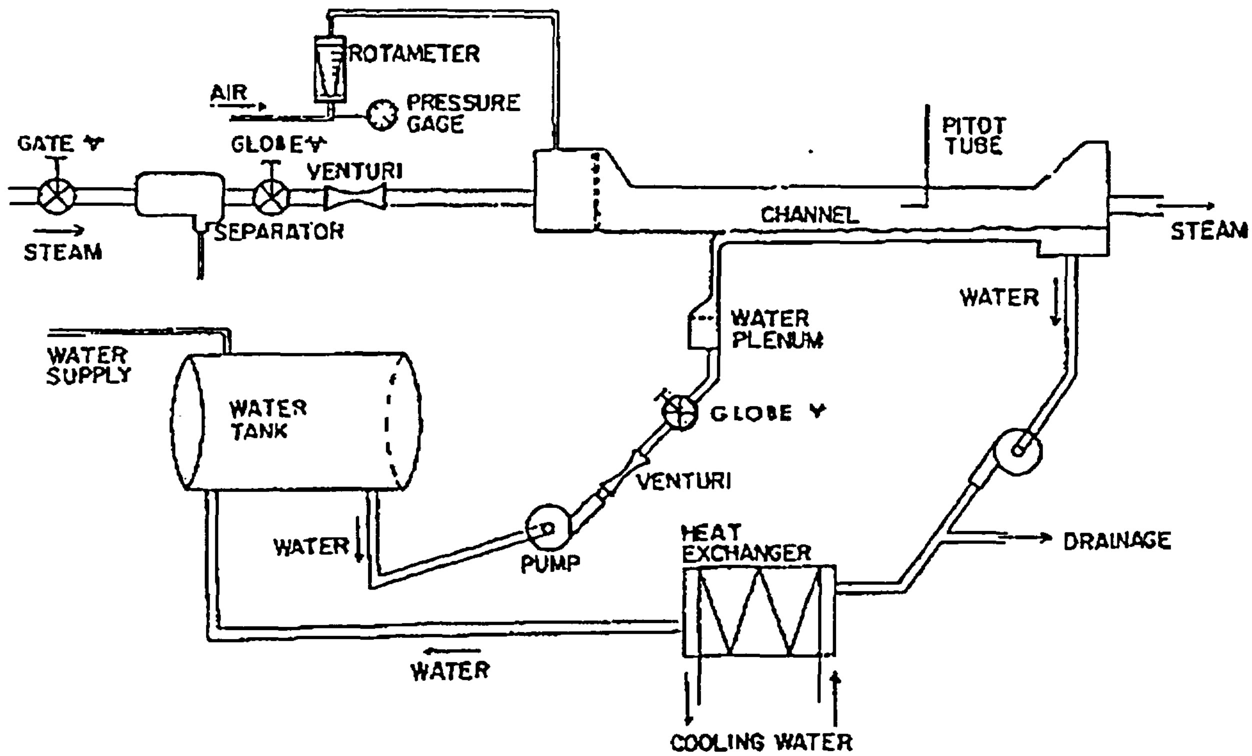

Figure 18-2. Schematic Diagram of the Experimental System (Lim, et al., 1981)

a,c

Figure 18-3. WCOBRA/TRAC Noding

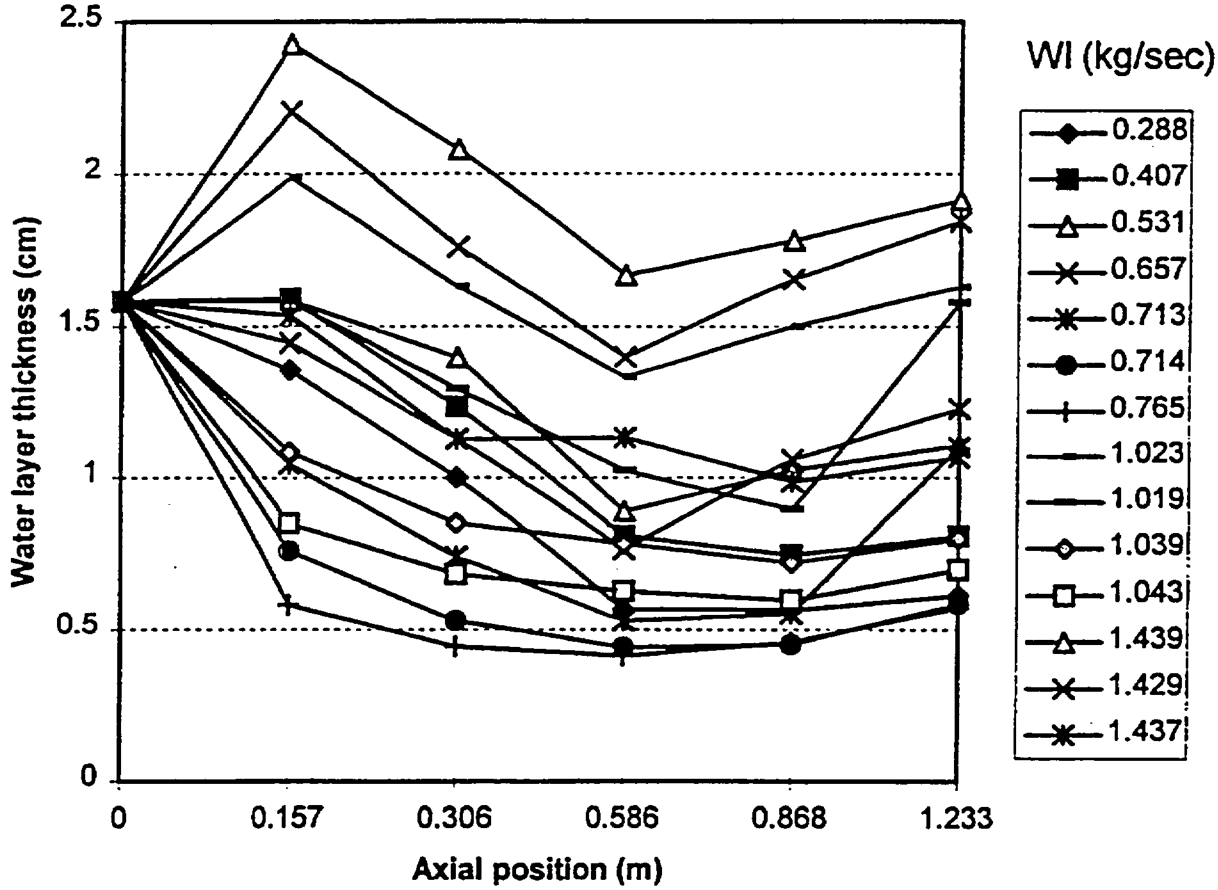

Figure 18-4. Measured Water Thickness Versus Axial Position for Various Liquid (WI) Flowrates and Inlet Water Layer Thickness of 1.583 cm

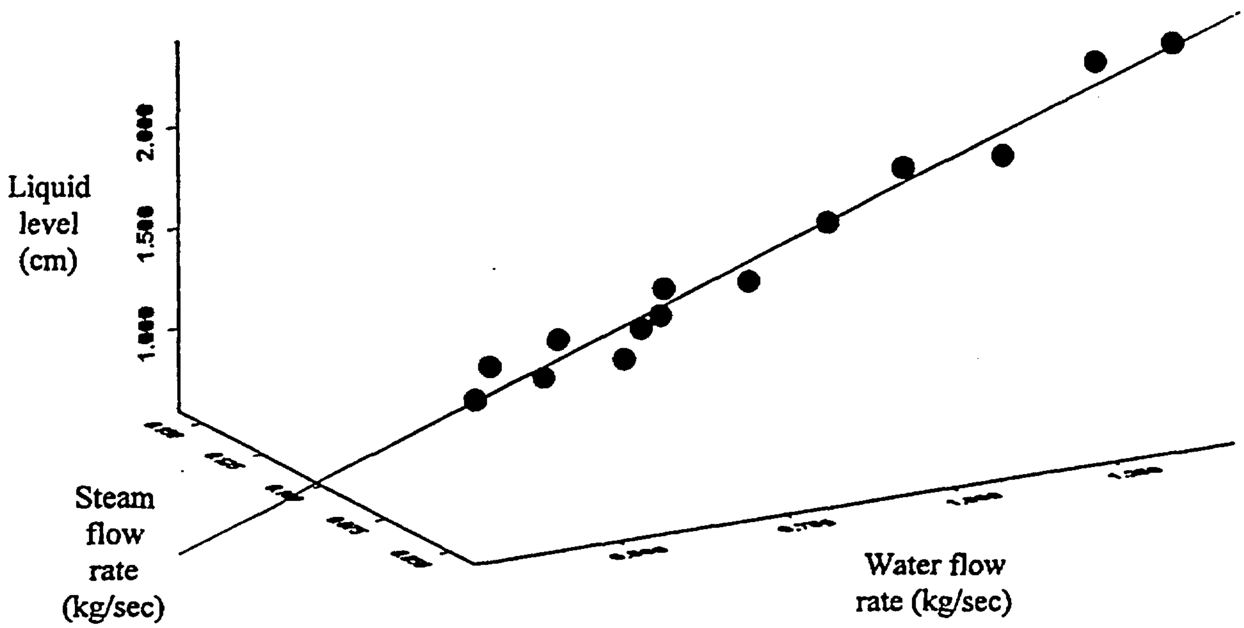

Figure 18-5. Measured Water Thickness at 0.157 m From the Channel Inlet Versus Liquid and Steam Flowrates

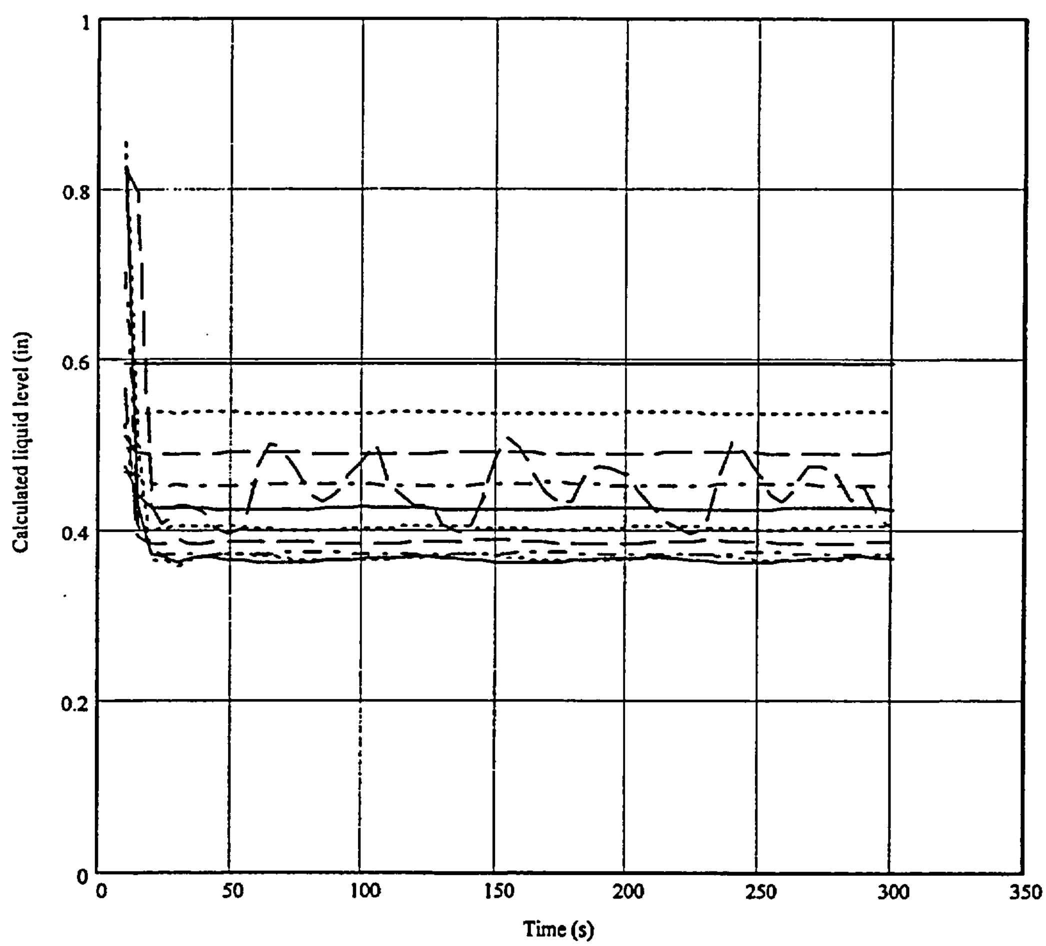

Figure 18-6. Calculated Liquid Level (Run 275)

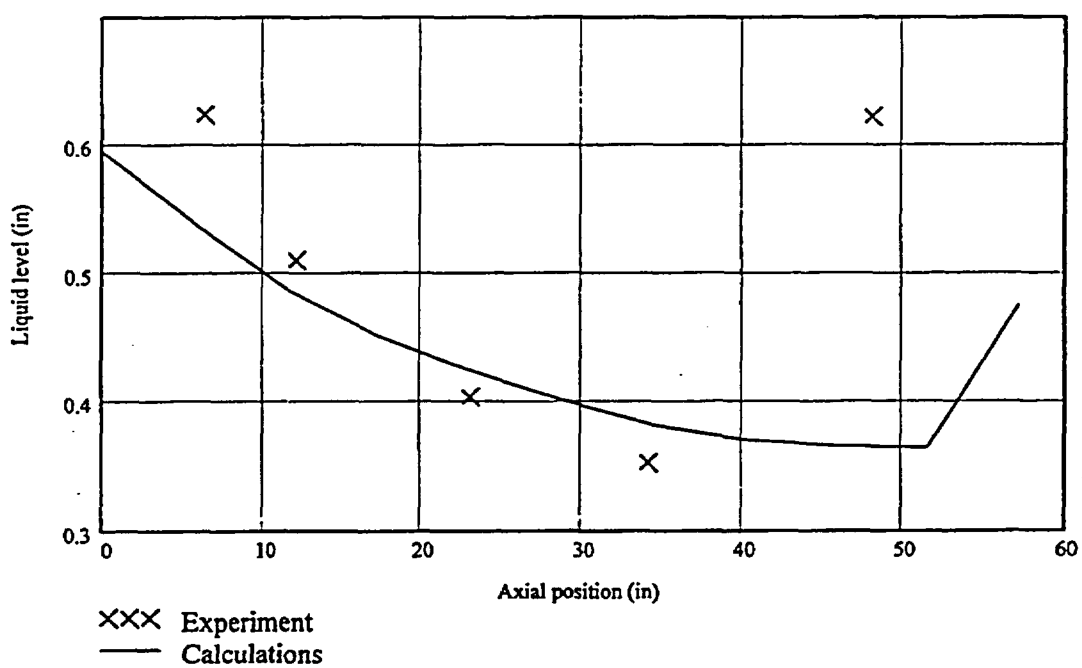

Figure 18-7. Calculated and Measured Liquid Levels Versus Axial Position (Run 275)

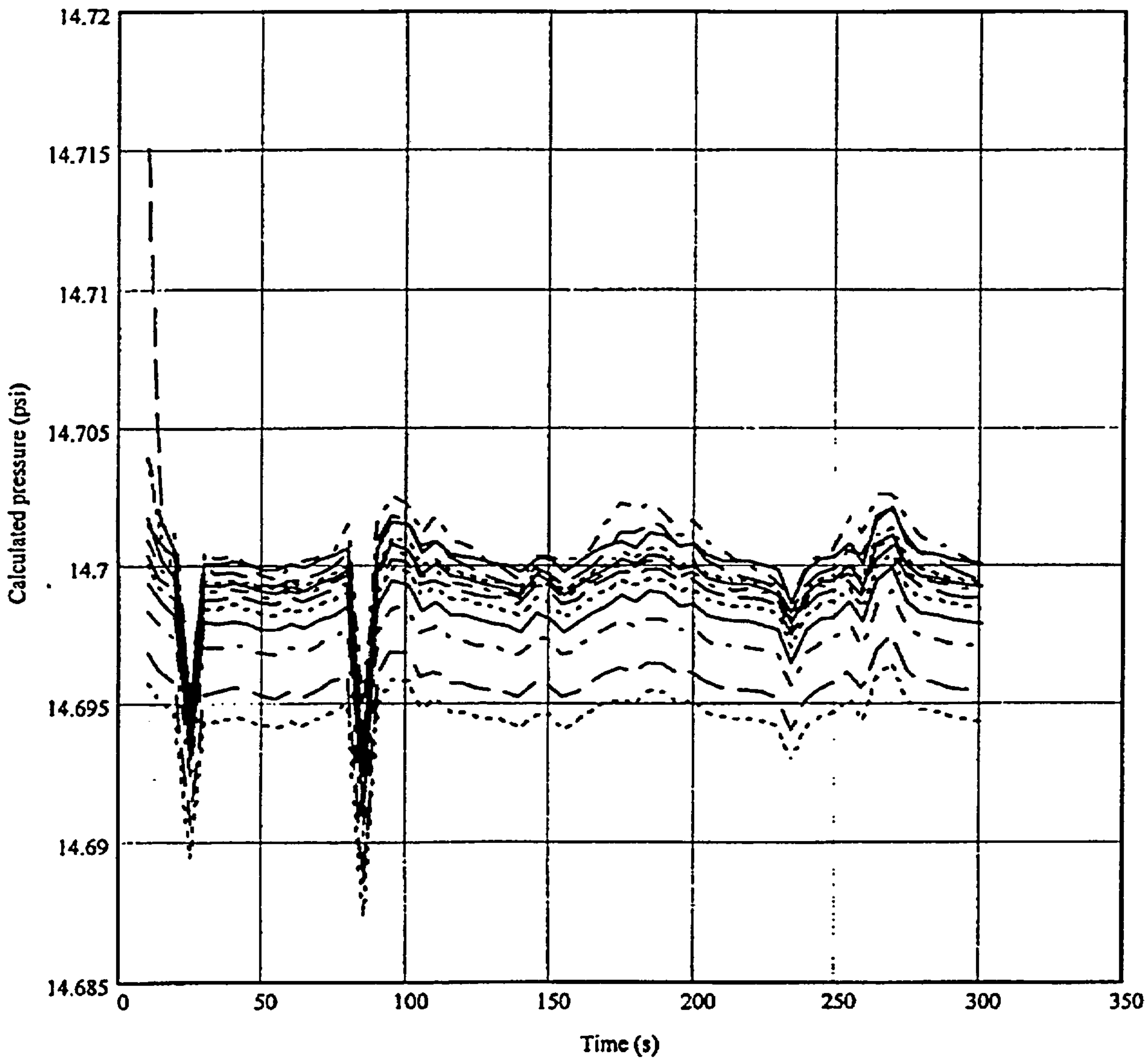

Figure 18-8. Calculated Steam Pressure (Run 275)

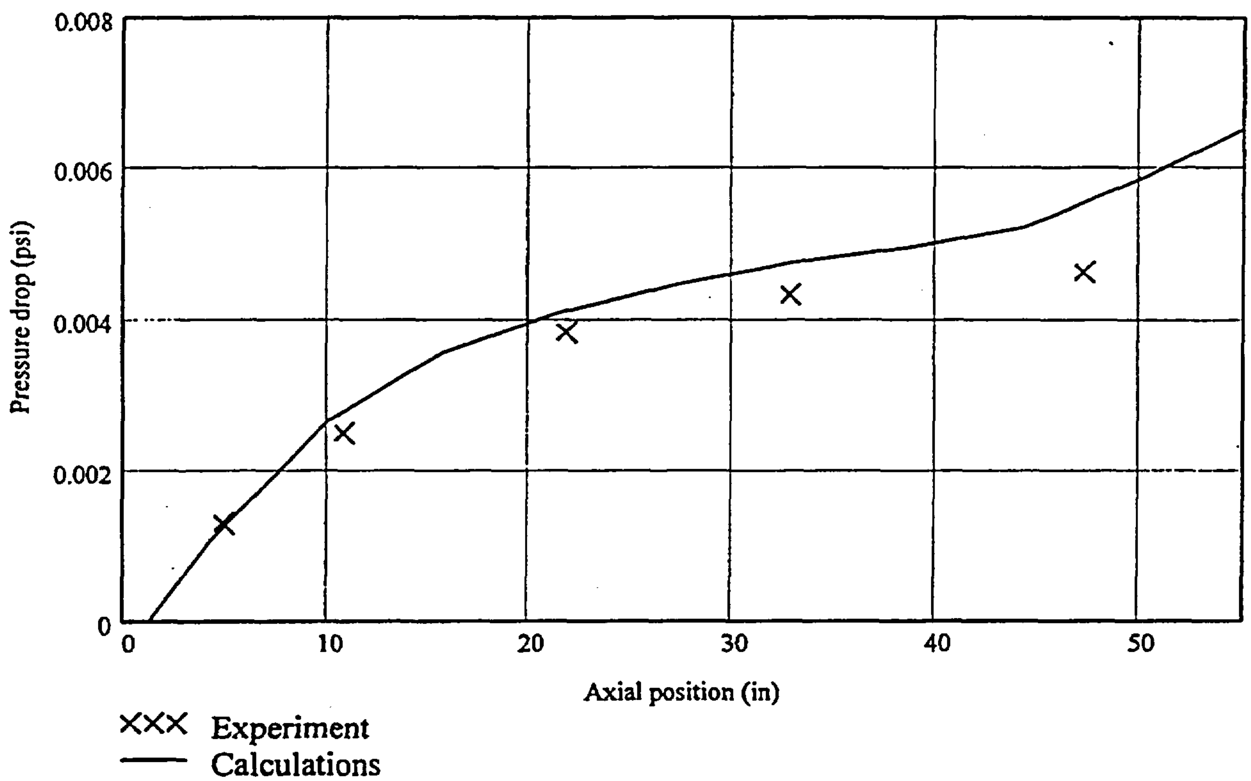

Figure 18-9. Calculated and Measured Steam Pressure Versus Axial Position (Run 275)

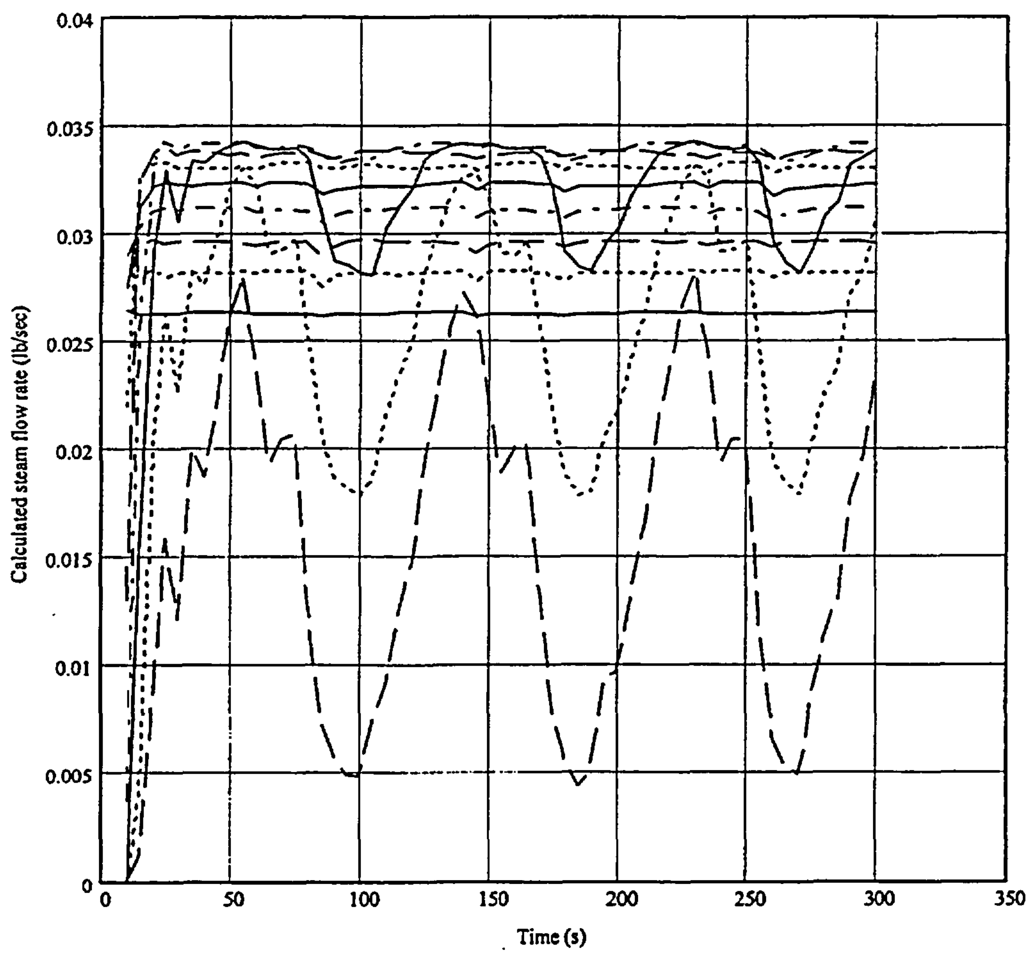

Figure 18-10. Calculated Steam Flowrate (Run 275)

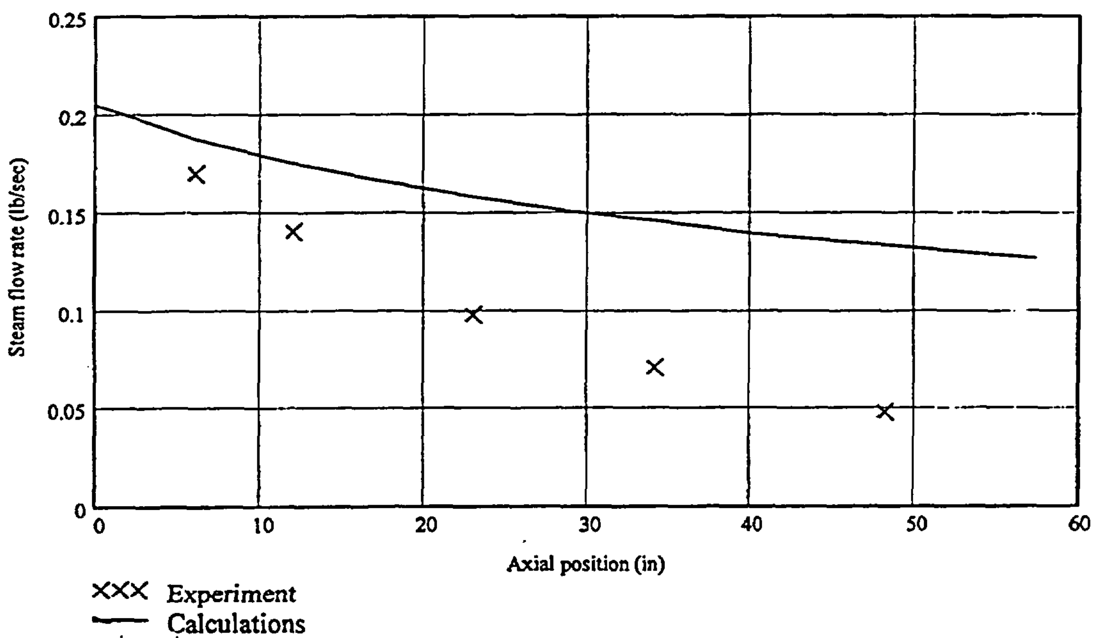

Figure 18-11. Calculated and Measured Steam Flowrate Versus Axial Position (Run 275)

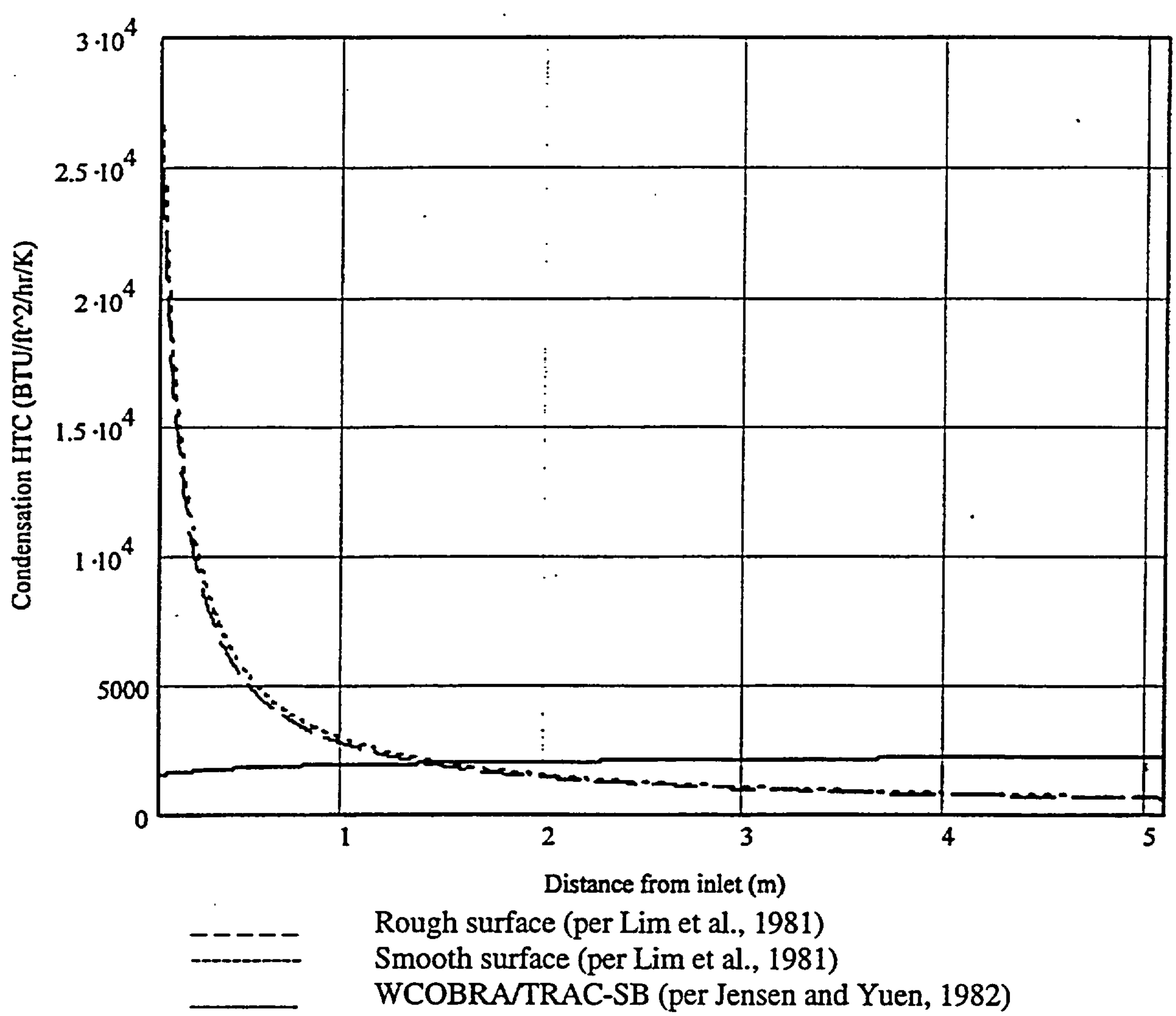

Figure 18-12. Comparison of Condensation Heat Transfer Correlations

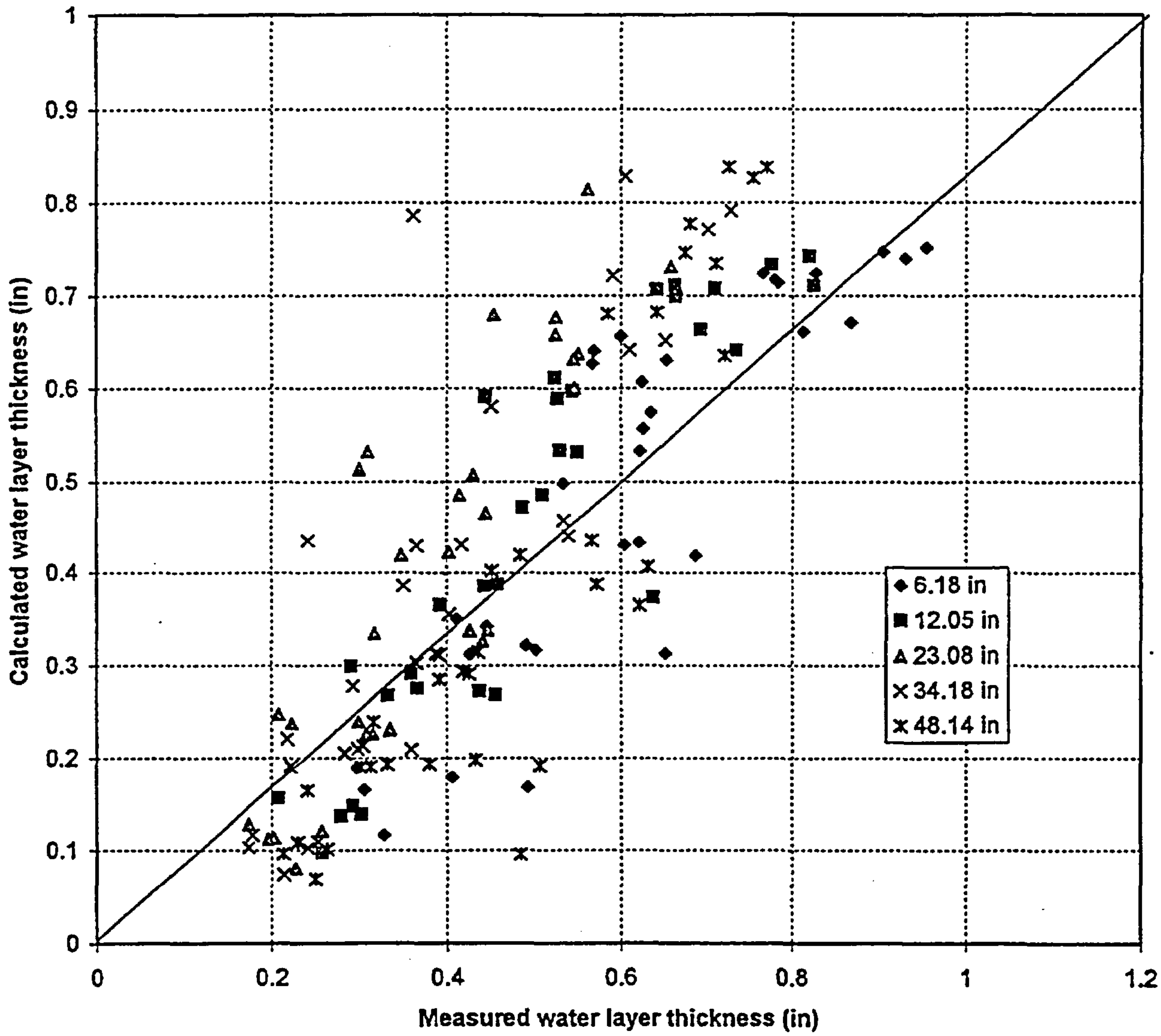

Figure 18-13. Predicted Versus Measured Liquid Level at Various Axial Locations

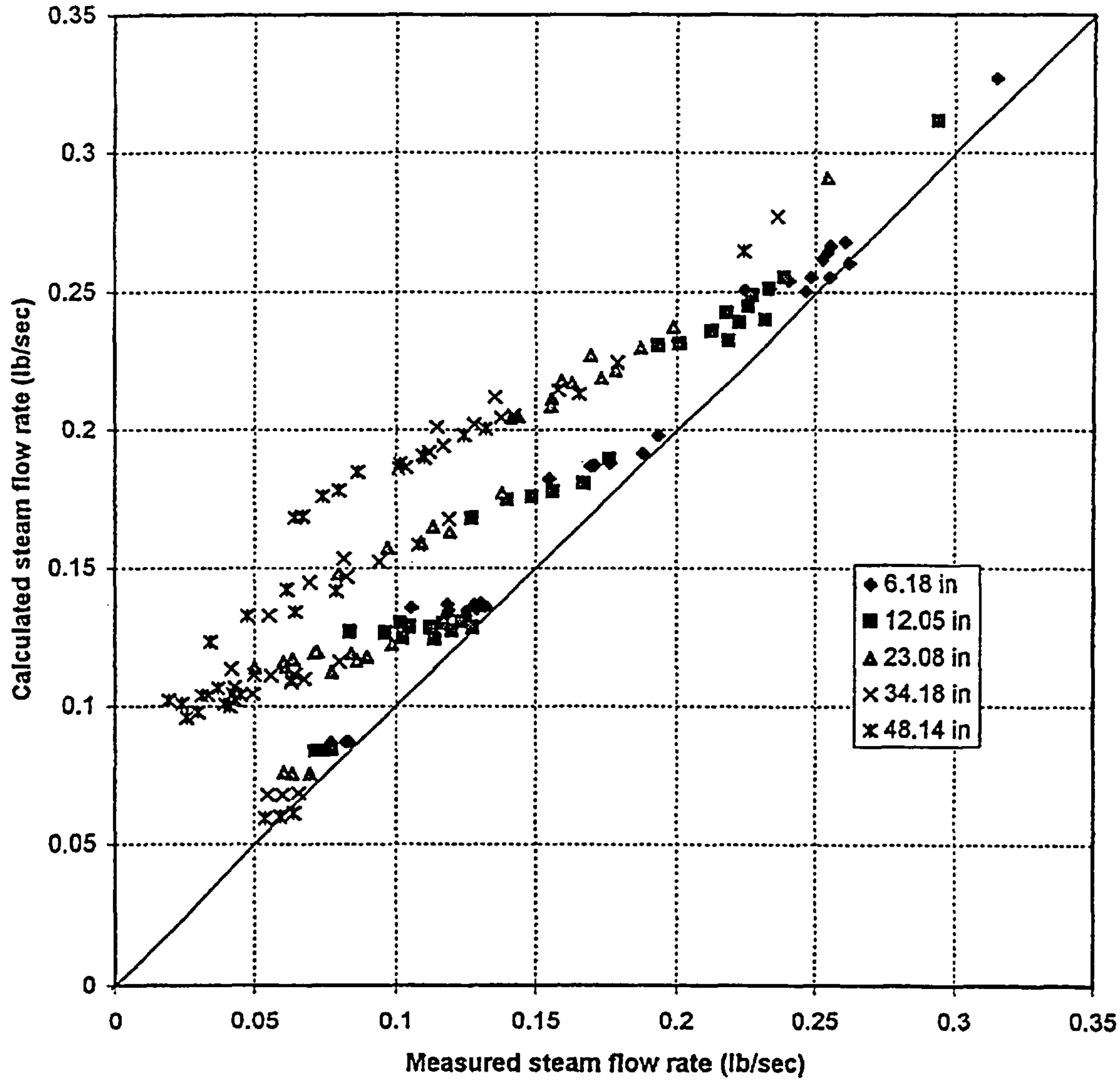

Figure 18-14. Predicted Versus Measured Steam Flowrate at Various Axial Locations

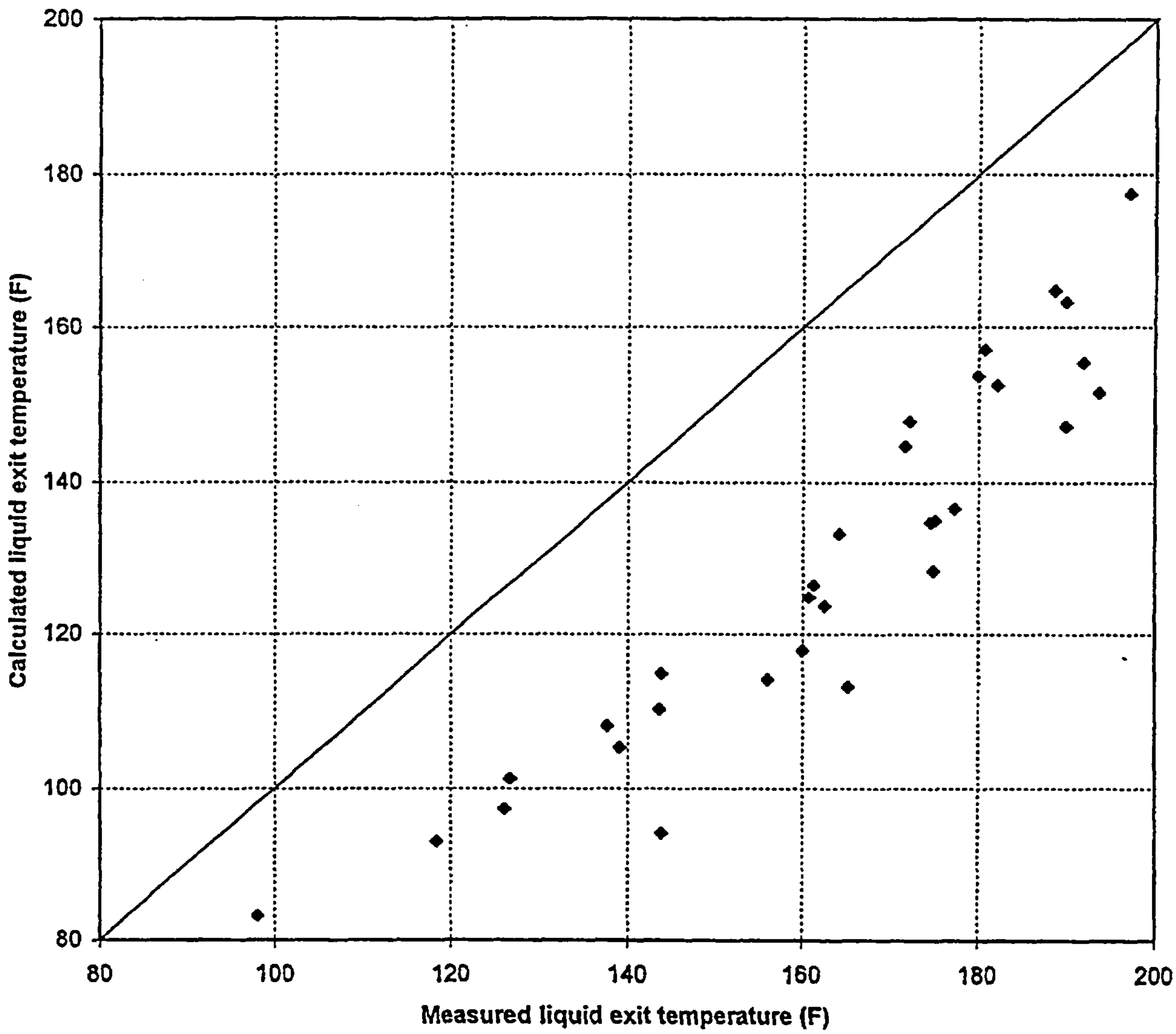

Figure 18-15. Predicted Versus Measured Liquid Temperature at the Channel Exit

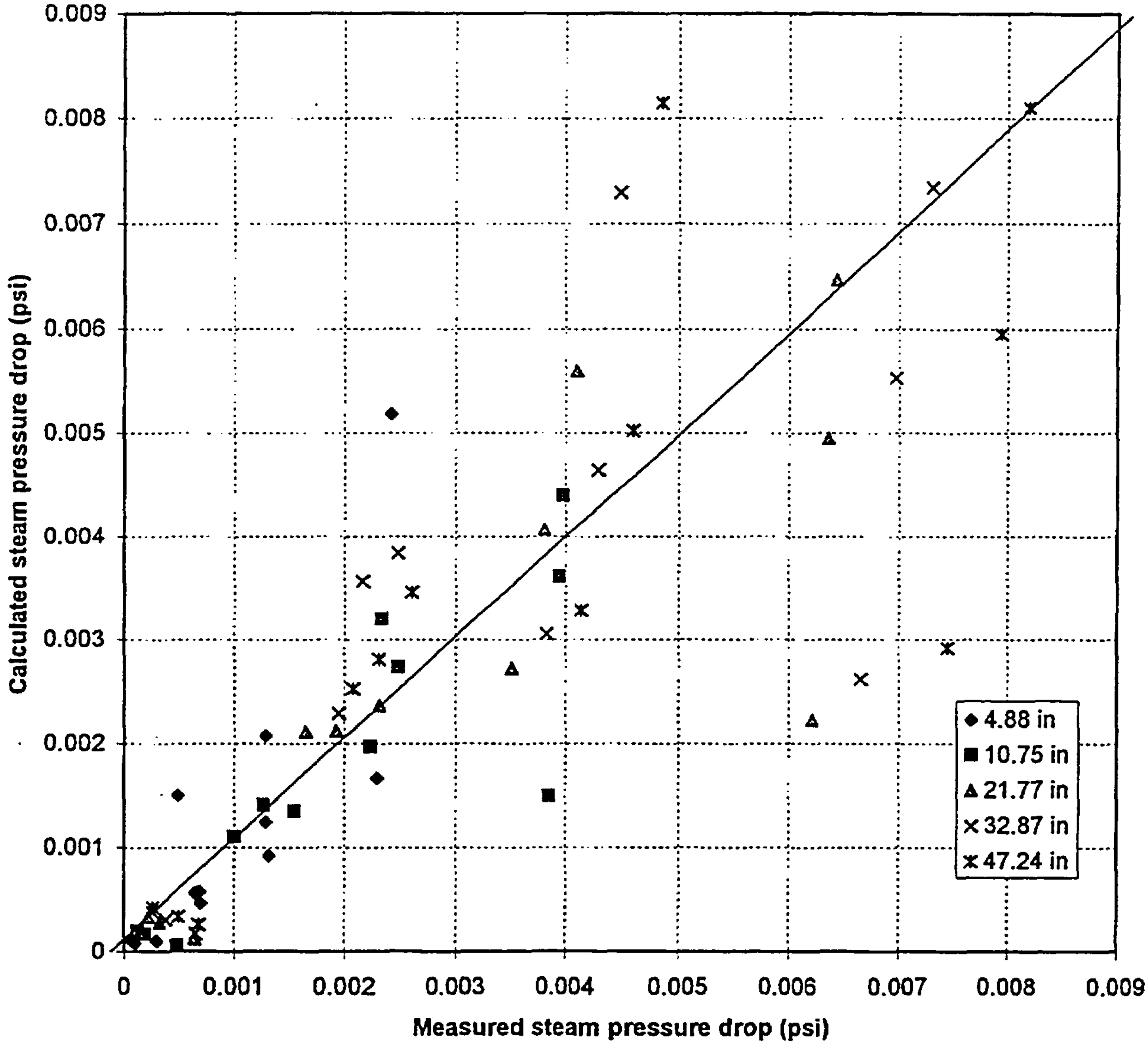

(Measurements were taken only during the following runs: 211, 231, 251, 253, 255, 257, 273, 275, 277, 293, 295, and 297)

Figure 18-16. Predicted Versus Measured Steam Pressure Drop at Various Axial Locations

SECTION 19
ROSA TEST SIMULATIONS

19-1 Introduction

The Rig-of-Safety Assessment Number 4 (ROSA-IV) program conducted a series of experiments to investigate the thermal-hydraulic behavior of a Westinghouse-designed four-loop PWR during small break LOCAs and operational transients using the Large Scale Test Facility (LSTF). The LSTF is a 1/48 volume scale representation of a Westinghouse four-loop 3423 MW_t PWR. Figure 19-1 is a schematic diagram of the facility. The LSTF consists of two equal volume loops, A and B, with the pressurizer attached to loop A. The elevations of the major components are full-scale to preserve natural circulation phenomena important to core cooling. The hot and cold legs, with a diameter of 8.15 inches, are sized to conserve volume scaling and the ratio of length to the square root of the pipe diameter ($L/\sqrt{D}$) of the reference PWR. Table 19-1 compares the major design characteristics of the LSTF and the PWR. The core contains 16 square 7x7 and 8 semicrescent heater rod assemblies. The heater rods are 0.374 inches in diameter and 12 feet in length.

The maximum power in the facility is 10 MW, which is equivalent to 14 percent of the scaled steady-state core power of the reference PWR.

The secondary coolant system consists of the steam generator, main and auxiliary feedwater pumps, and condensing system. The height of the LSTF steam generator is the same as in the reference PWR. The downcomer in the steam generators consists of four pipes located outside the steam generator vessel. The pipes are sized to give a representative volume and width. Each steam generator contains 141 U-tubes with 0.772 inches ID and 1.0 inches OD. Primary and secondary steam separators are included in each steam generator vessel.

The LSTF ECCS consists of a high pressure charging system, a high pressure injection system, a low pressure injection system, an accumulator system, and a residual heat removal system.

A detailed description of the facility is contained in the Japan Atomic Energy Research Institute (JAERI) document (JAERI-M 84-237, 1985).

This section describes the modelling and simulation of five ROSA tests using WCOBRA/TRAC-SB. The tests simulated were the 2.5-, 5-, and 10-percent cold leg breaks, each with the break at the middle of the pipe. This group of tests provides a break size sensitivity. Two other 2.5-percent cold leg break tests were also simulated: one with the break at the top of the pipe and the other with the break at the bottom. These provide a break orientation sensitivity. Comparisons between predicted and measured results are used to validate the WCOBRA/TRAC-SB code version and to identify possible compensating errors.

19-2 WCOBRA/TRAC Model of the LSTF

The WCOBRA/TRAC-SB nodalization of the LSTF uses a similar amount of detail in the vessel, steam generators, and loops as used in the PWR model. Figure 19-2 shows the WCOBRA/TRAC-SB noding of the LSTF pressure vessel. Because the LSTF is a two-loop facility, the vessel is modelled [

]a,c

The upper plenum modelling of the LSTF facility includes [

]a,c

Modelling of the LSTF hot and cold legs is shown in Figure 19-3. Each hot leg is modelled [ ]a,c

[

]a,c

The LSTF steam generators are shown in Figures 19-4 and 19-5. Primary flow enters the steam generator [

]a,c.

The steam generator secondary side includes sufficient detail to model recirculation in the downcomer and separation in the vapor dome region. [

]a,c

During steady-state simulation, and prior to reactor trip, steam leaving the generators passes through a TEE component and VALVE component to a constant pressure BREAK. At reactor trip, the main steam isolation valve (MSIV) is closed and flow goes through a VALVE component representing the main steam safety valve (MSSV) to a second BREAK component that provides a constant pressure boundary condition at the MSSV setpoint pressure.

Figure 19-6 shows the loop seal nodalization. Flow from the steam generator outlet passes through [

]a,c

The safety injection system is shown in Figure 19-7. Charging and high pressure safety injection flows to each loop are modelled [

]a,c

accumulator setpoint of 647.5 psia. The combined safety injection from the pumps and accumulators entered the cold legs through TEE components 10 and 19 to loops A and B respectively.

19-3 Steady-State Simulation

Verification that the WCOBRA/TRAC model of the LSTF adequately represented the facility was accomplished through a full-power, 100-second steady-state simulation. At the end of this 100-second simulation, predicted and measured flow parameters were compared to ensure reasonably good agreement by the model. Table 19-2 summarizes initial conditions used in the steady-state comparison.

Agreement was obtained between the simulated initial system pressure and initial test pressure. The comparison shows that the total core flow is underpredicted due to too high of an estimate of the core and loop flow resistance. As a result, T_{hot} is several degrees high. A good energy balance was achieved between the primary and secondary sides. The steady-state parameters are considered close enough for reliable transient calculations based on the WCOBRA/TRAC model of the facility.

19-4 Simulation of SB-CL-05, 5-Percent Cold Leg Break

Experiments as part of ROSA-IV were conducted for several different break areas. Test SB-CL-05 simulated a 5-percent cold leg break, which corresponds to approximately a 6-inch break in a PWR. The break was located in loop B and had a horizontal orientation. Safety injection flowrates corresponding to a single failure in the safety injection system were assumed. Experimental results are discussed by Kawaji (Kawaji, et al., 1986) and Tasaka (Tasaka, et al., 1988).

Operational setpoints for this test are listed in Table 19-3. The core power was scrammed once the primary pressure decreased below 1862 psia. At scram, the primary coolant pumps began to coast down, the main feedwater was stopped, and the steam generator secondaries were isolated by closure of the main steam isolation valves (MSIV).

In this test, the primary system rapidly depressurized to a pressure slightly higher than the secondary pressure, approximately 1150 psia, until the loop seal cleared at 140 seconds.

After loop seal clearance, the break quality changed from a low quality mixture to primarily vapor and the primary system continued to depressurize.

Test SB-CL-05 had a core depression during loop seal clearance that was considerably below the elevation of the bottom of the loop seal piping. Osakabe (Osakabe et al., 1987) attributed this to a large liquid holdup in the uphill steam generator tubes. During this core level depression, the cladding temperature increased by approximately 180°F reaching a maximum cladding temperature of approximately 830°F. After loop seal clearance, the core level recovered quickly. Accumulator injection began at 417 seconds and prevented a second core uncovery.

The WCOBRA/TRAC-SB simulation of the LSTF 5-percent cold leg break was initiated by attaching a PIPE component to the middle level of the loop B cold leg. The break unit in this test was aligned horizontally. Figure 19-8 shows the nodalization for modelling the break unit in the LSTF.

Table 19-4 compares the sequence of events in the simulation and the experiment. In the current modelling, the pressurizer pressure decreased more slowly than the experiment. This caused a delay in the generation of reactor trip and safety injection signal generation.

As the primary system continued to drain, a manometeric balance was set up between the core and downcomer, and the uphill and downhill sides of the loop seal piping. A deep depression in the core collapsed liquid level occurred as steam slipped through the loop seal piping toward the cold leg. The core level became depressed nearly to the bottom of the core, while liquid remained in the uphill side of the loop seal. At this time, the heater rods heated up rapidly. While most liquid had drained from the steam generator tubes, a level remained in the plenum and bottom of the uphill side.

After steam slipped through the loop seals, the core level recovered and most of the water was pushed out of both loop seals.

In this simulation, no core uncovery occurred following the loop seal clearance period. By 420 seconds, the primary system pressure decreased below 647.5 psia and accumulator injection began. At this time, the core remained covered with a low void fraction mixture and no heatup was predicted.

Figures 19-9 through 19-16 compare predicted and measured results for the 5-percent cold leg break test. Figure 19-9 compares predicted and measured primary system pressure. For the first 75 seconds of the simulation, the pressurizer pressure remains higher than the measurement while the pressure in the upper head is predicted lower than the data. Overprediction of pressurizer pressure for this period causes a delay in reactor trip and safety injection signals. The system depressurization slows down briefly near the hot leg saturation pressure; it then continues until both the primary and secondary pressures equilibrate at approximately 1200 psia in both the prediction and the test data. From about 100 seconds until loop seal clearance begins at 197 seconds, the predicted pressure increases approximately 50 psi. This increase is not observed in the data. The cause of this reduction in the primary to secondary heat transfer may be due to excessive liquid holdup/fluid stagnation in the steam generator tubes. As the liquid film hangs, the convective heat transfer from the primary side water to the tube is diminished. The primary pressure increases by an amount necessary to continue heat transfer with a higher primary to secondary temperature difference. After loop seal venting, the predicted pressure remains higher than the measurement. The accumulator setpoint pressure of 646 psia was reached 417 seconds into the test. The WCOBRA/TRAC-SB simulation depressurized to this value at 420 seconds.

Break flow is compared in Figure 19-10. Early in the transient, flow out of the break is subcooled, that is, single-phase liquid. During this period, with no discharge coefficient applied, WCOBRA/TRAC-SB slightly overpredicts the break flow. Between 50 and 150 seconds, the break flow is underpredicted in the simulation. During this period, break flow becomes two-phase in the calculation, some 100 seconds earlier than the test data. This mismatch is attributed partly to early overprediction of the break flow, which depleted the inventory faster, and to a higher core outlet initial temperature. Once the flow quality turns two-phase, the venturi meter used in the experiment becomes significantly unreliable and has great uncertainty at low mass flowrates. For that portion of the comparison, break mass flowrate derived from the catch-tank level is used. The derived flowrate is not responsive to the rapid changes in flow at the beginning of the transient. After 150 seconds, the break flow is slightly overpredicted compared to the data.

Loop seal venting occurs at approximately 140 seconds in the test. WCOBRA/TRAC-SB predicts loop venting initially at 195 seconds in the intact loop and continually through both loop seals after 200 seconds, as seen in Figures 19-11 and 19-12. The data also show venting through both loop seals. This delay relative to test data is likely due to the mismatch in break flow prediction.

As the loop seals vent, the collapsed liquid level in the core is depressed. Figure 19-13 compares the core liquid levels. During the initiation of loop seal venting, the predicted level is depressed nearly to the bottom of the core. The data also show a deep core level depression with the level decreasing well below the bottom of the loop seal piping to within 2 feet of the bottom of the core. After loop seal clearance, the core level recovers to approximately the level observed in the data.

Core heatup occurs during the loop seal clearance period while the core remains uncovered. Figure 19-14 compares the PCT predicted by WCOBRA/TRAC to the maximum cladding heatup observed in the data. The core uncovery period during the loop seal clearance event is overpredicted in the simulation. This results in a higher PCT compared to measured data.

The core uncovery during the loop seal clearance period depends upon the manometric balance between the core and downcomer, and the sum of pressure drops through the loop and uphill side of the loop seal piping. An important static head exists on the uphill side of the steam generator tubes, where water condensed in the tubes collects because of CCFL and flooding in the steam generator up-hill tubes. Figures 19-15 and 19-16 show collapsed liquid levels in the uphill steam generator tubes. The apparent high resistance in the bypass flow modelling between the downcomer and the upper head and excessive liquid holdup in the steam generators result in extended core level depression. Following loop seal clearance, the steam generator tubes drain briefly and then retain a small collapsed level.

Table 19-4 summarizes the predicted and recorded results for the 5-percent cold leg test.

19-5 Simulation of SB-CL-09, 10-Percent Cold Leg Side Break

One of the integral shakedown tests performed in the LSTF was a 10-percent cold leg break, which was the maximum break size for the facility design. This is a relatively large break size, corresponding to approximately a 9-inch break in a PWR, which could be considered more of an intermediate break as opposed to a small break LOCA. This break size is relevant, however, because limiting small break sizes may shift to larger equivalent diameters in other plants. The break was located in loop B, which was the loop without the pressurizer, and was oriented horizontally from the middle of the cold leg. The operational setpoints for this 10-percent break are listed in Table 19-5.

The 10-percent cold leg break test simulated using WCOBRA/TRAC-SB is the ROSA-IV experiment designated as run SB-CL-09. This test uses a conservative core power transient curve, which is significantly higher than the realistic power curve for the first 300 seconds of the transient. While the same experiment with realistic power curve, SB-CL-14, showed no significant rod heatup, this case exhibits large rod heatup during the loop seal clearing (Koizumi and Tasaka, 1988). In addition, lack of high pressure charging injection and high pressure safety injection resulted in the simulation predicting a core boiloff with rod heatup after the loop clearance event.

Predicted results for the 10-percent break are shown in Figures 19-17 to 19-24. Figure 19-17 depicts the primary system pressure. The prediction was found to depressurize rapidly during the first few seconds of the transient. By 30 seconds, the primary pressure equilibrates at the secondary side pressure until loop seal clearance. Accumulator injection begins at 198 seconds in the prediction.

The break flow is shown in Figure 19-18. Figure 19-19 shows the predicted core collapsed liquid level. The initial rapid depressurization of the primary side in the prediction causes the core to flash quickly. This is seen in the initial deep drop in the collapsed liquid level 12 seconds following the break. The broken side loop seal begins to clear at 80 seconds, and the intact side loop seal clears at 71 seconds as seen in Figures 19-20 and 19-21.

Liquid holdup on the uphill side of the steam generator tubes is shown in Figures 19-22 and 19-23. Both broken and intact side steam generators drain quickly because of the relatively large break size. The PCT prediction is shown in Figure 19-24; the calculated value does not reach the experimental value of 1135°F.

Table 19-6 summarizes the predicted results for the 10-percent cold leg test.

19-6 Simulation of 2.5-Percent Cold Leg Breaks

A set of three experiments – SB-CL-01, 02, and 03 – was conducted in the LSTF to investigate the effect of break orientation. All three tests simulated a 2.5-percent break in the cold leg, which approximates a 3-inch break in a PWR. In these experiments, the break was oriented at the side, bottom, and top of the loop B cold leg. Experimental results are summarized in the data report by Koizumi (Koizumi, et al., 1987). The test results showed that break orientation had only a small effect on system parameters such as pressure and core collapsed liquid level.

Figure 19-25 provides a description of the break geometry for these tests. These tests provide a useful means of evaluating the break flow model in WCOBRA/TRAC-SB for the effects of vapor pull-through and liquid entrainment near the break orifice.

Operational setpoints for the 2.5-percent cold leg break tests were the same as those shown in Table 19-3, with two exceptions. The charging and high pressure safety injection was delayed in these tests until 1200 seconds to force boiloff to occur, instead of the normal 12- and 17-second delays for these system flows. In addition, core power trip control turned the power off once the heater rod temperatures reached 1196°F in the experiment.

Figure 19-8 shows the break modelling used in the 2.5-percent cold leg break simulations. Results for the 2.5 percent cold leg side break are compared to data in Figures 19-26 through 19-30. Figure 19-26 compares the predicted and measured primary system pressure. Over the first 200 seconds of the transient, WCOBRA/TRAC-SB tends to slightly underpredict the pressure. By 200 seconds, however, both the predicted and measured pressures have equilibrated with secondary side pressure at approximately 1200 psia. Between 200 and 400 seconds, WCOBRA/TRAC-SB overpredicts the system pressure. Furthermore, WCOBRA/TRAC-SB predicted the pressure to slightly increase, which is not observed in the data. After loop seal clearance, the predicted and measured pressures are in good agreement.

Figure 19-27 shows a comparison of predicted and measured break flows. Early in the transient, until 350 seconds, the break flow is underpredicted, after which it is overpredicted for a time. The code underprediction of the SB-CL-01 breakflow leads to an overprediction of the time to loop seal clearance. A comparison of the vessel collapsed liquid level is shown in Figure 19-28. The agreement is good when comparing the times of loop seal clearance (462 seconds in the simulation versus 380 in the test). Neither the data nor the prediction shows enough of a core level depression to cause a significant core heatup at this time, as seen in Figure 19-29; one does occur later as the boiloff period begins. The reason for the lack of a severe loop seal clearance level depression in the core can be explained by Figure 19-30. Because of the small break size, the transient proceeds at a relatively slow rate. Liquid held up in larger breaks in the uphill steam generator tubes drains, and the tubes are nearly voided by the time loop seal venting occurs. The additional static head due to liquid in the steam generator tubes is not present, and less of a core level depression is required to maintain a manometric balance with the loop seal. The characteristic deep core uncovery during loop seal clearance in other ROSA-IV tests does not occur.

The boiloff period is turned around with the accumulator injection. In the experiments, the core power was tripped once the heater cladding temperatures reached almost 1200°F. The core remains covered with the help of safety injection, which was manually delayed until 1200 seconds. In the simulations, the power is tripped once the PCT reached 1196°F, stopping a further increase in the cladding temperatures. The power trip also reverses the core boiloff, and the core collapsed liquid level starts to recover. The transients for the top and bottom breaks were terminated before a full level recovery was observed for these cases.

The timing of key events for experiments with side, bottom, and top orientation is given by Tables 19-7 through 19-9, respectively.

Test results for the three 2.5-percent breaks showed relatively little difference in break flowrate (Koizumi, et al., 1988). The experimental break flowrates are shown in Figure 19-31A. A comparison of the predicted break flowrates is shown in Figure 19-31B. Similar to the experimental data, the break orientation had only a small effect on the predicted break flow. The test data for all three orientation breaks show no difference in break flowrate until 100 seconds. However, the test data show that the break flows diverge from each other when the break flow quality turns two-phase. First, the top break and side break discharge becomes two-phase, and the discharge flowrate reduces abruptly. The last to become two-phase is the bottom break. Change in the break flow from single-phase subcooled discharge to high-void two-phase discharge is predicted in a consistent manner for top and bottom break orientations. The bottom break takes longer to become two-phase because the level in the cold leg needs to drop to break location. However, because most of the liquid is exhausted, the break flowrate then reduces below the top orientation flow. This detail is predicted in the simulations. The side break case did not produce a consistent prediction with the data; it exhibits an increase in break flow after the initial abrupt drop.

While the test data showed that break orientation had only a minor effect on the break flowrate, the orientation did affect the timing of the loop seal clearance and core uncovery. In the test data, of Figure 19-32A, the side break orientation had the earliest loop seal clearance time, then the top break and the bottom break vented at almost the same time. Also, the bottom break produces an earlier and deeper uncovery in the boiloff period. In the simulations, as in the tests, the side break was the first one to vent; the bottom and top breaks vent later as shown in Figure 19-32B. The sequence in which loop seal clearing occurs as a function of break orientation is well predicted by WCOBRA/TRAC-SB, although the timing is delayed from the data in every case.

Figures 19-32A and 19-32B provide a comparison of measured and predicted core levels for the top, side, and bottom 2.5-percent breaks. In the test data, the start of the boiloff period for the bottom break occurs first, and the side break boiloff began prior to the top break. The timing of the onset of the core boiloff period in the predictions shows the top and side break begin at almost the same time, later than for the bottom break; as in the test data, the bottom break exhibits the most rapid core uncovery.

Figures 19-33A and 19-33B indicate that the WCOBRA/TRAC-SB simulations show the general two-phase level characteristics of the experiments. Top and side breaks maintain a higher mixture level in the broken cold leg compared to the bottom-oriented break.

The core heatup rate during the boiloff period is adequately predicted. Figure 19-34A shows the cladding temperature for an 8.67-foot rod elevation. Figure 19-34B depicts the code-predicted temperatures at the same elevation for 2.5-percent break cases. Simulations were ended at 975 seconds for the side-oriented case and 1114 seconds for the bottom-oriented case.

19-7 Summary of Results

This section describes the predicted results for five different ROSA-IV/LSTF small-break tests. The simulations provide an adequate representation of the test data. The loop seal clearance behaviors are predicted with acceptable accuracy, and core uncovery predictions that closely agree in magnitude with the test data produce cladding heatup predictions comparable to those in the data. Liquid holdup in the steam generator tubes appears to be predicted with good accuracy in the SB-CL-01 simulation, although in the 5-percent cold leg break simulation, the code prediction of liquid holdup in the steam generators appears to lead to a repressurization of the primary side.

WCOBRA/TRAC-SB results for the 5-percent cold leg break case show the discharge of single-phase subcooled liquid at high pressures is overpredicted slightly in the initial 50 seconds when compared against the available data, then underpredicted. The break flowrates in the 2.5-percent series of test simulations trend well with the data with the exception of an early surge in the side orientation case (SB-CL-01) result. In both the 5-percent and 2.5 percent break size predictions, the underprediction of break flow causes a delay in the predicted time of loop seal clearance.

The timing of the initiation and the turnaround of the boiloff period in the 2.5-percent bottom and side break cases are in general well predicted, although in the top break case the boiloff is predicted to begin earlier than in the SB-CL-03 data. Because the power was tripped at a preset heater temperature, the PCTs are exactly predicted.

19-8 References

JAERI-M 84-237, 1985, "ROSA-IV Large Scale Test Facility (LSTF) System Description."

Kawaji, M., et al., 1986, "ROSA-IV/LSTF 5% Cold Leg Break LOCA Experiment Data Report, Run SB-CL-05," JAERI-memo 61-056.

Koizumi, Y., et al., 1987, "ROSA-IV/LSTF 2.5% Cold Leg Break LOCA Experiment Data Report for Runs SB-CL-01, 02 and 03," JAERI-memo 62-399.

Koizumi, Y., et al., 1988, "Investigation of Break Orientation Effect During Cold Leg Small-Break LOCA at ROSA-IV LSTF," Nucl. Sci. and Tech., 25.

Koizumi, Y. and Tasaka, K., 1988, "Quick Look Report for ROSA-IV/LSTF 10% Cold Leg Break LOCA Test, SB-CL-14," JAERI-memo 62-262.

Osakabe, M., et al., 1987, "Core Liquid Level Depression due to Manometric Effect during PWR Small Break LOCA," J. of Nucl. Sci. and Tech., 24.

Tasaka, K., et al., 1988, "The Results of 5% Small Break LOCA Tests and Natural Recirculation Tests at the ROSA-IV LSTF," Nucl. Eng. Des., 108.

Table 19-1
Major Design Characteristics of LSTF and PWR

Characteristic	LSTF	PWR	PWR/LSTF
Pressure (psia)	2250	2250	1
Temperature (°F)	617	617	1
Number of fuel rods	1064	50,952	48
Core height (ft)	12	12	1
Fluid volume (ft^3)	255.2	12,254.2	48
Core power (MW)	10	3423(t)	342
Power density (kW/ft^3)	39.64	280.34	7.1
Core inlet flow (lbm/s)	97.6	33,400	342
Downcomer gap (in.)	2.09	10.24	4.9
Hot leg			
Diameter (D) (ft)	0.679	2.418	3.56
Length (L) (ft)	12.1	22.93	1.89
$L/\sqrt{D}$ ($ft^{1/2}$)	14.76	14.76	1.0
$\frac{\pi}{4} D^2 L$ (m^3)	0.124	2.98	24.0
Number of loops	2	4	2
Number of tubes in steam generator	141	3382	24.0
Length of steam generator tube (average) (ft)	66.3	66.3	1.0

Table 19-2
Steady-State Parameter Checklist

Parameter	Target	Predicted
Pressurizer pressure (psia)	2262	2257.9
Hot leg fluid temperature (°F)	619	626.2
Cold leg fluid temperature (°F)	557.6	553.7
Core power (MW)	10	10.0
Core inlet flowrate (lbm/s)	108.7	94.1
Pressurizer water level (ft)	8.53	8.64
Pump speed (rpm)	800	800.0
Pressure vessel top-bottom ΔP (psi)	10.76	10.99
Hot leg A ΔP (psi)	0.5	1.4
Steam generator loop A inlet to tube top ΔP (psi)	10.88	11.57
Cold leg A ΔP (psi)	0.1	0.04
Upper plenum - downcomer ΔP (psi)	0.6	3.85
Steam generator secondary pressure (psia)	1055	1055.0
Steam generator secondary level (ft)	33.78	31.23
Steam generator feedwater temperature (°F)	431.6	431.6
Steam generator feedwater flowrate (lbm/s)	5.95	6.09
Steam generator steam flowrate (lbm/s)	5.95	5.91/5.88

Table 19-3
Operational Setpoints for Run SB-CL-05

Event	Setpoint
Reactor scram signal (psia)	1862
Initiation of RCP coastdown	With reactor scram
Safety injection signal (psia)	1761.5
High pressure charging	12 s after safety injection signal
Safety injection	17 s after safety injection signal
Accumulator injection (psia)	647.5
Low pressure injection (psia)	185.2
Main feedwater termination	With reactor scram
Turbine throttle valve closure	With reactor scram
Auxiliary feedwater initiation	28 s after reactor scram

Table 19-4
Transient Results Summary for 5-Percent Cold Leg Side Break

Event	Data	Prediction
Break (s)	0	0
Reactor trip (s)	12	24.0
MSIV closure (s)	15	25.0
Safety injection signal (s)	17	32.1
Steam generator feedwater stop (s)	18	23.0
Charging injection ON (s)	31	44.1
High pressure safety injection ON (s)	34	49.1
Auxiliary feedwater ON (s)	40	51.0
Core uncovery (s)	120 to 155	135 to 210
PCT (°F)	830	850
Minimum vessel collapsed liquid level (ft)	1.4	1.9
Loop seal clearing (s)	140	197
Accumulator injection ON (s)	417	420
Accumulator injection OFF (s)	1447	> 500[a]

a. Transient calculation terminated at 500 seconds.

Table 19-5

Operational Setpoints for Run SB-CL-09

Event	Setpoint
Reactor scram signal (psia)	1862
Initiation of RCP coastdown	With reactor scram
Safety injection signal (psia)	1761.5
High pressure charging	Not actuated
Safety injection	Not actuated
Accumulator injection (psia)	647.5
Low pressure injection (psia)	185.2
Main feedwater termination	With reactor scram
Turbine throttle valve closure	With reactor scram
Auxiliary feedwater initiation	Not actuated

Table 19-6
Chronology of Events for Run SB-CL-09, 10-Percent Cold Leg Side Break

Events	Predicted Time (s)
Break	0.0
Reactor trip	10
Main steam line valve close	11
Loop seal clearing	71
Primary to secondary pressure reversal	104
Accumulator injection on (ACC-cold)	198

Table 19-7
Chronology of Events for Run SB-CL-01, 2.5-Percent Cold Leg Side Break

Events	Measured Time (s)	Predicted Time (s)
Break	0	0.0
Reactor trip	15	13
Safety injection signal	19	21
Main steam line valve close	20	14
RCPs stop	272	~280
Loop seal clearing	380	462
Primary to secondary pressure reversal (loop B)	380	464
Primary to secondary pressure reversal (loop A)	460	464
Core dryout	600 to 980	608 to 975[a]
Accumulator injection on (ACC-cold)	835	882
Core power trip	872	919
High pressure charging injection on	1199	>975[a]
High pressure safety injection on	1200	–
Low pressure injection on	1446	–
Accumulator injection off	1460	–
Experiment terminated (break unit close)	2429	–

a. Transient calculation is terminated at 975 seconds.

Table 19-8

Chronology of Events for Run SB-CL-02, 2.5-Percent Cold Leg Bottom Break

Events	Measured Time (s)	Predicted Time (s)
Break	0	0
Reactor trip	16	13
Safety injection signal	21	20
Main steam line valve close	21	14
RCPs stop	273	~280
Loop seal clearing	446	468
Primary to secondary pressure reversal (loop B)	450	471
Primary to secondary pressure reversal (loop A)	550	471
Core dryout	600 to 970	587 to 1093
Core power trip	846	877
Accumulator injection on (ACC-cold)	853	856
High pressure charging injection on	1201	>1114.3[a]
High pressure safety injection on	1201	–
Low pressure injection on	1464	–
Accumulator injection off	1471	–
Experiment terminated (break unit close)	2409	–

a. Transient calculation is terminated at 1114.3 seconds.

Table 19-9

Chronology of Events for Run SB-CL-03, 2.5-Percent Cold Leg Top Break

Events	Measured Time (s)	Predicted Time (s)
Break	0	0
Reactor trip	16	13
Main steam line valve close	20	14
Safety injection signal	21	20
RCPs stop	272	~280
Loop seal clearing	430	474
Primary to secondary pressure reversal (loop B)	430	474
Primary to secondary pressure reversal (loop A)	490	474
Core dryout	670 to 1030	618 to 1015
Accumulator injection on (ACC-cold)	914	889
Core power trip	957	1006
High pressure charging injection on	1201	1200
High pressure safety injection on	1201	1200
Accumulator injection off	1479	1396
Low pressure injection on	1507	N/A[(b)]
Low pressure injection system off	1961	N/A[(b)]
Experiment terminated (break unit close)	2731	–

a. Transient calculation is terminated at 2000 seconds.

b. This was not modelled.

Table 19-10
2.5-Percent Cold Leg Break Loop Seal Venting Times

Break Orientation	Measured (s)	Predicted (s)
Top	450	474
Side	380	462
Bottom	450	468

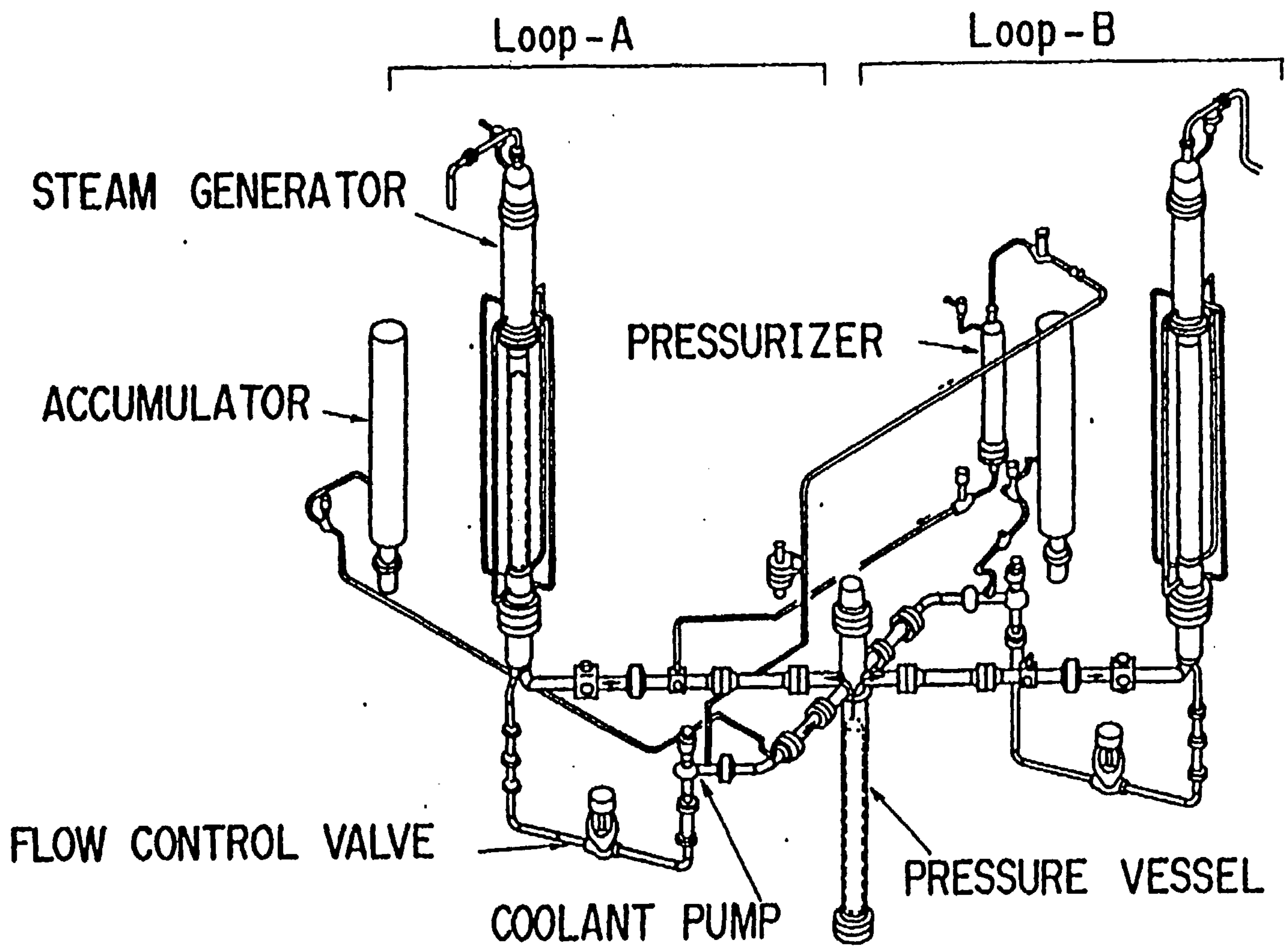

Figure 19-1. Schematic Diagram of LSTF

a,c

Figure 19-2. WCOBRA/TRAC-SB Model of LSTF Pressure Vessel

a.c

Figure 19-3. WCOBRA/TRAC-SB Model of LSTF Hot and Cold Legs

a,c

Figure 19-4. WCOBRA/TRAC-SB Model of LSTF Loop A Steam Generator

a,c

Figure 19-5. WCOBRA/TRAC-SB Model of LSTF Loop B Steam Generator

a,c

Figure 19-6. WCOBRA/TRAC-SB Model of LSTF Loop Seals

a,c

Figure 19-7. WCOBRA/TRAC-SB Model of LSTF Safety Injection

a,c

Figure 19-8. Nodalization of LSTF Break Unit

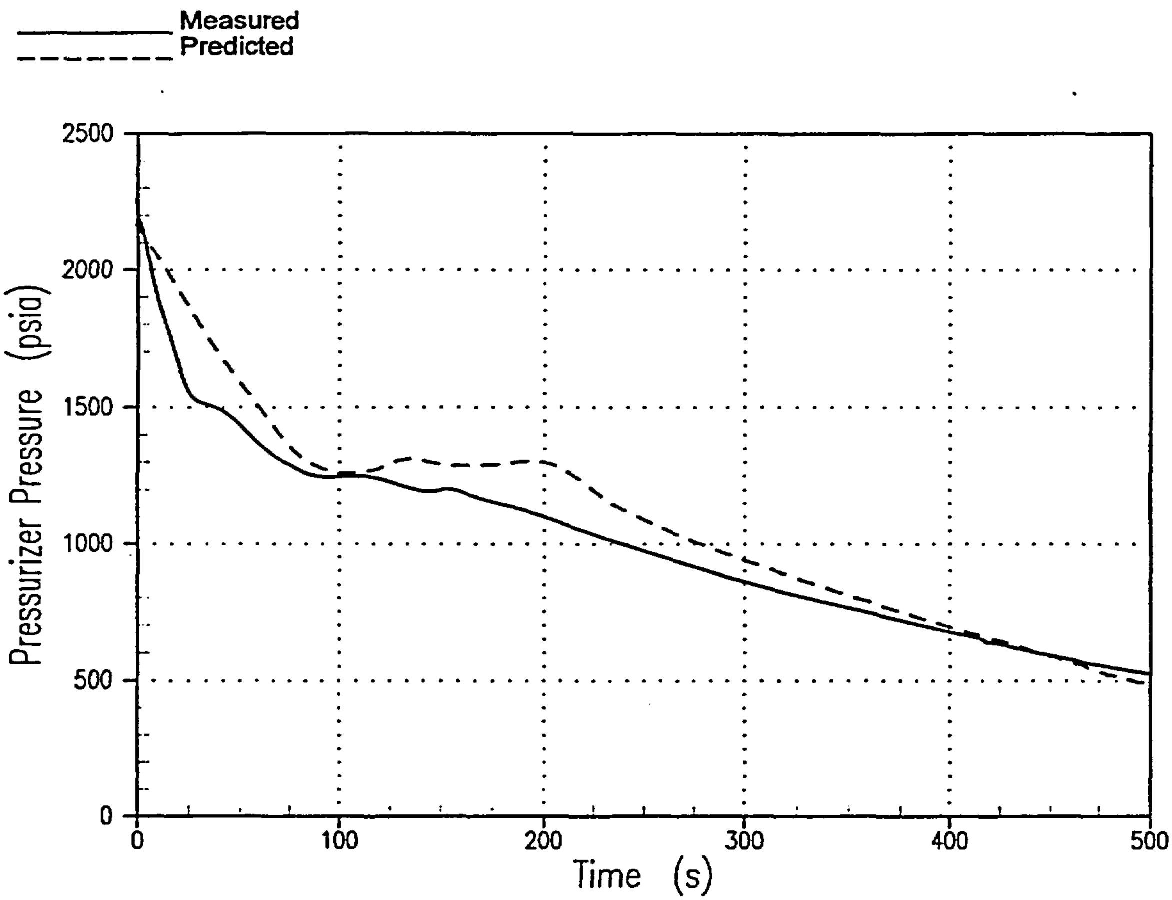

Figure 19-9. Comparison of Predicted and Measured Primary System Pressure, ROSA 5-Percent Cold Leg Side Break

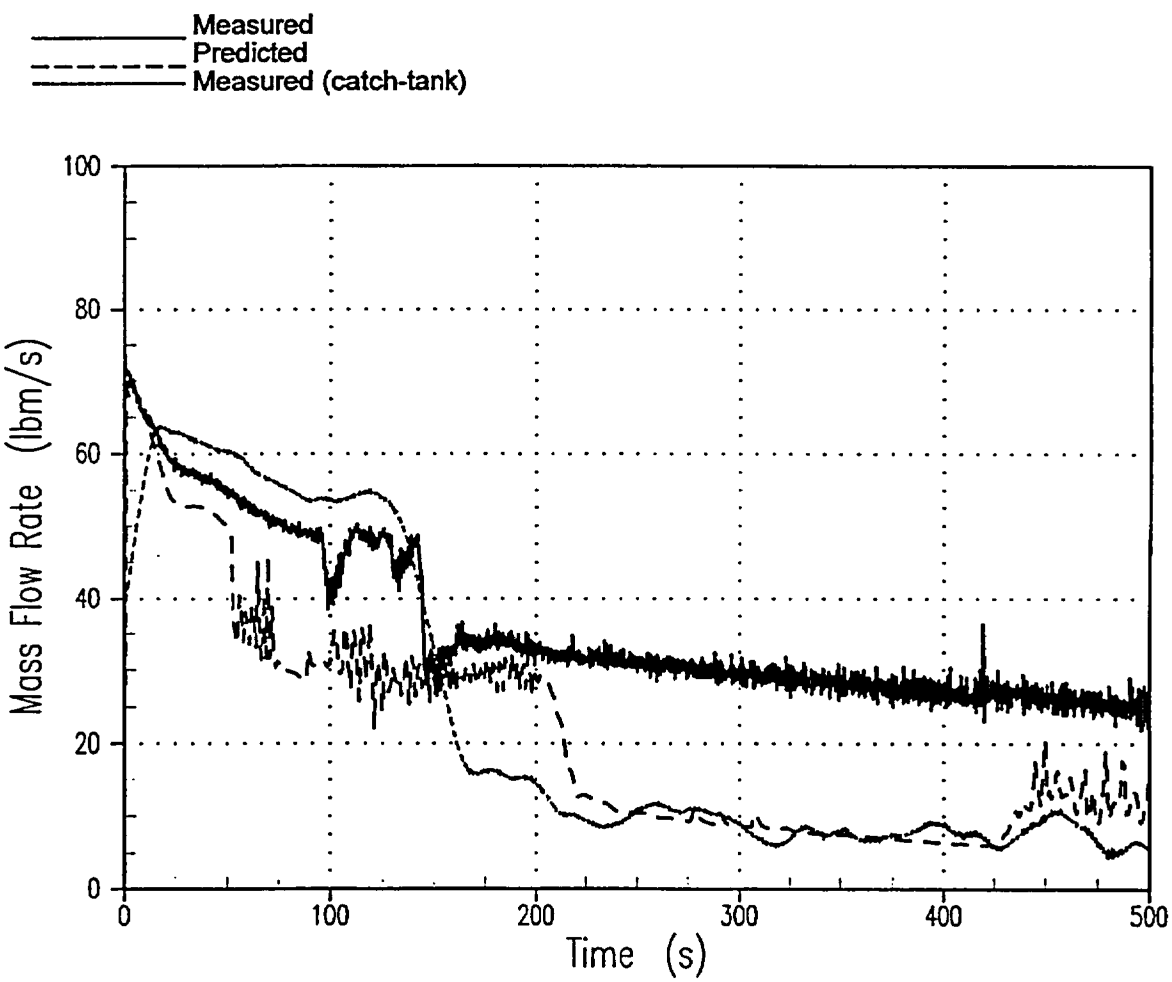

Figure 19-10. Comparison of Predicted and Measured Break Flowrates, ROSA 5-Percent Cold Leg Side Break

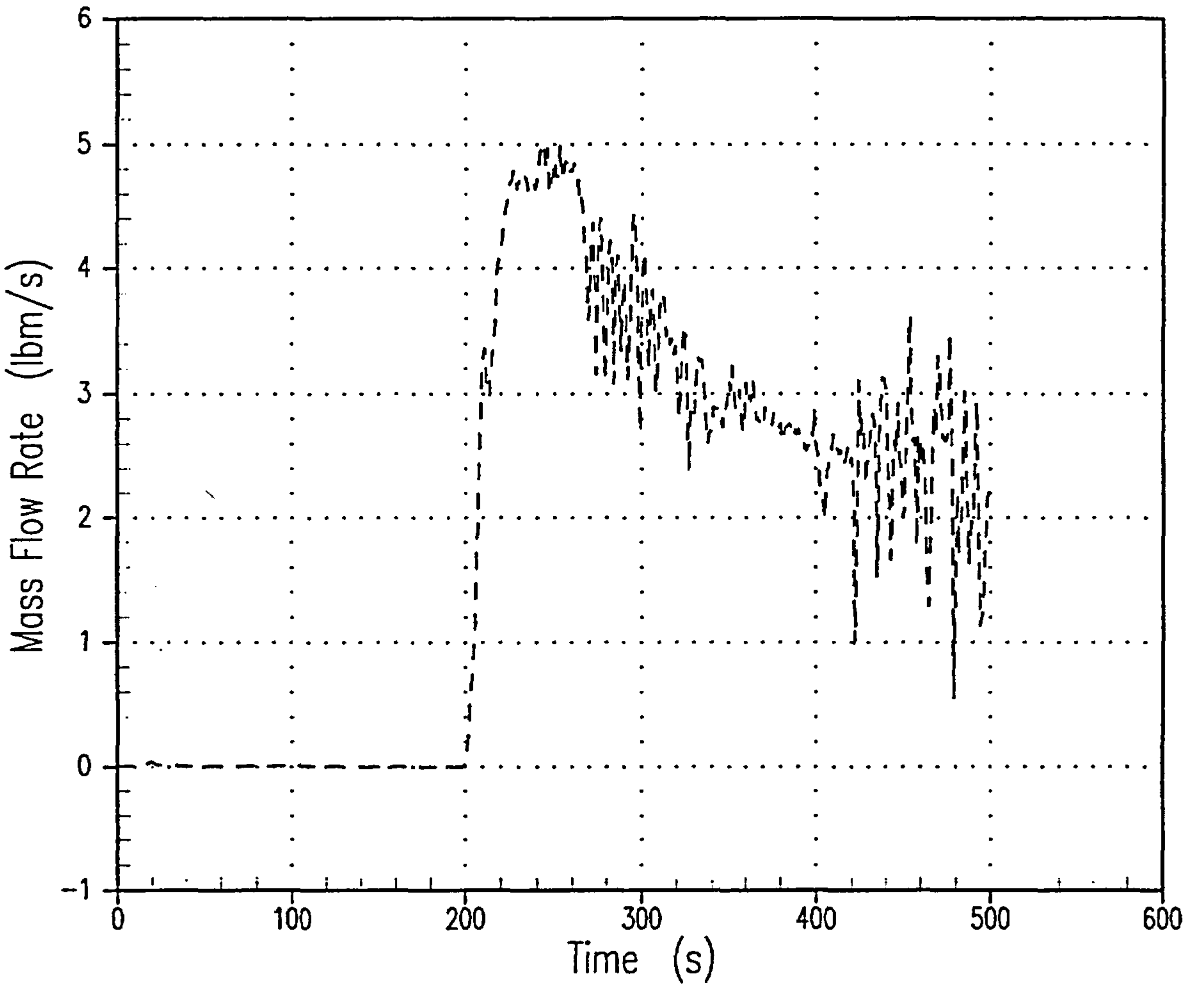

Figure 19-11. Predicted Intact Loop Seal Steam Flowrate, ROSA 5-Percent Cold Leg Side Break

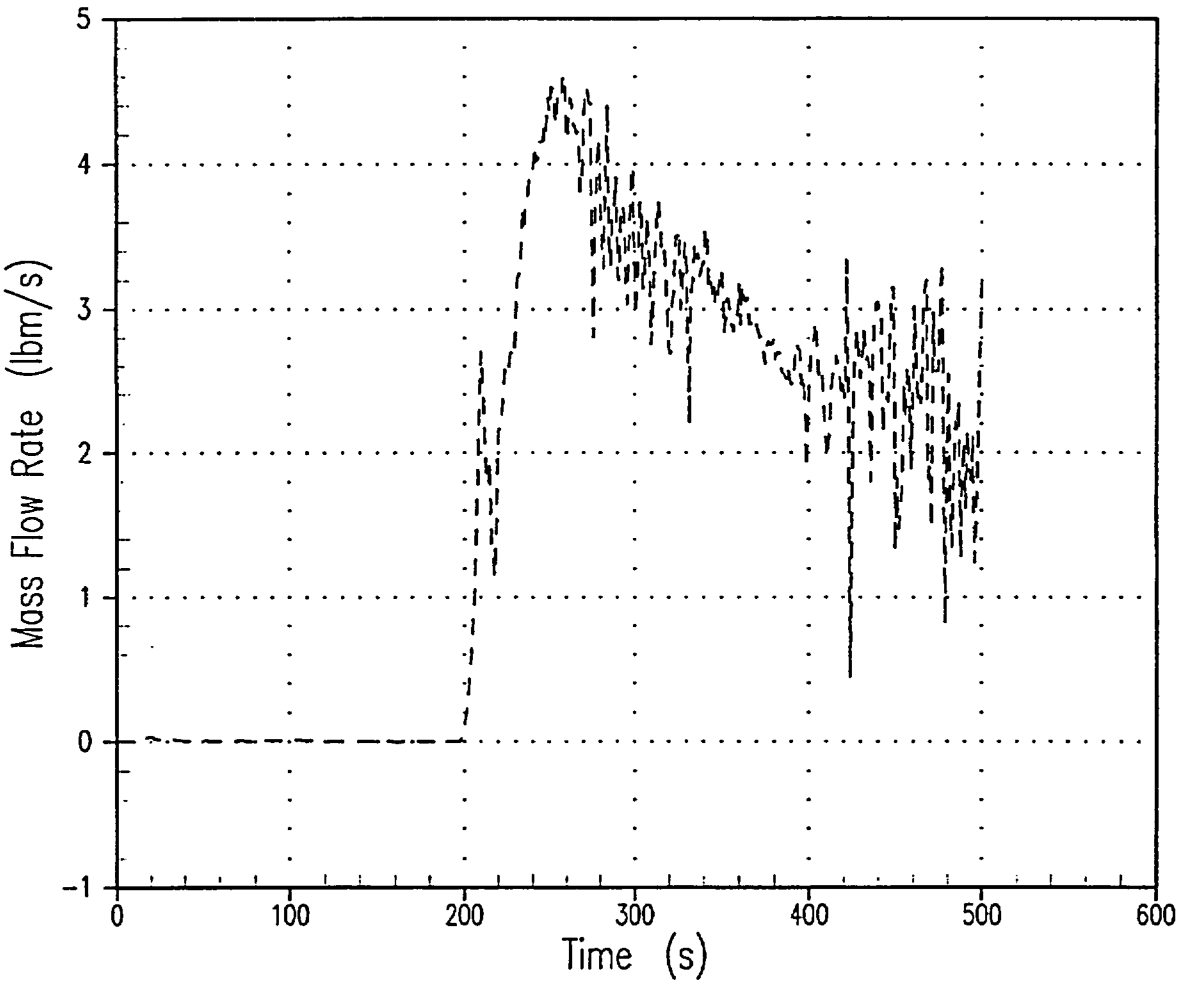

Figure 19-12. Predicted Broken Loop Seal Vapor Flowrate, ROSA 5-Percent Cold Leg Side Break

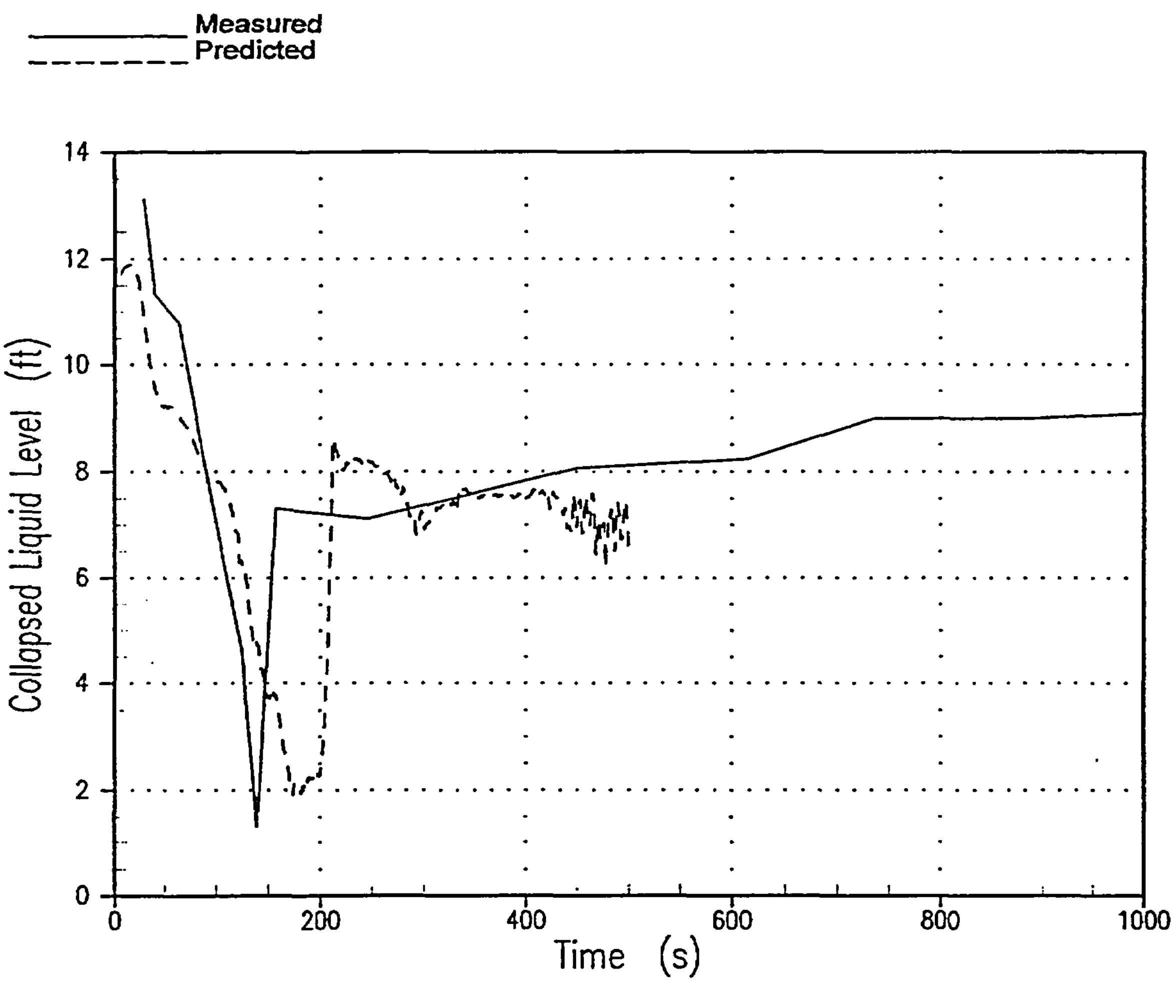

Figure 19-13. Comparison of Predicted and Measured Core Collapsed Liquid Levels, ROSA 5-Percent Cold Leg Side Break

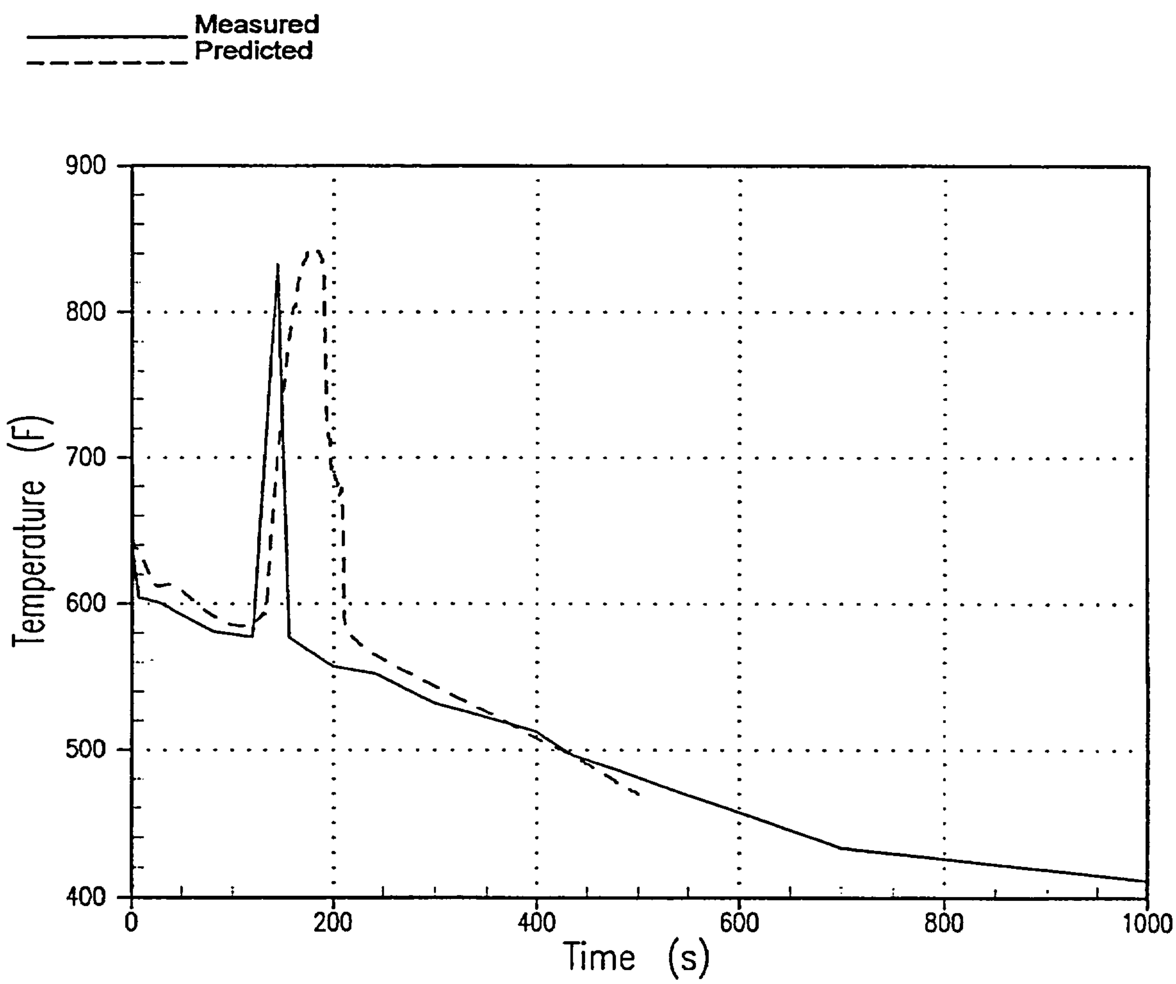

Figure 19-14. Comparison of Predicted and Measured PCTs, ROSA 5-Percent Cold Leg Side Break

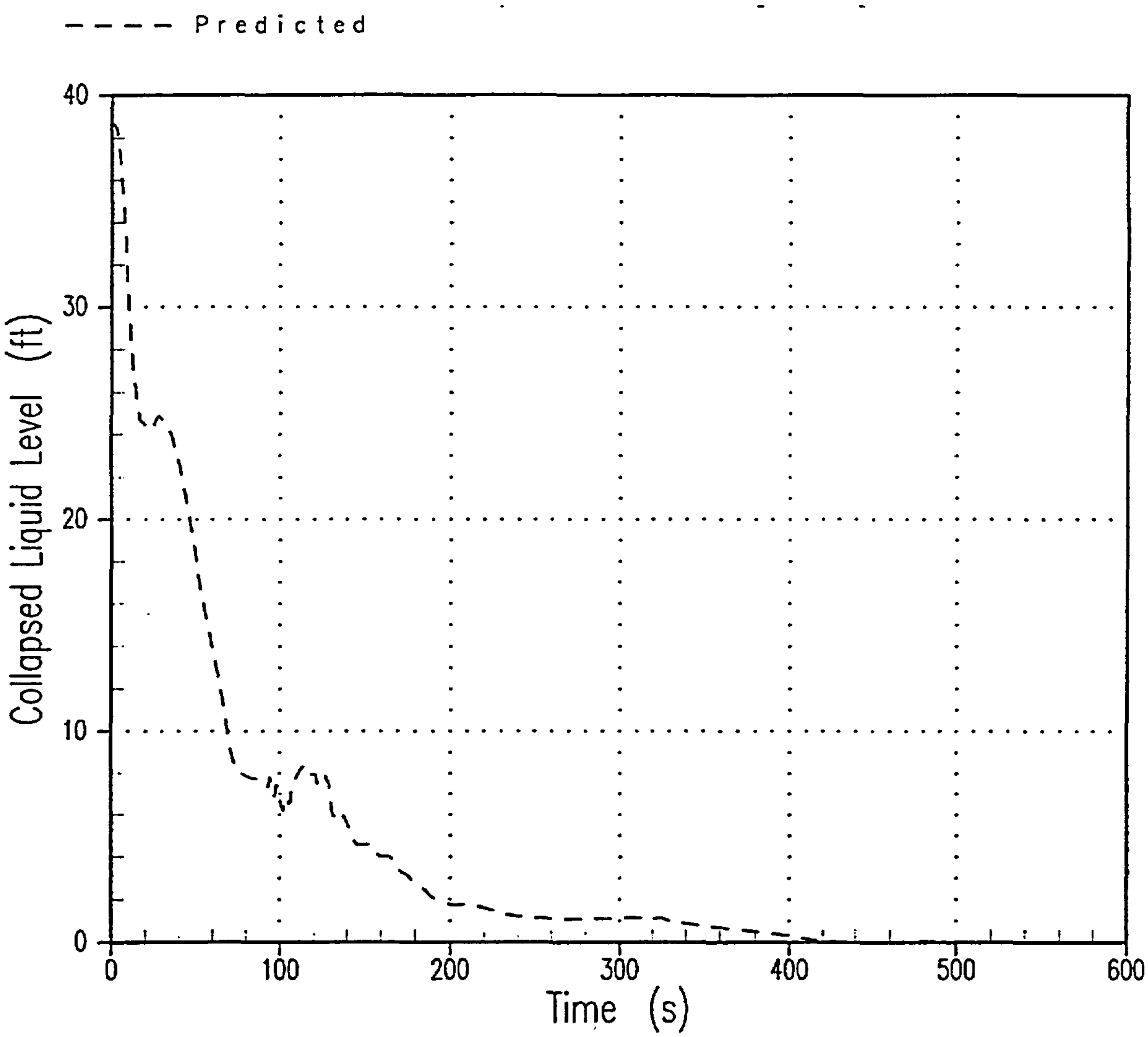

Figure 19-15. Predicted Intact Loop Uphill Steam Generator Tube Collapsed Liquid Level, ROSA 5-Percent Cold Leg Side Break

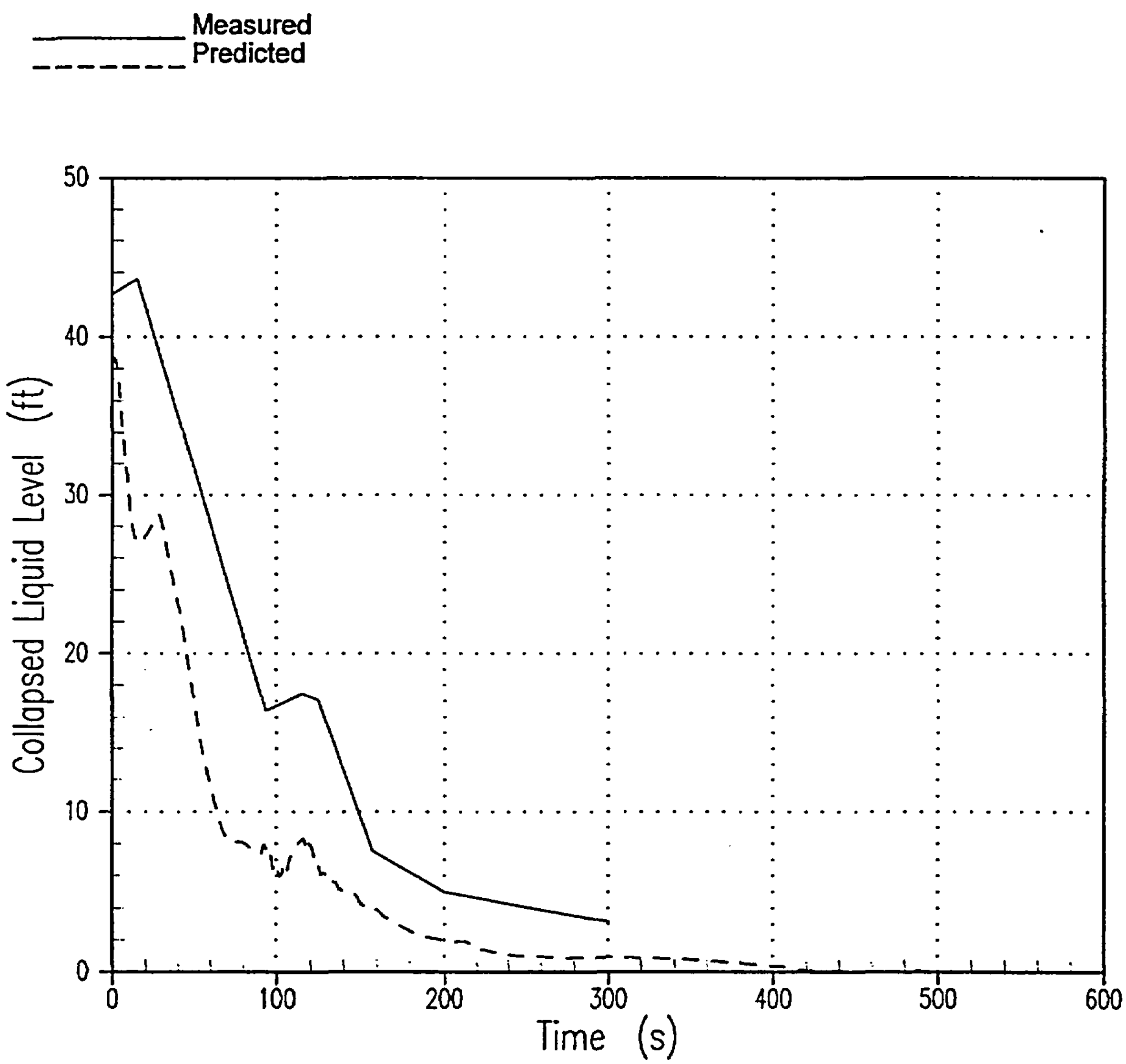

Figure 19-16. Comparison of Predicted and Measured Broken Loop Uphill Steam Generator Tube Collapsed Liquid Level, ROSA 5-Percent Cold Leg Side Break

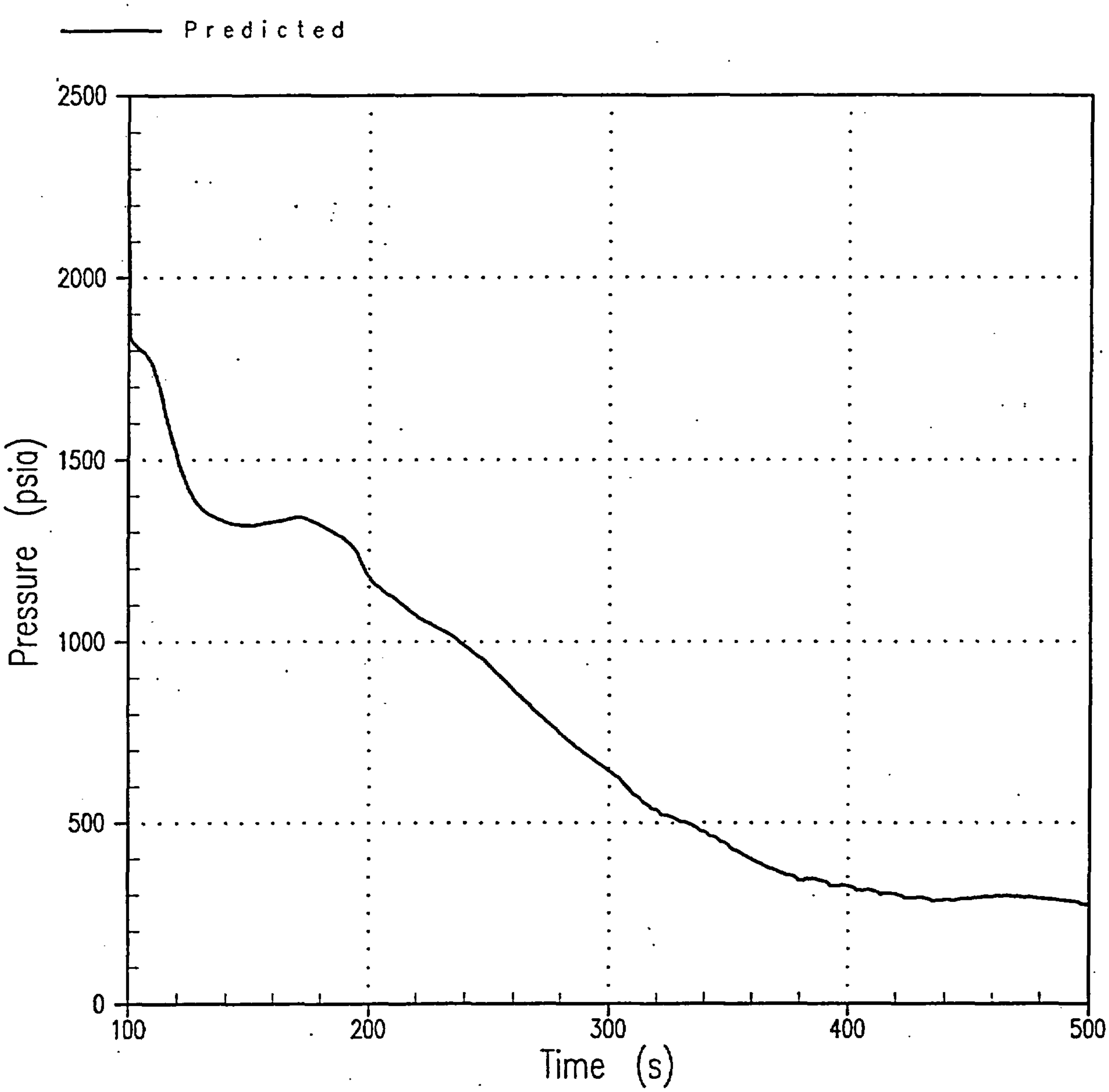

Figure 19-17. Predicted Primary System Pressure, ROSA 10-Percent Cold Leg Side Break

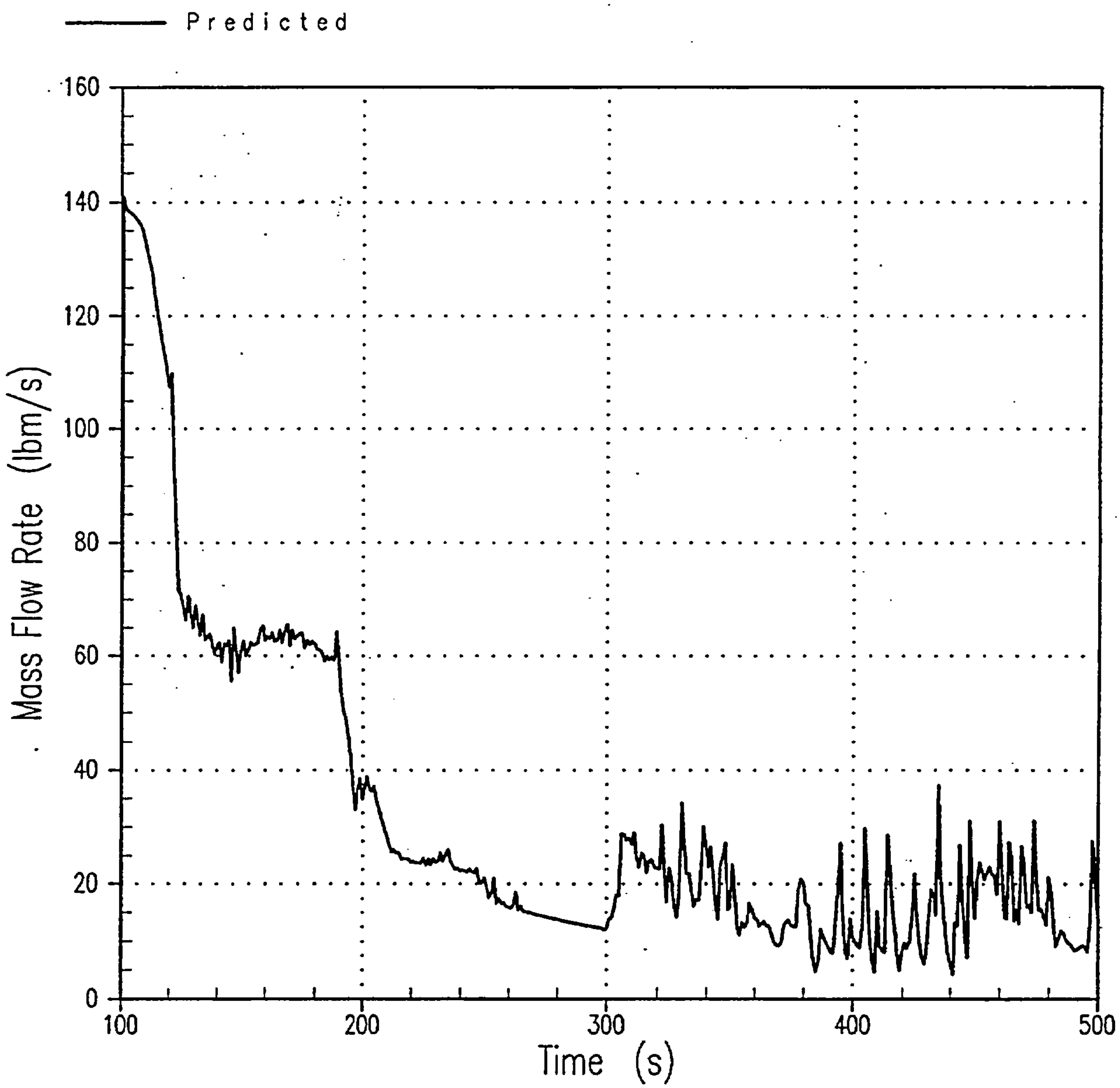

Figure 19-18. Predicted Break Flowrate, ROSA 10-Percent Cold Leg Side Break

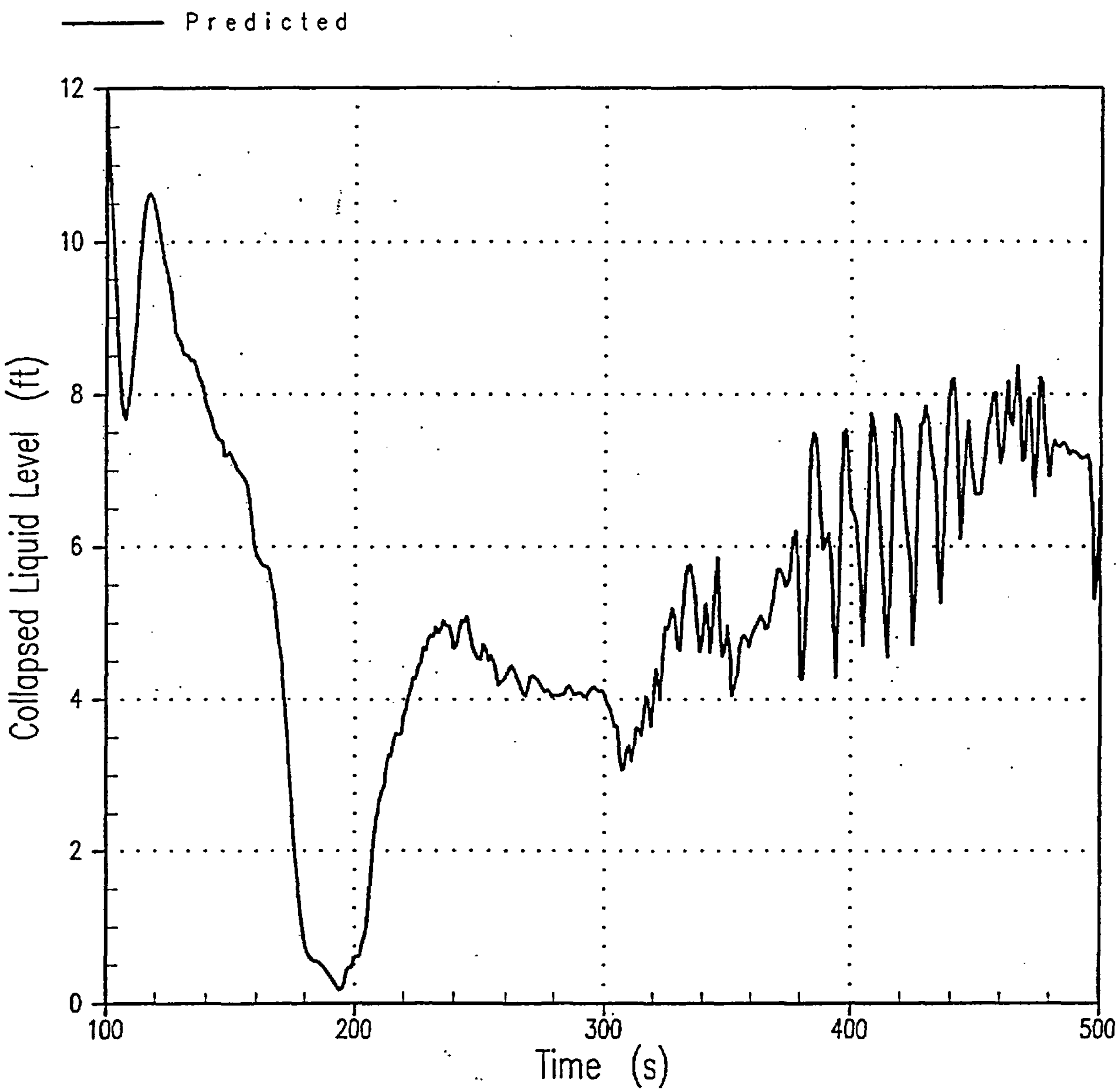

Figure 19-19. Predicted Core Collapsed Liquid Level, ROSA 10-Percent Cold Leg Side Break

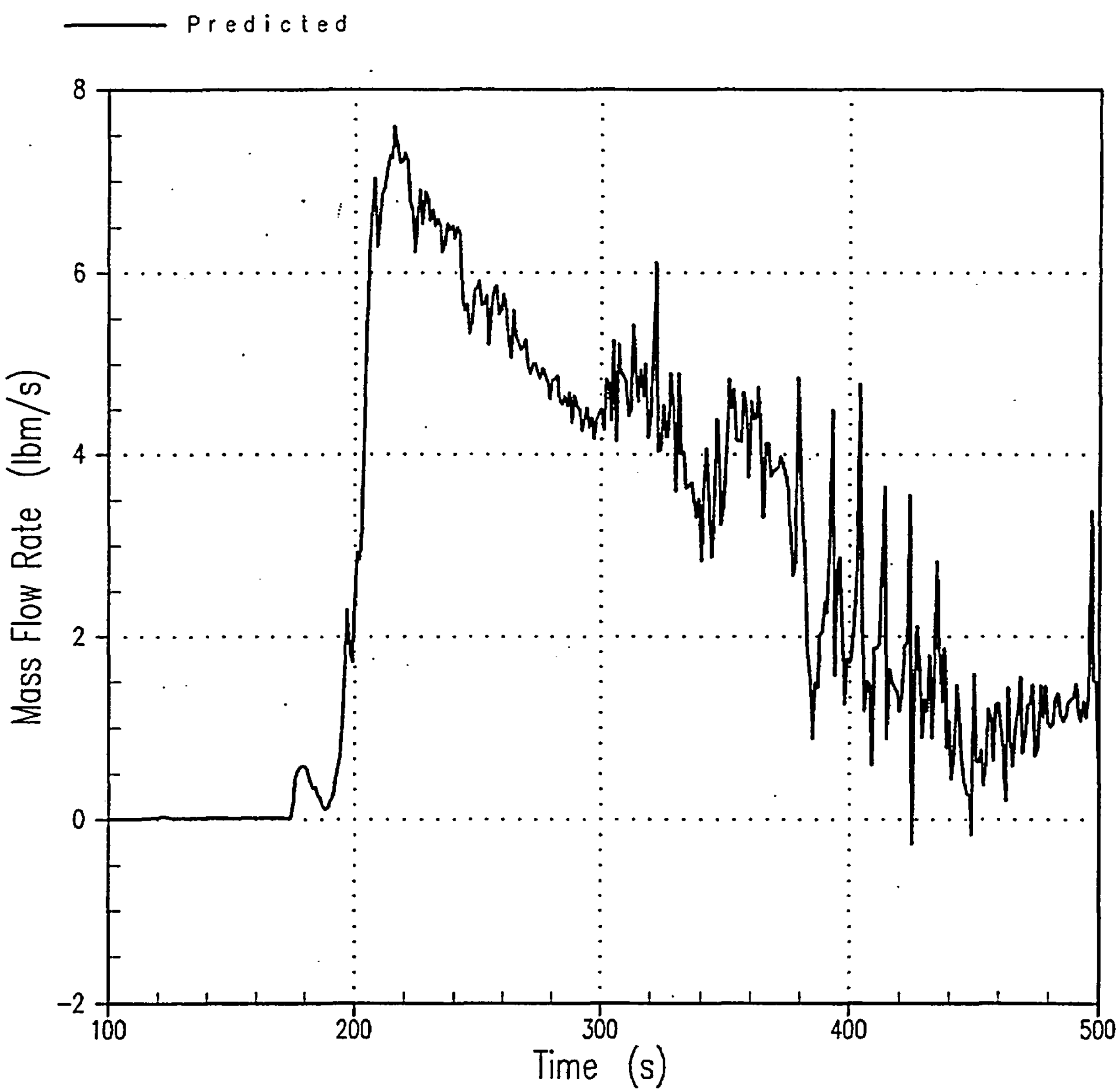

Figure 19-20. Predicted Intact Loop Seal Steam Flowrate, ROSA 10-Percent Cold Leg Side Break

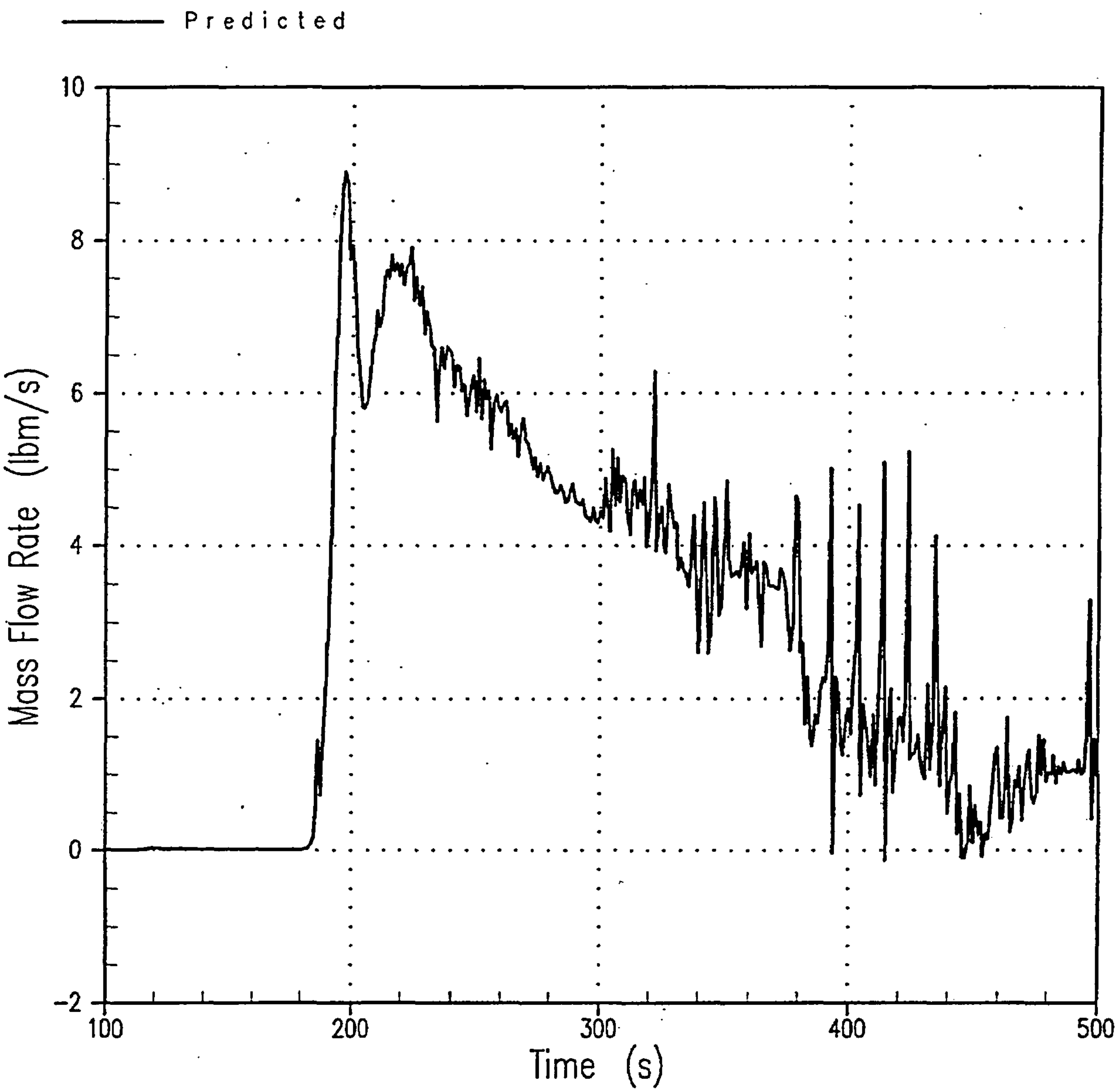

Figure 19-21. Predicted Broken Loop Seal Steam Flowrate, ROSA 10-Percent Cold Leg Side Break

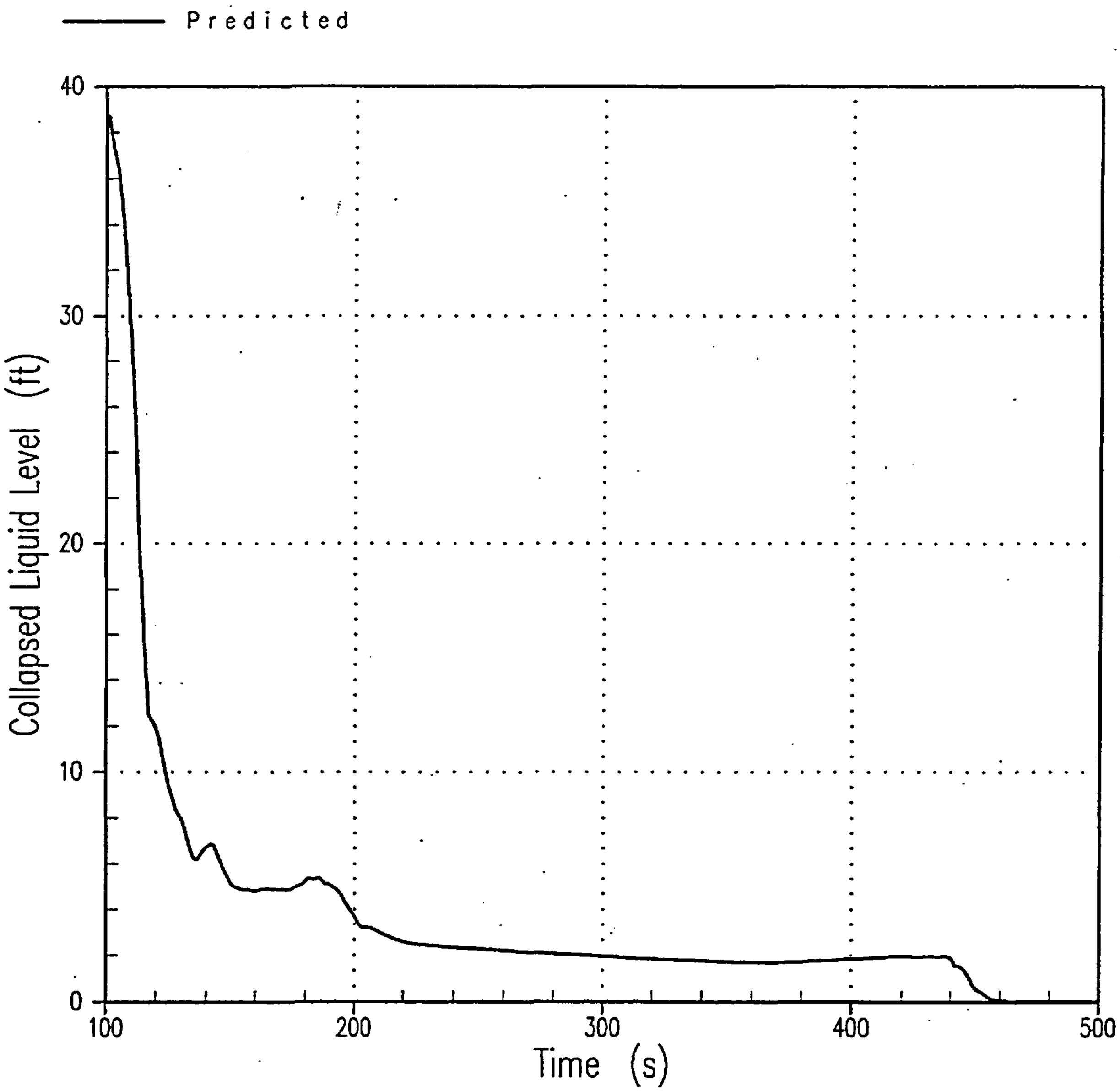

Figure 19-22. Intact Loop Uphill Steam Generator Tube Collapsed Liquid Level Prediction, ROSA 10-Percent Cold Leg Side Break

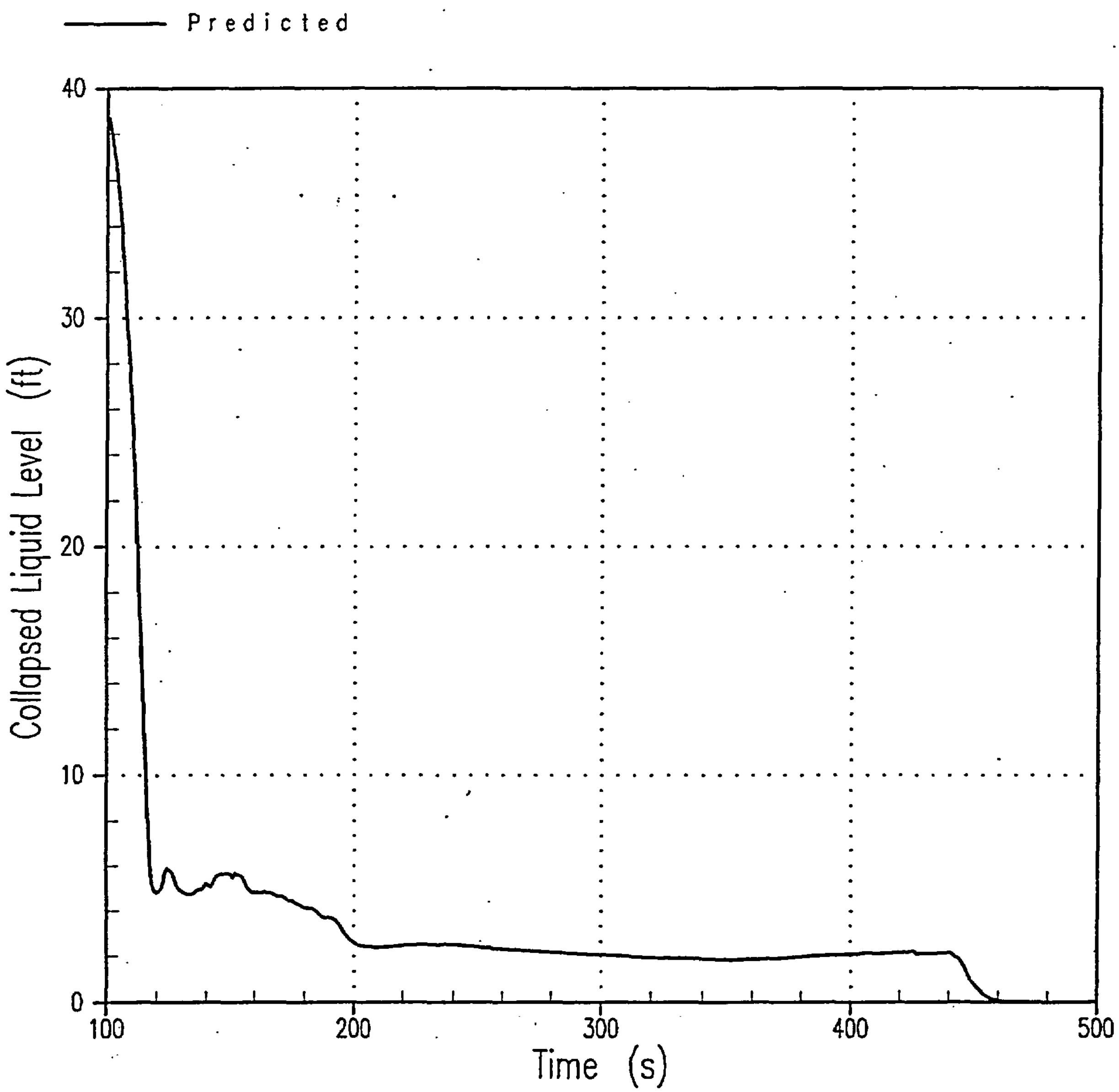

Figure 19-23. Broken Loop Uphill Steam Generator Tube Collapsed Liquid Level Prediction, ROSA 10-Percent Cold Leg Side Break

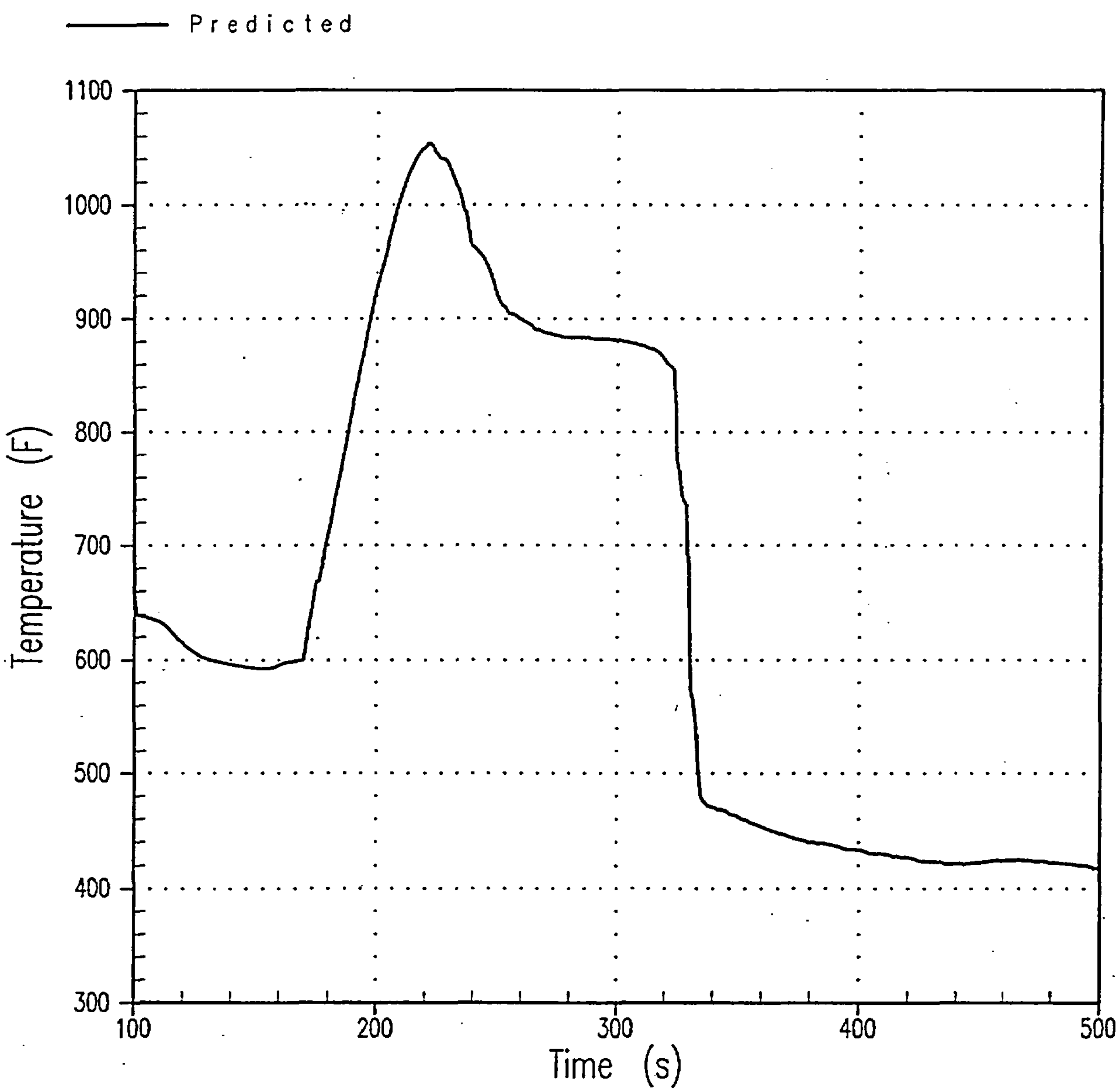

Figure 19-24. Predicted PCT, ROSA 10-Percent Cold Leg Side Break

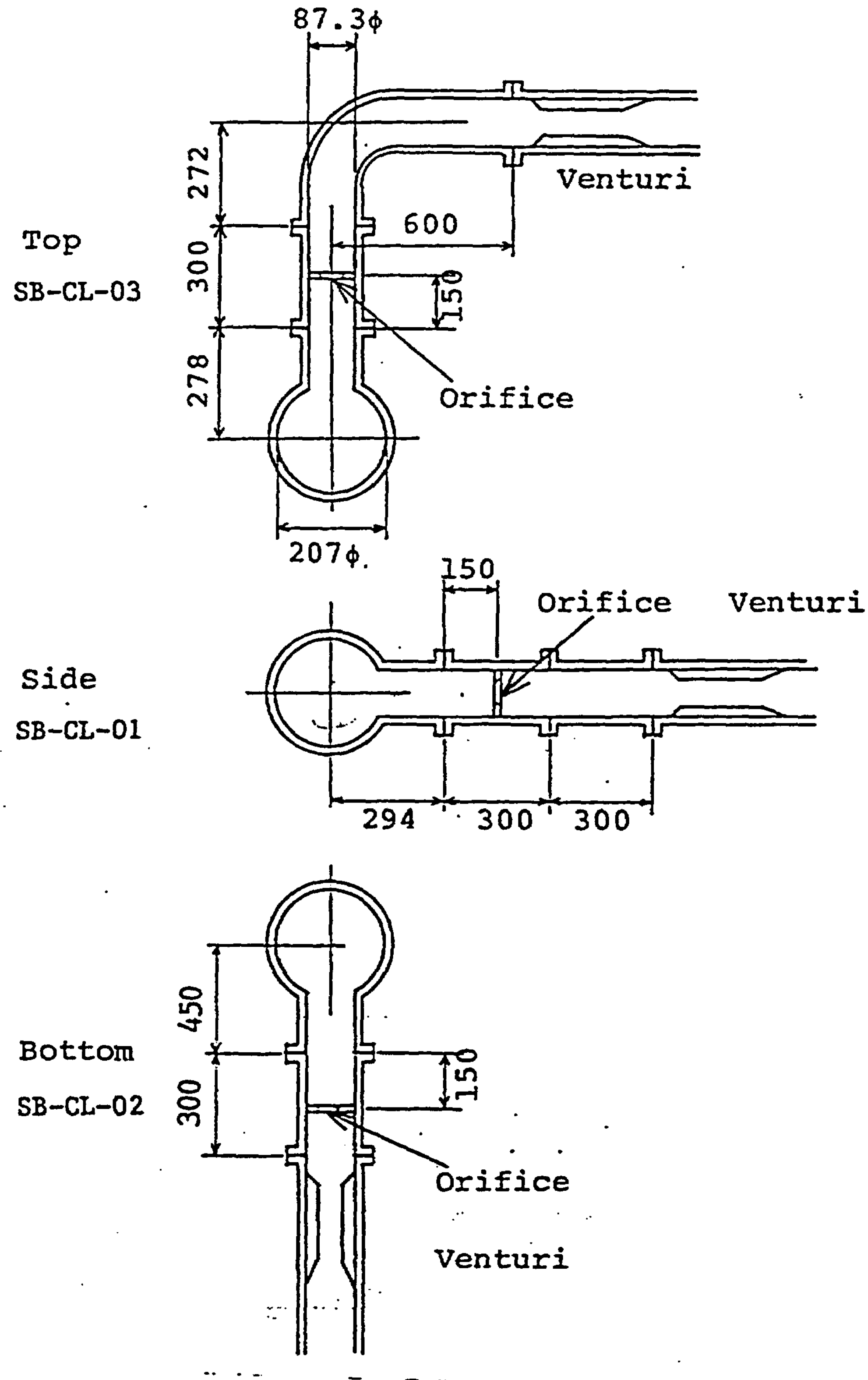

Figure 19-25. **Break Orientation in LSTF 2.5-Percent Cold Leg Break Tests (Koizumi, et al., 1987)**

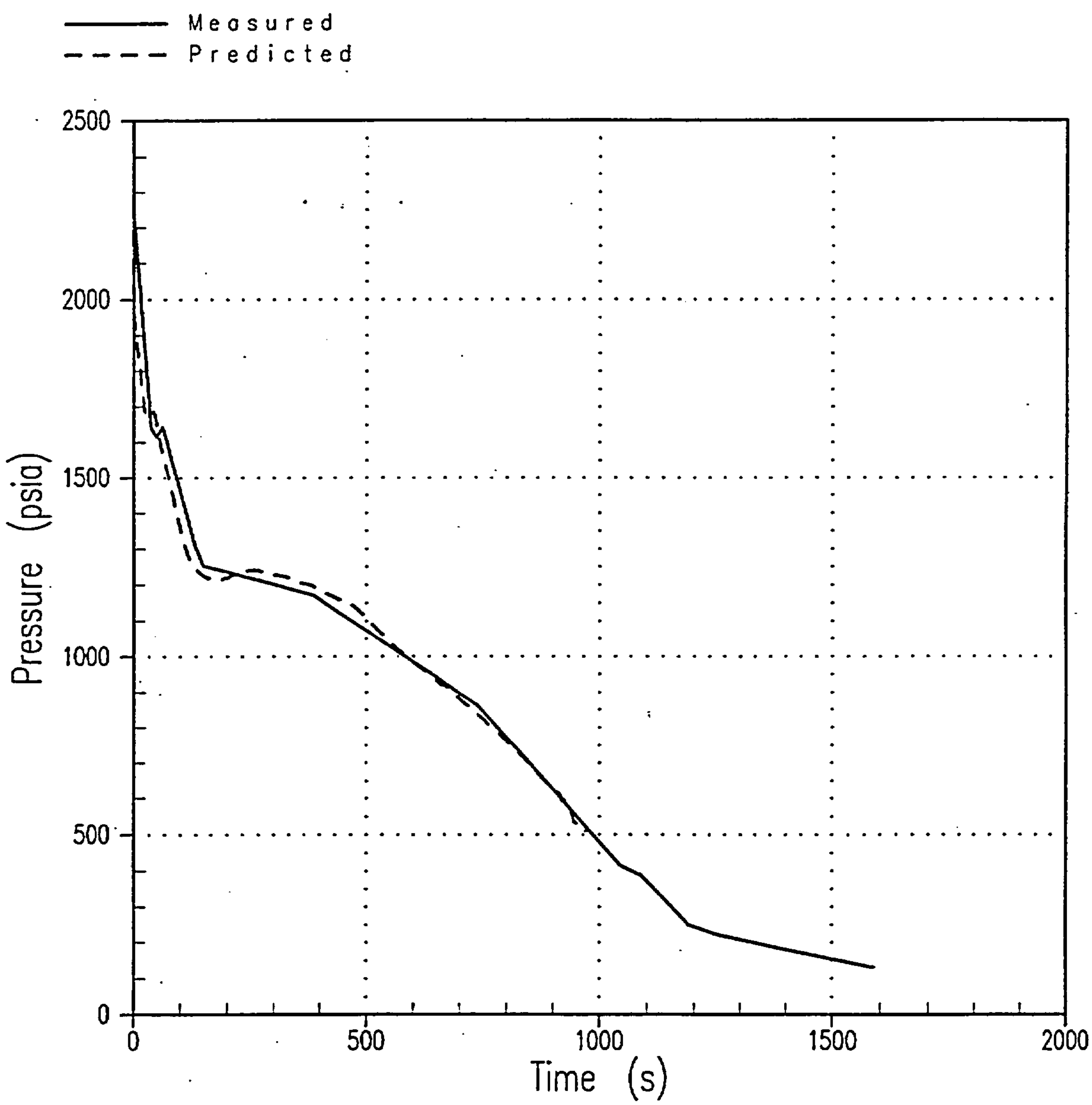

Figure 19-26. Comparison of Predicted and Measured Primary System Pressure, ROSA 2.5-Percent Cold Leg Side Break

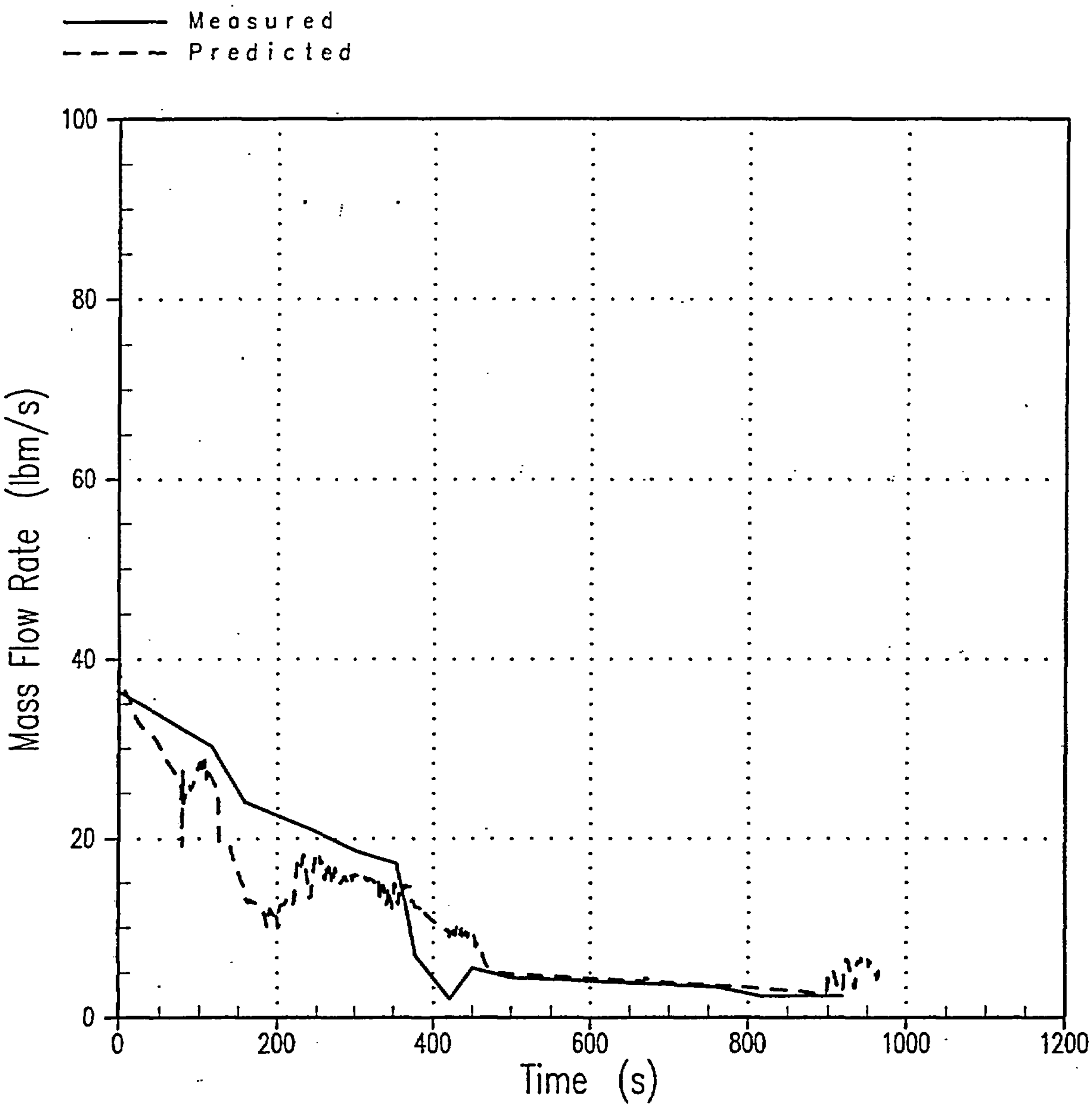

Figure 19-27. Comparison of Predicted and Measured Break Flowrates, ROSA 2.5-Percent Cold Leg Side Break

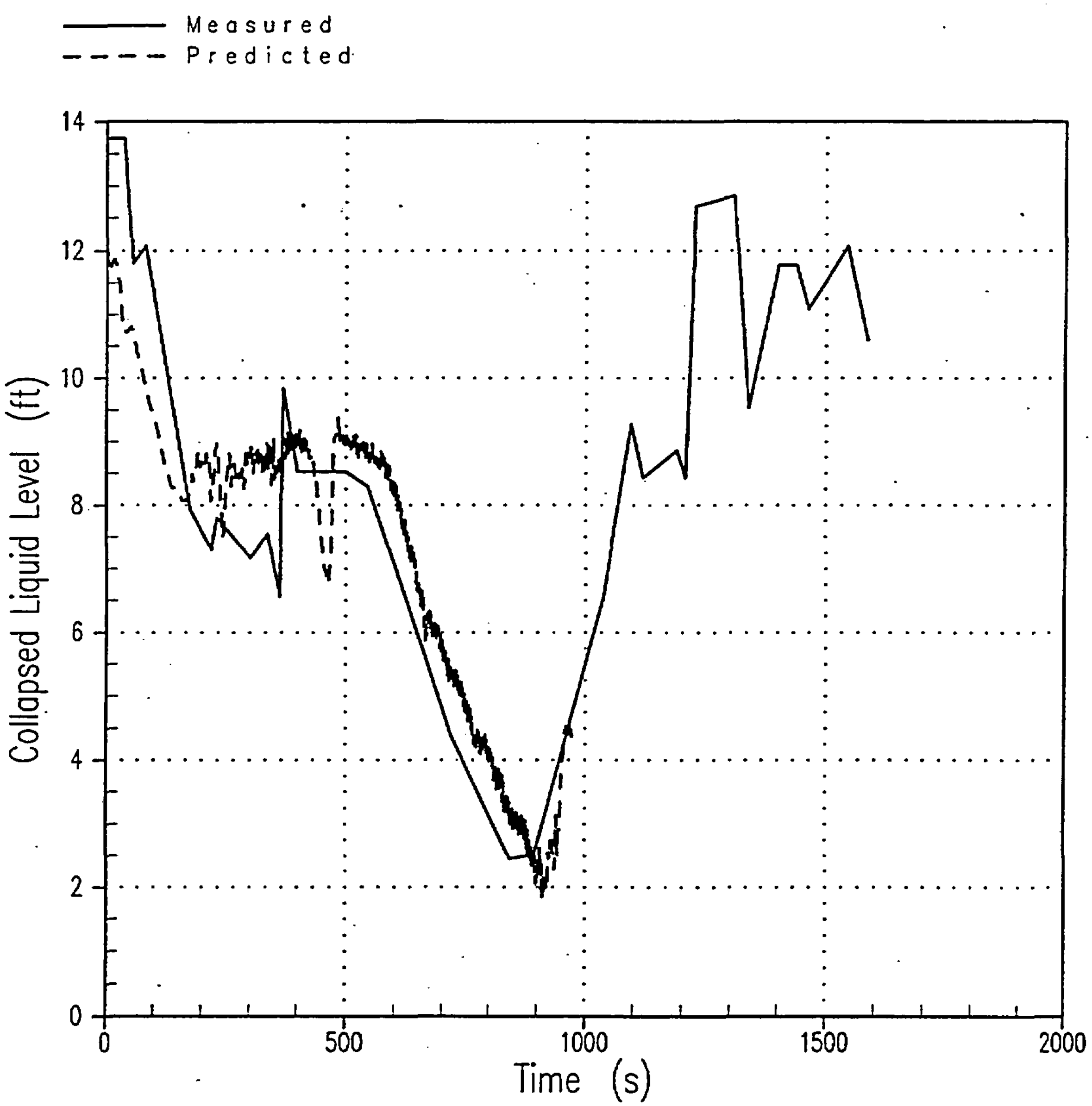

Figure 19-28. Comparison of Predicted and Measured Core Collapsed Liquid Levels, ROSA 2.5-Percent Cold Leg Side Break

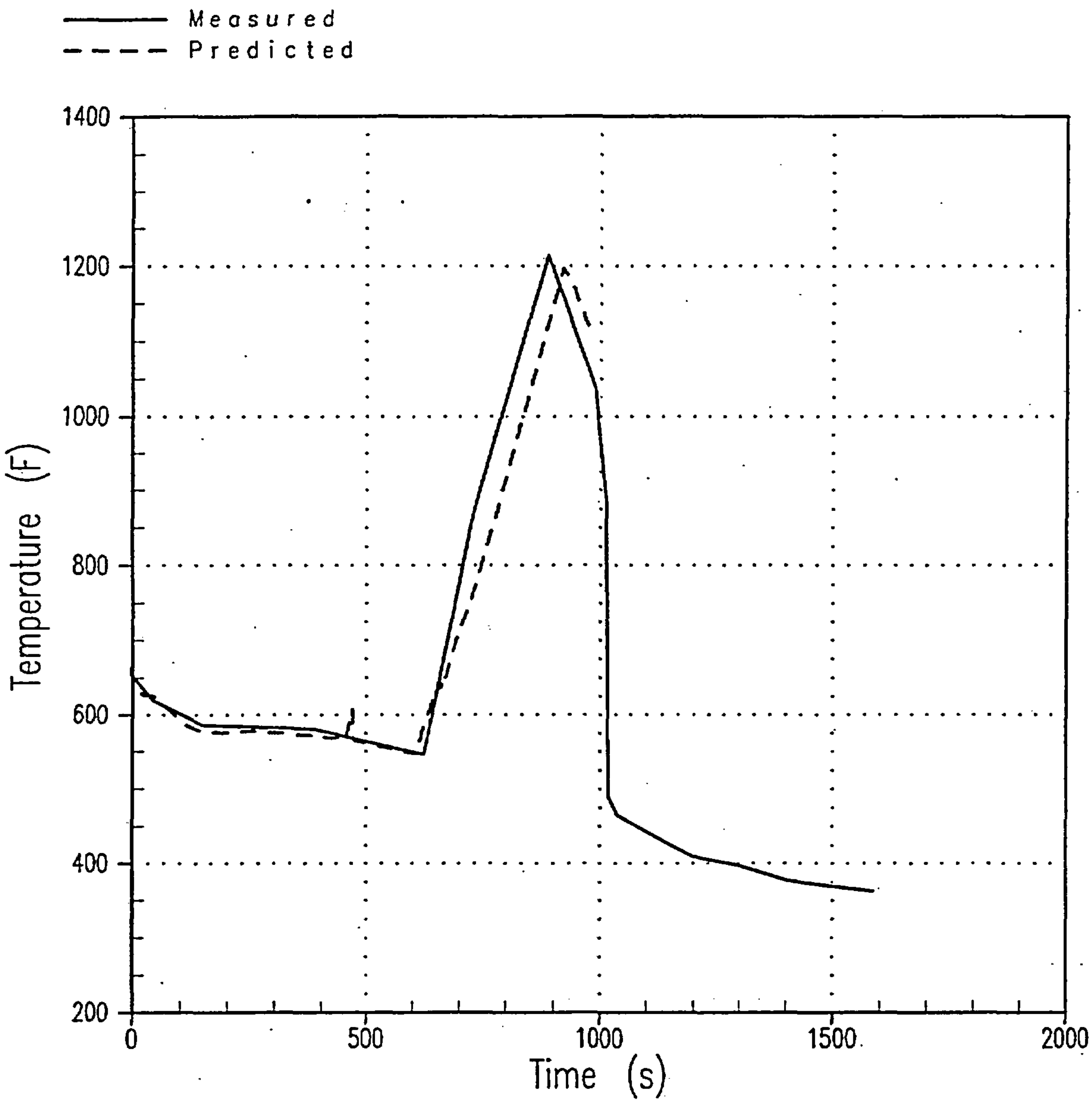

Figure 19-29. Comparison of Predicted and Measured PCTs, ROSA 2.5-Percent Cold Leg Side Break

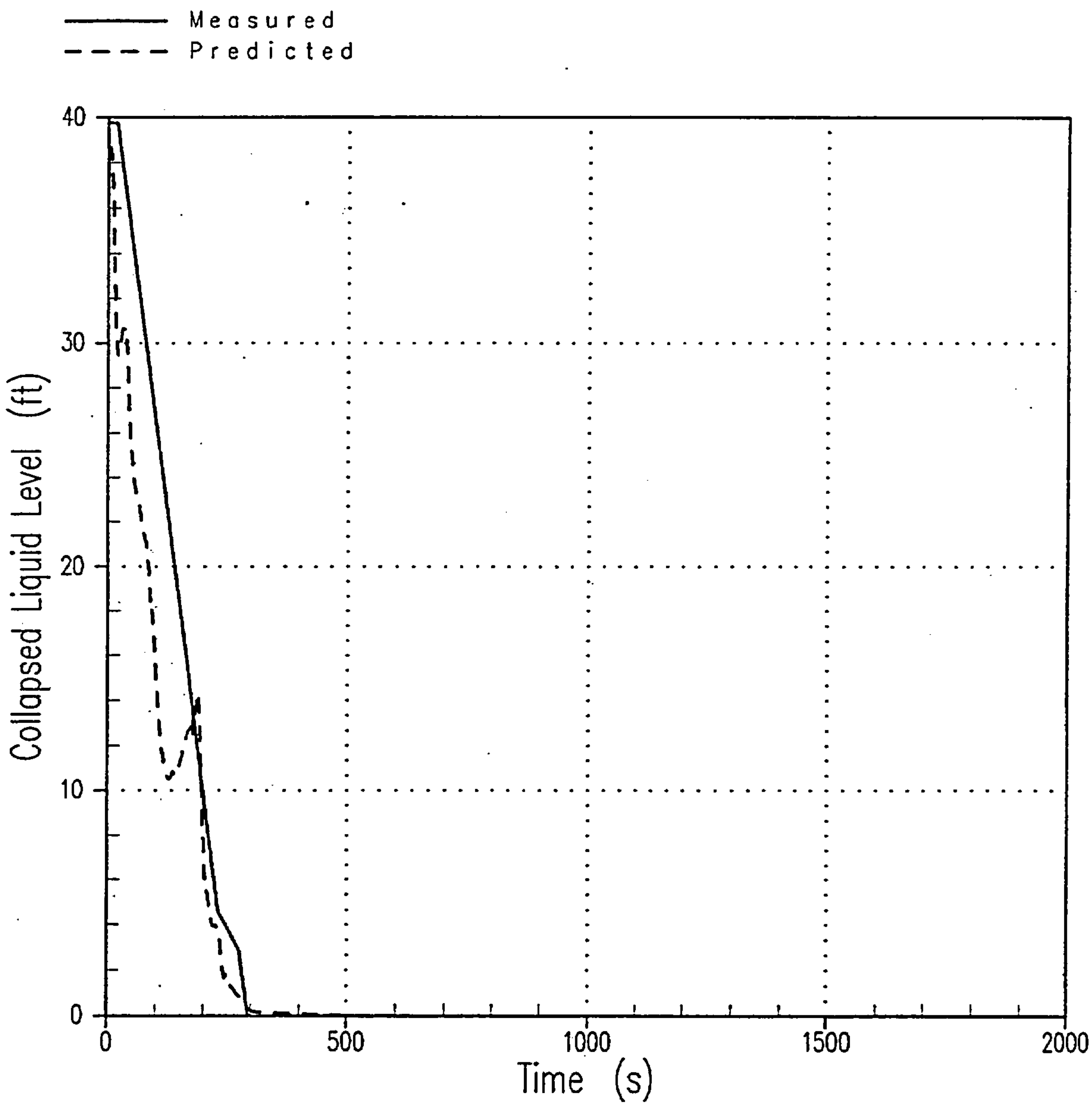

Figure 19-30. Comparison of Predicted and Measured Broken Loop Uphill Steam Generator Tube Collapsed Liquid Level, ROSA 2.5-Percent Cold Leg Side Break

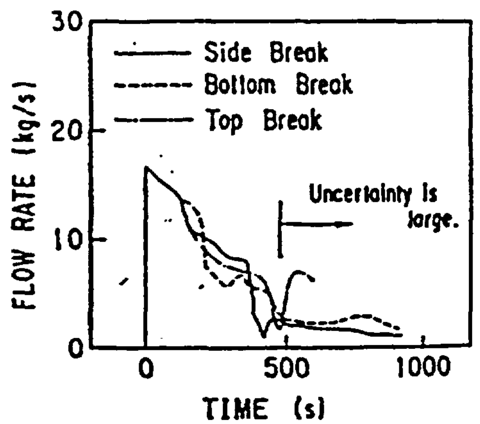

Figure 19-31A. Comparison of Experimental Break Flowrate for 2.5-Percent Top, Side, and Bottom Cold Leg Breaks (Koizumi, et al., 1988)

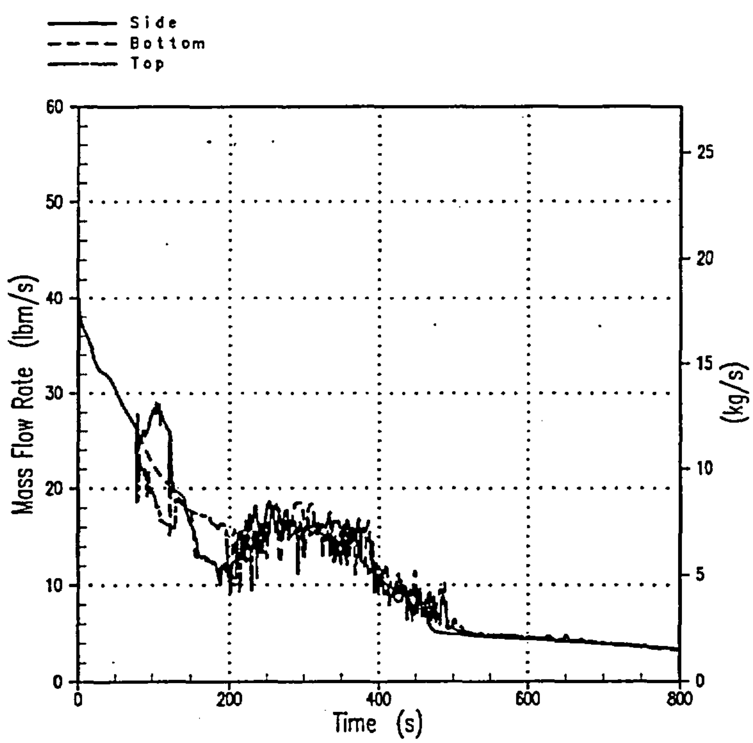

Figure 19-31B. Comparison of Predicted Break Flowrate for 2.5-Percent Top, Side, and Bottom Cold Leg Breaks

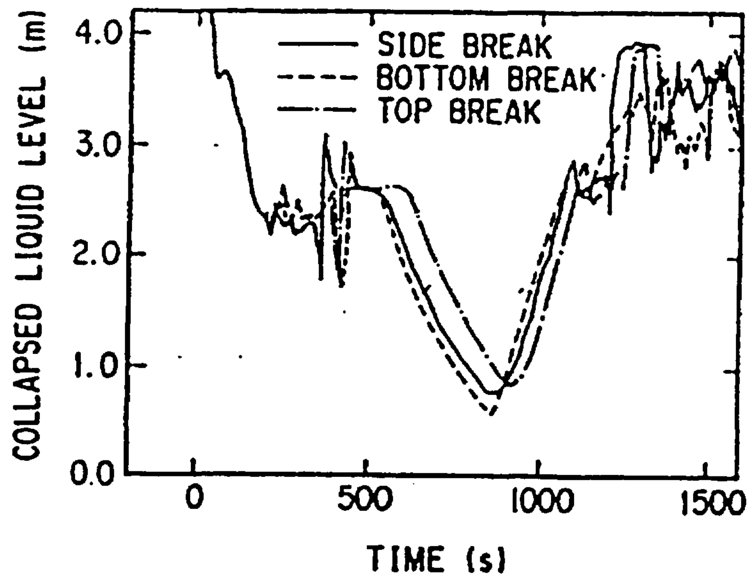

Figure 19-32A. Comparison of Experimental Core Collapsed Liquid Levels for 2.5-Percent Top, Side, and Bottom Cold Leg Breaks (Koizumi, et al., 1988)

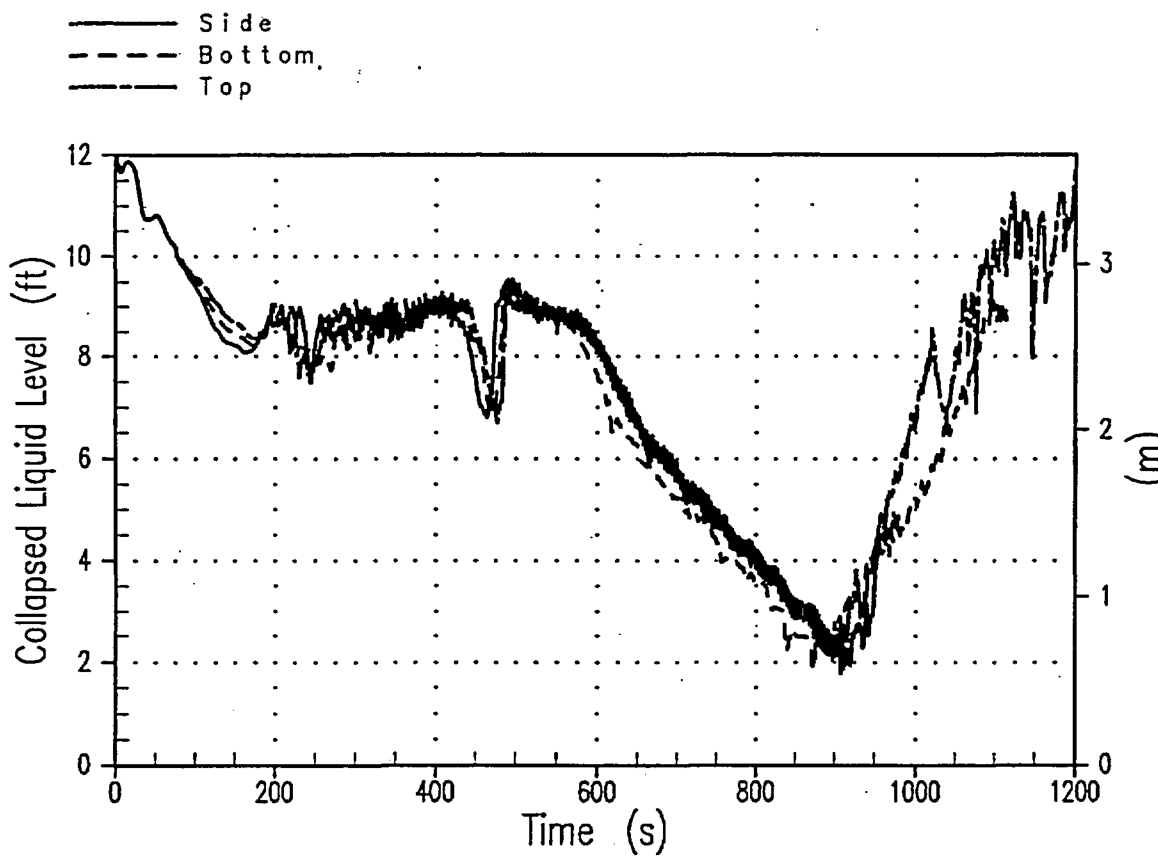

Figure 19-32B. Comparison of Predicted Core Collapsed Liquid Levels for 2.5-Percent Top, Side, and Bottom Cold Leg Breaks

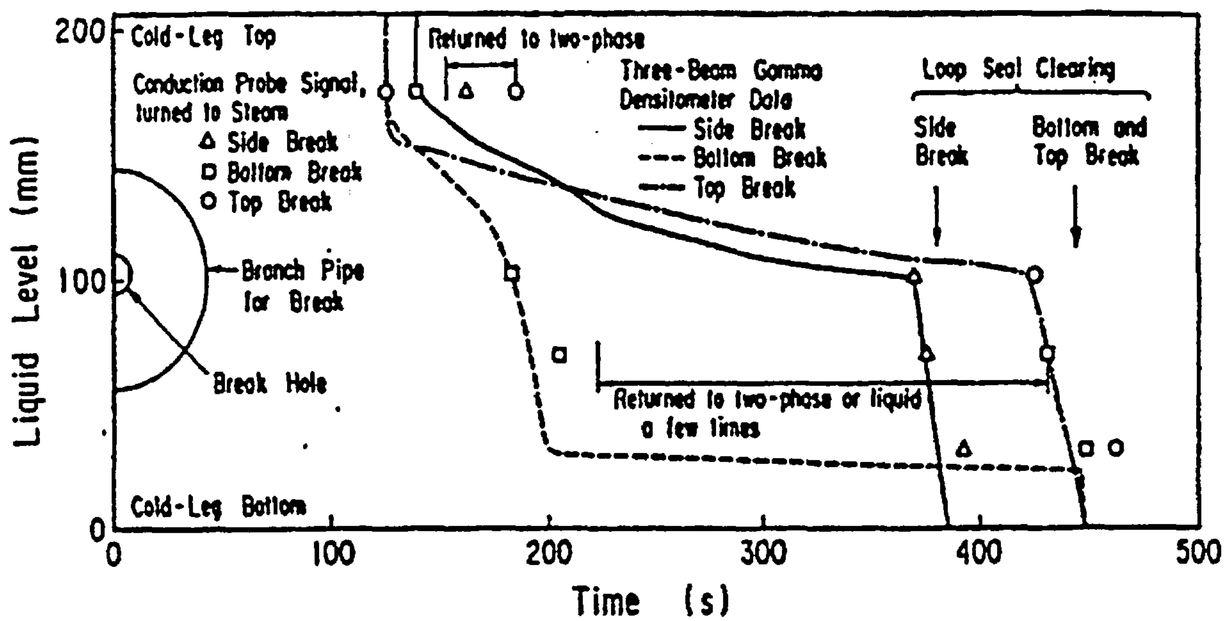

Figure 19-33A. **Mixture Levels in Broken Cold Leg Measured for Side, Bottom, and Top Break Experiments (Koizumi, et al., 1988)**

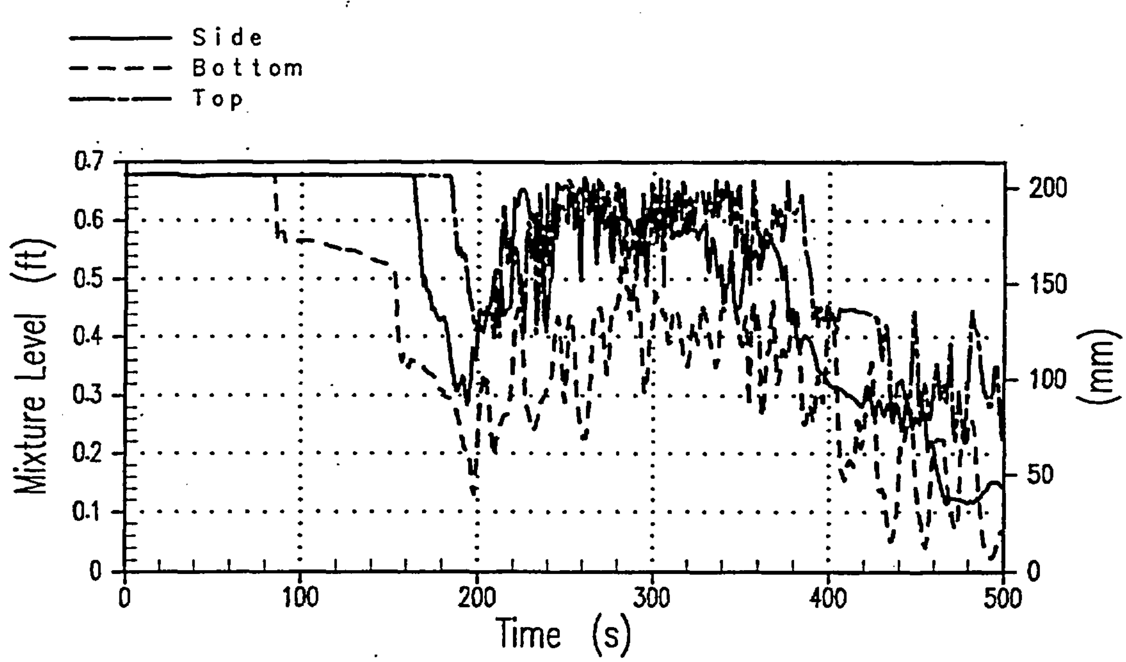

Figure 19-33B. **Two-Phase Mixture Level Prediction in Broken Cold Leg for 2.5-Percent Break Cases**

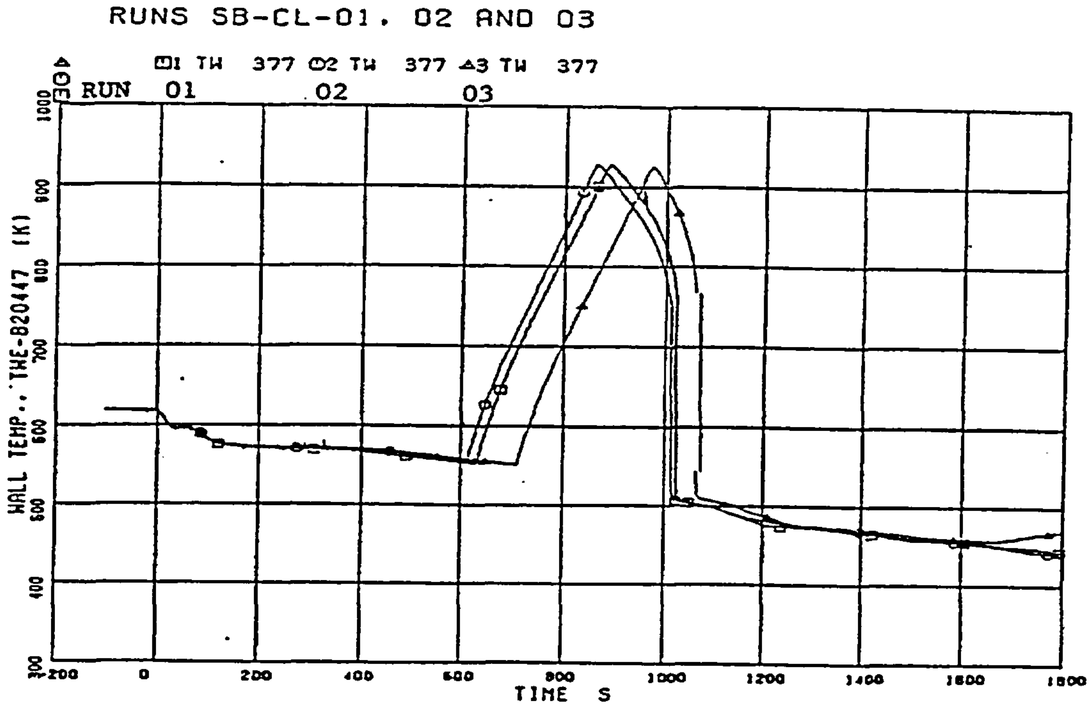

Figure 19-34A. Cladding Temperature of B-20 Rod at Position 7 (8.67-ft Elevation) for Side, Bottom, and Top Break Experiments (Koizumi, et al., 1987)

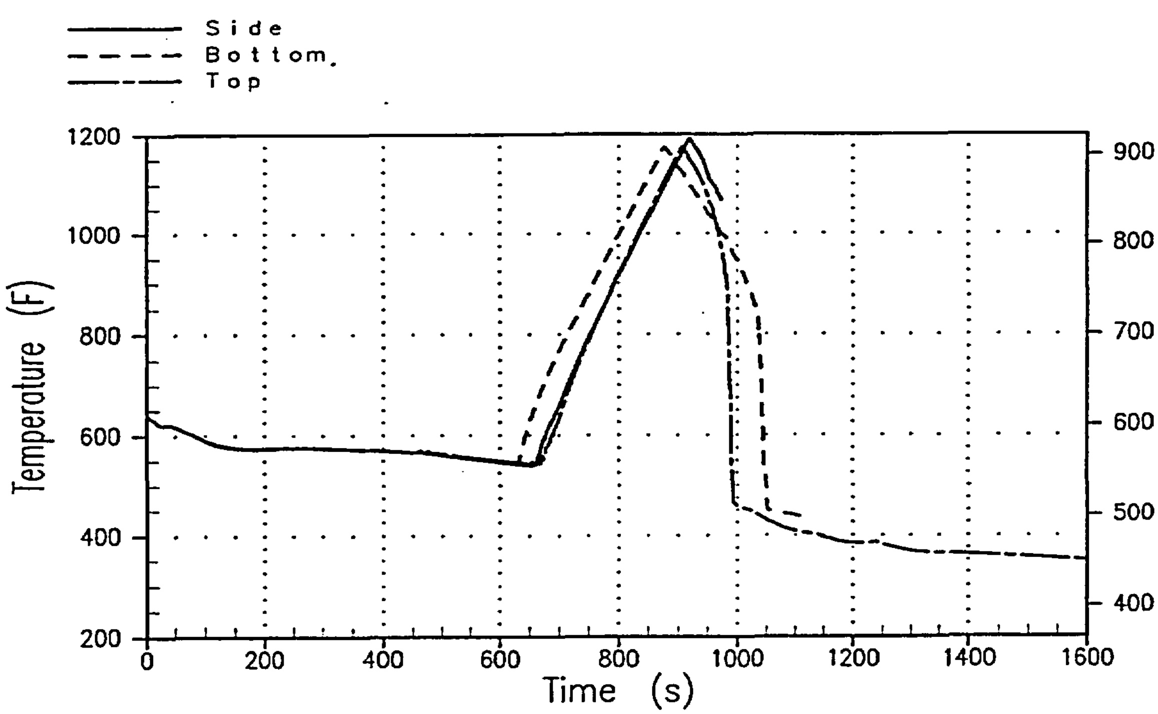

Figure 19-34B. Clad Temperature Predictions at 8.66-ft Elevation for 2.5-Percent Side, Bottom, and Top Break Experiments

SECTION 20
LOFT SIMULATIONS USING WCOBRA/TRAC-SB

20-1 Introduction

Other integral-systems tests that were simulated using WCOBRA/TRAC-SB are based on experiments conducted at the Loss-of-Fluid Test (LOFT) facility. The LOFT loss-of-coolant experiments (LOCEs) have been widely used for validation of PWR computer models due to the relatively large scale of the facility (1:60 volume scaling of a commercial four-loop PWR) and the use of a nuclear core designed to have the same physical, chemical, and metallurgical properties as a PWR core (Reeder, 1978). The large scale of the facility enables multidimensional effects which allow assessment of the ability of the code to predict these effects. Also, because LOFT is the only integral facility to use a nuclear core, the experiments are considered to be an essential part of the validation package for any PWR computer model.

The LOFT facility is designed to provide thermal-hydraulic data representative of a large rupture of a main coolant pipe. Consequently, the facility design and instrumentation are oriented toward fulfilling these goals. The LOFT facility contains a number of atypicalities to a large-scale PWR for large break LOCA simulations; for small break LOCAs, the facility contains even more atypicalities, some of which were not recognized until after some small break LOCEs had been completed. Nevertheless, the facility remains a valuable benchmark for model assessment, provided the atypicalities are recognized and do not overshadow the thermal-hydraulic behavior of interest. In general, LOFT fluid volumes were scaled according to the ratio of LOFT core power to PWR core power of a large plant. If practical, flow areas were scaled by the same ratio.

In this section, simulations of LOFT small break LOCEs L3-1, L3-7, and L3-5 using WCOBRA/TRAC-SB are presented and compared to various data acquired during the experiments. L3-1 and L3-5 simulate a 4-inch equivalent diameter break. The L3-1 break is located at the centerline of the inactive loop cold leg. For LOCE L3-5, the break is located in the active loop cold leg. The L3-1 experiment is of interest for model validation due to the influence of accumulator injection on the primary system response during the test; by comparison, LOCE L3-5, because of its location in the active loop, is more typical of the break geometry expected for a small break LOCA in a full-scale PWR. L3-7 simulates a 1-inch equivalent diameter break also at the centerline of the inactive loop cold leg. This experiment is of interest for model validation due to the extended period of natural circulation that was established and maintained during the test.

20-2 LOFT Facility Description

The following text describing the LOFT facility is summarized from NUREG CR-1145 (Bayless, et al., 1980) with additional information from NUREG CR-0247 (Reeder, 1978) and changes for readability where necessary.

Figure 20-2-1 (Bayless, et al., 1980) illustrates the layout of the LOFT facility. LOFT consists of five major components: the reactor vessel, the active loop, the inactive loop, the blowdown suppression system, and the emergency core cooling system (ECCS). A reflood assist bypass line (RABL) was also included in the inactive loop to provide additional safeguards capability in an emergency.

The LOFT reactor vessel is similar to a PWR reactor vessel in that it includes a nuclear core and an integral annular downcomer. However, the LOFT downcomer contains large metal filler blocks not found in a standard PWR downcomer to maintain volume scaling. Also, the LOFT vessel does not have an upper head typical of a PWR vessel. Figure 20-2-2 based on Reeder (Reeder, 1978) illustrates the LOFT reactor vessel and shows the various flowpaths that are available for coolant that enters through the vessel inlet nozzle.

The 5.5-foot LOFT nuclear core consists of nine fuel assemblies designed for a thermal output of 50 MW. As shown in Figure 20-2-3 (Bayless, et al., 1980), five assemblies have a 15×15 square cross section and the remaining four assemblies have a triangular cross section that represents a portion of the square cross-sectional design. The square assemblies have 225 pin locations, 21 of which are occupied by guide tubes except for the center assembly; the center guide tube is not installed to allow for additional instrumentation. The triangular assemblies have 78 pin locations, 8 of which are occupied by guide tubes. In all, the 9 LOFT assemblies contain 1,300 fuel rods, 136 guide tubes, and 1 open hole for instrumentation.

The LOFT active loop is similar to a PWR main coolant loop in that it includes a hot leg, an active steam generator (inverted U-tube and shell design), pump suction piping, and a cold leg. However, the LOFT active loop uses two coolant pumps in parallel, rather than a single coolant pump typical of a PWR loop, and the LOFT steam generator tubes are not full height. The LOFT secondary side steam flow is controlled on a pressure hysteresis following steam generator trip and is, therefore, also different from the PWR.

The LOFT inactive loop contains a hot leg, a steam generator simulator to represent the steam generator resistance, a reactor coolant pump (RCP) simulator to represent the pump resistance, and a cold leg. The hot and cold legs are connected on one side to the reactor vessel and on the other side to the quick-opening blowdown valves of the blowdown suppression system. The hot and cold legs are also connected by the RABL, normally closed during the LOCEs, but which provides additional safeguards capability by allowing steam generated in the core to be vented directly to the break in an emergency.

The LOFT blowdown suppression system consists of header pipes from the quick-opening blowdown valves in the inactive loop, connected to a blowdown suppression tank with a spray system for steam condensation. This system provides the backpressure to the RCS for the LOCEs and, therefore, simulates the containment in a PWR.

The LOFT ECCS consists of two accumulators; a high-pressure injection system (HPIS), consisting of two high-pressure injection pumps and a low-pressure injection system (LPIS), consisting of two low-pressure injection pumps. Generally, only one of each is active during a given experiment.

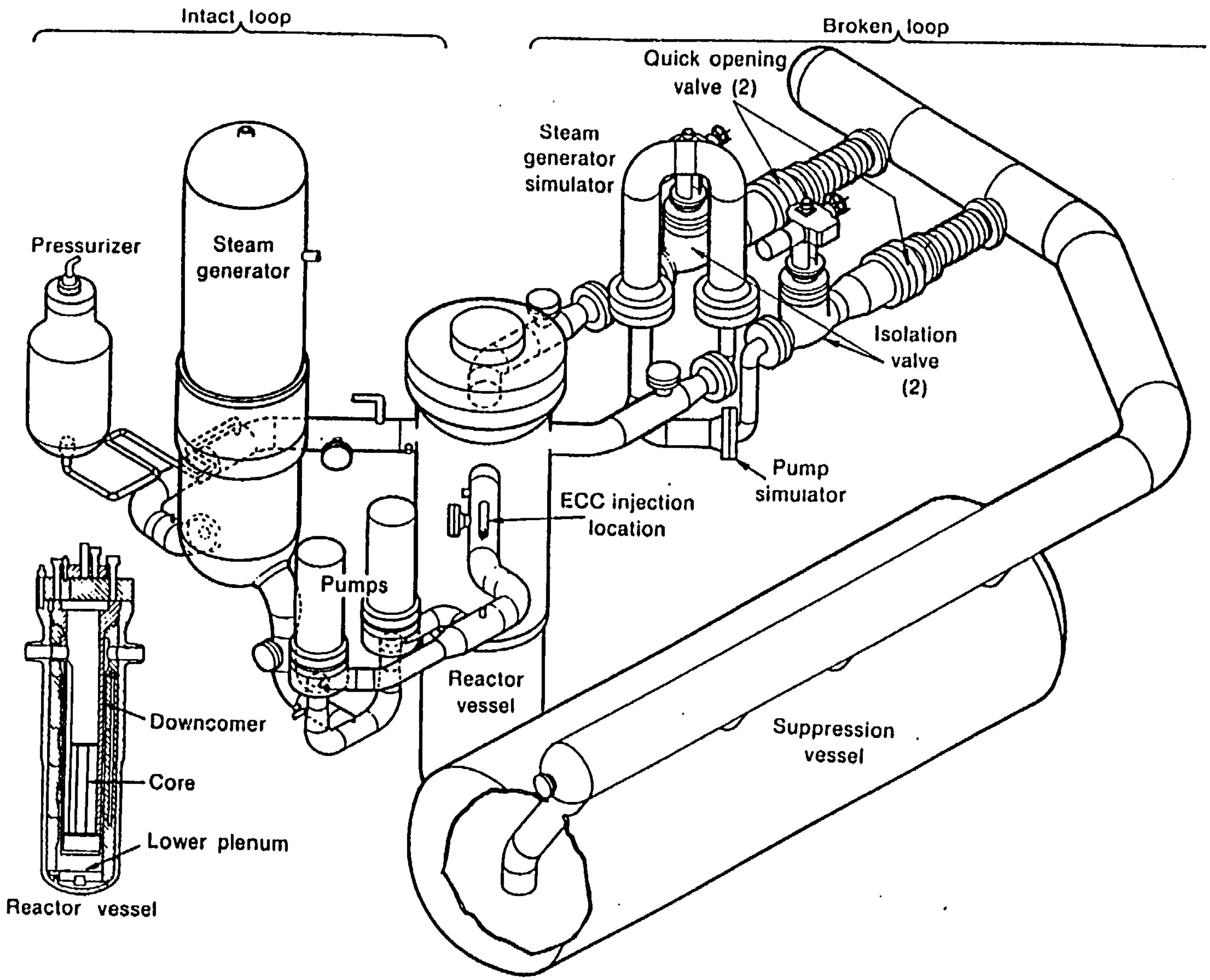

Figure 20-2-1. Diagram of LOFT Major Components (Bayless, et al., 1980)

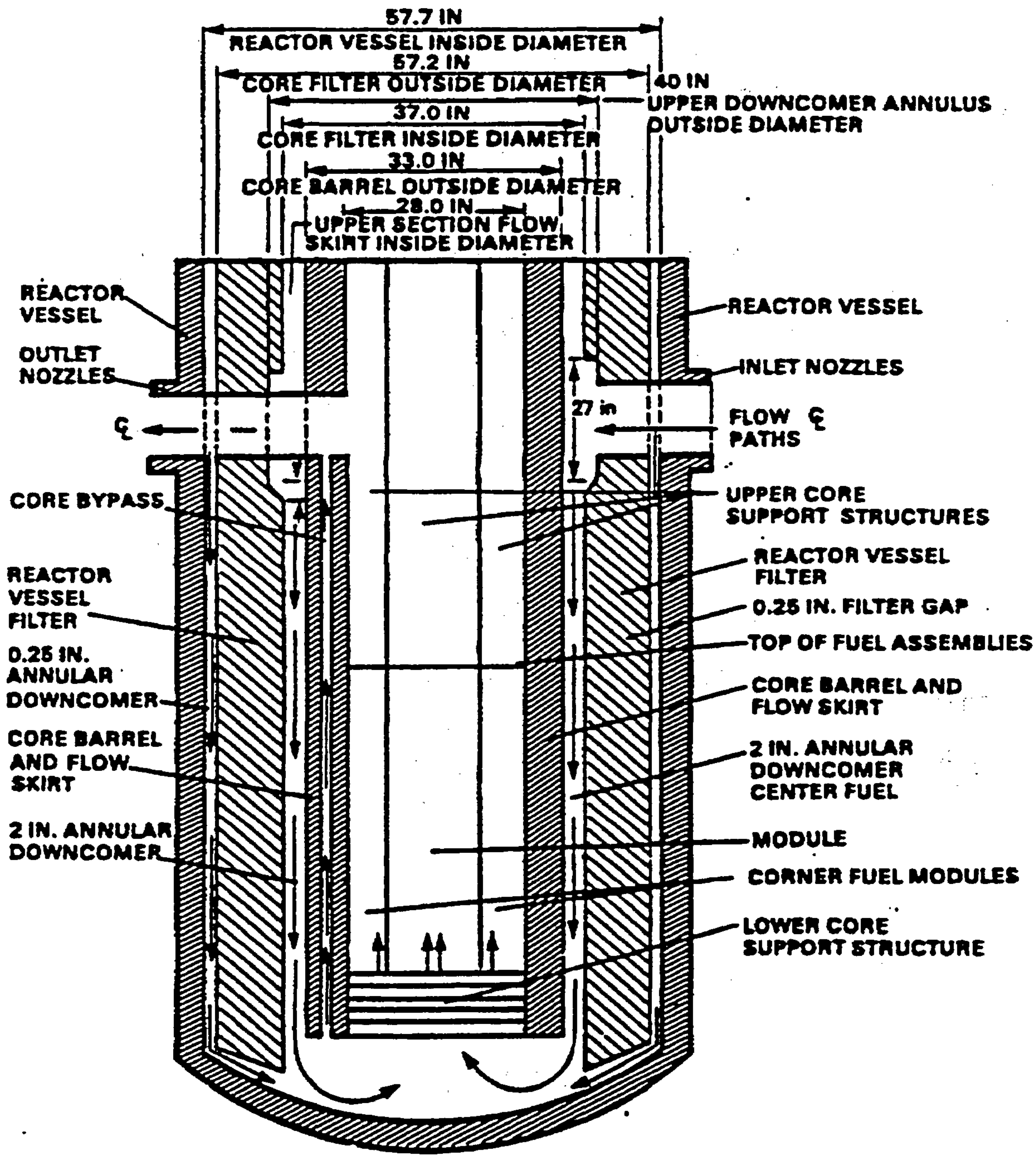

Figure 20-2-2. Diagram of LOFT Reactor Vessel and Flowpaths (Reeder, 1978)

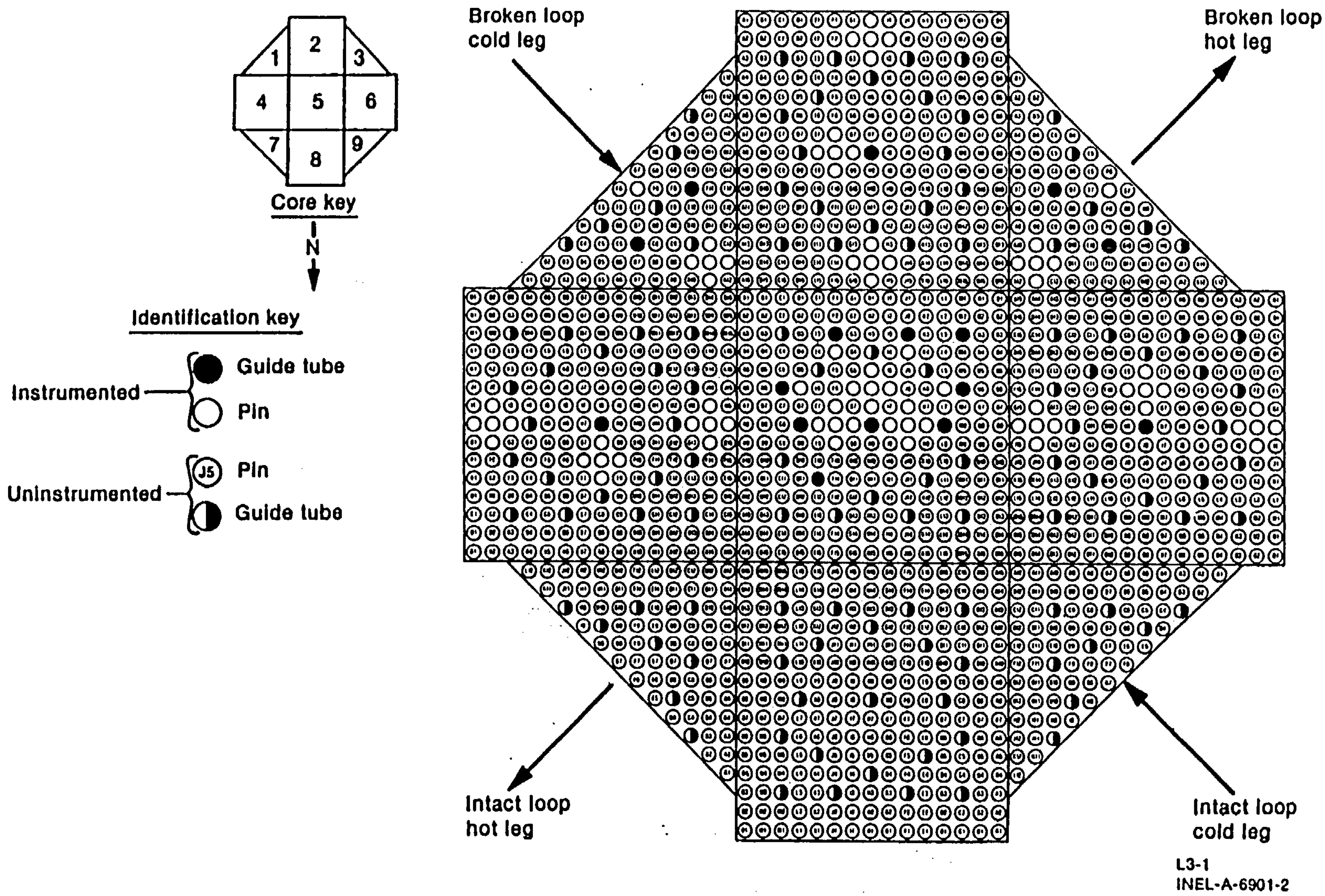

Figure 20-2-3. Cross Section of LOFT Core Arrangement (Bayless, et al., 1980)

20-3 WCOBRA/TRAC-SB Model for Simulation of LOFT Small Break LOCEs L3-1, L3-7, and L3-5

Section 14-1 of WCAP-12945-P-A (Bajorek, et al., 1998) describes the WCOBRA/TRAC model that was used to simulate LOFT large break LOCEs L2-2, L2-3, L2-5, and LB-1. For large break, the LOFT reactor vessel is modelled [

]^{a,c}

This section discusses the WCOBRA/TRAC-SB modelling for LOFT small break LOCEs L3-1, L3-7, and L3-5 using the large break modelling described in Section 14-1 as a basis. For small break, LOFT is modelled [

]^{a,c}.

20-3-1 Reactor Vessel Modelling

In the LOFT large break model, the reactor vessel is represented [

]^{a,c} Figure 20-3-1 illustrates the reactor vessel modelling for the WCOBRA/TRAC-SB simulations of LOCEs L3-1, L3-7, and L3-5.

The core power as a function of time for the LOFT small break LOCEs is supplied to WCOBRA/TRAC-SB as a boundary condition, based on Figure 21 of NUREG CR-1145 (Bayless, et al., 1980) for L3-1; Figure 4-2 of NUREG CR-1570 (Gillas and Carpenter, 1980) for L3-7; and Figure 2-2 of NUREG CR-1695 (Dao and Carpenter, 1980) for L3-5. Use of these best estimate curves in place of the WCOBRA/TRAC-SB kinetics and decay heat models ensures that the thermal-hydraulic predictions are not influenced by known differences in core power behavior between the code modelling and the experiments.

20-3-2 Active Loop Hot Leg, Pressurizer, and Steam Generator Inlet Piping Modelling

In the LOFT large break model, the active loop hot leg and pressurizer surge line are modelled [

]^{a,c} Figure 20-3-2 illustrates the active loop hot leg, pressurizer, and steam generator inlet piping modelling for the WCOBRA/TRAC-SB simulations of LOCEs L3-1, L3-7, and L3-5.

20-3-3 Active Loop Steam Generator Modelling

In the LOFT large break model, the active loop steam generator is modelled [

]^{a,c}

[ ]^{a,c} Figure 20-3-3 illustrates the active loop steam generator modelling for the W̲COBRA/TRAC-SB simulations of LOCEs L3-1, L3-7, and L3-5.

The LOFT steam control valve operates on a pressure hysteresis following steam generator trip and is, therefore, different from the PWR. For L3-1, L3-7, and L3-5, a nontrivial amount of leakage through this valve affected the experimental results. [

]^{a,c}

20-3-4 Active Loop Pump Suction Piping and RCP Modelling

In the LOFT large break model, the active loop pump suction piping was modelled [

]^{a,c}

Figure 20-3-4 illustrates the active loop pump suction piping and RCP modelling for the W̲COBRA/TRAC-SB simulations of LOCEs L3-1, L3-7, and L3-5.

The pump coastdown for the LOFT small break LOCEs is supplied to W̲COBRA/TRAC-SB as a boundary condition, based on Figures 59 and 60 of NUREG CR-1145 (Bayless, et al., 1980) for L3-1; Figure 5S-1 of NUREG CR-1570 (Gillas and Carpenter, 1980) for L3-7; Figures 3S-45 and 3S-46 of NUREG CR-1695 (Dao and Carpenter, 1980) for L3-5. Use of these experimentally obtained curves in place of the W̲COBRA/TRAC-SB pump coastdown calculations ensures that the thermal-hydraulic predictions are not influenced by known differences in RCP behavior between the code modelling and the experiments.

20-3-5 Active Loop Cold Leg Modelling

In the LOFT large break model, the active loop cold leg was modelled [

]^{a,c} Figure 20-3-5 illustrates the active loop cold leg modelling for the WCOBRA/TRAC-SB simulations of LOCEs L3-1 and L3-7.

The LOFT pumped injection enters the cold leg at a location near the reactor vessel, while the PWR injection point is typically further upstream. This results in distortion between the flow regimes observed in the LOFT cold leg and the flow regimes observed in a PWR cold leg and must be considered before using LOFT cold leg behavior to draw conclusions regarding the PWR small break model.

20-3-6 Accumulator and ECCS Modelling

In the LOFT large break model, the accumulator and ECCSs were modelled using: [

]^{a,c} For LOFT LOCEs L3-5 and L3-7 accumulators were valved out during the period of interest - only in LOCE L3-1 is the recommendation active in the simulation.

20-3-7 Inactive Loop Modelling

In the LOFT large break model, the inactive loop was modelled [

]^{a,c} For small break, the inactive loop modelling is as illustrated in Figure 20-3-6. The hot leg is modelled [

]^{a,c}

[

]a,c

The RABL connecting the inactive loop hot and cold legs was designed to remain closed during the experiments. For L3-1 and L3-7, however, a nontrivial amount of leakage through the RABL affected the overall system bypass, which must be modelled in the WCOBRA/TRAC-SB simulations. The RABL is modelled for the small break simulations, [

]a,c Also for L3-5, safety and accumulator injection are moved to the downcomer.

20-3-8 Break Modelling

L3-1 and L3-7 simulated single-ended breaks and used the same break units shown in Figures 20-3-7 and 20-3-8 of the inactive loop cold leg. For the WCOBRA/TRAC transient simulations, the break assembly is modelled, as shown in Figure 20-3-6, [

]a,c

For L3-5, the break unit is located in the intact loop cold leg through an instrument as shown in Figure 20-3-9 (Dao and Carpenter 1980). In this case, [

]a,c

a,c

Figure 20-3-1. Reactor Vessel Modelling for LOFT LOCEs L3-1, L3-7, and L3-5

a,c

Figure 20-3-2. Active Loop Hot Leg, Pressurizer, and Steam Generator Inlet Piping Modelling for LOFT LOCEs L3-1, L3-7, and L3-5

a,c

Figure 20-3-3. Active Loop Steam Generator Modelling for LOFT LOCEs L3-1, L3-7, and L3-5

a,c

Figure 20-3-4. Active Loop Pump Suction Piping and RCP Modelling for LOFT LOCEs L3-1, L3-7, and L3-5

a,c

Figure 20-3-5. Active Loop Cold Leg Modelling for LOFT LOCEs L3-1 and L3-7

a,c

Figure 20-3-6. Inactive Loop Modelling for LOFT LOCEs L3-1 and L3-7

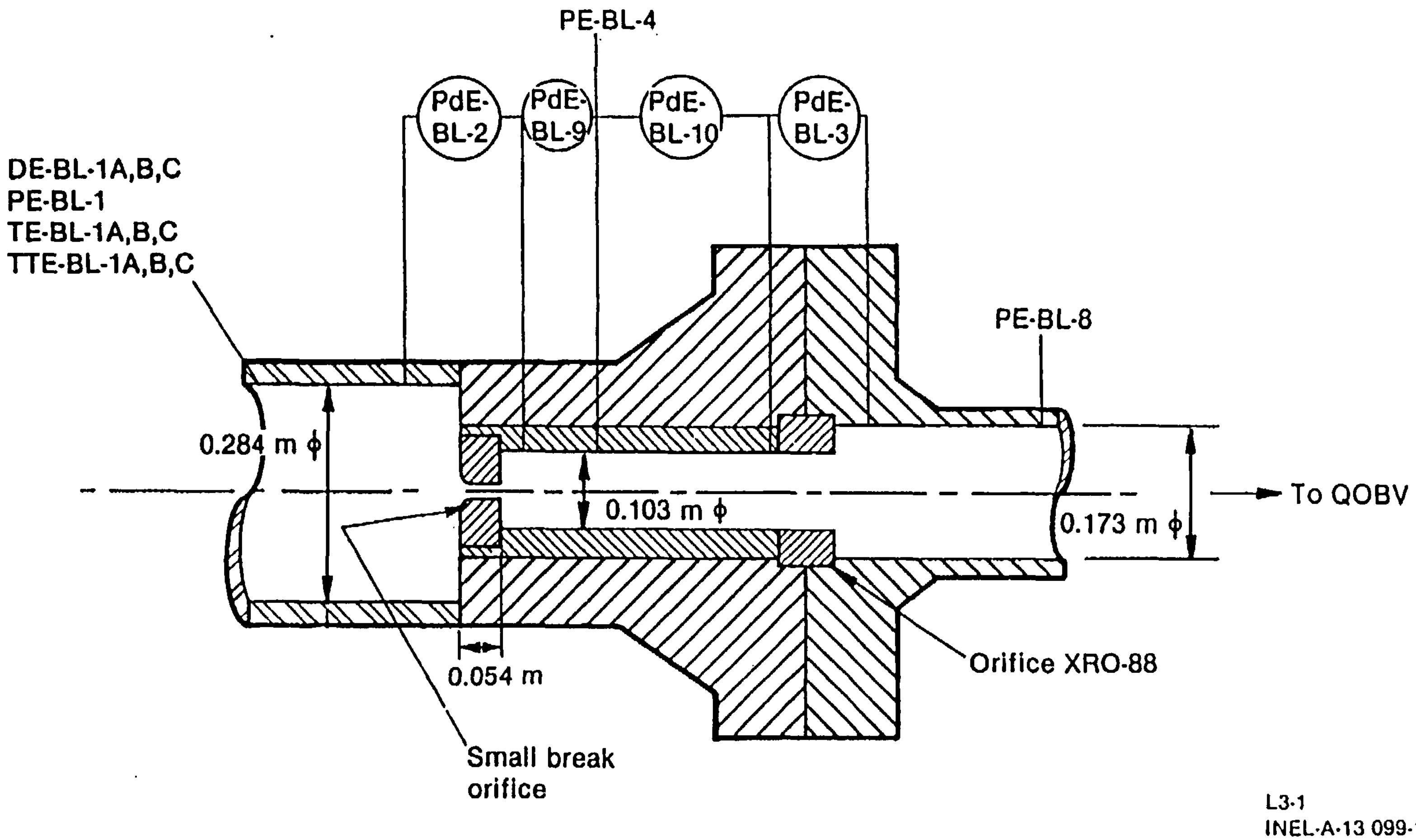

Figure 20-3-7. Break Orifice Assembly for LOFT LOCEs L3-1 and L3-5 (Bayless, et al., 1980)

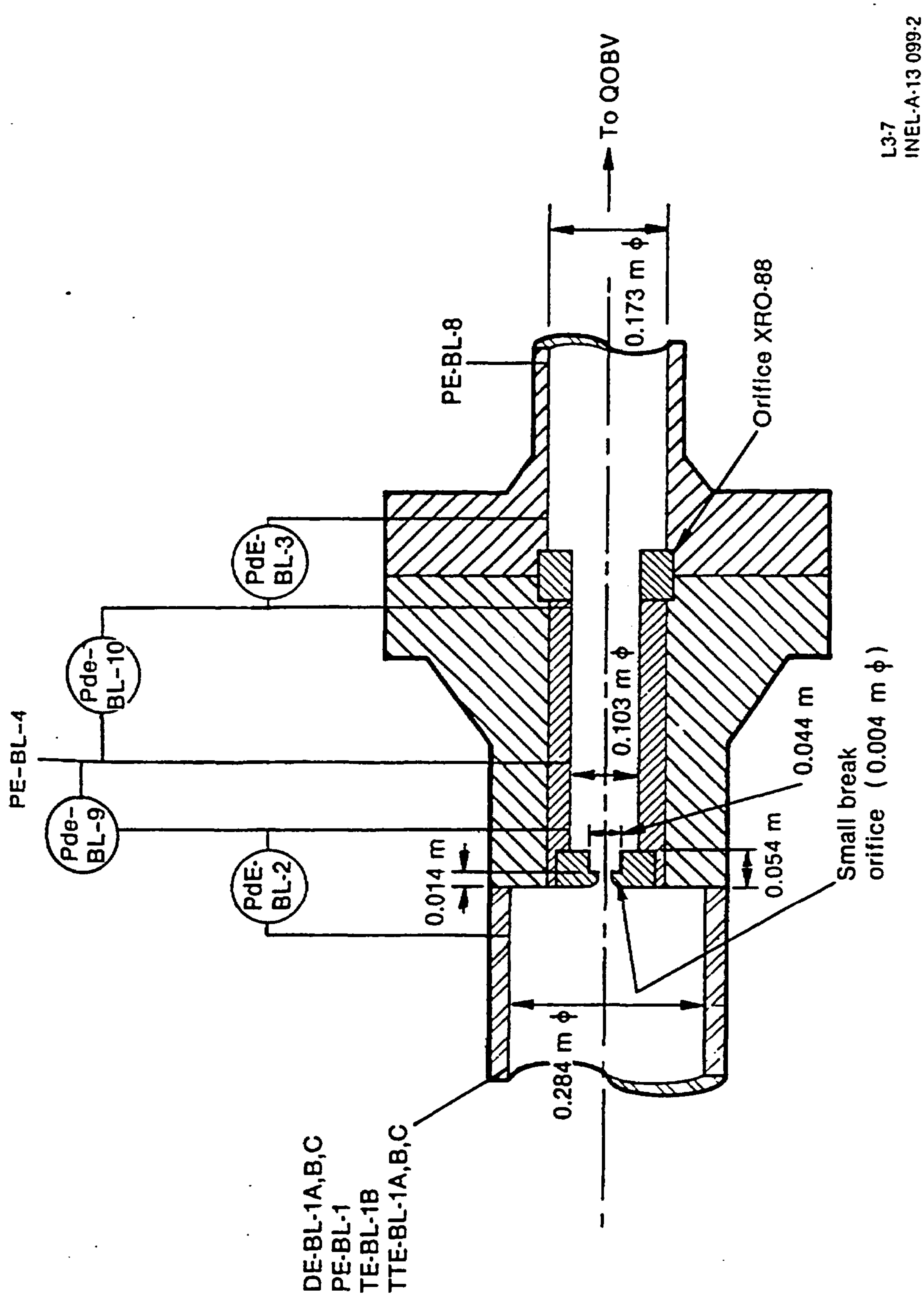

Figure 20-3-8. Break Orifice Assembly for LOFT LOCE L3-7 (Gillas and Carpenter, 1980)

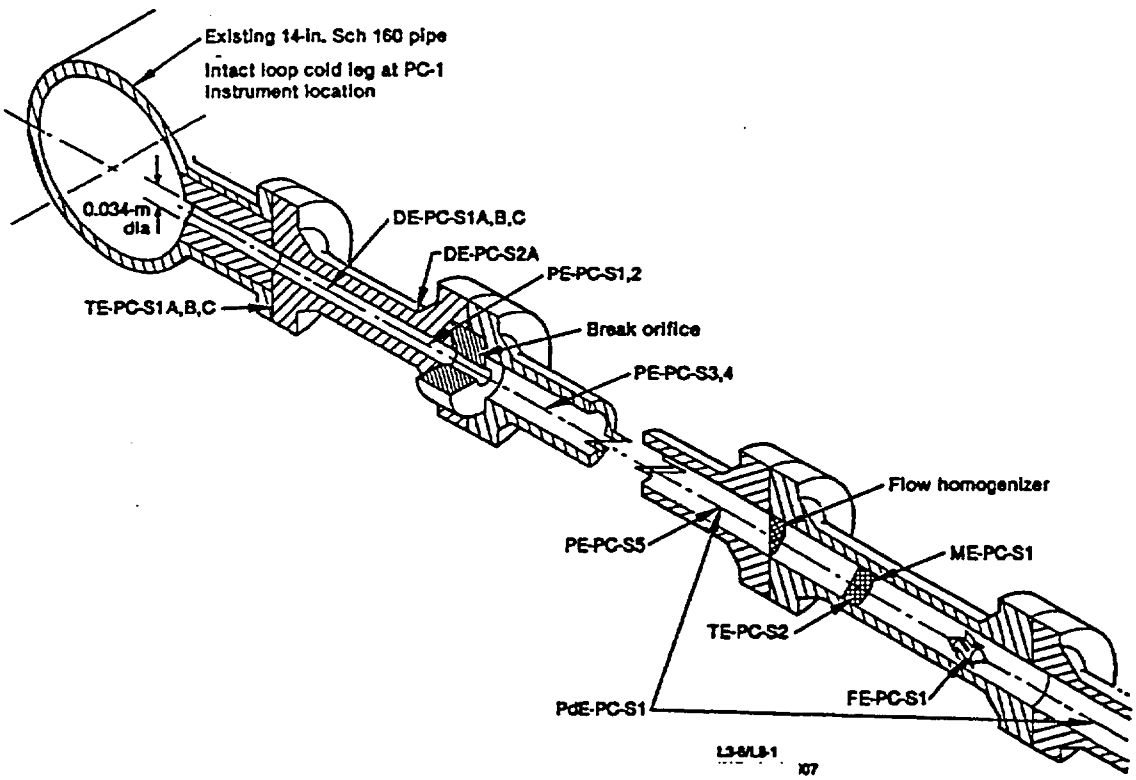

Figure 20-3-9. LOFT LOCE L3-5 Break Unit Configuration

20-4 Steady-State Simulations for LOFT Small Break LOCEs L3-1, L3-7, and L3-5

Prior to the transient simulations, a 200-second steady-state was run for each LOCE to ensure stable system behavior prior to break initiation. Parameters that are normally varied in large break LOCA test simulations to obtain satisfactory steady-state conditions are varied in these small break LOCE calculations. System coolant mass (i.e., enthalpy) is varied to obtain a primary system pressure within the stated data uncertainty. Pump speed is varied to obtain the desired primary system flow. Secondary system pressure is varied to obtain active loop hot and cold leg temperatures within specified limits. The average linear heat generation rate is varied to obtain the correct core power. Feedwater temperature is varied to obtain the appropriate secondary fluid temperature. With these parameters controlled, other parameters (such as the inactive loop hot and cold leg temperatures) may be within or outside of the limits specified by the data uncertainty.

20-4-1 Steady-State Simulation for LOFT LOCE L3-1

Table 20-4-1 compares the results of the 200-second WCOBRA/TRAC-SB steady-state simulation for LOCE L3-1 to the initial conditions identified in NUREG CR-1145, pages 28 and 29 (Bayless, et al., 1980). The following summarizes the results of the steady-state simulation for L3-1:

- The calculated active loop hot leg temperature predicts hot leg streaming. The temperature at the top of the hot leg is calculated to be greater than that calculated for the cells below. The numerical average of the calculated temperatures lies within the data uncertainty, as does the mixed liquid temperature for channel 88 at the steam generator unit.

- The calculated RABL flow is 1.5 percent of total active loop flow. This is below the estimated 3-percent bypass for the RABL.

- The calculated inactive loop cold leg and hot leg temperatures lie within the data uncertainty.

- The steam generator collapsed liquid level is approximately 9.4 feet; this is approximately 0.9 feet below the data minus uncertainty.

- The steam generator feedwater and steam flowrates are within the data and uncertainty. The steaming rate is approximately 1 percent higher than the feed water flowrate. This is consistent with a calculated liquid temperature at the bottom of the boiler approximately 5 °F greater than the data for the steam generator liquid temperature.

- The steam generator pressure was adjusted to give the correct primary side temperatures. [

  ]^{a,c}.

20-4-2 Steady-State Simulation for LOFT LOCE L3-7

The results of the L3-7 steady-state calculation, as summarized in Table 20-4-2, are within the limits of the data and uncertainties identified in NUREG/CR-1570 (Gillas, 1980) except as noted in the following. The steady-state values outside the limits of the data and uncertainty are judged to be minor and have no significant effect on the overall transient calculation.

- The calculated active loop hot leg temperature predicts hot leg streaming. The temperature at the top of the hot leg is calculated to be greater than that calculated for the lower cells. The numerical average of the calculated temperatures lies within the data uncertainty, while the mixed fluid temperature in channel 88 is 0.1 °F below the data and uncertainty.

- The calculated RABL flow is 1.5 percent of total active loop flow; this is below the estimated 3-percent bypass for the RABL.

- The calculated inactive loop cold leg temperature lies within the data uncertainty. Even with the lower RABL bypass flow, the inactive loop hot leg temperature is calculated to be approximately 1.3 °F below the data minus uncertainty.

- The steam generator level is approximately 9.3 feet and approximately 1 foot below the data minus uncertainty.

- Steam generator pressure is 29.3 psi below the data and uncertainty. As with L3-1, the secondary side pressure is adjusted to obtain desired primary side temperature. [

  ]a,c

20-4-3 Steady-State Simulation for LOFT LOCE L3-5

The results of the L3-5 steady-state calculation, as summarized in Table 20-4-3, are within the limits of the data and uncertainties identified in NUREG/CR-1695 (Dao and Carpenter, 1980) except as noted in the following. The steady-state values outside the limits of the data and uncertainty are judged to be minor and have no significant effect on the overall transient calculation.

- The calculated active loop hot leg temperature predicts hot leg streaming. The temperature at the top of the hot leg is calculated to be greater than that calculated for the lower cells. The numerical average of the calculated temperatures lies within the data uncertainty, as does the mixed fluid temperatures in channel 88.

- The calculated RABL flow is 1.5 percent of total active loop flow; this is below the estimated 3-percent bypass for the RABL.

- The calculated inactive loop hot leg temperature is greater than the data plus uncertainty by 1.4°F. The inactive loop cold leg temperature lies within the data and uncertainty.

- The steam generator level is approximately 9.3 feet and approximately 1 foot below the data minus uncertainty.

- The pressurizer temperature is approximately 0.4°F below the data minus uncertainty, which is consistent with the calculated pressurizer pressure.

- As in the L3-1 steady-state calculation, the secondary side pressure is adjusted to obtain the desired primary side temperatures, and is 19.4 psi below the data minus uncertainty. This translates to 4°F in secondary side saturation temperature – [

  ]a,c.

Table 20-4-1
Comparison of LOFT LOCE L3-1 Steady-State Calculation to L3-1 Data

Parameter	Calculated Value (190 sec)	Data[1,2]	Uncertainty[1,2] (±)
Reactor Power	48.9 MW	48.9 MW	1
Peak Linear Heat Generation Rate	16.099 kW/ft	15.75 kW/ft	0.305
Intact Loop			
Flow Rate	1065 lb/sec	1067.0 lb/sec	13.9
Hot Leg Pressure	2149.6 psia	2153.25 psia	5.8
Hot Leg Temperature			
Top Cell	577.2°F		
Average	573.9°F		
SG Entry Pipe	573.8°F	573.5°F	1.8
Cold Leg Temperature	540.2°F	537.5°F	5.4
Pressurizer			
Liquid Volume	21.9 ft^3	21.9 ft^3	0.28
Pressure	2146.5 psia	2147.5 psia	5.8
Temperature	6445.9°F	650.9°F	5.4
Broken Loop			
Cold Leg Temperature	540.3°F	543.5°F	9.0
Hot Leg Temperature[4]	554.8°F	552.0°F	9.0
Steam Generator Secondary			
Secondary Flowrate		55.1 lb/sec	0.88
Feedwater Flowrate	55.6 lb/sec		
Steam Flowrate[3]	55.8 lb/sec		
Pressure	760.9 psia	787.4 psia	16.0
Water Temperature		505.4°F	7.0
Downcomer	497.1°F		
Boiler	510.7°F		
Liquid Level	9.4 ft	10.34 ft	0.03

1. NUREG CR-1145 (Bayless, et al., 1980), see Appendix B for a copy of SS data
2. Converted from SI units
3. Value in the table represents value at 190 sec.
4. Average of 549.8, 554.6, and 560.4

Table 20-4-2

Comparison of LOFT LOCE L3-7 Steady-State Calculation to L3-7 Data

Parameter	Calculated Value (200 sec)	Data[1,2]	Uncertainty[1,2] (±)
Reactor Power	49 MW	49 MW	1
Peak Linear Heat Generation Rate	16.132 kW/ft	16.093 kW/ft	1.128
Intact Loop			
Flow Rate	1064.2 lb/sec	1061.1 lb/sec	13.9
Hot Leg Pressure	2162.0 psia	2160.5 psia	36.3
Hot Leg Temperature			
Top Cell	579.6°F		
Average	576.4°F		
SG Entry Pipe	576.3°F	577.3	0.9
Cold Leg Temperature	542.8°F	541.1°F	5.4
Pressurizer			
Liquid Volume	22.6 ft³	22.25 ft³	1.77
Pressure	2158.7 psia	2160.5 psia	5.8
Temperature	646.9°F	647.3°F	0.54
Broken Loop			
Cold Leg Temperature	542.9°F	544.2°F	4.5
Hot Leg Temperature[3]	556.7°F	550.9°F	4.5
Steam Generator Secondary			
Secondary Flowrate		61.7 lb/sec	0.88
Feedwater Flowrate	60.7 lb/sec		
Steam Flowrate	60.7 lb/sec		
Pressure	777.5 psia	808.5 psia	1.74
Water Temperature		519.5°F	0.36
Downcomer	511.06°F		
Boiler	515.5°F		
Liquid Level	9.3 ft	10.50 ft	0.20

1. NUREG CR-1570 (Gillas, et al., 1980)
2. Converted from SI units
3. Average of 551.0, 556.4, 562.6

Table 20-4-3

Results of LOFT LOCE L3-5 Steady-State Calculation to L3-5 Data

Parameter	Calculated Value (190 sec)	Data[1,2]	Uncertainty[1,2] (±)
Reactor Power	49 MW	49 MW	1
Peak Linear Heat Generation Rate	16.132 kW/ft	16.032 kW/ft	1.128
Intact Loop			
Flow Rate	1048.4 lb/sec	1050.3 lb/sec	13.9
Hot Leg Pressure	2160.0 psia	2154.7 psia	20.3
Hot Leg Temperature			
Top Cell	580.4°F		
Average	577.1°F		
SG Entry Pipe	577.0°F	577.1°F	3.6
Cold Leg Temperature	543.1°F	544.7°F	1.8
Pressurizer			
Liquid Volume	24.0 ft^3	24.0 ft^3	2.1
Pressure	2156.9 psia	2157.6 psia	2.9
Temperature	646.6°F	647.23°F	0.18
Broken Loop			
Cold Leg Temperature	543.2°F	541.1°F	4.5
Hot Leg Temperature[3]	557.8°F	551.9°F	4.5
Steam Generator Secondary			
Secondary Flowrate		58.2 lb/sec	2.2
Feedwater Flowrate	57.7 lb/sec		
Steam Flowrate[4]	57 lb/sec		
Pressure	781.0 psia	809.1 psia	8.7
Water Temperature		517.7°F	1.8
Downcomer	504.7°F		
Boiler	515.0°F		
Liquid Level	9.3 ft	10.30 ft	0.13

1. NUREG CR-1695 (reference 8, copy of reference table in Appendix B)
2. Converted from SI units
3. Average of 564.5, 557.4, 551.4
4. Slight oscillation about the steady-state feed flow, see figure, average about 190 sec = 57.0 lb/sec.

20-5 Transient Simulations for LOFT Small Break LOCEs L3-1, L3-7, and L3-5

20-5-1 Transient Simulation for LOFT LOCE L3-1

The LOFT LOCE L3-1 is a 4-inch equivalent break in the inactive loop cold leg. This experiment started from initial conditions similar to L3-5 with the same break orifice as described in this section. The reactor was tripped several seconds prior to opening the blowdown valves to initiate the break. The sequence of events is listed in Table 20-5-1-1 (Bayless, et al., 1980). The RCPs were tripped shortly after the break opening, and safety injection was initiated on low primary system pressure. Safety injection was directed into the active loop cold leg. The intent is to simulate L3-1 with WCOBRA/TRAC-SB based on the initial conditions described in Section 20-4-1 and the appropriate boundary conditions.

The physical arrangement of the inactive loop cold leg with the RABL connecting the inactive loop cold and hot legs coupled with the lack of a complete loop means that L3-1, like L3-7, is atypical of a full-scale PWR geometry. Leakage through the RABL equalizes pressure between the hot and cold legs and acts like loop seal clearing. While L3-1 and L3-7 may not represent typical behavior of a small break LOCA in a PWR, they remain useful in evaluating WCOBRA/TRAC-SB.

A comparison of the calculated and measured temperatures upstream of the break, as seen in Figure 20-5-1-1, shows that the calculated temperature (dashed curve) initially decreases several degrees, while the measured temperature indicates an initial increase of approximately 10°F. A comparison of the measured inactive loop hot and cold leg temperatures, as seen in Figure 20-5-1-2, equalizes within approximately 30 seconds into the transient. This indicates the possibility that flow reversal through the RABL occurred by 30 seconds into the transient.

The calculated time of flow reversal through the RABL is approximately 30 seconds into the transient as seen in Figure 20-5-1-3. If this is later than the actual time of flow reversal, or the calculated RABL flow is less than the actual flow, these errors allow the calculated temperature to remain low. After the calculated RABL flow reversal, the calculated cold leg temperature increases only slightly. The hot and cold leg temperatures equalize when the hot leg temperature has fallen to the cold leg temperature. Calculated saturation of the inactive loop cold leg is delayed by more than 200 seconds compared to the data as seen in Figures 20-5-1-2 and 20-5-1-4.

A comparison of the measured inactive loop mass flowrate and the indicator of the actual break flow, and the calculated break mass flowrate is shown in Figures 20-5-1-5a and 20-5-1-5b. The calculated mass flow is significantly greater than that indicated by the inactive loop flowrate after 200 seconds. This is consistent with the extended period of subcooled flow and lower than measured temperature. Even with an unrealistically high calculated mass ejection through the break, the calculated pressure stays higher than the data after saturation is reached as seen in Figure 20-5-1-6. This may be the result of an underprediction of the quality upstream of the break, as seen in Figure 20-5-1-7, which causes the break to remain plugged. Both the calculated break mass flowrate and system pressure remain higher than the data.

The extent to which the assumed RABL leakage area is a contributor to the errors in the simulation of L3-1 is not determinable without explicit knowledge of the RABL leakage during L3-1. At best, the sensitivity of the simulation to RABL leakage could be determined by additional calculations that vary the leakage area.

Table 20-5-1-1
Sequence of Events for LOFT LOCE L3-1
(Bayless, et al., 1980)

Event	L3-1 Measured Data (seconds)
LOCE initiated	0.0
Primary coolant pumps tripped	0.04 ± 0.01
HPIS injection initiated	4.6 ± 0.5
Pressurizer emptied	17.0 ± 1.0
Upper plenum reached saturation	24.4 ± 0.5
Auxiliary feed pump started	75.0 ± 1.0
Accumulator injection initiated	633.6 ± 0.5
Accumulator empty	1741.0 ± 1.0
Auxiliary feed pump tripped	1875.0 ± 1.0

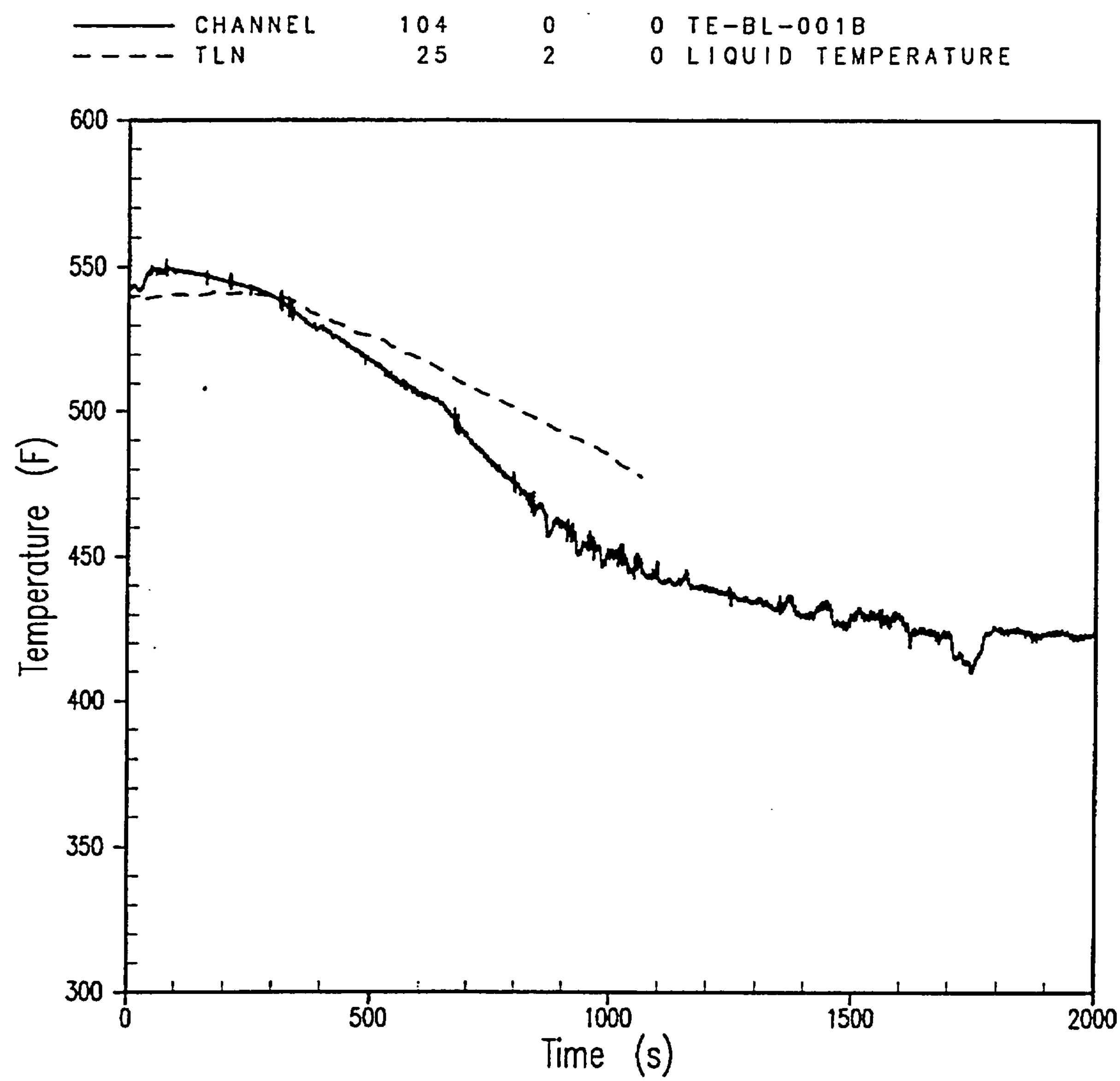

Figure 20-5-1-1. Comparison of Calculated and Measured Temperature Upstream of Break Orifice for LOFT LOCE L3-1

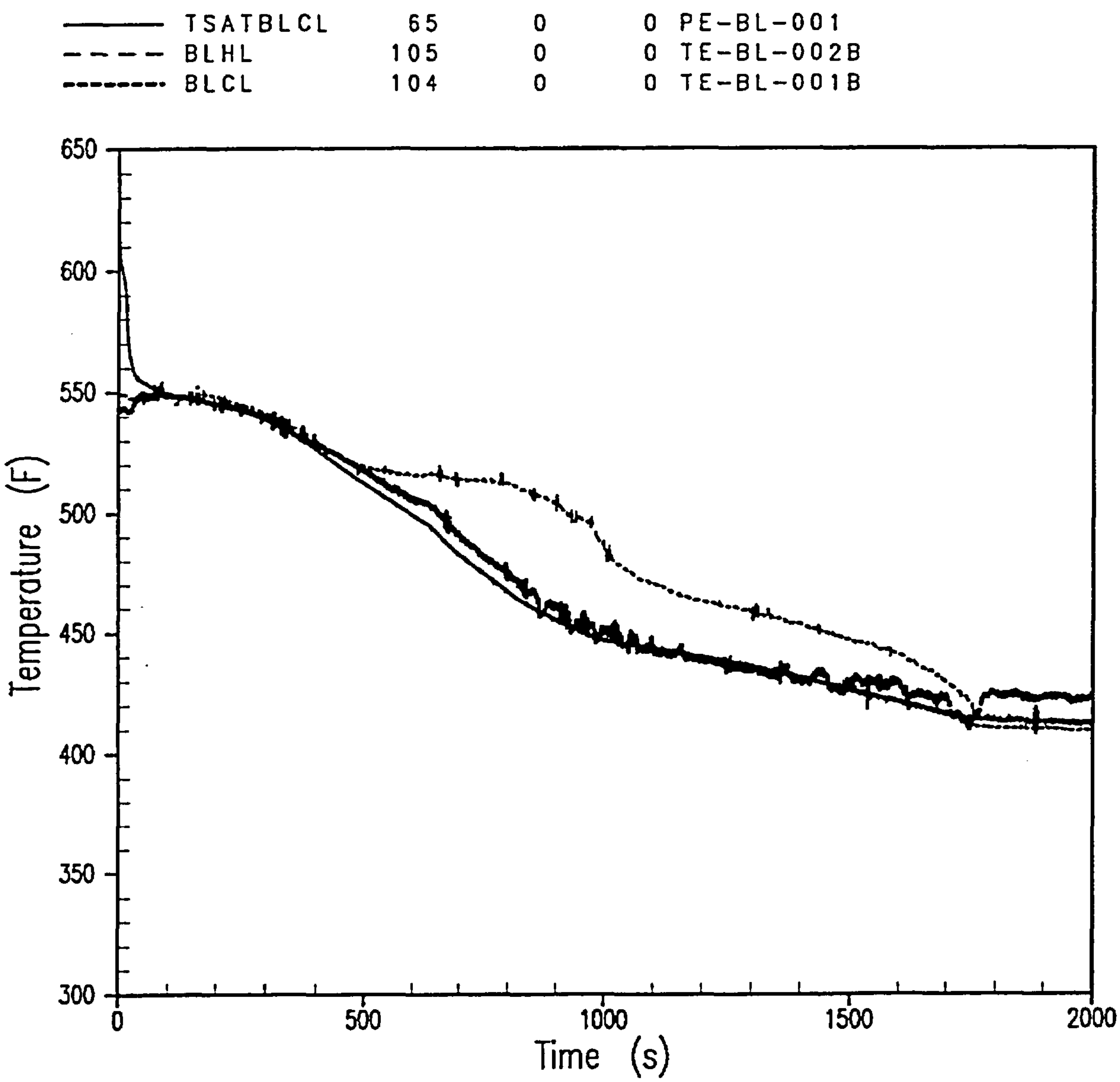

Figure 20-5-1-2. Comparison of Inactive Loop Cold Leg, Inactive Loop Hot Leg, and Saturation Temperature for LOFT LOCE L3-1 From Test Measurements

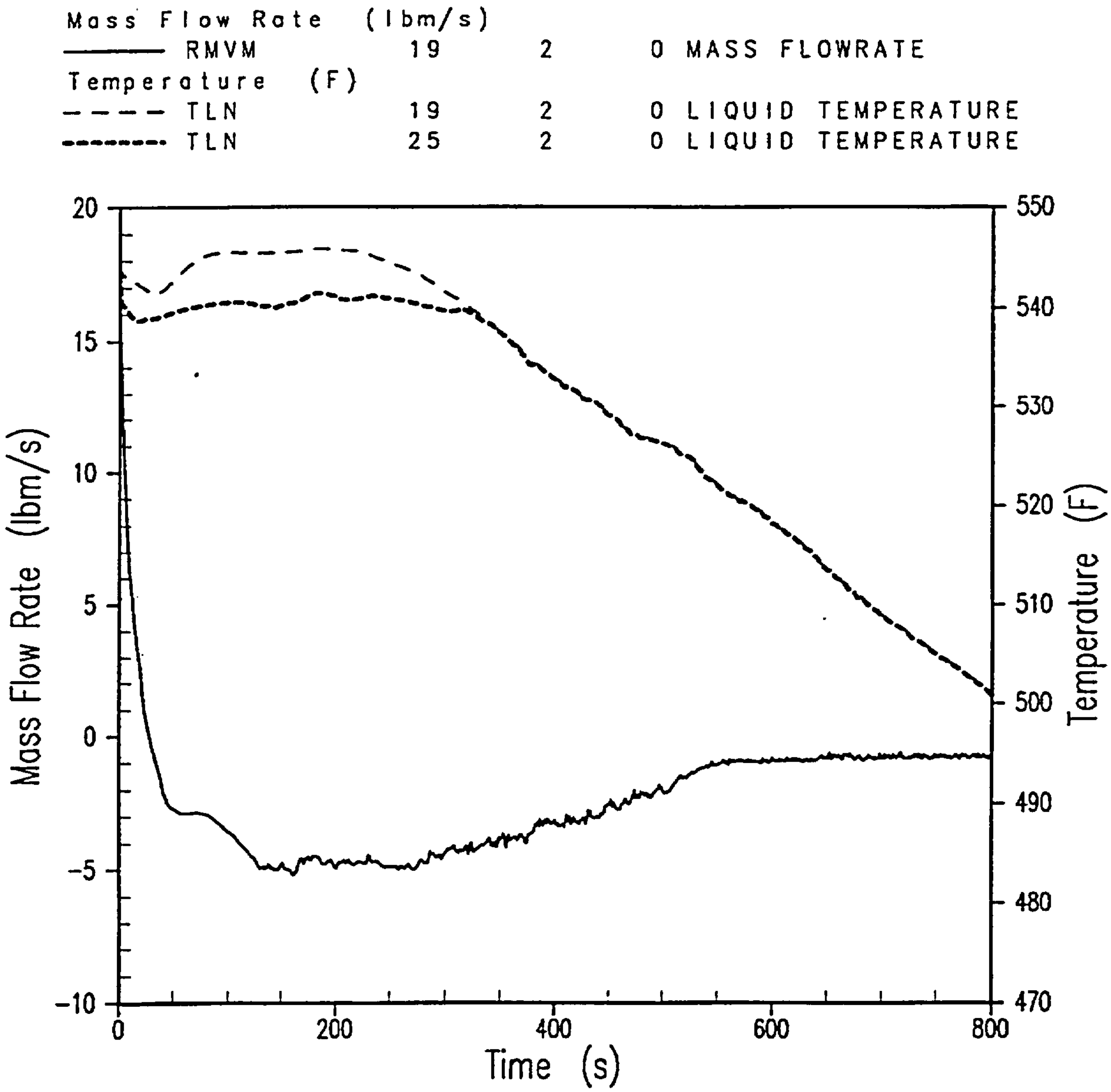

Figure 20-5-1-3. Comparison of Calculated Liquid Temperature Upstream of Break Orifice, Liquid Temperature in RABL, and RABL Mass Flowrate

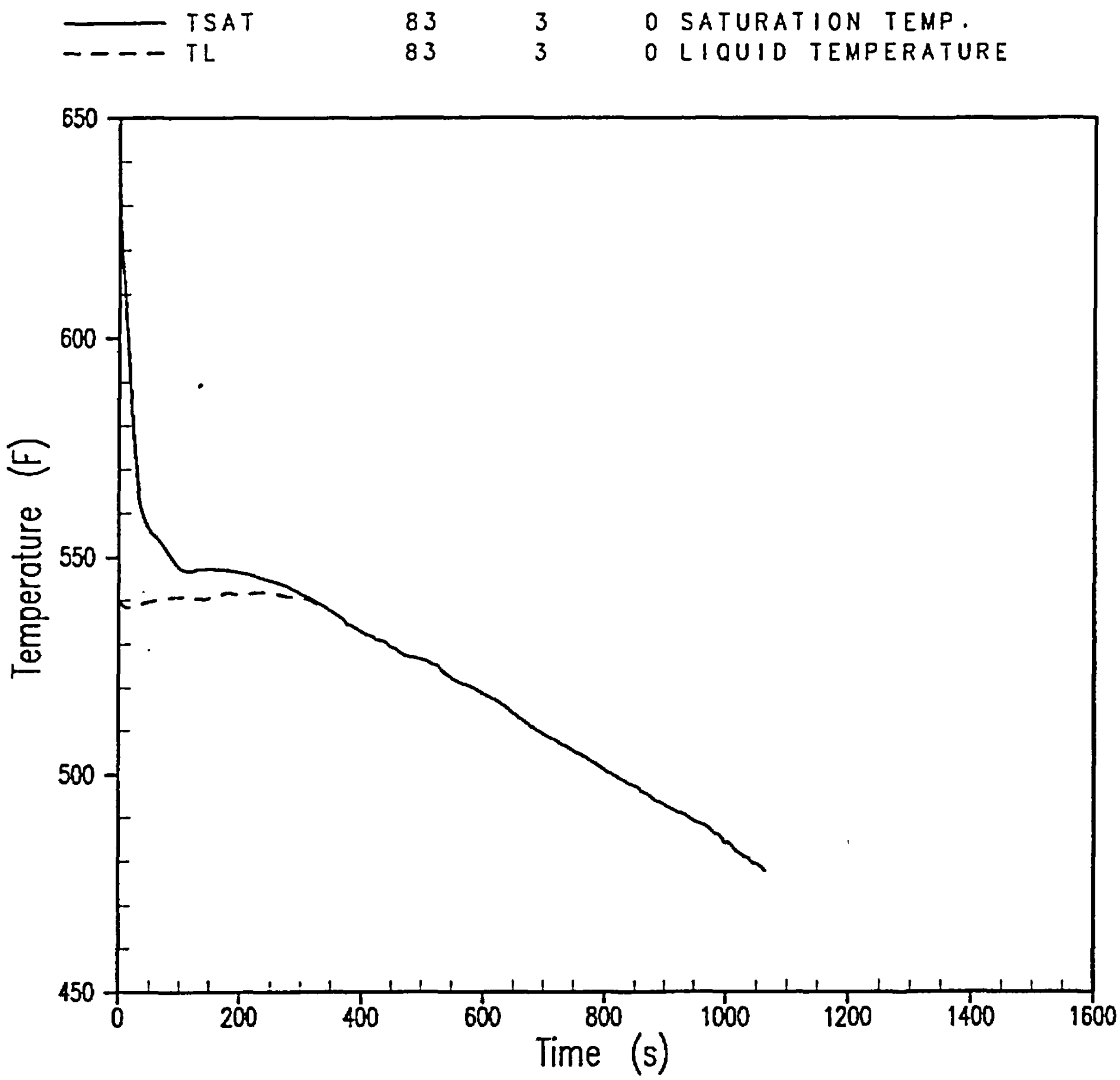

Figure 20-5-1-4. Comparison of Calculated Inactive Loop Cold Leg Liquid Temperature and Saturation Temperature

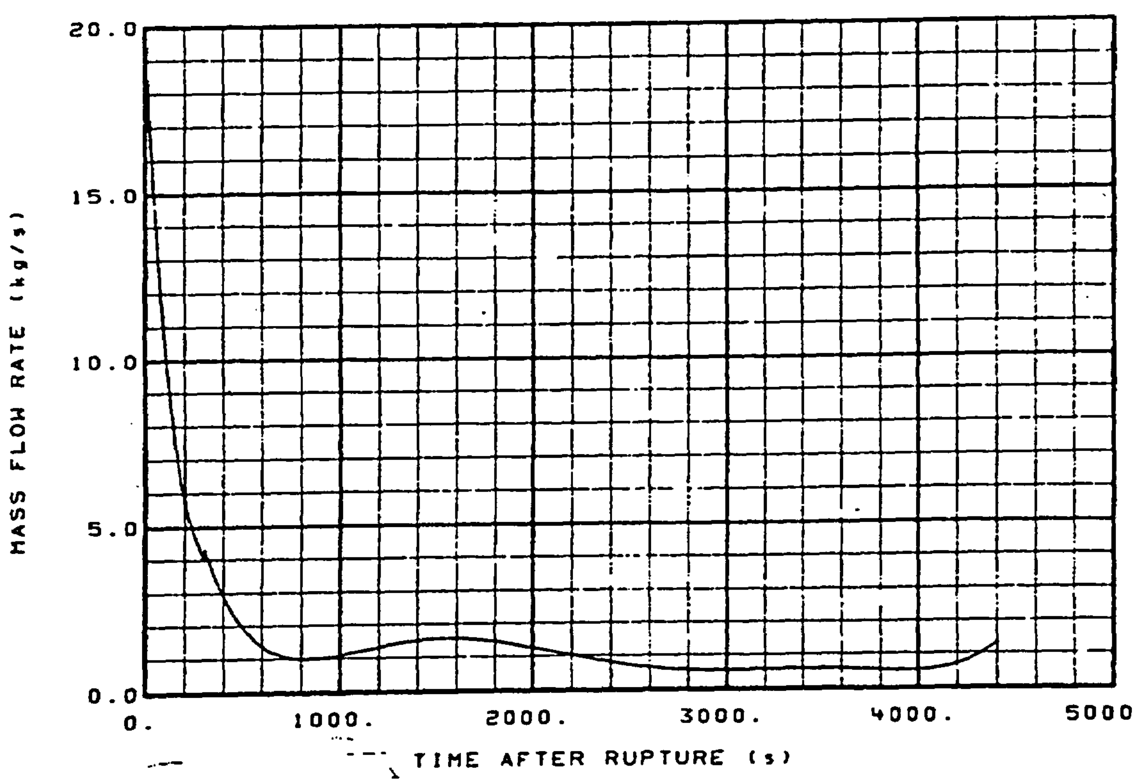

Figure 20-5-1-5a. Measured Mass Flowrate in Inactive Loop Cold Leg (Qualified) (Bayless, et al., 1980)

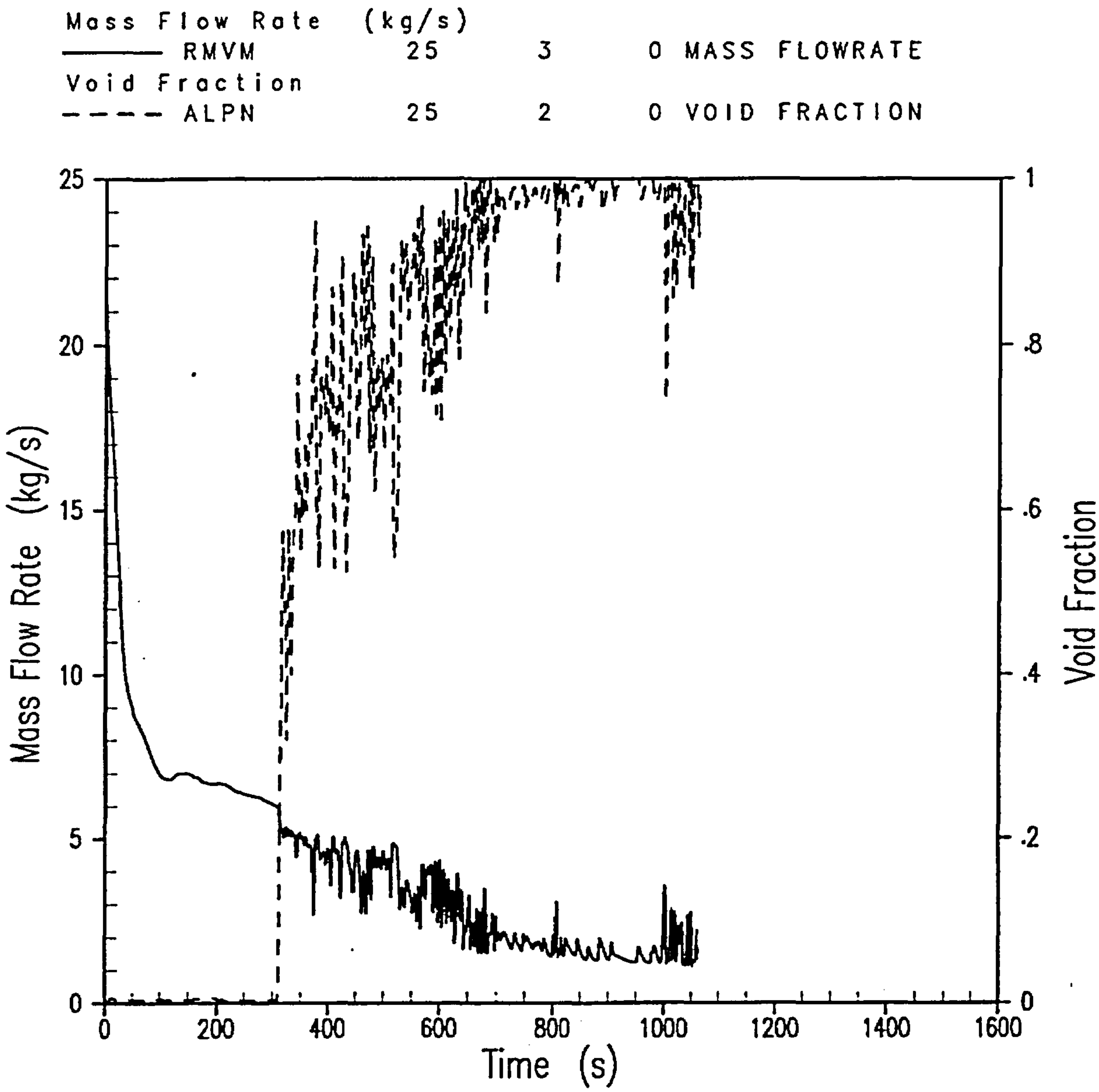

Figure 20-5-1-5b. Calculated Break Mass Flowrate and Upstream Void Fraction for LOFT LOCE L3-1

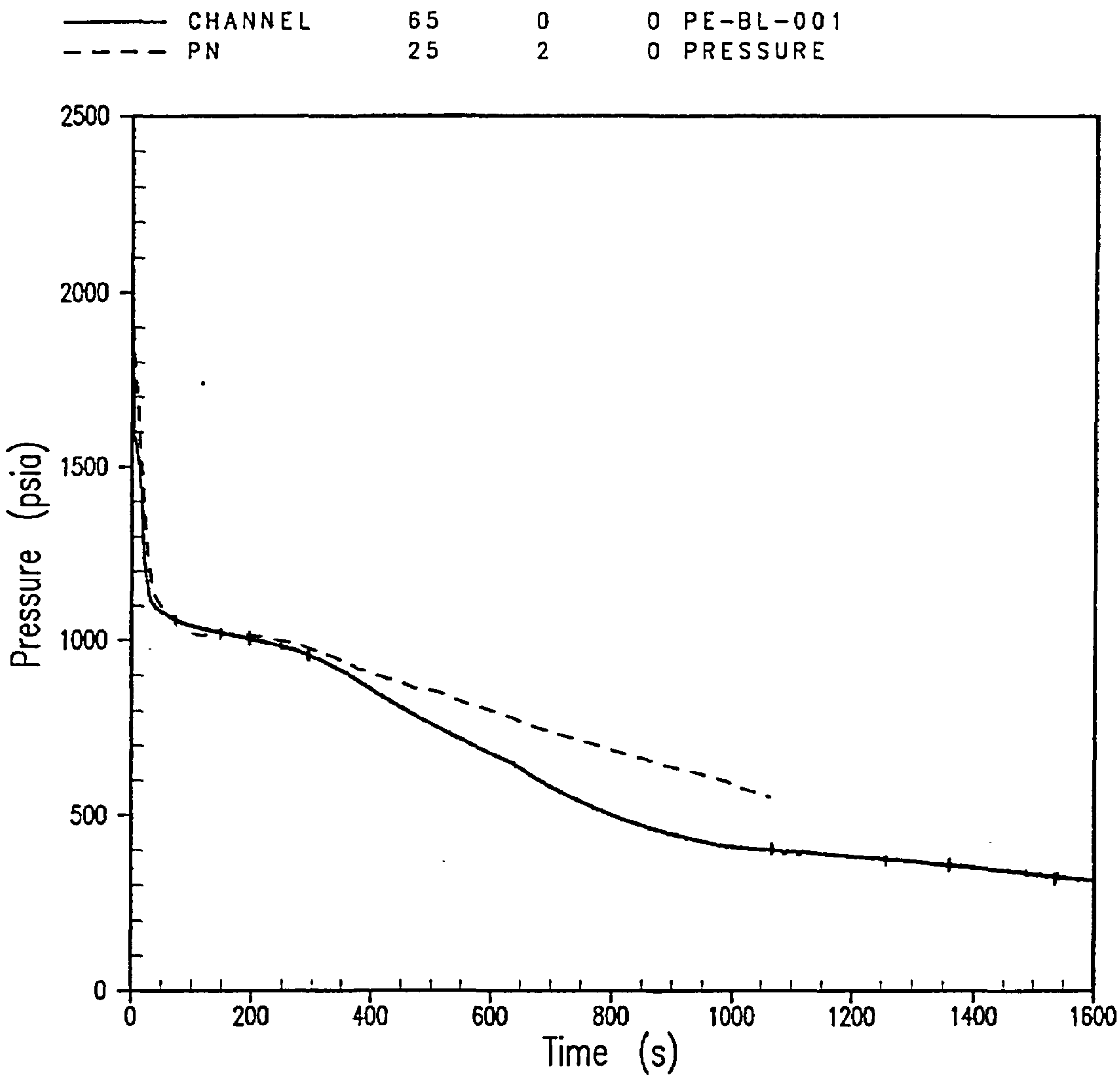

Figure 20-5-1-6. Comparison of Calculated and Measured Primary System Pressure for LOFT LOCE L3-1

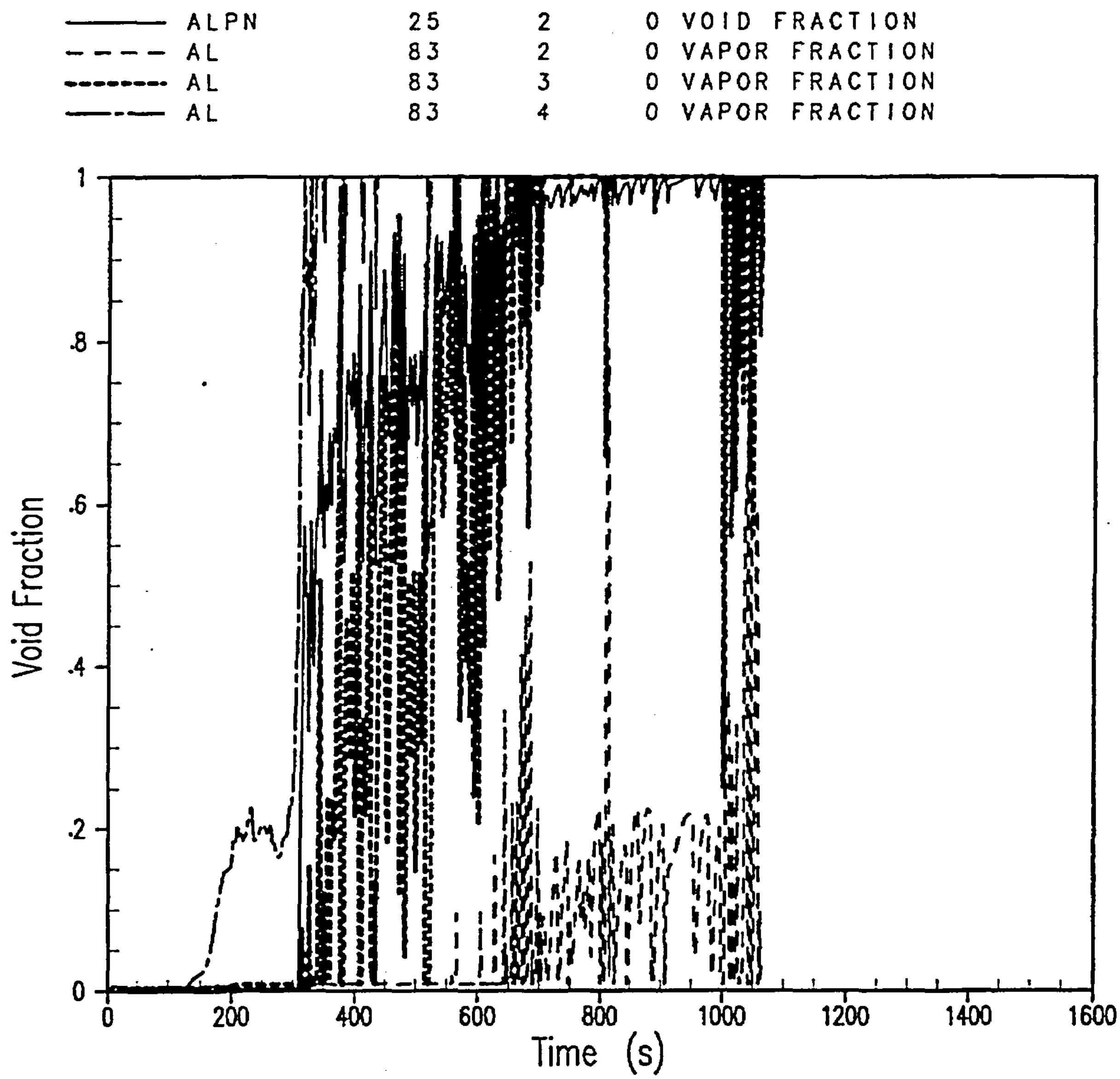

Figure 20-5-1-7. Calculated Void Fractions Upstream of Break Orifice and in 3-D Channel Connected to Break Unit for LOFT LOCE L3-1

20-5-2 Transient Simulation for LOFT LOCE L3-7

LOFT LOCE L3-7 is a 1-inch equivalent break (13.2 mm^2) using the spoolpiece depicted in Figure 20-3-8. The objective of L3-7 was to establish conditions conducive to long-term natural circulation. However, a geometric distortion exists in the form of the RABL upstream of the break plane. The RABL provides a direct leakage path between the hot and cold legs that does not exist in a full-scale PWR. This may influence the calculations favorably or unfavorably as discussed later in this section.

For L3-7, the facility was operated similarly to a full-scale PWR, unlike the other small break LOCEs. The reactor and RCP trips occurred on low pressure. The reactor trip occurred at 36 seconds, and the pump trip occurred at 39.3 seconds, as shown in the sequence of events in Table 20-5-2-1.

A comparison of the measured and calculated inactive loop cold leg temperatures upstream of the break, as seen in Figure 20-5-2-1, indicates the code overestimates the temperature during the first 800 seconds. Overall, the WCOBRA/TRAC-SB calculations follow the trend of the data, although the calculation predicts the decrease in temperature to occur approximately 200 seconds early. The final calculated temperature is under predicted by approximately 14K (25°F).

As shown in Figure 20-5-2a and -2b, the break/mass flow rate predicted by WCOBRA/TRAC-SB follows the unqualified measurement.

WCOBRA/TRAC-SB under predicts the unqualified measurement of break flow by approximately 0.2 kg/s by the end of the transient calculation. Since the data are unqualified only the trend can be judged, and the trend is judged to be adequate.

The WCOBRA/TRAC-SB prediction of inactive loop cold leg pressure adequately matches the data to 400 seconds when both the prediction and measurement are approximately 8 MPa (1100 psia). At 800 seconds the prediction and measurement are approximately the same. After 800 seconds the calculated depressurization rate increases and WCOBRA/TRAC-SB under predicts the data. By the end of the transient calculation the inactive loop cold leg pressure is under predicted by approximately 0.7 MPa (102 psia). The cause of the under prediction appears to be steam generator heat rejection.

As shown in Figure 20-5-2-4b, natural circulation is predicted to be established between 100 and 200 seconds into the transient. The predicted natural circulation flow is predicted to be between approximately 15 and 22 kg/s. This is less than half of the unqualified measurement (Gillas and Carpenter 1980). As noted previously for unqualified data, only the trend can be judged and the trend is judged to be adequately predicted. Also, shown in Figure 20-5-2-4a and -4b, are the measured and predicted steam generator inlet and outlet temperatures. The predicted temperature difference is greater than measured. Thus the primary system average temperature is significantly under predicted starting at approximately 800 seconds. The error in calculated temperature is a result of overestimation of the auxiliary feedwater flowrate. The result of the under prediction of the loop average temperature is underprediction of the primary system pressure as shown in Figure 20-5-2-3b.

Figure 20-5-2-5 compares decay heat and heat rejected to the secondary system. At approximately 700 seconds predicted heat rejection increases from approximately 200 KW to approximately 500 KW. This is consistent with the above observation on steam generator primary side temperature difference.

Table 20-5-2-1
Sequence of Events for LOFT LOCE L3-7
(Gillas and Carpenter, 1980)

Event	L3-7 Measured Data (seconds)
LOCE initiated	0.0
Reactor scrammed	36.0 ± 0.1
Control rods reached bottom	38.1 ± 0.1
Primary coolant pumps tripped	39.3 ± 0.5
HPIS injection initiated	65.6 ± 0.1
Auxiliary feed initiated	75.0 ± 3.0
Pressurizer emptied	264.0 ± 7.0
Upper plenum reached saturation	382.0 ± 6.0
End of subcooled break flow	1037.0 ± 10.0
Auxiliary feed terminated	1800.0 ± 5.0
HPIS flow terminated	1805.3 ± 0.1
SCS steam bleed initiated	3603 ± 1
HPIS flow reinstated	5974.2 ± 0.1
Accumulator injection initiated	6028 ± 5
Break isolated	7302.0 ± 0.1

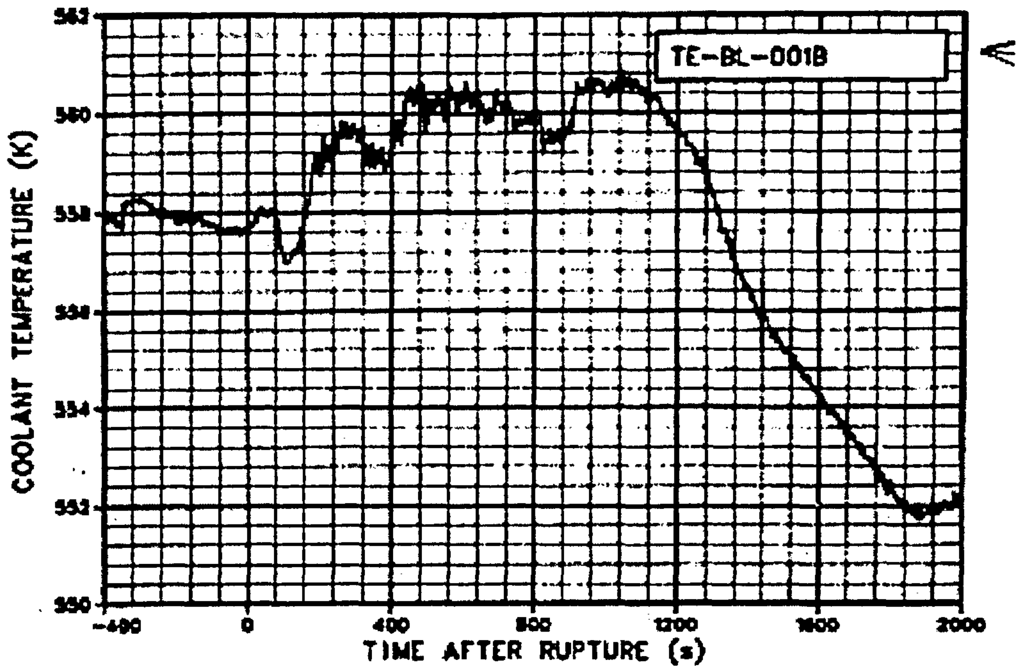

Figure 20-5-2-1a. Measured Inactive Broken Loop Cold Leg Temperature for LOFT LOCE L3-7 (Gillas and Carpenter, 1980)

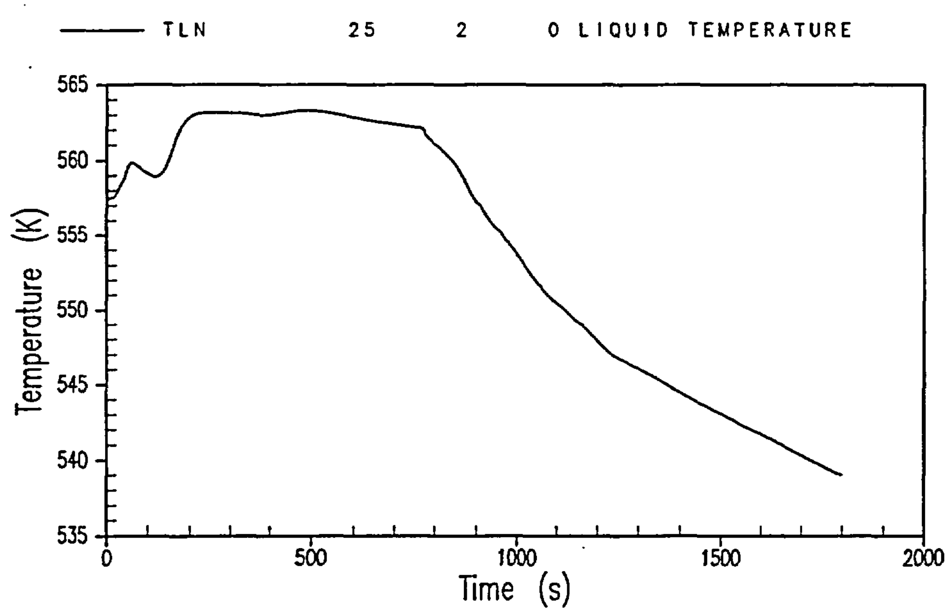

Figure 20-5-2-1b. Calculated Liquid Temperature Upstream of Break Orifice for LOFT LOCE L3-7

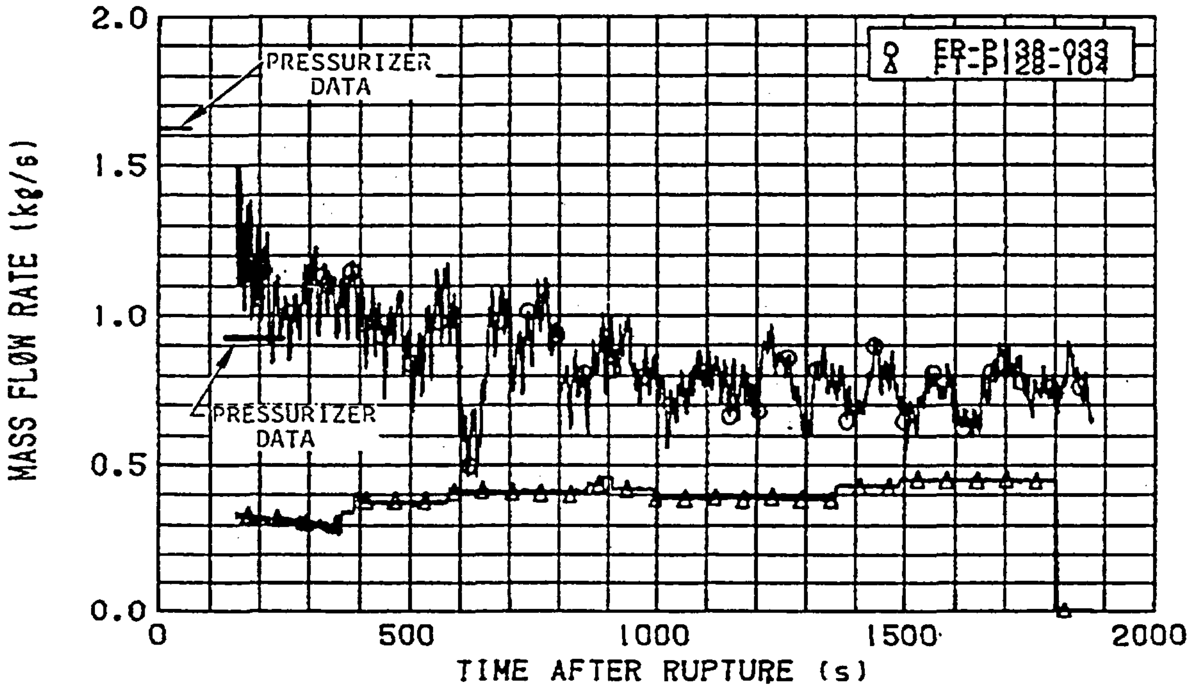

Figure 20-5-2-2a. Comparison of Measured Break Flow and ECCS Flow (Not Qualified) (McCreery, 1980)

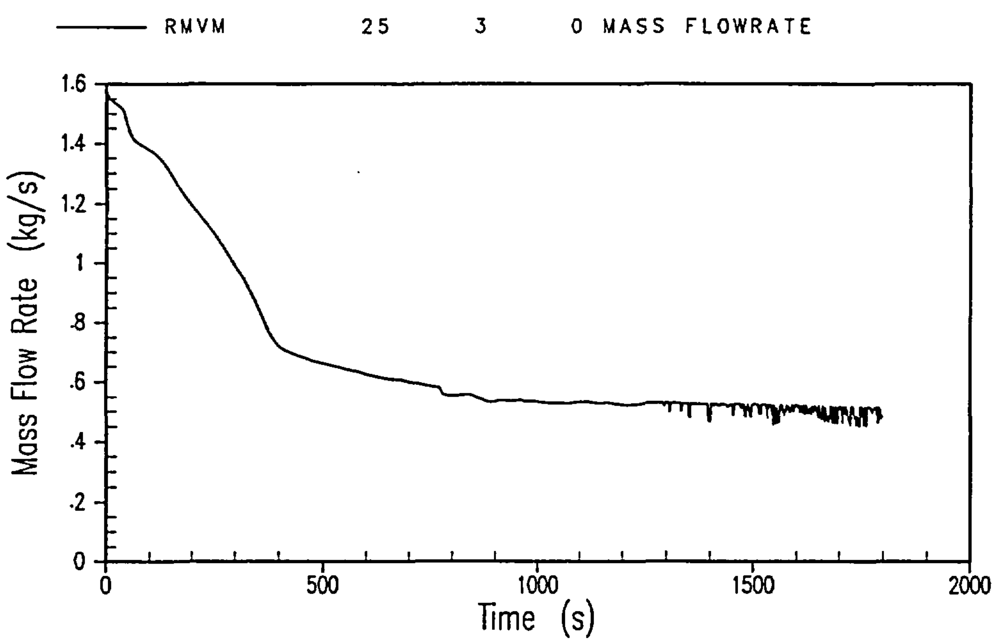

Figure 20-5-2-2b. Calculated Break Mass Flowrates for LOFT LOCE L3-7

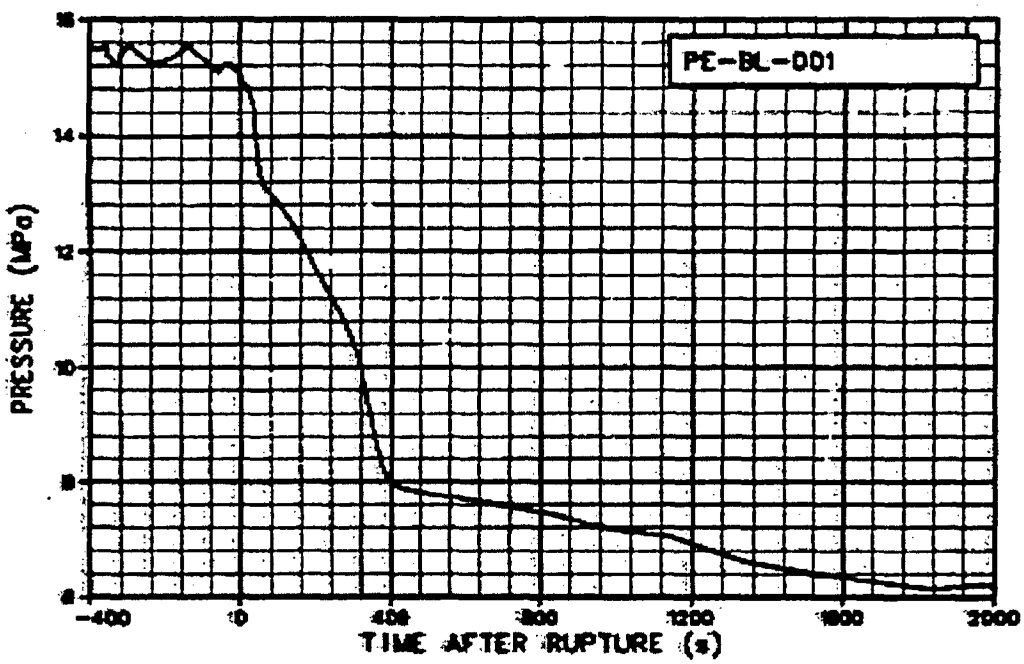

Figure 20-5-2-3a. Measured Inactive Loop Cold Leg Pressure for LOFT LOCE L3-7 (Gillas and Carpenter, 1980)

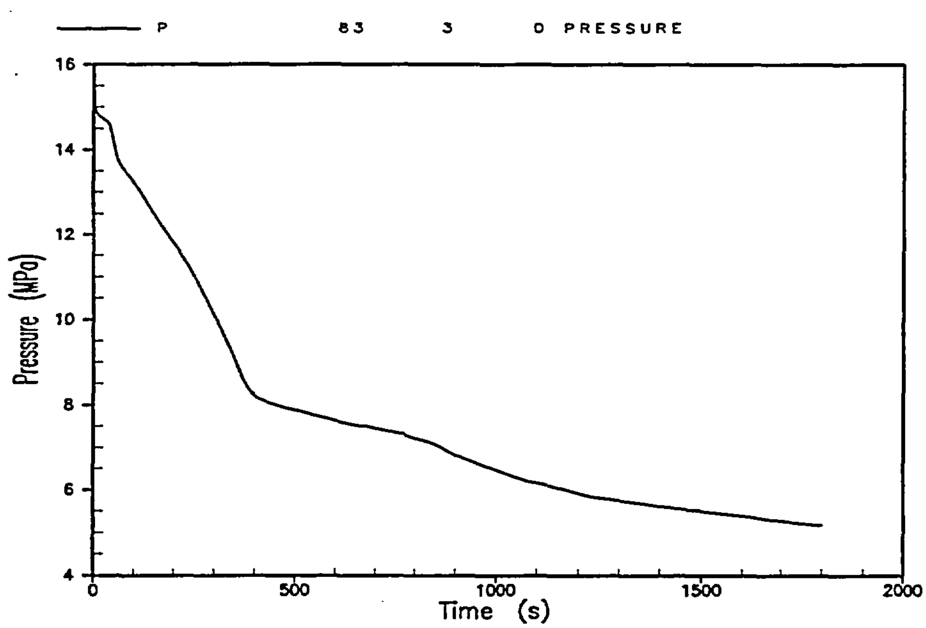

Figure 20-5-2-3b. Calculated Inactive Loop Cold Leg Pressure for LOFT LOCE L3-7

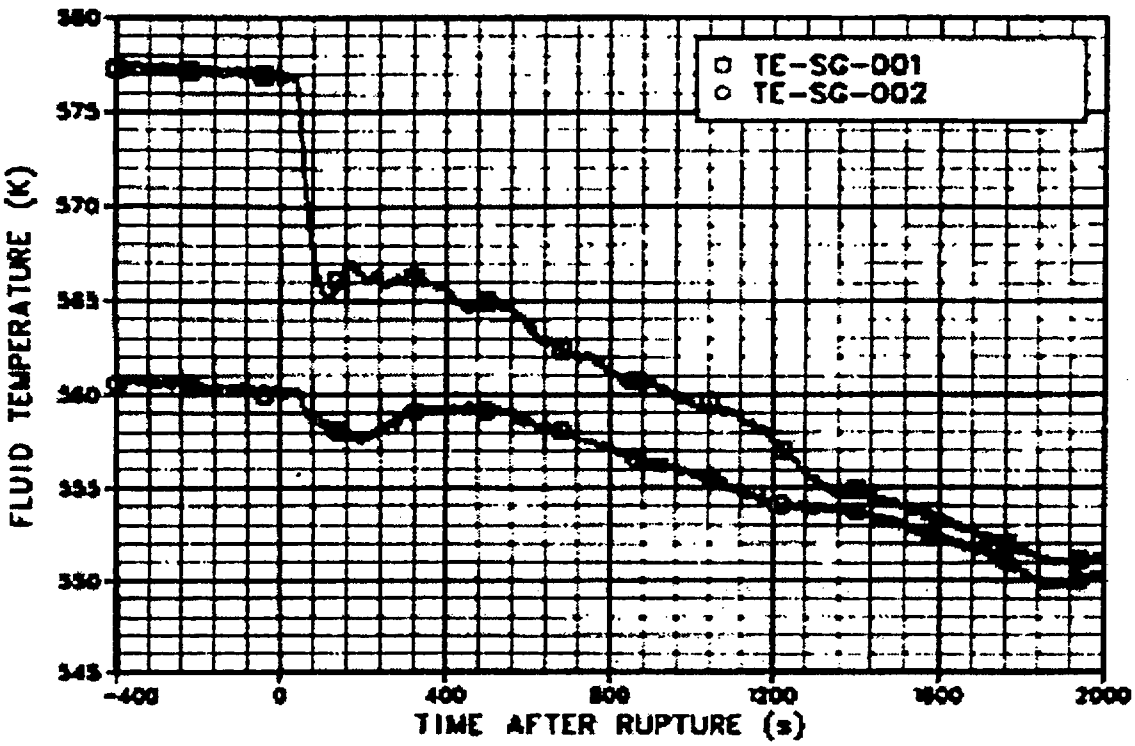

Figure 20-5-2-4a. Measured Steam Generator Inlet and Outlet Temperatures for LOFT LOCE L3-7

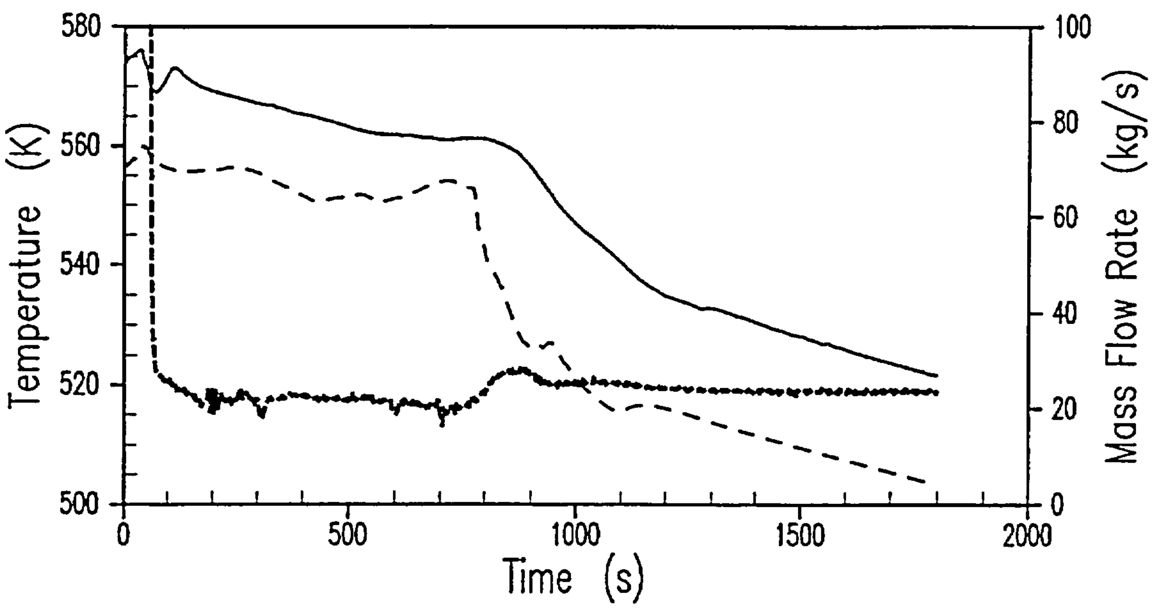

Figure 20-5-2-4b. Calculated Steam Generator Inlet and Outlet Temperatures Versus Calculated Active Loop Mass Flow Rate for LOFT LOCE L3-7

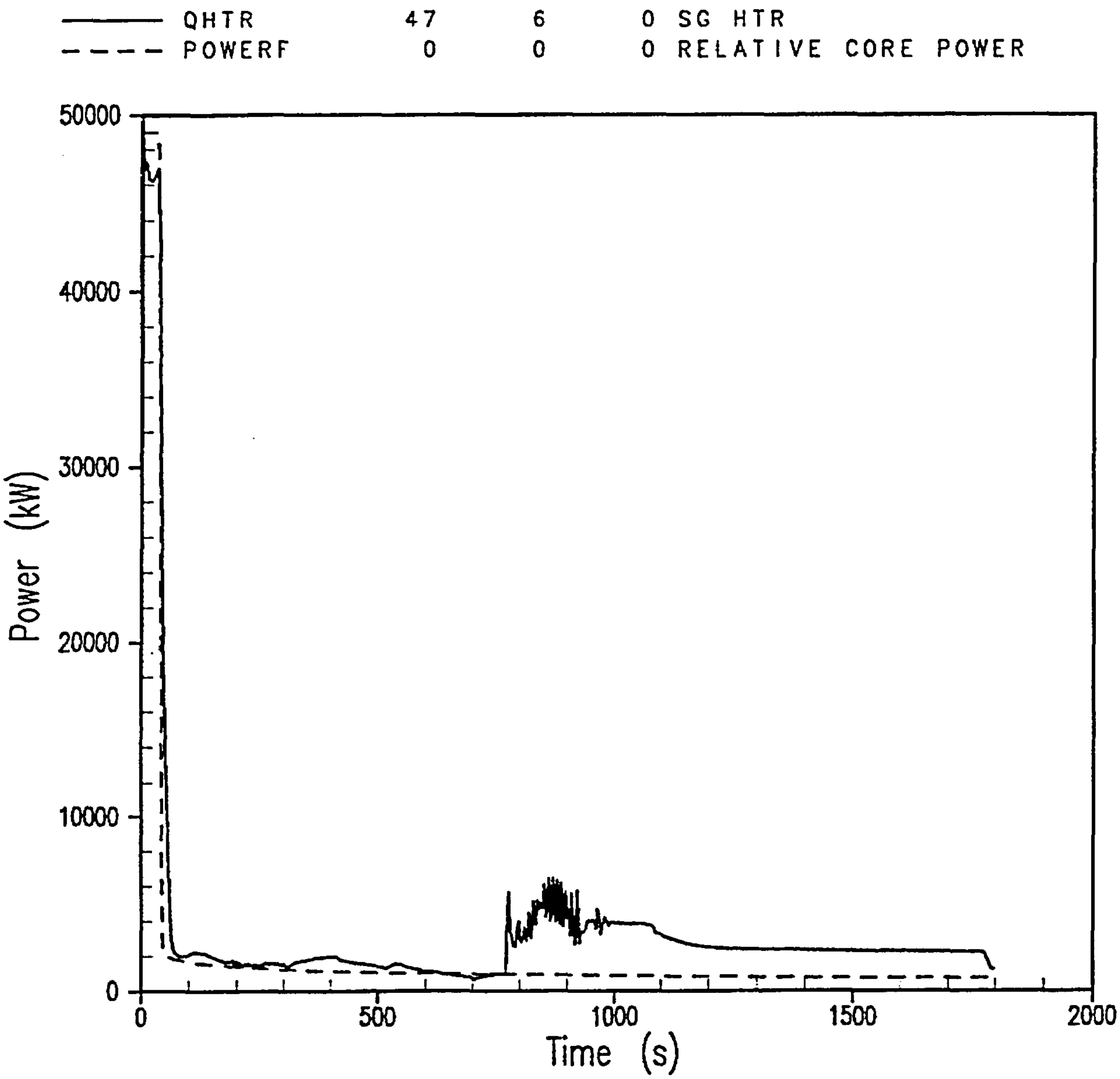

Figure 20-5-2-5. Calculated Steam Generator Heat Rejection versus Decay Heat for LOFT LOCE L3-7

20-5-3 Transient Simulation for LOFT LOCE L3-5

LOCE L3-5 is one of three tests in the LOFT facility that represent 4-inch diameter equivalent breaks in a full-scale PWR. It and the other tests, L3-1 and L3-6, all start from approximately the same boundary conditions. LOCE L3-5 was set up as a break in the active loop cold leg using the break unit depicted in Figure 20-3-9. The reactor was tripped several seconds prior to the initiation of the break as shown in the sequence of events in Table 2-5-3-1 (Dao and Carpenter, 1980). Once the break was opened, the RCPs were tripped and safety injection was initiated on low pressure directly to the downcomer. The accumulators were valved out to allow evaluation of the safety injection system. LOCE L3-5 was terminated at 2309 seconds with closure of the break and the safety injection system. LOCE L3-5 is the most typical of the three tests in its representation of a small break LOCA in a full-scale PWR.

The WCOBRA/TRAC-SB model used for the transient analysis is as previously described except that the break unit (PIPE 25) is connected to the center cell of channel 66. Safety injection is directed to the upper plenum bypass channel 33. In the WCOBRA/TRAC-SB LOFT model, channel 33 is in the downcomer segment opposite the active loop cold leg. This was done to best represent the injection path without increasing the number of downcomer segments.[1] Initial conditions for the analysis are as stated in Section 20-4-3.

Calculated and measured hot leg pressures are depicted in Figure 20-5-3-1. At approximately 125 seconds, both the data and the calculation show an increase in primary system pressure. The calculated repressurization ends at approximately 300 seconds. At approximately 300 seconds, the calculated pressure falls below the data and starts to parallel the data at approximately 750 seconds. The calculation ended at 1600 seconds. The potential causes of the calculated behavior are examined in the following paragraphs.

The repressurization probably results from a steam generator stall as the cold leg approaches saturation coupled with timing of the pump coastdown. A comparison of the calculated liquid flow at the steam generator inlet and calculated system pressure indicates that the repressurization starts when the liquid flow drops from approximately 65 lb/s to an average of

1. The actual injection point is midway between the active loop cold and hot legs. To connect the safety injection to the cell above the active loop cold leg will artificially inject cold water too close to the break.

approximately 10 lb/s as shown in Figure 20-5-3-2. Also, natural circulation appears to start at approximately 85 seconds as indicated by the increase in liquid flow. A near mirror image of this behavior is shown for the outlet of the steam generator in Figure 20-5-3-3 with liquid flow out of the steam generator ceasing at approximately 220 seconds. Thus by approximately 120 seconds, the steam generator is stalled and the active hot and cold legs are isolated from each other.

The stall occurs as the last RCP reaches zero rotational speed at 120 seconds. Natural circulation decreases as the hot and cold sides of the active loop approach the same temperature as shown in Figure 20-5-3-4. Because the cold side is still calculated to be below the saturation temperature (that is, hot leg temperature), break flow remains slightly subcooled as seen in Figure 20-5-3-5. Data from the experiment show that saturated conditions at the break started at approximately 93 seconds. This limited the pressure rebound in the data. Because the break remains subcooled in the WCOBRA/TRAC-SB calculation, the rate at which vapor is being generated in the core exceeds the volume flowrate out of the primary system. Primary system pressure rebounds, and the rebound is greater than the pressure rebound experienced in LOCE L3-5.

The measured hot leg pressure shows a decrease in the rate of depressurization from approximately 130 seconds to 150 seconds. WCOBRA/TRAC-SB is correctly modeling the phenomena of the pressure rebound as indicated by the pressure rebound present in the data. The magnitude of the pressure rebound may primarily be the amount of RABL leakage. As shown in Figure 20-5-3-6, the measured liquid level in the steam generator side of the loop seal shows a level depression starting at approximately 400 seconds. The level depression, as measured, does not reach the horizontal pipe run, and the loop seal is not cleared. Leakage through the RABL that results in pressure equalization between the hot and cold legs prevents loop seal clearing. Also, RABL leakage will bring fluid approaching the upper plenum temperature to the cold side of the facility bypassing the active loop steam generator. The effect of the leakage is an increase in active loop cold leg temperature sufficient to cause early voiding and saturation in the active loop cold leg, which results in an early transition to saturated break flow. WCOBRA/TRAC-SB is performing well and within the uncertainties associated with RABL leakage.

Because the break flow is calculated to remain subcooled during the pressure rebound, the break flow increases significantly and more mass is removed from the system than is indicated by the data as shown in Figure 20-5-3-5. Calculated break flow remains above the data until single phase vapor reaches the break. Because of the greater volume and mass flow out of the primary system, the primary system pressure drops below the data at approximately 400 seconds.

A comparison of the calculated collapsed liquid level and the measured liquid level between the centerline of the loop seal and the steam generator inlet is shown in Figure 20-5-3-6. The WCOBRA/TRAC-SB simulation predicts the level to decrease to the top of the elbow, bottom cell of channel 58, at approximately 260 seconds; and the loop seal to pass steam at approximately 300 seconds. Because pump injection was not modeled, level recovery in the loop seal is not indicated in the WCOBRA/TRAC-SB simulation. Primary system coolant inventory decreases to a minimum of approximately 3500 lb at 1800 seconds as seen in Figure 20-5-3-7. The overall influence of pump injection on the transient simulation is minor except for loop seal and total primary inventory.

Table 20-5-3-1
Sequence of Events for LOFT LOCE L3-5
(Dao and Carpenter, 1980)

Event	L3-5 Measured Data (seconds)
Reactor scrammed	-4.8 ± 0.1
Control rods reached bottom	-2.8 ± 0.1
LOCE initiated	0
Primary coolant pumps tripped	0.8 ± 0.2
HPIS injection initiated	4.0 ± 0.2
Core natural circulation first indicated	17 ± 3
Primary coolant pump coastdown completed	17.7 ± 0.2
Pressurizer emptied	22.2 ± 0.5
Upper plenum reached saturation pressure	28.4 ± 0.4
Active loop hot leg voiding began	30 ± 5
Secondary coolant system (SCS) auxiliary feed initiated	63 ± 3
Active loop cold leg voiding began	80 ± 5
End of subcooled break flow	92.9 ± 0.2
SCS pressure exceeded PCS pressure	745 ± 20
Primary coolant system (PCS) mass at a minimum	1480 ± 100
SCS auxiliary initial feed terminated	1800 ± 5
Reactor vessel mass at a minimum	2125 ± 180
Break isolated	2309.1 ± 0.5

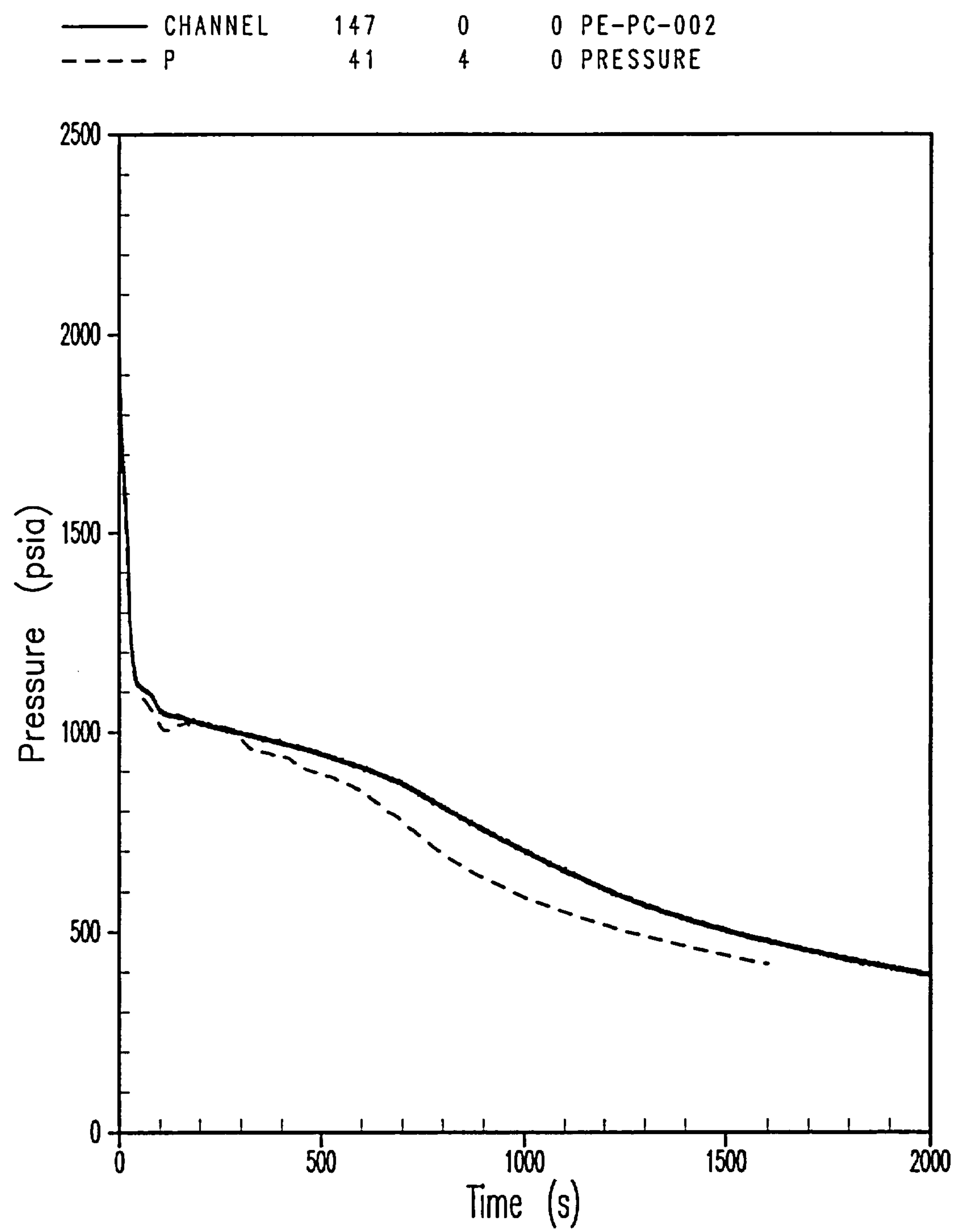

Figure 20-5-3-1. Comparison of Calculated and Measured Hot Leg Pressures for LOFT LOCE L3-5

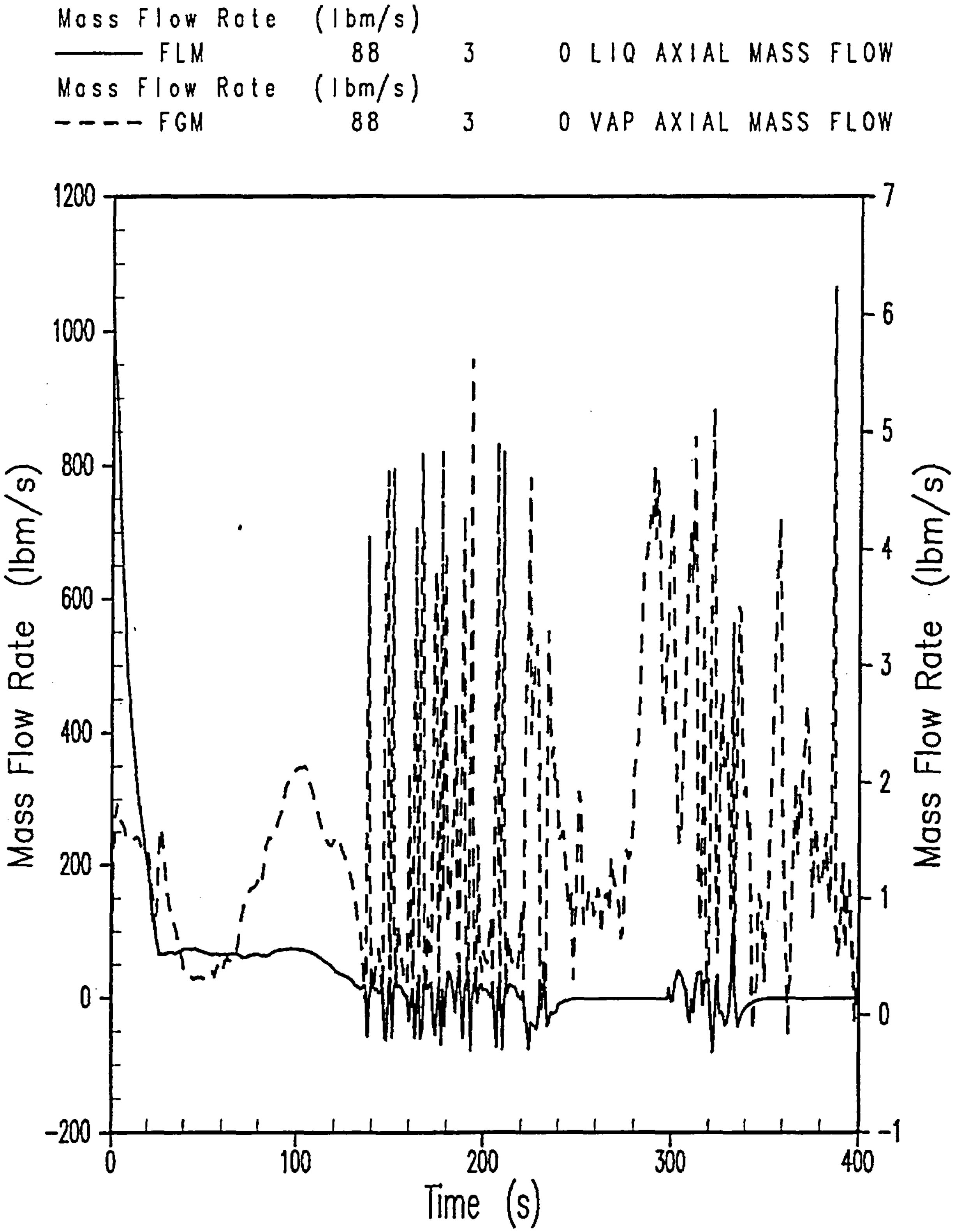

Figure 20-5-3-2. Comparison of Liquid and Steam Mass Flowrate at Steam Generator Inlet for LOFT LOCE L3-5

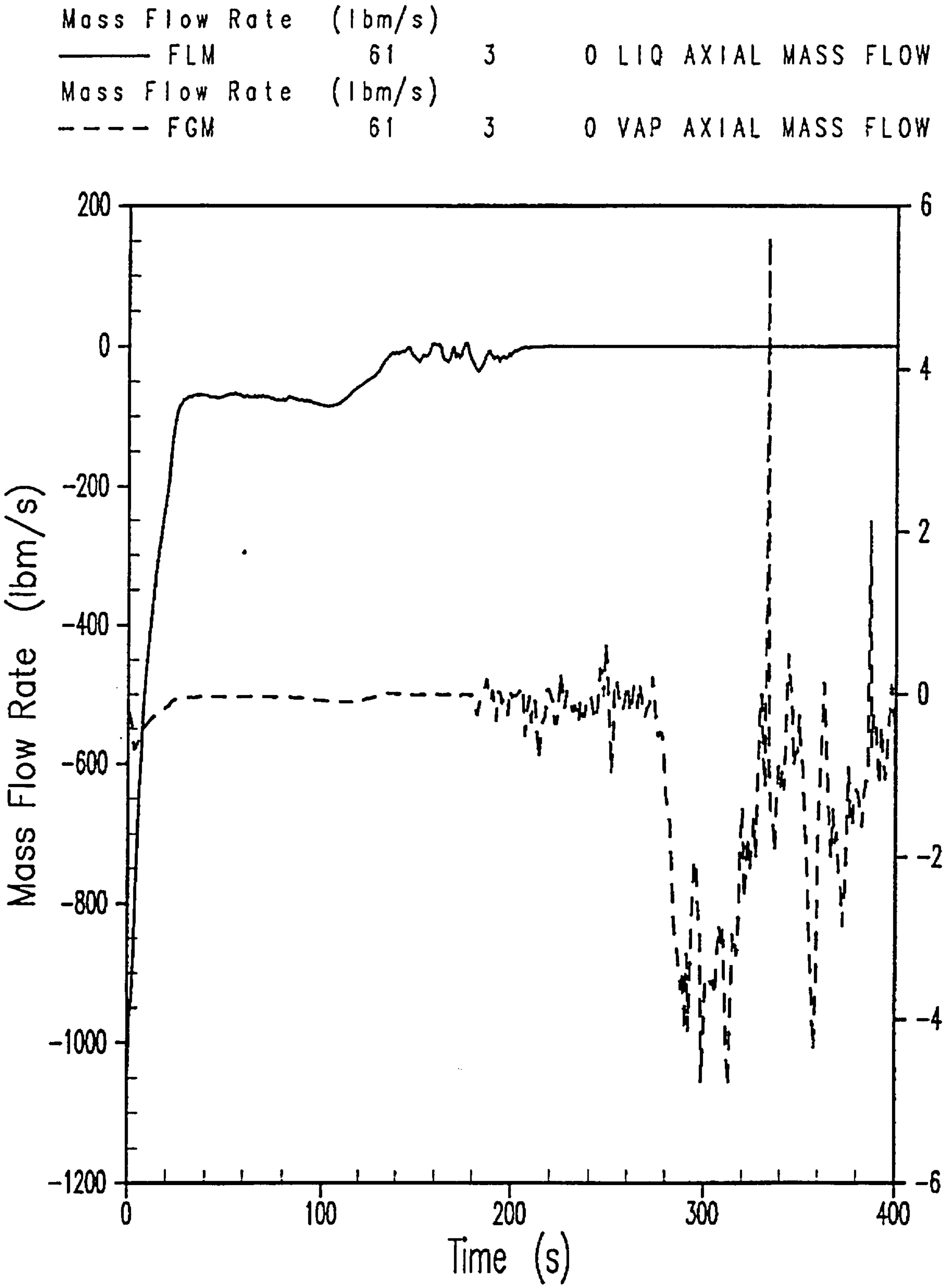

Figure 20-5-3-3. Comparison of Calculated Liquid and Steam Mass Flowrate at Steam Generator Outlet for LOFT LOCE L3-5

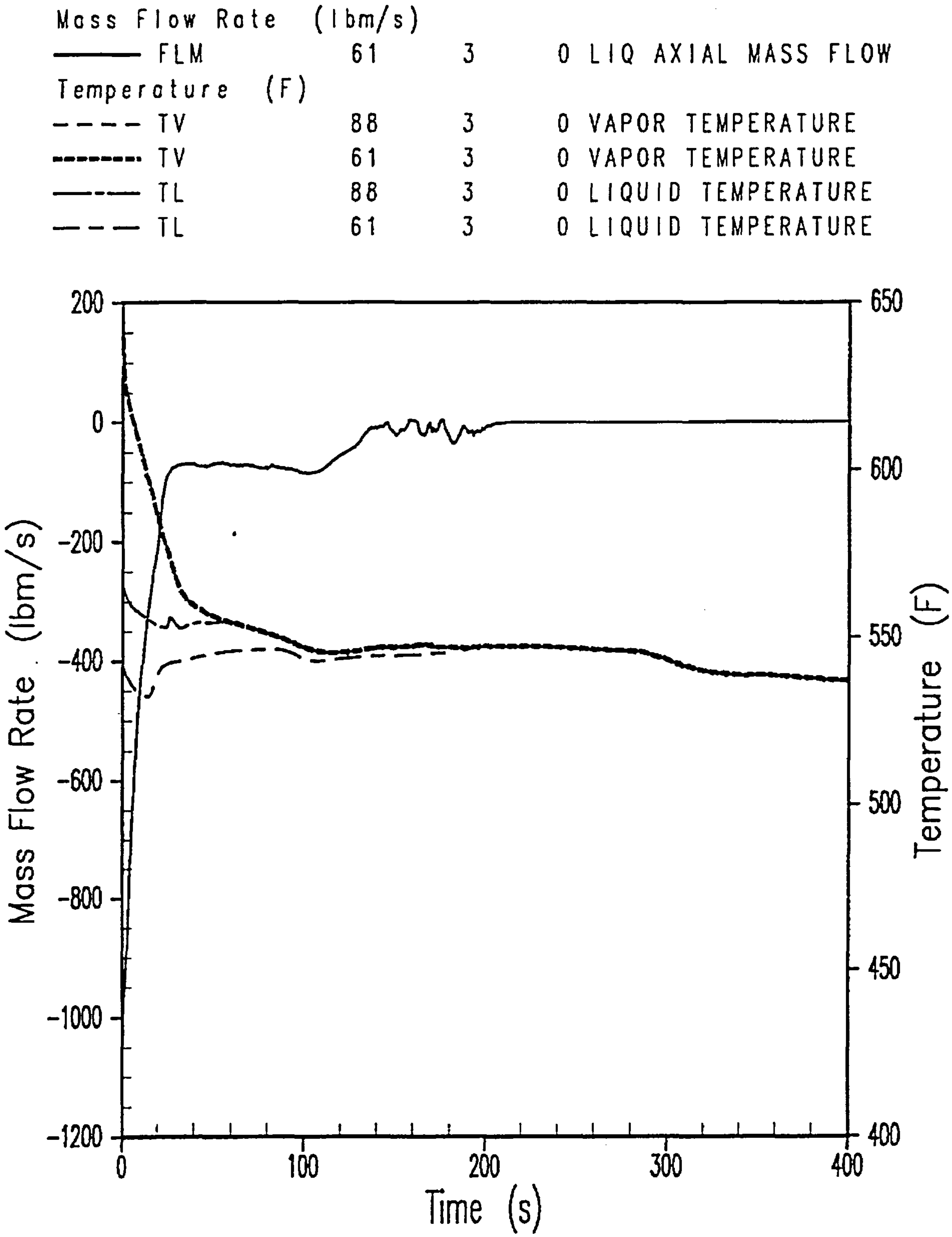

Figure 20-5-3-4. Comparison of Calculated Steam Generator Outlet Flow versus Active Loop Hot Leg and Cold Leg Temperatures for LOFT LOCE L3-5

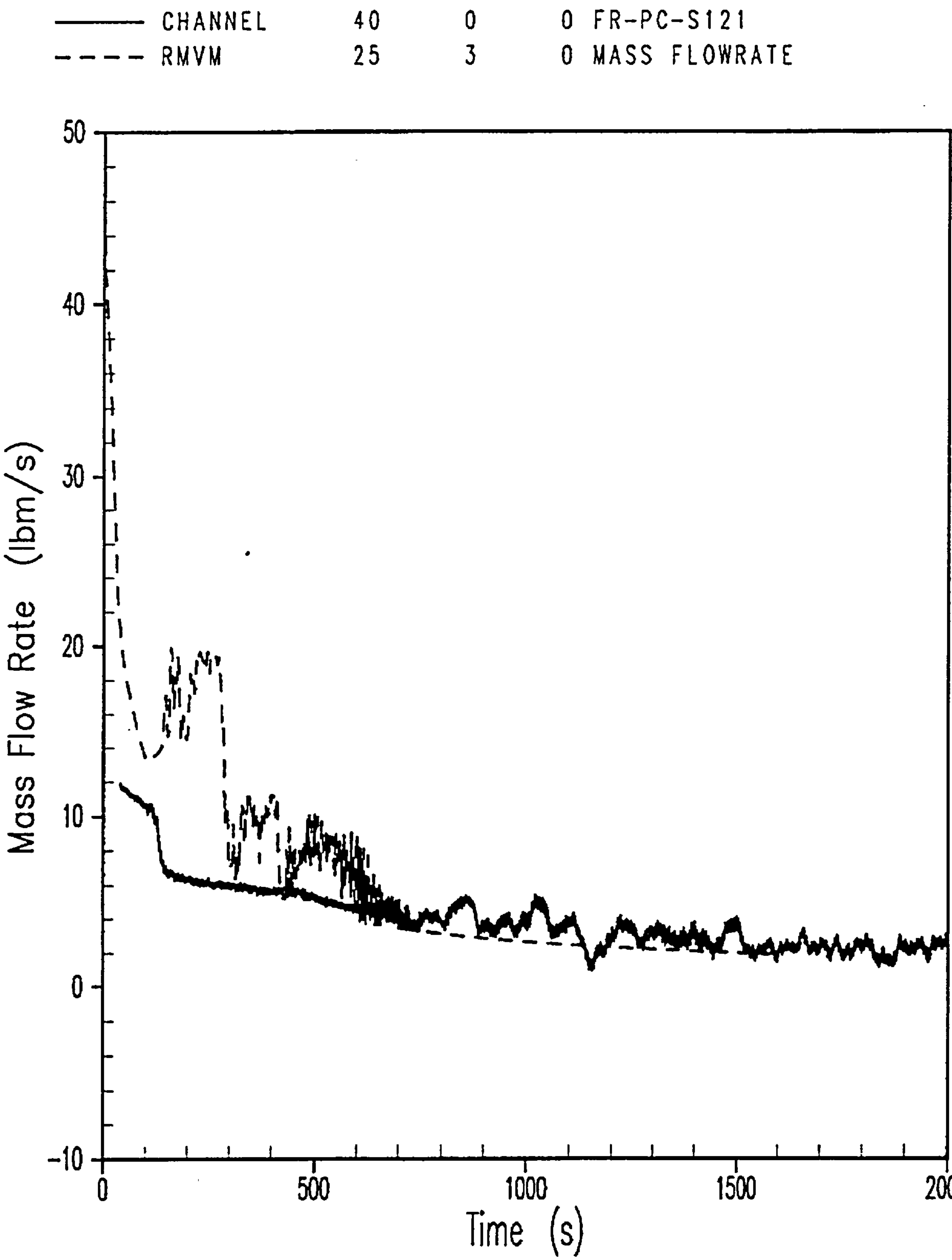

Figure 20-5-3-5. Comparison of Calculated and Measured Break Mass Flowrates for LOFT LOCE L3-5

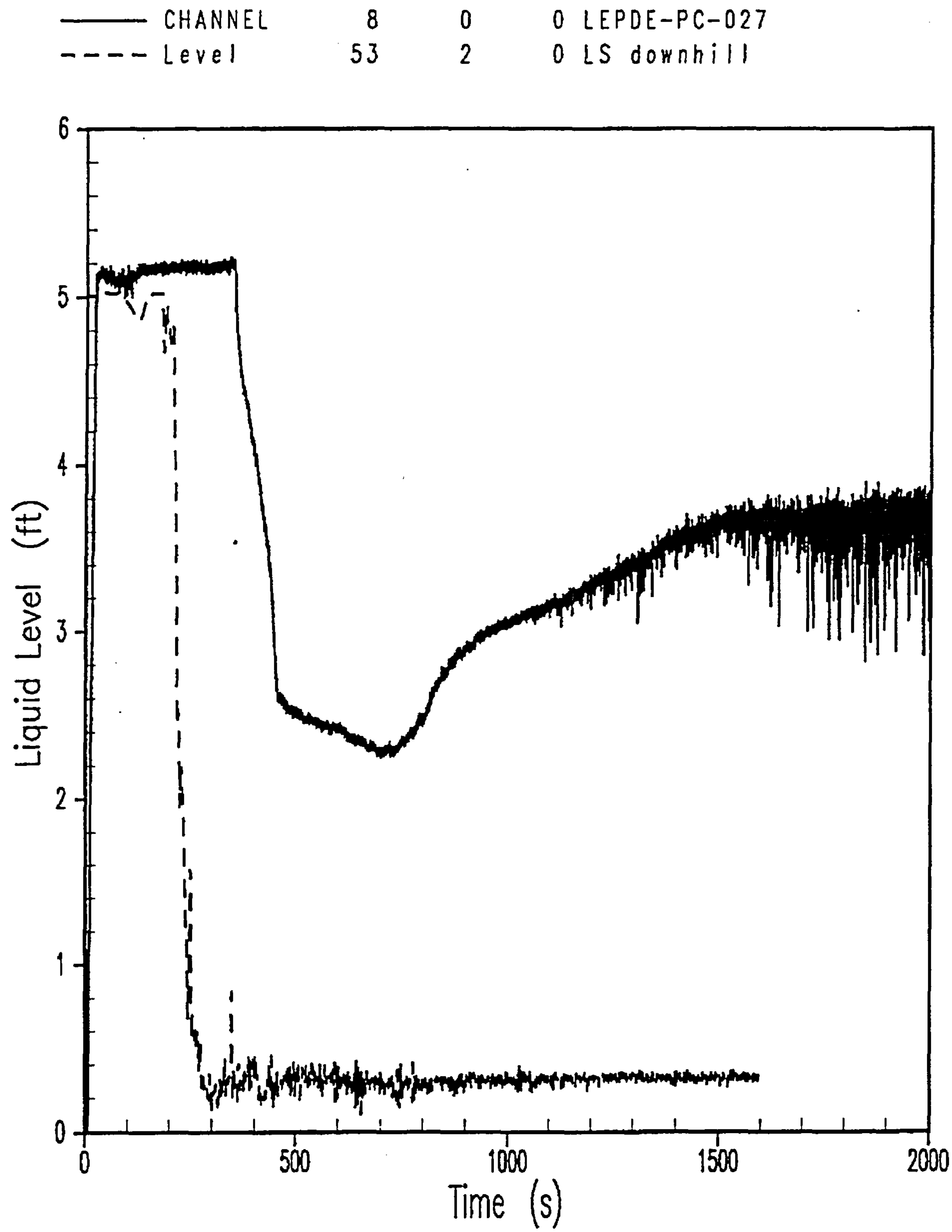

Figure 20-5-3-6. Comparison of Calculated and Measured Loop Seal Level for LOFT LOCE L3-5

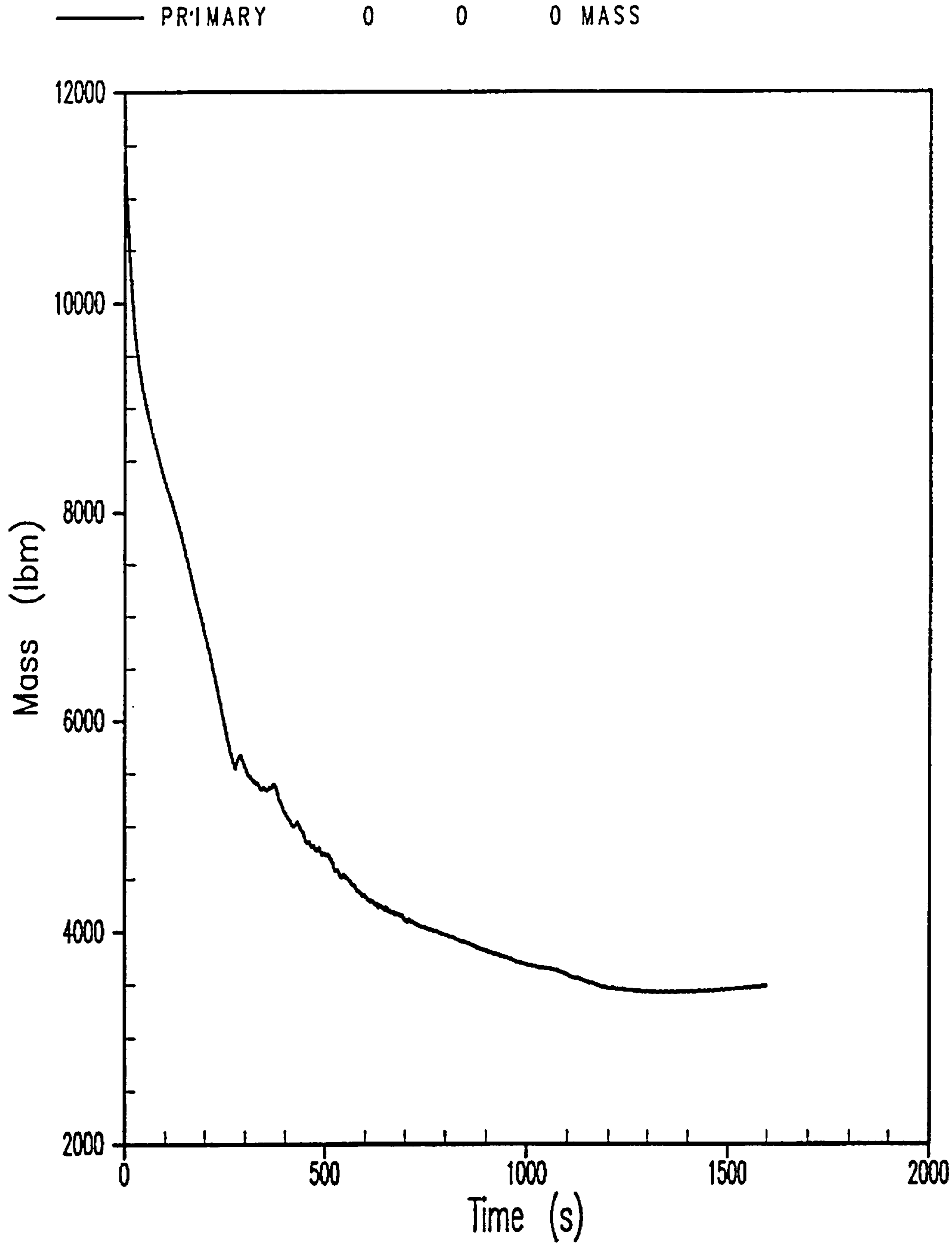

Figure 20-5-3-7. Calculated Primary System Coolant Inventory for LOFT LOCE L3-5

20-6 Conclusions

Overall, WCOBRA/TRAC-SB simulated the phenomenology of the LOFT LOCEs fairly well notwithstanding the probable influence of unknown experimental conditions important to accurate simulation of the experiments. WCOBRA/TRAC-SB simulated LOCE L3-5 well except for the transition from forced to all natural circulation flow that resulted in an extended period of subcooled break flow. The simulation of LOCE L3-1 is initially similar to LOCE L3-5 in that a distinct pressure rebound occurs following the end of forced flow. The effect of the RABL appears to have been underestimated leading to overestimation of system pressure. WCOBRA/TRAC-SB well simulated the natural circulation in LOCE L3-7, but underpredicted the depressurization that occurred during the experiment, which may also have resulted from an error in modeling the RABL leakage.

20-7 References

Adams, J. P., 1979, "Quick-Look Report on LOFT Nuclear Experiment L3-1," EGG-LOFT-5057.

Bajorek, S. M., et al., 1998, "Code Qualification Document for Best Estimate LOCA Analysis - Volume III: Hydrodynamics, Components, and Integral Validation," WCAP-12945-P-A, Vol. 3.

Bayless, P. D., et al., 1980, "Experiment Data Report for LOFT Nuclear Small Break Experiment L3-1," NUREG CR-1145/EGG-2007.

Condie, K. G., et al., 1981, "Four-Inch Equivalent Break Loss-of-Coolant Experiments: Posttest Analysis of LOFT Experiments L3-1, L3-5 (Pumps Off), and L3-6 (Pumps On)," EGG-LOFT-5480.

Czapary, L. S., 1980, "LOFT L3-1 Preliminary Comparison Report," EGG-CAAP-5255.

Dao, L. T. L. and Carpenter, J. M., 1980, "Experiment Data Report for LOFT Nuclear Small Break Experiment L3-5/L-35A," NUREG CR-1695/EGG-2060.

Gillas, D. L. and Carpenter, J. M., 1980, "Experiment Data Report for LOFT Nuclear Small Break Experiment L3-7," NUREG CR-1570/EGG-2049.

McCreery, G. E., 1980, Quick Look Report on LOFT Nuclear Experiment L3-7, EGG-LOFT-5792.

Reeder, D. L., 1978, "LOFT System and Test Description (5.5-ft. Nuclear Core 1 LOCEs)," NUREG CR-0247/TREE-1208.

SECTION 21
SIMULATION OF SEMISCALE SMALL BREAK LOCA EXPERIMENTS

21-1 Introduction

The Semiscale facility is a small scale (1:1705) replica of a Westinghouse RCS which includes all of the major components. Figure 21-1 shows the layout of the major components in the Mod-2C configuration. There are two loops in the facility, with one scaled as a single loop, and the other scaled as a combined three loops. The facility evolved through several major modifications over the course of approximately a decade of testing and was used for both large and small break experiments. Later modifications to the facility focused on small break LOCA phenomena, and extensive instrumentation was installed to measure key phenomena such as liquid levels and break discharge rates. The simulated reactor vessel houses an electrically heated bundle consisting of 25 heater rods with a total power of 2 MW. The overall scaling philosophy used in designing the facility is the maintenance of the power-to-volume ratio, coupled with a 1:1 elevation scaling criteria (Larson, et al., 1980 and Loomis, 1987). The facility is capable of operating at actual nuclear power plant pressures and temperatures, and therefore, a full range of pressures and fluid states occurs during a transient.

21-2 Key Phenomena

Due to the small scale, combined with 1:1 elevation scaling, the corresponding pipe and vessel sizes used to construct the facility are generally characterized as exhibiting 1-D fluid flow behaviors. Therefore, some scaling distortion is expected to be evident in comparisons with larger facilities or full-scale plants. However, the purpose of the experiments is to provide information concerning the overall flow behaviors and qualitative interaction of phenomena that occur throughout the various stages of a small break LOCA in a complete integral RCS. Comparisons of calculated results to the experiments will be focused on general phenomena such as the relative timing of events and the factors which influence fluid distributions within the RCS.

One particular phenomenon that the facility can be used to address is the integral effects nature of loop seal clearing. Due to size considerations, Semiscale is argued to exhibit a strong 1-D loop seal clearing behavior with liquid in the piping being moved and expelled in a plug-like fashion. While separate effects facilities address the 3-D phenomena given fixed fluid conditions, they do not provide information on the general aspects of how the loop seals behave over the course of a transient in relation to the fluid distribution in the entire RCS. The accuracy with which the code is able to calculate loop seal formation and clearing when the 3-D aspects are unimportant will be important in establishing its capability to model more complex system interactions, including phase separation and other phenomena for the nuclear power plant (NPP) calculations.

Another important phenomenon that influences the severity of small break transients is steam generator tube liquid holdup. This holdup phenomenon was first identified experimentally in a Semiscale small break LOCA experiment (Leonard, 1982); it has since been duplicated in other facilities such as ROSA (Osakabe, et al., 1987) and has been discussed extensively in the open literature (Leonard, 1983 and Loomis, 1985a). Steam generator liquid holdup is the result of liquid being condensed in the upflow side of the tubes relatively early during a small break LOCA transient. This liquid is unable to gravity-drain back through the hot leg because it is impeded by high upward steam flowrates. The large pressure drops induced by this holdup, in turn, affect the hydrostatic head balances throughout the RCS. Whether the pump suction seal clearing phenomenon discussed above results in core uncovery is significantly affected by the amount of liquid holdup.

21-3 Applicable Tests

Information from more than 40 small break LOCA tests, which were conducted in the various Semiscale configurations, is available in NUREG/CR-4393 and NUREG/CR-4945 (Loomis, 1985b and Loomis, 1987). Because the purpose of the comparisons is to study the more general behaviors during a small break transient, the experiments used for comparison are selected based upon data quality. Given this, the experiments conducted later in the program are better choices because the instrumentation and test procedures at that point were better refined for small breaks. The following are two experiments conducted in the final Semiscale Mod-2C configuration (Loomis and Streit, 1985a):

- S-LH-1: A 6-inch equivalent cold leg break with downcomer-to-upper head bypass set to 0.9 percent at steady-state

- S-LH-2: A 6-inch equivalent cold leg break with downcomer-to-upper head bypass set to 3 percent at steady-state

Both of these transients exhibited core uncoveries, which allow investigation of in-bundle mixture level swell and rod heat transfer (Loomis and Streit, 1985b and Shaw and Loomis, 1985). The purpose of varying the vessel upper head bypass was to investigate the influence of this relief path on the core liquid level depressions that occur from the manometric balances that form among the various sections of the RCS: the core/downcomer, pump suction crossover legs, and steam generator tubes. The transients exhibited a notable difference in the amount of core uncovery and rod heatup as a function of upper head bypass flow. The difference was attributed to the timing of upper head drain, which clears a relief path between the upper plenum and the downcomer/cold leg.

21-4 Facility Configuration for Tests S-LH-1 and S-LH-2

In conducting the small pipe break experiments, a tee spool piece is inserted in the loop that is scaled to represent a single NPP loop and is designated as the broken loop. The loop arrangement is shown in Figure 21-1, and a detail of the break spool is shown in Figure 21-2. The break orifice is scaled to represent 5 percent of the cold leg area of a full-size cold leg (27.5-inch inside diameter) and has a diameter of 0.1488 inches, which is equivalent to a 6.37-inch inside diameter break at full-scale. It is positioned at the horizontal centerline of the cold leg piping, so the break flow will be susceptible to flow regimes in the piping, such as stratification. All of the break effluent is passed through a system of condensing coils and is collected in a catch tank. This arrangement not only allows for accurate measurements of the integral break flow, but also allows for measurement of instantaneous break flow, other than the delay during the initial opening of the break at the start of the experiment.

The layout of the vessel upper head area is depicted in Figure 21-3. A bypass line connects the top of the downcomer to the upper head at elevations representative of the reference NPP. A replaceable orifice is inserted in the bypass line and used to adjust the bypass flow ratio to the desired value for the particular experiment. A single tube is scaled to represent the flow area and elevations for the aggregate of all the control rod guide tubes in an NPP. There are also two tubes representing upper internals support columns, which connect the upper head to the upper core plate. These were originally included for experiments modelling the internals configuration of upper head injection plants and were, therefore, plugged off for the experiments to be examined here.

The core in the Semiscale facility is composed of 25 electrically heated rods, each of which are geometrically similar to nuclear fuel rods in an NPP with 0.422-inch outside diameter cladding.

The rods are capable of operating at the full steady-state power of a PWR nuclear rod. The resistive element windings are sized such that a stepped cosine axial power profile results, as shown in Figure 21-4, with a peak linear power of approximately 11.2 kW/ft at full power.

The steam generators are scaled to a full 1:1 elevation matching the reference NPP, and each individual steam generator tube is made from the same tube stock: 0.776-inch inside diameter, 49.5-mil thick. There are a total of six tubes in the intact loop and two tubes in the broken loop steam generator in order to conserve the scaled heat transfer areas.

Elevation scaling is preserved 1:1 relative to the reference NPP. The Semiscale hot legs join together the vessel and the steam generator inlet plenums. This maintains the correct elevations relative to one another. The pump suction piping does not have a horizontal run, as in a full-size NPP, because the volume would have become excessive. In general, due to the use of standard piping sizes, the loop volumes are somewhat overscaled relative to the ideal, but this is not a significant distortion relative to the overall volume of the other major components.

21-5 Description of WCOBRA/TRAC-SB Model

Figure 21-5 shows the component layout of the WCOBRA/TRAC-SB model of the Semiscale Mod-2C system. The reactor vessel, the primary loop piping, and the steam generators are
[

]a,c

The break is modelled as proceeding from the middle cell of the broken cold leg, consistent with the break assembly elevation in the test facility. The break model as described in Section 13 of this volume is used as shown in Figure 21-5 with no discharge coefficient or flow area multiplier
[

]^{a,c} The WCOBRA/TRAC-SB model, therefore, represents the Semiscale Mod-2C test facility break geometry without any adjustments.

Due to the small scale of the facility, the general thermal-hydraulic behaviors are assumed to be close to 1-D. In particular, the formation and blowout of the pump suction loop seals tend to behave in a plug-like fashion. Experimental measurements in the horizontal piping, including video probe information, verified that there can be significant stratification even at this scale. Therefore, the modelling of the primary loops reflects the same approach as used on the other integral facilities.

Information used to compile the facility geometries, and the like, was obtained largely through the review of an available drawing. Where feasible, some parameters were compared to the facility description and RELAP model document of Leonard (Leonard, 1981). Additionally, personnel at INEL were contacted to reconcile some of the more ambiguous items, operating conditions, and procedures.

Figure 21-6 shows the nodalization of the simulated reactor vessel using the VESSEL component. The WCOBRA/TRAC-SB noding used for the Semiscale facility is consistent with the nodalizations of the other integral test facility simulations and the nodalization used in the PWR computations. The number of each section in the vessel is shown, together with the number of cells within each section, in parentheses. Figure 21-6 shows the elevation of the vessel for WCOBRA/TRAC-SB analysis. The section boundary heights are relative to the inside of the bottom of the vessel. Values within squares are channel numbers, and values within circles are gap numbers. WCOBRA/TRAC-SB assumes that a flow path exists between vertically connected channels, unless otherwise specified in the input. Transverse flow between channels in the same section only exists if the channels are specified as connected by gaps. The volume, axial flow area, and wetted perimeter of each channel is specified in the code input. There is also the capability to vary these quantities within a channel if the geometry warrants. As in the facility, the downcomer is a stand-alone pipe with a short annulus region at the top (Sections 7 and 8) where the cold leg piping is connected. The cold legs and hot legs [

]^{a,c}

Figures 21-7 and 21-8 show the models of the two steam generators for the intact and broken loops, respectively. Because the steam generator tubes remain mostly covered throughout the transients, the amount of axial detail shown is judged to be adequate for modelling the phenomena of interest. [

]^{a,c}

A set of reference points and four quadrant homologous curves are supplied for the primary recirculation pumps. However, in general, because the pumps are tripped relatively early in the transient, the contribution of the pumps is made during periods in which they are pumping a positive head of single-phase liquid. Because the Semiscale pumps physically do not have a scaled moment of inertia, they are controlled on a powered coastdown curve after the trip. This behavior is replicated in the input to WCOBRA/TRAC-SB.

Similarly, the electrical power to the core heater rods is controlled by a computer program to simulate a normalized decay heat curve, and this is duplicated as shown in Figure 21-10.

The pumped safety injection system used in the Semiscale facility uses positive displacement pumps. The pumps are controlled by a computer which uses a pressure measurement from the RCS as input to vary the injection rate as a function of pressure to follow a prescribed curve to simulate the performance of a centrifugal pump. Figure 21-11 shows the injection rates for the intact and broken loop safety injection pumps as a function of pressure, as actually derived by

INEL personnel during post-experimental data reduction. The curve for the intact loop pump shows an anomalous behavior over the range of pressures from about 400 to 800 psi. Because this is the best estimate of the actual safety injection pump characteristics, it has been modelled in the WCOBRA/TRAC-SB analysis as shown.

21-6 Steady-State Simulations

Steady-state operating conditions are attained in the WCOBRA/TRAC-SB model by running the code with no break in the system until conditions have stabilized. Table 21-1 compares the key parameters from test S-LH-1 to those obtained by the model; Table 21-2 provides the same information for test S-LH-2. All of the parameters are within acceptable tolerances for conducting validation simulations. The vessel upper head bypass flow ratios in the WCOBRA/TRAC-SB steady-state simulation match the S-LH-1 and S-LH-2 experiments well. Because upper head bypass was the critical parameter varied between the two tests in the LH test series, it is important in these simulations to obtain good agreement of the bypass flow to the experimental value.

The steady-state secondary masses do not agree well with the reported values from the experiment. However, this parameter has a large uncertainty associated with it; a review of related Semiscale documentation (Shimeck, 1983) shows that secondary mass has a large range of possible values. Also, in the description of the INEL simulation of the experiments with the RELAP5 code, it is stated that it was necessary to run the model with lower masses to maintain stable operation (Loomis and Streit, 1985b). The amount of secondary inventory in the WCOBRA/TRAC-SB model allows for substantial coverage of the tube bundles. Therefore, the effect on the transient predictions of any discrepancies in secondary mass (if in fact they exist) are judged to be insignificant.

21-7 Transient Simulations

The steady-state model conditions, as described in the previous section, were used to perform simulations of tests S-LH-1 and S-LH-2. This set of 5-percent small break LOCA experiments in the Semiscale MOD-2C facility addressed the sensitivity to vessel upper head bypass. Through review of the calculational results in comparison to the test data, it was determined that the holdup of liquid in the steam generator tubes, and associated phenomena in the hot legs and loop seal piping, was a dominant factor with regard to the ability to replicate the experimental results. The following discussion will compare the code predictions to data from tests S-LH-1 and S-LH-2.

21-7-1 S-LH-1 Simulation Results

Figure 21-12 shows the pressurizer pressure transient from the WCOBRA/TRAC-SB test S-LH-1 calculations (dashed line) compared to test data (solid line). At the opening of the break, the model predicts the pressure to drop to near the hot leg saturation value a bit more rapidly than the experimental data indicate. Once the calculation reaches hot leg saturation (approximately 1700 psi) agreement exists between the data and prediction as primary fluid begins to flash. Once the system depressurizes to cold leg saturation (approximately 1100 psi), the depressurization rate slows appreciably both in the experiment and the calculation. After this point, WCOBRA/TRAC-SB overpredicts, than underpredicts pressure. Overall, the WCOBRA/TRAC-SB calculation predicts the primary pressure well versus the test data all the way through the accumulator actuation. The time of accumulator injection is predicted to occur approximately 20 seconds earlier than in the test.

Figure 21-13 overlays the predicted primary pressure, as a solid line, along with the predicted steam generator secondary side pressures as dashed lines, with the intact loop steam generator — exhibiting a higher value than the broken loop value most of the time. Figure 21-14 overlays the broken and intact loop steam generator pressures against the test S-LH-1 data. In general for small break LOCAs, during the initial portion of the transient, the primary pressure hovers above the secondary pressure because the break energy removal is supplemented by continuing heat transfer to the steam generator secondary side fluid. Once the loop seals clear (approximately 190 seconds in the prediction), the break uncovers, the primary depressurizes, and the secondaries became heat sources. After loop seal clearance occurs, the steam generator secondary pressure becomes unimportant. During the early portion of the transient, the secondary pressures predicted by WCOBRA/TRAC-SB are higher than in the experiment. The first stage safety valve setpoint on the steam generator secondaries is set at 1047 psia. In the experiment, neither secondary pressure reached the setpoint, while in the calculation, the broken loop pressure is predicted to reach the setpoint. As discussed in Section 21-6 on the steady-state parameters, the amount of initial secondary inventory is suspected to be low in the calculation relative to the experimental conditions. Due to scaling distortions, the Semiscale steam generators have a large amount of structural mass relative to fluid volume, including some large "fillers" in the intact loop generator. Comparing the behavior of the predicted secondary pressures to the experiment, it is speculated that the misprediction is due at least in part to the liquid mass of the steam generator secondary in WCOBRA/TRAC-SB being too small relative to the metal mass. Focusing on the broken loop steam generator, once the initial peak has passed, the predicted and experimental pressures agree well until beyond the time of loop seal clearance. Then, heat transfer to the cooler secondary side metal causes the pressure in WCOBRA/TRAC to fall below the data. Toward the end of the transient, reverse heat transfer from the metal to the secondary side liquid holds up the predicted pressure versus the data.

Figure 21-15 compares the measured (solid line) and calculated break mass flowrates. The experimental data, obtained from a catch tank system, have good accuracy for integral flow but do not always reflect sudden flowrate changes. For instance, at the opening of the break, the measured break flow may lag somewhat because of the transit time and buffering effects of the condensing coil system. In general, it is seen that the WCOBRA/TRAC-SB calculation is in good agreement with the experimental measurement during the first 30 seconds of the transient. For the next 120 seconds of the transient, the predicted break flow is somewhat low (on the average by about 20 percent) as its trend follows the data. This leads to a collapsed liquid level prediction above the data in this time interval in Figure 21-16. At the time of loop seal clearance in the calculation, the predicted break flow drops suddenly. The same phenomenon occurs in the test data, but 20 seconds earlier. Following loop seal clearance, WCOBRA/TRAC-SB predicts a significantly larger break flow than the data for 60 - 70 seconds.

Figure 21-16 compares the collapsed liquid level predicted in the core region to the test data as provided by Loomis and Streit (Loomis and Streit, 1985b) and shown as the solid line. The notable differences between the data and the calculation are that the calculation predicts a depression and recovery of the level in the core approximately 20 seconds late during loop seal clearance and then predicts a collapsed liquid level that is approximately 2.5 ft low in the ensuing period until accumulator actuation. In the test data, the core level depression observed to bottom out at approximately 170 seconds is relieved by the intact loop pump suction seal blowout. In WCOBRA/TRAC-SB a very similar loop seal behavior is predicted. This indicates that there is a similar liquid holdup in the steam generator tubes in the prediction as in the test. Later on in the transient, the predicted core level is well below the measured value because WCOBRA/TRAC-SB predicts too high a break flow post-loop seal clearing.

Figures 21-17 and 21-18 show the calculated void fractions in the top two nodes in the pump suction piping for the intact and broken loops. The solid and dashed lines in the figures are the top and middle nodes, respectively. In test S-LH-1, once the intact loop seal cleared, the pressure relief temporarily removed the driving heads for clearing the broken loop seal, which eventually blew out at approximately 270 seconds. In the simulation, as in the test, the flow through the cleared intact loop is inadequate to prevent the broken loop from clearing. After the initial clearance of each loop seal, the loop seal refills partially. The broken loop loop seal middle node does refill completely for a short time and then reclears later on. The upflow sides of each of the pump suction legs were swept out gradually, which is in good agreement with the type of behavior observed in all Semiscale small break LOCA experiments.

Figure 21-19 compares the core heater rod temperature response of the lead rod in the test S-LH-1 data with the peak temperature predicted by WCOBRA/TRAC-SB indicated by the dashed curve. WCOBRA/TRAC does not predict a modest heatup of the heater rods during the loop seal clearance even though the severity of the core depression is predicted well. This indicates that the two-phase mixture level is overpredicted by WCOBRA/TRAC-SB. The code-predicted heatup above saturation temperature during the core boiloff portion of the transient is approximately 540°F, versus approximately 400°F in the test. As is evident in Figure 21-19, the predicted heater rod temperature excursion is of longer duration than in the test. This is a consequence of the code underprediction of collapsed level.

Figure 21-19 also indicates that there may be another overprediction of mixture level swell in the Semiscale heated rod bundle; the collapsed level at which the core boiloff excursion in clad temperature begins is about 0.2 feet lower than in the experiment. The heat transfer prediction in the uncovered core situation, as shown in Section 12 of this document, is close to the data. The WCOBRA/TRAC-SB underprediction of collapsed liquid level and overprediction of level swell in the core region compensate somewhat but produce a PCT value above the data.

Figure 21-20 provides a comparison of the integrated break mass flow between experiment and prediction. For the transient overall, the agreement is within 1 percent; the low break flow that occurs in WCOBRA/TRAC-SB at low subcooling/saturated liquid conditions before the clearance of the intact loop loop seal at 190 seconds, defines the largest point of departure in the WCOBRA/TRAC prediction from the data. The excessive break flow predicted by WCOBRA/TRAC-SB for two-phase flow after loop seal clearance brings the code's integrated total back to the data, and by the time the pressure decreases to the accumulator setpoint (630 psi), the integrated break flows are a close match. The error in overpredicting the two-phase flow compensates for the previous underprediction of the break flow.

21-7-2 S-LH-2 Simulation Results

Figure 21-21 shows that the integrated break mass flow comparison for the test S-LH-2 prediction and data follows the same trend as the test S-LH-1 result. Figure 21-22 shows the pressurizer pressure transient from the WCOBRA/TRAC-SB test S-LH-2 calculations (dashed line) compared to test data (solid line). As was the case for S-LH-1 at the opening of the break, the model over-predicts the pressure drop to near the hot leg saturation value. The initial depressurization of the system is totally dependent upon the draining of the pressurizer, which is restricted by the surge line to the hot leg. Once the calculation reaches hot leg saturation (approximately 1700 psi), agreement exists between the data and prediction as primary fluid begins to flash. Once the system depressurizes to cold leg saturation (approximately 1100 psi), the depressurization rate slows appreciably both in the experiment and the calculation. Then, the WCOBRA/TRAC-SB calculation over-predicts the primary pressure versus the test data for a time, but the predicted value decreases so that the predicted accumulator actuation time is approximately on the mark.

Figure 21-23 overlays the predicted primary pressure (solid line) along with the predicted steam generator secondary side pressures (dashed lines) with the intact loop steam generator — exhibiting a higher value than the broken loop unit most of the time. Figure 21-24 overlays the broken and intact loop steam generator pressures against the test S-LH-2 data. In general for small break LOCAs, during the initial portion of the transient, the primary pressure hovers above the secondary pressure because the break energy removal is supplemented by continuing heat transfer to the secondaries. Once the intact loop loop seal clears (approximately 200 seconds), the break uncovers and the primary side can depressurize below the secondaries. During the early portion of the transient, the secondary pressures are predicted to be higher than in the experiment. The first stage safety setpoint on the steam generator secondaries is set at 1047 psi. Contrary to the experiment, where neither secondary reached the setpoint, WCOBRA/TRAC-SB predicts the broken loop steam generator secondary pressure to reach the setpoint for a few seconds. As discussed in Section 21-7-1, the amount of initial secondary inventory is suspected to be low in the calculation relative to the experimental conditions and to the steam generator metal mass. The WCOBRA/TRAC predicted steam generator secondary pressures exceed the test values during the transient until after loop seal clearance occurs.

Figure 21-25 compares the measured (solid line) and calculated break mass flowrates. The experimental data, obtained from a catch tank system, have good accuracy for integral flow, but do not always reflect sudden flowrate changes. In general, it is seen that the

WCOBRA/TRAC-SB calculation is in good agreement with the experimental measurement during the first 25 seconds of the transient. For the next 90 seconds of the transient, the predicted break flow is somewhat low (about 35-40 percent) in the low subcooling/saturated liquid region. Clearing of the intact loop seal in the prediction (within a few seconds of the time that it cleared in the experiment) affects the break mass flow comparison thereafter, in the same way as in S-LH-1. The overprediction of two-phase break flow compensate for the previous underprediction of the break flow.

Figure 21-26 compares the collapsed liquid level predicted in the core region to the test data. The notable difference between the data and the calculation is the greater decrease in the predicted level after 350 seconds, before which the agreement is good. The calculation predicts a depression and recovery of the level in the core, and, consistent with the data, the pump suction seal depression and blowout causes no core uncovery. Not until the longer term boiloff begins at approximately 300 seconds into the experiment, causing a depletion of inventory, does any core heatup occur in test S-LH-2. The S-LH-2 prediction shows an increase in core collapsed level in the time interval between 485-510 seconds. This is caused by the sudden draining of liquid that has been held up in the intact loop hot leg back into the reactor vessel upper plenum. Once this draining is complete, the core region collapsed liquid level of WCOBRA/TRAC-SB agrees very well with the test value. The error in predicting the core collapsed level is compensated for by the draining of liquid that WCOBRA/TRAC-SB has held up in the hot leg due to its overprediction of CCFL.

Figure 21-27 shows the predicted void fractions in the intact loop pump suction piping middle and top nodes. Figure 21-28 provides void fractions in nodes in the pump suction piping for the broken loop as predicted by WCOBRA/TRAC-SB. The solid and dashed lines are the top and middle nodes, respectively, in these two figures. The WCOBRA/TRAC-SB model predicts no clearing of the broken loop loop seal, which is consistent with the test result. The steam relief flow path through the vessel upper head is sufficient, together with the cleared intact loop, to vent steam to the break. Figure 21-27 shows the middle node in the intact loop pipe tends to replug after clearing.

Figure 21-29 compares the core heater rod temperature response of the lead rod in the test S-LH-2 data with the peak temperature predicted by WCOBRA/TRAC-SB. In contrast to the test, WCOBRA/TRAC-SB predicts two periods of heatup of the heater rods during the transient. The mass addition from draining of the intact hot leg causes the code-predicted initial heatup above saturation temperature during the core boiloff portion of the transient to terminate. In

Figure 21-29, the second predicted heater rod temperature excursion begins at about the same time as the test excursion, but at a collapsed liquid level about 0.4 lower than in the test. This behavior is consistent with that previously noted in the test S-LH-1 discussion.

21-8 Conclusions

The S-LH-1 and S-LH-2 experiments of the Semiscale Mod-2C configuration have been simulated with the WCOBRA/TRAC-SB model using the boundary conditions from these small break LOCA experiments. A comparison of calculated steady-state conditions from the model to experimental data is generally in good agreement, and all parameters were within acceptable tolerances for performing transient simulations to ascertain the general ability of the code to predict the major thermal-hydraulic phenomena.

A review of the calculation results indicates that the code is generally doing a good job of predicting the key small break LOCA parameters. Notably, the expected top-down drain of the system and the formation of quasi-equilibrium hydrostatic balances associated with liquid inventories in the vertical components, particularly the core/downcomer and pump suction loop piping, are reasonable. Key transient parameters of depressurization rate and break mass discharge are predicted adequately. The predicted heater rod temperature excursions differ somewhat from the data; the lower collapsed liquid level in the core region in the S-LH-1 simulation leads to a higher PCT than was observed in the test, while a delayed hot leg draining leads to a dual temperature excursion in the test S-LH-2 simulation. Consistent with the findings reported in Chapter 13, in the Semiscale simulations WCOBRA/TRAC-SB underpredicts the critical mass flux for saturated liquid, then overpredicts critical flow for two-phase conditions.

21-9 References

Larson, T. K., et al., 1980, "Scaling Criteria and an Assessment of Semiscale Mod-3 Scaling for Small Break Loss Of Coolant Transients," EGG-SEMI-5121.

Leonard, M. T., 1981, "RELAP5 Standard Model Description for the Semiscale Moda System," EGG-SEMI-5692.

Leonard, M. T., 1982, "Vessel Coolant Mass Depletion During a Small Break LOCA," EGG-SEMI-6010.

Leonard, M. T., 1983, "An Analytical Study of a Small Break Loss-Of-Coolant Accident with Upper Head Injection," Nuclear Technology, Vol 62.

Loomis, G. G., 1985a, "Semiscale Liquid Holdup Investigations: A Comparison of Small Break LOCA Tests Performed in the Semiscale Moda and Mod-2C Facilities," 13th Annual Water Reactor Safety Research Information Meeting, Gaithersburg, MD.

Loomis, G. G., 1985b, "Summary of Semiscale Small Break Loss-of-Coolant Accident Experiments (1979 to 1985)," NUREG/CR-4393 (EGG-2419).

Loomis, G. G., 1987, "Summary of the Semiscale Program (1965-1986)," NUREG/CR-4945 (EGG-2509).

Loomis, G. G. and Streit, J. E., 1985a, "Quick Look Report for Semiscale Mod-2C Experiments S-LH-1 and S-LH-2," EGG-SEMI-6884.

Loomis, G. G. and Streit, J. E., 1985b, "Results of Semiscale Mod-2C 5% Small Break LOCA Experiments S-LH-1 and 2," NUREG/CR-4438 (EGG-2424).

Osakabe, M., et al., 1987, "Core Liquid Level Depression Due to Manometric Effect During PWR Small Break LOCA," J. of Nuclear Science and Technology 24(2), pp. 103-110.

Shaw, R. and Loomis, G. G., 1985, "Vessel Coolant Mass Depletion During a 5% Small Break LOCA in the Semiscale Mod-2C Facility," Specialists Meeting on Small Break LOCA Analysis in LWRs, 2, Piza, Italy, pp. 159-175.

Shimeck, D. J., 1983, "Analysis of Semiscale Moda System UHI/SBLOCA Experiments," NUREG/CR-3195.

Table 21-1
Comparison of Steady-State Conditions: Test S-LH-1

Parameter	Measured	WCOBRA/TRAC Model
Pressurizer pressure (psia)	2244	2214
Core power (kW)	2019	2019
Cold leg temperature (°F)		
Intact loop	552.1	550
Broken loop	555.6	554.3
Core ΔT (°F)	67.8	66
Primary flowrates (lbm/s)		
Intact loop	15.7	16.0
Broken loop	5.2	5.2
Upper head temperature (°F)	545	543
Upper head bypass (%)	0.90	0.957
Primary leakage rate (lbm/s)	0.004	0
Steam generator secondary pressures (psia)		
Intact loop	830	830
Broken loop	882	881
Steam generator secondary masses (lbm)		
Intact loop	421	269
Broken loop	95	84

Table 21-2
Comparison of Steady-State Conditions: Test S-LH-2

Parameter	Measured	WCOBRA/TRAC Model
Pressurizer pressure (psia)	2237	2204
Core power (kW)	2019	2019
Cold leg temperature (°F)		
Intact loop	552	549.4
Broken loop	556.2	553.2
Core ΔT (°F)	66.9	67
Primary flowrates (lbm/s)		
Intact loop	16.2	16.1
Broken loop	4.4	5.2
Upper head temperature (°F)	546	547
Upper head bypass (%)	3.0	3.1
Primary leakage rate (lbm/s)	0.004	0
Steam generator secondary pressures (psia)		
Intact loop	827	827
Broken loop	864	865
Steam generator secondary masses (lbm)		
Intact loop	421	269
Broken loop	106	89

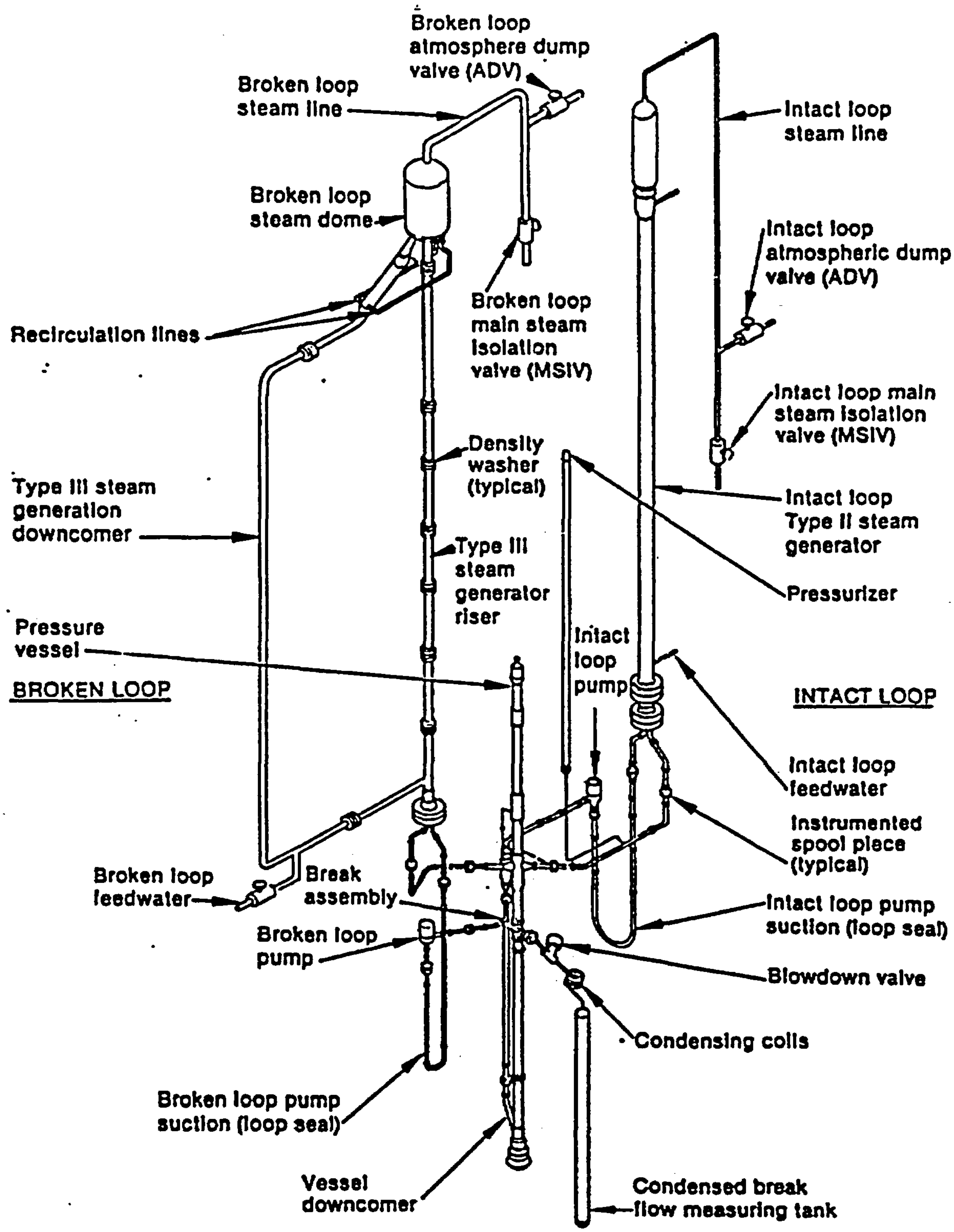

Figure 21-1. Semiscale Mod-2C System

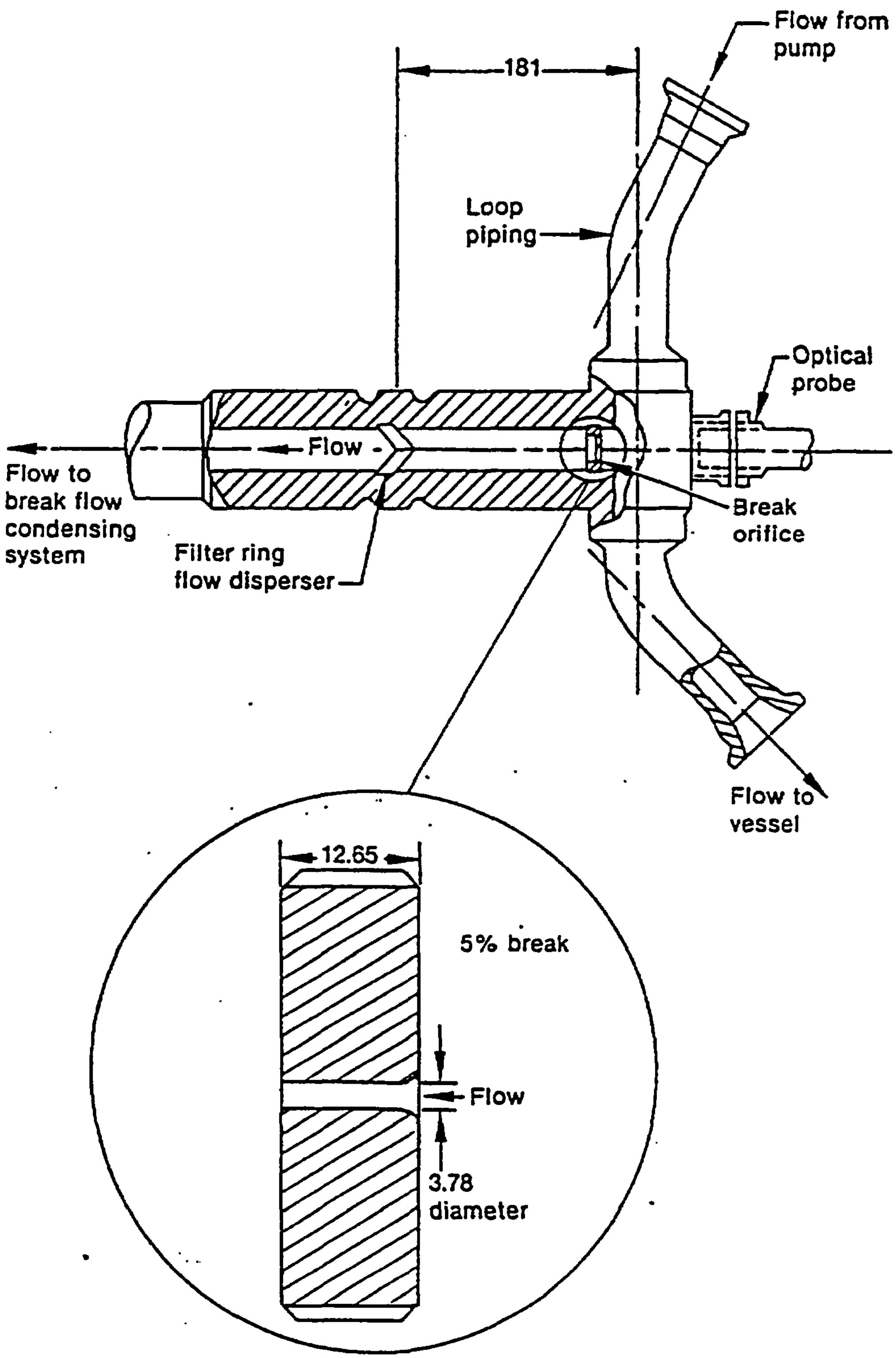

Figure 21-2. Cold Leg Break Assembly

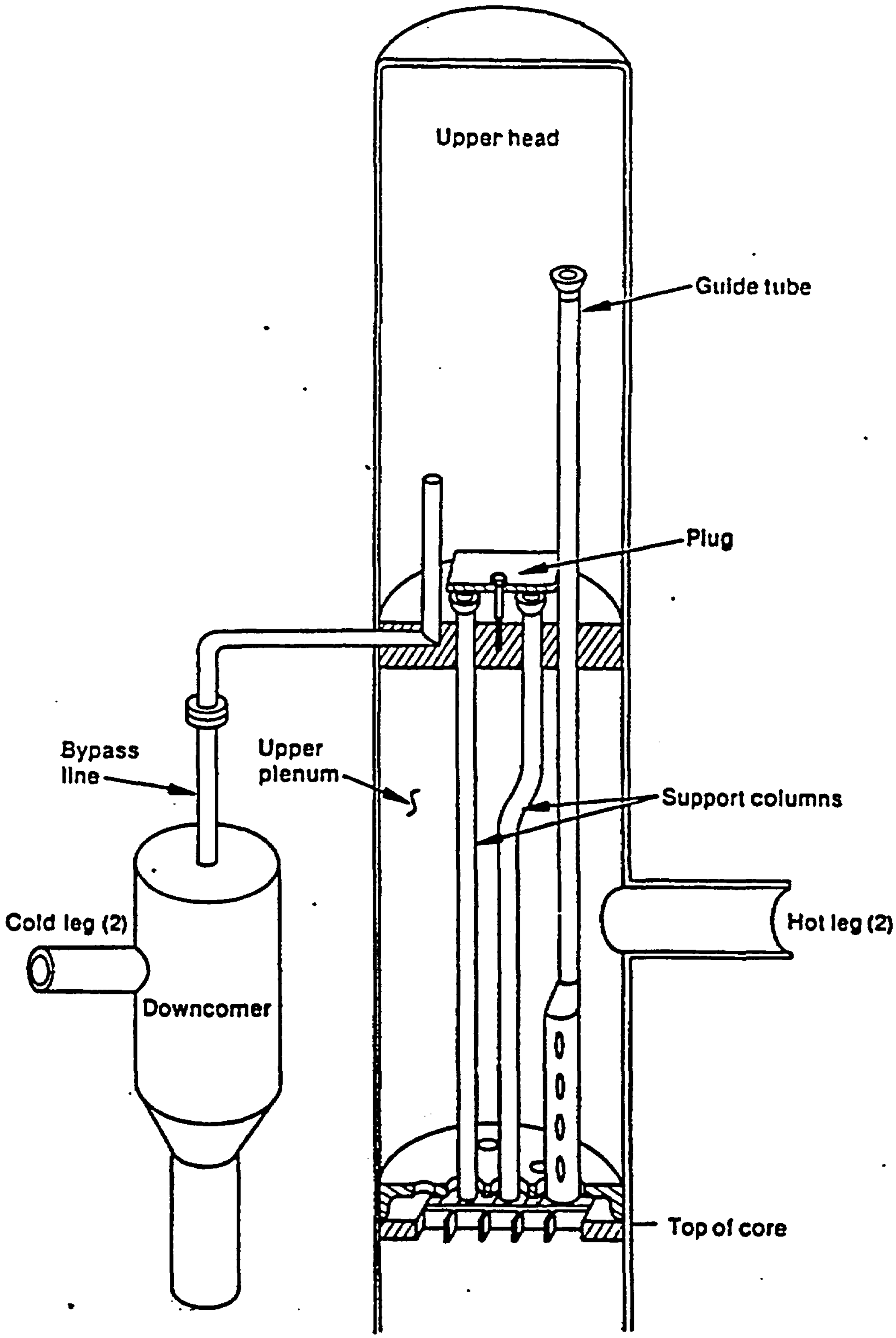

Figure 21-3. Vessel Upper Head Configuration

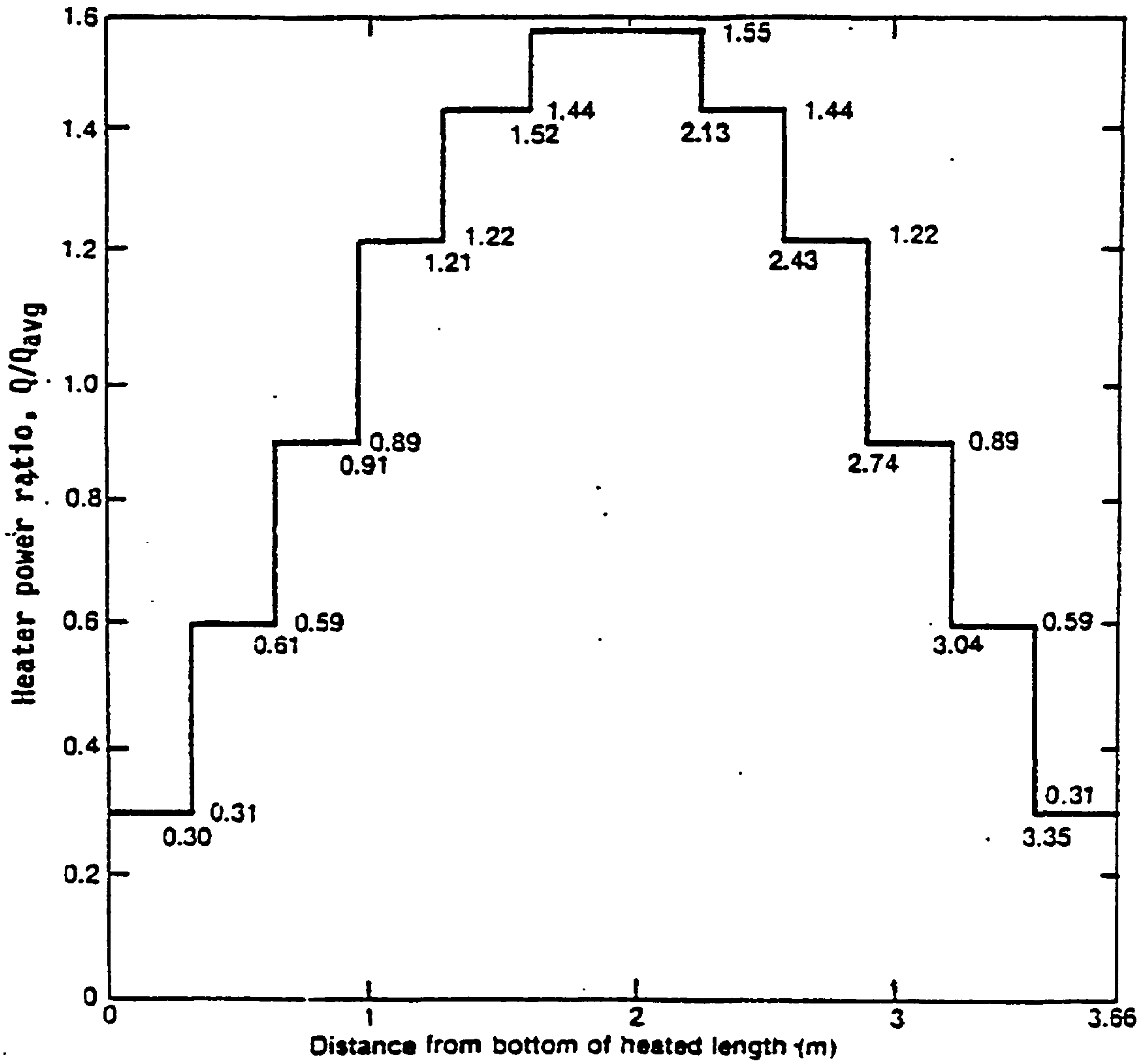

Figure 21-4. Core Heater Rod Axial Power Profile

a,c

Figure 21-5. WCOBRA/TRAC Model of Semiscale Mod-2C Component Layout

a,c

Figure 21-6. WCOBRA/TRAC Model of Semiscale Reactor Vessel

a,c

Figure 21-7. WCOBRA/TRAC Model of Semiscale Intact Loop Steam Generator

a,c

Figure 21-8. WCOBRA/TRAC Model of Semiscale Broken Loop Steam Generator

a,c

Figure 21-9. Semiscale Reactor Coolant Loop Noding

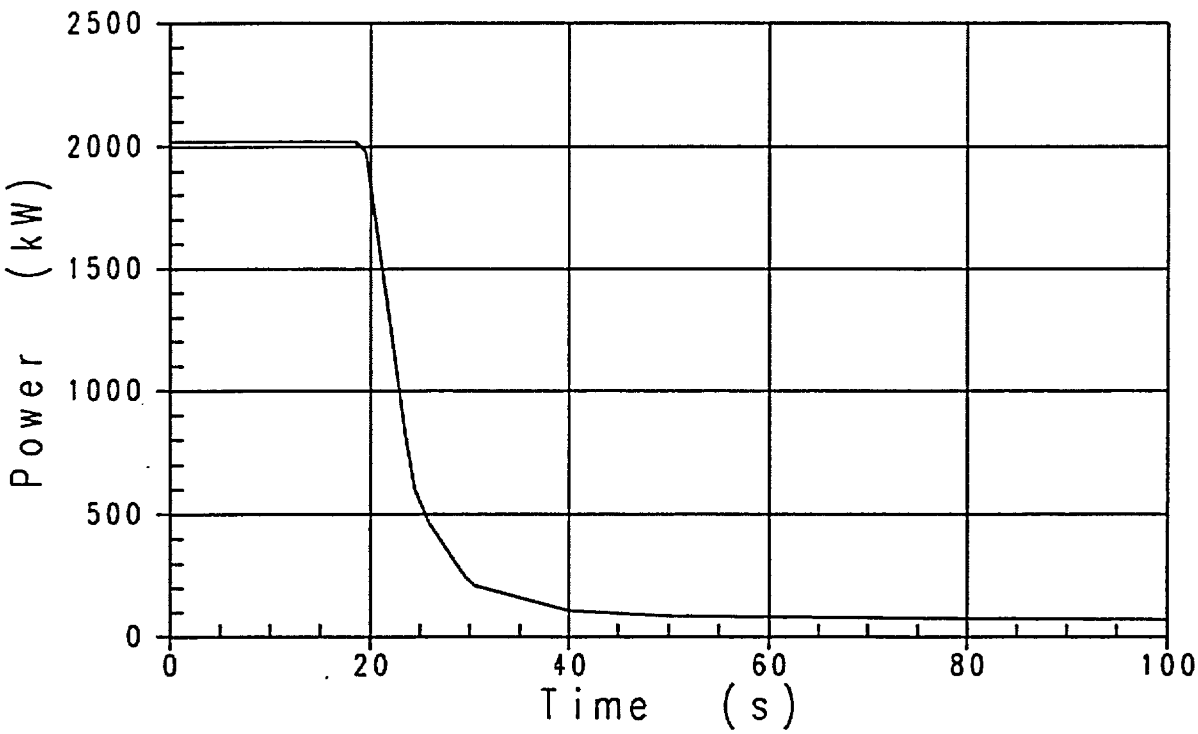

Figure 21-10. Core Power Versus Time Curve

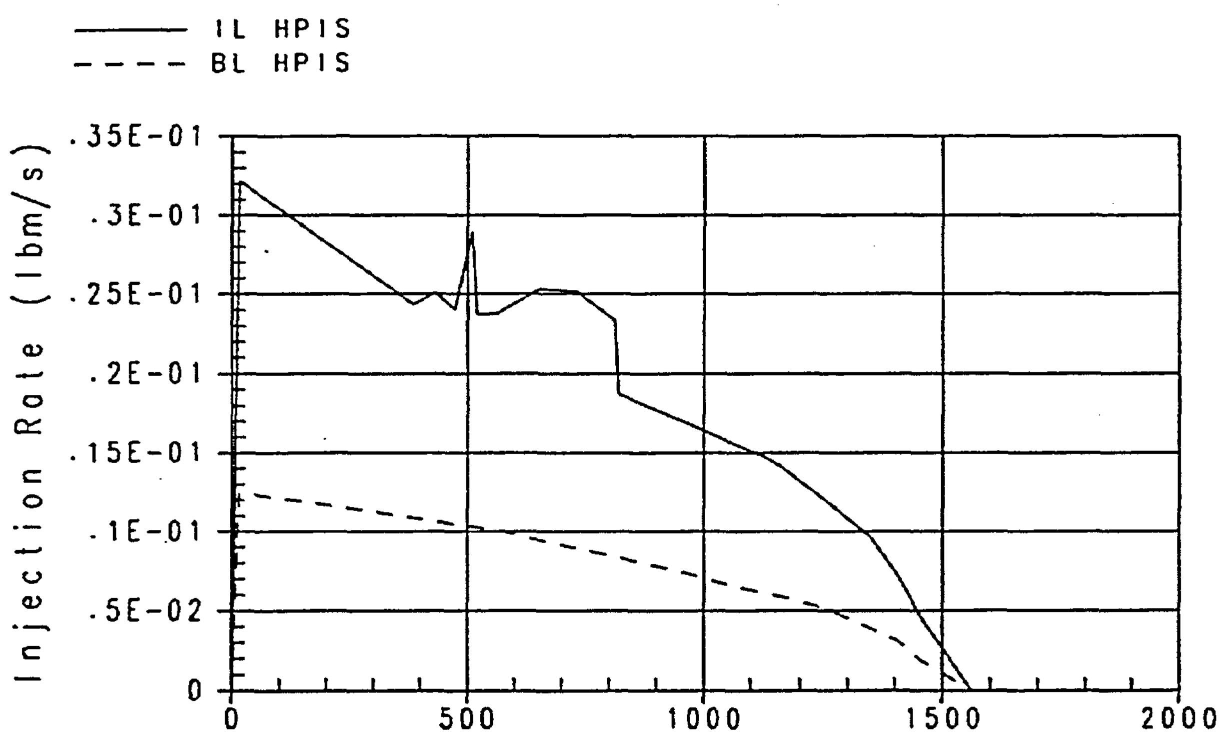

Figure 21-11. Safety Injection Rates as a Function of RCS Pressure

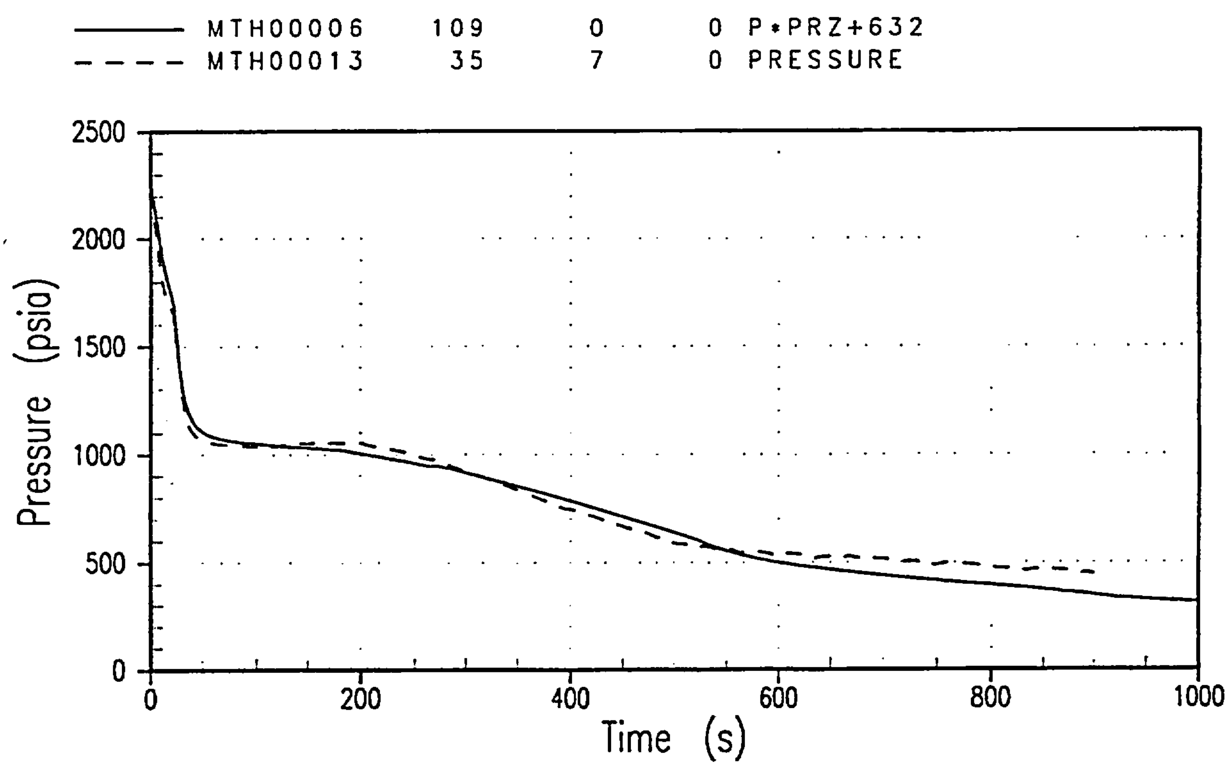

Figure 21-12. Pressurizer Pressure, Test S-LH-1

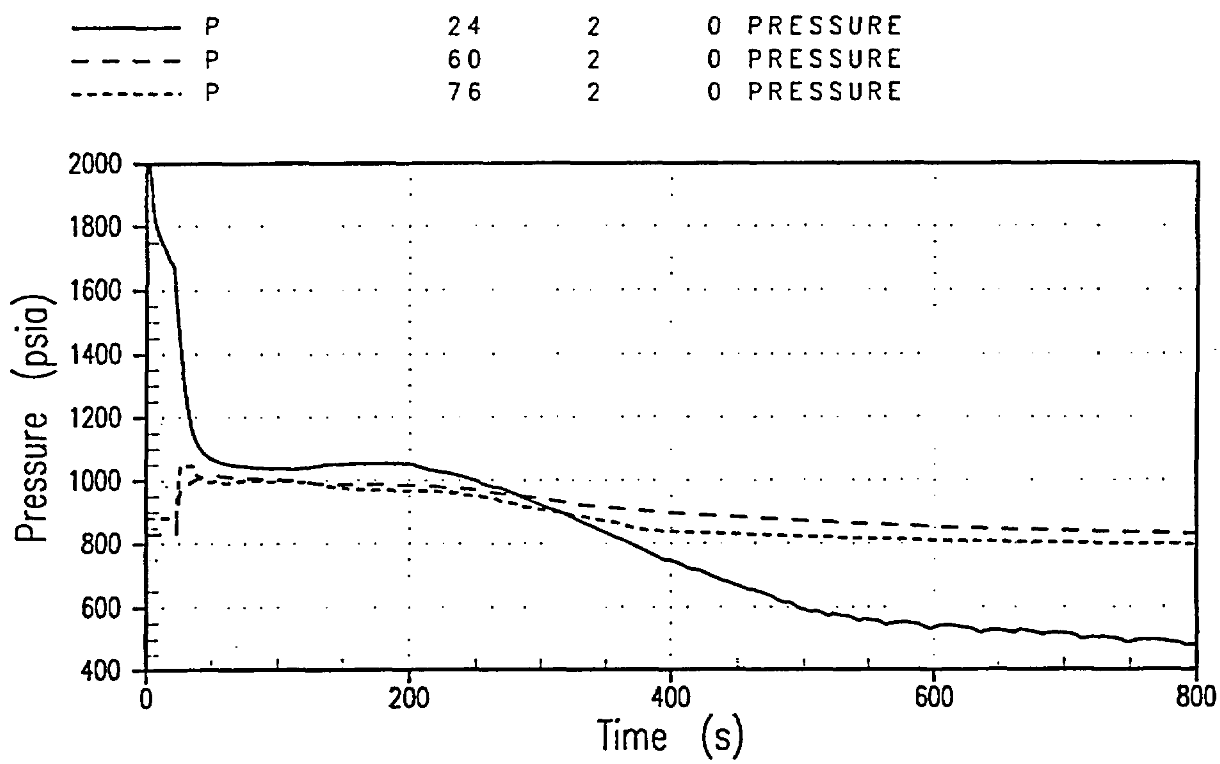

Figure 21-13. Primary and Secondary Predicted Pressures, Test S-LH-1

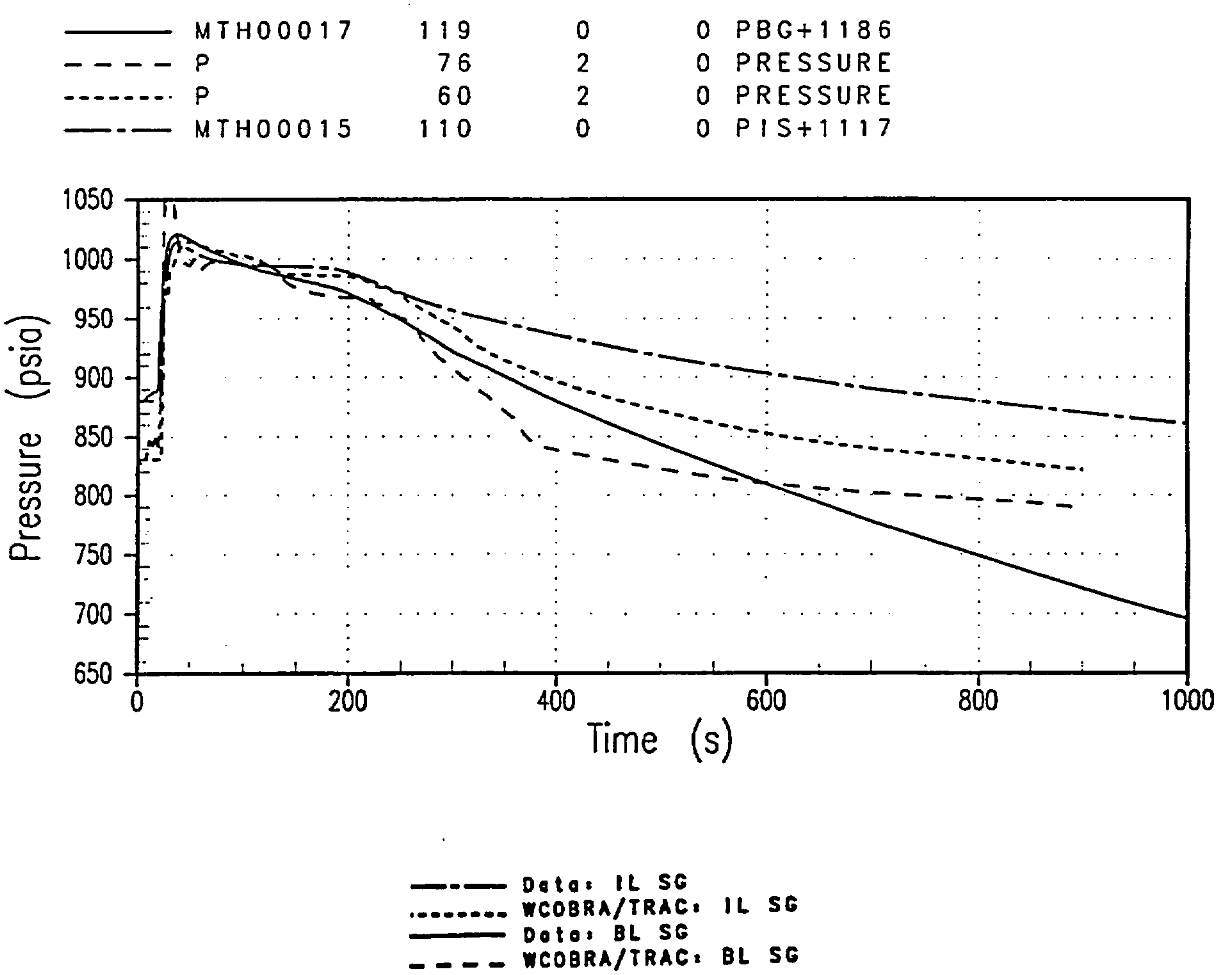

Figure 21-14. Broken and Intact Loop Secondary Pressure Predictions, Test S-LH-1

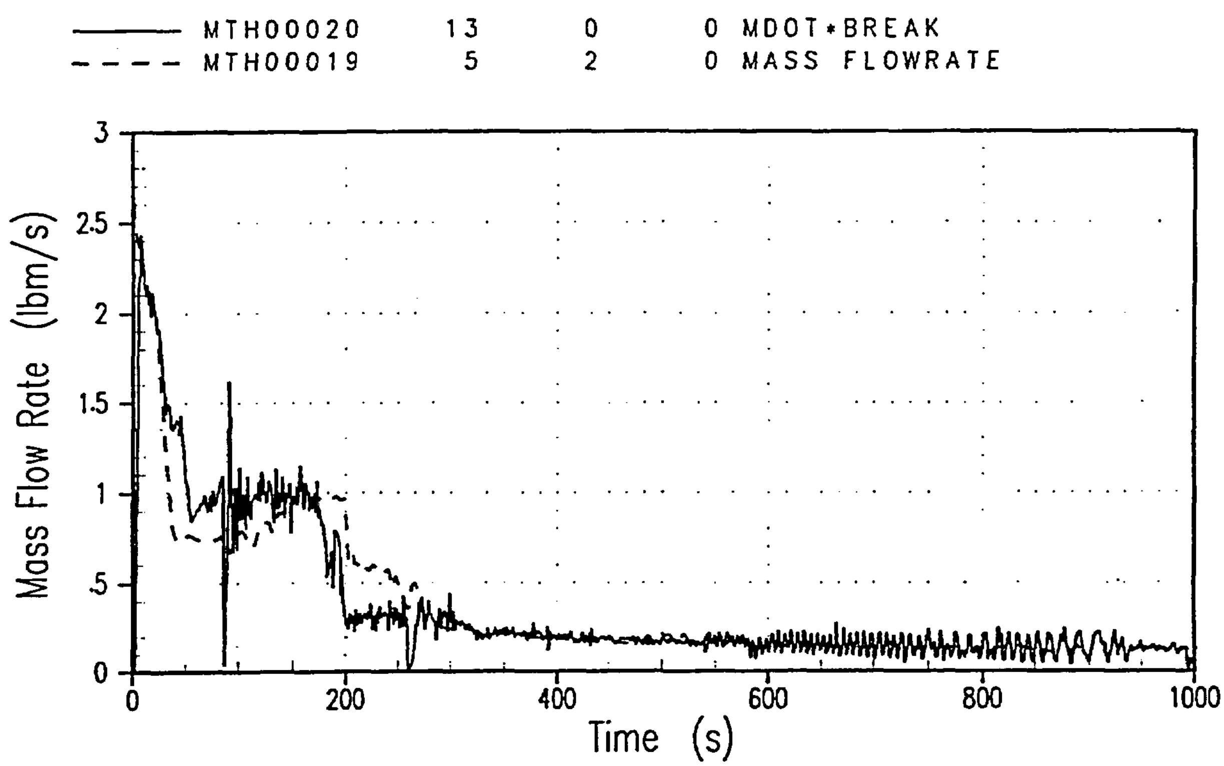

Figure 21-15. Break Mass Flowrates, Test S-LH-1

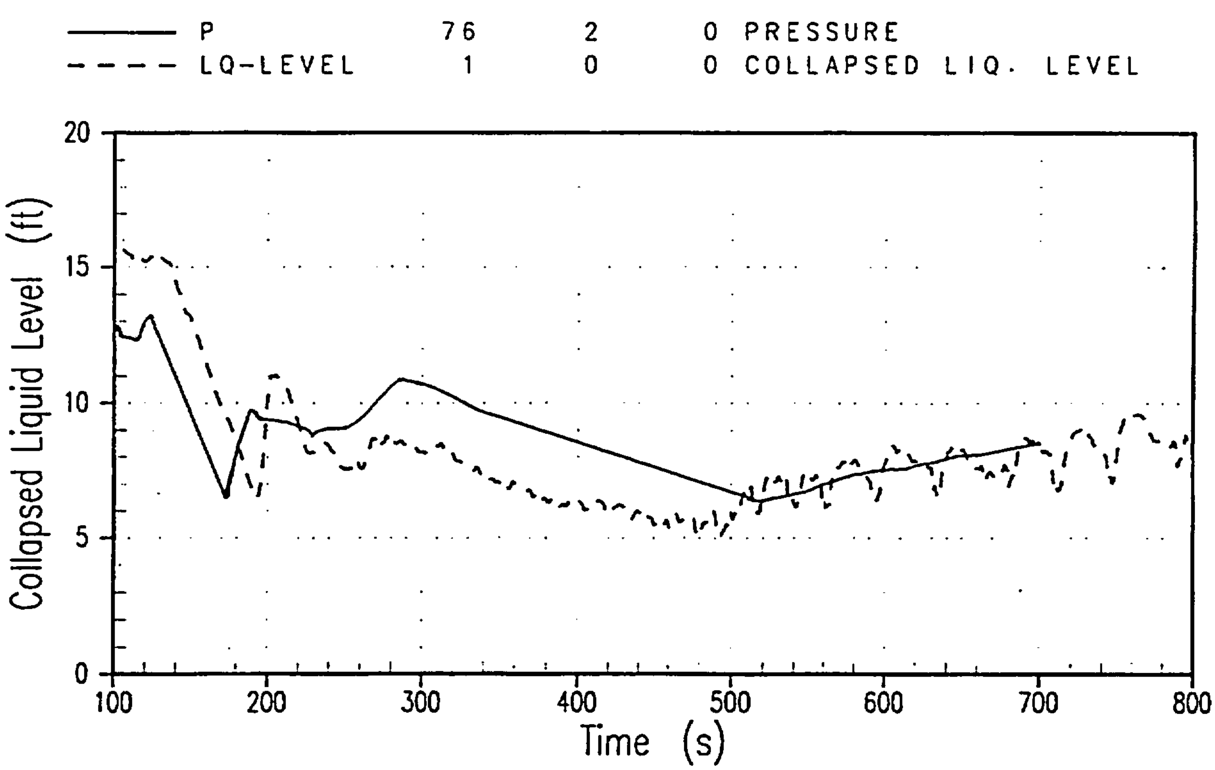

Figure 21-16. Core Collapsed Liquid Levels, Test S-LH-1

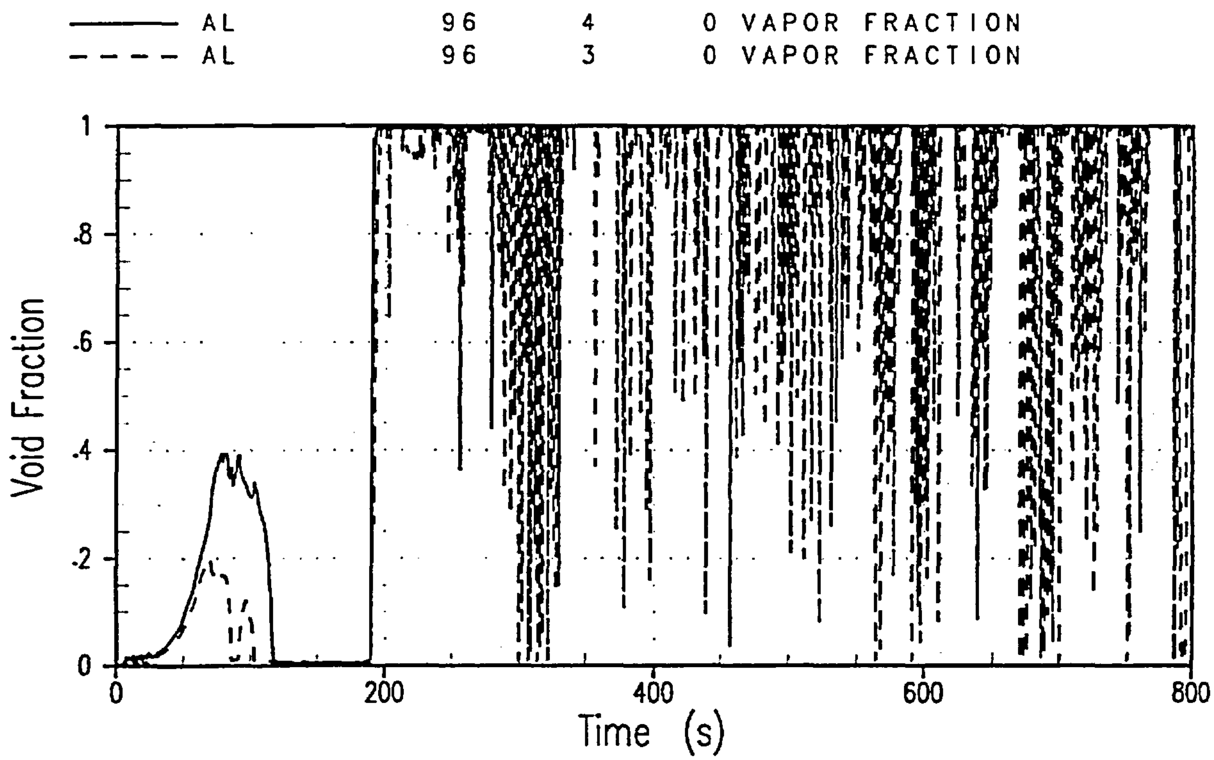

Figure 21-17. Calculated Void Fractions in the Intact Loop Pump Suction Piping, Test S-LH-1

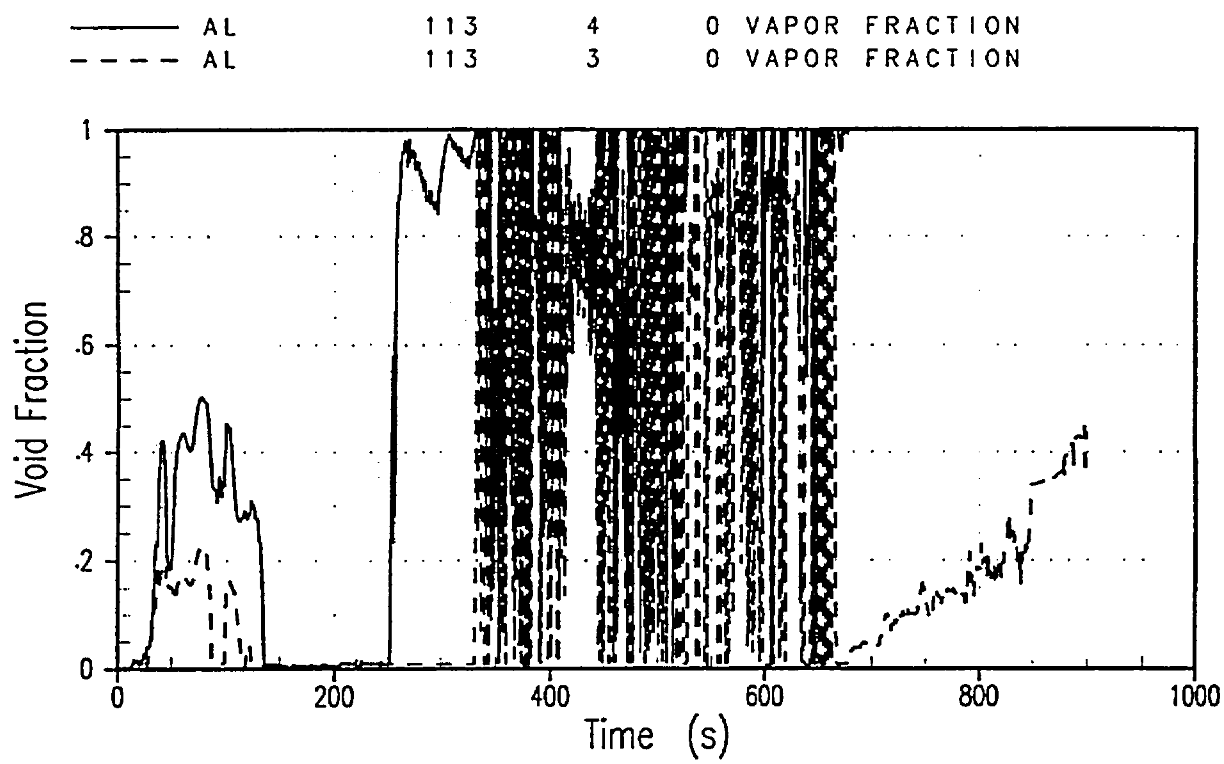

Figure 21-18. Calculated Void Fractions in the Broken Loop Pump Suction Piping, Test S-LH-1

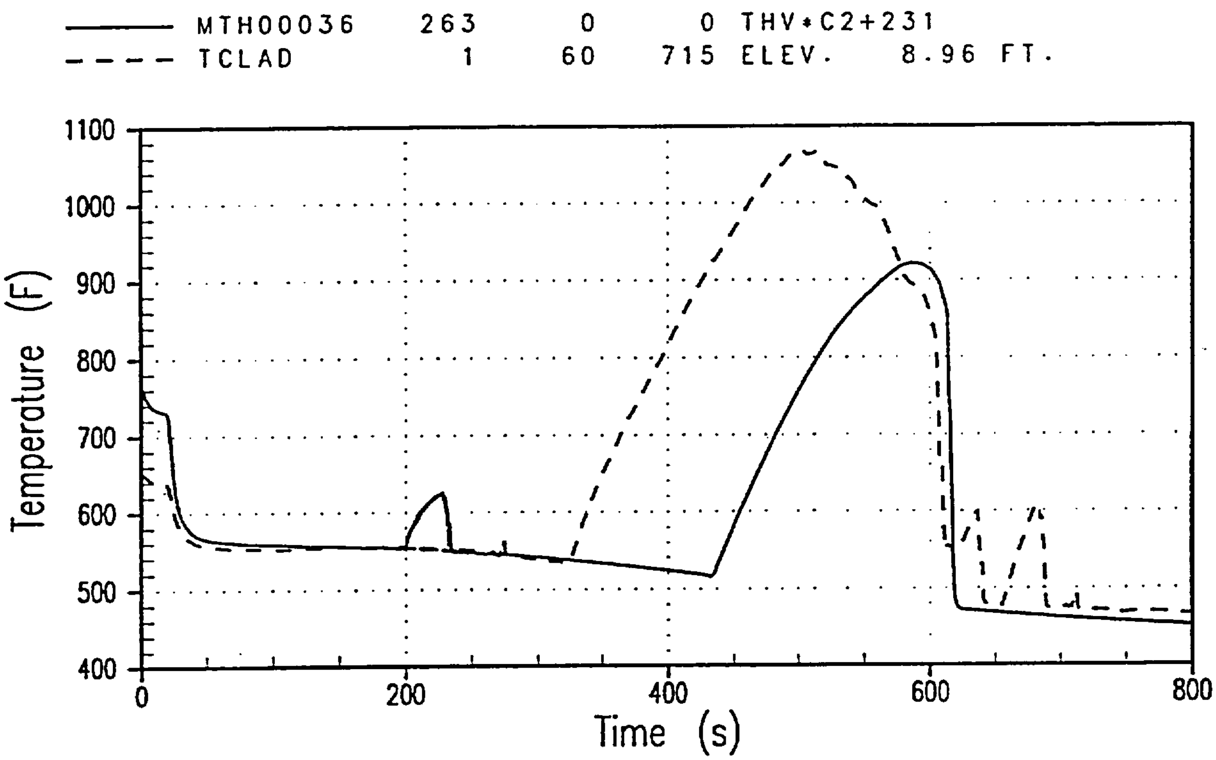

Figure 21-19. Core Heater Rod Temperature Response, Test S-LH-1

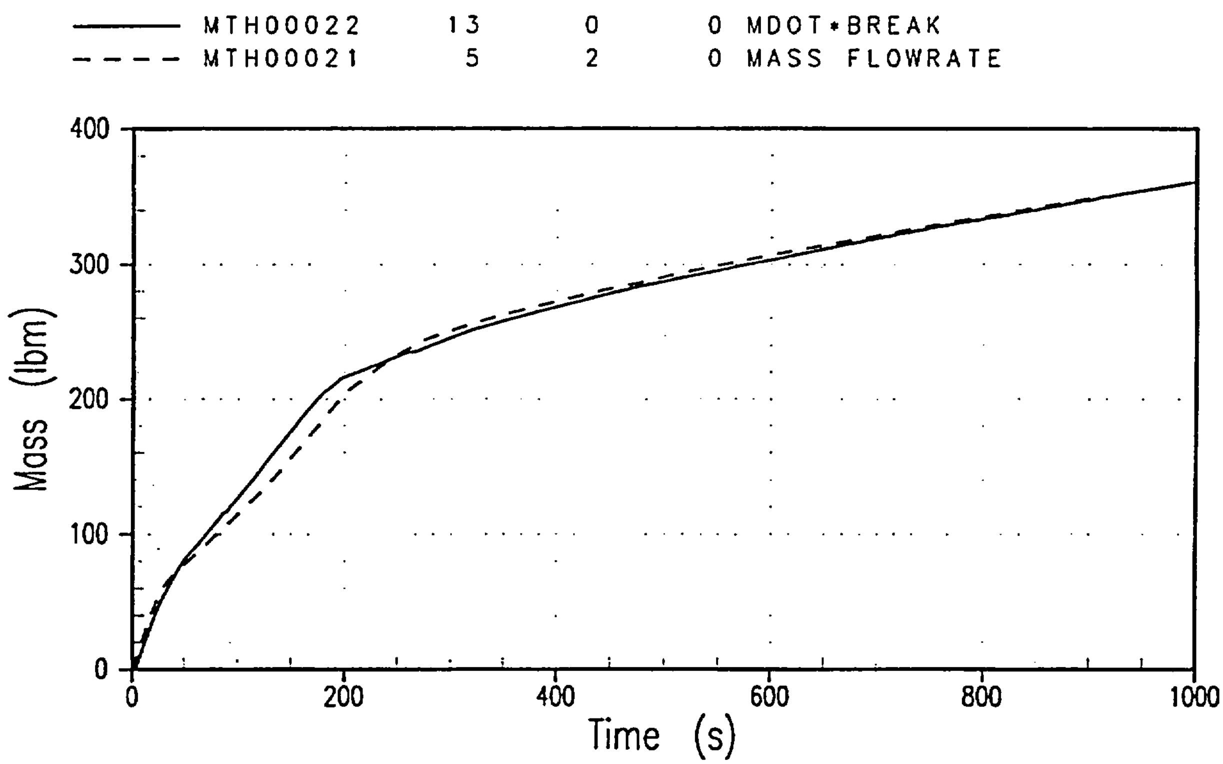

Figure 21-20. Integrated Break Mass Flow Comparison, Test S-LH-1

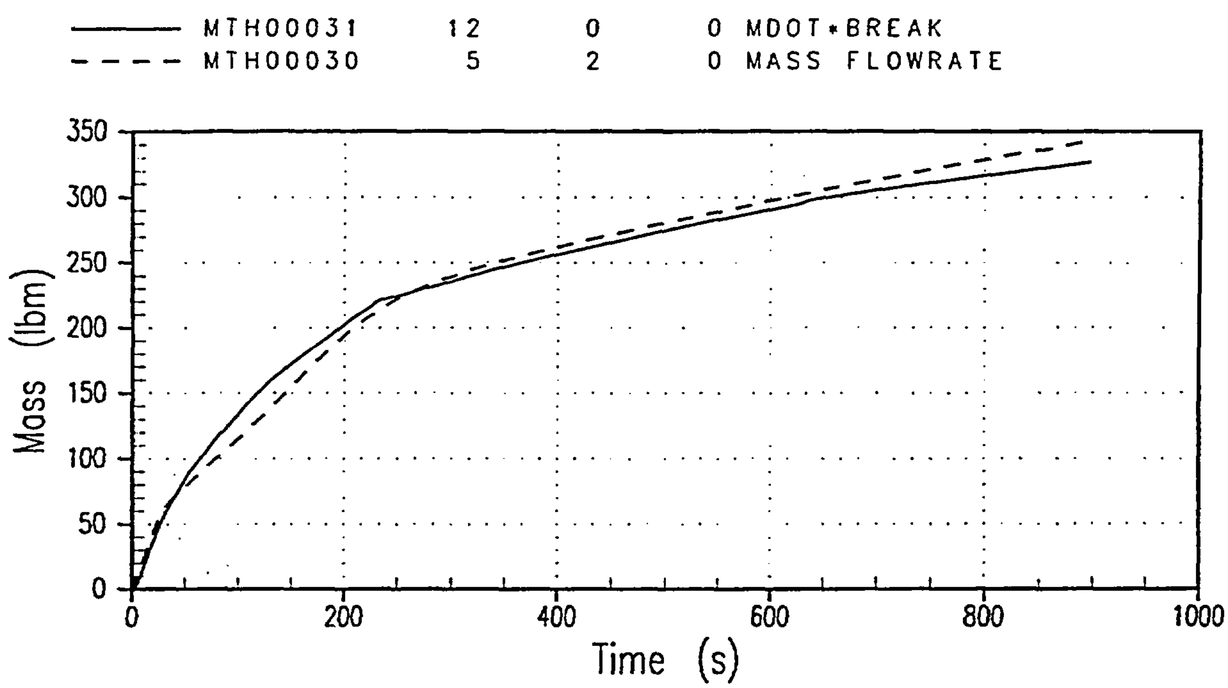

Figure 21-21. Integrated Break Mass Flow Comparison, Test S-LH-2

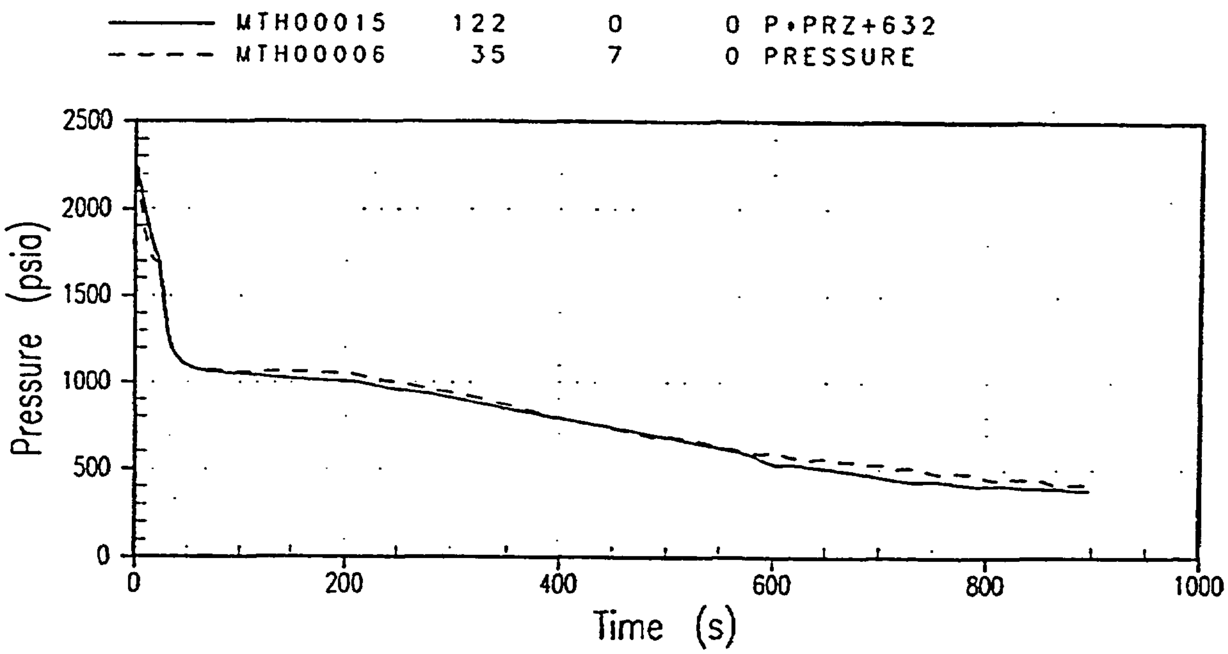

Figure 21-22. Pressurizer Pressure, Test S-LH-2

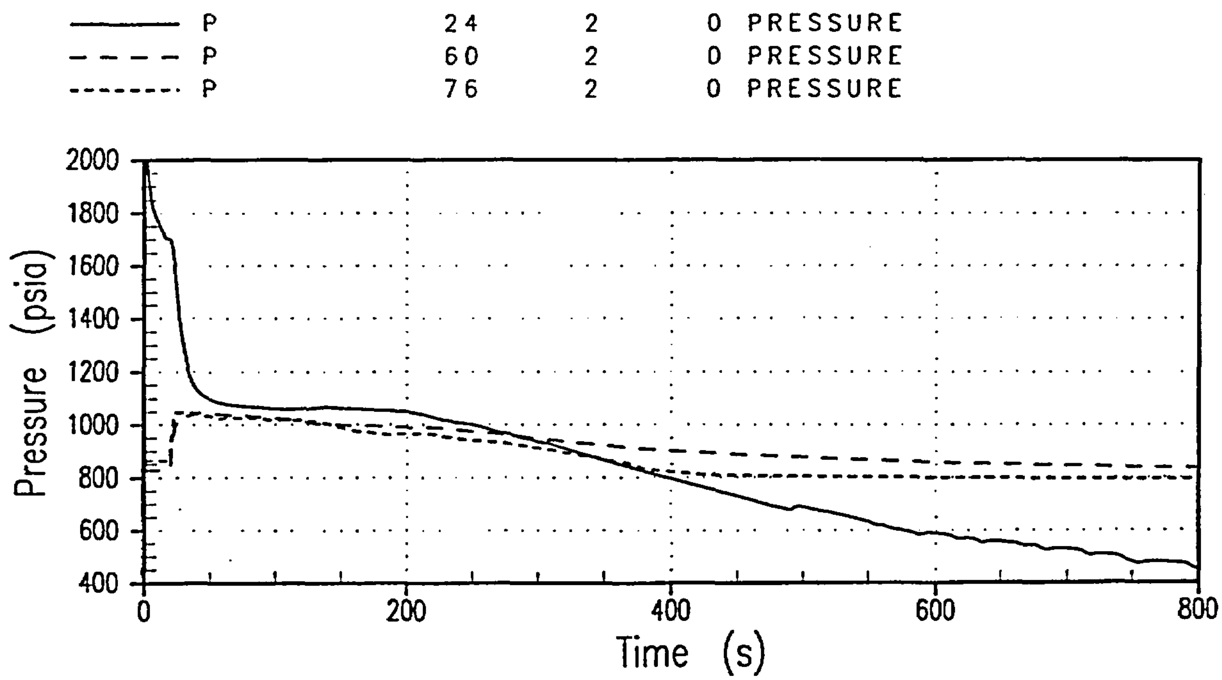

Figure 21-23. Primary and Secondary Predicted Pressures, Test S-LH-2

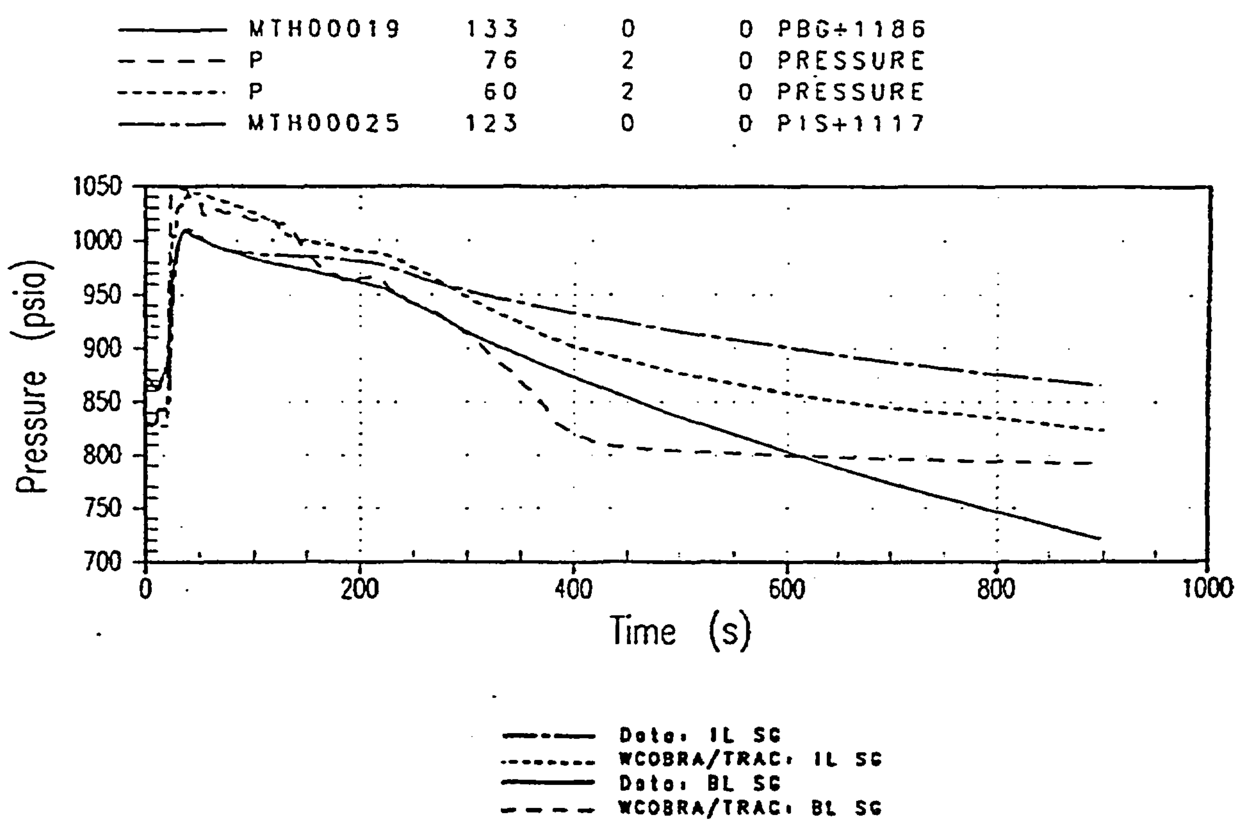

Figure 21-24. Broken and Intact Loop Secondary Pressure Predictions, Test S-LH-2

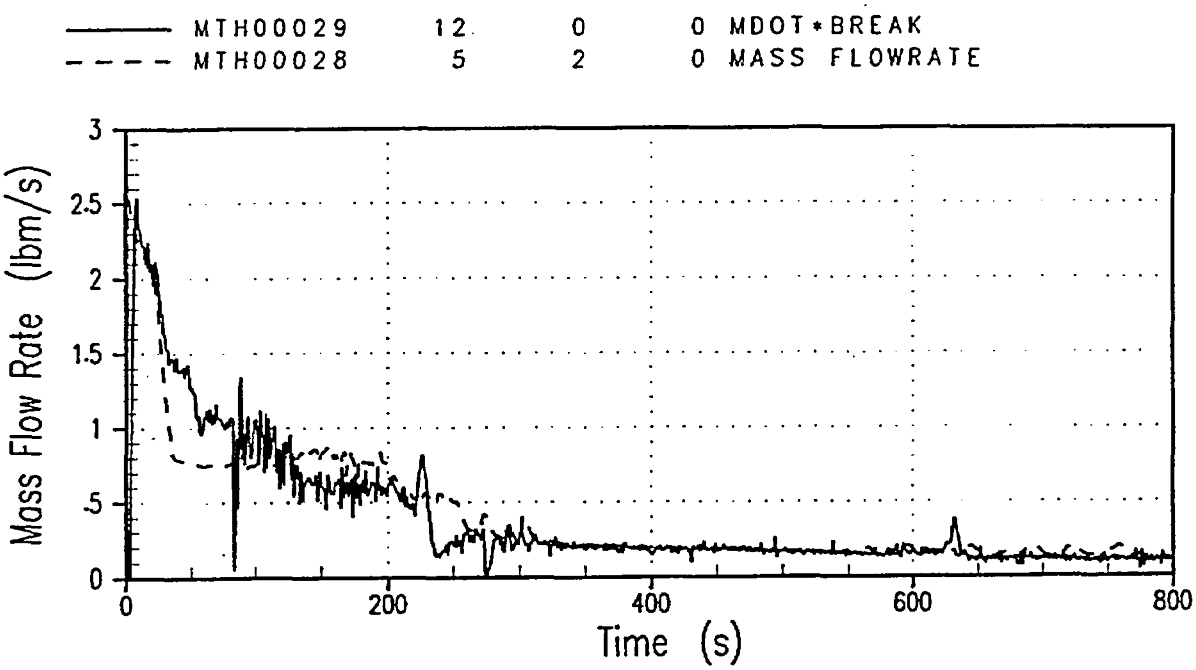

Figure 21-25. Break Mass Flowrates, Test S-LH-2

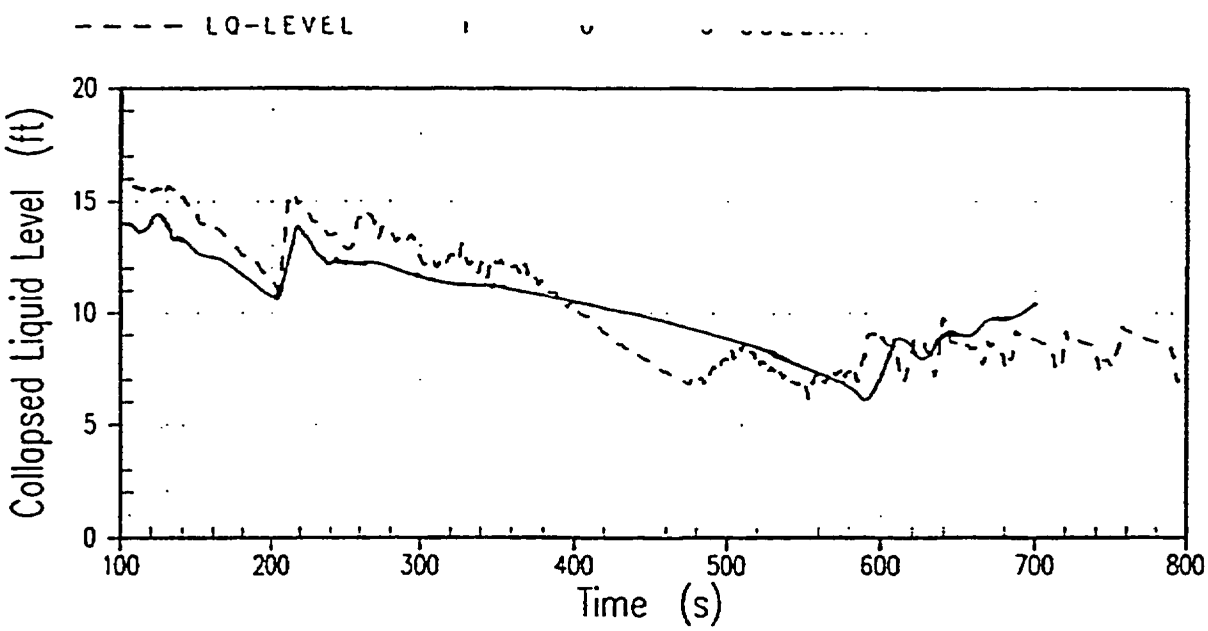

Figure 21-26. Core Collapsed Liquid Levels, Test S-LH-2

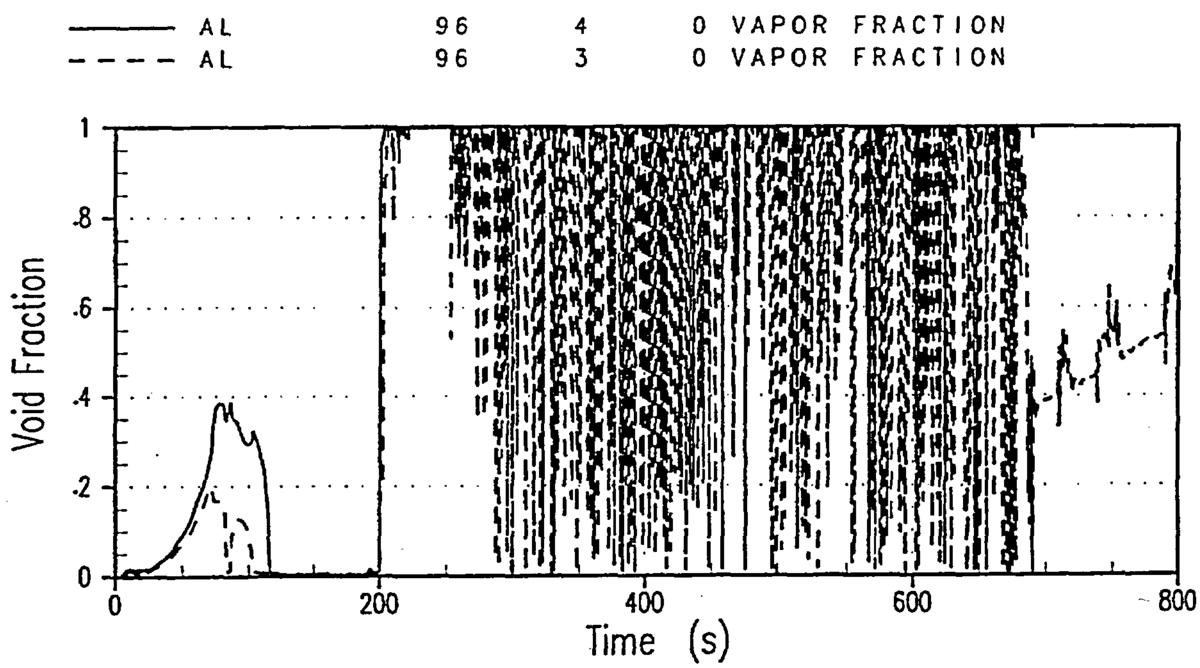

Figure 21-27. Calculated Void Fractions in the Intact Loop Pump Suction Piping, Test S-LH-2

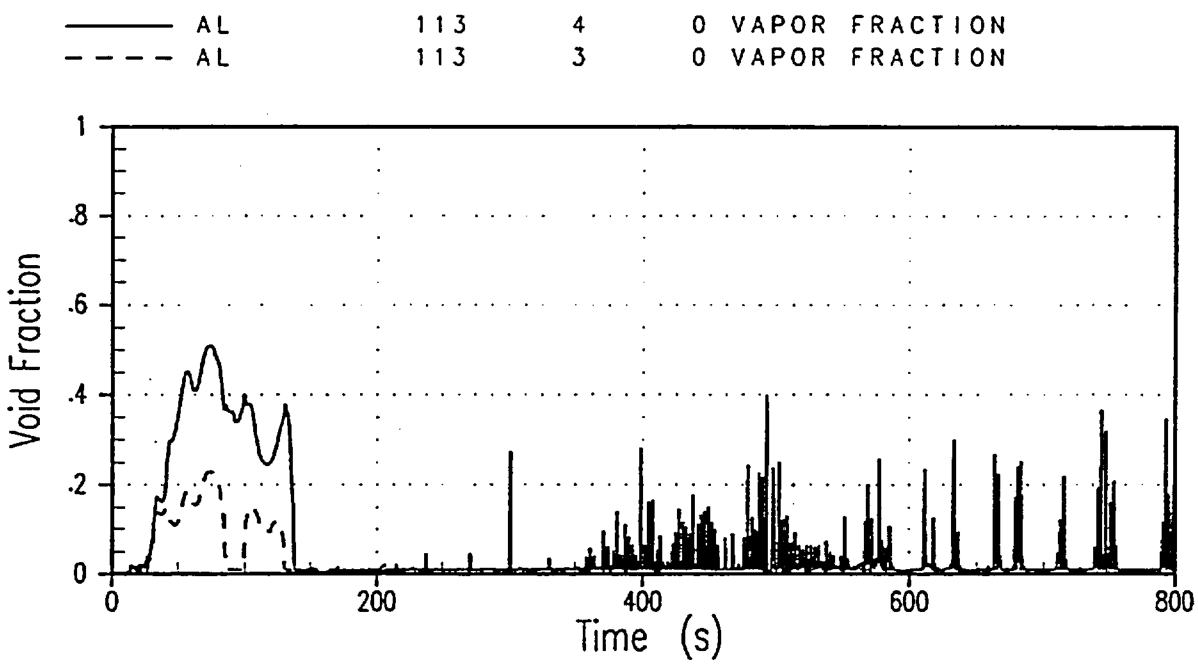

Figure 21-28. Calculated Void Fractions in the Broken Loop Pump Suction Piping, Test S-LH-2

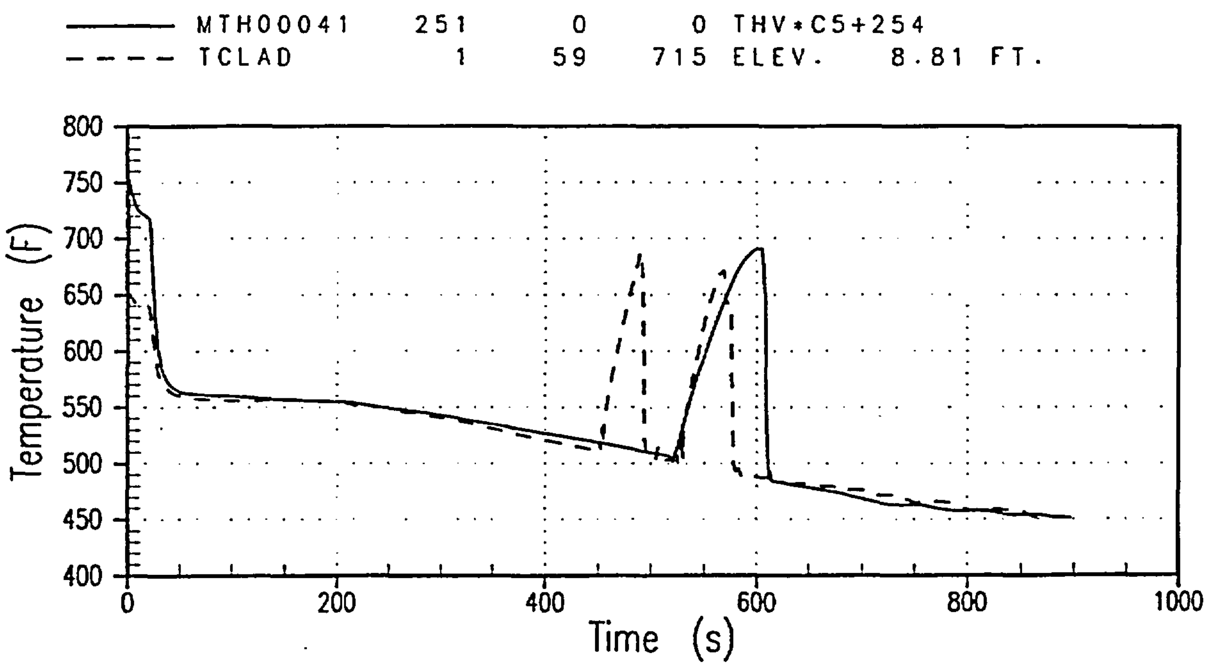

Figure 21-29. Core Heater Rod Temperature Response, Test S-LH-2

SECTION 22
NUCLEAR ROD AND COMPONENT MODEL ASSESSMENT

22-1 Nuclear Fuel Rod Model

22-1-1 Introduction

The fuel rod model in WCOBRA/TRAC is used to predict the following quantities:

a) Fuel Initial Stored Energy

During normal operation, the fuel average temperature in the high power rod is approximately 2000°F, controlled primarily by the relatively low conductivity of the fuel and the thermal resistance of the gap between the fuel and the cladding. During the LOCA, this stored energy is conducted to the cladding and is the primary contributor to the degree to which the cladding heats up early in the LOCA transient.

b) Fuel Rod Thermal Conduction

During the LOCA, residual power and stored energy accumulates in or is removed from the fuel. The change in fuel and cladding temperature is controlled primarily by the fuel conductivity and specific heat and by the changing thermal resistance in the fuel-clad gap.

c) Cladding Swelling and Burst

During the LOCA, internal pressure and high cladding temperature may cause the cladding to deform. This deformation is controlled primarily by the predicted cladding temperature and the burst and strain rate models used.

d) Cladding Rewet

Rewet may occur during the LOCA. This process may involve the rewetting of large areas of cladding surface as a result of the cladding cooling to temperatures below the minimum film boiling temperature, or the slower quenching process during reflood resulting from axial conduction in the fuel rod.

e) Cladding Reaction

Reaction between the zirconium in the cladding and the steam environment during the LOCA deposits additional energy into the cladding which must be removed. The reaction rate is controlled primarily by the cladding temperature and by the cladding surface area presented to the steam.

f) Residual Fission and Decay Heat

Throughout the LOCA, additional energy is deposited into the fuel. The rate of energy generation is controlled early in the transient by the rate of void generation in the core, which is the primary cause of shutdown of the fission process during the LOCA, and later in the transient by the assumed composition of the fuel as fission product decay continues.

The models used in WCOBRA/TRAC-SB to predict the above quantities are described in Volume 1, Sections 7 and 8, of this document. In the following sections, the ability of WCOBRA/TRAC-SB to predict the above quantities is assessed. Uncertainties in these models are considered in Section 25 of WCAP-12945-P-A (Bajorek, et al., 1998).

22-1-2 Fuel Rod Model Assessment

The following paragraphs discuss the fuel rod model:

a) Fuel Initial Stored Energy

The fuel temperature during normal operation depends, in complex ways, on fuel pellet condition and its properties. One of the most complex processes that affects this parameter is the relocation of the fuel pellet within the cladding and the resulting asymmetric fuel-clad gap. Complex fuel rod computer models have been developed to predict the fuel temperature as a function of power and burnup. For Westinghouse fuel, the fuel performance code PAD (Weiner, et al., 1985) is used. Incorporating all the detailed models necessary into WCOBRA/TRAC is not practical. The predicted WCOBRA/TRAC fuel temperature, during normal operation, is compared with values predicted from the PAD code for the fuel design being considered. Agreement between PAD and WCOBRA/TRAC predicted fuel temperature is obtained by adjusting the fuel-cladding gap width, which is an input quantity in WCOBRA/TRAC.

In predicting the LOFT experiments, as described in Section 14-1 of WCAP-12945-P-A (Bajorek, et al., 1998a), the initial fuel temperature for the LOFT core was obtained by using the PAD information for fuel of similar design and composition and using the same approach as in the PWR. No further adjustments were made. This, therefore, amounts to a "blind" prediction of the initial fuel temperature for LOFT. The reasonable agreement between the predicted and measured cladding temperatures for LOFT is evidence that the method for predicting this quantity in WCOBRA/TRAC is also reasonable.

b) Fuel Rod Thermal Conduction

Two experiments were used to assess the ability of WCOBRA/TRAC to predict the transient temperature of a fuel rod. The LOFT tests include comparisons with cladding and fuel temperatures. The composition of the gas in the LOFT fuel rods is similar to that of a PWR fuel rod; consequently, these comparisons provide evidence that the gap conductivity model is working properly.

The LOFT fuel rods were not highly pressurized. Therefore, the cladding did not deform significantly. Two National Research Universal (NRU) reflood tests were simulated to examine the gap conductance predictive capability of the code with deformed cladding. NRU test MT-3.06 used pressurized nuclear fuel rods, while test PTH-110 used unpressurized rods. These simulations are described in Sections 22-1-3 through 22-1-7 of WCAP-12945-P-A (Bajorek, et al., 1998).

c) Cladding Swelling and Burst

NRU test MT-3.06 is used to assess the models in WCOBRA/TRAC for cladding swell and burst. This test and the WCOBRA/TRAC simulation are described in Sections 22-1-3 through 22-1-6 of WCAP-12945-P-A.

d) Cladding Rewet

The cladding rewet model in WCOBRA/TRAC consists of two parts: the heat transfer coefficient model, described in Section 6-2-6 of this document, and the axial conduction model, described in Section 7-3-1 of this document. These combined models are extensively assessed in WCAP-12945-P-A, Volume II (Bajorek, et al., 1998b), and in the integral tests in Section 14 (Bajorek, et al., 1998a).

e) Cladding Reaction

The cladding reaction model in WCOBRA/TRAC is described in Section 7-5 of this document. Few tests other than those laboratory experiments used to derive the reaction rate formula are available for verification of this quantity. A few tests early in the FLECHT program were performed with zircaloy cladding. However, the contribution to cladding heatup resulting from the reaction could not be identified. The NRU tests did not reach cladding temperature high enough to cause the reaction rate to become significant. Therefore, the reaction rate equations are based directly on the oxidation test results reported in ORNL/NUREG-17 (Cathcart, et al., 1977) and WCAP-12610 (Burman, 1990).

f) Residual Fission and Decay Heat

The reactor kinetics and decay heat model are described in Section 8 of this document. This model was used in a manner analogous to the approach in the PWR, using values of the moderator temperature coefficient and initial boron concentration existing in the LOFT facility at the time of the experiment. The resulting predicted core power is compared with measured values in Section 14-1 of WCAP-12945-P-A and shows that the model adequately predicts residual power.

22-1-3 NRU Test Description

The NRU reactor at the Chalk River Nuclear Laboratories in Canada was used to conduct a series of experimental tests to investigate the thermal-hydraulic and mechanical deformation behavior of nuclear rods in a LOCA. The test bundles were made of full-length, 3-percent enriched, 17x17 fuel rods powered by low level nuclear fission to simulate decay heat. Two NRU tests were modelled and simulated with WCOBRA/TRAC: test PTH-110, which was primarily a thermal-hydraulic test, and test MT-3.06, which was a mechanical deformation test. The PTH-110 test is described in NUREG/CR-1882 (Mohr, et al., 1981) and the MT-3.06 test in NUREG/CR-2528 (Mohr, et al., 1983).

22-1-4 NRU Test Bundle Description

The NRU test train was approximately 30 feet long and consisted of six major sections: the inlet region, the test bundle, the shroud, the outlet region, the hanger, and the closure head. The entire test train was inside a pressure tube inside the NRU reactor. The closure region provided the pressure boundary between the test train and the NRU pressure tube. Figure 22-1-1 shows a configuration of the NRU test train and the NRU pressure tube. The hanger tube suspended the test bundle and shroud from the closure head. The 14-foot stainless steel shroud, constructed from two halves clamped together at 7-inch intervals, supported the test bundle.

The PTH-110 fuel bundle consisted of a 6x6 segment of a 17x17 PWR assembly with the four corner rods removed for easier insertion in the shroud. Figure 22-1-2 shows a cross section of the PTH-110 test section. The outer ring of 16 rods plus the corner rods of the next inner ring served as guard rod heaters during the tests. The central 11 rods with the instrument thimble (inside the dotted line in Figure 22-1-2), arranged in a cruciform pattern, were the test rods of interest. The nuclear fuel rods had a cladding outside diameter of 0.379 inches and a pellet diameter of 0.325 inches. The rod-to-rod pitch was 0.502 inches, and the chopped cosine power profile had a peak power of 0.55 kW/ft at the 6-foot elevation. None of the rods in test PTH-110 were prepressurized.

The MT-3.06 fuel bundle also consisted of a 6x6 segment of a 17x17 assembly with the four corner rods removed. In MT-3.06, however, the instrument tube was replaced by a fuel rod. Thus, the cross section of the MT-3.06 test section is the same as that shown in Figure 22-1-2 with a fuel rod in place of the instrument tube. In addition, the 12 central rods in the MT-3.06 bundle (inside the dotted line in Figure 22-1-2) were pressurized to 550 psia. All 12 of these rods ruptured during test MT-3.06.

Horizontal movement and/or bowing was restricted by seven typical PWR grid spacers at 21-inch intervals, starting at the beginning of the heated length. The shroud was insulated on the outer surface to reduce the amount of heat loss to the environment.

The experimental test conditions were obtained in two steps: a steady-state phase and a transient phase. During the steady-state phase, the rod power was slowly increased to the desired value for the particular test while the dry steam coolant flowrate was decreased to produce a peak cladding temperature of 800°F. The steady-state conditions were maintained at these values until the thermocouple readings stabilized. The transient phase was then initiated. The steam coolant flow was stopped as quickly as possible; then reflood was started at the desired flowrate. The time period between steam shutoff and reflood initiation was an adiabatic heatup period, which continued until the specified maximum peak cladding temperature was reached.

22-1-5 WCOBRA/TRAC Model of NRU

The NRU rod bundle is modelled using the VESSEL component. Boundary conditions are applied to the top and bottom VESSEL cells. The PIPE and zero-velocity FILL components are attached to the VESSEL solely to fulfill the requirement that the model contain at least one one-dimensional component. Figure 22-1-3 shows the WCOBRA/TRAC noding diagram of NRU which was used for the MOD7A analysis.

The VESSEL component is composed of four channels. Two channels are used to model the rod bundle section: channel 2 for the inner region of the bundle, with a cross-sectional flow area of 1.67 square inches, and channel 3 for the outer region, which includes the shroud wall with a cross-sectional flow area of 3.912 square inches. Channels 1 and 4 are used to represent entrance and exit regions, respectively. The axial lengths are shown in Figure 22-1-3 and are typically 10.5 inches.

For the simulation of test MT-3.06, the inner region modelled by channel 2 contains 11 test rods and an instrument tube. The test rods are represented by rod 1. For the simulation of test PTH-110, rod 1 represents the 12 interior test rods. The 20 guard rods in the outer region are modelled by rod 2 for both test simulations. Both rods are given the WCOBRA/TRAC default material properties of UO_2 fuel and Zircaloy-4 cladding. The shroud wall is modelled as an unpowered conductor with a tube geometry connected to channel 3.

The initial temperatures for the rods and the shroud were determined from the thermocouple measurements for each test. The cold gap size between the fuel pellet and the cladding was based on the initial undeformed dimensions. In the initialization and during the transient simulations, the WCOBRA/TRAC dynamic gap conductance model was used to predict the effective heat transfer coefficient across the fuel pellet-clad gap.

22-1-6 Simulation of NRU Test MT-3.06

Test MT-3.06 was simulated for the first 310 seconds of the transient using WCOBRA/TRAC-MOD7A. The flowrate into the bundle and the fluid temperature are shown in Figure 22-1-4. The initial flowrate was approximately 0.42 lbm/s, which decreased steadily after 50 seconds to a rate of just less than 0.1 lbm/s for the remainder of the transient.

The predicted and measured inner cladding temperatures at NRU level 15 are compared in Figure 22-1-5 for the inner rods (rod 1) and in Figure 22-1-6 for the guard rods (rod 2). This elevation was 97.3 inches from the bottom of the active fuel.

The predicted temperatures for the inner rods track the data for about the first 40 seconds of the transient; then they drop below the data. This point in time corresponds to the first sharp reduction in flooding rate (Figure 22-1-4) and reflects the resulting increase in entrainment. The predicted temperatures for the outer guard rods, which are at a higher average power, track the data for about 120 seconds before dropping below the data as the flooding rate is reduced to the minimum.

At NRU level 17, the predicted inner cladding temperatures exceed the data after about 140 seconds for the inner rods and after about 80 seconds for the guard rods. These comparisons are shown in Figures 22-1-7 and 22-1-8, respectively. At NRU level 18, which was located near the bundle exit (139.3 inches above the bottom of the active fuel), the predicted inner cladding temperature for the guard rods exceeds the data after about 50 seconds, as shown in Figure 22-1-9.

Comparisons of predicted and measured pellet centerline temperatures are shown in Figure 22-1-10 for the guard rod at level 15 and in Figure 22-1-11 for the inner rod at Level 17. These comparisons show the same general trends as the corresponding inner cladding temperatures, indicating that the gap conductance and fuel conductivity are reasonably predicted.

[

]a,c

Cladding deformation and burst information predicted by WCOBRA/TRAC are compared with the experimental data in Table 22-1-1. The information provided under the "Data" column is the averages of the data provided in Tables 6 and 7 of NUREG/CR-2528 (Mohr, et al., 1983). The burst times, temperatures, and strains predicted by MOD7A are in good agreement. The burst elevations require some additional discussion, which follows.

WCOBRA/TRAC predicts rupture of Zircaloy-4 cladding as a function of heatup rate and engineering hoop stress, as described in Section 7-4-1 of this document. This typically results in the burst elevation coinciding with the heat transfer node with the highest temperature at the time of rupture. This was true in the NRU MT-3.06 simulation. [

]^{a,c}

Figure 22-1-13 shows a comparison of the predicted rod 1 internal pressure to the measured plenum pressure of rod 2C. [

]^{a,c}

The pressure increase at 110 seconds in Figure 22-1-13 is due to heatup of the fuel above the quench front and dryout of the cladding at the top of the fuel rod. The MT-3.06 test used a variable (decreasing) flooding rate, which resulted in stagnation of the quench front. The resulting heatup of the gas in the pellet-cladding gap, the fuel stack, and the plenum lead to the calculated pressure increase.

The early underprediction of the rod pressure transient in Figure 22-1-13 raised questions whether a tendency exists to not calculate burst and blockage in a PWR transient, when burst realistically should occur. To resolve this issue, Westinghouse committed to increasing the hot assembly rod initial pressure until burst and blockage are achieved if the nominal calculation results in a hot assembly rod reflood PCT greater than 1600°F without burst. In these unlikely cases, the most limiting of the burst and nonburst cases will be used as input to the uncertainty evaluation.

22-1-7 Simulation of NRU Test PTH-110

Test PTH-110 was simulated using WCOBRA/TRAC-MOD7A. The inlet temperature transient used in the simulation was taken from the data report and is shown in Figure 22-1-14. The inlet flowrate was set to the nominal value of 1.9 in/s, based on Table 2 of NUREG/CR-1882 (Mohr, et al., 1981). Initial rod temperature data were reported at levels 13, 15, and 17 only for PTH-110. The initial temperature distribution in the lower regions of the bundle were, therefore, estimated using the more detailed initial distributions measured in the MT-3.06 tests.

Figures 22-1-15 through 22-1-17 compare the predicted and measured inner cladding temperatures at levels 17 and 18. Figures 22-1-18 and 22-1-19 compare the predicted and measured pellet centerline temperatures for the inner and guard rods, respectively. Each of these comparisons shows reasonable agreement with the data.

22-1-8 Summary and Conclusions

Simulations of LOFT and NRU were made using WCOBRA/TRAC to validate the nuclear rod models. Predictions of cladding temperatures in LOFT were in good agreement with the data as were the predictions of cladding and pellet temperatures in NRU test PTH-110. The simulation of NRU test MT-3.06 showed a tendency to [ ]^{a,c}. Even so, the simulation showed reasonable agreement with the test data for rupture and blockage. The underprediction of the measured rod pressure transient early in MT-3.06 raised questions regarding whether a tendency exists to not calculate burst and blockage in a PWR transient when burst realistically should occur. To resolve this issue, Westinghouse committed to increasing the hot assembly rod initial pressure until burst and blockage are achieved if a WCOBRA/TRAC calculation results in a hot assembly rod reflood PCT greater than 1600°F without burst. In these unlikely cases, the most limiting of the burst and nonburst cases will be used as input to the uncertainty evaluation.

Table 22-1-1

NRU Test MT-3.06 Rod Failure Data Comparison

Parameter	WCOBRA/TRAC	Data	Range
Burst time (s)	135.0	133.0	109 – 182
Burst elevation (in.)	113.1	104.3	102 – 106
Burst temperature (°F)	1456.0	1463.0	1430 – 1500
Burst strain	0.568	0.586	0.522 – 0.736

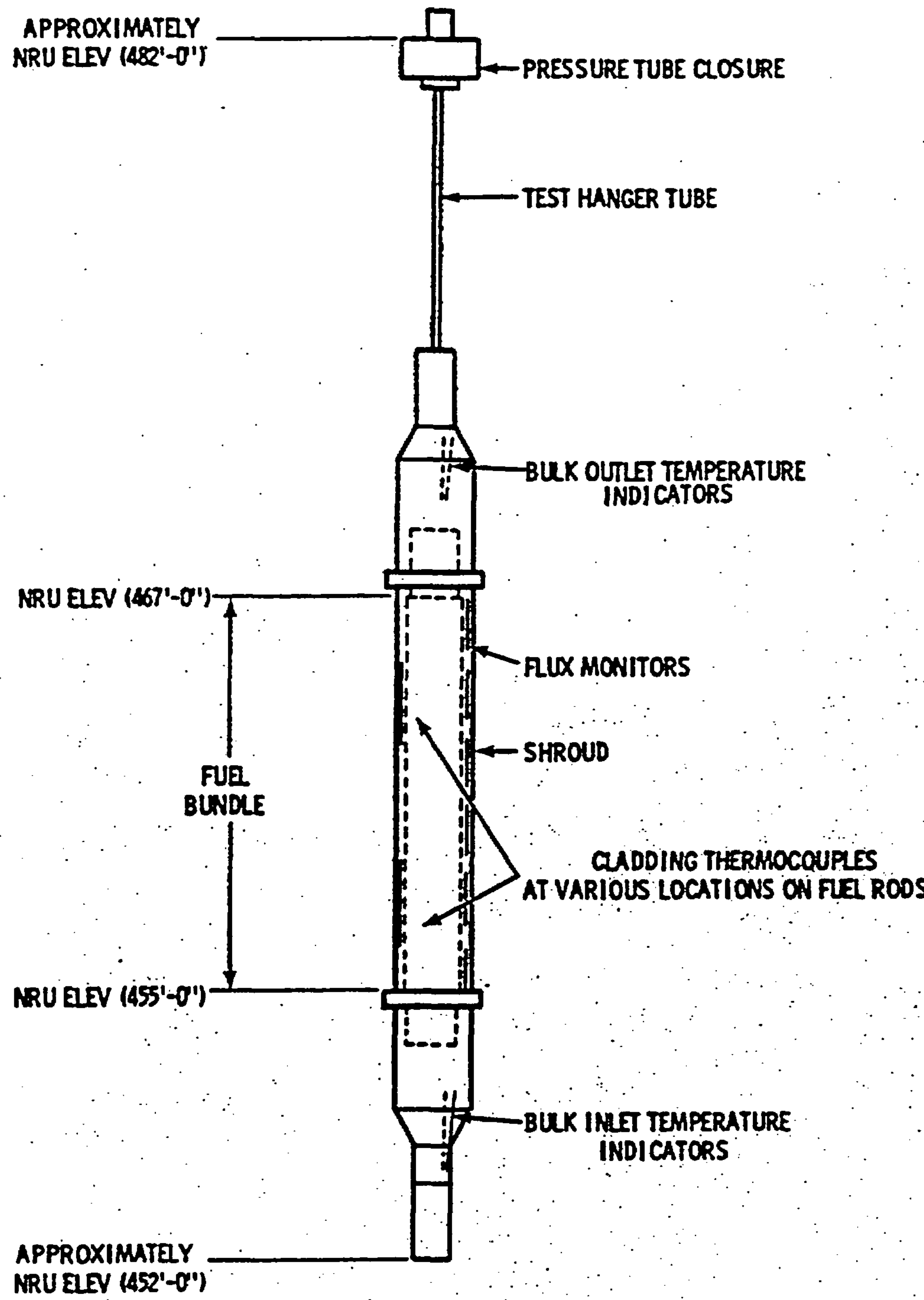

Figure 22-1-1. Vertical Test Train Configuration for NRU Reflood Experiments

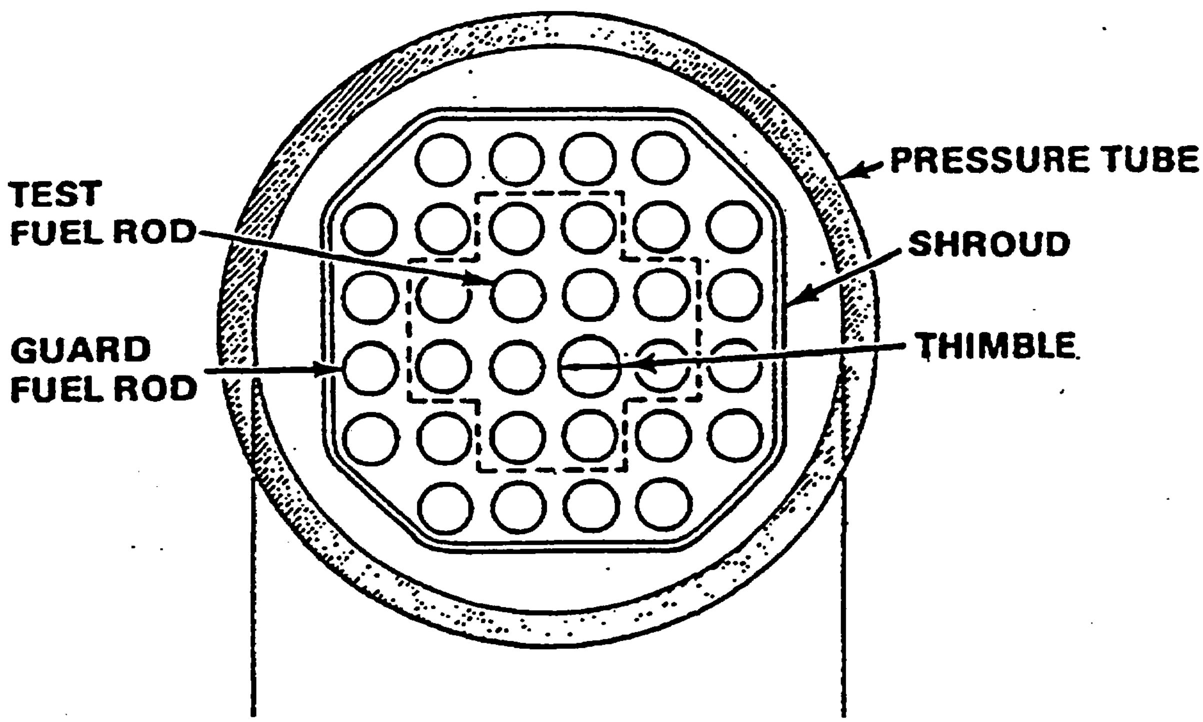

Figure 22-1-2. NRU Test Bundle Cross Section (Test PTH-110 Bundle Shown)

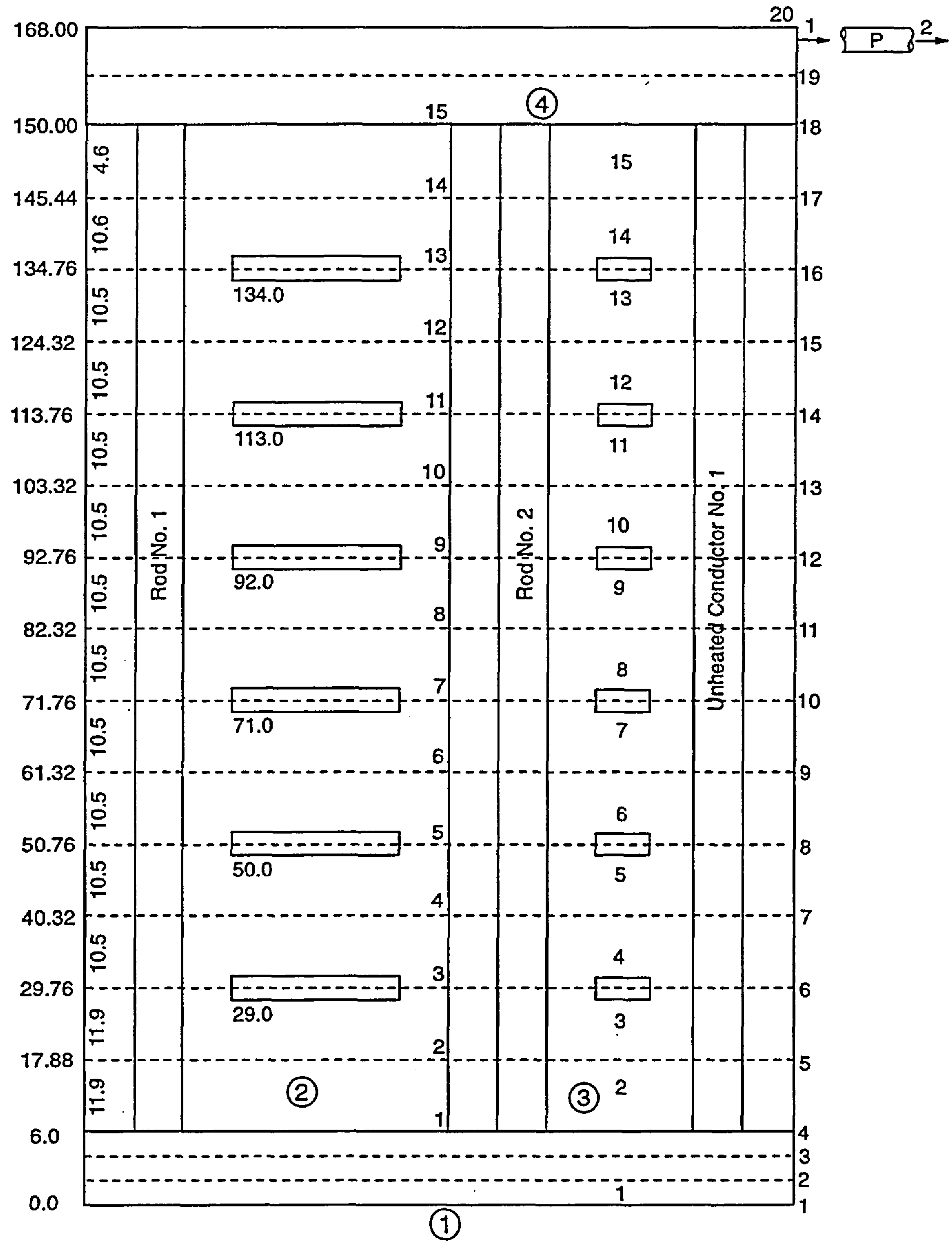

Figure 22-1-3. WCOBRA/TRAC Model of NRU

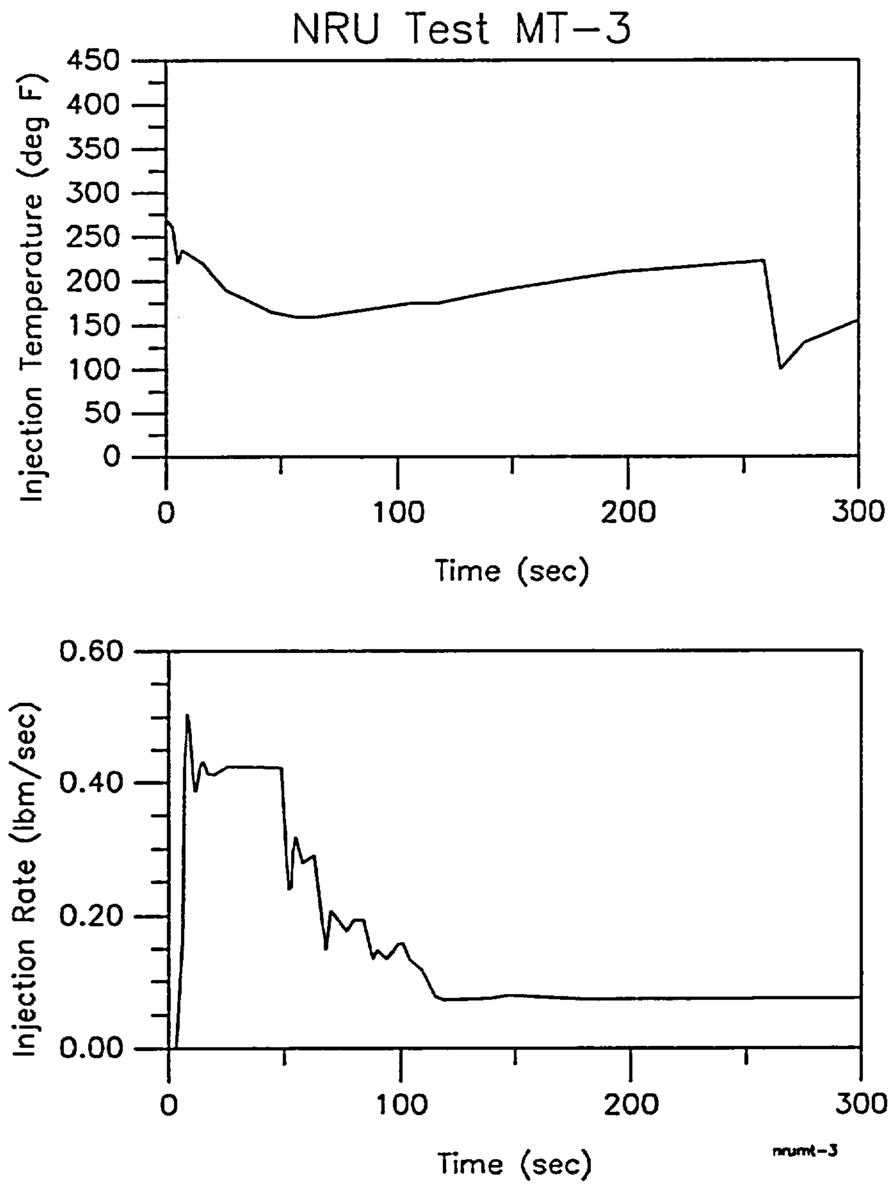

Figure 22-1-4. NRU Test MT-3.06 Injection Flowrate

a,c

Figure 22-1-5. Comparison of Rod 1 Predicted and Measured Inner Cladding Temperatures at Level 15 for NRU Test MT-3.06

a,c

Figure 22-1-6. Comparison of Rod 2 Predicted and Measured Inner Cladding Temperatures at Level 15 for NRU Test MT-3.06

a,c

Figure 22-1-7. Comparison of Rod 1 Predicted and Measured Inner Cladding Temperatures at Level 17 for NRU Test MT-3.06

a,c

Figure 22-1-8. Comparison of Rod 2 Predicted and Measured Inner Cladding Temperatures at Level 17 for NRU Test MT-3.06

a,c

Figure 22-1-9. Comparison of Rod 2 Predicted and Measured Inner Cladding Temperatures at Level 18 for NRU Test MT-3.06

a,c

Figure 22-1-10. Comparison of Rod 2 Predicted and Measured Pellet Temperatures at Level 15 for NRU Test MT-3.06

a,c

Figure 22-1-11. Comparison of Rod 1 Predicted and Measured Pellet Temperatures at Level 17 for NRU Test MT-3.06

a,c

Figure 22-1-12. Comparison of WCOBRA/TRAC Predicted Quench Front Elevations with MT-3.06 Data from NUREG/CR-2528

a,c

Figure 22-1-13. Comparison of Rod 1 Internal Pressure to the Measured Plenum Pressure of NRU Rod 2C for NRU Test MT-3.06

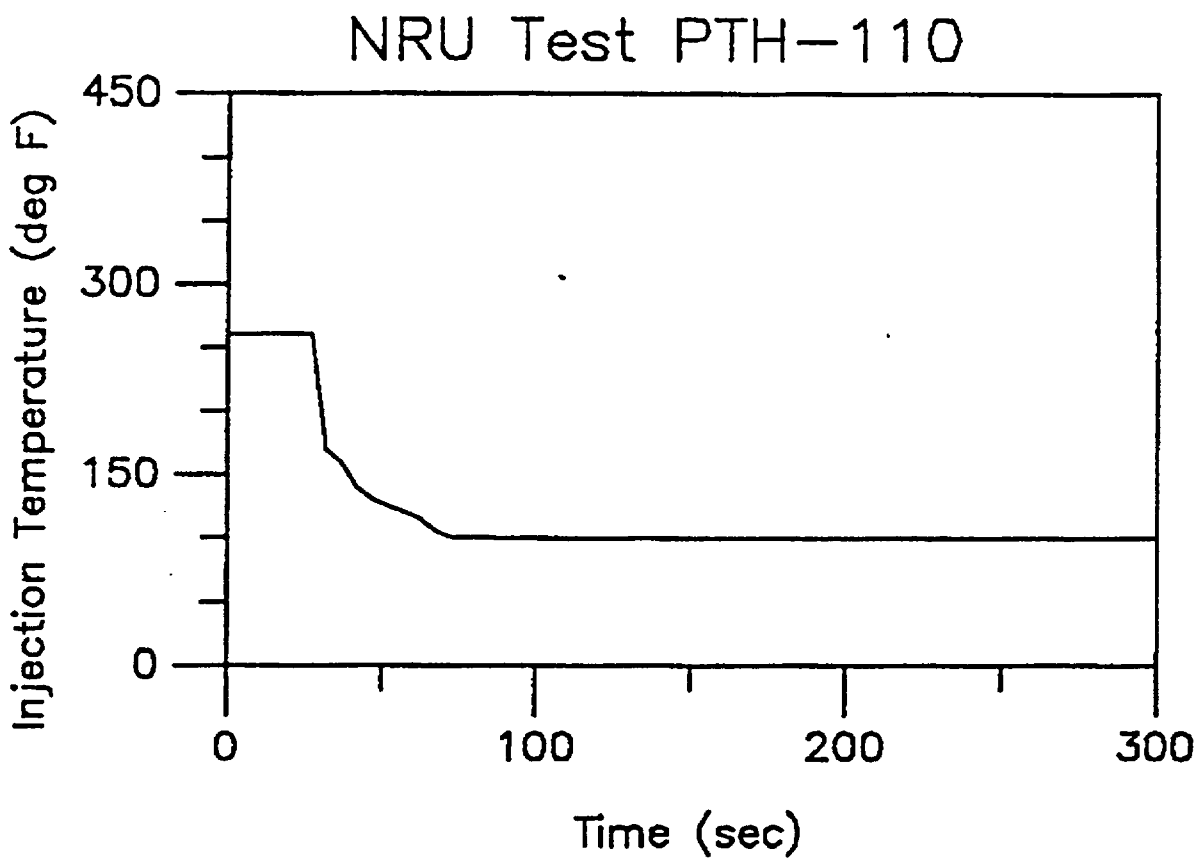

Figure 22-1-14. NRU Test PTH-110 Injection Temperature

a,c

Figure 22-1-15. Comparison of Rod 1 Predicted and Measured Inner Cladding Temperatures at Level 17 for NRU Test PTH-110

a,c

Figure 22-1-16. Comparison of Rod 2 Predicted and Measured Inner Cladding Temperatures at Level 17 for NRU Test PTH-110

a,c

Figure 22-1-17. Comparison of Rod 1 Predicted and Measured Inner Cladding Temperatures at Level 18 for NRU Test PTH-110

a,c

Figure 22-1-18. Comparison of Rod 1 Predicted and Measured Pellet Temperatures at Level 17 for NRU Test PTH-110

a,c

Figure 22-1-19. **Comparison of Rod 2 Predicted and Measured Pellet Temperatures at Level 17 for NRU Test PTH-110**

22-2 Accumulator Component

22-2-1 Introduction

The accumulator component model is described in Volume 1, Section 9-8, of this document. Section 9-8 also describes the phases of accumulator water injection, emptying, and accumulator nitrogen discharge. In verifying the application of the model to the PWR, WCOBRA/TRAC calculations were performed and the results were compared to available separate effects accumulator test data. In addition, nitrogen discharge effects were assessed.

22-2-2 Indian Point Unit 2 Accumulator Test

An accumulator blowdown test was performed at Indian Point Unit 2 in 1971 during startup testing. The initial gas pressure in the accumulator was about 100 psig, the gas volume was about 400 cubic feet, and the water volume was 700 cubic feet. Test runs were performed at ambient temperature (80°F) with an RCS back pressure of 0 psig. The cold legs were empty, and the water level in the vessel was well below the cold leg nozzle elevation. The control valves used to initiate the test runs were set to open from 0 to 100 percent in 10 seconds. Test runs were performed for the four accumulators that had various accumulator line lengths. The test runs would terminate when the pressure in the accumulator reached approximately 20 psig while the accumulator line was still in single-phase liquid flow. The measured pressure responses of the four accumulators were all similar. Pressure response for one of the accumulators was selected for WCOBRA/TRAC model verification. Figure 22-2-1 shows the layout of the accumulator piping.

22-2-3 WCOBRA/TRAC Model

A WCOBRA/TRAC model was constructed to simulate the accumulator test. A typical PWR model of the accumulator and its piping consists of up to four WCOBRA/TRAC model components: an accumulator, one or two valves, and a pipe, as shown in Figure 22-2-2. In this model, the RCS is simulated by a BREAK component, supplying a constant back pressure. The volume, height, length, and hydraulic diameter for the accumulator and the accumulator line are all preserved. The various levels and elevation changes in the actual line are simplified to some extent as shown by the dotted lines in Figure 22-2-1. The line resistance in the accumulator line is simulated in two ways: using the WCOBRA/TRAC built-in friction model (NFF = 4) and using the hydraulic resistance (fL/D) value obtained from measurement and uniformly distributed over the pipe length. Little difference is observed in the two approaches. The initial and boundary conditions are the same as those used in the 1971 Indian Point Unit 2 test. A steady-state run of 20 seconds was first performed, followed by a blowdown run initiated by opening a control valve in the accumulator line. The valve reached 100-percent opening within the first 10 seconds of the blowdown run.

The accumulator pressure predicted by WCOBRA/TRAC is compared to measured test data (the only data available) in Figure 22-2-3. WCOBRA/TRAC predicts a [

]^{a,c}.

22-2-4 WCOBRA/TRAC Model With PWR Line Noding

Although the accumulators are of the same design for all loops, the lines connecting the accumulator and the cold leg may vary from loop to loop. In the WCOBRA/TRAC PWR plant model, the accumulator and the connecting line in all loops are [

]^{a,c}.

22-2-5 Nitrogen Model Switching and Accumulator Noding

WCOBRA/TRAC calculates the accumulator blowdown before and after the accumulator becomes empty. With this continuous blowdown model, the accumulator will switch from the normal nitrogen model to the subcooled vapor model when the [

]^{a,c}.

The model described above predicts the behavior shown in Figure 22-2-9 for the Indian Point Unit 2 test. Nitrogen fills the pipe from the accumulator end, and a two-phase mixture appears at the pipe end at 100 seconds.

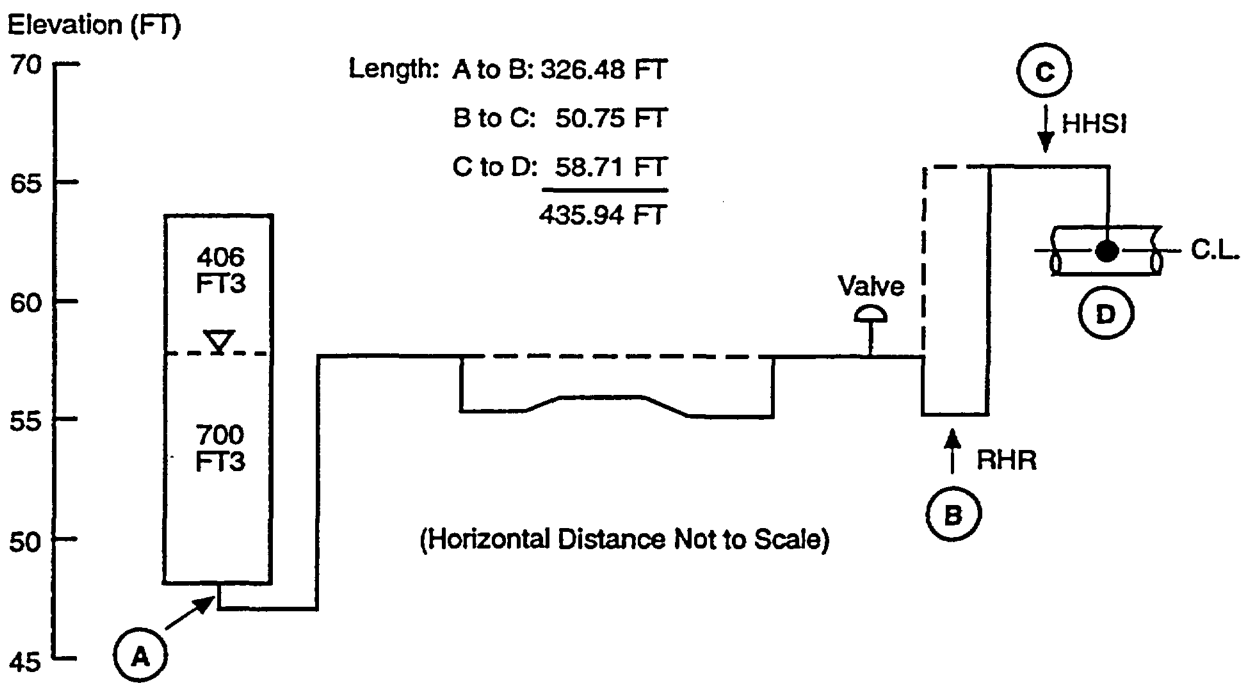

Figure 22-2-1. Indian Point Unit 2 Loop 21 Accumulator Line Schematic Diagram

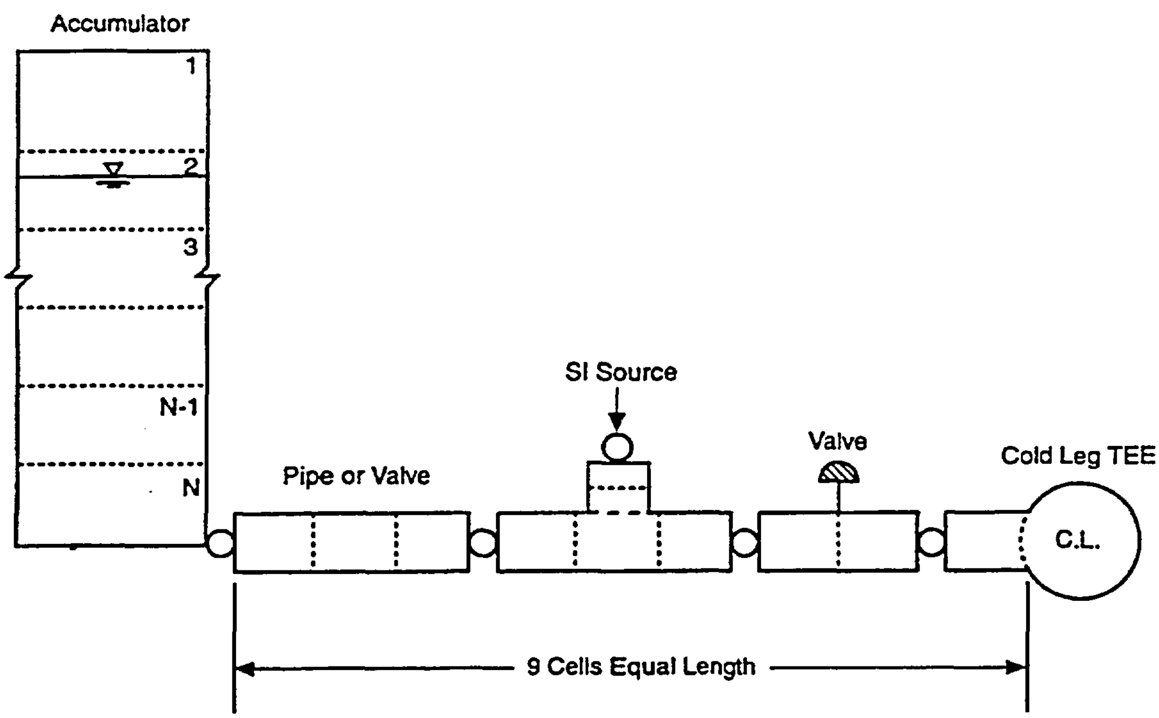

Figure 22-2-2. WCOBRA/TRAC Model of Accumulator and Safety Injection Line in a PWR

a,c

Figure 22-2-3. Predicted Accumulator Pressure (Solid Line) Compared With Measured Test Data (Dashed Line)

a,c

Figure 22-2-4. Predicted Accumulator Flowrate

a,c

Figure 22-2-5. Predicted Gas Temperature at Top of Accumulator

a,c

Figure 22-2-6. **Comparison of Predicted Pressure/Volume Relationship With Adiabatic Assumptions**

a,c

Figure 22-2-7. Comparison of Detailed Noding With Simplified PWR Noding Prediction of Accumulator Pressure

a,c

Figure 22-2-8. Basis for Transition from Water to Nitrogen Flow From Accumulator (Andreychek, et al., 1988)

a,c

Figure 22-2-9. Predicted Void Fraction at Accumulator Line Exit

22-3 Pump Component Model

The pump component model is described in Volume 1, Section 9-4, of this document. It is an empirical model in which the pressure differential generated by the pump, and the corresponding torque applied to the pump during single- and two-phase flow, is derived from single- and two-phase flow data in scaled pumps. In particular, the pump head and torque during two-phase flow is assumed to vary as a function of void fraction from the single-phase value to a "fully degraded" or minimum value which occurs at intermediate void fractions. For the pump head:

$$H = H_1 + M(\alpha) * (H_2 - H_1) \tag{22-3-1}$$

where:

H = pump head
H_1 = single-phase pump head
H_2 = fully degraded pump head
$M(\alpha)$ = two-phase multiplier

A similar equation is used for the pump torque (Equation 9-8 from Section 9-4) with the multiplier defined as $N(\alpha)$.

This is clearly an approximate description of the actual variation of the pump head. As described in NUREG/CR-5249 (Rohatgi, et al., 1989), the uncertainty associated with such a model is relatively large and needs to be considered in the code uncertainty. This section describes the basis for the empirical model used in the LOCA analysis of the PWR, establishes the basis for its uncertainty, and relates it to the pump model used in LOFT. Comparisons with LOFT data of the predicted pump head then serve as validation that the empirical model adequately predicts pump head for both LOFT and a PWR.

22-3-1 Westinghouse Pump Data

The Westinghouse pump model is based on the air and water data obtained from a scale model of a 93A model pump, designed to operate at a pump head of 92.6 feet, a flow of 7420 gpm, and an impeller speed of 1799 rpm. Figure 22-3-1 shows a scale model used to obtain single- and two-phase data. The model is designed to be geometrically similar to a full-scale Westinghouse model 93A pump with an equivalent specific speed. The specific speed of a centrifugal pump is defined as:

$$N_s = N\,Q^{1/2}/H^{3/4} \tag{22-3-2}$$

where:

N is in rpm
Q is in gpm
H is in feet of water

Specific speed is a convenient parameter in distinguishing the performance characteristics of different pumps. The specific speeds of Westinghouse pumps range from 5000 to 7000 rpm. In contrast, the specific speed of the LOFT pumps is 3300 rpm.

23-3-1-1 Single-Phase Data

Figures 22-3-2 and 22-3-3 show some of the test data used to determine the single-phase homologous curves for forward and reverse flow through the pump. The data consist of water data from the scale model of the 93A pump, as well as air data from the same scale model and test facility where two-phase data were obtained (Howland and Lamers, 1973). The air and water data agree well, indicating that the change in test fluid and test facility had little effect on the test results.

The uncertainty of the single-phase data was determined by evaluating two data sources. The first source was from the Westinghouse single-phase data cited above. A band can be drawn about the data in Figure 22-3-3 (the normalized head data are plotted against the inverse of the normalized flow in this figure). [

]a,c

The second source examined was from data developed by Cudlin (Cudlin, 1977). The normalized head in the forward flow, dissipative quadrant for a 1/3-scale model pump is shown in Figure 22-3-4. [ ]a,c

23-3-1-2 Two-Phase Data

The two-phase data were obtained by running air-water mixtures through the pump (Howland and Muench, 1975). The test facility is illustrated in Figure 22-3-5. Water was drawn from a large basin using a diesel-powered pump, mixed with air in a mixing chamber, and pushed through the scale model pump. Inlet line venturi meters and orifices were used to measure inlet flowrates. Pump pressure differential, impeller speed, and impeller torque were also measured. The inlet void fraction was not measured but was inferred from the flowrates. A correlation was used to estimate the void fraction from the flowrates. In addition, a homogeneous void fraction was used. The basic nature of the data was not affected by the choice of void fraction. In the following discussion, the homogeneous (zero slip) void fraction is used.

Typically, homologous head data are plotted using two x-axes: normalized flow divided by normalized speed (Figure 22-3-2), and normalized speed divided by normalized flow (Figure 22-3-3). An alternative way to plot the head data is as a function of normalized head divided by normalized speed squared, versus normalized flow divided by normalized speed, for all forward flow conditions. This results in the data in Figure 22-3-6, which more clearly shows the transition, as flow increases from a positive head or pumping mode, to a negative head or energy dissipation mode. As seen in Section 25-3 of WCAP-12945-P-A (Bajorek, et al., 1998), the intact loop pumps are operating in the pumping mode during the initial stages of a cold leg break LOCA, while the broken loop pump is operating in an energy dissipation mode during the entire transient. The two-phase data are also shown on this figure and indicate that the pumping mode data shows relatively little scatter, while the dissipation mode data show more scatter. The increased scatter may be due to the fact that when the downstream pressure is lower, the upstream conditions are no longer as accurate a representation of conditions within the pump. Also plotted on this figure are the single-phase head curve and a fully degraded head curve drawn through the lower bound data.

The method for determining the two-phase multiplier $M(\alpha)$ and $N(\alpha)$ in Equations 9-7 and 9-8 (in Section 9 of this document) from the pump data is as follows:

1. Determine single-phase homologous head and torque. The pressure difference across the pump and the torque applied to the pump impeller are measured under a variety of flow conditions. Homologous head and torque curves are derived by dividing these data by the appropriate quantities (rated flow, rated speed, and the like). Each pump model (designated 93, 93A, 100, and so on) designed by

Westinghouse has a set of homologous curves derived from scale model single-phase tests using both air and water.

2. Measure the pump pressure difference and torque under two-phase conditions over a range of void fractions. The lower boundary of the data, when converted to homologous form, is defined as the "fully degraded" homologous head and torque. These data were obtained from a 1/3-scale model pump with the same specific speed as the model 93A pump. The pump head data are shown in Figure 22-3-7, and the pump torque data in Figure 22-3-8. The single-phase and "fully degraded" curves constructed from these data are also shown in Figure 22-3-8 and Figures 9-4 to 9-7 in Volume 1, Section 9, of this document. The fully degraded curves are always drawn below the single-phase curves and bound nearly all the data.

   The two-phase data indicate that the amount of full degradation in head or torque is approximately a constant. That is, the fully degraded curve is offset from the single-phase curve by a constant. This is more easily seen in Figure 22-3-6. This observation allows the fully degraded curve to be extended into areas where data are sparse or lacking.

3. Assume that the homologous head and torque go from single-phase to fully degraded, back to single-phase values, as the pump inlet void fraction ranges from 0 to 1.0. Use Equation 22-3-1 in the following form to calculate $M(\alpha_i)$ for each pump head data point:

$$M(\alpha_i) = \frac{H(\alpha_i) - H(single\text{-}phase)}{H(degraded) - H(single\text{-}phase)}$$

   Use the $M(\alpha_i)$ data to define the appropriate shape of the $M(\alpha)$ function, as in Figures 22-3-9 and 22-3-10. Figure 22-3-9 includes only the pumping mode data, while Figure 22-3-10 includes all the data. Perform a similar exercise for the pump torque (Figure 22-3-11).

Data are lacking for void fractions greater than 70 percent. [

]^{a,c} This assumption is supported by test data from other design pumps, for example, Figure 2.1 on page L-9 of the code scaling, applicability, and uncertainty (CSAU) report (Boyack, et al., 1989).

The simple form of the M(α) function results in considerable scatter in the data in the dissipative, or turbine mode of pump operation. The effect of this uncertainty was examined in the PWR scoping studies by defining a new multiplier drawn through the lower bound of the data. The multiplier resulted in a relatively small effect due to the relatively short time that the pump is in the fully degraded, low void fraction two-phase regime. This result is consistent with results obtained in the CSAU report.

Most studies of pump model uncertainties focus only on the two-phase characteristics. The Westinghouse methodology examines and accounts for the uncertainty present in the single-phase head curves as well as discussed in Section 25-3-2 of WCAP-12945-P-A (Bajorek, et al., 1998).

[

]^{a,c}

[

]a,c.

22-3-2 Pump Model Comparison to Data

The only test that contains a powered pump is the LOFT test. Although the pumps in LOFT are of a different design than PWR pumps, they exhibit similar overall performance as can be seen from Figure 22-3-12. The pump model used in the LOFT simulations, described in Section 14-1 of WCAP-12945-P-A (Bajorek, et al., 1998a), is the same as that used in the PWR, except that the homologous curves and the two-phase multiplier used were the LOFT specific curves obtained from tests on the Semiscale pump (Reeder, 1978). Another difference was that the pump speed was input from the LOFT data, rather than calculated. This was done to specifically examine the pump head prediction. The resulting prediction for LOFT test L2-5 is shown in Figure 14-1-38 (Bajorek, et al., 1998a). These comparisons show that the predicted pressure difference across the pumps in the intact loops compares well with the measured pressure difference during blowdown.

The comparisons indicate that the relatively simple pump model in WCOBRA/TRAC adequately predicts pump behavior during a LOCA. Because pump performance is not of high importance in a small break LOCA, and the pumps are tripped early in the event, uncertainty is not considered.

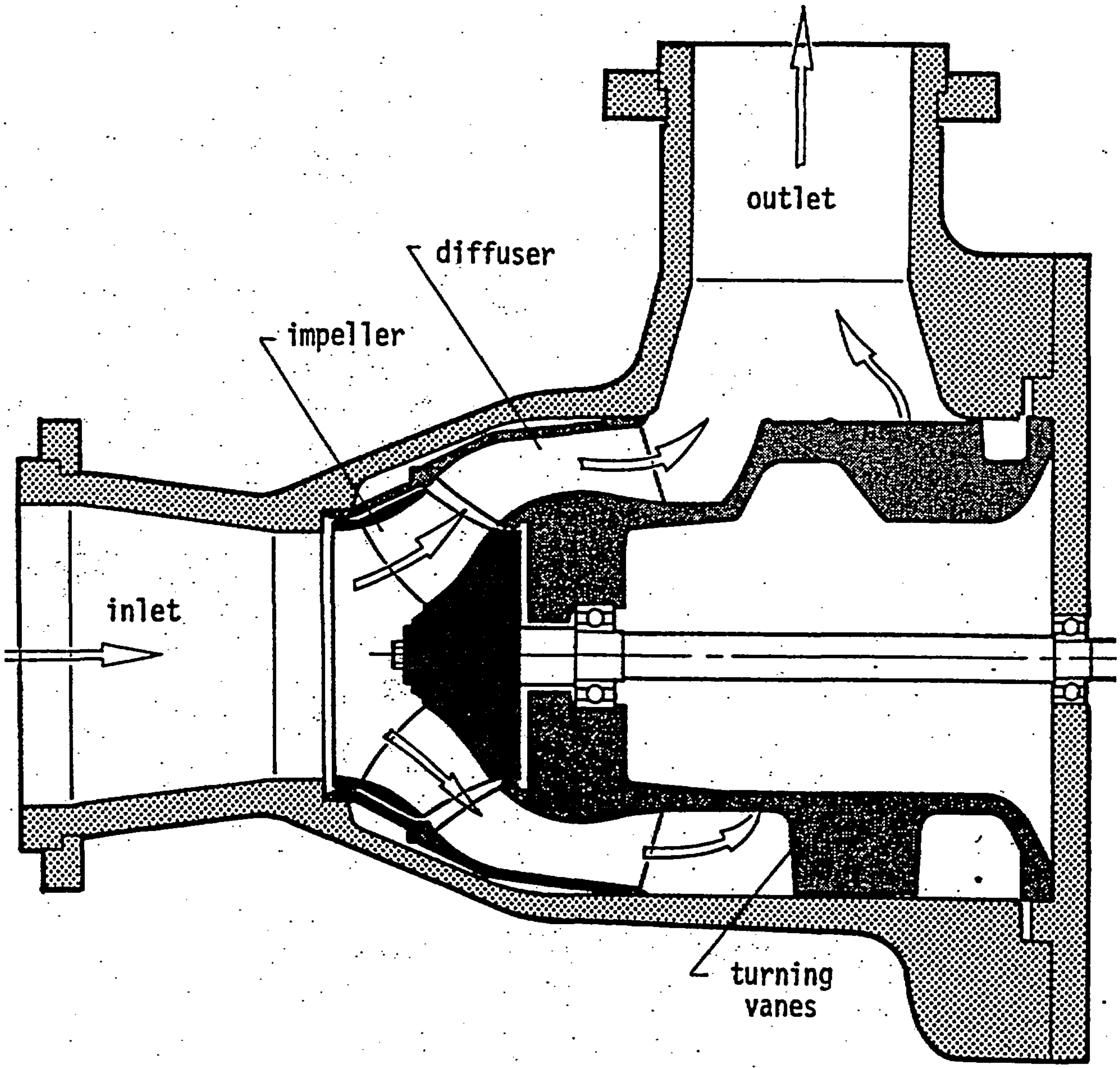

Figure 22-3-1. Cross-Sectional View of the Westinghouse Scale Model Pump

a,c

Figure 22-3-2. **Scale Model Homologous Head Single-Phase Data in the Pumping Mode, Forward and Reverse Flow**

a,c

Figure 22-3-3. Scale Model Homologous Head Single-Phase Data in the Dissipation Mode, Forward Flow

a,c

Figure 22-3-4. Data Scatter for Dissipative Mode 1/3-Scale Pump Data (Cudlin, 1977)

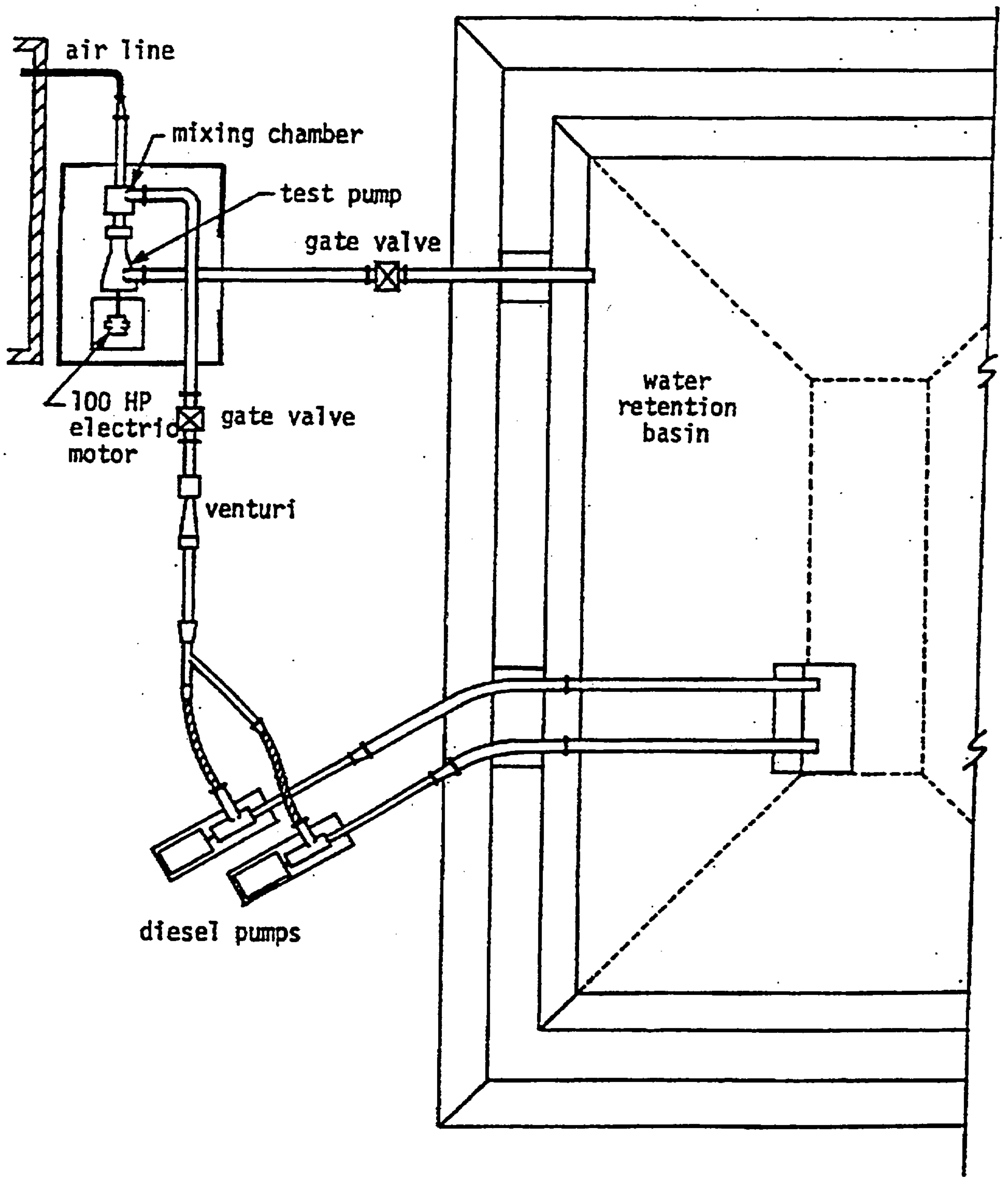

Figure 22-3-5. Schematic Diagram of the Air-Water Test Facility

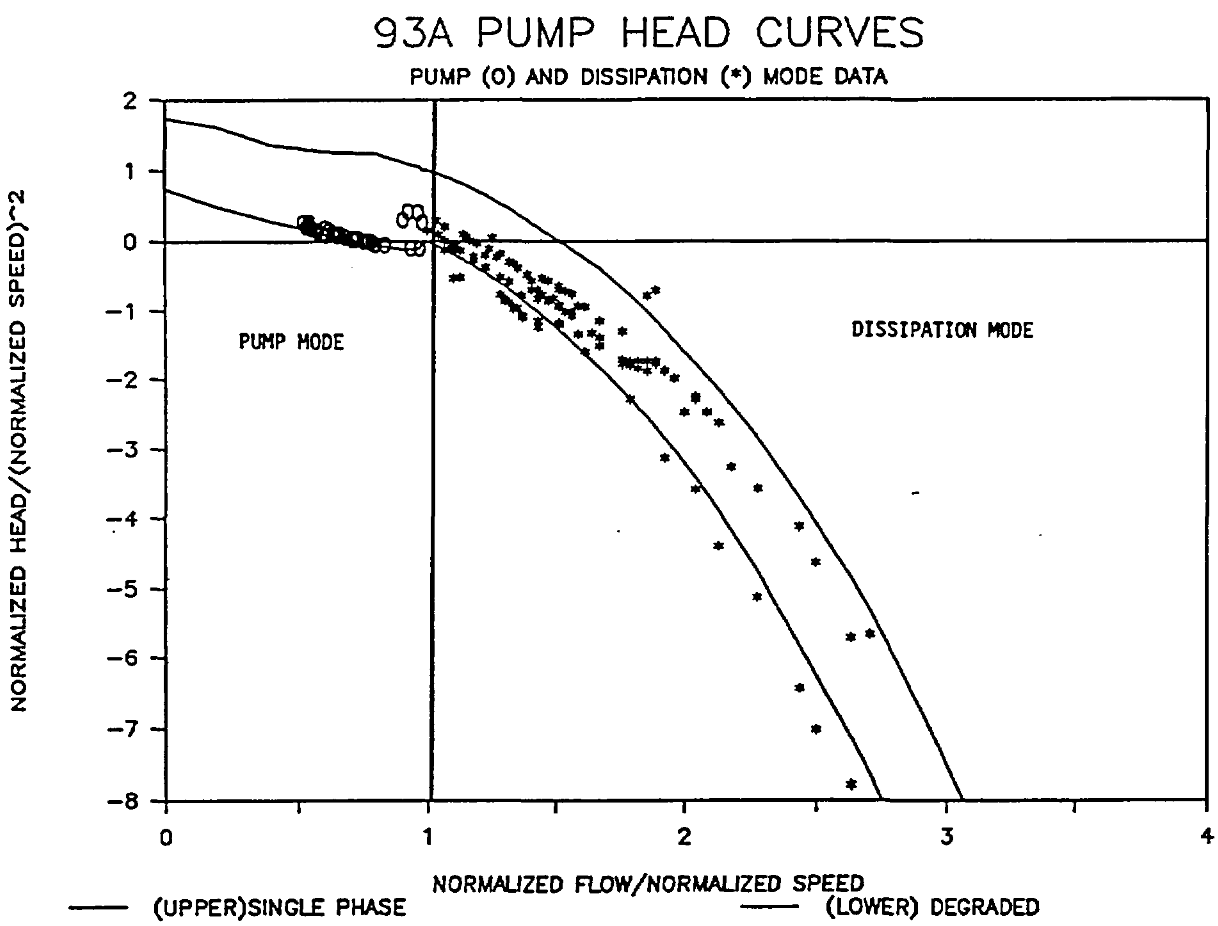

Figure 22-3-6. Homologous Head Curves and Westinghouse Air-Water Data

a,c

Figure 22-3-7. Single-Phase and Fully Degraded Pump Head Curves Compared With Two-Phase Data

a,c

Figure 22-3-8. Pump Single-Phase and Fully Degraded Torque Curves, Compared With Two-Phase Data

a,c

Figure 22-3-9. Two-Phase Multiplier and Pumping Mode Data

a,c

Figure 22-3-10. Two-Phase Multiplier and All Two-Phase Data

a,c

Figure 22-3-11. M(α) for Pump Torque (Referred to as N(α) in Equation 9-8 in This Document)

a,c

Figure 22-3-12. Westinghouse Pump Head Curves Compared With LOFT Pump Head Curves

22-4 References

Andreychek, T. A., et al., 1988, "Loss of RHRS Cooling While the RCS is Partially Filled," WCAP-11916.

Bajorek, S. M., et al., 1998, "Code Qualification Document for Best Estimate LOCA Analysis Volume V: Quantification of Uncertainty," WCAP-12945-P-A, Vol. 5.

Bajorek, S. M., et al., 1998a, "Code Qualification Document for Best Estimate LOCA Analysis Volume III: Hydrodynamics, Components and Integral Validation," WCAP-12945-P-A, Vol. 3.

Bajorek, S. M., et al., 1998b, "Code Qualification Document for Best Estimate LOCA Analysis Volume II: Heat Transfer Model Validation," WCAP-12945-P-A, Vol. 2.

Boyack, et al., 1989, "Quantifying Reactor Safety Margins," NUREG/CR-5249.

Burman, D. L., 1990, "ZIRLO™ High Temperature Oxidation Tests," WCAP-12610, Appendix E.

Cathcart, J. V., et al., 1977, "Zirconium Metal-Water Oxidation Kinetics IV - Reaction Rate Studies," ORNL/NUREG-17.

Cudlin, J. J., 1977, "1/3 Scale Air-Water Pump Program, Analytical Pump Performance Model," EPRI NP-160.

Howland, G. R. and Lamers, R. P., 1973, "Air Test Program to Establish the Complete Pump Characteristics of WEMD 93A Model Reactor Coolant Pump," Westinghouse Research Report 73-7E9-TAPSC-R1.

Howland, G. R. and Muench, R. A., 1975, "Air/Water Mixed Flow Testing of the WEMD 93A Model Reactor Coolant Pump," Westinghouse Research Report 75-7E9-CORCL-R1.

Mohr, C. L., et al., 1981, "Prototypic Thermal-Hydraulic Experiment in NRU to Simulate Loss-of-Coolant Accident," NUREG/CR-1882.

Mohr, C. L., et al., 1983, "LOCA Simulations in the National Research Universal Reactor Program" NUREG/CR-2528.

Reeder, D. L., 1978, "LOFT System and Test Description," NUREG/CR-0247.

Rohatgi, et al., 1989, "Quantifying Reactor Safety Margins," NUREG/CR-5249.

Weiner, R. A., et al., 1988, "Improved Fuel Performance Models for Westinghouse Fuel Design and Safety Evaluations," WCAP-10851-A (Proprietary), WCAP-11873-A (Non-Proprietary).

SECTION 23
CODE ASSESSMENT SUMMARY AND CONCLUSIONS

23-1 Introduction

Sections 12 through 22 in this volume provide comparisons of WCOBRA/TRAC-SB predictions to experimental test results involving small break LOCA processes. This section summarizes the code performance in simulating the separate and integral effects tests necessary to demonstrate that WCOBRA/TRAC-SB produces satisfactory results for small break LOCA processes. These simulations provide a consistent set of information that can be used to determine the bias and uncertainty for the WCOBRA/TRAC-SB computer code.

These test simulations also provide a comprehensive validation of the code capability. A wide range of test facilities and conditions was selected for simulation, not only to establish code applicability, but also to provide a means of isolating and assessing individual model and correlation packages. Tests in the assessment matrix were selected to validate the ability of the code to model the important phenomena that occur during a small break LOCA in a PWR.

At the beginning of the development effort, Westinghouse generated a small break LOCA PIRT (Section 1-4, Volume 1, of this document). To a great extent, the important processes identified by an independent expert panel were in agreement with the Westinghouse table. In fact, Westinghouse technical experts revised their original ranking process to coincide with the rankings assigned by the independent panel (Attachment A, Volume 1, of this document). This final PIRT will be used as a checklist to demonstrate that WCOBRA/TRAC-SB is capable of performing best-estimate small break LOCA analysis.

23-2 Separate Effects Test Simulations

The separate effects tests simulated provide insight into the capability of WCOBRA/TRAC-SB to predict high-ranked PIRT phenomena as discussed below.

Section 12 presents simulations of heat transfer experiments relevant to post-CHF core uncovery conditions using the WCOBRA/TRAC-SB heat transfer package. During small break LOCA events, this process is ranked high in the PIRT. A comparison between measured and predicted heat transfer coefficients is available in the Reynolds number regime of interest from the ORNL and INEL experiments. The minimum and maximum values of the multiplier to adjust the code-predicted coefficient to match the test value [

]a,c

Section 13 compares the WCOBRA/TRAC-SB break model predictions against data for a wide range of experimental critical flow geometries and conditions to validate the code for this highly ranked process. Uncertainty in the break flow model is accommodated in the uncertainty methodology by varying the break size to identify the limiting size in the plant break spectrum. [

]a,c.

Section 14 describes the implementation of the safety injection jet heat transfer correlation from the COSI experiment into WCOBRA/TRAC-SB. The agreement of the code prediction for this low-ranked process with COSI data is adequate.

In Section 15, the mixture level swell in the core (a high ranked PIRT item) is examined for the ORNL and G-1 facilities, with heater rod bundles, and the GE facility test vessel. The interfacial drag multiplier is adjusted to enable the predicted WCOBRA/TRAC-SB level swell to match the ORNL and G-1 experimental data, and the median YDRAG value to match the experimental data from both facilities is 0.78. This supports the use of YDRAG = 0.8 in the core in integral test simulations and the reference PWR studies. [

]a,c.

For the loop seal clearing period of the small break LOCA transient, the PIRT identifies a number of high-ranked processes. The capability of WCOBRA/TRAC-SB to predict loop seal clearance phenomena is established by simulating the full-scale UPTF test facility in Section 16. Overall, the code predicts the trends in behavior observed in the UPTF experiment.

Section 17 considers a number of phenomena pertinent to upper plenum/hot leg/steam generator region hydraulics during a small break LOCA event. The CCFL prediction of WCOBRA/TRAC-SB in the relevant flow situations matches the data well. The condensation heat transfer modeling of the code has been examined by simulating the NC test series 60-kW core power test in the Semiscale Mod-2A facility. The agreement in these natural circulation two-phase flow and heat transfer predictions is judged to be adequate based on commentary from the experimenters.

Chapter 18 validates the WCOBRA/TRAC-SB computer code for the prediction of horizontal stratified flow phenomena in the PWR loop piping; horizontal flow is a high-ranked process in the PIRT. WCOBRA/TRAC-SB was used to simulate a test facility that used a rectangular channel to measure condensation of steam in concurrent, horizontal flow. The channel is constructed of stainless steel with Pyrex glass windows. The 32 experiments simulated with WCOBRA/TRAC-SB included a range of steam and water flowrates and temperatures, and water layer thickness at the inlet. Inlet steam pressure was approximately 1 atmosphere. Steam velocity, static pressure, and water layer thickness as measured at five locations along the channel were compared with the WCOBRA/TRAC-SB predictions. The code was shown to predict pressure variation reasonably well and to underpredict condensation occurring at the interface. [

]^{a,c}

23-3 Integral Test Facility Simulations

Facilities of varying scales and characteristics were simulated using consistent nodalization to evaluate the capability of WCOBRA/TRAC-SB to predict experimental small break LOCA transients. The small scale Semiscale Mod-2C facility provides single-effect sensitivity tests (S-LH-1 and S-LH-2) which assess the impact of upper head flow bypass on the scaled equivalent of a 6-inch diameter cold leg break. The depressurization rate is predicted well for these tests. The break flow is underpredicted and then overpredicted at different times, and the S-LH-2 core heater rod temperature transient is influenced by compensating errors in the mass inventory and hot leg draining predictions. The predictions mirror the test results in identifying the significant impact of the upper head bypass flow on transient behavior.

The LOFT breaks simulated with WCOBRA/TRAC-SB range from a small break size (L3-7, the scaled equivalent of a 1-inch break) to the 4-inch equivalent diameter break series of cases: L3-1 in the broken loop, and L3-5 in the intact loop cold leg. The L3-7 predictions are adequate, demonstrating the capabilities of the code for small break LOCA cases. The set of 4-inch equivalent break cases reinforces the importance of the high-ranked PIRT item regarding conditions upstream of the break; the code performance is judged based on detailed evaluation to be adequate when the atypicalities of the LOFT facility are taken into account.

The ROSA tests analyzed provide a set of 2.5-percent break size cases that examine the impact of break orientation (top, side, and bottom locations). WCOBRA/TRAC-SB predicts the general trends observed in the different results for the three orientations. The 5-percent ROSA test is the larger scale equivalent of the Semiscale cases in break size, and it illustrates the effect of scale on the adequacy of code predictions to be minor. The 10-percent break ROSA test provides an intermediate size small break LOCA to illustrate WCOBRA/TRAC-SB capabilities for the larger breaks in the small break LOCA spectrum.

Among the 6-inch equivalent diameter break simulations, both of the Semiscale cases and the ROSA-IV SB-CL-05 break flowrate predictions exhibit flowrates less than the data values in the saturated liquid flow regime prior to loop seal clearance. This is followed by critical flowrate predictions that exceed the data once two-phase flow is established after loop seal clearance. The global model sensitivity cases performed as part of the PWR uncertainty methodology consider this variability by ranging the two-phase break flow discharge coefficient after loop seal clearance.

23-4 Nodalization Consistency

The performance of the code in the ROSA, LOFT, and Semiscale simulations supports its use in PWR calculations in a best estimate methodology for small break LOCAs. The PWR nodalization scheme is consistent with the schemes used in the integral test facility simulations.

The nodalizations used in the integral test facility simulations and the PWR calculation are reviewed by region or component.

Hot Leg and Cold Leg

[

]a,c

[

]a,c

Steam Generators

[

]a,c

Horizontal Crossover Leg Piping

[

]a,c

[

]a,c

RCPs

[ ]a,c.

Lower Plenum

[ ]a,c.

Core

[

]a,c

The PWR model is [

]a,c

Upper Core Plate

[

]a,c

Upper Plenum - Below the Hot Leg

[

]a,c

Upper Plenum - Above the Hot Leg

[

]a,c

[

]a,c

Upper Head

[

]a,c

Downcomer

[

]a,c

Downcomer-to-Upper Head Bypass

[

]a,c.

Summary

The only notable differences among the various facility models are those that are forced by some of the facility-specific requirements, and in the lower upper plenum region where there is a combination of necessary differences caused by the core nodalization and other differences related to modeling of jet channels.

23-5 Conclusions

Based on the separate effects test and integral test simulations, Westinghouse has made the following conclusions about the performance of WCOBRA/TRAC-SB for small break LOCA processes:

1. The model for critical break flow was validated in separate effects test simulations. It provides acceptable results for a wide range of break sizes, geometries, and inlet conditions. The code-predicted break flow shows reasonable agreement with the data in the integral effects tests over a range of scales.

2. The WCOBRA/TRAC-SB correlations for heat transfer in highly voided conditions show good agreement with ORNL and INEL data. The application of the WCOBRA/TRAC-SB heat transfer package to integral effects tests simulations was successful.

3. The models affecting mixture level swell provide agreement with a bias and a range of uncertainty for mixture level swell tests over a series of tests conducted under small break LOCA conditions. Interfacial drag in the core will be ranged according to these results in PWR global model sensitivity studies.

4. Mass retention in the loop seal during loop seal clearance is adequately predicted, and the loop seal clearing predictions of integral effects test simulations were found to agree well with the data.

5. The horizontal stratified flow model was incorporated [

   ]^{a,c} The option to cause the code to identify the horizontal flow regimes was used in both separate and integral effects test simulations successfully.

6. The COSI model for condensation in the cold leg on the jet of safety injection water in WCOBRA/TRAC-SB shows suitable agreement with the test data.

7. Simulations of various facilities were performed to assess the WCOBRA/TRAC-SB prediction of upper plenum/hot leg/steam generator hydraulic phenomena. The code performance is shown to be adequate for important small break LOCA processes.

8. The integral test facility simulations investigated and affirmed the capability of WCOBRA/TRAC-SB to predict experimental small break LOCA transients at different scales:

   - The code exhibited the capability to predict the trends associated with the different upper head bypass configurations of Semiscale tests S-LH-1 and S-LH-2. Predicted results were consistent with the code biases observed in the separate effects tests.

   - WCOBRA/TRAC-SB predictions of the suite of LOFT small break LOCA tests exhibit agreement ranging from good to marginal with the data. Specific reasons for misprediction have been discussed.

   - The ROSA series of 2.5-percent break test simulations shows the general ability of the code to distinguish between top, bottom, and side break locations. The code is also used to predict larger small break LOCA tests (5-percent and 10-percent breaks). As is true for the Semiscale predictions, the predicted core behavior during the loop seal clearance and boiloff periods is satisfactory.

Volume 3 of this document reports the results obtained using the WCOBRA/TRAC-SB computer code to perform small break LOCA analyses for Indian Point Unit 2. The Indian Point Unit 2 noding is consistent in principle with the nodalizations used to model the test facilities. Volume 4 of this document describes the bias and uncertainty characterizations of the WCOBRA/TRAC-SB code for the small break LOCA application. An uncertainty methodology is developed and applied to Indian Point Unit 2.